AFRL-RQ-WP-TR-2013-0198

HIGH WORK, HIGH-EFFICIENCY TURBINES FOR UNINHABITED AERIAL VEHICLES (UAVs)

Rolf Sondergaard

Turbomachinery Branch
Turbine Engine Division

SEPTEMBER 2013
Final Report

AIR FORCE RESEARCH LABORATORY
AEROSPACE SYSTEMS DIRECTORATE
WRIGHT-PATTERSON AIR FORCE BASE, OH 45433-7542
AIR FORCE MATERIEL COMMAND
UNITED STATES AIR FORCE

NOTICE AND SIGNATURE PAGE

Using Government drawings, specifications, or other data included in this document for any purpose other than Government procurement does not in any way obligate the U.S. Government. The fact that the Government formulated or supplied the drawings, specifications, or other data does not license the holder or any other person or corporation; or convey any rights or permission to manufacture, use, or sell any patented invention that may relate to them.

This report was cleared for public release by the USAF 88th Air Base Wing (88 ABW) Public Affairs Office (PAO) and is available to the general public, including foreign nationals.

Copies may be obtained from the Defense Technical Information Center (DTIC) (http://www.dtic.mil).

AFRL-RQ-WP-TR-2013-0198 HAS BEEN REVIEWED AND IS APPROVED FOR PUBLICATION IN ACCORDANCE WITH ASSIGNED DISTRIBUTION STATEMENT.

*//Signature//

ROLF SONDERGAARD
Project Engineer
Turbine Branch
Turbine Engine Division

//Signature//

CHARLES W. STEVENS
Branch Chief
Turbine Branch
Turbine Engine Division

//Signature//

JEFFREY M. STRICKER
Chief Engineer
Turbine Engine Division
Propulsion Directorate

This report is published in the interest of scientific and technical information exchange, and its publication does not constitute the Government's approval or disapproval of its ideas or findings.

*Disseminated copies will show "//Signature//" stamped or typed above the signature blocks.

REPORT DOCUMENTATION PAGE

Form Approved
OMB No. 0704-0188

1. REPORT DATE *(DD-MM-YY)*	2. REPORT TYPE	3. DATES COVERED *(From - To)*
September 2013	Final	01 May 2005 – 30 June 2013

4. TITLE AND SUBTITLE
HIGH WORK, HIGH-EFFICIENCY TURBINES FOR UNINHABITED AERIAL VEHICLES (UAVs)

5a. CONTRACT NUMBER
In-house

5b. GRANT NUMBER

5c. PROGRAM ELEMENT NUMBER
61102F

6. AUTHOR(S)
Rolf Sondergaard

5d. PROJECT NUMBER
2307

5e. TASK NUMBER

5f. WORK UNIT NUMBER
Q0EB

7. PERFORMING ORGANIZATION NAME(S) AND ADDRESS(ES)
Turbomachinery Branch (AFRL/RQTT)
Turbine Engine Division, Air Force Research Laboratory, Aerospace Systems Directorate
Wright-Patterson Air Force Base, OH 45433-7542
Air Force Materiel Command, United States Air Force

8. PERFORMING ORGANIZATION REPORT NUMBER
AFRL-RQ-WP-TR-2013-0198

9. SPONSORING/MONITORING AGENCY NAME(S) AND ADDRESS(ES)
Air Force Research Laboratory
Aerospace Systems Directorate
Wright-Patterson Air Force Base, OH 45433-7542
Air Force Materiel Command
United States Air Force

10. SPONSORING/MONITORING AGENCY ACRONYM(S)
AFRL/RQTT

11. SPONSORING/MONITORING AGENCY REPORT NUMBER(S)
AFRL-RQ-WP-TR-2013-0198

12. DISTRIBUTION/AVAILABILITY STATEMENT
Approved for public release; distribution unlimited.

13. SUPPLEMENTARY NOTES
PAO Case Number: 88ABW-2013-4167; Clearance Date: 23 Sep 2013. Report contains color. References in this report to RZ and RB are to former directorates within AFRL that were consolidated into RQ in 2012. On many of the papers, the U.S. Government is joint author and has the right to use, modify, reproduce, release, perform, display, or disclose the work.

14. ABSTRACT
This report documents the activities and results of an AFOSR-funded, in-house, basic research effort. The effort was focused on the fluid mechanics and heat transfer that is associated with advanced turbine aerodynamic designs, particularly for small engines. The objectives of this task were to identify and evaluate loss mechanisms for very highly loaded turbines and turbines intended to operate at low Reynolds number, and investigate passive and fluidic techniques for the control of separation, reattachment, blade row outlet air angle deviations, secondary flows, and similar loss producing phenomena. The results are applicable to both military and civil applications of gas turbine engines.

The following titles published in professional journals and conference proceedings are provided in the appendix:

- "Secondary Flow Loss Reduction Through Blowing for a High-Lift Front-Loaded Low Pressure Turbine Cascade"
- "Surface Stress Sensitive Film as a Separation Control Sensor"
- "An Investigation of Reynolds Lapse Rate for Highly Loaded Low Pressure Turbine Airfoils with Forward and Aft Loading"
- "Experimental Comparison of DBD Plasma Actuators for Low Reynolds Number Separation Control"
- "Endwall Loss Reduction of High Lift Low Pressure Turbine Airfoils Using Profile Contouring – Part I: Airfoil Design"
- "Endwall Loss Reduction of High Lift Low Pressure Turbine Airfoils Using Profile Contouring – Part II: Validation"
- "Endwall Loss and Mixing Analysis of a High Lift Low Pressure Turbine Cascade"
- "Surface Stress Sensors for Closed Loop Low Reynolds Number Separation Control" (dissertation)

15. SUBJECT TERMS
turbine aerodynamics, turbine pressure loss, turbine efficiency, turbine end-wall flows, low Reynolds number aerodynamics, turbine flow control

16. SECURITY CLASSIFICATION OF:			17. LIMITATION OF ABSTRACT:	18. NUMBER OF PAGES	19a. NAME OF RESPONSIBLE PERSON (Monitor)
a. REPORT	b. ABSTRACT	c. THIS PAGE			Rolf Sondergaard
Unclassified	Unclassified	Unclassified	SAR	306	19b. TELEPHONE NUMBER *(Include Area Code)* N/A

Table of Contents

Section **Page**

List of Figures

Figure **Page**

1.0 SUMMARY

This report documents the activities and results of an AFOSR-funded, in-house, basic research effort focused on the fluid mechanics and heat transfer associated with advanced turbine aerodynamic designs, particularly for small engines. The objectives of this task were to identify and evaluate loss mechanisms for very highly loaded turbines and turbines intended to operate at low Reynolds number, and investigate passive and fluidic techniques for the control of separation, reattachment, blade row outlet air angle deviations, secondary flows, and similar loss producing phenomena. The results are applicable to both military and civil applications of gas turbine engines.

This report is intended to be a broad summary of the activities performed under this research effort and will necessarily gloss over many of the technical details and specific results of the research. For detailed technical descriptions and results refer to the list of publications produced under this effort presented in the Appendix.

2.0 RESEARCH ACTIVITIES AND RESULTS

The aerodynamic loading and efficiency of the turbine components play a large role in the overall efficiency and power output of gas turbine engines. The low pressure turbine presents significant opportunities for improvements in this regard. A typical commercial aircraft turbine engine or ground power unit can have anywhere between five and twelve low pressure turbine stages. Low bypass engines used in high performance military engines will typically have two to four low pressure turbine stages. Increasing blade loading in the low pressure turbine, while maintaining efficiency, allows for significant reduction in part count, and has the potential to allow the removal of whole stages of the low pressure turbine module, which translates into performance improvements and signficant weight and cost savings.

The primary obstacle to increasing turbine blade loading is maintaining efficiency. For the low pressure turbine (LPT) a major cause of loss of efficiency is flow separation on the rear of the turbine airfoil, where there is a strong adverse pressure gradient. Controlling this separation requires reenergizing the boundary layer flow in order to make it more separation resistant. There are many techniques for accomplishing this, but they can be separated into two broad categories: active techniques, which rely an the application of external energy; and passive techniques, which rely on making fixed surface or profile modifications to the airfoil in order to influence the boundary layer, where losses are generated. Both passive and active separation control techniques were studied under this work unit, as followons to previous research performed under work units 2302NP01 and 2307NP01 (AFRL/PRTT and AFRL/RZTT respectively).

In addition to midspan losses, losses at the turbine endwalls – where the blade profile meets the hub and case – can be major contributers to overall stage loss. Increased blade loading increases the intensity of three-dimensional structures in the endwall areas, which, if not addressed, can lead to loss increases that completely overwhelm any benefits gained from loading enhancements even if midspan losses are controlled.

The following sections will discuss research performed under this project that address the design of several generations of low pressure turbine airfoils, the characterization of the performance of those, and earlier baseline, designs, and the exploration of flow control strategies to mitigate aerodynamic losses, both at the midspan and the end-walls.

2.1. Turbine Aerodynamic Characterization

The initial focus of this project was to characterize and understand the performance of low pressure turbines under low-Reynolds number conditions. Such conditions occur for aircraft operating at high altitudes, and are particularly acute for the relatively small engines that typically power unmanned aircraft. Low Reynolds number conditions can be particularly troublesome, as the higher viscosity, lower momentum flow over the turbine airfoils is prone to difficult to predict separation and turbulence transition effects driven by the adverse pressure gradient on the suction surface of the blades. Low Reynolds number operating conditions, particularly in the LPT section, can result in major performance degradation due to this flow separation. This loss of aerodynamic performance as the Reynolds number drops is referred to as Reynolds lapse.

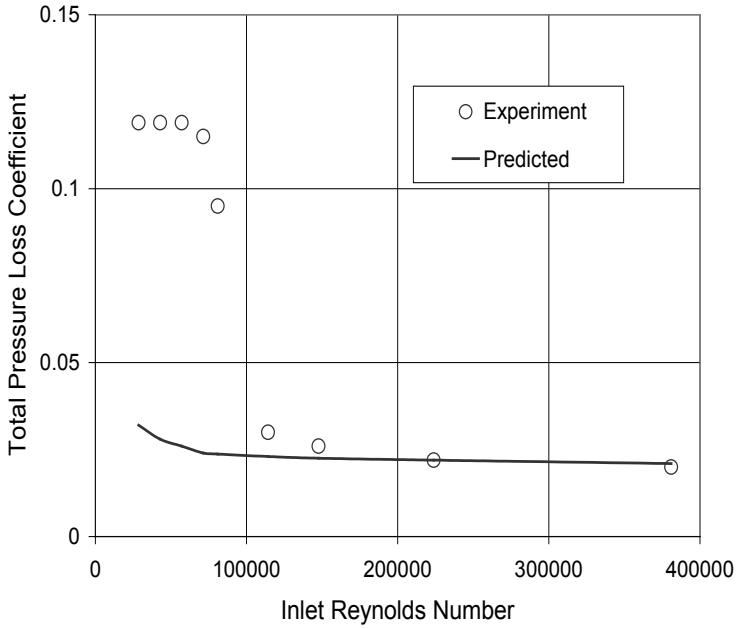

Figure 1: Reynolds Lapse for Pack-B LPT Profile
(Experiment and prediction.)

The baseline experimental model used for the study of Reynolds lapse was the Pratt & Whitney designed Pack-B low pressure turbine blade profile. Designed for research purposes in the mid-1990s, it represented a state-of-the-art loading at the time, and was available to the research community for study. The Reynolds lapse curve for the Pack-B, as experimentally measured in the RQT Low Speed Wind Tunnel Cascade Facility, is shown in Figure 1. Also shown is a numerical prediction using RANS based computational code which was available at the time. Two things are clear from this plot. First is that the losses grow rapidly below a certain critical Reynolds number, and second is that the predictive tools available at the time were only reliable at high Reynolds numbers, where transition effects are not important, and failed to properly predict low Reynolds number behavior.

The performance and aerodynamic behavior of the Pack-B was carefully studied over a wide range of Reynolds numbers, and with low turbulence, high turbulence, and periodically unsteady (simulated wake passing) inlet conditions. The primary cause of the Reynolds lapse was the change of the blade suction side boundary layer from a primarily turbulent condition to a transitional or fully laminar condition, even in the presence of free-stream turbulence or wake passing unsteadiness, as the Reynolds number dropped. The non-turbulent boundary layer, in the presence of the adverse pressure gradient at the rear of the blade results in a separation which, depending on inlet conditions and Reynolds number, could range from a small closed bubble to a fully erupted separation. The separation reduced the effective turning of the flow and greatly increased the pressure losses, both highly undesirable effects.

2.2. Turbine Aerodynamic Flow Control

In order to counteract these negative effects of low Reynolds number conditions, a variety of boundary layer flow control techniques were investigated. The techniques encompassed both

passive (geometric changes) and active (powered actuator) techniques, several of which are discusses in the next sections.

2.2.1. Passive Boundary Layer Contol

Passive separation control techniques studied included suction side v-grooves, slots, trips, turbulators, and spherical and asymmetric dimples. Of the passive techniques studied, the dimples proved to be the most effective at flow separation suppression at low Reynolds number conditions while causing a minimum of adverse affects on the airfoil loss characteristics at higher Reynolds number conditions.

A combined experimental and computational study of two dimple shapes on the Pack-B LPT blade design at low Reynolds numbers was performed. The performance of the Pack-B blades were tested at Reynolds numbers of between 100k and 25k with freestream turbulence levels of 1% (low turbulence) and 4% (moderate turbulence). The cascade was configured either with the baseline Pack-B blades, or the Pack-B blades with either asymmetric or spherical dimples at several chord locations, as shown in Figure. Boundary layer profiles and total pressure loss coefficient were obtained and compared to three dimensional computations of the same geometries.

Figure 3 shows samples of the computation of the flow over a single row of spherical dimples and asymmetric dimples respectively. The effect of the dimples is to generate highly unsteady streamwise vorticity in the boundary layer near the wall. This vorticity serves to pump high energy fluid from outside the boundary layer down into the boundary layer near the wall, energizing the boundary layer. It also serves to trip a laminary boundary layer, speeding transition to turbulence, which again increases the boundary layer's resistance to separation.

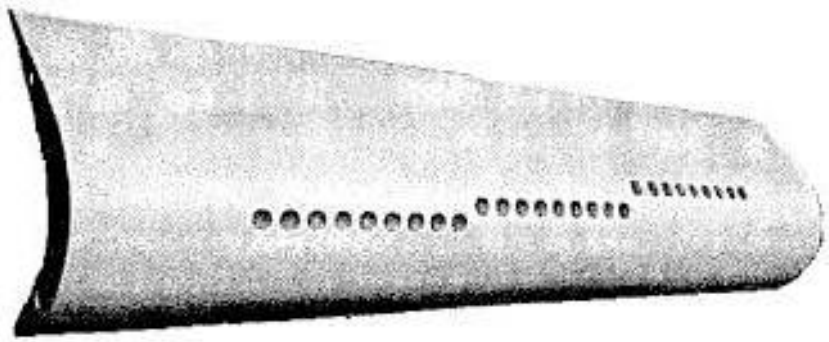

Figure 2: Pack-B Test Blade with Sperical Dimples at Three Axial Locations

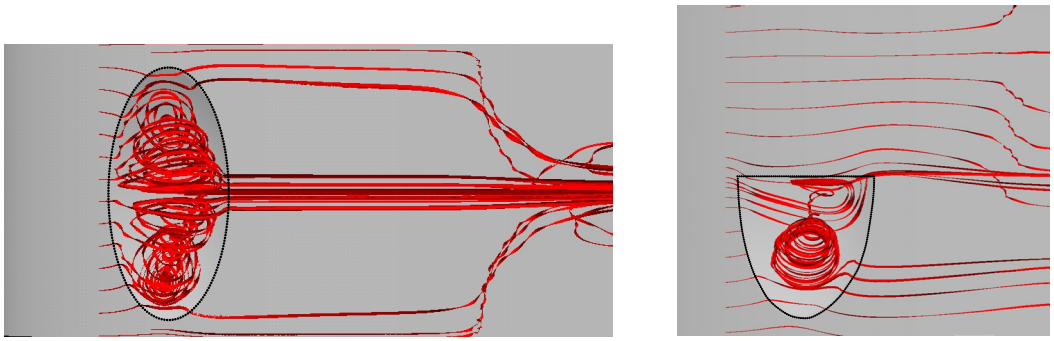

Figure 3: Computed Flow over Dimples
(Suction side of a low pressure turbine airfoil with spanwise periodic boundary conditions. Left: Spherical dimple; Right: Asymmetric dimple.)

Experimental results also indicated that dimples serve to trip the flow from laminar to turbulent and transition the separated flow to a re-attached turbulent boundary layer. Both dimple shapes proved to be effective, increasing the range of Reynolds numbers where the blade losses were low, but the spherical dimples were determined to have a more robust performance.

2.2.2. Active Boundary Layer Control: Vortex Generator Jets

A number of active boundary layer control actuators were considered for study, including Helmholtz resonators, micro-electro-mechanical devices (MEMS), thermal actuators, plasma actuators, and Vortex Generator Jets (VGJs). The last, VGJs, were chosen to be the focus of study because of their proven effectiveness in external flows, and because of their physical similarity to the film cooling technologies already found in gas turbine engines. More recent work has examined the use of plasmas for forcing. That work will be discussed in the next section.

Vortex Generator Jets are small jets that are injected through the airfoil surface into the boundary layer. VGJs are typically configured with a low pitch angle (30-45 degrees) and aggressive skew angle (45-90 degrees) to the local freestream flow direction. Here pitch angle is defined as the angle the jet makes with the local surface and skew angle is defined as the angle of the projection of the jet onto the surface relative to the local freestream direction. In this skew configuration, the VGJ creates a horseshoe vortex pair with one very strong leg accompanied by a weak leg of opposite sign. The result is a single, dominant, slowly-decaying streamwise vortex downstream rather than the two weaker counter-rotating horseshoe vortices generated by a jet with 0 degrees skew or a symmetric passive boundary-layer obstruction. It has been shown that this single-sign vortex energizes the separating boundary-layer by effectively bringing high momentum freestream fluid down to the wall.

Figure 4 shows the effect of VGJ blowing on the pressure loss though low pressure turbine cascade at low Reynolds number. The blowing ratio is the ratio of the momentum flux per unit area exiting the VGJ to the momentum flux per unit area of mid-channel flow outside the hole. At a blowing ratio of 0 (no flow through the VGJs) the flow over the LPT is separated and the loss coefficient (a normalized measure of the energy lost going though the cascade) is large.

Once the blowing ratio is increased above a certain critical value, here approximately B=1.0 for steady blowing, the flow separation is greatly reduced and the loss is cut by approximately 60%.

Also shown on Figure 4 are the results for pulsed VGJs. Here the jet flow is turned on periodically for only a fraction of the total cycle time. The effect is to greatly reduce the required mass flow from the VGJs, while still maintaining effective flow control. As can be seen in Figure 4, a pulsed VGJ with an effective average blowing ratio of B=0.02 still effectively suppresses the separation and drives the losses down by 60%. Detailed results from these experiments are available in publications listed in the Appendix.

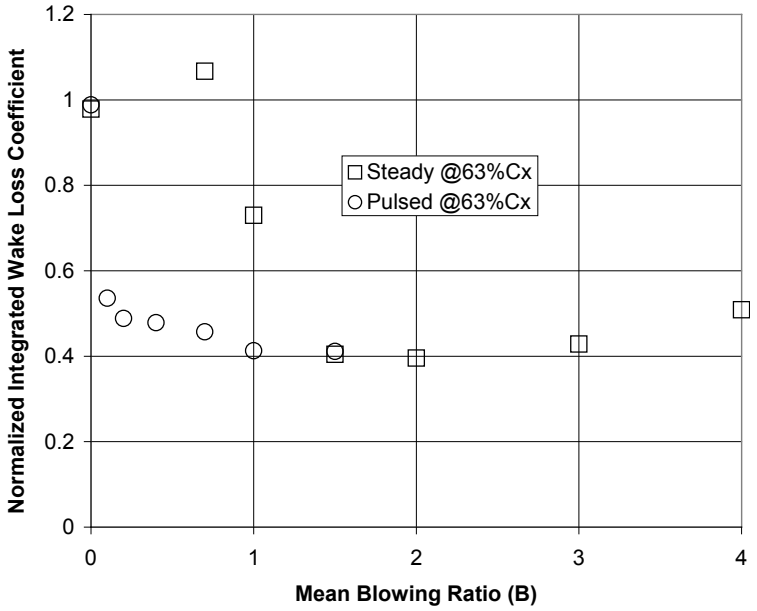

Figure 4: Effect of VGJ Blowing on Loss
(Low pressure turbine blade pressure loss coefficient, steady and unsteady VGJ flow.)

2.2.3. Active Boundary Layer Control: Atmospheric Plasmas

The other technology for separation control that was studied was dielectric barrier discharge (DBD) plasma actuators. DBD actuators, also known as glow discharge actuators, work by using a high voltage, high frequency driver electrode to locally ionize the gas passing over the actuator. The ionized gas is then driven by the strong electric field gradient around the actuator to produce fluid pumping.

Both high frequency AC and pulsed DC sources of excitation were studied. AC driven DBDs have the advantage of simplicity, but DC pulsed DBDs can be driven to much higher power levels because higher voltages can be used to deposit energy into the flow without breaking down the dielectric barrier. For the experiments, the discharge impedance was inductively and frequency matched for high frequency AC excitation and resistively matched for the pulsed DC cases. Uniform atmospheric AC glow discharges were obtained on test electrodes for driver frequencies from 1 kHz to 10 kHz and for electrode lengths of 25 cm to 78 cm. Uniform Pulsed DC glow discharges were obtained for similar electrodes with pulse widths from 22 nanoseconds

to 2 microseconds at a pulse rate of 100 pulses per second. Calculated pulsed discharge peak instantaneous power levels exceeded 50kW. The DBD actuators with various electrode configurations were installed in a 2D boundary layer tunnel for study. Figure 5 shows boundary layer profiles with and without plasma actuation showing an augmentation of the wall velocity of roughly 3.3 m/s.

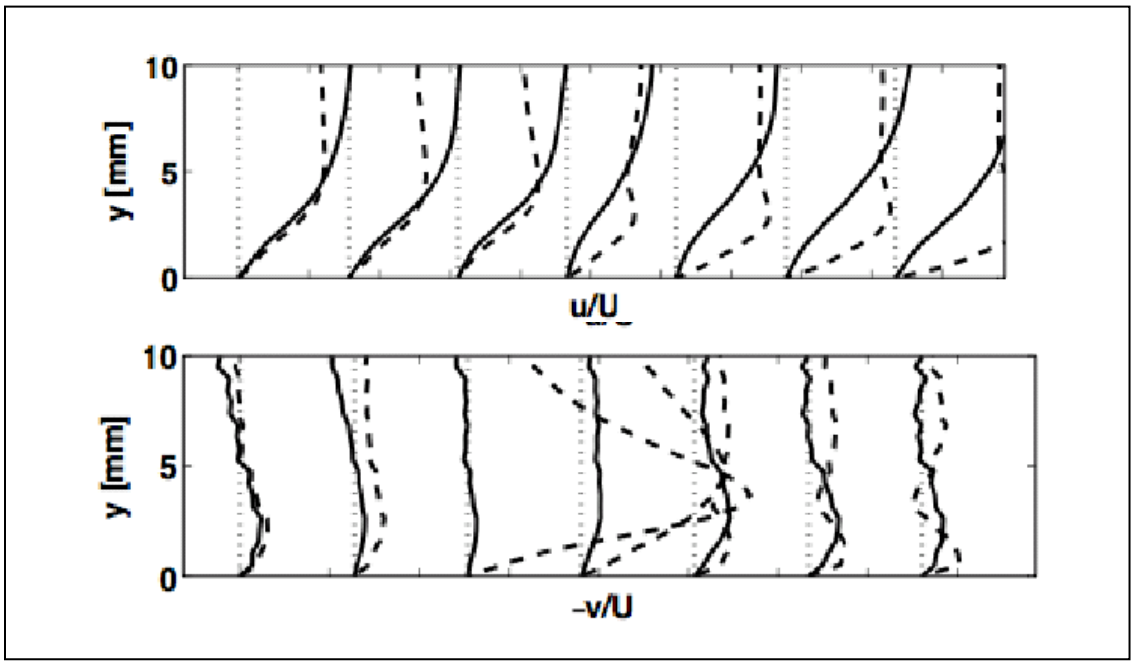

Figure 5: Boundary Layer Velocity Profiles
(Profiles of u (streamwise) and v (wall normal) boundary layer velocity without (solid) and with (dashed) plasma discharge forcing, U∞ =1.0 m/s.)

To study the usefulness of the DBD actuators for separation control, three plasma actuator electrode configurations were installed on an airfoil in the low speed wind tunnel. Two of the actuator configurations were implemented with the intent of generating three-dimensional, or streamwise vorticity to improve momentum entrainment from the freestream into the boundary layer: one as an array of same-sign vortex generators; and one as an array of vertical jets. The third configuration was designed to provide streamwise pumping of the flow to directly energize the viscous sublayer of the boundary layer in the flow direction. The actuators were studied at two different blade Reynolds numbers. Without actuation, at a Reynolds number of 50,000, laminar separation without reattachment was observed over the blade. At a Reynolds number of 100,000 the boundary layer separated, transitioned, and then naturally reattached prior to the trailing edge of the test blade.

Three parameters were used to compare the performance of each actuator: suction surface pressure profile, surface shear (measure with the S3F sensor technique described in later sections), and pressure loss. At the lowest Reynolds number tested, where the flow was fully separated, reattachment locations indicated the plasma actuator configured as a spanwise array of linear vertical jets reattached the flow and moved the mean reattachment upstream as voltage was increased. Though the pressure coefficients did not recover to the calculated inviscid profile, this configuration also resulted in the largest improvement in pressure loss at the lowest

applied voltage. At the higher Reynolds number, where the baseline flow showed a closed separation bubble, all the plasma actuator moved the reattachment point upstream, with the straight streamwise pumping configuration showing the best performance. Figure 6 shows a sample flow visualization that demonstrates the plasma actuation suppressing the boundary layer separation.

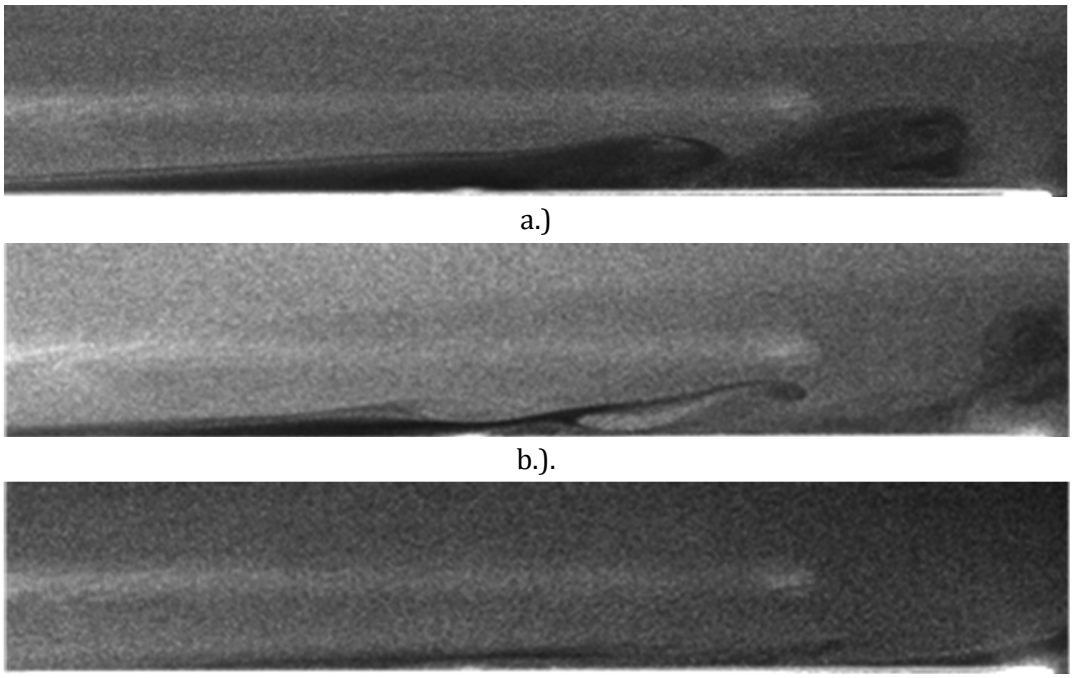

a.)

b.).

c.)

Figure 6: Flow visualization of effect of DBD plasma actuator.
(a.) No actuation, fully separated; b.) Actuation at 5.6 kV, reduced separation; and c.) Actuation at 7.2 kV, separation suppressed.)

Because of the ease of controlling electrical circuitry, use of the DBD plasma actuators in a closed-loop separation control system was also studied. An experimental blade was configured with a continuously monitored S3F shear sensor in the region of the known separation and a DBD actuator at a location upstream of the separation. The shear sensor output was analyzed to provide the location of the separation bubble reattachment point and that information was fed back into the DBD control circuitry to drive the actuator to suppress the separation. Figure 7 shows one of the experiments. The flow is established at a Reynolds number that is free of separation ($t < 0s$) as demonstrated by the positive shear stress (open symbols and fitted thin line). In the absence of separation, the actuator voltage is zero. At t=0s the flow Reynolds number is reduced to a value that would normally result in a large separation. The shear sensor detects a separation (negative shear) and drives the actuator voltage up to suppress it. At t=25s the Reynolds number is raised again, and the system responds by shutting off the actuator. The inset in Figure 7 shows the shear stress profile over the rear of the blade during the period when the actuator is on. This experiment demonstrated the feasibility of using a plasma actuator with a shear sensor as a closed loop flow control system.

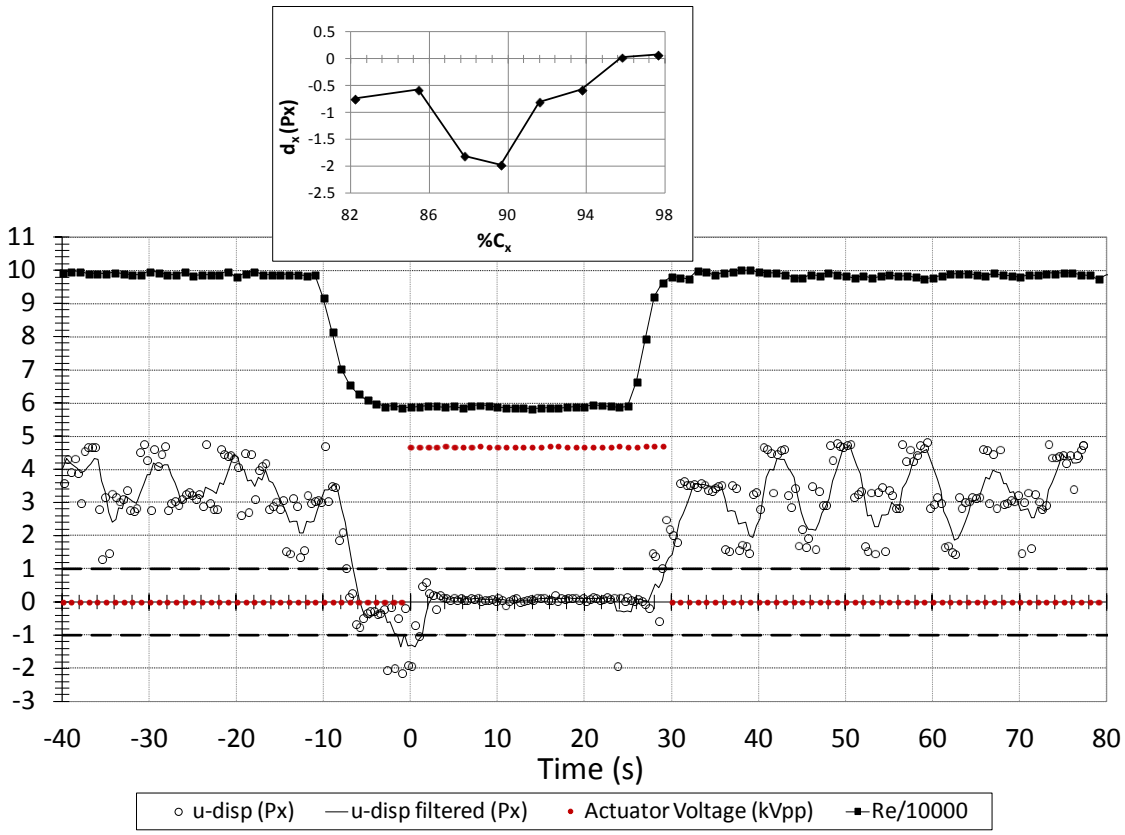

Figure 7: Response of Measured Sheer Stress to Closed Loop DBD Actuation

2.3. High Lift Low Pressure Turbine Design

In addition to the low Reynolds number flow control work performed, significant work was performed under this project to extend the design space available for low pressure turbines (for technical details see the papers by Clark et al., Praisner et al., and McQuilling et al. referenced in the Appendix). Starting from the Pratt and Whitney designed Pack-B research turbine, considered cutting edge ca. 1998, two generations of low pressure turbine airfoils, the L1x and L2x families, were designed and characterized.

Using the AFRL in-house turbine design system (TDAAS) developed by John Clark (AFRL/RQTT) and incorporating a turbomachinery specific turbulence transition model developed by Praisner and Clark, the L1x family was designed ca. 2004 with a blade loading 17% higher than the Pack-B, while holding the inlet and outlet conditions fixed. The implication of a 17% loading increase is that if the Pack-B technology blades on a turbine wheel were replaced with L1x technology blades, 15% fewer blades would be required to provide the same wheel work output. A reduced turbine blade count can lower part counts, maintenance, and weight of an engine, thus lowering the overall system cost.

Holding the inlet and outlet conditions fixed allowed direct comparison of the L1x blades to the Pack-B baseline. Forward- (L1F), mid- (L1M), and aft- (L1A) versions of the L1x family, all with the same overall loading but different surface pressure distributions, were designed,

fabricated, and evaluated in the AFRL/RQTT Low Speed Cascade Facility. Overall performance was found to be very favorable compared to the Pack-B baseline, with equal or lower mid-span losses, and more favorable Reynolds lapse (loss increase as operating Reynolds number decreases) behavior. The improved low-Reynolds performance promises increased efficiency, reduced fuel consumption, longer loiter times, and higher maximum operating altitudes compared current designs.

Having multiple pressure profiles with the same loading allowed the study of the performance of forward- vs. aft-loaded designs. The forward- and mid-loaded versions of the L1x blade proved to have superior low Reynolds number behavior, a significant factor for small, high altitude engines which can be required operate at conditions that result in very low flow Reynolds numbers in the turbine section.

The second generation family of blade profiles, the L2x, was designed ca. 2006 using the same design tools, while applying lessons learned from the evaluation of the L1x blade profiles. The L2x family has a loading 38% higher than the Pack-B baseline, representing a 28% decrease in blades for the same turbine wheel work. Again, the inlet and exit conditions were held fixed to allow direct comparisons between the baseline Pack-B, the L1x family, and the L2x family, and forward-, mid- and aft-loaded versions were produced (L2F, L2M, and L2A).

A study performed by Ryan Battelle and others in the AFRL/RQTE Cost and Performance group modeled the impact of applying L2x magnitude loadings to the LPT of a transport class engine, the CFM56. They modeled applying the loading increase in three ways: replacing the blades on each stage of the turbine with 1/3 fewer blades; keeping the blade counts the same, but reducing the axial lengths of each stage by 1/3; and keeping the blade counts the same but removing one of the five LPT stages on the machine. The study showed that LPT weight could be reduced by roughly 35% (or roughly 7% of engine weight) and the LPT module cost reduced by roughly 14%. Those savings represent significant system level improvements.

2.4. Turbine Endwall Flows

One of the major impediments to the adoption of high lift turbine aerodynamics is the fact that as the blade loading is increased, the three-dimensional secondary flows at the juncture of the blade profile and the hub and case of turbine become stronger. These end-wall flows are a major contributor to the overall blade aerodynamic losses, and the fraction of the loss produced by the end-wall flows grows as the blade loading is increased. In order for high lift aerodynamics to be practical, the end-wall losses must be addressed.

2.4.1. Turbine Endwall Loss Characterization

The pressure loading of an LPT airfoil plays an important role in the performance of the blade. Front loading (designing with the peak of the pressure coefficient forward of the half-chord point) is known to allow designs that are much more highly loaded and separation resistant because the flow turning occurs early on the blade where the boundary layer is thin. The L2F design discussed above fit in that mold. However, a long accepted premise of LPT turbine design was has been that front loading exacerbates end-wall losses because it subjects the end-wall boundary layer to strong cross-stream pressure gradients for a longer time. Several

experiments by other researchers have demonstrated this trend. This has driven turbine designers to tend to design aft-loaded (pressure peak behind mid-chord) profiles to minimize end-wall losses.

The in-house design capability developed under this project allowed a unique opportunity to revisit this topic. The other researchers who had studied front- versus aft-loading had done so by using a single blade profile and then restaggering (adjusting the blade angles relative to the inlet plane) in order to shift the pressure profile peak forward or aft. The problem with this approach is that restaggering changes not just the loading profile, but the total loading, the inlet and exit angles, and the axial chord. Consequently, the results of the experiments are not solely a function of the loading profile.

Studying the custom-designed L2x family of blades avoided this problem. The forward-loaded L2F and the aft-loaded L2A were specifically designed to have the same inlet, exit, stagger (chord angle relative to the inlet plane) and total loading conditions, so the only aerodynamic parameter that changed was the location of the peak pressure.

The study of the end-wall losses of the L2F and L2A revealed that the traditional idea that aft-loading reduced end-wall losses was incorrect. In fact the important parameter was in fact the stagger angle, with high stagger blades presenting more blockage to the incoming end-wall boundary layer. The greater blockage induces more mixing of the low-momentum boundary layer with the high-momentum free-stream, resulting in increased losses.

With this new understanding, a low-stagger blade with the same pressure profile as the L2F, designated the L2F-LS, was designed and tested. It demonstrated a 23% lower end-wall loss then either the L2F, while maintaining the mid-span loading. The mid-span performance of the L2F-LS, however, was slightly worse than the L2F, due to the larger surface area of the L2F-LS design, as can be seen in Figure 8. That result prompted the decision to study methods of keeping the mid-span performance of the L2F while simultaneously using the low-stagger philosophy to minimize end-wall losses.

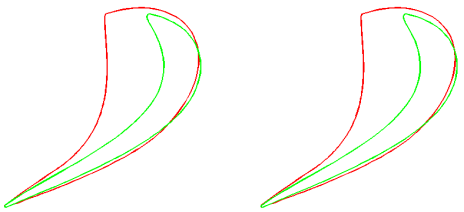

Figure 8: Standard and Low-stagger Front-loaded Profiles
(Green L2F; Red L2F-LS.)

2.4.2. Turbine Design for Endwall Loss Control

The first approach to combining the L2F with its excellent mid-span performance with the L2F-LS with its superior end-wall performance was simply to smoothly transition from the first profile at mid-span to the second at the end-wall. This essentially produced a large fillet at the interface of the blade profile and the end-wall. Unlike the large number of fillets that had been

studied previously by other researchers, however, the size and shape was determined using a specific low-stagger design goal. The result was a 17% improvement in end-wall losses over the L2F blade. This initial success was sufficient to warrant a more in-depth optimization of the blade contouring, which is ongoing as of the submission of this report.

2.5. Instrumentation Development

During the wide ranging research performed under this project, a number of instrumentation capabilities were developed and implemented. A novel skin shear stress measurement technique, S3F, and Particle Image Velocimetry (PIV) and Laser Doppler Velocimetry (LDV) capabilities were among them.

2.5.1. Shear and Stress Sensitive Film (S3F)

Some of the research described in the report made use of a unique sensor called Surface Stress Sensitive Film (S3F). S3F is n thin elastic film applied to an aerodynamic surface that responds to flow pressure gradients and wall shear stress, allowing optical measurement of wall pressure gradients and skin friction. Originally developed by Innovative Scientific Solutions Incorporated (ISSI), a new method for installing the S3F sensor to assure a smooth interface between the wall and wetted S3F surface was developed and proven out. In addition, new formulations of the S3F polymer were developed in cooperation with ISSI in order to measure the extremely low forces presented in the law speed facilities used by this project. During the course of this project the S3F shear modulus was decreased from approximately 100 Pa to 7.7 Pa, an increase in sensitivity by a factor of 15. Work was also done with ISSI to develop alternate packaging approaches for the S3F sensor that would make it both easier to handle and more sensitive. That work is ongoing.

2.5.2. Particle Image Velocimetry (PIV) and Stereo PIV

Evaluating the complex flows around turbine airfoils, and particularly near the blade end-walls, required instrumentation capabilities that allow capture of field data rapidly. To that end, project funds were expended on acquiring the hardware and software necessary to assemble a Particle Image Velocimetry (PIV) system. PIV works by seeding the flow of interest with small particles, typically smoke, illuminating the region of interest with a carefully focused sheet of laser light, and taking a pair of images of the illuminated particles separated by a small know time offset. By calibrating the image size to a known standard, knowing the time between images, and analyzing the distance the particles moved between images, the two-dimensional projection of the fluid velocities in the plane of the PIV image can be extracted. The technique can be extended by imaging the illuminated region with a pair of cameras viewing simultaneously from different angles. This stereoscopic view allows the analysis to extract the full three-dimensional velocity field in the illuminated plane. Figure 9 shows typical PIV data, with velocities and calculated vorticity in a plane near the exit of the end-wall region of the L2F LPT profile.

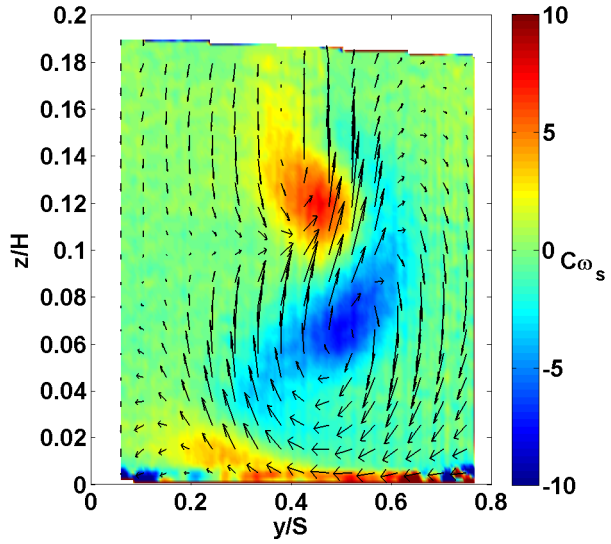

Figure 9: PIV Data Showing Cut Through Flow Near End-wall of LPT Airfoil

While the use of PIV was not unique to this project, a variation of the technique was developed which is. Turbine aerodynamic flows present a problem for the application of PIV, because of the large curvature of both the blade surfaces and the resulting flow fields. The flat imaging planes used in typical PIV are difficult to orient in a way that captures important flow features. To address this issue a new technique, Curved Sheet PIV, was developed and implemented. By use of custom optics, the laser sheets that define the PIV measurement region were formed into curved sheets that approximately matched the curvature of the streamlines in the flow of interest, in this case the curvature of the turbine blade suction side. This allows, for example, the imaging and collection of velocity data from the curved boundary layer that hugs the blade profile. Imaging the boundary layer allowed better understanding of the mechanisms leading to separation and reattachment. Figure 10 shows a sample Curved Sheet PIV data set taken over the highly curved surface of an LPT airfoil. The separation, transition, and turbulent reattachment is evident near the middle of the image and velocity field. This work resulted in the award of a US patent for the technique.

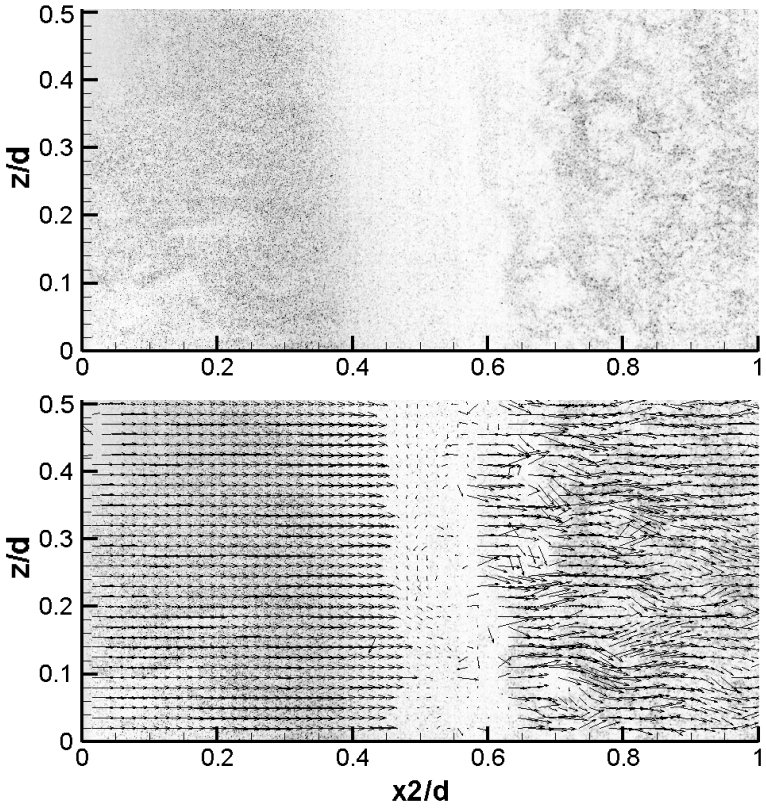

Figure 10: Curved Sheet PIV Example
(Top, typical image. Bottom, processed velocity data. Both show separation, transition, and reattachment near the center of the field of view.)

2.5.3. LDV

While PIV is excellent for obtaining field data, some fluid parameters of interest such as turbulence statistics and correlations, require three component data at frequencies that PIV, with its limitations imposed by laser speed and image acquisition, cannot provide. To fill that gap, a developmental laser velocimetry system from SBIR company Applied University Research (AUR) was acquired. LDV uses the fringe patterns in tightly focused crossed laser beams to illuminate passing flow seed particles and extract flow velocity. The unique requirements of turbine research required the development of new optics in cooperation with AUR. Those optics are now being commercialized by AUR for sale to other users.

2.6. Engine LPT application

Some of the technologies developed under this project are transitioning towards applications. The Low Reynolds number LPT work is progressing to investigation of application of passive control approaches (dimples) to the low pressure turbine of an existing turbine engine to mitigate losses incurred at altitude. Three sets of scaled cascade blades were fabricated from the LPT design of an operational engine: the first vane, first rotor, and third rotor, Figure 11. In 2005 and 2006 these were run in back to back tests without and with dimples in the linear cascade to demonstrate the dimple technology and to determine the relative importance of individual stage losses

In addition, dimples have been machined on two high pressure turbine first vanes on a full annular turbine rig, Figure 12. Pressure transducers for the Turbine Research Facility's (TRF) rakes were upgraded for the Reynolds number range of interest. TRF tests were run in 2004 and 2005 at nine Reynolds numbers with a rainbow array of HPT vanes. The array included 3 dimpled vanes, two rough vanes, and six clean vanes. A high Reynolds number TRF wake traverse of the rainbow array is illustrated in Figure 13.

Figure 11: Engine LPT Cascade Blades

Figure 12: Dimpled HPT Vanes for TRF

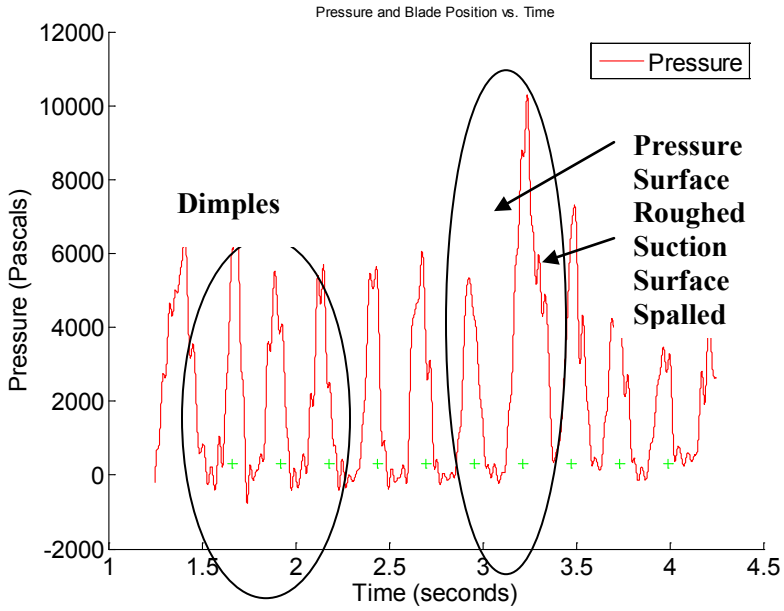

Figure 13: TRF Wake Traverse of Dimples on Roughened Vanes
(Re = 272,500)

Finally, the high lift aerodynamics developed and demonstrated under this program has been applied to the design of research LPT for the University of Notre Dame full scale rotating rig. Designed by John Clark using the TDAAS code, turbine shown in Figure 14 represents a significant advancement in turbine aerodynamics. Initial results from Notre Dame rig have been very promising.

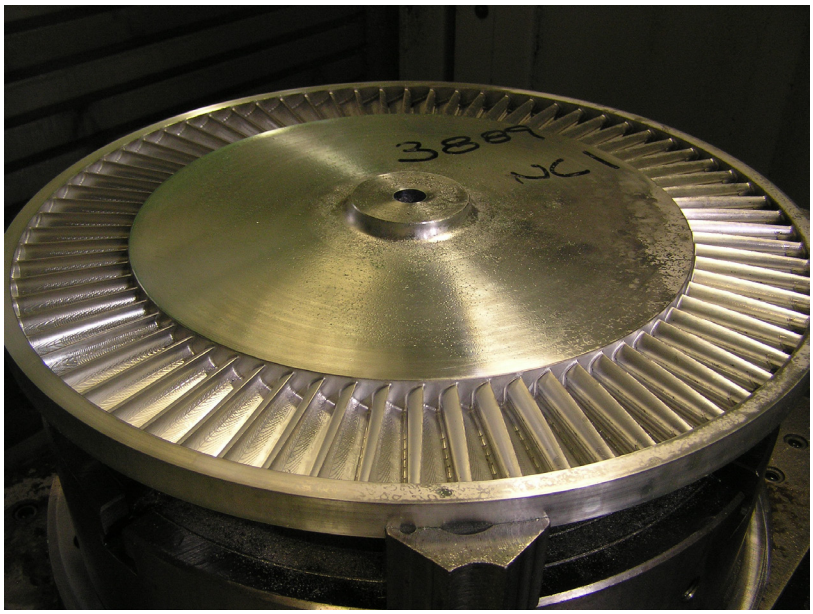

Figure 14: Notre Dame Turbine Designed Using TDAAS Code

3.0 CONCLUSIONS

This project has provided a broad ranging contribution to a variety of technologies related to the turbine component of gas turbine engines. The results have substantially added to the understanding of high lift turbine aerodynamics and the mitigation and control of losses associated with both high lift and low Reynolds number turbine operations.

APPENDIX A: LIST OF PUBLICATIONS

M. Lyall, R. Sondergaard, J. Clark, and P. King, "Endwall Loss Reduction of High Lift Low Pressure Turbine Airfoils Using Profile Contouring – Part I: Airfoil Design," GT2013-95000, Proc. ASME Turbo Expo, San Antonio, TX, June 3-7, 2013.

K. Sangston, M. Lyall, J. Little, and R. Sondergaard, "Endwall Loss Reduction of High Lift Low Pressure Turbine Airfoils Using Profile Contouring – Part II: Validation," GT2013-95002, Proc. ASME Turbo Expo, San Antonio, TX, June 3-7, 2013.

S. Benton, C. Bernardini, J. Bons, and R. Sondergaard, "Parametric Optimization of Unsteady Endwall Blowing on a Highly Loaded LPT," GT2013-95113, Proc. ASME Turbo Expo, San Antonio, TX, June 3-7, 2013.

C. Marks, R. Sondergaard, M. Wolff, and R. Anthony, "Experimental Comparison of DBD Plasma Actuators for Low Reynolds Number Separation Control," *J. Turbomachinery*, Vol. 135, pp. 011024: 1-11, January 2013.

S. Benton., J. Bons, and R. Sondergaard. "Secondary Flow Loss Reduction Through Blowing for a High-Lift Front-Loaded Low Pressure Turbine Cascade," Accepted *J. Turbomachinery*, July 2, 2012.

M.E. Lyall, P. King, R. Sondergaard, J. Clark, and M. McQuilling, "An Investigation of Reynolds Lapse Rate for Highly Loaded Low Pressure Turbine Airfoils with Forward and Aft Loading," *J. Turbomachinery*, Vol. 134, September 2012.

M.E. Lyall, P. King, and R. Sondergaard, "Endwall Loss and Mixing Analysis of a High Lift Low Pressure Turbine Cascade," GT2012-68709, Proc IGTI Turbo Expo, Copenhagen, Denmark, June 11-15, 2012.

C. Marks, R. Sondergaard, and M. Wolff, "Surface Stress Sensitive Film as a Separation Control Sensor," AIAA-2012-746, Proc. 50th AIAA Aerospace Sciences Meeting, Nashville, TN, January 9-12, 2012.

M.E. Lyall, P. King, R. Sondergaard, J. Clark, and M. McQuilling, "An Investigation of Reynolds Lapse Rate for Highly Loaded Low Pressure Turbine Airfoils with Forward and Aft Loading," GT2011-46328, Proc IGTI Turbo Expo, Vancouver, Canada, June 6-10, 2011.

C. Marks, R. Sondergaard, M. Wolff, and R. Anthony, "Experimental Comparison of DBD Plasma Actuators for Low Reynolds Number Separation Control," GT2011-45397, Proc IGTI Turbo Expo, Vancouver, Canada, June 6-10, 2011.

K. Rouser, P. King, F. Schauer, R. Sondergaard, and J. Hoke, "Performance Evaluation of an Unsteady Turbine Driven by a Pulse Detonation Combustor," GT2011-45396, Proc IGTI Turbo Expo, Vancouver, Canada, June 6-10, 2011.

N. Longo, P. King, F. Schauer, R. Sondergaard, and J. Hoke, "Heat Transfer Experiments on a Pulsed Detonation Driven Radial Turbine Exhaust," AIAA-2011-579, 49th AIAA Aerospace Sciences Meeting and Aerospace Exposition, Orlando, FL, January 4-7, 2011.

K. Rouser, P. King, F. Schauer, R. Sondergaard, and J. Hoke, "Time-Accurate Flow Field and Rotor Speed Measurements of a Pulsed Detonation Driven Turbine," AIAA-2011-577, 49th AIAA Aerospace Sciences Meeting and Aerospace Exposition, Orlando, FL, January 4-7, 2011.

J. Estevadeordal, C. Marks, R. Sondergaard, and M. Wolff, "Curved laser-sheet for conformal surface flow diagnostics," *Experiments in Fluids*, Vol. 50, No. 3, pp. 761-768, August 29, 2010.

D. Sanders, W. O'Brien, R. Sondergaard, M. Polanka, and D. Rabe, "Predicting Separation and Transitional Flow in Turbine Blades at Low Reynolds Numbers - Part I: Development of Prediction Methodology," *Journal of Turbomachinery*, Vol. 132, July 2010, pg. 103003: 1-11.

D. Sanders, W. O'Brien, R. Sondergaard, M. Polanka, and D. Rabe, "Predicting Separation and Transitional Flow in Turbine Blades at Low Reynolds Numbers - Part II: The Application to a Highly Separated Turbine Blade Cascade Geometry," *Journal of Turbomachinery*, Vol. 132, July 2010, pp. 104003: 1-8.

D. Sanders, C. Nessler, R. Sondergaard, M. Polanka, C. Marks, M. Wolff, and W. O'Brien, "A CFD and Experimental Investigation of Unsteady Wake Effects on a Highly Loaded Low Pressure Turbine Blade at Low Reynolds Number," GT2010-22977, ASME Conf. Proc. 2010, 2511 (2010).

D. Sanders, W. O'Brien, R. Sondergaard, M. Polanka, and D. Rabe, "Unsteady Wake Effects on a Highly Loaded Low Pressure Turbine Blade - Part II: Prediction of Separation and Transitional Flow" ASME Paper GT2010-22991, IGTI Turbo Expo, Glasgow, UK, June 14-18, 2010.

M. McQuilling, M. Wolff, S. Fonov, J. Crafton, and R. Sondergaard, "Experimental Investigation of a High-Lift Low-Pressure Turbine Suction Surface" *AIAA Journal*, Vol. 48, No. 11, 2010, pp. 2465-2471.

K. Rouser, P. King, F. Schauer, R. Sondergaard, and J. Hoke, "Parametric Study of Unsteady Turbine Performance Driven by a Pulse Detonation Combustor," AIAA-2010-6536, 46th AIAA/ASME/SAE/ASEE Joint Propulsion Conference and Exhibit, Nashville, TN, July 25-28, 2010.

K. Rouser, P. King, F. Schauer, R. Sondergaard, and J. Hoke, "Unsteady Performance of a Turbine Driven by a Pulse Detonation Engine," AIAA-2010-1116, 48th AIAA Aerospace Sciences Meeting and Aerospace Exposition, Orlando, FL, January 4-7, 2010.

H. Fasel, A. Gross, J. Bons, R. Rivir, and R. Sondergaard, Fundamentals and Applications of Modern Flow Control, vol 231,Chapter 9: Turbomachinery Applications, American Institute of Aeronautics and Astronautics, December 2009 (ISBN: 1563479834).

D. Sanders, W. O'Brien, R. Sondergaard, M. Polanka, and D. Rabe, "A Mixing Plane Model Investigation of Separation and Transitional Flow at Low Reynolds Numbers in a Multistage Low Pressure Turbine," AIAA 2009-1467, 46th AIAA Aerospace Sciences Meeting and Exhibit, Orlando, FL, January 4-8, 2009.

D. Sanders, W. O'Brien, R. Sondergaard, M. Polanka, and D. Rabe, "Turbulence Model Comparisons for Mixing Plane Simulations of a Multistage Low Pressure Turbine Operating at Low Reynolds Numbers," AIAA 2009-4928, 45th AIAA Joint Propulsion Conference, Denver, CO, August 3-5, 2009.

C. Nessler, C. Marks, R. Sondergaard, and M. Wolff, "PIV Investigation of Periodic Unsteady Wakes over a Highly Loaded LPT Blade," AIAA-2009-5107, 45th AIAA/ASME/SAE/ASEE Joint Propulsion Conference & Exhibit, Denver, CO, August 2-5, 2009.

C. Marks, C. Nessler, R. Sondergaard, J. Crafton, S. Fonov, and M. Wolff, "High Lift LPT Blade Suction Surface Flow Investigation Using Surface Stress Sensitive Film," AIAA-2009-5106, 45th AIAA/ASME/SAE/ASEE Joint Propulsion Conference & Exhibit, Denver, CO, August 2-5, 2009.

D. Sanders, W. O'Brien, R. Sondergaard, M. Polanka, and D. Rabe, "Turbulence Model Comparisons for Mixing Plane Simulations of a Multistage Low Pressure Turbine Operating at Low Reynolds Number," AIAA-2009-4928, 45th AIAA/ASME/SAE/ASEE Joint Propulsion Conference & Exhibit, Denver, CO, August 2-5, 2009.

C. Nessler, C. Marks, R. Sondergaard, and M. Wolff, "Investigation of Losses on a Highly Loaded Low Pressure Turbine Blade with Unsteady Wakes," AIAA-2009-302, 47th AIAA Aerospace Sciences Meeting, Orlando, FL, January 5-8, 2009.

C. Marks, R. Sondergaard, M. Wolff, and J. Estevadeordal "PIV Investigation of a Highly-Loaded LPT Blade Using a Curved Laser Sheet," AIAA-2009-301, 47th AIAA Aerospace Sciences Meeting, Orlando, FL, January 5-8, 2009.

D. Sanders, W. O'Brien, R. Sondergaard, M. Polanka, and D. Rabe, "A Mixing Plane Model Investigation of Separation and Transitional Flow at Low Reynolds Numbers in a Multistage Low Pressure Turbine," AIAA-2009-1467, 47th AIAA Aerospace Sciences Meeting, Orlando, FL, January 5-8, 2009.

T. Praisner, E. Grover, D. Knezevici, I. Popovic, S. A. Sjolander, J. Clark, and R. Sondergaard, "Toward the Expansion of Low-Pressure-Turbine Airfoil Design Space," GT2008-50898, IGTI Turbo Expo 2008, June 9-13, 2008, Berlin, DE.

D. Sanders, W. F. O'Brien, R. Sondergaard, M. Polanka, and D.C. Rabe, "Predicting Separation and Transitional Flow in Turbine Blades at Low Reynolds Numbers," GT2008-50283, IGTI Turbo Expo 2008, June 9-13, 2008, Berlin, DE.

R. Sondergaard, "LPT Flow Control at AFRL," AIAA-2008-4156, 38th Fluid Dynamics Conference and Exhibit, Seattle, WA, June 23-26, 2008

M. McQuilling, M, Wolff, S. Fonov, J. Crafton, and R. Sondergaard, "An Experimental Investigation of a Low-Pressure Turbine Blade Suction Surface using a Shear and Stress Sensitive Film," *Expts. in Fluids*, Vol. 44, No. 1, January 2008, pp. 73-88.

M. McQuilling, S. Fonov, J. Crafton, and R. Sondergaard "An Experimental Investigation of Suction Surface Flow Features on a High-Lift LPT," AIAA-2008-79, 46th AIAA Aerospace Sciences Meeting and Exhibit, Reno, NV, January 2008.

R. Anthony and R. Sondergaard, "What is Needed in Experimental Methods Instruction – Perspectives from a Government Laboratory," AIAA-2008-705, 46th AIAA Aerospace Sciences Meeting and Exhibit, Reno, NV, January 2008.

N. Woods, R. Sondergaard, M. McQuilling, and M. Wolff, "Study of the Effects of the Blowing Ratio or Vortex Generator Jets in a Low Pressure Turbine," AIAA-2007-5102, 43rd AIAA/ASME/SAE/ASEE Joint Propulsion Conference and Exhibit, Cincinnati, OH, July 2007.

N. Woods, R. Sondergaard, M. McQuilling, and M. Wolff, "Study of Separation Suppression in a Low Pressure Turbine using Pulsed Vortex Generator Jets," AIAA-2007-4217, 37th AIAA Fluid Dynamics Conference and Exhibit, Miami, FL, June 2007.

N. Woods, I. Boxx, and R. Sondergaard, "Investigation of Separation Control in a Low Pressure Turbine using Pulsed Vortex Generator Jets," 42nd AIAA/ASME/SAE/ASEE Joint Propulsion Conference and Exhibit, Sacramento, CA, July 2006.

M. McQuilling, M. Wolff, S. Fonov, J. Crafton, and R. Sondergaard, "Experimental Investigation of Low Pressure Turbine Blade Suction Surface Stresses using S3F," AIAA-2006-19, 44th AIAA Aerospace Sciences Meeting and Exhibit, Reno, NV, January 2006.

K. Moore, M. Wolff, M. Polanka, and R. Sondergaard, "A Large-Scale Investigation of a Flat-Plate Pulsed Vortex Generator Jet in Crossflow using PIV," AIAA-2005-4221, 41st AIAA/ASME/SAE/ASEE Joint Propulsion Conference, Tucson, AZ, July 2005.

J.P. Bons**,** L.C. Hansen, J.P. Clark, P.J. Koch, and R. Sondergaard, "Designing Low-Pressure Turbine Blades with Integrated Flow Control," Proceedings of ASME TurboExpo 2005: International Gas Turbine Conference, *IGTI*, 2005.

K. Moore, M. Wolff, R. Sondergaard, and M. Polanka, "A PIV Study of Pulsed Vortex Generator Jets," AIAA-2004-3927, 40th AIAA/ASME/SAE/ASEE Joint Propulsion Conference and Exhibit, Fort Lauderdale, FL, July 2004.

J. Casey, P. King, and R. Sondergaard, "Parameterization of Boundary Layer Control Dimples on a Low Pressure Turbine Blade," AIAA-2004-3570, 40th AIAA/ASME/SAE/ASEE Joint Propulsion Conference and Exhibit, Fort Lauderdale, FL, July 2004.

R. Sondergaard, R.B. Rivir, J.P. Bons, and N. Yurchenko, "Control of Separation in Turbine Boundary Layers," AIAA-2004-2201, 2nd AIAA Flow Control Conference, Portland, OR, June 2004.

R. Sondergaard, R.B. Rivir, and J.P. Bons, "Control of Low Pressure Turbine Separation using Vortex Generator Jets," *J. Propulsion and Power*, Vol. 18, No. 4, 2002, pp. 889-895.

R. Sondergaard, J.P. Bons, M. Sucher, and R.B. Rivir, "Reducing Low-Pressure Turbine Blade Count Using Vortex Generator Jet Separation Control," GT2002-30602, ASME Turbo Expo, Amsterdam, The Netherlands, June 2002.

J.P. Bons, R. Sondergaard, and R.B. Rivir, "The Fluid Dynamics of LPT Blade Separation Control Using Pulsed Jets," *J. Turbomachinery,* Vol. 124, No. 1, January 2002, pp. 77-85.

J.P. Bons, R. Sondergaard, and R.B. Rivir, "Turbine Separation Control Using Pulsed Vortex Generator Jets," *J. Turbomachinery*, Vol. 123, No. 2, April 2001, pp. 198-206.

R.B. Rivir, R. Sondergaard, J. Bons, J. Lake, "Application of Longitudinal Vortices for Control of Separation in Turbine Boundary Layers," Intl. Workshop on Org. Vort. Motion as a Basis for Boundary-Layer Control, Kiev, Ukraine, September 2000.

R.B. Rivir, R. Sondergaard, J.P. Bons, and J.P. Lake, "Passive and Active Control of Separation in Gas Turbines," AIAA Fluids 2000 Conference, AIAA-2000-2235, Denver, CO, June 2000.

R. Sondergaard, J.P. Bons, and R.B. Rivir, "Control of Low-Pressure Turbine Separation Using Vortex Generator Jets," *J. Propulsion and Power,* Submitted June 2000.

R. Sondergaard, "Low Pressure Turbine Loss Control," *AFRL Technology Horizons PR-99-01*, June 2000.

J.P. Bons, R. Sondergaard, and R.B. Rivir, "Turbine Separation Control Using Pulsed Vortex Generator Jets," Proceedings of TURBOEXPO 2000: International Gas Turbine Conference, ASME-2000-GT-0262, Munich, Germany, May 2000.

J.P. Lake, P.I. King, R.B. Rivir, and R. Sondergaard, "Low Reynolds Number Loss Reduction on Turbine Blades with Dimples and V-Grooves," 38th Aerospace Sciences Meeting & Exhibit, Reno, NV, AIAA 00-0738, January 2000.

J.P. Bons, R. Sondergaard, and R.B. Rivir, "Control of Low-Pressure Turbine Separation Using Vortex Generator Jets," 37th Aerospace Sciences Meeting & Exhibit, AIAA 99-0367, Reno, NV, January 1999.

C. Murawski, R. Sondergaard, R. Rivir, T.W. Simon, K. Vafai, and R.J. Volino, "Experimental Study of the Unsteady Aerodynamics in a Linear Cascade with Low Reynolds Number Low Pressure Turbine Blades," The International Gas Turbine & Aeroengine Congress & Exhibition, ASME 97-GT-95, Orlando, FL, June 1997.

R.B. Rivir, R. Sondergaard, M. Dalhstrom and E.E. Ervin. "Low Reynolds Number Turbine Blade Cascade Calculations," The Sixth International Symp. on Transport Phenomena and Dynamics of Rotating Machinery, Vol. 2, p. 132, Honolulu, HI, February 1996.

APPENDIX B

Proceedings of ASME Turbo Expo 2012
GT2012
June 11-15, 2012, Copenhagen, Denmark

GT2012-68812

SECONDARY FLOW LOSS REDUCTION THROUGH BLOWING FOR A HIGH-LIFT FRONT-LOADED LOW PRESSURE TURBINE CASCADE

Stuart Benton*
Jeffrey P. Bons
Department of Mechanical and Aerospace Engineering
The Ohio State University
Columbus, Ohio 43235
Email: benton.53@osu.edu

Rolf Sondergaard

Propulsion Directorate
U.S. Air Force Research Laboratory
Wright Patterson AFB, OH, 45433

ABSTRACT

Efforts to increase individual blade loading in the low pressure turbine have resulted in blade geometries optimized for midspan performance. Many researchers have shown that increased blade loading and a front-loaded pressure distribution each contribute separately to increased losses in the endwall region. A detailed investigation is performed of the baseline endwall flow of the L2F profile, a high-lift, front loaded profile. In-plane velocity vectors and total pressure loss maps are obtained in five planes oriented normal to the blade surface, for three Reynolds numbers. A row of pitched and skewed jets are introduced near the endwall on the suction surface of the blade. The flow control method is evaluated for four momentum coefficients at the high Reynolds number, with a maximum reduction of 42% in the area averaged total pressure loss coefficient. The same blade is also fitted with midspan vortex-generator jets and is tested at a Reynolds number of 20,000, resulting in a 21% reduction in area averaged total pressure loss.

NOMENCLATURE

A area
B jet blowing ratio, U_j/U_l
C blade chord
C_X blade axial chord
C_P pressure coefficient, $(P_{T,1}-P_{S,l})/q_1$
C_μ momentum coefficient (eq. 2)
D jet diameter
N_j number of active jets
P pressure
Re Reynolds number, $U_1 C_X/\nu$
S blade pitch
Tu turbulence intensity
$\overline{U}$ average velocity magnitude
Zw Zweifel loading coefficient (eq. 1)
h blade span
q dynamic pressure
u x-component of velocity
v y-component of velocity
w z-component of velocity
x axial or measurement plane normal direction
y pitchwise or blade normal direction
z spanwise direction

Greek

Π flow power
α flow angle in relation to the axial direction
γ total pressure loss coefficient, $(P_{T,1}-P_{T,l})/q_1$
$\overline{\gamma}$ averaged total pressure loss coefficient
η_j flow control efficiency parameter
θ jet pitch angle
ν kinematic viscosity
ρ density
ϕ jet skew angle

*Address all correspondence to this author.

Superscripts

M mass-weighted average quantity
A area-weighted average quantity

Subscripts

1 inlet quantity
2 outlet quantity
BL measurement on the baseline case (no flow control)
EW corresponds to an endwall measurement
FC measurement on the flow control case
MS corresponds to a measurement at midspan ($z/h = 0.5$)
T stagnation quantity
S static quantity
def quantity refers to a deficit
j jet exit quantity
l local quantity

INTRODUCTION

Blade reduction through increased loading in the low-pressure turbine (LPT) has been shown as a clear opportunity for reduced weight and complexity through reduced part count. However, with increased blade spacing, reduced efficiency becomes more of an issue. Profile losses in the two-dimensional region can result in significant losses due to boundary layer separation caused by increased adverse pressure gradients. The increased magnitude of the pressure gradient also increases the strength of the endwall flow field resulting in further losses.

A popular strategy to allow for increased blade loading while maintaining high efficiency has been to use a blade profile with an aft loaded pressure distribution. Aft loaded pressure distributions have been shown to have reduced losses at the endwall [1, 2]. However, the aft loading results in a strong adverse pressure gradient that can result in a non-reattaching boundary layer separation at low Reynolds numbers. This behavior is potentially detrimental to an aircraft engine, but has been shown to be easily controlled though the use of various passive and active flow control mechanisms [3–6]. A front loaded pressure distribution allows for a reduction in the magnitude of the adverse pressure gradient on the aft portion of the blade. A recent design effort by McQuilling [7] has demonstrated that through the use of optimization techniques a front loaded distribution can be designed at a very high loading level that exhibits no full boundary layer separation even at very low Reynolds numbers.

$$Zw = 2\left(\frac{S}{C_X}\right)cos^2\alpha_1(tan\alpha_1 - tan\alpha_2) \quad (1)$$

This design effort is a part of an ongoing effort at the Air Force Research Laboratory to expand the design space of the LPT using optimization techniques, advanced analysis tools and flow control. The LPT designs stem from a Pratt & Whitney research profile, the Pack-B, which was designed with a Zweifel loading coefficient (eq. 1) of $Zw = 1.15$ and a flow turning of 95°. The first generation of profiles is made up of an aft loaded profile (L1A) [8,9] and a mid loaded profile (L1M) [10], both designed with a loading level of $Zw = 1.34$ and the same flow turning as the Pack-B. Using vortex generator jets (VGJs) as active flow control, it was shown that these aggressive profile designs could perform at low Reynolds numbers without experiencing full boundary layer separation. The second generation of profiles is made up of the L2F designed by McQuilling [7] and the L2A which appeared recently in the open literature [11], each designed with a loading of $Zw = 1.59$. Work by Praisner et.al. [12] looks at the limits of the design space of highly loaded LPTs and studies multiple highly loaded designs, including front loaded profiles up to a loading of $Zw = 1.8$.

The mitigation of endwall losses has been approached from many angles. Passive flow control methods have been investigated in the form of leading edge modifications [13], endwall boundary layer fences [14, 15], and endwall profiling [16].

Gbadebo et al. [17] studied four tailored methods of slot suction computationally and verified the best design experimentally on a compressor cascade. A loss reduction of 22% was demonstrated experimentally. Bloxham and Bons [18] investigated two methods of active flow control through suction on a LPT cascade of L1A profiles. Two separate optimized patterns of holes on the endwall were tested to focus on either the removal or the redirection of the passage vortex. A total pressure loss reduction of 27% was demonstrated using the removal approach.

Active flow control has also been investigated on compressor cascades in the form of blowing through a small slot located on the endwall [19–21]. Using slot blowing on the endwalls and suction surface, Hecklau et al. [19] demonstrated an 8% loss reduction with steady blowing and a 13% loss reduction with pulsed blowing. Aunapu et al. [22] studied two methods of blowing on a representative LPT passage. The first method used six jets near the vortex saddle point and the second method followed the recommendations of Chung and Simon [15] and the results of oil flow visualizations to place 12 jets on the endwall. Both methods were designed to alter the trajectory of the passage vortex. No loss reduction was demonstrated due to increased turbulence levels, but the passage vortex trajectory was shown to be altered and the vortex strength was reduced.

The current study looks to take advantage of the front loaded pressure distribution for its exceptional midspan performance at low Reynolds numbers while seeking to mitigate the increased losses at the endwall through an active flow control strategy. This is done with the L2F blade design, which has 19% higher loading than the L1A studied in [18].

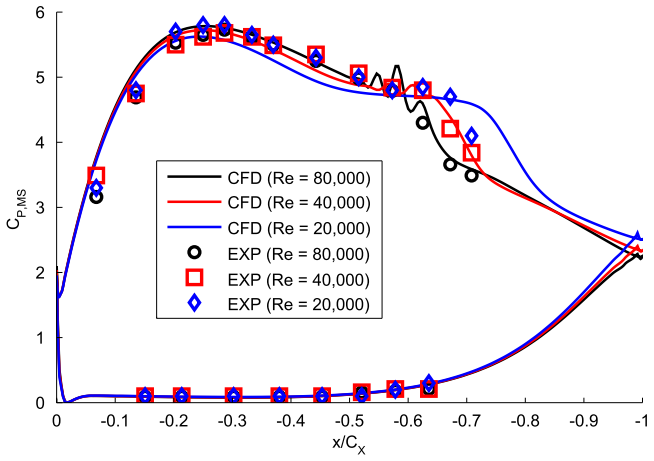

FIGURE 1: PRESSURE COEFFICIENTS AT THE REYNOLDS NUMBERS OF INTEREST.

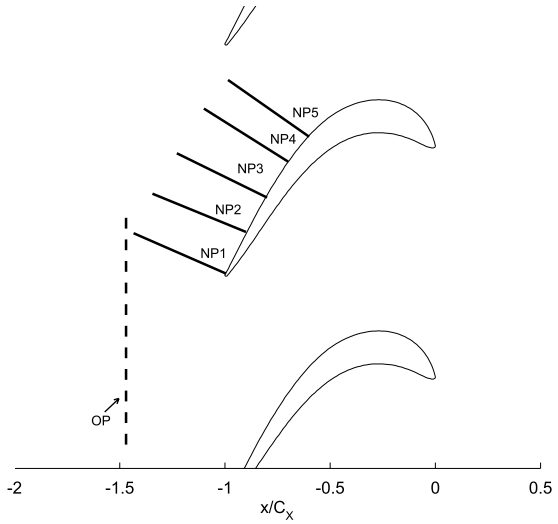

FIGURE 2: LOCATION AND DOMAIN OF MEASUREMENT PLANES.

EXPERIMENTAL SET-UP

Experiments are performed on Ohio State's Low-Speed Linear Cascade facility. The LPT profile for this study is the L2F blade profile. The L2F has an axial chord of 152.4mm and a solidity of 1.221. This profile was designed by McQuilling [7] with a Zweifel loading coefficient of $Zw = 1.59$ and a peak C_P at 26% axial chord. The cascade is operated with a grid-generated inlet turbulence intensity of $Tu = 3\%$. Tailboards and inlet bleeds are adjusted to match the surface pressure coefficients to computations performed with a periodic boundary condition. Figure 1 shows the experimental and computational pressure coefficients. The computation is performed on a steady-state two-dimensional model in ANSYS Fluent, used by Lyall et.al. [11]. Transition and turbulence are modeled using the $k-k_l-\omega$ model.

To model the endwall flow region, a splitter plate is used to properly condition the endwall boundary layer. The splitter plate extends 31mm from the endwall reducing the effective blade span from 380mm to 350mm. At the junction of the endwall and the blade profile a clay fillet with a radius of 10mm is implemented to seal the junction and to model engine manufacturing procedures. The leading edge of the splitter plate is manufactured in an elliptic shape and extends $2C_X$ upstream of the leading edge of the blade row in the axial direction. Immediately after the elliptic leading edge, a 3.2mm boundary layer trip is used to ensure a turbulent boundary layer. Bloxham and Bons [18] used a similar splitter plate and provide more details on the construction.

Measurements are made in six different planes within the linear cascade. The outlet axial plane is placed $-1.47C_X$ from the leading edge of the blade and is aligned such that all of the relevant losses are captured. This plane is one pitch wide and spans from the endwall to $0.4h$. The outlet plane (OP) is used to evaluate the overall effect of flow control and blade performance. Five planes normal to the blade suction surface are used for a more detailed investigation. These planes stem from the blade suction surface at $-.995C_X$ (NP1), $-0.9C_X$ (NP2), $-0.8C_X$ (NP3), $-0.7C_X$ (NP4), and $-0.6C_X$ (NP5) and extend in the direction normal to the blade surface.

Pressure measurements are performed using a standard pitot-static probe and a Kiel probe. The Kiel probe has a head diameter of 3mm. Two GE Druck differential pressure transducers with ranges of 0 - 0.1 "H_2O and 0 - 0.5 "H_2O are used to make measurements for the low and high Reynolds number cases. Different transducers are used for different measurements in order to maximize accuracy at various Reynolds numbers. The inlet velocity is measured using a pitot-static probe, centered at the inlet of the tunnel. Total pressure loss is determined by measuring the difference between the total pressure port of the inlet pitot-static probe and the Kiel probe located in the measurement plane.

Particle Image Velocimetry (PIV) is used to measure the in-plane velocity vectors at five planes normal to the suction surface of the blade. The laser is introduced from the top of the cascade and is split into a sheet using a cylindrical lens prior to entering the tunnel through the clear Plexiglas ceiling. The camera is placed at the exit of the cascade and captures the measurement area unabated. Each data set represents the average of 1000 individual image pairs. The time separation in between images is first estimated based upon the laser sheet thickness (2.5mm) and

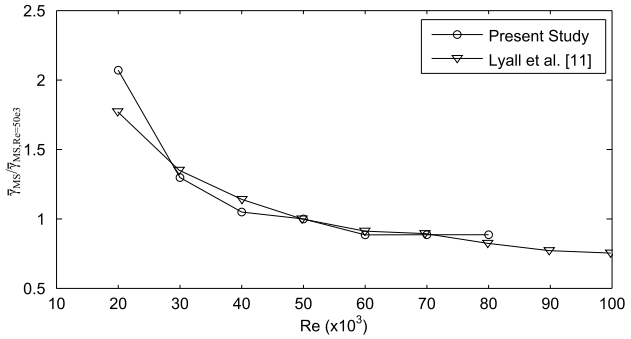

FIGURE 3: NORMALIZED MIDSPAN LOSS VS. REYNOLDS NUMBER OF THE PRESENT STUDY COMPARED TO EXPERIMENTAL DATA OF LYALL ET AL. [11].

the local velocity, small data sets were acquired for different time steps and an optimal was chosen. Images are captured and processed using the LaVision Davis 7.2 software. One sweep of a 64x64 pixel window and two sweeps of a 16x16 pixel window are used to perform the correlation and determine the velocity vectors. During the flow control measurements, the jet air is not seeded. The authors acknowledge that this can introduce a velocity bias, but since the measurements are taken downstream of the jet exit and the jet mass flow is very low ($< 1\%$) compared to the passage mass flow, this error is assumed to be minimal.

In the outlet axial plane, velocity vectors are measured using an X-wire probe. A TSI IFA-300 is used as the anemometry system. For each case, two sweeps are performed. For the first sweep the X-wire is oriented to measure the v-velocity component and the second sweep the X-wire is oriented to measure the w-velocity component.

In this study the cascade Reynolds number is based upon axial chord and inlet velocity. However, to facilitate conversion to multiple definitions of cascade Reynolds number, the velocity ratio across the cascade is $\overline{U}_2/\overline{U}_1 = 1.55$ and the chord to axial chord ratio is $C/C_X = 1.21$.

UNCONTROLLED FLOW FIELD

The flow field is investigated at three different Reynolds numbers to determine the effect of Reynolds number on the behavior of the secondary flow field. These Reynolds numbers are chosen based upon the Reynolds lapse results of Lyall et al. [11]. The lowest Reynolds number is past the "knee" of the lapse curve (Figure 3) and represents a case with significant shear layer thickening. The highest Reynolds number represents a condition well above the loss knee where the average total pressure loss coefficient is relatively constant with increasing Reynolds number.

PIV measurements and total pressure loss contours in the

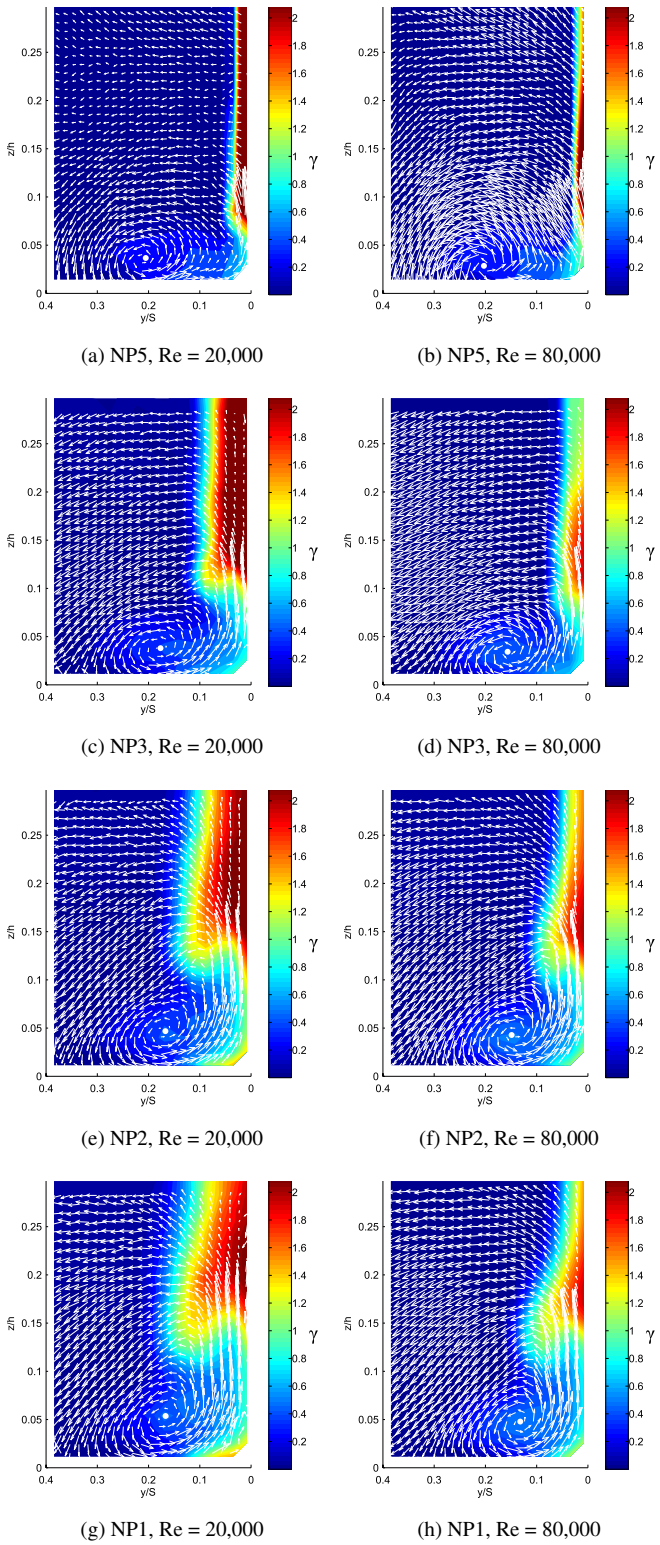

(a) NP5, Re = 20,000 (b) NP5, Re = 80,000

(c) NP3, Re = 20,000 (d) NP3, Re = 80,000

(e) NP2, Re = 20,000 (f) NP2, Re = 80,000

(g) NP1, Re = 20,000 (h) NP1, Re = 80,000

FIGURE 4: PIV VELOCITY VECTORS OVERLAID ON CONTOURS OF TOTAL PRESSURE LOSS COEFFICIENT.

normal planes (Figure 2) describe the vortex movement and loss development. The contrast between the high and low Reynolds number cases is seen in Figure 4. Loss development is the only main difference between the two Reynolds number cases. Figure 5 tracks the vortex to blade distance throughout the passage (the white dot in Figure 4 is the vortex center) and indicates that the vortex remains further from the wall for the low Reynolds numbers than for the higher Reynolds number, however this is hardly noticeable in Figure 4. The main feature of interest, which seems to correlate with total pressure loss, is the spanwise jet of fluid (effectively a "wall jet") emanating from the base of the blade. Figure 4a indicates that the "wall jet" begins before the vortex reaches the surface. Classic descriptions of secondary flow development suggest that the pressure-side leg of the horseshoe vortex becomes or merges with the passage vortex, this image supports this interpretation. The pressure gradient in the passage creates the lateral movement across the endwall and the upward movement of fluid on the suction surface (i.e. the "wall jet"). This behavior is consistent with the sense of the pressure-side leg of the horseshoe vortex and works to increase the size and strength of the vortex.

To better quantify the effect of Reynolds number on endwall loss development, a method is proposed to decompose the endwall and midspan losses. Each contour of total pressure loss in Figure 4 represents a grid of data points of individual total pressure loss measurements. To decompose this grid (Figure 6), two data sets of the same size are created and area-averaged. The first data set is the top most row of the grid continued down to the endwall, representing the case where no endwall flows exist and the blade exhibits purely two-dimensional behavior. This assumes that the topmost row in Figure 4 is in the two-dimensional loss regime. The area average total pressure loss ($\overline{\gamma}^A_{MS}$) of this extended two-dimensional profile versus x/C_X for three Reynolds numbers is shown in Figure 7. The second data set represents the losses attributed to the endwall flows. In this case, the top most row of the data set is subtracted from the entire data set. This loss difference is area averaged to obtain $\overline{\gamma}^A_{EW}$, which is also shown in Figure 7. This highlights loss peaks and loss reductions attributed to the endwall flows, compared to the case of pure midspan flow. In Figure 7, both of these loss measurements are normalized by the area averaged loss from the original data grid (Figure 4) at the respective Reynolds number. As such, the sum of the $\overline{\gamma}^A_{MS}/\overline{\gamma}^A$ and $\overline{\gamma}^A_{EW}/\overline{\gamma}^A$ is always equal to unity. It is noted that for the lowest Reynolds number, the endwall actually provides a benefit in terms of total pressure loss since the midspan results in such high loss behavior due to the thick shear layer. However, for the higher Reynolds number the endwall losses contribute to nearly half of the total loss in the region $z/h < 0.3$. This would indicate that control benefits will most likely be realized at the higher Reynolds numbers.

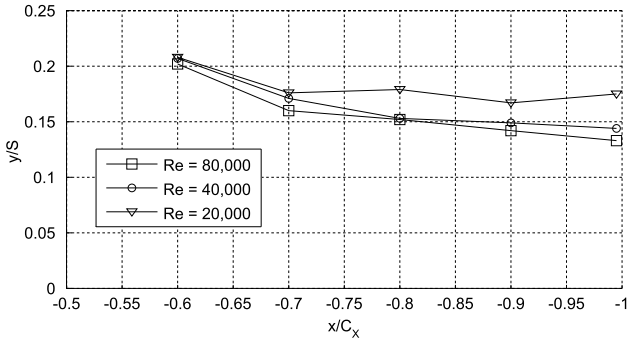

FIGURE 5: DISTANCE BETWEEN VORTEX CORE AND BLADE SUCTION SURFACE FOR THE BASELINE CASES.

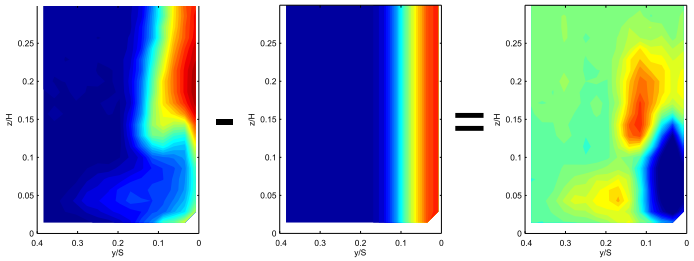

FIGURE 6: SCHEMATIC OF LOSS DECOMPOSITION PROCESS.

FLOW CONTROL DESIGN AND IMPLEMENTATION

The initial idea to focus on endwall control was to use a flow control system that is mounted on the blade surface as a means to remain consistent with current technologies in flow control and film cooling where a hollow plenum within the blade provides pressurized air. With this in mind, three main objectives are proposed for the flow control scheme to accomplish:

1. Distance the passage vortex from the suction surface.
2. Decrease the spanwise penetration of the vortex system and wall jet.
3. Provide loss reduction through momentum injection while minimizing mixing losses.

To accomplish these goals, the use of pitched/skewed jets is proposed. The pitch angle is defined as the angle between the jet exit direction and the blade surface and the skew angle is the angle between the jet exit and the local streamwise direction. In accordance with the above goals, a pitch angle of 30° and a skew angle of 30° are proposed. The low pitch angle will allow for jet injection in the flow direction with reduced mixing loss. The skew angle is angled downward towards the endwall to counteract the wall jet, while a majority of the injected momentum

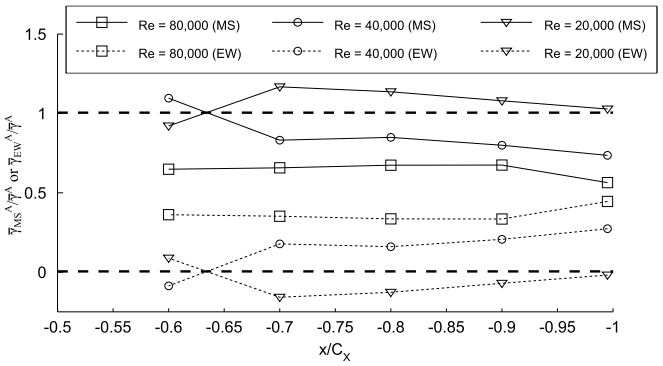

FIGURE 7: DECOMPOSED ENDWALL AND MIDSPAN AREA-AVERAGED LOSSES AS A FRACTION OF TOTAL AREA-AVERAGED LOSS.

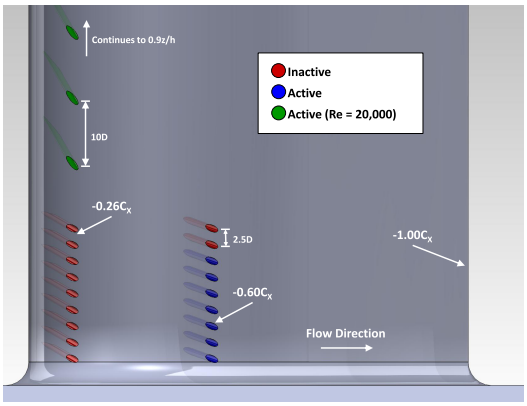

FIGURE 8: CAD MODEL SHOWING FLOW CONTROL PLACEMENT.

is in the streamwise direction. A row of nine endwall jets are placed at $-0.26C_X$ and $-0.6C_X$. The upstream location corresponds to the midspan suction peak. Since this is the location with the strongest crossstream pressure gradient, this would be an acceptable early stage to change the flow physics and prevent increased loss development downstream. By the second location (at $-0.6C_X$) the flow has seen a majority of the turning, and the injected momentum will not be working against the passage pressure gradient.

The jets for endwall flow control have a diameter of 2.8mm and are spaced 2.5D apart, spanning from approximately $0.03h$ of the blade span up to $0.2h$ of the blade span. Midspan jets are placed only at the $-0.26C_X$ location. These jets also have an exit diameter of 2.8mm and a pitch angle from the surface of 30°. The skew angle is manufactured at 60° toward the endwall from the streamwise direction. This is chosen based upon recommendations by Evans et al. [23]. These jets are spaced 10D apart and span from $0.27h$ to $0.9h$ span. These jets are expected to provide benefits at the low Reynolds number case to increase blade loading and efficiency. Work by Bloxham and Bons [18] provides evidence through total pressure loss contours that midspan VGJs may help to suppress the endwall flows as well. The flow control layout is shown graphically in Figure 8. Flow control is fed by pressurized air regulated from 100 psi to 30 psi. Using a rotameter, the volume flow into the plenum is monitored. Jet exit velocity is determined by assuming incompressible flow and equal densities at the jet exit.

The amount of blowing is quantified using a parameter similar to that defined by Bae et al. [24]. The momentum coefficient is defined as the ratio of the momentum flux introduced by the jet, normalized by the momentum flux into half of the passage. This definition is used to scale the flow control system with a single endwall region, therefore allowing the study to apply to both a rotor and a stator.

$$\begin{aligned} C_\mu &= \frac{\rho_j \overline{U}_j^2 (N_j \cdot A_j)}{\rho \overline{U}_1^2 \frac{1}{2} h Scos(\alpha_1)} x100\% \\ &= \frac{1}{2}\left(\frac{\overline{U}_j}{\overline{U}_1}\right)^2 \frac{\pi N_j D_j^2}{h Scos(\alpha_1)} x100\% \end{aligned} \tag{2}$$

In the low Reynolds number case, the momentum coefficient is used only to determine the blowing from the endwall jets. Blowing from the midspan jets is quantified in terms of the blowing ratio (B), the ratio of the average jet velocity to the local edge velocity.

From the multiple hole locations and combinations tested, the configuration which best satisfied the three objectives stated above was chosen. This is identified in the legend of Figure 8 as the seven "active" endwall holes at $-0.6C_X$. It was found that this downstream location was superior for several reasons: the passage vortex is closer to the suction surface at this point, the majority of turning is completed, and the jet can exit in the streamwise direction due to the low local curvature. Seven holes were used instead of the nine available when a sensitivity study indicated that the top two holes had minimal benefit relative to the additional mass flow required.

HIGH REYNOLDS NUMBER FLOW CONTROL

For this final "active" configuration the highest Reynolds number is evaluated at four momentum coefficients, 1%, 2%, 3%, and 4%. The momentum coefficient is related to the mass flow fraction by the jet/inlet velocity ratio. For the case of a stator with an aspect ratio of $h/C_X = 2.3$ and blowing on both endwalls, the above momentum coefficients would result in mass

flow percentages of 0.40%, 0.56%, 0.70%, and 0.80% of the passage flow.

Total pressure loss contours overlaid with X-wire velocity vectors are shown in Figures 9 and 10. The flow control suppresses the main vortex structure to a small region and eliminates the vertical jet structure as well. In the outlet plane, almost $0.2h$ span of clean flow is added. Mass-averaged values across the entire pitch are presented as a function of span in Figure 11. The exit angle can be used to estimate blade loading as a function of span. This suggests that loading is increased in the section of span from $0.12h$ to $0.3h$ over the baseline.

As stated earlier, one strategy of loss reduction is to alter the trajectory of the passage vortex such that it does not impinge on the blade suction surface. Figure 12 shows that the vortex to blade distance increases for increased blowing. The trajectory of the vortex is shown to move away from the suction surface as it exits the passage. For the maximum momentum coefficient studied, the vortex core moves from approximately $-0.13S$ to $-0.21S$. This trend is also seen in the outlet plane velocity vectors in Figures 9 and 10.

Figure 13 shows inplane velocity vectors at plane NP1. With increased blowing, the PIV vectors show that the wall jet is suppressed and nearly eliminated in the highest blowing case. In this case, the downward component of velocity due to the skewed nature of the jets is clearly visible.

Area averaged total pressure loss in the outlet plane shows a near linear reduction in total pressure loss with increasing momentum coefficient (Figure 14). Losses are reduced by as much as 42% for the highest blowing case.

In comparison to the aforementioned active flow control studies, these results suggest a significant development. Bloxham and Bons [18] demonstrate a similar linear loss reduction behavior through their removal approach. Maximum loss reduction is demonstrated at a reduction of 27% while removing approximately 4% of the passage mass flow. PIV velocity vectors (in a plane similar to plane NP1) show similar behavior, where the wall jet is reduced. Hecklau et al. [20] uses a similar PIV plane at the trailing edge of the compressor cascade to visualize the effect of endwall slot blowing on the passage vortex. A significant spanwise suppression and trajectory diversion is shown for very low mass flows of approximately 0.5% of the passage flow. Pulsed blowing is demonstrated as well to further reduce the required mass flow; however the vortex location is not suppressed for the entire pulsing period. In terms of the present study, a comparable mass flow is used and similar results are demonstrated in terms of the function of the flow control in altering the passage vortex. Since the L2F represents a worst case scenario for endwall flows, it suggests that the results of the current study are significant.

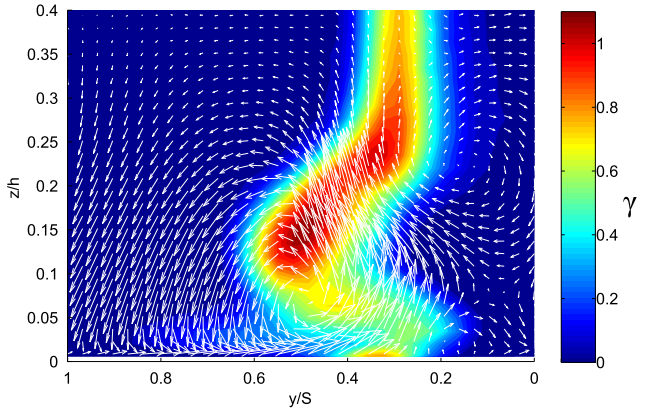

FIGURE 9: TOTAL PRESSURE LOSS COEFFICIENT AND STREAMWISE-NORMAL VELOCITY VECTORS IN THE OUTLET PLANE FOR THE BASELINE CASE, $RE = 80,000$.

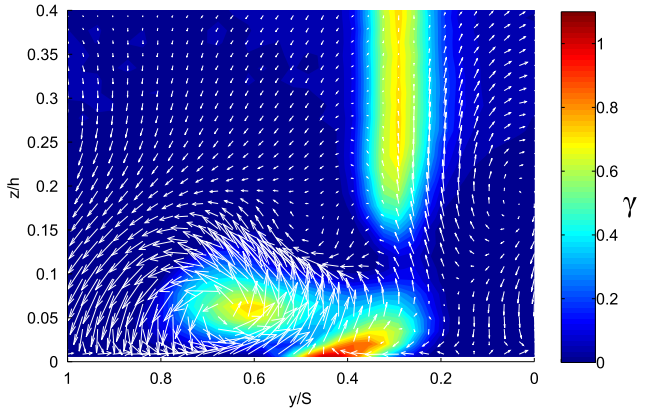

FIGURE 10: TOTAL PRESSURE LOSS COEFFICIENT AND STREAMWISE-NORMAL VELOCITY VECTORS IN THE OUTLET PLANE FOR THE CONTROLLED CASE OF $C_\mu = 4\%$, $RE = 80,000$.

LOW REYNOLDS NUMBER FLOW CONTROL

For the low Reynolds case it is decided that due to the loss issues associated with the midspan, the midspan VGJs located at the peak C_P will be used in combination with the endwall jets at $-0.6C_X$. VGJs have been shown to provide benefits such as increased loading and improved flow turning. Although the L2F exhibits exceptional behavior at low Reynolds numbers, these benefits may still be realized if the internal plenum is in place for endwall control or film cooling.

The midspan jets and endwall jets share the same internal

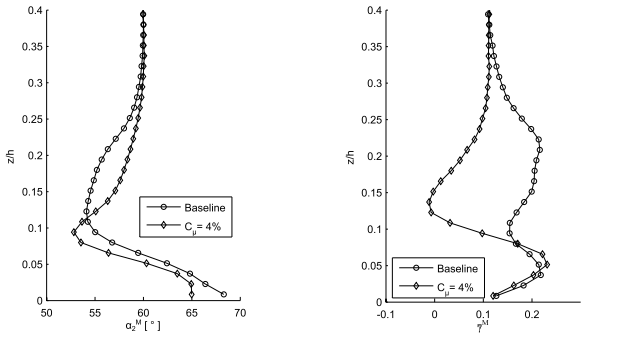

(a) Exit Angle (b) Total Pressure Loss Coefficient

FIGURE 11: MASS AVERAGED VALUES AS A FUNCTION OF SPAN, $RE = 80,000$.

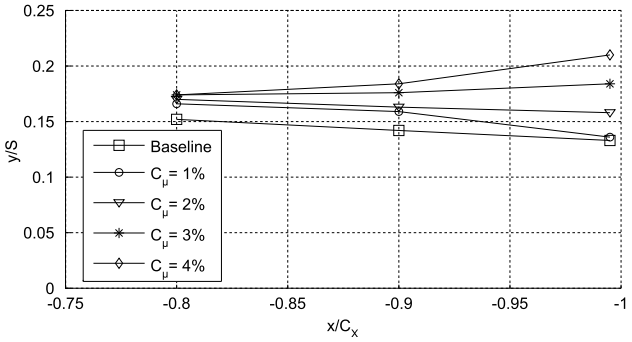

FIGURE 12: DISTANCE BETWEEN VORTEX CORE AND BLADE SUCTION SURFACE, $RE = 80,000$.

plenum. Therefore the blowing ratio for the midspan VGJs at $-0.26C_X$ and the momentum coefficient for the endwall jets cannot be varied independently. For the low Reynolds number case, only endwall momentum coefficients of 2% and 4% are studied. Assuming equal discharge coefficients for all injection points, the midspan blowing ratios are approximately 1.5 and 2.1. In the case of a stator with aspect ratio $h/C_X = 2.3$, this results in the addition of three midspan jets to each half-span. The added blowing results in mass flow ratios of 0.80% and 1.14% compared to the mass flow ratios of 0.56% and 0.80% at the higher Reynolds number, for the cases of C_μ equal to 2% and 4% respectively.

The endwall control scheme seems to work well in the case of the low Reynolds number as well. In plane velocity vectors in Figure 13 show that the wall jet is suppressed with increased blowing and that the vortex trajectory is altered from $-0.17S$ to $-0.21S$ at NP1.

Contours of total pressure loss in the outlet plane (Figures 15

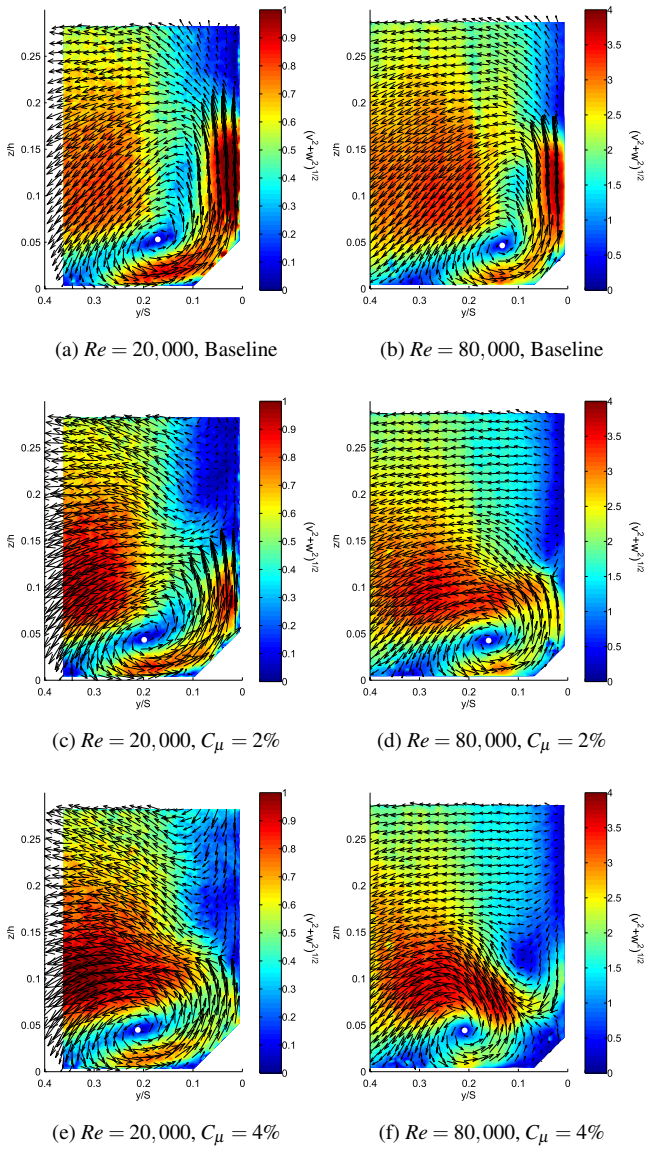

(a) $Re = 20,000$, Baseline (b) $Re = 80,000$, Baseline

(c) $Re = 20,000$, $C_\mu = 2\%$ (d) $Re = 80,000$, $C_\mu = 2\%$

(e) $Re = 20,000$, $C_\mu = 4\%$ (f) $Re = 80,000$, $C_\mu = 4\%$

FIGURE 13: PIV VELOCITY VECTORS OVERLAID ON CONTOURS OF IN-PLANE VELOCITY MAGNITUDE AT PLANE NP1.

and 16) show a spanwise suppression of the main loss core. The midspan VGJs also appear to reduce the magnitude of the profile loss by thinning the shear layer. The area averaged total pressure loss coefficient is reduced by approximately 21%. Contrary to the high Reynolds number case, loss reduction does not appear to drop linearly with C_μ (Figure 14), though the data are too sparse to be conclusive.

Compared to other studies which demonstrate both endwall and midspan control the loss reduction is comparable. Bloxham

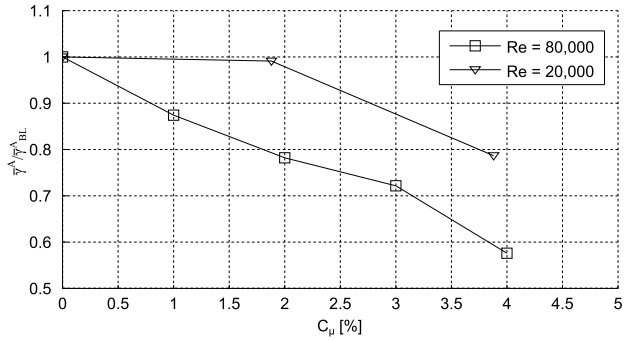

FIGURE 14: AREA-AVERAGED TOTAL PRESSURE LOSS COEFFICIENT IN THE OUTLET PLANE FOR THE CONTROLLED CASES.

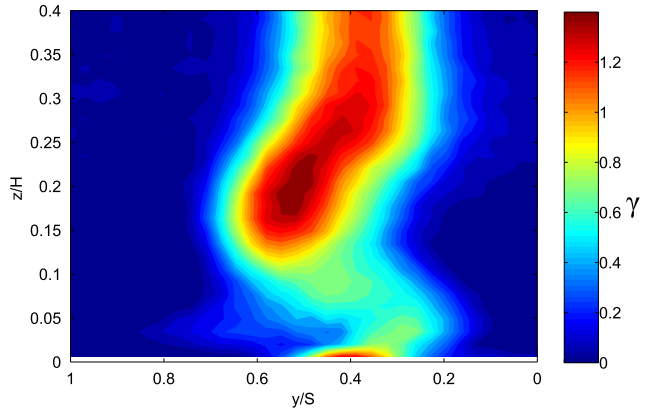

FIGURE 15: TOTAL PRESSURE LOSS COEFFICIENT IN THE OUTLET PLANE FOR THE BASELINE CASE, $RE = 20,000$.

and Bons [18] demonstrate loss reductions between 5% and 69%; however the aft-loaded blade was experiencing a non-reattaching separation in the baseline case. Hecklau et al. demonstrate up to a 13% loss reduction using pulsed slot blowing on the endwall and suction surface of a highly loaded compressor. They also recorded other benefits including increased flow turning and increased static pressure rise. In the present study, major benefits are not realized due to the relatively acceptable midspan losses of the L2F, however it would be assumed that improvements such as increased loading and turning are obtained with the midspan VGJs that are not included in the area averaged loss coefficient.

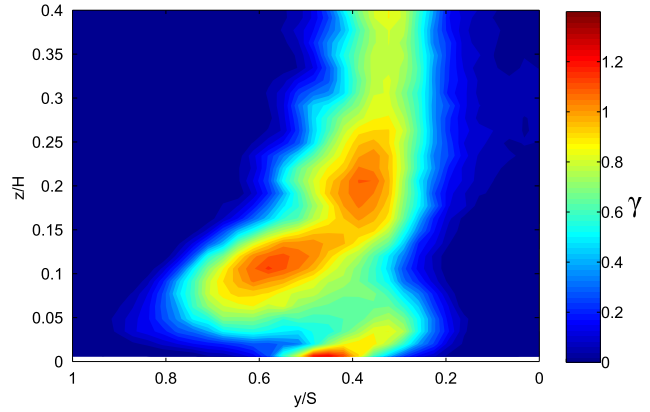

FIGURE 16: TOTAL PRESSURE LOSS COEFFICIENT IN THE OUTLET PLANE FOR THE CONTROLLED CASE OF $C_{\mu,EW} = 4\%$ & $B_{MS} = 2.1$, $RE = 20,000$.

FLOW CONTROL EFFICIENCY

Flow control efficiency is evaluated using a method similar to that presented by Bae et al. [24] and used by other researchers [21]. The basic idea is a comparison of the flow power recovered through total pressure loss reduction ($\Delta\Pi_{def}$) and the flow power cost through the jet power, hence representing an efficiency parameter based purely on the fluid mechanics interactions within the cascade.

A modification to this method is proposed. The assessment of [24] assumes that all of the jet power "cost" is lost. The present assessment revises the jet power to only include the streamwise normal component of the jet (Π_j). The two terms in the efficiency calculation are shown in equations 3 and 4.

$$\Delta\Pi_{def} = \rho\overline{U}_1^3 cos(\alpha_1)\frac{hS}{4}(\overline{\gamma}_{BL}^M - \overline{\gamma}_{FC}^M) \tag{3}$$

$$\Pi_j = \rho\frac{N_j A_j}{2}\overline{U}_j^3(1 - cos^2(\phi)cos^2(\theta)) \tag{4}$$

Using this analysis, it is shown that 79% of the streamwise normal jet power is recovered in the outlet plane through total pressure loss reduction, for the high Reynolds number at $C_\mu = 4\%$. The method of Bae et al. [24] can be rearranged to show the dependency on momentum coefficient in relation to total pressure loss, as seen in equation 5.

$$\eta_j = \frac{\Delta\Pi_{def}}{\Pi_j} \propto \frac{1}{C_\mu^{3/2}}(\overline{\gamma}_{BL}^M - \overline{\gamma}_{FC}^M) \quad (5)$$

Since the results for the high Reynolds number indicate a nearly linear reduction in total pressure loss as a function of momentum coefficient (Figure 14), the flow control efficiency is maximized at the lower blowing magnitudes. Though instructive, η_j does not account for other real benefits to the LPT namely: weight reduction, additional power extraction, and the compounding effects of a cleaner inlet profile on downstream stages.

CONCLUSIONS

A detailed investigation of the endwall flows for a highly-loaded LPT with a front-loaded pressure distribution is presented. The baseline investigation was performed for three Reynolds numbers. It was shown that decreasing Reynolds number results in a slightly increased distance between the passage vortex and the suction surface wall, presumably due to the thickening shear layer. A method for decomposing the endwall and profile losses is demonstrated. The method suggests that endwall control is more important at higher Reynolds numbers, where the endwall loss contributes over 40% of the total loss (for short aspect ratio blades).

A flow control strategy is implemented to perform three main functions. The method seeks to move the passage vortex further from the suction surface, suppress the spanwise fluid motion from the endwall, and reduce losses through momentum injection. Initial investigations indicate that a position slightly aft is preferred such that the jet momentum does not work against the passage pressure gradient to perform the desired turning. The main conclusion of the initial investigation is that blowing magnitude has a clear first order effect on loss reduction in the outlet plane.

The flow control is first investigated on the high Reynolds number case. PIV measurements verify that the wall jet is suppressed from $0.2h$ to about $0.1h$. The outlet plane also shows a suppression of the endwall flows by at least $0.1h$. The passage vortex is successfully deflected further from the suction surface, with a maximum deflection by as much as $0.08S$ in the plane normal to the trailing edge. Mass averaged total pressure loss in the outlet plane is reduced by as much as 41%. Exit angle results from an X-wire survey verify that loading is improved for as much as 15% span.

Endwall flow control is then extended to the low Reynolds number case. Midspan flow control in the form of VGJs is included for its proven benefits in reducing profile losses and improved loading. In this case, area averaged total pressure loss coefficient indicates a reduction of 21% over the baseline flow.

An evaluation of the flow control efficiency indicates that 79% of streamwise normal component of the jet power is regained in terms of total pressure loss. Unaccounted for in this analysis is the added loading to blade span and the efficiency benefit of having a cleaner inlet loss profile for downstream blade rows.

This study verifies that endwall flow control to improve efficiency is possible, allowing for highly-loaded LPTs with front-loaded pressure distributions to become a potential option for engine designers. Future investigations will seek to optimize the system for maximum blade loading and efficiency with less cost to the gas turbine system.

ACKNOWLEDGEMENTS

The authors would like to acknowledge the financial support of The Dayton Area Graduate Studies Institute through the AFRL/DAGSI Ohio Student-Faculty Research Fellowship.

REFERENCES

[1] Weiss, A., and Fottner, L., 1995. "The influence of load distribution on secondary flow in straight turbine cascades". *ASME Journal of Turbomachinery,* ***117***(1), pp. 133–141.

[2] Zoric, T., Popovic, I., Sjolander, S., Praisner, T., and Grover, E., 2007. "Comparative investigation of three highly loaded lp turbine airfoils: Part i - measured profile and secondary losses at design incidence". No. GT2007-2753, ASME Turbo Expo.

[3] Rivir, R., Sondergaard, R., Bons, J., and Lake, J., 2000. "Passive and active control of separation in gas turbines". No. AIAA-2000-2235, AIAA Fluids 2000 Conference and Exhibit.

[4] Sondergaard, R., Rivir, R., and Bons, J., 2002. "Control of low-pressure turbine separation using vortex-generator jets". *AIAA Journal of Propulsion and Power,* ***18***(4), pp. 889–895.

[5] Bons, J., Sondergaard, R., and Rivir, R., 2001. "Turbine separation control using pulsed vortex generator jets". *ASME Journal of Turbomachinery,* ***123***(2), pp. 198–206.

[6] Volino, R., 2003. "Separation control on low-pressure turbine airfoils using synthetic vortex generator jets". *ASME Journal of Turbomachinery,* ***125***(4), pp. 765–777.

[7] McQuilling, M., 2007. "Design and validation of a high-lift low-pressure turbine blade". PhD thesis, Wright State University.

[8] Bons, J. P., Pluim, J., Gompertz, K., Bloxham, M., and Clark, J., 2008. "The application of flow control to an aft-loaded low pressure turbine cascade with unsteady wakes". No. GT2008-50864, ASME Turbo Expo.

[9] Bons, J., Pluim, J., Gompertz, K., Bloxham, M., and Clark, J., 2012. "The application of flow control to an aft-loaded

low pressure turbine cascade with unsteady wakes". *ASME Journal of Turbomachinery,* ***134***(3).

[10] Bons, J., Hansen, L., Clark, J., Koch, P., and Sondergaard, R., 2005. "Designing low-pressure turbine blades with integrated flow control". No. GT2005-68962, ASME Turbo Expo.

[11] Lyall, M. E., King, P. I., Sondergaard, R., Clark, J. P., and McQuilling, M. W., 2011. "An investigation of reynolds lapse rate for highly loaded low pressure turbine airfoils with forward and aft loading". No. GT2011-46328, ASME Turbo Expo.

[12] Praisner, T., Grover, E., Knezevici, D., Popovic, I., Sjolander, S., Clark, J., and Sondergaard, R., 2008. "Toward the expansion of low-pressure-turbine airfoil design space". No. GT2008-50898, ASME Turbo Expo.

[13] Sauer, H., Muller, R., and Vogeler, K., 2000. "Reduction of secondary flow losses in turbine cascades by leading edge modifications at the endwall". *ASME Journal of Turbomachinery,* ***123***(2), pp. 207–213.

[14] Chung, J., Simon, T., and Buddhavarapu, J., 1991. "Three-dimensional flow near the blade/endwall junction of a gast turbine: Application of a boundary layer fence". No. 91-GT-45, ASME Turbo Expo.

[15] Chung, J., and Simon, T., 1993. "Effectiveness of the gas turbine endwall fences in secondary flow control at elevated freestream turbulence levels". No. 93-GT-51, ASME Turbo Expo.

[16] Harvey, N., Rose, M., Shahpar, S., Taylor, M., Hartland, J., and Gregory-Smith, D., 2000. "Non-axisymmetric turbine end wall design: Part i- three-dimensional design system". *ASME Journal of Turbomachinery,* ***122***(2), pp. 278–285.

[17] Gbadebo, S., Cumpsty, N., and Hynes, T., 2008. "Control of three-dimensional separations in axial compressors by tailored boundary layer suction". *ASME Journal of Turbomachinery,* ***130***(1).

[18] Bloxham, M., and Bons, J., 2010. "Combined blowing and suction to control both midspan and endwall losses in a turbomachinery passage". No. GT2010-23552, ASME Turbo Expo.

[19] Hecklau, M., Zander, V., Peltzer, I., Nitsche, W., Huppertz, A., and Swoboda, M., 2010. "Experimental afc approaches on a highly loaded compressor cascade". Vol. 108, Active Flow Control II, NNFM, Springer-Verlag, pp. 171–186.

[20] Hecklau, M., Zander, V., Nitsche, W., Huppertz, A., and Swoboda, M., 2010. "Active secondary flow control on a highly loaded compressor cascade by periodically pulsating jets". Vol. 112, Numerical & Experimental Fluid Mechanics VII, Springer-Verlag, pp. 199–207.

[21] Nerger, D., Saathoff, H., Radespiel, R., Guemmer, V., and Clemen, C., 2012. "Experimental investigation of endwall and suction side blowing in a highly loaded compressor stator cascade". *ASME Journal of Turbomachinery,* ***134***(2).

[22] Aunapu, N., Volino, R., Flack, K., and Stoddard, R., 2000. "Secondary flow measurements in a turbine passage with endwall flow modification". *ASME Journal of Turbomachinery,* ***122***(4), pp. 651–658.

[23] Evans, S., Hodson, H., Hynes, T., Wakelam, C., and Hiller, S.-J., 2008. "Controlling separation on a simulated compressor blade using vortex generator jets". No. AIAA-2008-4317, AIAA 4th Flow Control Conference.

[24] Bae, J., Breuer, K., and Tan, C., 2005. "Active control of tip clearance flow in axial compressors". *ASME Journal of Turbomachinery,* ***127***(2), pp. 352–362.

APPENDIX C

Surface Stress Sensitive Film as a Separation Control Sensor

Christopher Marks[1], Rolf Sondergaard[2], Mitch Wolff[3]
U. S. Air Force Research Laboratory, WPAFB, OH, 45433

Low Reynolds number boundary layer separation causes reduced aerodynamic performance in a variety of applications such as MAVs, UAVs, and turbomachinery. The inclusion of a boundary layer separation control system offers a way to improve efficiency in conditions that would otherwise result in poor performance. Many effective passive and active boundary layer control methods exist. Active methods offer the ability to turn on, off, or adjust parameters of the flow control system with either an open loop or closed loop control strategy using sensors. This research investigates the use of a unique sensor called Surface Stress Sensitive Film (S3F) in a closed loop, low Reynolds number separation control system. S3F is an elastic film that responds to flow pressure gradients and shear stress along its wetted surface, allowing optical measurement of wall pressure and skin friction. The S3F sensor was integrated into the curved airfoil surface so as not to perturb the boundary layer. In this proof of concept investigation the S3F image signal was acquired via high speed interface and analyzed on an off board control system. The S3F displacement signal was used directly in a closed loop separation control system to drive a Dielectric Barrier Discharge (DBD) plasma actuator used to control laminar boundary layer separation on an Eppler 387 airfoil over a range of low Reynolds numbers. Operation of the plasma actuator resulted in a 33% reduction in section drag coefficient and reattachment of an otherwise separated boundary layer. A simple On/Off controller and Proportional Integral (PI) controller were used to close the control loop.

Nomenclature

C_x	=	axial chord
F_x	=	Force in the x direction (tangential)
f_o	=	natural frequency
h	=	S3F thickness
P	=	Normal Stress, or Pressure
Re	=	Reynolds number, $Re = \rho V_{in} C_x / \mu$
d_x	=	tangential reaction of the film
d_z	=	normal reaction of the film
u	=	shear displacement in the streamwise direction
V	=	velocity magnitude
V_{in}	=	inlet velocity
ρ	=	density
τ	=	wall tangential shear stress
μ_m	=	shear modulus
v	=	applied voltage peak to peak

[1] Formerly Graduate Student Researcher, Propulsion Directorate, Currently Research Engineer, University of Dayton Research Institute, Member AIAA.
[2] Engineer, Turbines Branch, Turbine Engine Division, Propulsion Directorate, Bldg 18, 1950 Fifth Street, Associate Fellow AIAA.
[3] Scientific Advisor, Power Division, Propulsion Directorate, Bldg 18, 1950 Fifth Street, Associate Fellow AIAA.

I. Introduction

The field of flow control is broad and encompasses systems with many different specific engineering objectives unique to a particular application, such as separation control, lift enhancement, and noise reduction. Even though specific applications have unique design goals, all flow control systems operate by altering the natural flow field around a wetted surface or object in order to obtain a performance improvement. Flow control systems are generally classified as either passive or active. Passive techniques are usually fixed to the surface of which the flow is being controlled. They have the benefit of being simple, but cannot be turned off. Examples of passive techniques include surface treatments like dimples, or vortex generators. Active control methods can be turned on and off, removing any penalty at off-design conditions, but require additional complexity and weight. Both an active flow control actuator and also a sensor are required. In this work a new type of separation control sensor is investigated for use at low Reynolds number with the objective of using it to close the control loop in a separation control system.

The focus of this work is low Reynolds number flows which are classified, as others have (see Lissaman[1] and Gad-el-Hak[2]), to be flows with Reynolds number between 10^4 and 10^6. At these conditions boundary layer behavior plays a large role in aerodynamic losses of an object, and the transition process is more sensitive to free stream disturbances and aberrations of the airfoil geometry[3].

In this range of Reynolds numbers, the maximum lift-to-drag ratio for smooth airfoils decreases by two orders of magnitude as Reynolds number decreases[4,2]. Turbomachinery components such as compressors, and low pressure turbines also suffer a lapse in performance as Reynolds number decreases. At cruise altitude, Reynolds number drops below 100,000 and in some cases below 25,000[5,6]. At low Reynolds number, separation, transition and reattachment can all occur within a short distance and dramatically affect the performance of lifting surfaces[2]. Depending on flow conditions, such as freestream turbulence, Reynolds number, surface curvature, roughness, and pressure distribution, the boundary layer can remain laminar beyond the minimum pressure location. The adverse pressure gradient beyond the minimum pressure point on the suction surface can cause the laminar boundary layer to separate and become a free shear layer. When a laminar boundary layer separates, it rapidly undergoes transition to a turbulent flow[1]. The separated shear layer is unstable and depending on the Reynolds number and flow conditions, in some cases reattaches, forming a closed separation bubble. In other cases the free shear layer will remain separated over the remainder of the airfoil. The paper by Mueller[7] describes several types of boundary layer behavior which occur at low Reynolds number: Laminar separation without reattachment occurring at high angle of attack ("stall"), or low angles of attack due to adverse pressure gradient over the aft portion of the airfoil; natural transition of the boundary layer prior to reaching the adverse pressure gradient, eliminating separation and increasing airfoil performance; an extension of the laminar separation case in which the separated shear layer reattaches shortly after separation often after transitioning to a turbulent boundary layer. The description by Mueller was in the context of external flow such as those over aircraft airfoils, but a similar situation occurs in turbomachinery as well. In turbomachinery airfoil performance is also affected by three dimensional effects, periodic unsteadiness, and an adverse passage pressure gradient in compressors, and a favorable pressure gradient in turbines[8].

Significant research is currently under way in all areas of active flow control, from actuators to sensors, to control logic for closed loop active control. Options for active flow control actuators are vast; examples include synthetic jet actuators[9-12], vortex generator jets[5,6], and dielectric barrier discharge (DBD) plasma actuators (for examples, see Corke et al.[13]), to name a few. Synthetic jets have been generated by small flush mounted surface devices and also by plasma actuators with no moving parts.

Useful flow control sensors measure pressure, shear stress, or temperature, and different application requirements make it impossible to define a single set of requirements for sensors in all aspects of active flow control[14]. Viable options for pressure based separation control sensors are point sensors as in the case of either diaphragm type, or piezoelectric, or field sensors as in the case of pressure sensitive paint (PSP). Piezoelectric transducers are typically smaller and have quicker response than the diaphragm type[15]. The small sizes of modern piezoelectric transducers make them a practical choice as a flow control sensor if mounted flush to a surface. Pressure based separation sensor signal analysis has been by frequency based techniques[16], or by simply comparing upstream and downstream static surface measurements as was demonstrated by Becker et al.[17].

Thermal based sensors take advantage of the proportional relationship between wall shear stress and heat transfer rate. Many different types of sensors useful for separation control exist and the trend is toward high density and miniaturization using fabrication methods based on MEMS development. Useful separation sensors include double hot-wire sensors[18,19], high density vacuum-insulated diaphragm-type thermal shear stress sensors[20], flexible arrays of thin film resistors[21], and MEMS sensor clusters consisting of multiple types of sensors in one[22]. Optical or image

based methods have also been developed to detect separation as in the case of thermal tufts by Baughn et al.[23], and Gregory et al.[24]. More direct methods of measuring wall shear stress measuring the deflection of micropillars or surface fences protruding into the vicous sublayer. Deflection of micropillars formed of an elastomer material has been measured optically by Grobe et al.[25,26] and Gnanamanickam et al.[27] and each use the linear relationship between wall shear stress and near wall velocity gradient. Surface fences have been used in a variety of ways to measure shear stress. A technique described by Fernholtz et al.[28] use precision micro pressure transducers to measure the change in pressure upstream and downsteam of the fence and calculate skin friction which is a function of the pressure difference. vonPapen et al.[29,30], and Shober et al.[31] describe the development of a micro surface fence capable of measuring wall shear stress magnitude and direction.

Relatively few closed loop separation experiments have been described in literature, and feedback based systems vary in control complexity. Many of the feedback control experiments use surface pressure measurements analyzed in a variety of ways to deduce flow state. Examples of three different methods of exploiting surface pressure measurements are by Patel et al.[32], Pinier et al.[33], and Becker et al.[17]. Patel et al.[32] describe closed loop experiments leading to a stall control system implemented on a NACA 0020 wing in a low speed wind tunnel. They use a closed loop system consisting of active vortex generators and embedded pressure sensors for predicting flow separation. Predetermined threshold values of pressure signal standard deviation are used to turn on the flow effectors and delay stall during a 2 deg/s change in angle of attack. Pinier et al. [33] used wing surface pressure measurements along with partial orthogonal decomposition and modified linear/quadratic stochastic measurements to estimate the state of the flow and then apply proportional feedback control. Becker et al.[17] used a pair of surface pressure measurements to determine if the flow was attached or separated by comparing the difference in C_p between measurement locations. The separated case gave a ΔC_p around zero and fully attached flow resulted in a ΔC_p greater than 1. Pulsed jets were used with a modeless extremum-seeking control scheme to demonstrate an increase in lift due to minimization or delay of flow separation.

Surface pressure sensors measure surface normal stress, but sensors that are sensitive to surface tangential stresses are also a natural fit for separation control systems. Recently Poggie et al.[34] demonstrated a stall control system on a morphing airfoil at a chord Reynolds number of 9.0×10^5 using the signal from a hot-film sensor in a turbulent boundary layer state. The sensor signal was used to sense flow separation and trigger on a dielectric barrier discharge (DBD) plasma actuator resulting in a 10% lift improvement.

This paper describes a complete closed loop low Reynolds number separation control system developed to investigate the use of a new type of surface stress sensor called Surface Stress Sensitive Film (S3F). S3F is an optical sensor that uses a low shear modulus elastomeric film that is inherently sensitive to both surface tangential stress (shear) and pressure gradient [35]. Optical measurements of markers on the surface of the film and embedded luminescent molecules are used to determine the tangential stress and pressure gradient on the film. S3F has been used to measure surface stresses in a variety of aerodynamic (e.g. Fonov et al.[35]) and hydrodynamic (Crafton et al.[36]) flows. The separation control system developed using S3F was successfully used to control laminar flow separation on the suction surface of an Eppler 387 (E387) airfoil. The experiments were carried out in the U.S. Air Force Research Laboratory (AFRL) Propulsion Directorate's Low Speed Wind Tunnel (LSWT) Facility. The reactive flow control system uses a unique S3F sensor for feedback into the control system, and a spanwise array of linear vertical jets generated by a DBD plasma actuator is used as a flow effecter. The closed loop operation is demonstrated using two simple control strategies, on/off feedback control, and a Proportional Integral (PI) controller. The paper details the prototype S3F separation control sensor system, closed loop separation control experiments, as well as a discussion and recommendations for improvement in the sensor system design.

II. Experimental Configuration

Experiments were carried out in the U.S. AFRL Propulsion Directorate's Low Speed Wind Tunnel (LSWT) located at Wright-Patterson Air Force Base, Ohio. The facility is comprised of two wind tunnels, the first is a large, variable angle linear cascade primarily used for aerodynamic investigation of turbomachinery components. The second wind tunnel, referred to as the Developmental Wind Tunnel (DWT) was used in this study. The DWT is a smaller open circuit tunnel with a straight 30.5 cm x 30.5 cm x 61 cm test section. It has good optical access, and an airspeed range of 4.5 – 65 m/s generated with a 7.5 kW electric motor. The inlet has a series of flow straighteners and turbulence-reducing screen followed by a 9.5:1 contraction providing an advertised turbulence level of less than 0.2%.

A. Airfoil Model

In an effort to make research applicable across design domains, a low

Reynolds number Eppler 387 airfoil geometry was chosen. The E387 was selected for the experiments based on the presence of laminar flow separation on the suction surface at small angles of attack. This assured a small wind tunnel flow blockage. The airfoil model was mounted across the full span of the wind tunnel with a chord length of 16.5 cm.

The E387 test article was fabricated out of a polycarbonate ABS mixture. A cavity was added to the suction surface in which a S3F carrier containing the S3F sensor was installed as shown in Figure 1. This method of S3F installation was used previously[38] to ensure that the S3F itself did not perturb the boundary layer. The S3F carrier was a thin sheet of plastic with a shallow cavity. The cavity in the carrier was filled with S3F flush to the surface of the carrier and then installed in the airfoil and held by either adhesive tape or countersunk screws near the trailing edge.

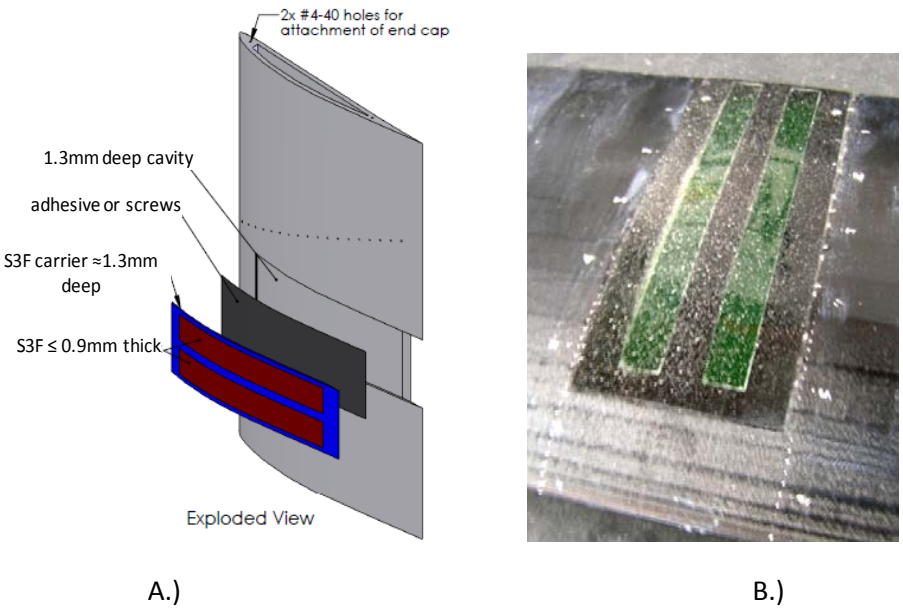

Figure 1. A.) Diagram of S3F installation on airfoil surface, and B.) example of S3F installed on an airfoil.

B. Airfoil characterization

Static pressure, flow visualization and particle image velocimetry (PIV) were used to understand the boundary layer behavior in the area of the separation sensor with both the sensor and actuator installed. AllSensor® pressure transducers were used for pressure measurements with nominal 0.05% and maximum 0.25% linearity full scale. A 0-125 Pa (31.1 Pa/V) sensor was used for inlet dynamic pressure, and a 0-249 Pa (62 Pa/V) transducer was used for C_p measurements. Uncertainty in the C_p measurements is nominally 1.5% at the pressure minimum, and 3.1% in the trailing edge area at Re = $5x10^4$. At Re = 1.0 x 10^5 uncertainty in C_p is nominally 0.5% at the

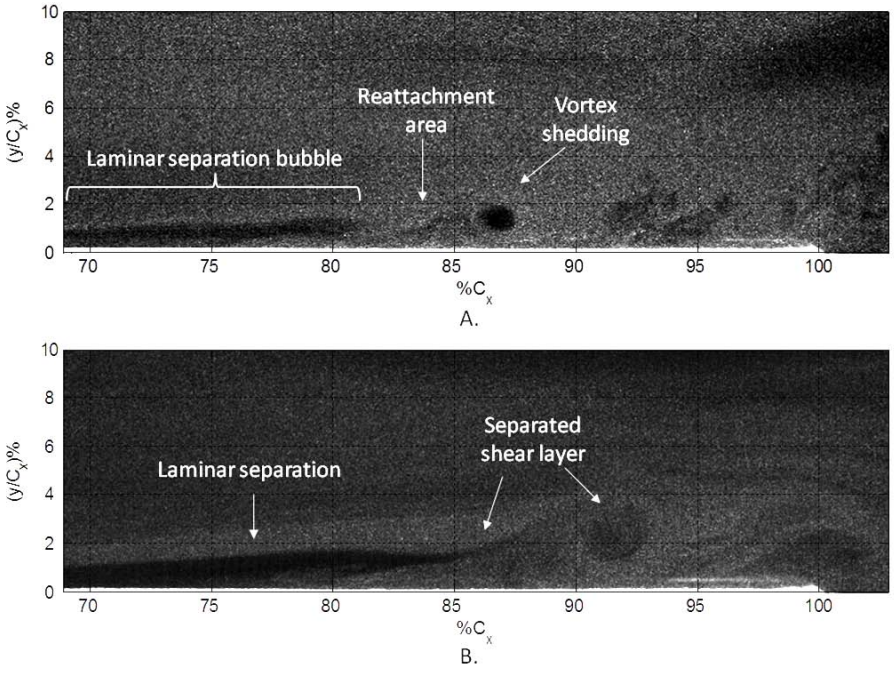

Figure 2. Instantaneous flow visualization over the E387 suction surface trailing edge region with actuator installed and powered off. Image A is at Re = 1.0 x 10^5. Image B is at Re = 6.0 x 10^4.

pressure minimum and 1.1% in trailing edge area.

PIV images and flow visualization were captured using a PCO 1600 camera and illuminated with a New Wave® Solo 120 laser. The laser sheet was formed by Dantec® sheet forming optics mounted to an articulating laser arm. The laser sheet thickness in this setup was approximately 1 mm. Investigation into clean flow seeding methods by Reeder et al. [39] inspired the use of water vapor generated from a Sussman® 9 kW steam generator. The steam was injected in line with the wind tunnel approximately 2 meters upstream of the inlet. Commercially available PIV software was used to calculate two-dimensional velocity fields.

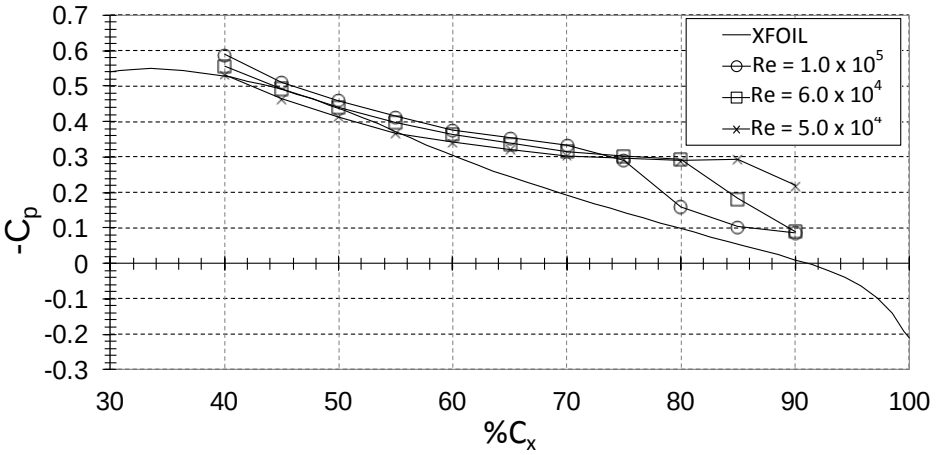

Figure 3. Example of Suction Surface C_p in the trailing edge region at various Reynolds numbers with actuator installed.

Examples of instantaneous flow visualization are shown in Figure 2. At a Reynolds number of 1.0 x 10^5 the laminar boundary layer separates, transitions to turbulent and reattaches. In the area of reattachment vortices are shed from the separation bubble and travel downstream along the boundary layer. At Re = 6.0 x 10^4 and below the boundary layer behavior is complex and very unsteady near the trailing edge. The boundary layer often did not reattach and large coherent eddies were observed convecting down the separated shear layer leading to instances of both reattached and separated boundary layer near the leading edge.

Mean static pressure across the trailing edge region of the airfoil suction surface with the actuator installed is shown in Figure 3 for various Reynolds number compared to the inviscid solution calculated in XFOIL. The plateau in suction pressure gradient beginning near C_x=55% is characteristic of boundary layer separation. At a Reynolds number of 1.0x10^5 the pressure recovers in the vicinity of C_x = 80-85% which is characteristic of mean shear layer reattachment. At the two lower Reynolds numbers, the mean reattachment point moves downstream towards the trailing edge, or does not reattach. The loading on the suction surface of the airfoil increases as Reynolds number increases. The reattachment points have moved upstream significantly compared to the open loop experiments.

III. Flow Effecter

Plasma synthetic jet configurations have been proposed in both annular[40,41] and linear configurations [42,43]. Experiments by Santhanakrishnan and Jacobs showed that steady operation produced induced velocities that behaved like a synthetic jet in crossflow, and pulsed operation formed multiple counter-rotating vortex rings. In a previous study[38] we compared three different types of plasma actuators electrode arrangments in an open loop configuration to reduce the extent of laminar separation on the E387 airfoil based test article. The use of a spanwise array linear vertical jets just upstream of the laminar separation location resulted in a 33% reduction of drag at Re = 5 x 10^4 and a greater than 6% C_x decrease in separation bubble length at Re = 1.0 x 10^5 while using less power per length of electrode. The control authority of the spanwise array of linear vertical jets was considered adequate for the current closed loop experiments over the entire Reynolds number range (1.0 x 10^5 – 6.0 x 10^4)

Figure 4. Plasma actuator configuration mounted in the wind tunnel.

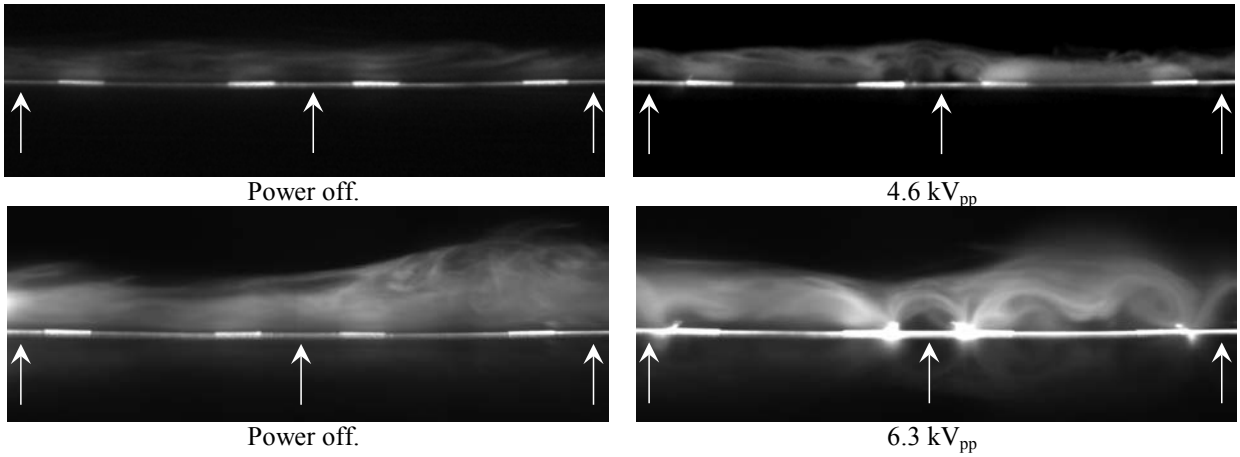

Figure 5. Plasma actuator flow visualization using CO_2 generated fog. Arrows indicate location of vertical jets.

considered here. The actuator was mounted upstream of the separation point and consisted of 9 linear vertical jets spaced 23.8mm on center and extending approximately 20.3mm in the streamwise direction.

The plasma actuators were fabricated in the U.S. AFRL Propulsion Directorate's thin film lab by photolithography and etching double-sided copper clad Kapton. The Kapton was 5 mil thick and the copper electrodes were 1.4 mil thick. The plasma actuators were attached to the airfoil suction surface by 2 mil thick adhesive transfer tape and were wrapped around the entire leading edge of the airfoil to reduce the chance of tripping the boundary layer. Surface irregularities added by the plasma actuators on the suction surface were limited to a 36 μm (1.4 mil) step up at the exposed electrode and an approximately 178 μm (7 mil) step down at the trailing edge of the actuator. Nonetheless, variation in extend of the mean laminar separation bubble has been observed between different installations of the plasma actuators onto the airfoil. This is due to variation in attachment of the plasma actuators. The plasma actuator was wrapped around the leading edge. Any change in the shape at the leading edge or a discontinuity could move the reattachment point upstream. For consistency the data reported in this paper has been obtained using the same plasma actuator.

The plasma actuators were powered by two Titan Series power supplies from Compact Power and the voltages were stepped up to kilovolt levels by an Industrial Test Equipment Co. transformer. The plasma actuators were powered by a steady continuous sinusoidal waveform. Measurements showed that it took 200 ms to reach steady state actuator voltages.

Flow visualization of the actuator induced velocity is shown in Figure 5. In the figure an actuator was fixed to a flat plate with a uniform layer of adhesive transfer tape and placed on a bench top. A class 3 laser was used to illuminate a plane normal to the surface of the actuator running along the spanwise direction. Fog generated by a mixture of water and dry ice was directed over the actuator (traveling towards the reader in the view of Figure 5). Two different actuator voltages are shown along with corresponding power off images taken just before each power on image. At the lower voltage vortical structures are observed in the region of the plasma marked by the middle arrow. Induced velocity jets are formed in the region of plasma at the inner edge of the exposed upper electrodes, directed towards each other. At the higher voltage the plasma area at the inner edge of the exposed electrodes looks

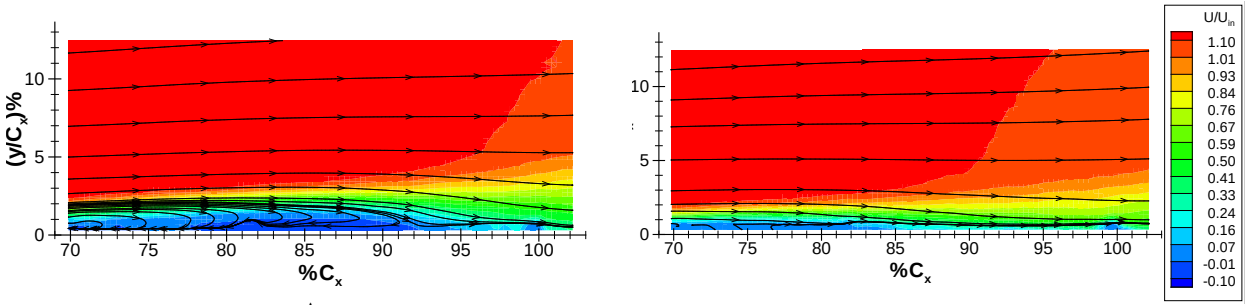

Figure 6. PIV mean velocity field at Re = 6.0×10^4 with plasma actuator A.) off, B.) on with v = 6.4 kV_{pp}.

like a pair of sinks, entraining fluid and drawing it through the plasma region and ejecting it into the vertical jet between electrodes. At the higher voltage an interaction between vertical jets is clearly observed producing streamwise vortical structures in between the vertical jets. No effort to optimize the electrode configuration was made, but this type of spanwise configuration of vertical jets has great potential as a flow effector due to the potential for generating three-dimensional vorticity and boundary layer instability.

The mean velocity field obtained by PIV with the actuators off and on at a Reynolds number of 6.0×10^4 are shown in Figure 6. Comparing the actuator on and off plots clearly shows an upstream shift in the mean reattachment point and significant decrease in the thickness of the mean separation bubble.

IV. Sensor System

The sensor system uses S3F technology (from ISSI Inc.) to infer boundary layer state. S3F is an elastic film placed on a wetted surface to measure surface stresses. The film has two types of sensors; the first is used to measure normal force (pressure) on the film by a fluorescent probe embedded in the S3F. The second consists of markers distributed across the surface of the film. Marker displacement under load from the fluid flow is recorded using a digital camera and compared to a flow-off image to determine film tangential displacement field. Recently Fonov et al.[37] used stereo photogrammetry to measure and reconstruct the deformed S3F surface which enables measurement of normal and tangential displacement using only cross correlation techniques. Once the S3F deformation field is measured, the normal and tangential wall forces can be calculated from the film displacement by solving an inverse elasticity problem using FEA [35]. For additional background and application of the S3F method the reader is directed to refs. 35-37,47-53.

Through analysis of the response of S3F using both experimental and analytical techniques ISSI Inc. has reported that with spatial loading frequencies (thickness/contact surface) below 0.1, film response can be modeled mathematically by[50]:

$$d_X = \frac{h}{\mu}\left(\tau_X - \frac{h}{2}\frac{\partial P}{\partial x}\right) \qquad d_Z = \frac{h}{\mu}\left(\frac{h^2}{3}\frac{\partial^2 P}{\partial x^2} - \frac{h}{2}\frac{\partial \tau_X}{\partial x}\right) . \tag{1}$$

In Equation (1), the surface normal (d_y) and tangential (d_x) reaction of the film is written in terms of the film thickness (h), shear modulus (μ_m), tangential stress (τ_x), and normal stress (P). These equations give insight into designing a film to have a higher response to shear than pressure, or vice-versa. The tangential reaction of the film is a function of tangential stress and pressure gradient scaled by thickness. A thin film will have a higher relative response to shear forces than to pressure gradients. Conversely, a thicker film will show a higher response to pressure forces over shear forces[50]. Another important insight from Equation (1) is that in the presence of small pressure gradients, shear stress is linearly related to tangential displacement. This key attribute was used in this work to develop the separation control sensor.

The frequency response of the S3F has been described with a simple mass-spring-damper model that assumes the film is purely elastic [50]. The first natural frequency of tangential oscilliation of the film is calculated by:

$$f_0 = \frac{1}{2\pi}\sqrt{\frac{\mu}{\rho\, h^2}} \quad . \tag{2}$$

The film frequency response is thus a function of shear modulus (μ), density (ρ), and thickness (h), which enables the frequency response to be adjusted in the range of 0.3 to 10 kHz[50]. For a constant shear modulus, and film density, frequency response is proportional to the inverse of thickness as in Equation 2[50].

Previous investigations have demonstrated the potential of S3F in air flows at low Reynolds numbers[44]. Experiments on a low pressure turbine blade by McQuilling et al. [45-46] found that film sensitivity is critical due to the an order of magnitude variation in shear stress gradients from leading edge to trailing edge, repeatability of measurements was difficult at such low velocities, and that sources of uncertainty needed to be addressed. Sources of uncertainty were thought to be due to tunnel vibration, blade deformation, and disturbances to the flow due to the S3F not being perfectly flush with the blade surface. More recently[38] S3F was used as an additional data source to compare the ability of three different dielectric barrier discharge (DBD) plasma actuator to reattach separated flow over an E387 airfoil at low Reynolds number. The S3F tangential response was used to estimate the shift in separated shear layer reattachment location. This previous work set the stage for the use of S3F as a separation control sensor. The unique capability of S3F to indicate the tangential displacement and its linear relationship to

shear stress under the presence of low pressure gradients and spatial loadings[8] make it useful as a separation control sensor.

In our experimental setup we have addressed the areas of uncertainty identified by McQuiling et al.[44]. To ensure the S3F was flush with the airfoil surface it was formed in a cavity in a plastic carrier (See Fig. 1) prior to installation on the curved airfoil surface. Early measurements by S3F in our facility indicated that airfoil/camera relative motion and rotation was significant compared to S3F displacement. In order to track airfoil/camera motion a calibration region just above the S3F and just below the S3F that was fixed rigid to the airfoil was sprayed with markers. Relative motion across the field of view was calculated using two-dimensional interpolation based on the movement of the calibration regions. This was an extra step in the analysis routine that required significant computational time due to the extra calculations in the calibration regions. Future S3F based sensors that are packaged discretely as shown in Figure 8b would not suffer from camera/airfoil relative motion problem and could operate at a higher frame rate.

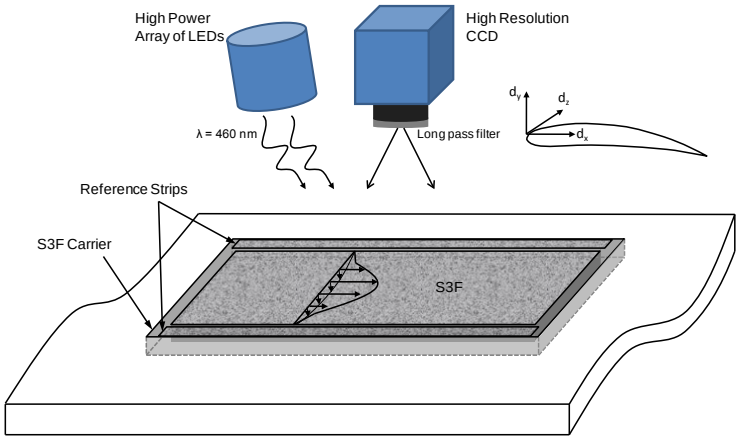

Figure 7. S3F Experimental Setup

The S3F experimental arrangement is shown in Figure 7. S3F was installed along the suction surface of the E387. Images were acquired with a commercial, high resolution CCD camera (PCO 4000) with a resolution of 4008 x 2680 pixels. A Nikkor 200 mm f4 lens with long pass filter was fitted to the camera and rigidly fixed to the wind tunnel test section. A Novatron flashlamp with flash-on time on the order of several hundred microseconds, and an ISSI Inc. high power LED lamp (460 nm wavelength) were used to illuminate the S3F. The Novatron flashlamp provided a high intensity light source but speed is limited to 0.33 Hz. The high power LED lamp can be operated in steady mode or high speed pulsed mode driven by an external signal generator. Images were transferred to CPU RAM over a high speed Cameralink interface. A Labview based software program controlled image acquisition and calculated film displacement using single pass cross-correlation. Frame rate (sampling speed) and exposure were controlled by a Quantum Composer 9300 Pulse generator.

A. System Design Considerations

S3F is naturally sensitive to both pressure gradient and shear stress, however; in low pressure gradients Crafton et al. showed that film tangential response is essentially uncoupled from pressure gradient[50]. This implies that tangential displacement itself can be used as a direct indicator of shear stress direction and magnitude. Exploiting the direct relationship between S3F tangential displacement and shear stress enables the use of S3F as a separation sensor. In regions with low pressure gradient relative to shear stress the tangential displacement direction can be a direct indicator of attached and separated flow. In areas with mild pressure gradient the measured tangential

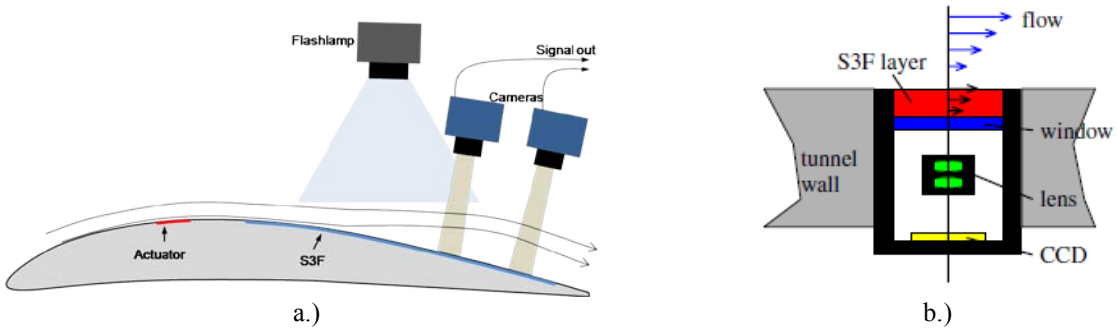

Figure 8 a.) Prototype S3F Separation Sensor used in current study. b.) Discrete S3F based skin friction sensor from Crafton et al.[50].

response can also be used as a predetermined control system input. In this investigation the tangential S3F displacement is used directly as a separation sensor output signal.

The determination of appropriate S3F material properties for a given application is a trade-off between film displacement, frequency response, and pressure gradient effects. Equation (1) implies that for a given surface load, thinner films have a higher response to shear stress than pressure gradient. Thinner films also have a higher frequency response, but lower overall tangential film displacement. The optics system must provide a large enough magnification so that film displacement is detectable and uncertainty acceptable. In this proof of concept research effort the light source and camera were mounted external to the test article as shown in Figure 8. Development of a better packaging concept for an S3F based sensor for flow control is currently underway. A useful sensor package for flow control will need to include an integrated method to measure film displacement rather than an external camera and light source. In this experiment, the length scale of the airfoil, target experimental Reynolds number, and properties of air required that a very sensitive S3F, with high magnification factor be used. Ultimately, a miniaturized version of the discrete skin friction sensor system similar to the description in Crafton et al.[50] would be a more useful package when integrated into an aerodynamic surface. This type of sensor would be useful in a variety of aerodynamic systems, with potential for using thinner films, higher frequency response, and increased sensor sampling speed..

The shear stress on the surface of the airfoil is low; on the order of 1 Pa. Figure 9 gives estimates of tangential film response for a 1 Pa shear stress with a 100 Pa/m pressure gradient over a range of S3F thicknesses and shear modulus calculated using Equation (2). The film must have an extremely low shear modulus (< 100 Pa) to provide adequate tangential displacement on the order of 1 px. A high resolution camera and high focal length lens was required to obtain a high image magnification factor. Image field of view height was on the order of 15mm, magnification factor >100 px/mm, and film thickness 0.9mm enabling measurement of displacements on the order of tens of microns. Ultra low shear modulus S3F (120 Pa and less) has a frequency response as high as 500 Hz if thin films are used, and lower frequency response around 50 Hz if thicker films are used.

The S3F based separation sensor assumes that local pressure gradient is low relative to shear stress and the S3F tangential displacement is an indicator of surface shear stress direction and magnitude. In reality the pressure gradient over the surface of the airfoil also contributes to tangential film displacement introducing spatial error into the sensor signal. The error is dependent on film properties, pressure gradient, and shear stress. In regions in which the local pressure gradient relative to shear stress is higher, the tangential film response can still be a useful control system input if S3F response is characterized over a range of flow conditions.

Several factors put a limit on sensor speed in our experimental setup: illumination intensity, camera frame rate, image processing speed, film response, and experimental setup. The factors are not independent of one another. Image processing speed was set by the system hardware and image processing algorithm. The camera frame rate was limited by image sensor resolution and magnification factor required to sense film displacement. A high resolution camera was required to achieve adequate film displacement, which had a maximum resolution frame rate of only 5 fps. The intensity of the pulsed light source set a minimum exposure time of approximately 40ms.

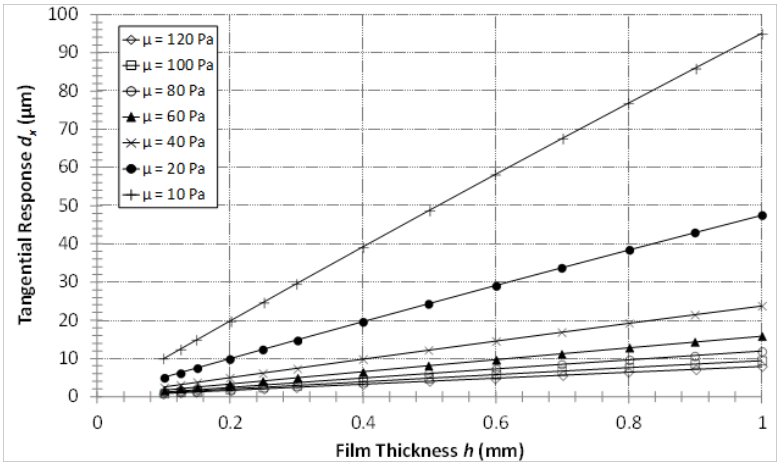

Figure 9. Estimated S3F tangential displacement for a 1 Pa surface shear stress and 100 Pa/m pressure gradient.

B. Signal Analysis

Film tangential displacement is determined by calculating the shift of particles in the "wind-on" and "wind-off" images. Two dimensional cross-correlation was chosen for its relative simple digital implementation and efficiency compared to other techniques. Many image preprocessing methods and advanced algorithms exist to increase the

accuracy of digital cross correlation. Since the objective here was to use S3F as a separation control sensor the image processing speed was essential, thus single-pass cross correlation was used. The image analysis process from signal (image) acquisition to two dimensional film displacement calculation is outlined in Figure 10. The two images were divided into interrogation regions of size $N \times N$ each containing an adequate number of markers. Cross-correlation of the interrogation region results in a spatial correlation plane in which the peak is an estimation of the film displacement to integer values. Displacement calculation to sub-pixel accuracy was achieved by using a three point Gaussian curve fitting function around the correlation peak given by Willert and Gharib[54,55]. Several key system parameters significantly influence processing speed and accuracy. Most noticeably marker size and density placed a bound on interrogation window size. Smaller interrogation window sizes result in a faster processing speed, but were only possible when SNR was high, and particle diameters and densities are appropriate.

Investigation of the uncertainty of the implementation of the cross correlation described above indicated that significant improvement in accuracy was gained by implementing the correlation multiplication technique proposed by Hart et al.[56] as a noise reduction technique. Correlation multiplication involves multiplying the correlation planes of two adjacent, partially overlapped interrogation windows. As long as the displacement gradient is small, this multiplication has the effect of reducing noise and amplifying the correlation peak. For this investigation two adjacent correlation planes offset by 50% were multiplied with each other. The calculation of an extra correlation plane has the negative impact of essentially doubling the time it takes to calculate one displacement vector.

Mean bias error (ε_b)and rms error ($\varepsilon_{b)}$ associated with cross correlation were estimated by single pass cross correlation using 500 interrogation regions extracted from images of the S3F used in this work. Peak error is at sub-pixel displacement with nearly 9% ε_{rms} and 3.2% ε_b**.** Both types of errror significantly decrease as displacement increases up to a marker displacement of 10 pixels. The minimum interrogation size used in this work was 128 pixels by 128 pixels. RMS error was higher for smaller interrogation windows size. Bias error was higher for the larger interrogation window size at sub-pixel displacement, with comparable, very small amount of error near integer displacements.

Other sources of error in the displacement calculation include airfoil movement relative to the camera. Airfoil motion was compensated for by calculating the displacement of markers just above and below the S3F. The top and bottom region of markers were rigidly fixed to the airfoil. The displacement of the airfoil itself was subtracted from the calculated S3F displacement along the midspan using 2D interpolation. An investigation into the uncertainty associated with correcting for airfoil movement was undertaken by installing a flat plate with markers into the cavity of the airfoil in which the S3F carrier was installed. Images of marker displacement with the wind tunnel on were recorded and displacement analyzed using ISSI Inc. hybrid cross correlation/optical flow software[57], then correcting for displacement using the method described above in Matlab®. Marker displacement after correction for airfoil motion should have resulted in zero displacement. The analysis indicated that second order curve fits of airfoil motion in the streamwise direction worked better than linear or third order curve fitting. First order curved fits were used in the spanwise (vertical) direction. Analysis indicated a mean displacement error of approximately +/- 0.015 pixels could be obtained using averages of 25, 50, and 100 images. This is an estimate of the accuracy of the airfoil rotation correction method.

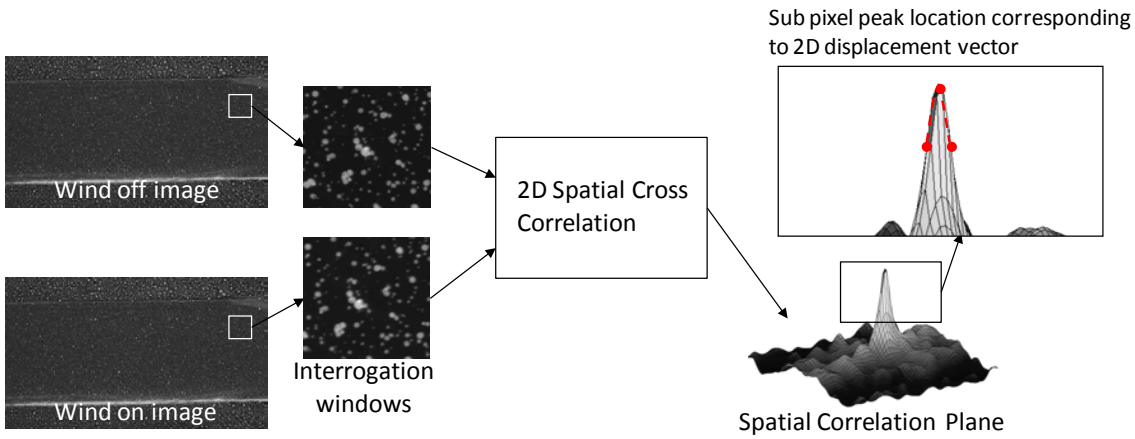

Figure 10. Two dimensional film displacement calculation using cross correlation.

C. Mean S3F displacement field

Several different formulations of S3F were tested on the airfoil. In each of the final three formulations of S3F the shear modulus was reduced significantly. This has the effect of increasing marker displacement, but decreasing the S3F frequency response. Nonetheless, the frequency response remained well above the camera maximum frame rate. Table 1 describes the last three S3F formulations tested. Frequency response was approximated using Equation (3) and shear modulus measurements were provided by ISSI Inc. The method used to measure such low shear modulus was improved over the course of the work by S3F #2 the reported uncertainty in the shear modulus measurement was +/-10%.

Table 1. S3F properties.

Version	Shear Modulus (Pa)	Mag Factor (px/mm)	Thickness (mm)	Freq. Response (Hz)
S3F #1	100	157	0.9	59
S3F #2	37 +/- 10%	145-147 typ.	0.9	32
S3F #3	7.7 +/- 10%	156	0.9	16

An example of S3F mean tangential displacement field calculated using ISSI Inc.'s hybrid cross correlation/optical flow method[57] is shown in Figure 11. Flow in the images is left to right. The film tangential displacement is in the negative flow direction from up to a zero crossing location near 94% C_x after which the displacement is positive. The negative S3F displacement implies mean flow separation with mean reattachment near the zero crossing location. No zero crossing in the measurements which would imply that the mean boundary is separated to extent of the S3F. Review of S3F displacement data, flow visualization, PIV, and C_p measurements implied that at the lower Reynolds numbers tested (Re = 6 x 10^4) the pressure gradient near the trailing edge is large enough relative to shear stress that the tangential displacement is actually a coupled response between pressure gradient and shear stress. Regardless of whether the local minimum was created by a coupling of forces or not, it was hypothesized that this minimum would shift spatially depending on reattachment location. This would make the tangential film displacement useful at the lower Reynolds number even if the shift in minimum is due to a coupled forcing affect. Estimations of skin friction coefficient that included pressure gradient showed that the mean separation point could shift spatially in excess 6% C_x from the perceived separation point based on tangential displacement. Near the reattachment point the inclusion of pressure gradient only shifted the mean zero crossing 2% C_x.

V. Separation Control System Software

A custom LabVIEW® virtual instrument was developed to read and analyze images of the S3F, record wind tunnel conditions, send plasma actuator control signals, and execute the closed loop separation control system logic. The film tangential displacement was calculated using frequency domain, single pass cross correlation.

The top level system diagram shows signal sources, paths, and interaction between the equipment used in the separation control system. Two different control methods were implemented in the code: On/off control and PI control. The wind-off image is recorded prior to execution of the separation control code. Upon execution of the separation control code, and during initialization of variables, the regions of interest in the wind-off image are loaded into computer RAM. This occurs only once during initial execution of the software. The wind-on images are transferred to the computer immediately after each exposure using camera FIFO protocol via a high speed Cameralink interface. A high resolution PCO 4000 scientific camera that has 4008 x 2600 pixel CCD image sensor was used in the experiments to obtain high magnification rates required to detect film displacement. While the PCO 4000 provided high resolution, low noise data, the features of the camera limited frame rate and processing speed. Data representing each image was large and can only be transferred to computer RAM as 16 bit data. Because the motion of the airfoil relative to the camera needs to be calculated and corrected for during each exposure, three different regions of interest were required: a top region just above the S3F, a middle region along the mid span of the S3F, and a bottom region just below the S3F. Since only one region of interest can be designated with the PCO 4000, the full image data was transferred to the computer RAM upon each exposure. The use of a high resolution camera with the ability to transfer 8bit image data and multiple regions of interest, rather than the entire image, would increase the sampling rate over the system described and used in this work.

Sampling speed was limited by the experimental setup and hardware, ultimately set by the high resolution camera and illumination requirements to approximately 3 Hz. Sampling rates were typically kept to 0.5-2.5 Hz and were sufficient for experimental setup and control method used. The most appropriate way to increase the sensor

system speed is by creating a miniature discrete sensor package similar to Figure 8b which would improve system speed by:

1. Increasing the frame rate by using lower resolution image sensors
2. Eliminate the need for airfoil/camera motion correction
3. Decrease the illumination intensity required.

In addition, a real time processor using GPUs optimized to perform the FFTs required for cross correlation would increase processing speed and allow the use of more accurate multi-pass algorithms that achieve higher accuracy.

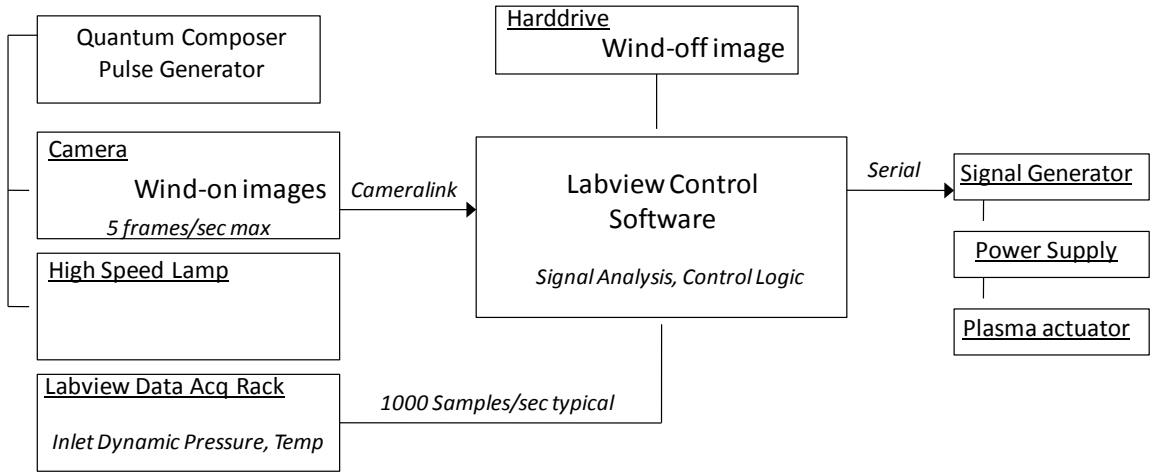

Figure 11. Top level system diagram.

VI. Separation Control System

A system block diagram of the feedback separation control system is shown in Figure 13. A simplistic approach was taken in this work to develop a simple controller with the objective of demonstrating that the S3F can be used a separation control sensor. An on/off controller and a PI controller were implemented.

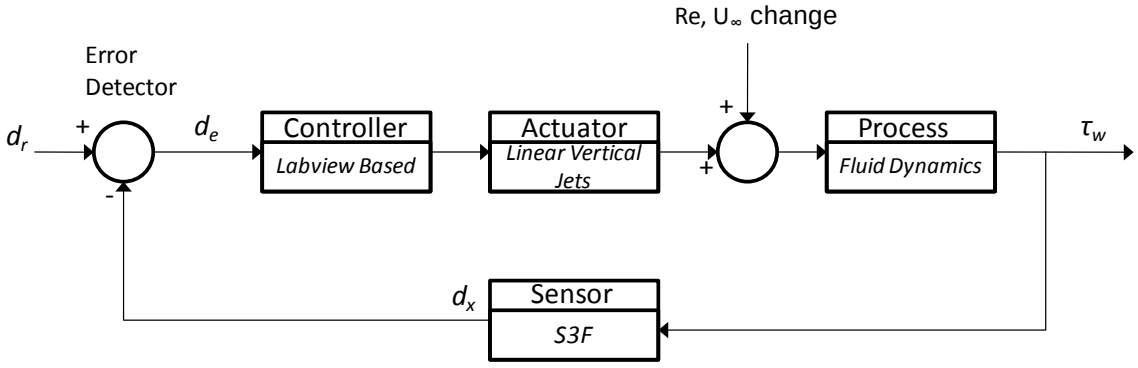

Figure 12. Feedback control system diagram.

A. System Response

Mean and transient response of the S3F at several different plasma actuator voltages were used to determine threshold values for an on/off controller and set point for the PI controller. Typically one region of the film was monitored, which simulated a discrete mounted S3F based sensor. Figure 14 shows the mean S3F tangential response for various plasma actuator voltages. At Re = 1.0 x 10^5 a location just upstream of the trailing edge was monitored. The mean response with increase in plasma actuator voltage was nonlinear. The higher Reynolds number of 1.0 x 10^5 shows a linear response with increase in actuator voltage until a 5.5 kV_{pp} applied voltage in which a further increase in actuator voltage resulted in little change in tangential film displacement. The plateau in

the response curve is consistent with observations using the same plasma actuator electrode geometry in a previous open loop investigation[38]. This implies there is a threshold voltage of approximately 5.5 kV_{pp} above which there is very little additional decrease in separation length. A maximum upstream shift in reattachment point of 6.1 %C_x was observed at Re = 1.0 x 10^5 with 7.2 kV_{pp} applied voltage. The reattachment location implied by the S3F tangential displacement is further downstream than was observed with PIV. With the plasma actuator off the mean zero crossing location was at 90% C_x with an upstream shift to approximately 84% C_x with 7.2 kV_{pp} applied voltage. At the lower Reynolds number the same linear range is visible but a drop off in shear displacement occurs at the highest plasma actuator voltage. The mean displacement actually changes to a negative value. Mean reattach point shifted upstream to as high as 89% C_x with a 6.4 kV_{pp} applied voltage. This is an upstream shift of approximately 9% C_x. The upstream shift in reattachment point is consistent with PIV measurements that indicated a 10% upstream shift; however, the location of zero crossing is nearly 7% further upstream than the reattachment point measured with PIV.

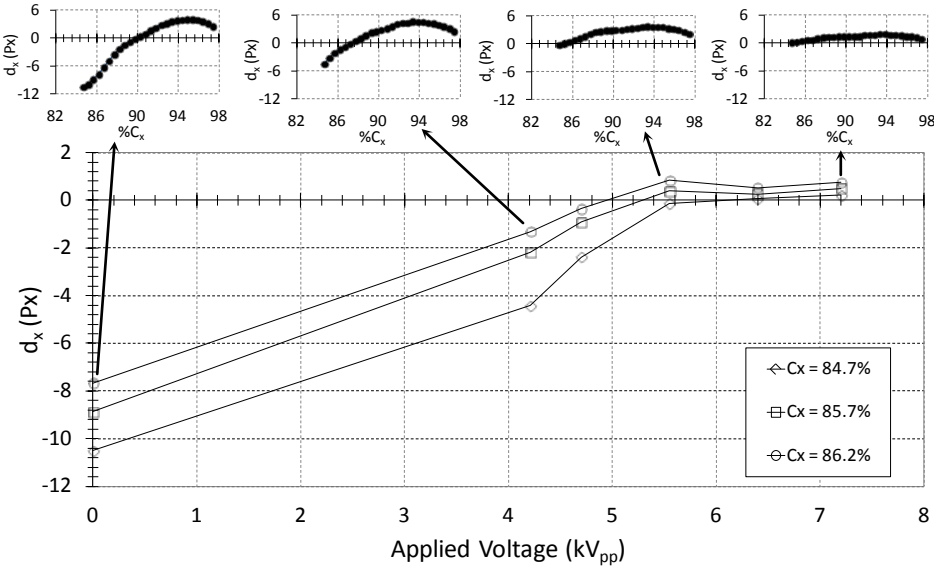

a.)

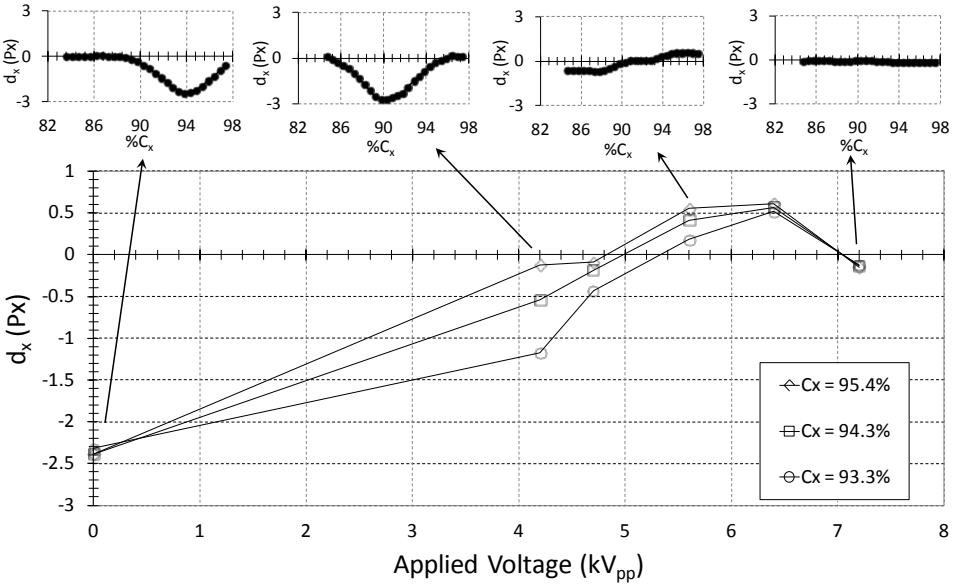

b.)

Figure 13. S3F mean response at various sensor locations, a.) Re = 1.0 x 10^5, b.) Re = 6 x 10^4.

Understanding the response of the S3F at a high level of plasma actuator voltage is complicated. Several factors could play a role in the change in S3F tangential displacement: frequency response of the S3F, pressure gradient effects, changes in pressure gradient and shear stress, and uncertainty in the displacement calculation. A mean negative displacement at Re = 6.0×10^4 and the highest actuator voltage could be due to the uncertainty in the single pass cross correlation method as displacement approaches zero.

The time resolved response of the S3F when the plasma actuator is powered on indicated that the film responds to load change within 1 second. The response of the highly sensitive, ultra low shear modulus, viscoelastic S3F may require further development and material property testing to fully understand. Nonetheless, the response of the S3F shown in Figure 14 makes it useful in a feedback separation control system. With the plasma actuator off the S3F tangential displacement is certainly negative, and when the plasma actuator is turned on the S3F tangential displacement moves positive or towards zero.

The S3F behavior is certainly useful as a sensor for On/off control of the plasma actuator. In order to better understand the time resolved S3F signal response as flow conditions change and separation control is turned on the wind tunnel speed was reduced from a speed at which the S3F displacement was positive and the boundary layer attached to a speed in which the boundary layer is separated over the monitor point. The sampling speed was set to 2.5 Hz and a point at C_x=95.4% was monitored. In one case the actuator was triggered to come on as separation was detected at the S3F monitor point, and the other flow control was left off. The results of both cases are shown in Figure 15. At a Reynolds number of 1.0×10^5 the S3F tangential displacement oscillates from just around zero to approximately 3.5 pixels. Oscillation of the signal is consistent with unsteadiness in the boundary layer downstream of the laminar separation bubble observed in the flow visualization in Figure 2b. The frequency of oscillation is not accurate due to the low natural frequency of the S3F, and slow sampling speed. For the two cases shown, the magnitude of displacement at a Re = 1.0×10^5 is not the same indicating either error in the measurement, or a small change in the boundary layer behavior between runs due to the sensitivity of the laminar boundary layer to minute changes in freestream unsteadiness. When the tunnel speed is decreased the S3F displacement quickly decreases to a negative displacement implying the reattachment point has moved downstream of the monitor point. There is a 6 second transient response period from the time the tunnel inlet Reynolds number reaches 6 x 10^4 until the displacement reaches a consistent value centered about approximately -3 px. For the case in which the plasma actuator is triggered on at an S3F filtered displacement of -1 px the boundary layer separation is significantly diminished within approximately 1.5 second. The actuator significantly increases the S3F displacement at the monitor point to a value that fluctuates between positive and negative with a mean value of -0.1 px.

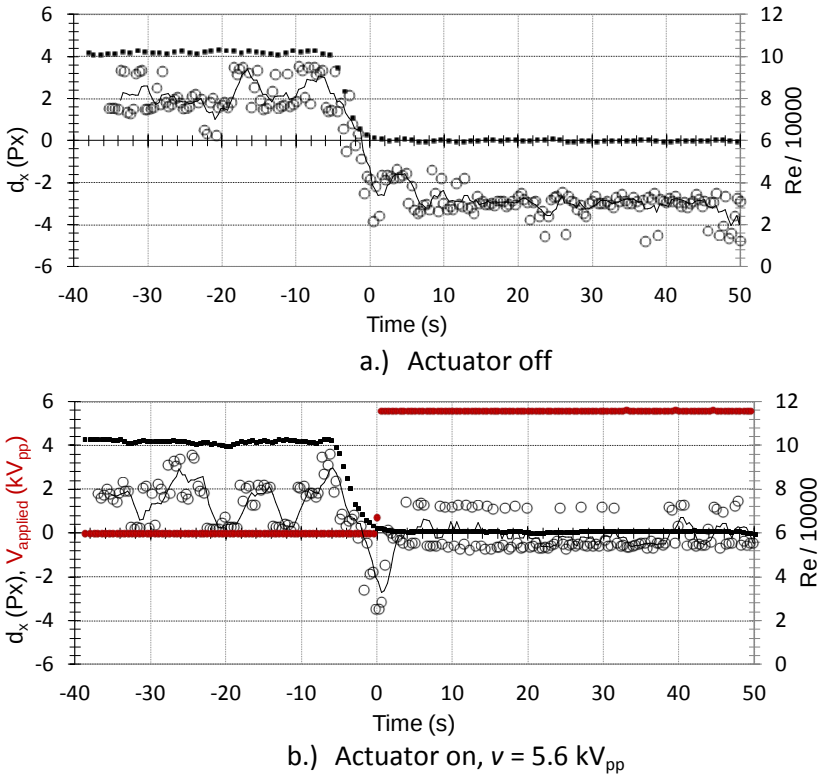

Figure 14. Comparison of S3F response for a sudden drop in free stream velocity, with and without flow control. Triggering of plasma actuator at dx = -1 px, fs=2.5 Hz, monitor point at 95.4%C_x.

B. On/off Controller

As a first demonstration of the closed loop system, the S3F sensor signal was used with an on/off controller. This is similar to the stall control system demonstrated by Poggie et al.[34] using hot film gauges, but with the ability to turn the actuator back off when flow conditions become more favorable. The system used the S3F signal as a trigger to turn on and off the plasma actuator at a predetermined sensor low and high signal level. If the S3F displacement changed to a value less than the lower set point the actuator would be turned on to a predetermined value. If the displacement increased to a value higher than the upper set point the actuator would be turned off. When the displacement was between the upper and lower set points the actuator would remain at its previous setting. Due to the unsteady signal and latency of the boundary layer response, delay logic was built into the controller. Once the actuator state changed, no control changes could be made for a period of t_d. This assured that the system did not oscillate. The sensor signal was low pass filtered to reduce noise.

An example of the on/off controller is shown in Figure 16. The sampling frequency was set to 2.5 Hz and the wind tunnel speed was set to provide a Reynolds number of 1.0 x 10^5 then decreased to the 6 x 10^4. The sensor location was at C_x = 95.4%. The actuator was set to 4.7 kV_{pp} and the sensor signal implies that flow separation was removed in under 2 seconds. With the actuator on, the S3F displacement at the monitoring point was 0.1 pixels. As the wind tunnel speed was increased and the controller detected a positive displacement larger than the upper set point the actuator was powered off. After several seconds the displacement begins to oscillate in a similar manner as prior to the actuator being turned on.

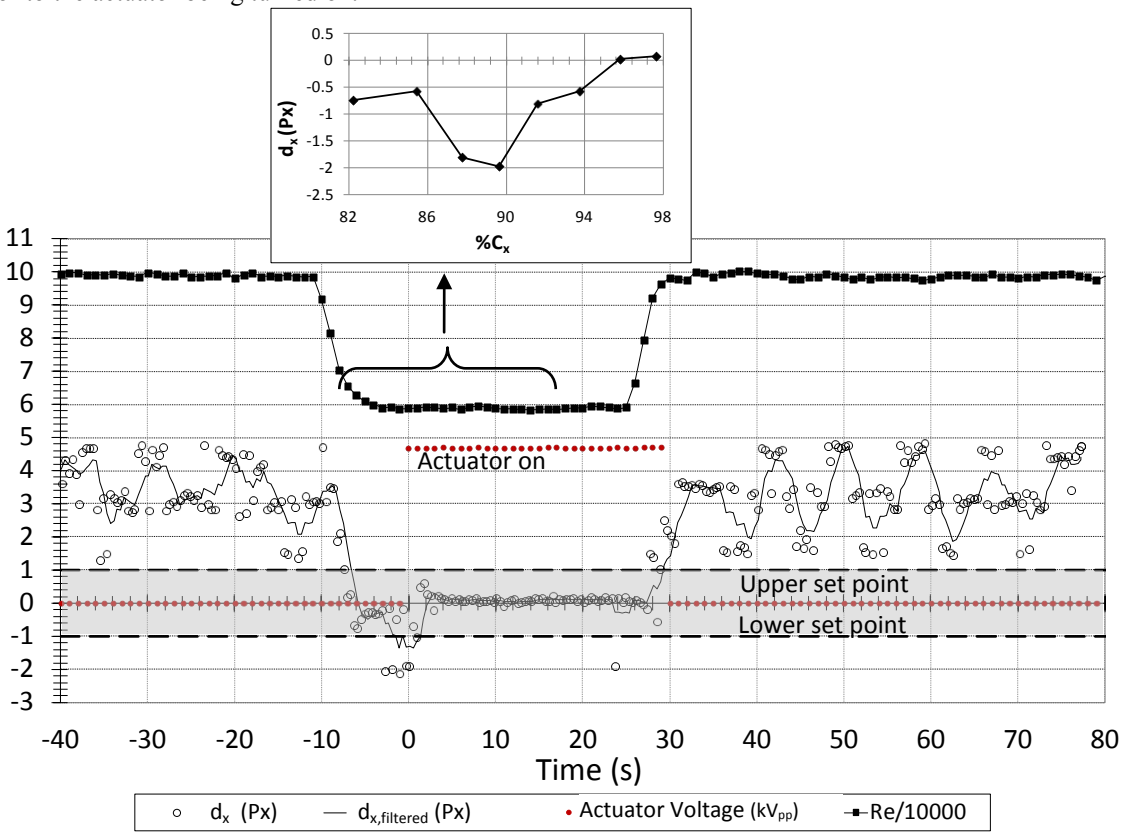

Figure 15. On/off controller, f_s = 2.5 Hz, v = 4.7 kV_{pp}.

C. PI Controller

A proportional integral (PI) controller was implemented to demonstrate closed loop control with a simple automatic controller. The standard form of a PI controller is given by:

$$u(t) = K_P \cdot d_e(t) + K_I \cdot \int_0^t d_e(\varphi) d\varphi \tag{3}$$

where *u(t)* is the output signal.

A discrete version of the PI controller was implemented in the control software. First the sensor signal was low pass filtered, compared to the reference value, then PI controller output calculated by:

$$u(t) = K_P \cdot \bar{d}_e(t) + K_I \cdot \sum_{i=1}^{k} \bar{d}_e(t_i) \cdot \Delta t \tag{4}$$

where $\bar{d}_e(t)$ is the low passed filtered error signal calculated by:

$$\bar{d}_e(t) = d_r - \bar{d}(t) \tag{5}$$

$$\bar{d}(t) = \frac{1}{m} \cdot (d(t) + d(t-1) + d(t-2) \cdots d(t-m-1)). \tag{6}$$

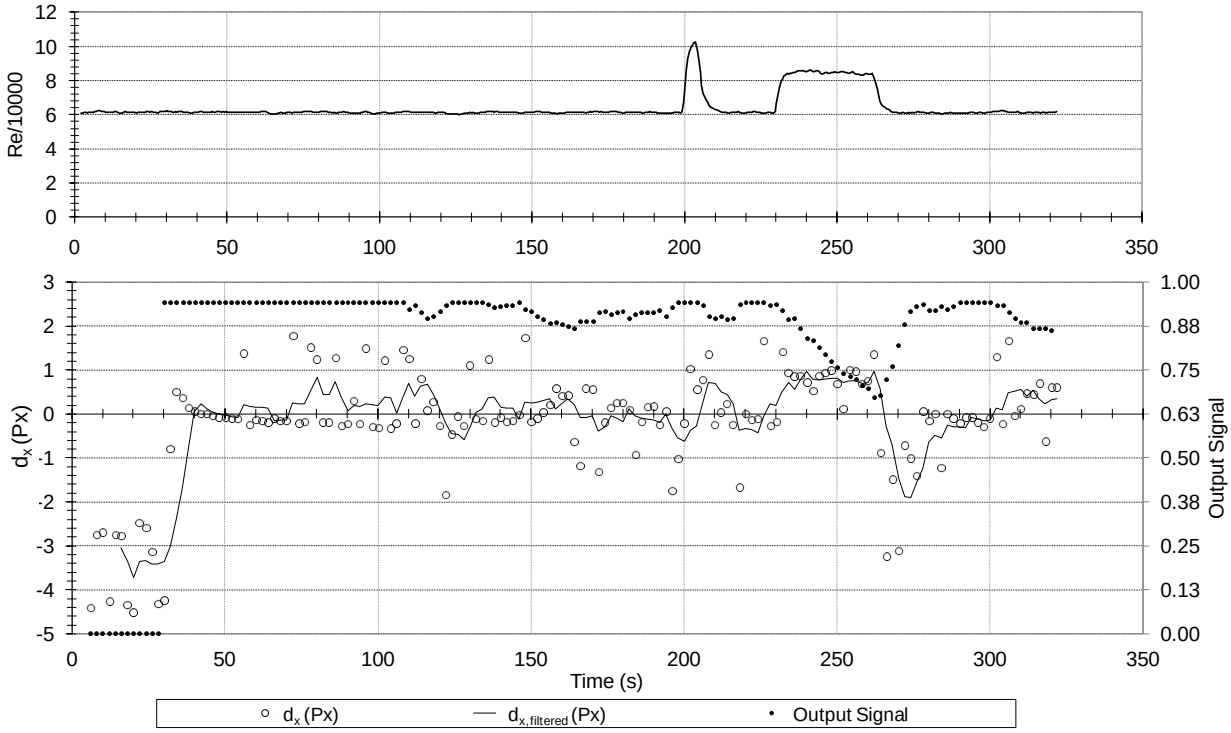

Figure 16. Controller response to external disturbances. Set point d_r = 0 px at C_x = 96%.

The controller gains were manually tuned, first by adjusting the proportional gain, then by adding and increasing the integral gain until a satisfactory response was obtained. It is important to remember that the PI controller used here was un-optimized and a better controller would likely yield better performance. The system sampling rate was typically between 0.5 Hz and 2.5 Hz, which was limited by the hardware available. Only one interrogation window in the field of view was used to simulate a discrete shear stress sensor. In a first example shown in Figure 17 the sampling rate was 0.5 Hz, the reference displacement d_r was 0 pixels at C_x=96%, and the output signal was limited to 0.94 (5.6 kV_{pp}). When the control system is turned on the controller commands maximum actuator output and boundary layer separation was eliminated. After approximately 30 seconds from the start of control the response becomes unsteady and the mean increases slightly resulting in a reduction of the output signal. The reason for the unsteadiness in unknown but assumed to be due to a change in boundary layer behavior. The time resolved reattachment point of the boundary layer with flow control on is spatially unsteady due to the shedding of vortices that form in the separated shear layer as shown in Figure 2. The simple un-optimized PI controller used here does a reasonable job at maintaining the set point even with the highly unsteady signal. At *t*=200s an impulse disturbance is introduced by increasing the flow velocity to a Reynolds number of 1.0×10^5. At the higher Reynolds number the sensor signal would typically be much higher than zero, but the disturbance happens in too short of a time scale to overcome the inherent damping in the system. At *t*=230s a step disturbance is introduced for 30 seconds resulting in a significant increase in sensor signal. The controller responds by decreasing the output signal to maintain the set

point. As the disturbance is removed the controller increases the output signal. The PI controller response is slow, but necessary due to the unsteady input signal. As a second example of the PI controller the wind tunnel was set to a speed providing a Re = 6.0 x 10^4, and the controller turned on. The output signal was increased over the previous example. Figure 18 shows the system response and the top three plots show the mean tangential displacement across the full sensor field of view at three different phases of the run. Three distinct phases of boundary layer response are shown. The first phase is with the feedback control system off. Reverse flow is observed at the trailing edge corresponding to a mean reversed flow vortex inside a separation area. When the control system is turned on the PI controller commands maximum actuator output and the separation was eliminated. After the initial transient response to the actuator step disturbance, the controller begins to decrease the actuator output signal. As the output signal is adjusted the response begins to oscillate with the controller trying to respond and maintain the reference value. The response in Phase 3 shows a mean reattachment point in the vicinity of the monitor point. The unsteadiness in the signal is most likely due to shedding of vortices.

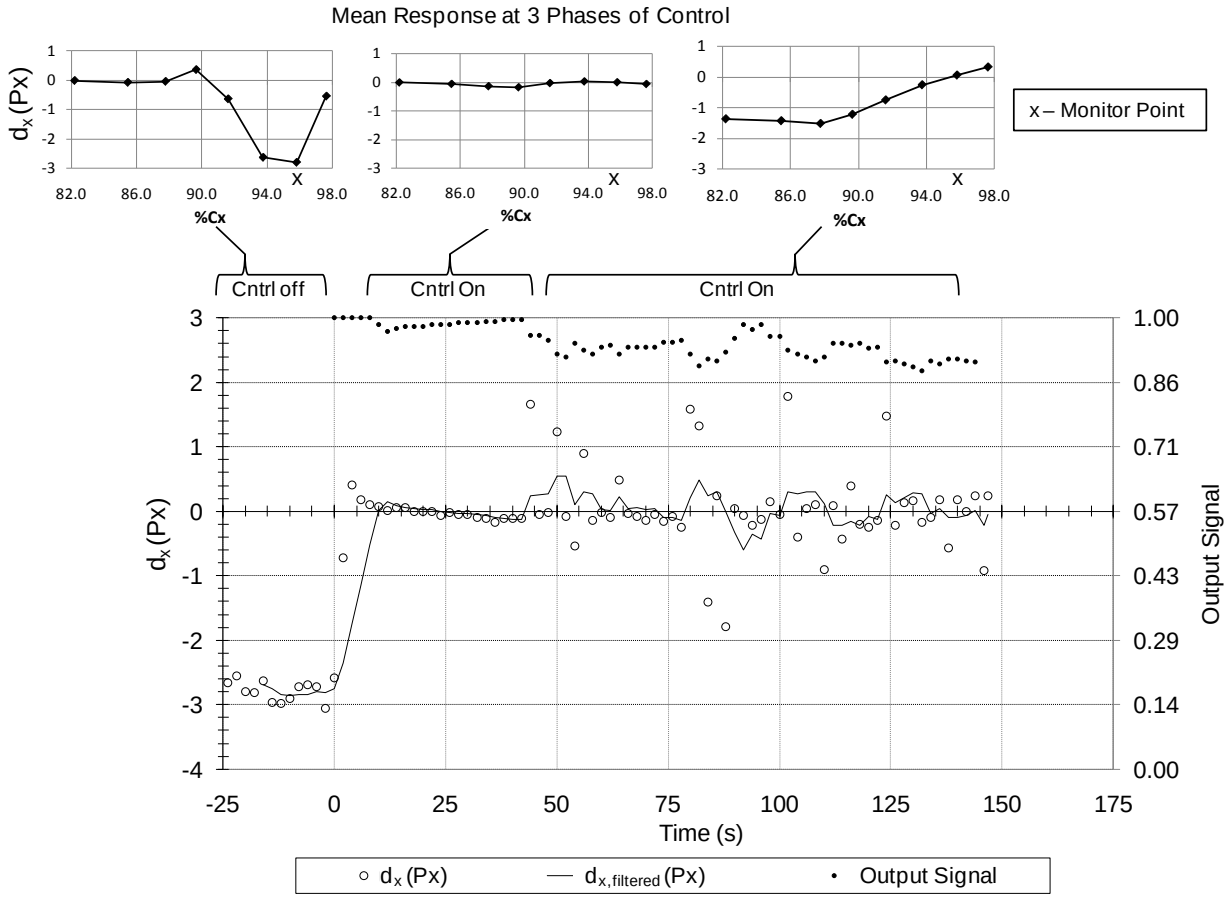

Figure 17. Example of separation control using a PI controller at Re = 6.0x104, fs=0.5 Hz.

The example provided here using a PI controller demonstrates that the S3F sensor signal can be used in a closed loop separation control system. The use of a different type of controller, hardware, and S3F packaging could provide a higher sampling rate, and quicker system response. The system response time using the ultra low S3F in this study are slow and would only make the use of the S3F sensor here useful in a limited number of flight environments. Future efforts should work towards increasing the S3F based sensor sampling speed.

VII. Conclusions

The use of the tangential displacement from an S3F sensor has been used in this study to control low Reynolds number flow separation over an E387 airfoil. A comparison of S3F tangential displacement with C_p and PIV data

indicated that tangential film displacement itself could be used to infer reattachment location. At a Reynolds number of 1.0 x 10^5 a zero crossing was observed that moved upstream in relation to a shift in mean reattachment point. At the lower Reynolds number a strong minimum point was observed that shifted upstream with reattachment point, inferring an upstream shift in reattachment. Examining the mean frequency response of the S3F at two different Reynolds numbers showed a non-linear response curve. Time resolved response of the S3F indicated that the S3F responded in less than 1 second, which was the limit of the sampling rate. The use of S3F with two different, simple, un-optimized feedback controllers was demonstrated in the AFRL/RZ DWT. An On/off controller and PI controller were used to control boundary layer separation as the inlet Reynolds number was reduced from Re = 1.0 x 10^5 to Re = 6 x 10^4. Decreasing the wind tunnel speed resulted in an increase in the extent of separation. By using the S3F signal as an input to a closed loop control system, the increase in separation was detected and subsequently reduced by powering on a plasma actuator.

Future work should focus on increasing frequency response, sampling rate, and repackaging the system into an all-in-one discrete sensor that includes S3F and displacement detection system. This work has demonstrated that a repackaged system, small enough to cleanly integrate into aircraft surfaces, would make a useful flow control sensor for a variety of aerodynamic systems.

References

[1] Lissaman, P. B., 1983. Low-Reynolds-Number Airfoils. *Ann. Rev. Fluid Mechanics 15*, 223-239.

[2] Gad-El-Hak, M. 2000. Flow Control Passive, Active, and Reactive Flow Management 1-2. Cambridge University Press.

[3] Mueller, T. J., Pohlen, L. J., Conigliaro, P. E., And Jansen, B. J., Jr. 1983. The Influence of Free-Stream Disturbances on Low Reynolds Number Airfoil Experiments. *Experiments in Fluids 1*, 3-14.

[4] Mcmaster, J. H., And Henderson, M. L., 1980. Low Speed Single Element Airfoil Synthesis. *Technical Soaring 6*, 1-21.

[5] Bons, J., Sondergaard, R., And Rivir, R., 2001. Turbine Separation Control Using Pulsed Vortex Generator Jets *J. of Turbomachinery 123*, 198-206.

[6] Sondergaard, R., Rivir, R., And Bons, J., 2002. Control of Low-Pressure Turbine Separation Using Vortex-Generator Jets. *J. of Propulsion and Power 18*, 889-895.

[7] Mueller, T. J. 1985. Low Reynolds Number Vehicles. AGARD-AG-288.

[8] Mayle, R. E., 1991. The Role Laminar-Turbulent Transition in Gas Turbine Engines. *J. of Tubomachinery 113*, 509-531.

[9] Smith, D., Amitay, M., Kibens. K., Parekh, D., And Glezer, A., 1998. Modification of lifting body aerodynamics using synthetic jet actuators. *AIAA Paper 98-0209*

[10] Amitay, M., Smith, B. L. And Glezer, A., 1998. Aerodynamic flow control using synthetic jet technology. *AIAA Paper 98-0208.*

[11] Amitay, M., Kibens, V., Parekh, D. E. And Glezer, A., 1999. The Dynamics of Flow Reattachment over a Thick Airfoil Controlled by Synthetic Jet Actuators. *AIAA Paper 99-1001*

[12] Gleazer, A., And Amitay, M. 2002. Synthetic Jets. *Annu. Rev. Fluid Mech. 34*, 503-529.

[13] Corke, T., And Post, M., 2005. Overview of Plasma Flow Control: Concepts, Optimization, and Applications. *AIAA Paper No. 2005-563.*

[14] Wright, K. D., Washburn, A. E., Jordan, J. D., Leighty, B. D., Waltkins, A. N., Ingram, J. L., Oglesby, D. M., Fleming, G. I., Scott, M. A., Balla, R. J., Hart, R. C., Herring, G. C., Fletcher, M. T., Schwartz, R. J., 2002. Measurement Technology for Use in Active Flow Control. *22nd AIAA Aerodynamic Measurement Technology and Ground Testing Conference,* 24-26 June 2002, St. Louis, MO.

[15] Barlow, J., Rae, W., And Pope, A., 1999. "Low-Speed Wind Tunnel Testing", 3rd Edition, John Wiley & Sons, New York.

[16] Bowles, P. And Corke, T. 2009. Stall detection on a leading-edge plasma actuated pitching airfoil utilizing onboard measurement. *AIAA Paper 2009-93.*

[17] Becker, R., And King, R., 2007. Adaptive Closed-Loop Separation Control on a High-Lift Configuration Using Extremum Seeking. *AIAA Journal, 45*, pp 1382-1392.

[18] Spazzini, P., Iuso, G., Onorato, M., Zurlo, N., 1999. Design, test and validation of a probe for time-resolved measurements of skin-friction. *Meas. Sci. Technol. 10,* 631-639.

[19] Buder, U., Petz, R., Kittel, M., Nitsche, W., Obermeier, E. (2008). AeroMEMS Polyimide based wall double hot-wire sensors for flow separation detection. *Sensors and Actuators A: Physical, 142*, 130-137.

[20] JIANG, F., LEE, G., TAI, Y., HO, C., 2000. A flexible micromachine-based shear-stress sensor array and its application to separation-point detection. *Sensors and Actuators 79*, 194-203.

[21] LIU, K., YUAN, W., DENG, J., MA, B., AND JIANG, C. 2007. Detecting boundary-layer separation point with a micro shear stress sensor array. *Sensors and Actators A 139*, 31-35.

[22] KAHNG, S., SCOTT, M., BEELER, G., BARTLET, J., AND COLLINS, R., 2000. An Integrated MEMS Sensor Cluster System for Aerospace Applications. NASA Langley Research Center, Doc ID: 20040086577.

[23] BAUGHN, J. W., BUTLER, R. J., BYERLEY, A. R., AND RIVIR, R. B. 1995. An Experimental Investigation of Heat Transfer, Transition and Separation on Turbine Blades at Low Reynolds Number and High Turbulence Intensity. *ASME Paper 95-WA/HT-25*.

[24] GREGORY, J. W., BAUGHN, J. W., PORTER, C. O, AND BYERLEY, A. R. 2008. Optical Method for Measuring Low Wall Shear Stresses Using Thermal Tufts. *AIAA Journal 46*, 1088-1095.

[25] GROBE, S, SCHRODER, W., AND BRUCKER, C., 2006. Nano-Newton drag sensor based on flexible micro-pillars. *Measurement Science and Technology 17*, 2689-97.

[26] GROBE, S., AND SCHRODER, W. 2008. Mean wall-shear stress measurements using the micro-pillar shear-stress sensor MPS^3. *Measurement Science and Technology 19*, 1-12.

[27] GNANAMANICKAM, E. P., AND SULLIVAN, J. P. 2008. Image Based Sensor for Distributed Wall Shear Stress Measurement. *46th AIAA Aerospace Sciences Meeting and Exhibit, 7-10 January 2008, Reno, NV*.

[28] FERNHOLZ, H., JANKE, G., SCHOBER, M., WAGNER, P., AND WARNACK, D., 1996. New developments and applications of skin-friction measuring techniques. *Measurement Science Technology 7*, 1396-1409.

[29] von Papen, T., Steffes, H., Ngo, H., Obermeier, E., (2002). A micro surface fence probe for the application in flow reversal areas. *Sensors and Acutators A 97-98*, 264-270.

[30] von Papen, T., Buder, U., Ngo, H., Obermeier, E., (2004). A second generation MEMS surface fence sensor for high resolution wall shear stress measurement. *Sensors and Acutators A 113*, 151-155.

[31] Schober, M., Obermeier, E., Pirskawetz, S., Fernholz, H. (2004). A MEMS skin-friction sensor for time resolved measurements in separated flows. *Experiments in Fluids 36*, 593-599.

[32] PATEL, M. P. TILMAN, C. P., NG, T. T., 2003. Active Transparent Stall Control Systems for Air Vehicles. *Journal of Aircraft, 40*, pp. 993-997.

[33] PINIER, ,J., AUSSEUR, J., GLAUSER, M., AND HIGUCHI, H. 2007. Proportional Closed-Loop Feedback Control of Flow Separation. *AIAA Journal 45,* 181-190.

[34] POGGIE, J., TILMAN, C., FLICK, P., SILKEY, J., OSBORNE, B., ERVIN, G., MARIC, D., MANGALAM, S., MANGALAM, A., 2010. Closed-Loop Stall Control System. *Journal of Aircraft, 47*, pp. 1747-1755.

[35] FONOV, S., JONES, G., CRAFTON, J., FONOV, V., AND GOSS, L. 2006. The development of optical techniques for the measurement of pressure and skin friction. *Meas. Sci. Technol. 17*, 1261-1268.

[36] CRAFTON, J., FONOV, S., JONES, E., GOSS, L., FORLINES, A., AND FONTAIN, A. 2008. Measurements of skin friction in water using surface stress sensitive films. *Meas. Sci. Technol. 19*, 801-811

[37] FONOV, S., CRAFTON, J., FORLINES, A., GOSS, L. 2010 Demonstration of a Surface Stress Sensitive Film for Skin Friction Measurements in a Variety of Flows. *27th AIAA Aerodynamic Measurement Technology and Ground Testing Conference, AIAA Paper No. 2010-4800.*

[38] Marks, C., Sondergaard, R., Wolff, M., Anthony, R. "Experimental Comparison of DBD Plasma Actuators for Low Reynolds Number Separation Control" *Proceedings of ASME Turbo Expo 2011*, ASME Paper: GT2011-45397 (submitted).

[39] REEDER, M., CRAFTON, J., ESTEVADEORDAL, J., DELAPP, J., MCNIEL, C., PELTIER, D., AND REYNOLDS, T., 2009. Clean seeding for flow visualization and velocimetry measurements. *Exp. Fluids*, DOI:10.1007/S00348-009-0.

[40] Jacob, J., Ramakumar, K., Anthony, R., Rivir, R., "Control of Laminar and Turbulent Shear Flows Using Plasma Actuators" 4th *International Symposium on Turbulence and Shear Flow Phenomena*, Williamsburg, VA June 27-29, 2005.

[41] Santhanakrishnan, A., and Jacob, J., "Flow Control with Plasma Synthetic Jet Actuators" *J. Phys. D: Appl. Phys. 40* (2007) pp 637-651.

[42] Santhanakrishnan, A., and Jacob, J., "Characterization of Linear Plasma Synthetic Jet Actuators". AIAA Paper No. 2008-538.

[43] Santhanakrishnan, A., Reasor, J., and Lebeau, R. "Characterization of linear plasma synthetic jet actuators in an initially quiescent medium". *Physics of Fluid 21*, 2009, DOI:10.1063/1.3097004.

[44] McQuilling, M., Wolff, M., Fonov, S., Crafton, J., Sondergaard, R., "An Experimental Investigation of a Low-Pressure Turbine Blade Suction Surface Using a Shear and Stress Sensitive Film", *Experiments in Fluids*, V. 44, No. 1, pp. 73-88.

[45] McQuilling, M., Wolff, M., Fonov, S., Crafton, J., and Sondergaard, R., "An Experimental Investigation of Suction Surface Flow Features on a High-Lift LPT", AIAA Paper No. 2008-79.

[46] McQuilling, M., "Design and Validation of a High-Lift Low-Pressure Turbine Blade," Ph.D. Dissertation, Mechanical and Material Engineering Dept., Wright State Univ., Dayton, OH, 2007.

[47] Fonov, S., Goss, L., Jones, E., Crafton, J., Fonov, V. "Identification of pressure measurement system based on surface stress sensitive films," *44th AIAA Aerospace Sciences Meeting,* AIAA Paper No. 2006-1043.

[48] Crafton, J., Fonov, S., Goss, L., Jones, G., Gnanamanickam, E., Sullivan, J., "Validation of an Image-Based Skin Friction Sensor in a Fully Developed Channel Flow," *25th AIAA Aerodynamic Measurement Technology and Ground Testing Conference*, AIAA Paper No. 2006-3839.

[49] Fonov, S., Jones, E., Crafton, J., Goss, L., Fonov, V., "Measurements of Non-Steady Pressure and Skin Friction Fields on Wall Mounted Cube Using Surface Stress Sensitive Film," *45th AIAA Aerospace Sciences Meeting*, AIAA Paper No. 2007-1264.

[50] Crafton, J., Fonov, S., Forlines, A., Goss, L., "Skin Friction Measurements Using Elastic Films", *AIAA Aerospace Sciences Meeting*, AIAA, Orlando, FL, 2010.

[51] Fonov, S., Crafton, J., Goss, L., Jones, G., Schulze, B., "Investigation of Pressure and Friction Force Distributions on a Model Tail Wing Using Pressure Sensitive Paint and Surface Stress Sensitive Film," *22nd International Congress on Instrumentation in Aerospace Simulation Facilities, 2007*, p 147-150, 2007.

[52] Fonov, S., Jones, E., Crafton, J., Goss, L., "Using surface stress sensitive films for pressure and friction measurements in Mini-and Micro-channels," *22nd International Congress on Instrumentation in Aerospace Simulation Facilities, 2007,* p 59-65, 2007.
[53] Crafton, J., Fonov, S., Hsu, K., Carter, C., Gruber, M., "Optical Measurements of Pressure and Shear on a Strut in Supersonic Flow," *45th AIAA Joint Propulsion Conference and Exhibit, 2009*, AIAA Paper No: 2009-5033.
[54] WILLERT, C., AND GHARIB, M., 1991. Digital particle image velocimetry. *Exp. Fluids, 10*, pp 181-193
[55] HUANG, H., DABIRI, D., GHARIB, M., 1997. On errors of digital particle image velocimetry. *Measurement Science Technology*, *8*, pp. 1427-1440.
[56] HART, D. (2000). PIV error correction. *Exp. Fluids 29*, 13-22.
[57] FONOV, V., FONOV, S., JONES, G., CRAFTON, J. 2004. Image Processing Technique for Shear-Stress Optical Measurements. *11th International Symposium on Flow Visualization*, University of Notre Dame, USA.

APPENDIX D

Proceedings of ASME Turbo Expo 2011
GT2011
June 6-10, 2011, Vancouver, Canada

GT2011-46328

AN INVESTIGATION OF REYNOLDS LAPSE RATE FOR HIGHLY LOADED LOW PRESSURE TURBINE AIRFOILS WITH FORWARD AND AFT LOADING

M. Eric Lyall
Air Force Institute of Technology
Wright-Patterson AFB, OH, USA

Paul I. King
Air Force Institute of Technology
Wright-Patterson AFB, OH, USA

Rolf Sondergaard
Air Force Research Laboratory
Wright-Patterson AFB, OH, USA

John P. Clark
Air Force Research Laboratory
Wright-Patterson AFB, OH, USA

Mark W. McQuilling
Saint Louis University
St. Louis, MO, USA

ABSTRACT

This paper presents an experimental and computational study of the midspan low Reynolds number loss behavior for two highly loaded low pressure turbine airfoils, designated L2F and L2A, which are forward and aft loaded, respectively. Both airfoils were designed with incompressible Zweifel loading coefficients of 1.59. Computational predictions are provided using two codes, Fluent (with k-k_l-ω model) and AFRL's Turbine Design and Analysis System (TDAAS), each with a different eddy-viscosity RANS based turbulence model with transition capability. Experiments were conducted in a low speed wind tunnel to provide transition models for computational comparisons. The Reynolds number range based on axial chord and inlet velocity was 20,000 < Re < 100,000 with an inlet turbulence intensity of 3.1%. Predictions using TDAAS agreed well with the measured Reynolds lapse rate. Computations using Fluent however, predicted stall to occur at significantly higher Reynolds numbers as compared to experiment. Based on triple sensor hot-film measurements, Fluent's premature stall behavior is likely the result of the eddy-viscosity hypothesis inadequately capturing anisotropic freestream turbulence effects. Furthermore, rapid distortion theory is considered as a possible analytical tool for studying freestream turbulence that influences transition near the suction surface of LPT airfoils. Comparisons with triple sensor hot-film measurements indicate that the technique is promising and is a worthwhile topic for future research.

INTRODUCTION

Understanding low pressure turbine (LPT) Reynolds number effects is important for engines which must operate at high altitudes, and also for engines with LPT airfoils with very high aerodynamic loading. High-flying aircraft such as unmanned aerial vehicles (UAVs) experience large Reynolds number variation between take-off and cruise conditions. At low Reynolds numbers, which occur at high altitude, the boundary layers contain less energy and thicken, thereby making them more susceptible to separation when subjected to adverse pressure gradients. Although turbines operate with an overall favorable pressure gradient, the suction surface curvature causes localized regions of adverse pressure gradient, which can cause boundary layer separation and increased losses at low Reynolds numbers in LPTs. The loss or efficiency plotted against the Reynolds number is commonly called the Reynolds lapse.

Increasing the aerodynamic load on airfoils is desirable to reduce airfoil count and LPT weight. For given gas angles (constant work coefficient), increasing the aerodynamic load not only results in increased pitchwise spacing, but also in more highly curved airfoils. Increased curvature on the suction surface has potential to strengthen local adverse pressure gradients and cause separation at higher Reynolds numbers as compared to airfoils with reduced loading. The Zweifel loading coefficient, Z_w, is typically used to describe aerodynamic loading and is historically of the order of 1.0 [1]. Recent studies in the literature have focused on much higher loading levels. For example, Praisner et al. [2] investigated the loss behavior for airfoils with $1.15 < Z_w < 1.8$ with the aim of

U.S. Air Force Public Affairs Office Case No. 88ABW-2011-0903

reducing airfoil count. Furthermore, low Reynolds number performance is also strongly dependent on the pressure coefficient profiles.

This paper focuses on the computational challenges of predicting midspan low Reynolds number performance. The airfoils used in the study are discussed first, followed by the transition models employed. Computational methods are presented next, followed by a discussion of the experimental arrangement and instrumentation for providing benchmark transition models. The results are then presented, which focus on the predictive quality of the transition models, and the interpretation of the results relative to the way the transition models were developed and calibrated. Finally, rapid distortion theory is discussed as a possible analytical technique to study turbulence effects that eddy viscosity models fail to capture.

AIRFOIL DEVELOPMENT

Recently, the Propulsion Directorate of AFRL developed a series of low pressure turbine airfoils for studying low Reynolds number, high-lift aerodynamics. These airfoils were designed in keeping with the Pratt & Whitney Pack B gas angles. The first pair of blades, L1M and L1A, were designed with incompressible Zweifel coefficients 17% greater than Pack B (i.e., Z_w=1.34 for L1M and L1A, Z_w = 1.15 for Pack B) and both mid- and aft-loaded pressure distributions, respectively. The L1M (level one increase in lift, mid-loaded), was first tested and analyzed outside of AFRL by Bons et al. [3] experimentally, and computationally by Gross and Fasel [4]. The airfoil was shown to have a significantly better Reynolds-lapse characteristic than the Pack B airfoil. The L1A (aft-loaded) airfoil was designed to the same level of loading as L1M, but it had too high a degradation in performance at low Reynolds numbers to make it more suitable for flow control studies under the NASA Fundamental Aeronautics Program [5, 6]. Subsequently, both airfoils were used in an investigation of the aerodynamic challenges in the operation of variable-speed power turbines for rotor-craft applications [7].

More recently another pair of cascade airfoils with incompressible Zweifel coefficients of 1.59 was designed to the Pack B gas angles. Again, the airfoils differed with respect to their loading conventions. The first one, designed by McQuilling [8], was front-loaded (L2F) whereas the second one that appears for the first time here, is more aft-loaded (L2A). This pair of airfoils was designed to test the limits of high lift, low Reynolds-number operation enabled by increases in the fidelity of CFD transition modeling. Both airfoils were predicted to have better Reynolds-lapse characteristics than the P&W Pack B despite increases in loading that were of order 38% over that high-lift airfoil.

Like the L1A and L1M, the AFRL L2-series of high-lift airfoils were designed using in-house analysis tools (TDAAS) that include the profile generator of Huber [9]. That algorithm uses Bezier curves in conjunction with typical leading- and trailing-edge specifications (e.g., wedge angles, edge radii of curvature, gage areas, and uncovered turning) to define airfoil shapes using a small number of control points in keeping with the method described by Casey [10]. Once the profile was defined, the grid generator and RANS solver described by Dorney and Davis [11] were used along with an ad hoc implementation of the transition models of Praisner and Clark [12] to determine airfoil performance. Graphical User Interfaces (GUIs) and both design optimization [13] and design-of-experiments techniques [14] were used during the design process to define the shape of the profiles.

DISCUSSION OF TRANSITION MODELS

Both codes used in the present study, TDAAS and Fluent, utilized transition models for low Reynolds number calculations. Walters and Leylek [15, 16] developed the transition model implemented in Fluent, which is the k-k_l-ω three-equation model, designed for modeling both natural and bypass transition. In natural transition, laminar boundary layers grow, eventually becoming unstable with the formation of Tollmien-Schlichting waves. As the flow continues, the Tollmein-Schlichting waves break down, forming turbulent spots, which are followed by a fully turbulent boundary layer. In bypass transition, freestream turbulence causes the natural process to be bypassed. (Schlichting and Gersten [17] discuss both types of transition.) The three transport equations in Fluent are used to solve for the turbulent kinetic energy, k, the laminar kinetic energy, k_l, and the specific dissipation, ω. Walters and Leylek [15, 16] added the transport equation for k_l to model streamwise laminar fluctuations in a pre-transitional boundary layer that eventually transitions to a turbulent boundary layer. After transition initiates, k_l is transferred to k to model the transition to full turbulence.

The k-k_l-ω model in Fluent was originally proposed as k-k_l-ε [15], where ε is the farfield turbulence dissipation rate. The authors then recast the transport equation for ε in terms of ω [16]. The model constants were determined from direct numerical simulations of fully turbulent channel flow and flat plate boundary layer experiments [16]. The latter model [16] is commercially available in Fluent and was used in the present study.

Because the Fluent k-k_l-ω model is recent, there are few studies in the literature using it. Sanders et al. [18, 19] reported that the model is a more accurate predictive tool for LPT airfoils as compared to conventional RANS based models. Cutrone et al. [20] compared the predictive quality of the k-k_l-ω model with five other transition models, all derived by combining a transition onset correlation with an intermittency factor based transition model to model the transition length. Cutrone et al. [20] concluded that the k-k_l-ω model performed best in all cases, except a flat plate case that had a strong pressure gradient in the transition region.

The separated flow transition model of Praisner and Clark [12] was employed in TDAAS for the present study. This model utilizes a single correlation from experiments to predict the turbulent reattachment point of a laminar separation bubble. The transition model is coupled with the Baldwin-Lomax [21] algebraic turbulence model to close the RANS equations. The

model was derived from 47 experimental test cases for separated flow transition. Using dimensional analysis, Praisner and Clark [12] found that the separation bubble length correlated well according to Eq. (1),

$$\frac{B}{SS_{sep}} = 173.0 Re_{\theta,sep}^{-1.227} \quad (1)$$

where B is the distance from separation onset to turbulent reattachment (bubble length), $Re_{\theta,sep}$ is the momentum thickness Reynolds number at separation onset, and SS_{sep} is the suction surface distance from the leading edge to the separation point. The predictions presented in this paper did not utilize Praisner and Clark's [12] attached flow transition model. It is believed that using only the separated flow model is more conservative, since depending on the turbulence level, transition may occur in the experiment upstream of separation.

Praisner et al. [22] presented experimental validation data for the attached and separated flow models. The models accurately predicted the Reynolds lapse at midspan for the pack B profile, based on cascade experiments of Bons et al. [23]. Multistage 3D simulations were compared with experimental data from Binder et al. [24]. Where the flow was primarily two-dimensional, efficiency predictions using the attached and separated flow transition models agreed well with experiment, outperforming fully turbulent predictions, which underpredicted the efficiency between 1% and 2%. Transition modeling did not improve agreement in the endwall regions. Schmitz et al. [25] applied the Praisner and Clark [12] separated flow transition model for designing a research LPT stage, which was tested in a high-speed rotating rig. Total pressure loss predictions were performed as low as Re = 20,000, indicating stall-free operation for all Reynolds numbers. The researchers operated the rig as low as Re = 14,000 (based on inlet velocity and true chord), without observing separation. Again however, spanwise efficiency predictions were poor in the endwall region. With or without transition modeling, RANS-based turbulence models predict total pressure loss and efficiency poorly in the endwall region.

COMPUTATIONAL METHODS

The authors provide computational predictions using both the commercial code Fluent, and AFRL's TDAAS system. The computational procedures were quite different for the two codes. In Fluent, the pressure-based solver was used for all calculations due to low Mach numbers in the experiment ($M_{ex} < 0.06$). The RANS equations were closed using the k-k_l-ω transition model [16]. Second order accurate finite volume spatial discretization was utilized. For time integration, either steady or unsteady formulations were used, depending on the Reynolds number. In general, the steady solver was used for high Reynolds numbers. At low Reynolds numbers, solutions usually failed to converge using the steady solver, which was evident by the lift coefficient and scaled residuals not reaching steady state. In that case, unsteady solutions were computed with an implicit, dual time-stepping formulation with second order accuracy. Solutions were assumed converged when the lift coefficient became steady periodic, indicating that all effects of initialization had decayed.

The domain modeled in Fluent was based on a single airfoil, with the inlet extending an axial chord upstream of the leading edge. The outlet was placed two axial chords downstream of the trailing edge. Periodic boundaries were assigned mid-pitch from the pressure and suction surfaces to model a single blade passage. The calculations were carried out using two dimensional, multi-block hybrid grids. A structured block with an O-type topology was used for discretizing the boundary layer around the airfoil surface, while an unstructured block was used for discretizing the remainder of the domain. Refining the grid to approximately 60,000 cells gave grid-independent results. In addition, boundary layers were sufficiently refined, with y^+ levels less than unity along the wall.

McQuilling [8] provides a detailed discussion of the computational procedures using TDAAS. Relevant details of the solver, grids and calculation procedure are discussed here for convenience. The grid generator and flow solver is that described by Dorney and Davis [11]. The solver is density-based and is used to solve the RANS equations using an implicit dual time stepping, time-accurate approach. The time integration scheme is second order accurate, with convergence being obtained when the pressure field downstream of the trailing edge becomes steady periodic. The spatial discretization is based on a third order accurate, finite difference upwinding scheme. Since the Dorney and Davis [11] flow solver was not preconditioned to handle low Mach number flows, the exit Mach number was set at $M_{ex} = 0.2$ to reduce the stiffness of the governing equations while maintaining incompressible flow. Reynolds numbers were matched by reducing the fluid density.

Due to using finite differencing, the solver in TDAAS required structured grids. The grids were based on a multi-block O-H topology. The O-type mesh was used for discretizing the boundary layer, with H-type meshing used for the remainder of the domain. Due to higher order finite differencing and structured meshing, grid independent results were achieved with approximately 7,000 grid points for the 2D passage. Furthermore, y^+ levels along the wall were less than unity.

Implementation of the Praisner and Clark [12] separated flow transition model in TDAAS requires a two-step procedure. A converged fully laminar solution is computed first to obtain $Re_{\theta,sep}$ and SS_{sep} as inputs for Eq. (1). After using Eq. (1) to define the reattachment point, the turbulent wall boundary layer downstream of the separation bubble is computed using the Baldwin-Lomax algebraic model [21]. Note that for reattachment points predicted beyond the trailing edge, only the laminar solution is utilized, resulting in outright separation. For more information regarding implementation, the reader is referred to Praisner and Clark [12].

EXPERIMENTAL METHODS

The experiments were conducted using the AFRL low speed wind tunnel facility. This wind tunnel is an open loop induction type, with the flow entering a bell-mouth contraction and passing through a turbulence-generating. The turbulence grid is comprised a lattice of horizontal and vertical 25.4 mm round bars, with 76.2 mm center spacing. The center blade of the cascade is approximately 90 bar diameters downstream of the grid. The turbulence grid produces a turbulence intensity of Tu = 3.1%, with an integral scale of L_{in} = 39.2 mm at about $1.4C_{ax}$ upstream of the cascade. Aft of the cascade, the flow passes through the exit duct to enter the fan.

A schematic of the test section is given in Fig. 1. As shown, the cascade is comprised of seven airfoils. The end-flow adjusters were used to control the bypass flow around the outside of the cascade to achieve periodicity. A single outer tailboard was used to set the exit angle at Re = 100k. The authors acknowledge that the exit angle will change as Re decreases, approaching stall. Exit traverse data were collected at midspan, $0.75C_{ax}$ downstream of the cascade in the axial direction. The traverse plane origin is defined downstream of the middle blade as the intersection of the tangent line projected from the pressure side of the trailing edge, and the traverse plane. The tangent line projected from the pressure side of the trailing edge originates from the intersection of the trailing edge circle and the pressure surface. An additional traverse plane is defined inside a single passage at midspan, at $0.5C_{ax}$. The origin of this traverse plane is defined at the blade suction surface. The same cascade definitions are used for both airfoils in the present study, the L2A and L2F. Table 1 summarizes the relevant geometric data and flow conditions. The flow angles are design point values.

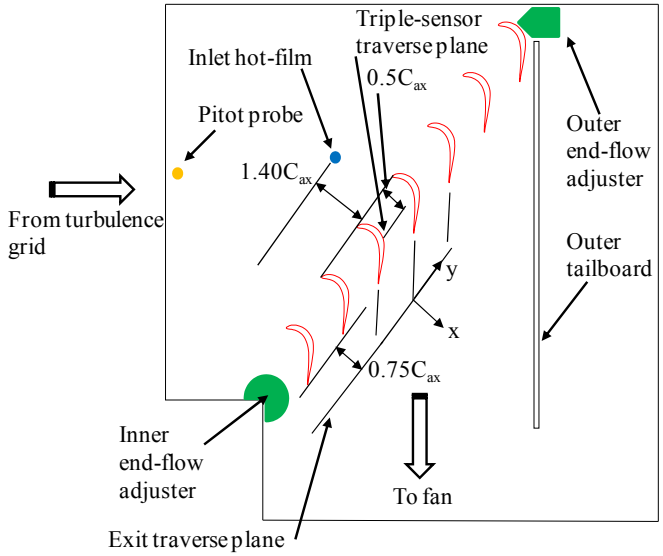

Figure 1. Schematic of AFRL low speed wind tunnel test section.

An upstream stationary pitot probe and a kiel probe in the exit traverse plane were used to measure total pressure loss. At 3.2 mm, the kiel probe diameter was less than 2% of the blade pitch, providing sufficient resolution within the wakes. The ambient pressure was measured with a laboratory barometer and freestream fluid temperatures were measured using type J thermocouples. An IFA300 constant temperature anemometer was used with single normal hot-film probes (TSI 1211-20) for obtaining velocities, turbulence intensities, and integral length scales at the inlet, and exit traverse. A TSI 1299-20-18 triple sensor hot-film probe was used to obtain freestream turbulence measurements within the triple sensor traverse plane (Fig. 1), but only for the L2A cascade. All three sensors of the triple probe were contained in a 2 mm measurement diameter. The probe stem however, was 4.6 mm in diameter.

Table 1. Cascade Geometry and Flow Conditions

Axial chord, C_{ax}	152.4 mm
Pitch/axial chord, P/C_{ax}	1.221
Span/axial chord, H/C_{ax}	5.75
Zweifel coefficient, Z_w	1.59
Inlet flow angle, α_{in}	35°
Exit flow angle, α_{ex}	58°
Inlet turbulence Intensity, Tu_{in}	3.1%
Streamwise integral scale at inlet, L_{in}	39.2 mm
Max exit Mach number, M_{ex}	0.053

All hot-film probes were calibrated using a TSI Model 1127 velocity calibrator. Typical calibration curves included 18 points, spanning the measured velocity range in the experiment. Table 2 displays the calibration velocity ranges for the probes. During calibration, the triple sensor probe was placed in a zero pitch/yaw configuration for the entire velocity range. An analytical technique, similar to that described by Lekakis et al. [26] was used to obtain the velocity angles and magnitudes in the experiment, given effective cooling velocities from the three sensors. In the experiment, flow angles relative to the probe axis were small, at less than 6°. Angle measurements on the calibration stand however, were within ± 0.5° of the actual velocity vector for ±12° pitch and yaw.

Table 2. Calibration velocity ranges for hot-film probes.

Probe	Min Velocity, m/s	Max Velocity, m/s
Inlet film	1.5	11.5
Exit film	10	18.5
Triple-film	5	29

Besides ambient pressures, all other data were sampled using National Instruments hardware and software. When capturing data used for computing the integral scales, the analog signal was conditioned with a low pass filter at a 5 kHz cutoff frequency. The analog signal was sampled at 20 kHz, well above the Nyquist criterion to prevent aliasing. The

integral length scales were computed by first calculating the autocorrelation function, as given by Eq. (2).

$$R_{xx}(s) = \frac{\int_0^T u(t)u(t+s)dt}{\int_0^T u(t)u(t)dt} \quad (2)$$

The integral time scale, τ, was then taken as the value of *s* such that $R_{xx}(s)= 1/e$, as proposed by Tritton [27]. The integral length scales were then computed for the streamwise direction by invoking the frozen turbulence approximation and multiplying τ by the mean velocity.

All uncertainties were calculated at 95% confidence. Uncertainties for the Reynolds number and total pressure loss coefficients were estimated using the partial derivative and root-sum-square method of Kline and McClintock [28]. The uncertainty of the peak loss coefficients and Reynolds numbers were less than 5% and 3.5%, respectively, of the measured values over the entire Reynolds number range. Hot-film velocity measurements were the largest source of uncertainty.

The uncertainty of the turbulence measurements downstream of the cascade was estimated by constructing confidence intervals for ensembles of 25 data sets for each measurement location. Within the wakes, the precision error of the integral scales was within 5% of the measured values. In the freestream between the wakes, the precision error was larger, but typically within 10% of the measured values. (Roach [30] reported that uncertainties in calculating integral scales can easily reach 10%.) The precision uncertainty for the turbulence intensity was lower, at less than 3% of the mean measured value. Upstream of the cascade, sufficient data were captured to reduce the precision uncertainty of the inlet integral scale and turbulence intensity to less than 2% of the mean values. Precision error also dominated for the triple sensor measurements. Mean square velocity fluctuations were within 10% of the measured values for the triple sensor probe.

RESULTS AND DISCUSSION

In this section of the paper, comparisons between computational and experimental data are presented and discussed in terms of predictive quality. Discrepancies between predictions and experiments are then discussed relative to the way the transition models emulate the flow physics.

Reynolds Lapse Predictions

It is imperative that the designer has confidence in the general trend of the predicted lapse curve. Said another way, it is necessary to know whether the boundary layer will separate, transition, and re-attach with only a modest increase in loss with decreasing Reynolds number, or whether the viscous layer separates without re-attachment. If the latter prevails, then the designer needs to know the Reynolds number at which this occurs.

The Reynolds lapse for the front-loaded L2F airfoil is presented in Figure 2. As shown, the losses for this airfoil increase modestly with decreasing Reynolds number as compared to the Pack B. This result, first observed by McQuilling [8] is significant, considering that the Pack B and L2F were designed with $Z_w = 1.15$ and $Z_w = 1.59$, respectively. McQuilling [8] also presented detailed suction surface boundary layer measurements for L2F. Based on shear stress measurements, McQuilling [8] showed that a separation bubble is present on the airfoil in the range of 25k < Re < 75k. McQuilling [8] also presented hotwire measurements down to 1 mm from the suction surface without observing reversed flow, indicating an extremely thin separation bubble. The Reynolds number at separation onset is unknown for L2F.

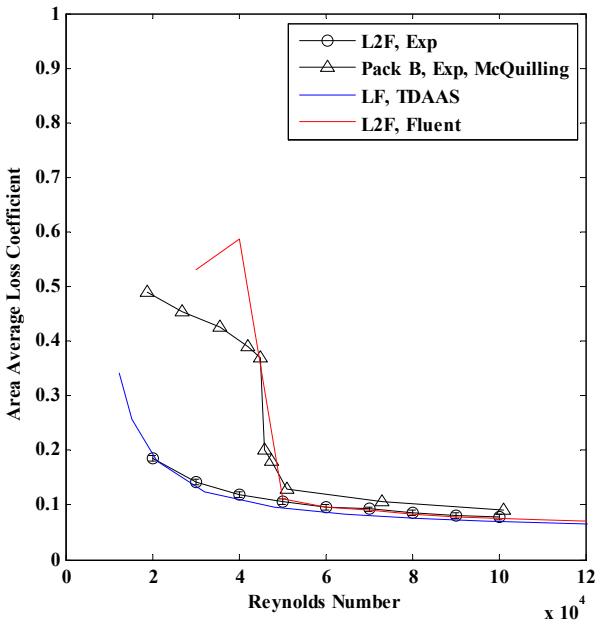

Figure 2. Experimental and computational Reynolds lapse for L2F. The Pack B results are from McQuilling [8].

Predictions for L2F using TDAAS agree well with the measurements across the entire Reynolds number range, being only slightly below the error bars. The calculations using Fluent however, predicted L2F to stall below Re = 50k, similar to Pack B. Before stall occurs, the Fluent predictions are within experimental uncertainty. Fluent predictions were not computed at lower Reynolds numbers because they were considered unnecessary after determining the stall location.

Figure 3 presents the Reynolds lapse for the L2A airfoil. Unlike L2F, the measurements indicated stall below Re = 40k, which is still a slight improvement over Pack B. At present, no suction surface boundary layer measurements are available for L2A. Overall, lapse predictions using TDAAS follow the trend quite well, but under-predict the loss magnitude within the range of 40k < Re < 90k. The TDAAS calculations also reasonably predict the Reynolds number at which stall occurs. The Fluent calculations predict earlier stall at nearly twice the Reynolds number of the measured stall location. Similar to L2F, the Fluent loss predictions for L2A are within experimental uncertainty before the airfoil stalls. Additionally,

neither code agrees well with the measured losses once stall occurs.

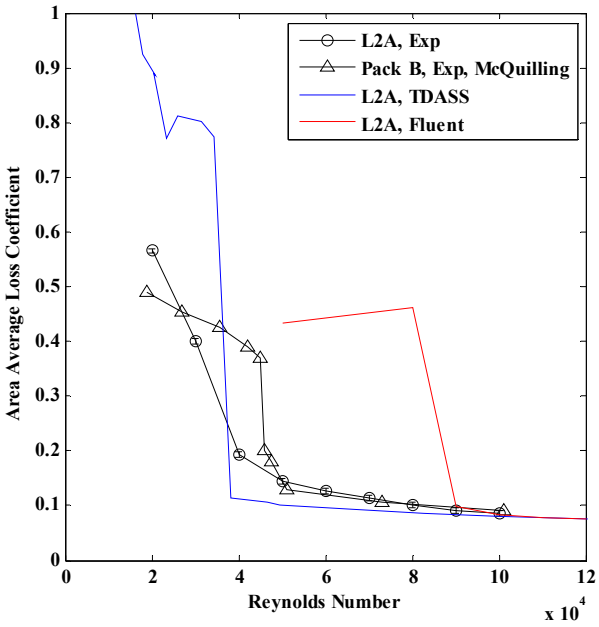

Figure 3. Experimental and computational Reynolds lapse for L2A. The Pack B results are from McQuilling [8].

The differences in the Reynolds lapse for the L2A and L2F airfoils are best explained by examining the pressure loading distributions. Figure 4 shows the pressure coefficients for both airfoils at midspan. These data were obtained computationally using Fluent's implementation of Shih et al.'s [31] realizable k-ε turbulence model. The fully turbulent computations eliminated separation bubbles present on the suction surface to provide cleaner plots for illustrative purposes. Inviscid calculations using the Navier-Stokes grids had instabilities near the trailing edge and were not used. As shown, the loading is significantly different for the two airfoils. Peak loading for L2F and L2A occur at 25% and 60% axial chord, respectively. Because of front loading, the diffusion length on the suction surface of L2F is nearly 1.9X longer than L2A's diffusion length. As a result, the adverse pressure gradient is more severe for L2A, resulting in stall at higher Reynolds numbers. The improved stall performance of L2F however, does not make it an obvious design choice over L2A. Front loaded airfoil performance is much more sensitive to small changes in geometry [1], and generally result in higher endwall losses [32]. These factors must be considered during design.

It is easier to understand the differences in measured airfoil performance than the differences in computational predictions. As described above, the two transition models used in the present study were developed using very different design philosophies. The transition model implemented in TDAAS is correlation based, and was calibrated using a database of cascade results, comprised of both compressors and turbines. This model yielded superior stall predictions because it was developed using flows with high streamline curvature and straining, similar to the flow being studied. Because this model requires a previously converged laminar solution before implementing the turbulent solution, users may consider its use cumbersome.

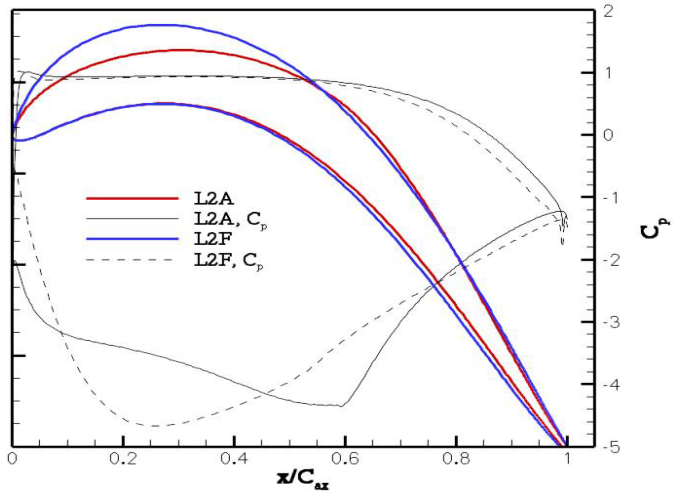

Figure 4. Pressure loading distributions for the L2A and L2F airfoils.

The k-k_l-ω model, which is available in Fluent, requires only a turbulent integral scale and intensity as boundary conditions, similar to fully turbulent RANS based, eddy viscosity turbulence models. The high loading levels present for the L2A and L2F airfoils were challenging for this model, which predicted stall prematurely for both airfoils. The model constants were calibrated with fully turbulent channel flow and flat plate boundary layer experiments [16], which may not accurately model the turbulence development when the flow is highly strained.

Furthermore, it is important to consider the methods for determining the turbulent boundary conditions implemented in Fluent to give confidence that they were not the cause of premature stall. The inlet turbulence intensity was determined to be 3.1% ± 0.062% at 95% confidence (2% of mean measured value). Since the turbulence intensity is obtained with straightforward statistical calculations, this result is believed to be a unique and valid inlet boundary condition. On the other hand, various methods exist for computing the turbulent integral scale, implying that the measured integral scale in the present study is not unique.

Sanders et al. [18] however, performed a parameter study using Fluent's version of the k-k_l-ω model to investigate the effect of inlet turbulence integral scale on the maximum wake loss coefficient of a cascade of LPT airfoils. The LPT airfoils modeled in their study were designed for use in the same experimental facility described in this paper, but with lower loading (Z_w = 0.94, C_{ax} = 177.8 mm). Sanders et al. [18] found that for L_{in} > 14 mm, the results were insensitive to the integral scale. Since the measured integral scale in the present study is L_{in} = 39.2 mm, a 10% variation due to a difference in calculation procedures as suggested by Roach [30], is not

expected to influence the present results. Differences between the predictions and measurements are therefore attributed to the way the flow physics are modeled. The next section of the paper explores this topic.

Reasons for k-k_l-ω Stall Behavior

This section of the paper presents midspan turbulence measurements inside a single passage of the L2A cascade (see Fig. 1). Considering that freestream turbulence interacts with developing boundary layers and influences transition, it is important to understand the difference between the measured and predicted turbulence development. The turbulent kinetic energy development at $0.5C_{ax}$ is given in Fig. 5. As shown, the predicted and measured turbulence development is qualitatively different. The measured turbulence energy decreases towards the wall, whereas the predicted turbulence energy increases. Also observe for the predicted turbulence development, that the kinetic energy goes to zero inside the boundary layer. It is interesting that Fluent predicted stall prematurely, even with computed turbulence energy levels more than 20% higher than the measured values in the freestream near the edge of the boundary layer. The measured Reynolds stresses give additional insight into the discrepancy.

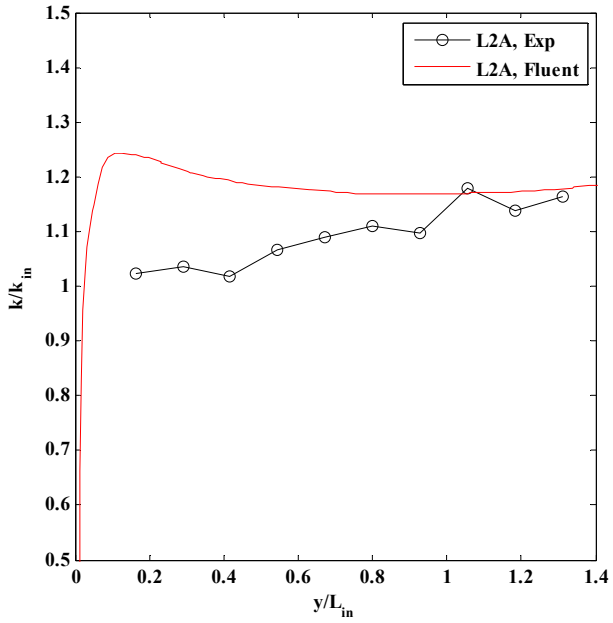

Figure 5. Turbulent kinetic energy at $0.5C_{ax}$ for the L2A cascade, normalized by the inlet turbulent kinetic energy. Re = 100k.

Figure 6 shows the measured components of the Reynolds shear stress tensor across the passage at $0.5C_{ax}$. The triple sensor results are presented in streamline coordinates. Therefore, u-fluctuations are in-line with the mean velocity vector, and the v and w-fluctuations are orthogonal to the mean velocity vector with zero mean velocity. Furthermore as the probe position approaches the wall, the v-velocity fluctuations become closer to the wall-normal direction. Because the turbulence entering the cascade was generated using a square lattice grid and was in the latter stages of decay (Tu = 3.1%), the turbulence is nearly isotropic, as described by Roach [30]. As shown in Fig. 6 however, the effect of high strain rates to accelerate the flow over the suction surface, and also streamline curvature has a dramatic effect on the incoming turbulence. Recall from Fig. 5 that the measured overall turbulent kinetic energy close to the wall is nearly the same value as the incoming turbulence. The turbulence energy is therefore redistributed directionally. The spanwise fluctuation component, $\langle w^2 \rangle$, is amplified close to the wall. The $\langle u^2 \rangle$ component gradually increases approaching the wall, whereas $\langle v^2 \rangle$ is damped.

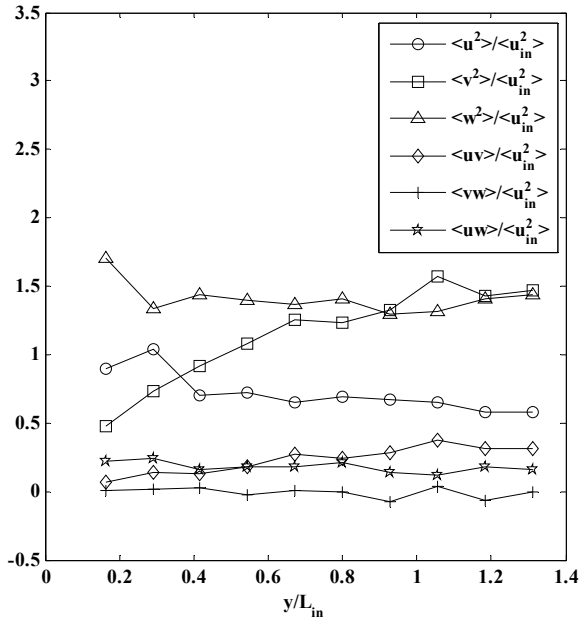

Figure 6. Measured components of the Reynolds stress tensor within the passage at $0.5C_{ax}$ for the L2A cascade. Re = 100k.

The Reynolds shear stresses are most interesting in Fig. 6. As shown, the <uv> and <uw> components are positive across the measurement range. The <vw> term is near zero, indicating negligible correlation between the two fluctuation components. The <uv> component decreases across the passage approaching the wall, whereas <uw> increases. The increasing <uw> term approaching the wall is a very interesting result. Since the measurements were taken at midspan of the passage, the RANS x-momentum equation indicates a negligible effect on the mean flow due to <uw>, based on symmetry. Furthermore, the z-direction momentum equation simply becomes a balance in shear stress gradients at midspan. The <uw> term does not appear in the y-momentum equation. Although <uw> does not have an apparent effect on the mean flow, it may actually be an instability mechanism. If <uw> remains significant approaching the wall, it may interact with streamlines in the edge of the developing boundary layer. Considering that <uw>

indicates a correlation between the streamwise, and dominant spanwise fluctuation components, its effect may be to buckle the streamlines and influence transition. This mechanism occurs in the x-z plane as opposed to instabilities in the x-y plane, possibly influencing both attached and separated flow transition processes.

The primary implication for turbulence modeling is that <uw> is zero by definition according to the eddy-viscosity hypothesis for two-dimensional flows. Any significant effect of <uw> in the experiment was not captured using Fluent. Wilcox [36] points out that the eddy-viscosity hypothesis fails for flows with high streamline curvature and extra rates of strain, both of which are present for high lift LPT flows. Researchers typically apply corrections to turbulence models to improve performance for challenging flows. The freestream turbulence measurements presented in this paper provide a possible explanation for the k-k_l-ω model's poor performance in predicting the Reynolds lapse, primarily due to a failure in the eddy-viscosity hypothesis. Because the TDASS predictions were based on empirical modeling for similar cascade flows, all the anisotropic turbulence effects were captured implicitly. This is why TDASS predicted stall more accurately than the Fluent predictions using the k-k_l-ω model.

As a consequence of high strain rates near the suction surface of LPT airfoils, rapid distortion theory may provide a means outside of DNS and LES to gain insight into the freestream turbulence field that interacts with the developing boundary layer. The purpose is to examine an alternative technique that does not require supercomputing facilities to study freestream turbulence effects. Improved knowledge of the freestream turbulence field can be used to apply corrections to eddy viscosity based transition models. The next section of this paper investigates this possibility.

Freestream Turbulence and Rapid Distortion Theory

Governing equations for the fluctuating velocity components in a turbulence field are obtained by subtracting the RANS from the Navier-Stokes equations. Pope [33] presents these equations in incompressible form while neglecting the energy equation as,

$$\frac{Du_j}{Dt} = -u_i \frac{\partial \langle U_j \rangle}{\partial x_i} - u_i \frac{\partial u_j}{\partial x_i} + \upsilon \nabla^2 u_j - \frac{1}{\rho}\frac{\partial p}{\partial x_j} \qquad (3)$$

and

$$\frac{1}{\rho}\nabla^2 p = -2\frac{\partial \langle U_i \rangle}{\partial x_j}\frac{\partial u_j}{\partial x_i} - \frac{\partial^2 u_i u_j}{\partial x_i \partial x_j}, \qquad (4)$$

where the bracketed and lower case terms are mean, and fluctuating quantities, respectively. Note that the *i* and *j* indices represent three space dimensions in a Cartesian coordinate system. Only the mean velocity gradients appear and not the mean velocity. These mean velocity gradients are taken to be known, and can be time dependent. The idea with rapid distortion theory is that if the turbulence field is subjected to large strain rates, the linear terms containing the mean velocity gradients will dominate over the turbulence-turbulence interaction terms. Therefore, the second and third terms on the right hand side of Equation (3), along with the second term on the right hand side of Equation (4) can be neglected, resulting in linear equations which are more easily solved. In their linear form, the governing equations for the fluctuating velocity and pressure are called the rapid distortion equations.

It is important to first assess whether or not rapid distortion theory applies to LPT flows. Hunt and Carruthers [34] provide the essential criterion for rapid distortion theory to apply in terms of turbulent scales. This criterion is given by Eq. (5),

$$\frac{\sqrt{< u^2 >}}{L}\left(\frac{l}{L}\right)^{-\frac{2}{3}} << \max\left(\frac{\Delta\langle U \rangle}{d}, \frac{1}{T_D}\right) \qquad (5)$$

where l is a turbulent scale to be evaluated, L is the turbulent integral scale, d is the distance along which the distortion occurs, and T_D is the time required for the distortion to occur. Equation (5) indicates that rapid distortion theory is most applicable for large turbulent scales.

Assuming that the energy containing eddies occur for scales in the range of $1/6L < l < L$ [33], the right hand side of Eq. (5) was approximated to be between 4X and 13X larger than the left hand side for the L2-series airfoils. To calculate the ratio, mean velocities were extracted from computational results approximately a half axial chord upstream of the leading edge, and at mid-axial chord, just outside of the boundary layer in the freestream. Because the inlet integral scale and turbulence intensity are insensitive to the Reynolds number for grid generated turbulence [30], taking the ratio of the right to left hand sides of Eq. (5) is also expected to be insensitive to the Reynolds number. Therefore, Eq. (5) is expected to apply over the experimental Reynolds number range.

Figure 7 is a contour plot of velocity magnitude, scaled by the inlet velocity, to give insight into the parts of the flow domain where rapid distortion theory may apply. As shown, the highest velocities will occur within the freestream, close to the suction surface. The boxed region in the figure indicates the high strain region. Furthermore, a fluid particle in the freestream passing over the suction surface must double its velocity in a distance shorter than an axial chord. Hence, rapid distortion theory is expected to be most applicable in that part of the flow. Additionally, it is flow along the suction surface that will interact with a developing boundary layer, influencing turbulent transition. Flow acceleration is less severe near the pressure side of the passage, suggesting that rapid distortion theory does not apply in that part of the flow.

Whether or not a rapid distortion event has occurred can also be determined by examining the turbulent integral scales downstream of the distortion. Hunt and Carruthers [34] claim that for rapidly distorted, inhomogeneous turbulence near a rigid surface, with or without mean shear, the two-point spatial correlations of the turbulence field change little during the distortion. Hence, the integral scales which are obtained from two-point spatial correlations are also expected to change little near a rigid boundary, similar to the suction surface of the high

lift LPT airfoils. Therefore, the size of the turbulent eddies that pass through the high strain region of the freestream near the airfoil suction surface is expected to remain approximately constant.

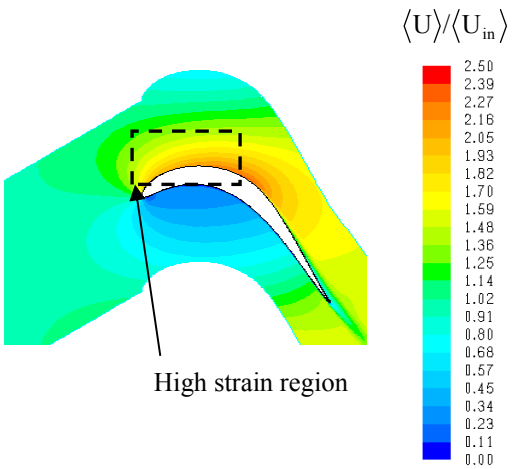

Figure 7. Contour plot of the scaled velocity magnitude for the L2A airfoil.

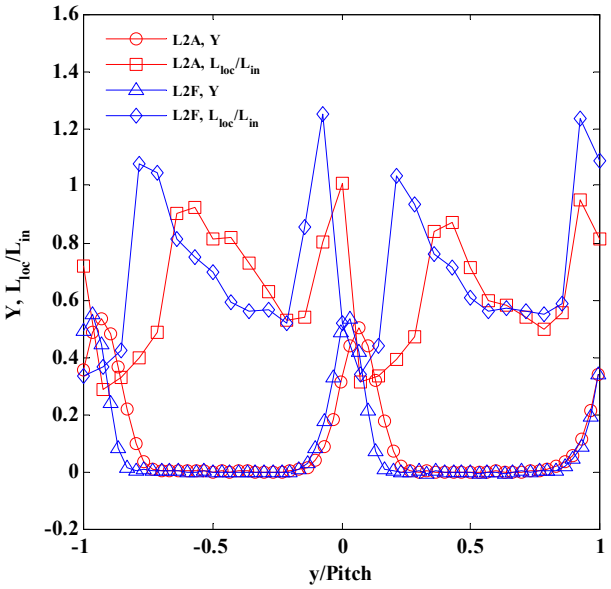

Figure 8. Pitchwise integral scale development in the exit traverse plane for the L2A and L2F airfoils. Data were captured at Re = 100k.

To investigate the effect of the airfoils on the integral scales, integral length scale measurements were taken at the exit traverse plane, and normalized by the measured values taken at the cascade inlet. These measurements are presented in Fig. 8 along with total pressure loss coefficients to indicate the blade wakes. The subscript "loc" indicates a measurement in the exit traverse plane. The right side of the wakes corresponds to the suction side of the airfoils. If a rapid distortion event occurs, $L_{loc}/L_{in} = 1.0$ is the expected result. As shown, the normalized integral scales for both airfoils are near unity just outside of the wake on the suction side (y/Pitch ≅ -0.7). This result suggests that rapid distortion theory provides a reasonable description of turbulence development along the airfoil suction surface within the freestream. The integral scales decrease farther towards the airfoil pressure surface, followed by an abrupt increase as the freestream interacts with the shear layer from the blade pressure surface. The integral scales are smallest within the blade wakes, which are due to mixing within the wake and not from the incoming grid generated turbulence.

Considering that scaling arguments and integral scale measurements both indicate that rapid distortion may be present, we will now examine the turbulent kinetic energy development. Goldstein and Durbin [35] solved the rapid distortion equations for two-dimensional contractions with various incoming turbulence integral scales, and contraction ratios. The incoming turbulence was isotropic for all cases. Their geometry is sketched in Fig. 9, which consisted of a plane strain contraction. The important aspect of Goldstein and Durbin's [35] results was the effect of high strain on the turbulence approaching the wall, but outside the boundary layer. Goldstein and Durbin [35] presented their plane strain results for the normal Reynolds stresses in terms of the parameters δ_1/δ_2 and $2\delta_2/L_{in}$. Both of these parameters significantly influence turbulence amplification near the wall.

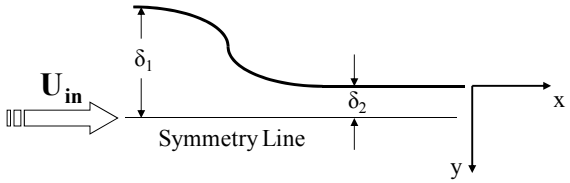

Figure 9. Sketch of Goldstein and Durbin's [35] geometry.

Figure 7 was used to obtain the required parameters for use with the Goldstein and Durbin [35] results. As shown, the space between the suction surface and the top of the high strain region in Fig. 7 was approximately $0.25C_{ax}$ and is taken to be the downstream contraction height, $2\delta_2$. Additionally, $0.25C_{ax} \cong L_{in}$, so the inlet integral scale is approximately equal to the downstream contraction height ($L_{in} \cong 2\delta_2$). As for contraction ratio, the fluid speed near the suction surface is approximately double the incoming fluid speed. This correlates by continuity to $\delta_1/\delta_2 = 2.0$. The parameters $\delta_1/\delta_2 = 2.0$ and $2\delta_2/L_{in} = 1.0$ were used as inputs in obtaining predictions using the Goldstein and Durbin [35] plane strain results.

The plane strain turbulence development is compared with the measured results from the L2A cascade in Fig. 10. Note that $\langle u^2 \rangle$ is for the streamwise direction, $\langle v^2 \rangle$ is for the wall-normal, or y-direction, and $\langle w^2 \rangle$ is for the spanwise direction (in and out of page for Fig. 9). Similar to the measurements, the predictions indicate highly anisotropic turbulence development due to large strain rates. The predicted spanwise fluctuation component, $\langle w^2 \rangle$, is clearly dominant, similar to

experiment. The predicted turbulent kinetic energy increases approaching the wall, but remains near unity until $y/L_{in} < 0.1$. The measured $\langle v^2 \rangle$ component decays more rapidly approaching the wall than the predicted values for plane strain, indicating that the wall damping effect is more significant than rapid distortion theory suggests. The predicted streamwise component, $\langle u^2 \rangle$, is consistently less than the measured values.

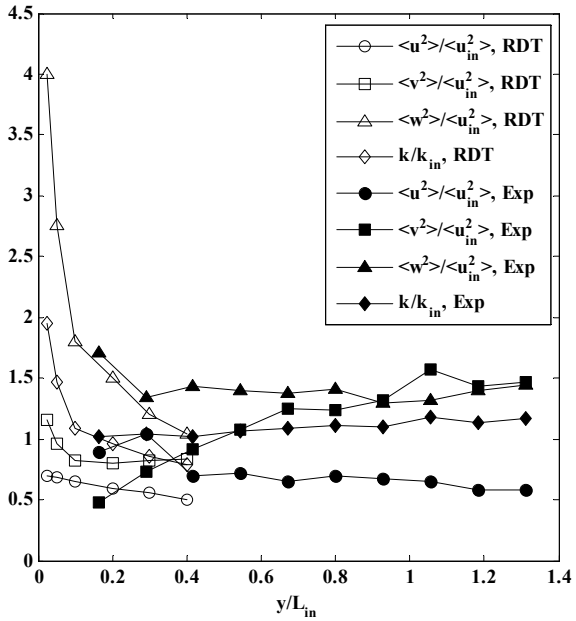

Figure 10. Comparison of L2A midspan turbulence development at $0.5C_{ax}$ with plane strain rapid distortion. Re = 100k for experimental results. ($\delta_1/\delta_2 = 2.0$ and $2\delta_2/L_{in} = 1.0$ for plane strain results of Goldstein and Durbin [35])

The results presented in Fig. 10 indicate that rapid distortion theory can capture the physical processes that redistribute the fluctuation energy. The magnitudes however, were clearly different. This result was not surprising considering that the rapid distortion predictions were based on a plane strain contraction. This flow is considerably different than the LPT airfoils. Furthermore, measurements could not be made any closer to the wall in the present study, due to concerns of probe interference with the flow and probe damage. Measurements are needed close to the wall, along with rapid distortion predictions for an equivalent flow to make a complete assessment of rapid distortion theory for this application. The idea is to find a tool to study turbulence development with less computational overhead than LES and DNS. These insights can be used to modify eddy-viscosity models to improve low Reynolds number performance.

CONCLUSIONS

The Reynolds lapse behavior for linear cascades of L2A and L2F airfoils was investigated experimentally and computationally. Experiments were conducted over a Reynolds number range of 20,000 < Re < 100,000 with an inlet turbulence intensity of 3.1% and a streamwise integral scale of 39.2 mm. The front-loaded L2F airfoil experienced only modest loss increases with decreasing Reynolds number, attributed mainly to a weak adverse pressure gradient on the suction surface. This airfoil did not stall. The aft-loaded L2A airfoil however, stalled catastrophically for Re < 40,000 as a result of a strong adverse pressure gradient on the suction surface.

Reynolds lapse predictions obtained using AFRL's TDAAS system, which included Praisner and Clark's [12] separated flow transition model, agreed well with experiments for both airfoils. Predictions using Fluent's implementation of the k-k_l-ω model [15, 16] however, were overly conservative, predicting stall for both airfoils, which was not observed during the experiments. For the L2A airfoil, the Fluent calculations predicted stall at nearly twice the experimental stall Reynolds number. The k-k_l-ω model's stall behavior is likely attributed to a failure in the eddy-viscosity hypothesis to fully resolve the anisotropic turbulence effects caused by high strain rates and turning. This argument is based on triple sensor hot-film measurements within the freestream for the L2A airfoil. Because the transition model in TDASS was empirically derived from similar flows, the freestream turbulence effects were captured implicitly, leading to improved results.

As a consequence of high strain rates near the suction surface of LPT airfoils, rapid distortion theory may provide a means outside of DNS and LES to gain insight into the freestream turbulence field that interacts with the developing boundary layer. This information may provide a physical basis for modifying eddy-viscosity based transition models for use with low Reynolds number LPT flows.

NOMENCLATURE

B	separation bubble length
C_{ax}	axial chord
C_p	pressure coefficient, $C_p = \left(P_s - P_{s,in}\right)/0.5\rho\langle U_{in}\rangle^2$
d	distance over which a rapid distortion occurs
H	blade span
k	turbulent kinetic energy, $k = 0.5(\langle u^2 \rangle + \langle v^2 \rangle + \langle w^2 \rangle)$
k_l	laminar kinetic energy
M	Mach number
l	arbitrary turbulent scale
L	turbulence integral scale
p	fluctuating static pressure
P	blade pitch
P_s	static pressure
P_t	total pressure
RANS	Reynolds-averaged Navier-Stokes
Re	Reynolds number based on inlet velocity and axial chord
R_{xx}	autocorrelation function
SS	suction surface
t	time variable
T_D	time duration for a rapid distortion

Tu	turbulence intensity, $\sqrt{< u^2 >}/\langle U \rangle \times 100\%$
U(t)	instantaneous velocity
$\langle U \rangle$	mean velocity
u(t)	velocity fluctuation, $u(t) = U(t) - \langle U \rangle$
$<u^2>$	x-direction mean square fluctuation
$<v^2>$	y-direction mean square fluctuation
$<w^2>$	z-direction mean square fluctuation
x	axial direction coordinate
y	pitchwise direction coordinate
Y	total pressure loss coefficient, $Y = \left(P_t - P_{t,in} \right) / 0.5 \rho \langle U_{in} \rangle^2$
Z_w	Zweifel loading coefficient, $Z_w = 2\left(\frac{P}{C_{ax}} \right) \cos^2 \alpha_{ex} \left(\tan\alpha_{in} - \tan\alpha_{ex} \right)$

Greek

α	cascade gas angle
δ_1, δ_2	contraction heights
ε	turbulence dissipation rate
θ	momentum thickness
ρ	density
τ	turbulence integral time scale
υ	kinematic viscosity
ω	turbulence specific dissipation

Subscripts

ex	exit location
i,j,k	Cartesian indices, can be 1, 2, or 3
in	inlet location
loc	local location
sep	separation location

REFERENCES

[1] Wilson, D.G., and Korakianitis, T., 1998, "The Design of High-Efficiency Turbomachinery and Gas Turbines," 2nd Edition. Upper Saddle River, New Jersey: Prentice Hall Inc.

[2] Praisner, T.J., Grover, E.A., Knezevici, D.C., Popovic, I., Sjolander, S.A., Clark, J.P., and Sondergaard, R., 2008, "Toward the Expansion of Low-Pressure-Turbine Airfoil Design Space," ASME Paper GT2008-50898.

[3] Bons, J. P., Hansen, L. C., Clark, J. P., Koch, P. J., and Sondergaard, R., 2005, "Designing Low-Pressure Turbine Blades with Integrated Flow Control," ASME Paper No. GT2005-68962.

[4] Gross, A. and Fasel, H. F., 2007, "Investigation of Low Pressure Turbine Separation Control," AIAA Paper No. 2007-520.

[5] Bons, J. P., Reimann, D., and Bloxham, M., 2008, "Separated Flow Transition on an LP Turbine Blade with Pulsed Flow Control," ASME *J. of Turbomachinery*, Vol. 130, pp. 021014-1:02101-8.

[6] Volino, R. J., 2010, "Separated Flow Measurements on a Highly Loaded Low-Pressure Turbine Airfoil," ASME *J. of Turbomachinery*, Vol. 132, pp. 011007-1:011007-10.

[7] Welch, G. E., 2010, "Assessment of Aerodynamic Challenges of a Variable-Speed Power Turbine for Large Civil Tilt-Rotor Application," 66th Forum of the American Helicopter Society, Phoenix, AZ, 11-13 May.

[8] McQuilling, M., 2007. "Design and Validation of a High Lift Low-Pressure Turbine Blade," PhD Thesis, Wright State University, Dayton, OH.

[9] Clark, J. P., Koch, P. J., Ooten, M. K., Johnson, J. J., Dagg, J., McQuilling, M. W., Huber, F., and Johnson, P. D., 2009, "Design of Turbine Components to Answer Research Questions in Unsteady Aerodynamics and Heat Transfer," AFRL Report No. AFRL-RZ-WP-TR-2009-2180.

[10] Casey, M. V., 1994, "Computational Methods for Preliminary Design and Geometry Definition in Turbomachinery," in Turbomachinery Design Using CFD, AGARD Lecture Series 195, pp. 1-1:1-22.

[11] Dorney, D. J. and Davis, R. L., 1992, "Navier-Stokes Analysis of Turbine Blade Heat Transfer and Performance," ASME *J. of Turbomachinery*, Vol. 114, pp. 795-806.

[12] Praisner, T. J. and Clark, J. P., 2007, "Predicting Transition in Turbomachinery, Part I – A Review and New Model Development," ASME *J. of Turbomachinery*, Vol. 129, pp. 1-13.

[13] Vanderplaats, G. N., 1984, Numerical Optimization Techniques for Engineering Design: With Applications, McGraw-Hill, New York.

[14] Santner, T. J., Williams, B. J., and Notz, W. I., 2003, The Design and Analysis of Computer Experiments, Springer-Verlag, New York.

[15] Walters, D.K., and Leylek, J.H., 2004, "A New Model for Boundary Layer Transition Using a Single-Point RANS Approach," *J. of Turbomachinery*, Vol. 126, pp. 193-202.

[16] Walters, K.K., and Leylek, J.J., 2005, "Computational Fluid Dynamics Study of Wake-Induced Transition on a Compressor-Like Flat Plate," *J. of Turbomachinery*, Vol. 127, pp. 52-63.

[17] Schlichting, H. and Gersten, K., 2000, "Boundary Layer Theory," 8th Edition. New York, New York: Springer-Verlag.

[18] Sanders, D.D., O'Brien, O.F., Sondergaard, R., Polanka, M.D., and Rabe, D.C., 2011, "Predicting Separation and Transitional Flow in Turbine Blades at Low Reynolds Numbers--Part I: Development of Prediction Methodology," *J. of Turbomachinery*, Vol. 133, pp. 031011-1:031011-10.

[19] Sanders, D.D., O'Brien, O.F., Sondergaard, R., Polanka, M.D., and Rabe, D.C., 2009, "A Mixing Plane Model Investigation of Separation and Transitional Flow at Low Reynolds Numbers in a Multistage Low Pressure Turbine," AIAA Paper 2009-1467.

[20] Cutrone, L., De Palma, P., Pascazio, G., and Napolitano, M., 2007, "An Evaluation of Bypass Transition Models for

Turbomachinery Flows," *International Journal of Heat and Fluid Flow*," Vol. 28, pp. 161-177.
[21] Baldwin, B., and Lomax, H., 1978, "Thin Layer Approximation and Algebraic Model for Separated Turbulent Flows," AIAA Paper No. AIAA-78-257.
[22] Praisner, T.J., Grover, E.A., Rice, M.J., and Clark, J.P., 2007, "Predicting Transition in Turbomachinery-Part II: Model Validation and Benchmarking," *J. of Turbomachinery*, Vol. 129, pp. 14-22.
[23] Bons, J.P., Sondergaard, R., and Rivir, R., 2001, "The Fluid Dynamics of LPT Blade Separation Control Using Pulsed Jets," ASME Paper No GT-2001-0190.
[24] Binder, A., Schröder, T.H., and Hourmouziadis, J., 1988, "Turbulence Measurements in a Multistage Low-Pressure Turbine," ASME Paper No. 88-GT-79.
[25] Schmitz, J.T., Morris, S.C., Ma, R., Corke, T.C., Clark, J.P., Kock, P.J., and Puterbaugh, S.L., 2010, "Highly Loaded Low-Pressure Turbine: Design, Numerical, and Experimental Analysis," ASME Paper GT2010-23591.
[26] Lekakis, I.C., Adrian, R.J., and Jones, B.G., 1989, "Measurement of Velocity Vectors with Orthogonal and Non-Orthogonal Triple-Sensor Probes," *Experiments in Fluids*, Vol. 7, pp. 228-240.
[27] Tritton, D.J, 1988, "Physical Fluid Dynamics," 2nd Edition. New York, New York: Oxford University Press.
[28] Kline, S.J., and McClintock, F.A., 1953, "Describing Uncertainties in Single Sample Experiments," *Mechanical Engineering*, Vol. 75.
[29] Figliola, R.S., and Beasley, D.E., 2000, "Theory and Design for Mechanical Measurements," 3rd Edition. New York, New York: John Wiley and Sons, Inc.
[30] Roach, P.E., 1986, "The Generation of Nearly Isotropic Turbulence by Means of Grids," *International Journal of Heat and Fluid Flow*, pp. 82-92.
[31] Shih, T.H., Liou, W.W., Shabbir, A., Yang, Z., and Zhu, J., 1995, "A New k-ε Eddy-Viscosity Model for High Reynolds Number Turbulent Flows-Model Development and Validation," *Computers and Fluids*, Vol. 24 (No. 3), pp. 227-238.
[32] Weiss, A.P., and Fottner, L., 1995, "The Influence of Load Distribution on Secondary Flow in Straight Turbine Cascades," *J. of Turbomachinery*, Vol. 117, pp. 133-141.
[33] Pope, S.B., 2000, "Turbulent Flows," 1st Edition. Cambridge, UK: Cambridge University Press.
[34] Hunt, J.C.R., and Carruthers, D.J., 1990, "Rapid Distortion Theory and the 'Problems' of Turbulence," *J. of Fluid Mechanics*, Vol. 212, pp. 497-532.
[35] Goldstein, M.E., and Durbin, P.A., 1980, "The Effect of Finite Turbulence Spatial Scale on the Amplification of Turbulence by a Contracting Stream," *J. of Fluid Mechanics*, Vol. 98, pp. 473-508.
[36] Wilcox, D.C., 1998, "Turbulence Modeling for CFD," 2nd Edition. La Cañada, California: DCW Industries Inc.

APPENDIX E

Proceedings of ASME Turbo Expo 2011
GT2011
June 6-10, 2011, Vancouver, Canada

GT2011-45397

EXPERIMENTAL COMPARISON OF DBD PLASMA ACTUATORS FOR LOW REYNOLDS NUMBER SEPARATION CONTROL

Christopher Marks **Rolf Sondergaard** **Mitch Wolff** **Rich Anthony**

U.S. Air Force Research Laboratory, Propulsion Directorate
Wright Patterson AFB, OH 45433, USA

ABSTRACT

This paper presents experimental work comparing several Dielectric Barrier Discharge (DBD) plasma actuator configurations for low Reynolds number separation control. Actuators studied here are being investigated for use in a closed loop separation control system. The plasma actuators were fabricated in the U. S. Air Force Research Laboratory Propulsion Directorate's thin film laboratory and applied to a low Reynolds number airfoil that exhibits similar suction surface behavior to those observed on Low Pressure (LP) Turbine blades. In addition to typical asymmetric arrangements producing downstream jets, one electrode configurations was designed to produce an array of off axis jets, and one produced a spanwise array of linear vertical jets in order to generate vorticity and improved boundary layer to freestream mixing. The actuators were installed on an airfoil and their performance compared by flow visualization, surface stress sensitive film (S3F), and drag measurements. The experimental data provides a clear picture of the potential utility of each design. Experiments were carried out at four Reynolds numbers, $1.4x10^5$, 1.0×10^5, 6.0×10^4, and 5.0×10^4 at a -1.5° angle of attack. Data was taken at the AFRL Propulsion Directorate's Low Speed Wind Tunnel (LSWT) facility.

INTRODUCTION

The environment in a low pressure (LP) turbine at high altitude can reach Reynolds numbers below 25,000 [15]. Highly loaded blades with large turning angles are prone to flow separation and reduced efficiency at low Reynolds number. Researchers have studied different active and passive flow control techniques to increase the efficiency of the turbine blades at low Reynolds number – see summary by Rivir et al. in 2004 [17]. Dielectric Barrier Discharge (DBD) plasma actuators used in this paper are a low power, active separation control method. The work presented here is part of an effort to develop a laboratory level Low Reynolds number closed loop separation control system. The DBD plasma actuators configurations evaluated are being considered as an additional alternative to other actuation methods being studied.

In order to most efficiently use a plasma actuator as a separation control method, it is important to understand the mechanism by which a separated boundary layer can be reattached or forced into early transition. With respect to control of turbine blades, Rivir et al. points out that successful techniques have introduced longitudinal or streamwise vortices which "reenergize the wall boundary layer flow by entraining and redistributing momentum from the primary flow to the wall layer" [17]. Three different methods of controlling highly loaded LP turbine blades have been demonstrated in a low speed linear cascade at the AFRL Low Speed Wind Tunnel (LSWT) facility that introduce streamwise vorticity. Passive separation control was demonstrated by Lake [1] using dimples applied to the suction surface of the Pack-B LP turbine profile. Flow visualization by Mahmood et al. [2] showed that dimples act as a vortex generator, introducing multiple longitudinal vortices. The use of steady and pulsed vortex generator jets (VGJ) were demonstrated by Sondergaard et al. [3] and Bons et al. [4] to reattach low Reynolds number separated flow. An aggressive skew angle relative to the freestream of 45-90 degrees resulted in one strong slow decaying longitudinal vortice that was shown by Johnston et al [5] to be more effective at transferring momentum from the freestream to the wall.

Dielectric barrier discharge (DBD) plasma actuators have also been used in a number of LP turbine separation control studies [18][19][20][21][35], and are typically a single asymmetric spanwise plasma actuator which pulls high momentum fluid from the freestream into the boundary layer. Pulsed actuator operation has been shown to generate spanwise coherent vortical structures that are more effective at transferring momentum to the boundary layer while using less power [19][21]. In each of these approaches the actuators acted as an instability generating mechanism.

U.S. Air Force Public Affairs Office Case No. 88ABW-2010-6254

The objective of this study was to verify that the DBD plasma actuator could control the flow over an Eppler 387 (E387) airfoil at Low Reynolds number, and evaluate the capability of three different electrode configurations for use in a Low Reynolds number separation control system. The uniqueness of this study is the head to head comparison of three different DBD plasma actuator electrode configurations. Two different electrode arrangements were compared to an asymmetric spanwise electrode arrangement in hopes of generating increased control authority by generating streamwise vorticity. The E387 was chosen because the suction surface flowfield was similar to previous LP turbine blade design at low Reynolds number tested in the U.S. Air Force Research Laboratory Propulsion Directorate (LSWT) facility. The E387 airfoil allowed the use of a straight section wind tunnel rather than linear cascade, and simplified optical access, setup, and mounting of the S3F sensor to the airfoil.

Application of DBD to Low Pressure Turbine Blades

The standard configuration of an asymmetric DBD with the electrode interface mounted perpendicular to the flow direction has been shown to entrain momentum from the primary flow into the wall layer (see Figure 2) [43]. A perpendicular orientation to the primary flow has been demonstrated to reattach a separated LP turbine boundary layer at low Reynolds number by a number of researchers described below.

List et al. in 2003 [35] applied a single DBD plasma actuator for control of laminar separation of a linear cascade of Langston turbine blades in which a laminar separation bubble was observed at low Reynolds numbers ($Re=3.0x10^4$ & $7.4x10^4$). A DBD plasma actuator was placed just upstream of the separation location and voltage was increased until the separation bubble was eliminated.

Huang et al. published two papers, the first in 2003 [18] and the second in 2006 [19] that investigated the use of a single DBD plasma actuator applied to a linear cascade of Pack-B LP turbine blades for flow control.

The first work focused on identifying the flowfield around the Pack-B blade in a linear cascade wind tunnel and comparing the use of a single DBD plasma actuator and vortex generator tabs to control the suction surface laminar flow separation. The authors placed one spanwise actuator upstream of the separation line with electrodes mounted perpendicular to flow direction creating a two dimension steady wall jet. The actuators shifted reattachment location upstream. The authors noted a threshold driving voltage amplitude at which a further increase in applied voltage would yield very little movement of reattachment point [18].

The second paper of Huang et al. [19] compared the use of steady AC driving waveform versus unsteady AC driving waveform for separation control of the Pack-B. They found both unsteady and steady actuators to be effective, but labeled the unsteady actuator the more effective of the two. Huang et al. suggests the steady actuators are turbulence tripping, and the unsteady actuators generate a train of spanwise structures that promote mixing. The optimum excitation frequency for the unsteady actuators to reattach flow was at a Strouhal number equal to unity. The Strouhal number was calculated based on length of separated zone and local freestream velocity.

Rizzetta and Visbal [20][21] performed a computational study focusing on the identification of effective strategies for separation control of highly loaded low pressure turbine blades. Numerical simulations were performed on a simulated Pack-B blade set. The actuators were modeled by momentum addition and the model did include the actual actuator physics. Both steady and unsteady actuators were examined, with the unsteady actuators introducing unsteady forcing. Co-flow and counter-flow configurations were evaluated. The computational study indicated higher power levels exerted greater control, pulsed excitation was more effective than continuous actuation due to enhanced mixing, and the pulsed counter-flow actuator configuration provided the most effective control with the least expenditure of energy [20].

DBD Plasma Actuator Background and Overview

A simple schematic of an asymmetric configuration of DBD is shown in Figure 1. This configuration has been studied significantly in recent literature.

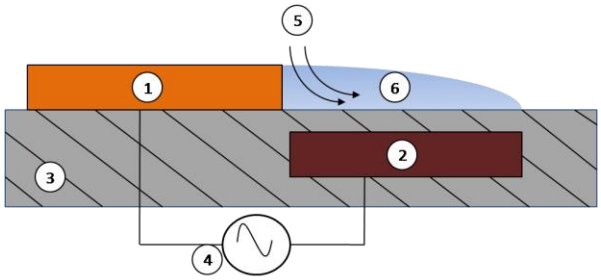

Figure 1. Asymmetric configuration of DBD plasma actuator.

The encapsulated electrode is typically grounded and the voltage potential is alternated between positive and negative. Typically high voltage AC is applied to the electrodes with voltage amplitudes of several kV_{p-p} to tens of kV_{p-p} and frequencies from around 1 kHz to tens of kilohertz. For detailed information and background on the physics of the plasma discharge readers should refer to other papers [7]-[9], the topical review paper by Fridman et al. [12] and a paper by Moreau [1].

An electrostatic force of Equation 1[8], acts in the charged species located in the plasma which results in an electric wind or induced velocity, in the form of a wall jet.

$$\vec{F} = \rho_e \vec{E} = -(\varepsilon_0/\gamma_D^2)\phi\vec{E} \quad (1)$$

In equation 1, ρ_e is the net charge density, E is the electric field, ε_0 is the permittivity of free space,and γ_D is the debye length. The thrust produced by the force has been reported to be in the range of 10 mN or less [9]. The induced air flow can be several

meters per second, but larger velocities have been generated [1]. An induced velocity and low power requirement make a DBD plasma actuator a viable candidate for low speed flow control applications. The use of DBD plasma actuators in a LP turbine will require additional research including operation in a harsh environment, scaling to higher Mach number flows, and reliability.

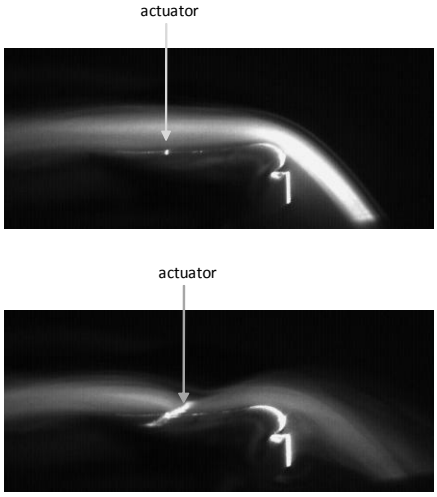

Figure 2. Visualization of the induced velocity generated by a DBD plasma actuator single asymmetric electrode configuration. Top image: actuator off. Bottom image: actuator on. Flow is from left to right.

Alternate DBD Plasma Actuator Configurations

A majority of fundamental research and application of DBD plasma actuators for flow control has utilized the linear asymmetric electrode arrangement illustrated in Figure 1. This configuration generates an induced velocity in the form of thin wall jet pointing downstream over the buried electrode. This configuration is effective at reenergizing the boundary layer by transferring momentum from the freestream to the boundary layer. The height of the jet is typically only several millimeters above the surface [11]. As mentioned above this configuration was used experimentally by Huang et al. to reattach and decrease the length of a separation bubble over the Pack-B airfoil. The jet was oriented downstream along the surface of the airfoil just upstream from separation adding momentum to the boundary layer with the objective of overcoming the adverse pressure gradient aft of the negative pressure peak. Huang et al. concluded the actuator acted as a turbulent trip, promoting earlier transition to turbulent boundary layer [19]. A nearly analogous computational study by Rizzetta and Visbal found the same steady actuator configuration mounted facing upstream more effective then the downstream facing plasma actuator. They predicted that the upstream jet created a local small scale separation and subsequent formation of vorticity and turbulent mixing [21]. It should be noted that both Huang et al. and Rizzetta and Visbal investigated pulsed configurations in their studies and found them to be more effective while using less power. Their performance gain was attributed to the generation of more coherent spanwise vortical structures that transferred high momentum fluid from the outer boundary layer to the blade surface [21],[19].

As alternatives to the asymmetric electrode arrangement several researchers have proposed different electrode configurations with objective of improved control authority. Roy and Wang have proposed horseshoe and serpentine electrode configurations in a numerical study that showed promise for generating induced flows with three-dimensionality [22].

Plasma synthetic jet configurations have been proposed in both annular [24] [25] and linear configurations [27][28][32]. Santhanakrishnan and Jacobs experimentally studied both a steady and pulsed annular arrangement. Steady operation behaved like a synthetic jet in crossflow, and pulsed operation formed multiple counter-rotating vortex rings. Linear plasma synthetic jets were experimentally and numerically studied by Santhanakrishnan et al. in quiescent air using PIV [27]. The researchers found that similar findings as the annular array in that steady operation resulted in a zero-mass flux jet, and unsteady operation resulted in counter-rotating vortical structures. They also found a low peak velocity located close the actuator compared to the higher velocities observed with traditional synthetic jets.

Porter et al. [29][30] investigates improving upon the linear plasma synthetic jet by modifying the shape of the buried electrode to produce spanwise variation or "waviness" in the normal jet. They create spanwise waviness in the vertical jet by removing portions of the buried electrode (either diamond or square shapes) at specified spatial frequency. This limits the extent of the plasma to areas in which the bottom electrode has not been removed creating spanwise variation in the body force. They found that their electrode arrangements had the ability to generate vertical jets with spanwise spatial variation [30] .

The objective of alternative electrode configurations over the traditional linear plasma jet is generation of induced jets with three dimensionality and vorticity for enhanced boundary layer control. Jet vectoring is another interesting approach to generating increased vorticity and mixing by controlling the direction of the jet produced by linear plasma synthetic jets. Variations of jet vectoring have been suggested by Porter et al.[29][30], Bolitho and Jacobs[31], and Sherman[32]. The work of Porter et al. is very interesting in that they vary the voltage applied to each of the two exposed electrodes that form a linear plasma synthetic jet. They demonstrate ≈ +/- 60 degrees of jet directional control by varying the voltage between exposed electrodes. In addition they demonstrate oscillation of the jet by frequency modulation, greatly expanding the design space of linear plasma synthetic jets.

CURRENT STUDY

The three electrode configurations evaluated in the current work are shown in Figure 3. The first actuator configuration, DBD-01 was a spanwise array of 11 linear actuators spaced

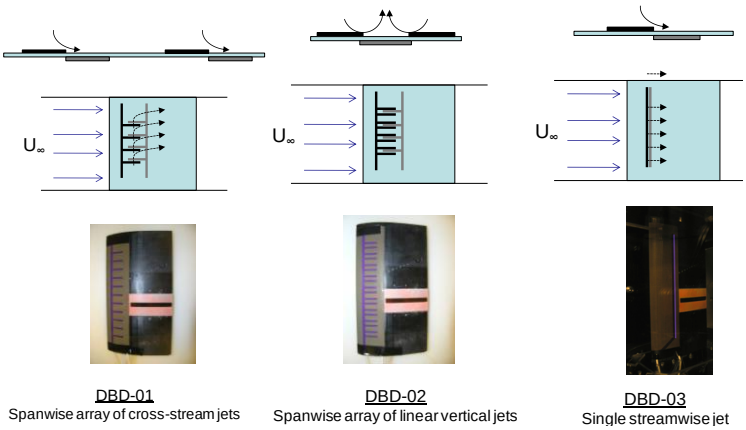

Figure 3. DBD Plasma Actuator Electrode Configurations.

20.6 mm on center, mounted parallel to the flow. This configuration produced an array of cross stream jets with the intent of generating longitudinal vorticity [43]. The second actuator, DBD-02 was a spanwise array of linear plasma synthetic vertical jets spaced 23.8 mm on center. Vertical jet arrangements can be created as annular or linear configurations, and operated steady or pulsed [24]-[28]. DBD-03 is a single asymmetric electrode across the span of the airfoil centered at 35% C_x. This type of geometry produces a downstream jet along the span of the airfoil.

Experimental Setup

Experiments were carried out in the AFRL Propulsion Directorate's LSWT facility 12" low speed wind tunnel. The straight section wind tunnel has a 30.5cm x 30.5cm x 61cm test section and an airspeed range of 4.5 – 65 m/s generated with a 7.5 kW electric motor. The inlet has a series of flow straighteners and turbulence-reducing screen followed by a 9.5:1 contraction providing an advertised turbulence level of less than 0.2%. The airfoil was mounted across the full span of the wind tunnel and had a 16.5cm chord length.

The E387 airfoil was rapid prototyped out of a polycarbonate ABS mixture. It is slightly modified in two ways. First a shallow cavity was created on the suction side of the airfoil to install a Surface Stress Sensitive Film (S3F) carrier. S3F is surface stress sensor used in this study to indicate shear stress. The S3F was formed external of the airfoil in the S3F carrier to ensure that it was smooth and flush with the surface of the carrier, and thus the surface of the airfoil. The S3F carrier was then installed into the cavity and held by either adhesive tape or countersunk screws near the trailing edge. The second modification to the airfoil is installation of surface pressure taps and plumbing. Due to the small thickness of the E387 (9.1%) the pressure tap lines (1.3mm diameter) were run along the pressure side of the airfoil and covered with tape. The modifications on the pressure side of the airfoil had little effect on the suction side boundary layer behavior, but as would be expected there is variation of drag along the span and an increase in drag over an unmodified airfoil.

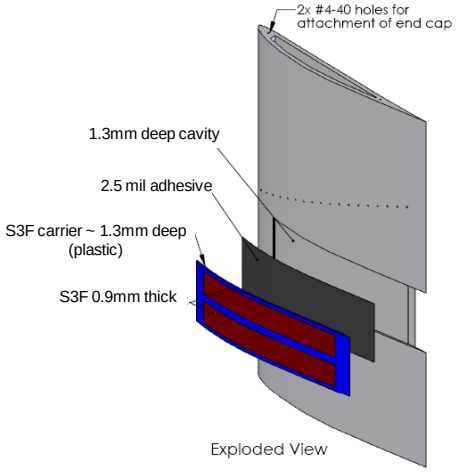

Figure 4. Modified E387 airfoil showing S3F mounting

Pressure coefficients, profile drag, shear direction by S3F, and flow visualization was obtained for each electrode configuration. An arrangement of AllSensor pressure transducers was used for pressure measurements with nominal 0.05% and maximum 0.25% linearity full scale. A 0-125 Pa (31.1 Pa/V) sensor was used for wake pressure measurements and inlet dynamic pressure. A 0-249 Pa (62 Pa/V) transducer was used for Cp measurements.

Drag was calculated by wake traverses using the method of Jones [42] using a Pitot-static probe located in a slot $0.5C_x$ downstream from the trailing edge.

$$C_d = \frac{2}{C_x}\int^{W} \frac{\sqrt{P_{T,w} - p_w}}{\sqrt{P_{T,in} - p_{in}}}\left(1 - \frac{\sqrt{P_{T,w} - p_{in}}}{\sqrt{P_{T,in} - p_{in}}}\right) dy$$

No corrections were applied to the data. Uncertainty in the Cp measurements is nominally 1.5% at the pressure minimum, and 3.1% in the trailing edge area at Re = $5x10^4$. At Re = 1.0 x 10^5 uncertainty in Cp is nominally 0.5% at the pressure minimum and 1.1% in trailing edge area. Uncertainty in the drag measurements omitting errors related to the probes is less than 1%.

Flow visualization was captured using a PCO 1600 camera and illuminated with a New Wave Solo 120 laser. The laser sheet was formed by Dantec sheet forming optics mounted to an articulating laser arm. The laser sheet thickness in this setup was ≈1 mm. The flow was seeded using water vapor generated from a Sussman 9 kW steam generator. The steam was injected in line with the wind tunnel approximately 2 meters upstream of the inlet. It should be noted that flow seeding will contaminate the plasma actuator, reducing its performance. The extent and uniformity of the plasma was affected by seeding contamination especially at lower voltage levels. Surface contamination from flow seeding was also noted in previous studies [26]. Flow visualization for each actuator was taken after wake traverse, Cp, and S3F data was acquired to minimize contamination.

S3F is a technique that enables the measurement of surface stresses over a wetted surface [23]. In many flows, both

pressure and shear fields can be measured simultaneously. The S3F technique consists of an elastic polymer film of known shear modulus and thickness applied to the surface being measured. The film deforms under to applied normal and tangential forces along the wetted interface. Film displacement is measured optically, then spatially cross-correlated with a wind-off image to obtain the two dimensional tangential displacement field. The normal force can be measured using the fluorescence signal emitted from a fluorescent probe embedded in the S3F. The shear stress and pressure gradients are calculated from the displacement field by solving the inverse problem using a finite element model of the elastic film [23]. The film has been used successfully for measurements in both high and low Reynolds number environments [23].

Previous experience using S3F at *low Reynolds number* has shown that it useful as a qualitative sensor and has potential as a quantitative sensor [38][38][39] [40]. In our low Reynolds number experiments very low shear modulus film is required (order of 100 Pa) to achieve adequate film sensitivity. Under a small pressure gradient the film displacement is linearly related to shear stress [23]. The raw film displacement vector field is an immediate indicator of surface shear direction. In a moderate and higher surface pressure gradient the raw displacement vectors are influenced by the pressure gradient as well as surface tangential stresses.

In this study the S3F tangential surface displacement was used as a direct indicator of shear stress direction. This is a valid assumption in flows with a small pressure gradient. Experiments have indicated that raw film tangential displacement near the E387 trailing edge reattachment can be shifted up to 2.5% axial chord by pressure gradient effect. Nonetheless it is deemed a worthwhile indicator of shifts in reattachment point for comparison of different actuator configurations tested in this study. In addition when S3F is applied in a filled cavity there will be an edge effect that decreases tangential displacement within several film thickness of the edge.

A PCO 4000 camera with 4008 x 2672 pixel resolution was used to obtain S3F flow-on and flow-off images. One strip of 0.9mm thick by 10mm wide S3F from C_x=42% to 98% was installed on the airfoil. The image field of view was 27.3mm x 18.2 mm with a magnification factor of 146.6 px/mm. Airfoil deformation and motion relative to the camera on the order 25-50 μm (3.5-7 pixels) was corrected for using 2D interpolation. Strips of patterned area just above and below the S3F rigidly fixed to the airfoil were used to correct for blade motion in each image pair.

Displacement maps were calculated using ISSI Inc. custom software that uses multipass optical flow to calculate displacement vectors. The displacement fields were then corrected for airfoil motion in Matlab. Accuracy of the optical flow technique used to calculate displacement vectors is better than 1/100 of a pixel [23]. In order to estimate the accuracy of the method used to correct for airfoil deformation a solid plastic filler panel was installed in place of the S3F. A fluorescent pattern was sprayed on the filler panel and flow-on and flow-off images were analyzed using the same process used for S3F images. For a series of 100 image pairs, correction for airfoil motion resulted in an average displacement field of +/- 0.015 pixels maximum. This is an indicator of the accuracy of the analysis method and airfoil motion correction technique, however, the actual accuracy is dependent on the pattern, signal to noise ratio, in addition to other factors.

Each electrode configuration was attached to the E387 airfoil using a uniform layer of 2 mil thick adhesive transfer tape. The DBD plasma actuators were fabricated in the U.S. AFRL Propulsion Directorate's thin film lab by photolithography and etching double-sided copper clad Kapton. The dielectric material was 5 mil thick Kapton with 1 oz copper (1.4 mil thick) electrodes. The top and bottom electrodes were formed flush with each other with no overlap. To assure the installation of the DBD plasma actuator on the airfoils did not trip the boundary layer, the actuators were wrapped completely around the leading edge of the airfoil. Only a 36 μm (1.4 mil) step up at the exposed electrode and an approximately 178 μm (7 mil) step down existed at the trailing edge of the actuator.

The electrodes were powered by two Titan Series power supplies from Compact Power. Each of the power supply output voltages were increased by an Industrial Test Equipment Co. transformer to kilovolt levels. In this work the DBD plasma actuators were operated in steady mode with continuous sinusoidal waveforms.

RESULTS AND DISCUSSION

Data was taken at four different Reynolds numbers with a focus here on performance at Re = 5 x 10^4, and Re = 1.0 x 10^5. At the lower Reynolds number the laminar boundary layer separates and large eddies are formed in the separated shear layer; the flow however, does not fully reattach. At the higher

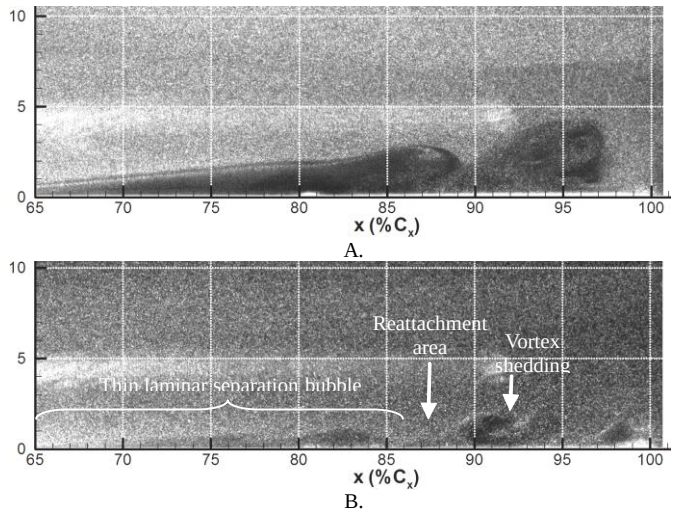

Figure 5. Flow visualization over the E387 suction surface from Cx = 67% to trailing edge with DBD-01 installed. Image A is at Re = 5 x 10^4. Image B is at Re = 1.0 x 10^5.

Reynolds number the boundary layer separates then transitions to turbulent and reattaches. The closed separation bubble sheds vortices which travel down the suction surface to the trailing edge. The large scale Kelvin-Helmholtz instabilities that develop in the separated shear layer lead to periodic vortex shedding observed in Figure 5B. Previous analysis has shown that time averaged measurements of the laminar separation look very similar to measurements of a traditional laminar separation bubble [33][34].

Figure 6 shows the suction surface Cp distribution with each plasma actuator installed at each Reynolds number tested along with inviscid results obtained in XFOIL [41]. The Cp distribution is consistent across each plasma actuator installed with regard to the presence of laminar separation without reattachment at Reynolds numbers tested below $6.0x10^4$, and laminar separation with reattachment for Reynolds numbers tested equal to $1.0x10^5$ and higher. Differences between the Cp profiles include higher peak Cp for DBD-01 than DBD-02 and DBD-03, with DBD-03 having the lowest peak Cp. In addition,

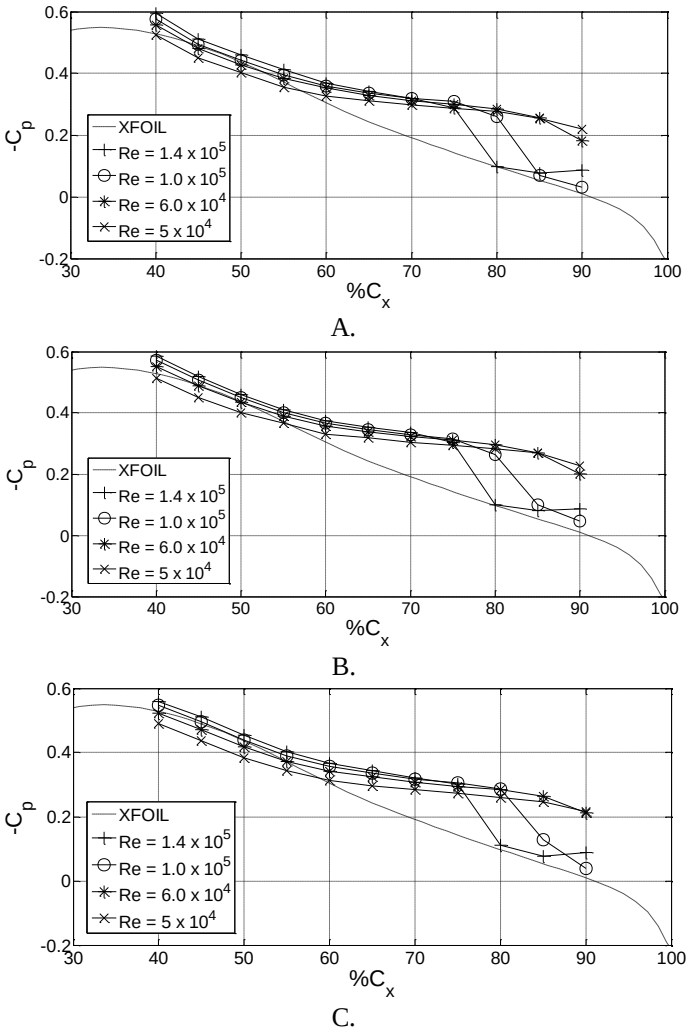

Figure 6. Suction surface Cp distribution with plasma actuators powered off. Plot A: DBD-01, B: DBD-02, C: DBD-03.

Cp plots indicate a difference in reattachment location for the three different plasma actuators tested. This difference is most noticeable in the Cp plot of DBD-03 at $Re=1.0x10^5$ in which the reattachment point noticeably shifts downstream 5% axial chord to Cx≈90%. It is important to keep in mind the spatial resolution of Cp data due to the limited amount of pressure taps. The S3F displacement field vector plots of Figure 9 indicate that the reattachment point is not uniform along the span, so a discrepancy of several percent axial chord is not unexpected. The difference in max Cp is likely due to the shift in mean reattachment location. The difference in data for each case is presumably due to two things: variation in the quality of installation of each plasma actuator, and the possibility that the electrode geometry caused small scale perturbations in the laminar boundary layer.

A summary of the separation and reattachment locations (extracted from Cp data) is provided in Figure 7 for each plasma actuator configuration tested.

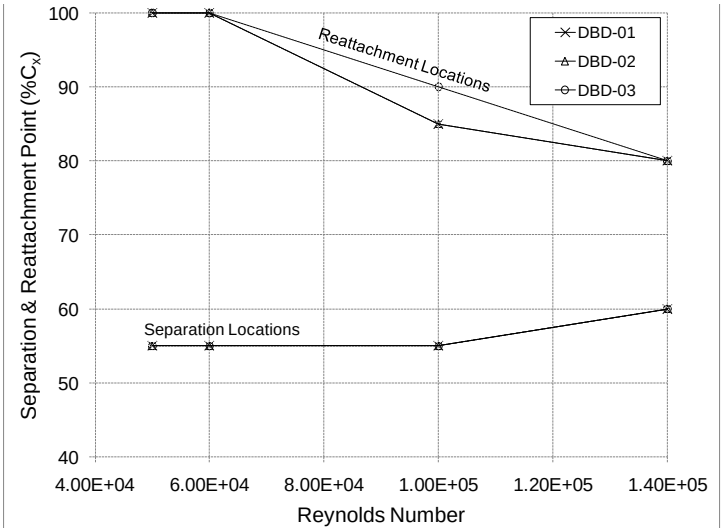

Figure 7. Mean suction surface separation and reattachment points for each plasma actuator configuration tested powered off.

Results at Re = 5 x 10^4

Cp and wake profile plots for each plasma actuator tested at a Reynolds number of $5x10^4$ are shown in Figure 8. A range of input voltages are shown in each plot. DBD-01 and DBD-02 drastically improve the surface pressure distribution with the time averaged measurements indicating flow reattachment. Powering on each actuator resulted in a significant narrowing of the airfoil wake. The wake of DBD-01 decreased in width as input voltage increased up to 5.6 kV_{pp} then increased width as voltage was amplified further. As the voltage of DBD-02 was increased beyond 4.2 kV_{pp} the wake gradually increased in width up to a voltage of 5.6 kV_{pp}. At input voltages above 5.6 kV_{pp} the wake began to narrow at its base with a significant increase in peak velocity deficit. Increasing the voltage of DBD-03 did not decrease the wake considerably beyond the lowest input voltage applied.

The use of S3F allows a unique view of the surface tangential displacement which directly corresponds to surface shear stress direction. Figure 9 is a series of mean surface tangential displacement vector plots obtained from S3F for DBD-01 actuator off and a range of applied plasma actuator voltage. The plots clearly show the effect of the plasma actuator. For actuator off conditions a strong reverse flow vortex is present at the trailing edge of the airfoil with a dead air region of separated flow just upstream from the vortex. As the plasma actuator is turned on the reverse flow vortex gradually shifts upstream with increase in voltage. There is a significant upstream shift and movement of the reverse flow vortex out of the view at the highest applied voltage of 7.2 kV_{pp}. At the highest voltage the mean flow appears to be reattached at $C_x \approx 93\%$ indicated by a zero crossing and downstream pointing displacement vectors. Figure 10 shows mean S3F tangential streamwise displacement for each plasma actuator tested at a spanwise location at $z = 5.5\%C_x$ (reference views in Figure 9). From Figs. 8-10 the following conclusions are made for operation at $Re=5 \times 10^4$:

DBD-01 – array of cross stream jets:

- Narrowing of the wake when the actuator is turned on indicates a decrease in drag and decrease in separation angle
- Mean S3F streamwise displacement in Figure 9 indicate that boundary layer reattachment and subsequent decrease in separated region does not occur until an applied voltage of 5.6 kV_{pp} and higher.
- Cp measurements agree with S3F in that there is no reattachment and/or minimal shift in reattachment point until higher actuator voltages are applied.

DBD-02 – array of vertical jets:

- Cp, S3F, and wake profile data all indicate that DBD-02 has a much larger effect on the flow at lower applied voltages compared to DBD-01.
- The reverse flow vortex moves upstream several percent chord when the plasma actuator is turned on at the lowest voltage. This is an improvement over DBD-01 and implies that the separated boundary layer is reattached or nearly reattached at the trailing edge at a voltage of 4.2 kV_{pp}. When the voltage is increased to 5.6 kV_{pp} the mean flow is clearly reattached as shown in the Cp and S3F data.

DBD-03 – downstream jet:

- DBD-03 has the least significant change in Cp distribution and S3F streamwise displacement when the actuator is turned on and voltage is increased.
- Decrease in wake profile at the lowest plasma actuator voltage indicates that there is an effect on the separated flow by the actuator.

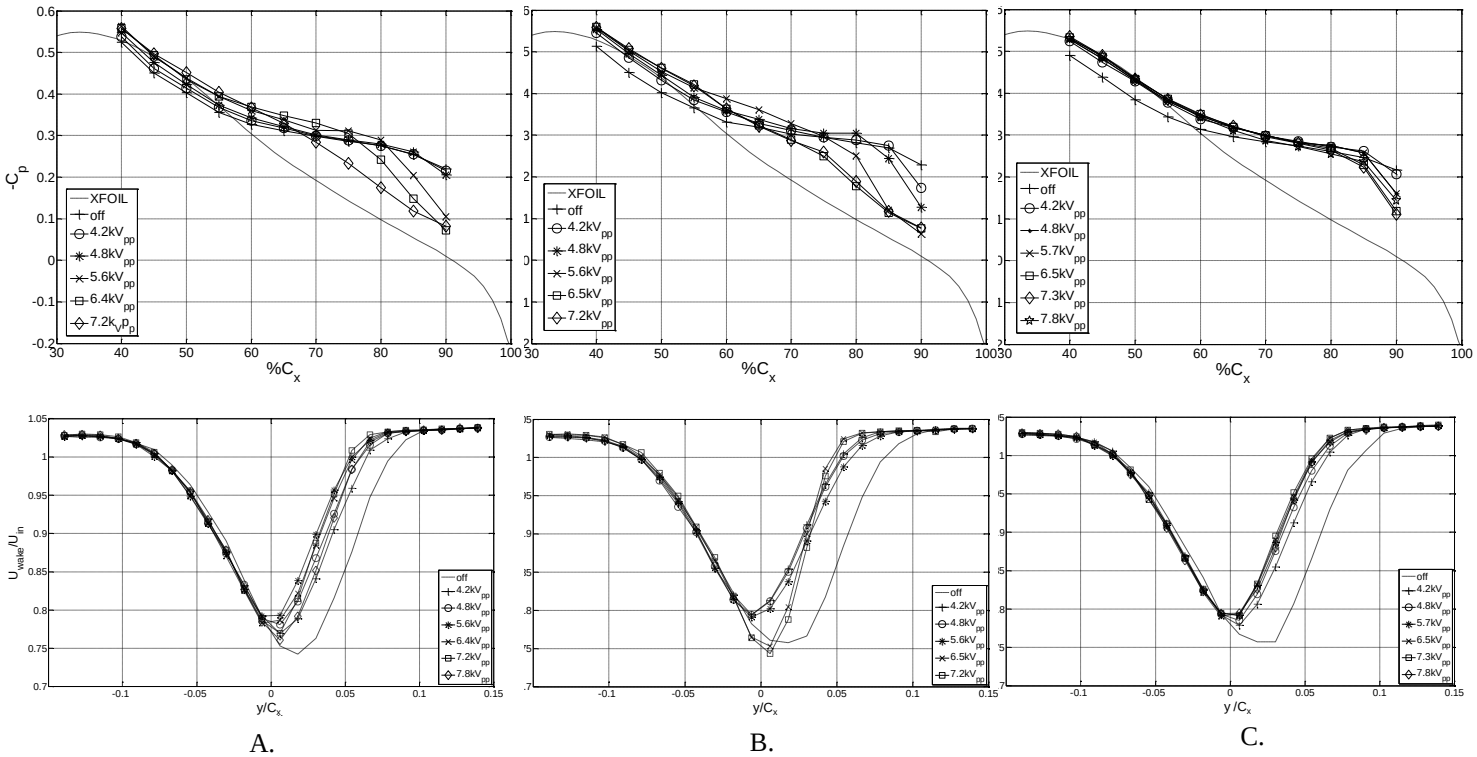

A. B. C.

Figure 8. Suction surface Cp distribution and wake profile for each plasma actuator tested at 5 x 10^4. Column A: DBD-01, B: DBD-02, C: DBD-03.

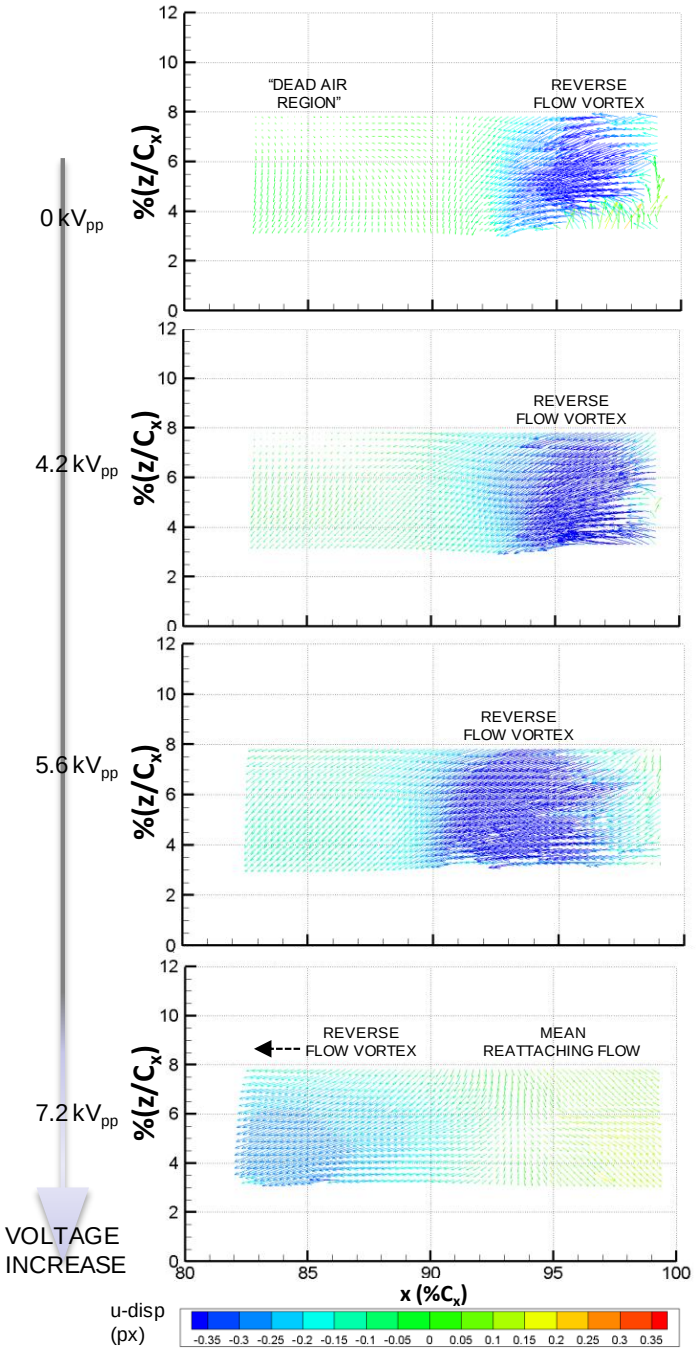

Figure 9. S3F measured surface tangential displacement of airfoil with DBD-01 installed. Flow speed is Re = 5 x 10^4 with various plasma actuator voltages

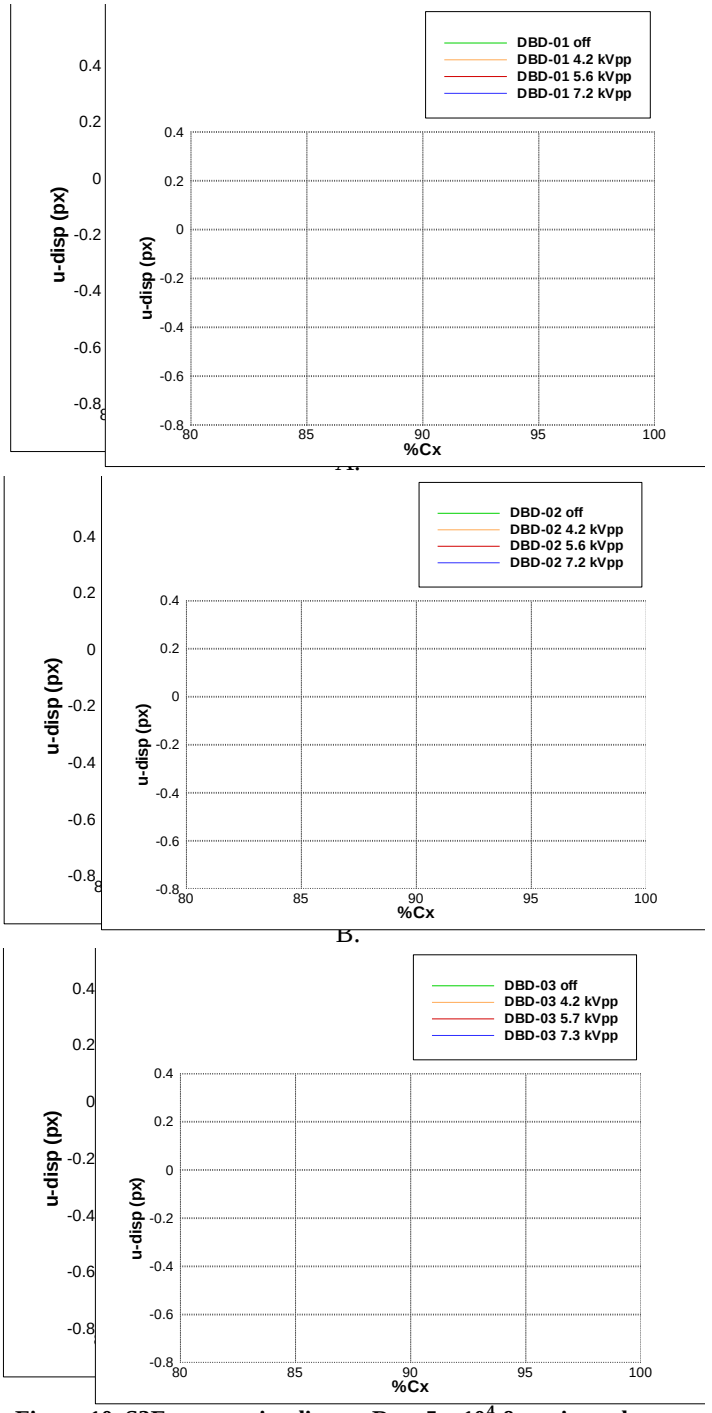

Figure 10. S3F streamwise disp. at Re = 5 x 10^4 & various plasma actuator voltages. Plot A: DBD-01, B: DBD-02, C: DBD-03.

Results at Re = 1.0 x 10^5

Figure 13 shows Cp and wake profiles at Re=1.0x10^5 for which there is laminar separation with reattachment when the actuator is powered off. The Cp profiles for each plasma actuator show an effect on suction surface Cp distribution when the actuator is turned on. The wake profiles (omitted here) however, show no decrease in wake width or depth with actuation; instead they remain constant or grow wider.

When the actuator is powered on the mean reattachment point gradually moves upstream as much as 5%C_x for DBD-01. The plateau region of the Cp distribution is flattened as voltage is increased for DBD-02 and DBD-03, first with a shift upstream of the reattachment point, then overall smoothing of

the pressure gradient. The S3F streamwise displacement in agrees with the Cp distributions in that there is a larger shift in reattachment point caused by DBD-02 and DBD-03, than for DBD-01. In fact, based on S3F data at the trailing edge and Cp data the mean flow reattaches far upstream of C_x=80% for DBD-02 with an applied voltage of 7.3 kVpp. This is a significant decrease in the extent of the mean separation bubble length. Earlier transition to turbulence with less dominance from large scale inviscid type instability and more viscous small scale turbulence in the boundary layer would support the increase in wake velocity deficit seen in DBD-02 at Re=1.0 x 10^5.

Based on the plots of Figures 11-13 the following conclusions are made for operation at Re = 1.0 x 10^5:

- All three plasma actuators move the mean reattachment point upstream as voltage is increased.
- Cp data indicates an upstream shift in reattachment point for DBD-01 of at least 5% Cx. S3F data indicates an upstream shift in mean reattachment of nearly 4% Cx at the S3F midpoint, but the reattachment point is not uniform in along the airfoil span.
- Cp data of DBD-02 shows a significant upstream shift in reattachment location as plasma actuator voltage is increased. The plateau in Cp that marks the separation bubble smoothes out significantly at an voltage of 6.5kVpp and above. The peak velocity deficit in the wake increases with voltage. S3F data shows a significant upstream shift in mean reattachment location as the voltage is increased culminating with a reattachment point upstream of the view which ends at C_x=83%.

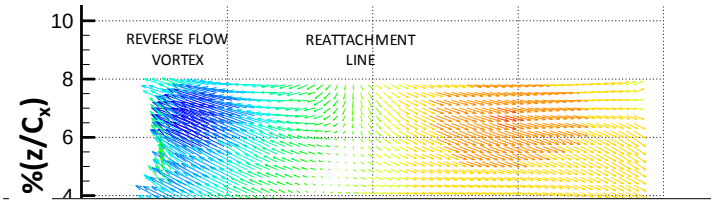

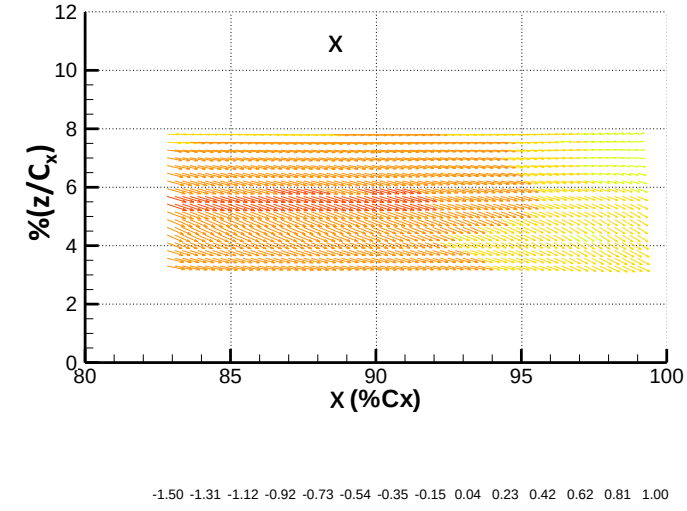

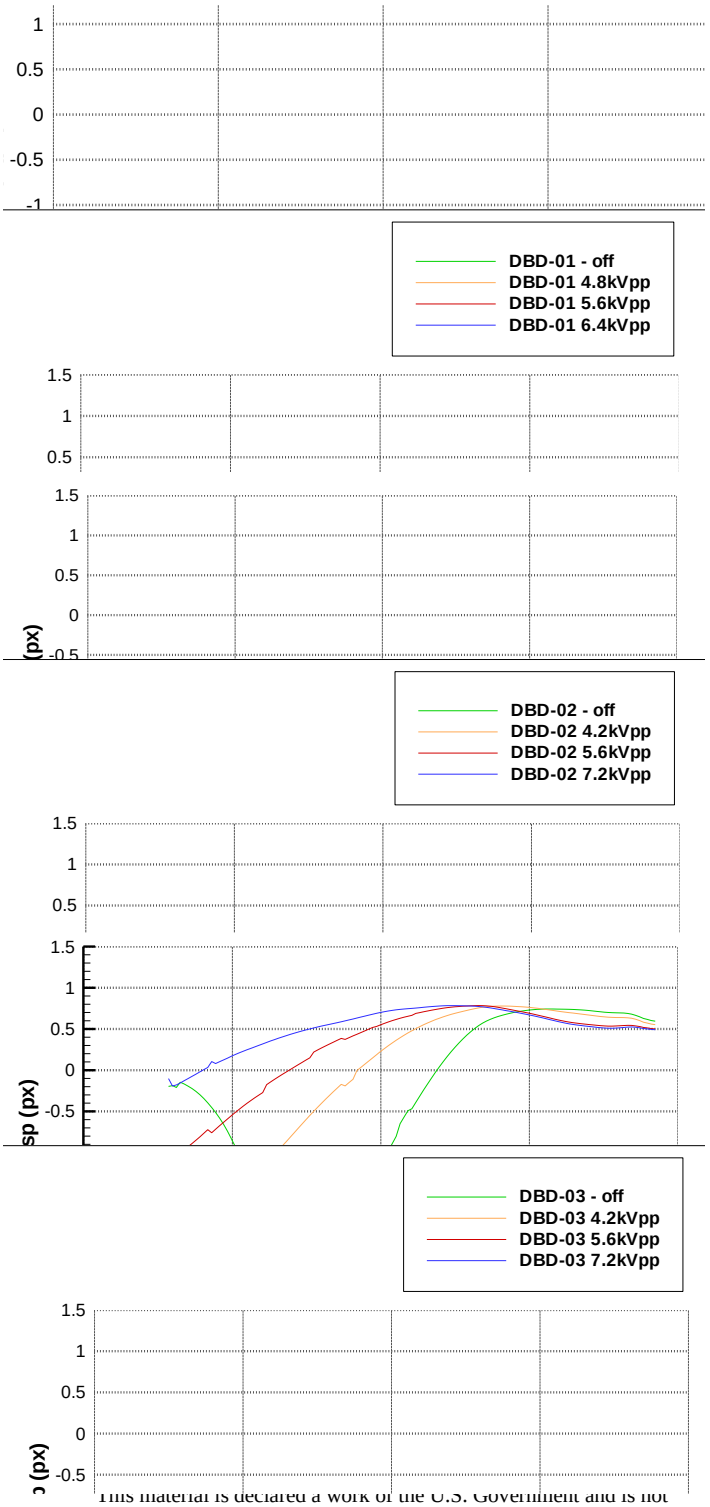

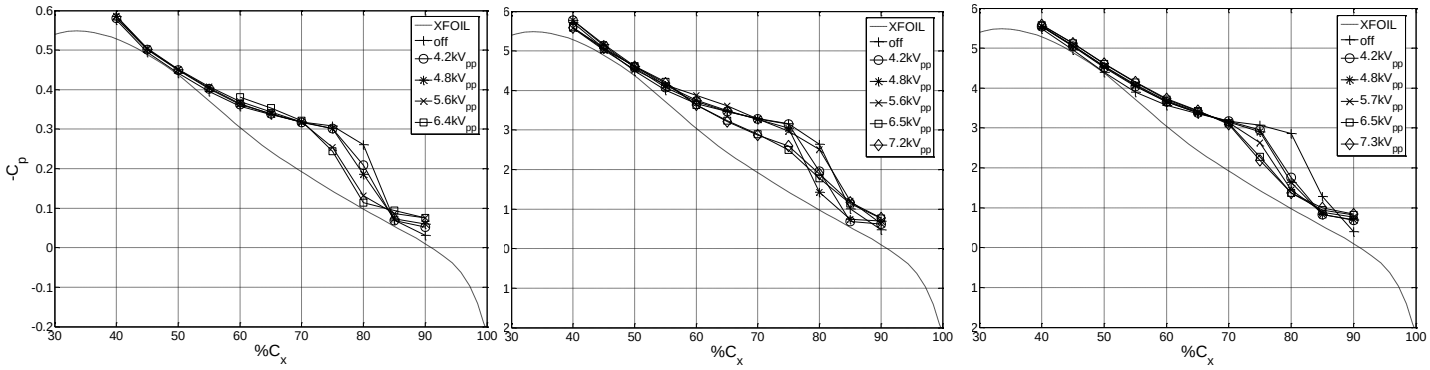

Figure 13. Suction surface Cp distribution and wake profile for each plasma actuator tested at 1.0 x 10^5. Column A: DBD-01, B: DBD-02, C: DBD-03.

- Powering on plasma actuator DBD-03 shifts the reattachment point upstream with increases in voltage providing further upstream shift in reattachment. S3F indicates a nearly 8% upstream shift in mean reattachment point as voltage is increased to 7.3 kVpp.

Discussion

Each actuator clearly had an effect on suction surface laminar boundary layer separation as summarized in the plots of Figure 14 that show the S3F indicated mean reattachment points. At the lower Reynolds number $5.0x10^4$ in which there was laminar separation without reattachment, powering on actuators DBD-01 and DBD-02 clearly resulted in a significant upstream shift in mean reattachment location. Electrode configuration DBD-02, the spanwise array of linear vertical jets led the actuators tested with reattachment at Cx=87%. This is confirmed by Cp data that shows significant smoothing of the plateau in pressure gradient that marked flow separation. DBD-03 did not definitively result in mean reattachment at the highest voltage tested, but did result in a significant decrease in wake width when the actuator was powered. It is possible that higher plasma actuator voltage would have resulted in mean reattachment.

At the higher Reynolds number, $1.0x10^5$, laminar boundary separation with mean reattachment was present with the plasma actuator off. In these flow conditions powering on DBD-03 significantly shifted the mean reattachment line upstream 8%Cx. Less of an upstream shift was observed for DBD-01, the spanwise array of cross stream jets, however S3F data was not obtained at 7.2kVpp to compare to the other actuators, and further upstream shift may have resulted. Electrode configuration DBD-02 had the largest apparent effect with an S3F indicate shift in mean reattachment point beyond the field of view (reattachment at Cx<83%).

Drag data is presented in Figure 15 for each actuator tested. Powering on each actuator resulted in a decrease in drag at $Re=5x10^4$, with each actuator reaching a minimum drag value. DBD-02, the spanwise array of linear vertical jets reached its minimum at the lowest plasma actuator voltage, with a 33% reduction in drag. DBD-03 the downstream facing jet also had a significant decrease in drag 30% at $Re=5.0x10^4$. At the $Re=1.0x10^5$ powering on the actuators did not result in a decrease in drag. In fact the drag gradually increased with increase in voltage for each actuator. This is most likely due to the increased length of turbulent boundary layer as the separation bubble decreases in length, resulting in no improvement in drag. The drag plot shown in Figure 15 also displays the difference in drag due to variation in the quality of installation of each plasma actuator on the airfoil. The airfoil with DBD-03 has the largest initial drag when the plasma actuator is powered off.

Flow visualization images are shown in Figs. 16-19 in order to further understand the effect of each actuator. Figure 16 shows a large decrease in separation and boundary layer thickness as the actuator power is increased. The effect of the actuator at lower voltage settings is decrease in separation angle and smaller, less dominate large scale inviscid structures in the separated shear layer. At the higher voltage a thin separation bubble is formed. This explains the earlier minimum observed in drag. As the voltage increases past 5.6 kV_{pp} and the separated boundary layer reattaches, no additional gains are made in drag due to increased turbulent boundary layer length.

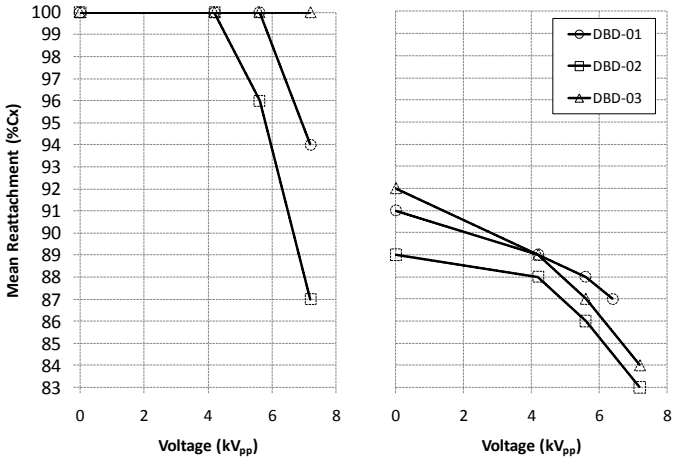

A. $Re= 5x10^4$ B. $Re = 1.0x10^5$

Figure 14. S3F indicated shifts in mean reattachment locations with increase in voltage.

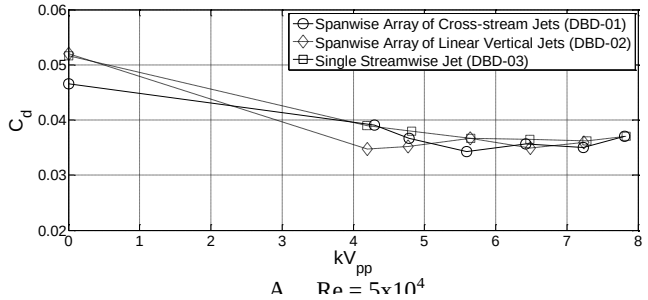

A. Re = $5x10^4$

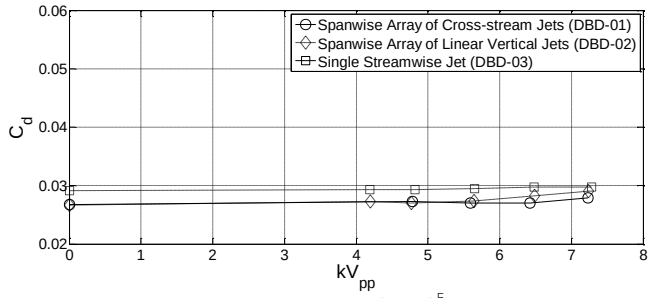

B. Re = 1.0×10^5

Figure 15. Drag for each actuator tested.

In Figure 17 flow visualization in the area of the plasma actuator and boundary layer separation is shown. The actuator on image is very interesting and shows eddies formed downstream of the actuator. The laser sheet in this case was placed centered with one of the plasma actuator vertical jets. The eddies were only observed at the highest voltage tested 7.3 kV_{pp}. The linear vertical jet is aligned with the streamwise direction and is expected to introduce three dimensional vorticity by creating a local separation region. This bottom image in Figure 17 clearly shows that, at the least spanwise coherent eddies form entraining higher momentum flow from the freestream to the wall.

The effect of plasma actuator DBD-03 at the trailing edge is shown in Figure 18. This plasma actuator was least effective at the lowest Reynolds number tested. The flow visualization indicates that as voltage is increased the separated shear layer develops into a boundary layer with large scale streamwise structures. This orientation acts as a wall jet entraining momentum from the freestream and adding momentum to the boundary layer. The flow visualization in this study indicates the configuration was less effective at promoting transition and reattachment of the boundary layer. The large scale inviscid structures are maintained and do not appear to break up into small scale structures. It did however, decrease drag by 30%. At the higher Reynolds number of Re=$1.0x10^5$ in which a mean reattaching separation bubble was present in the actuator off case, the plasma actuator DBD-03 was very effective at moving the reattachment point upstream (see Figure 19).

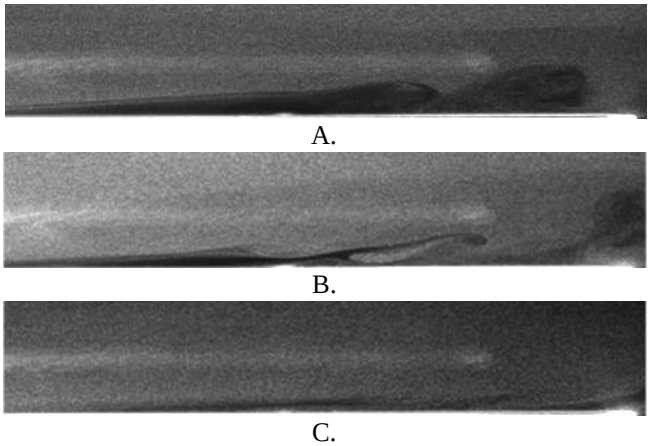

A.

B.

C.

Figure 16. Flow visualization of plasma actuator DBD-01 at the trailing edge from Cx=65% to 101% at a Re = 5 x 10^4. Image A: actuator off, B: 5.6 kV_{pp}, C: 7.2 kV_{pp}

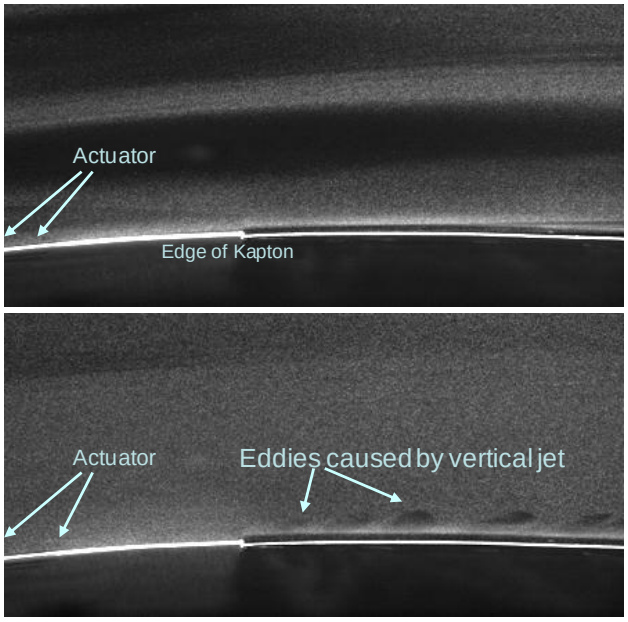

Figure 17. Flow visualization showing spanwise coherent unsteadiness generated by the vertical jets of DBD-02 with Re=$5x10^4$. Top: actuator off, Bottom: actuator voltage 7.2 kVpp. View is from approximately Cx=30% to 60%.

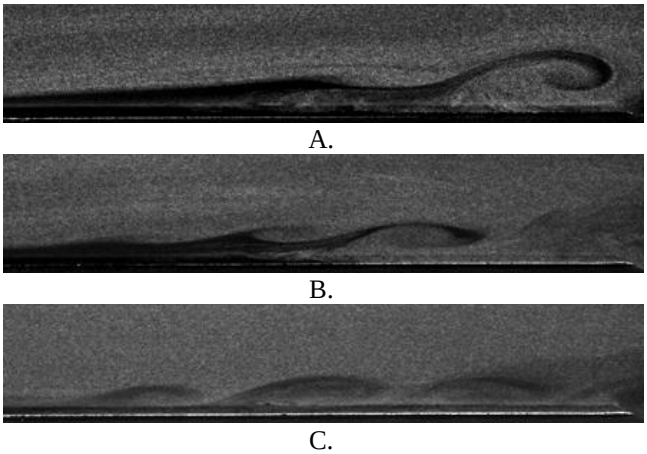

A.

B.

C.

Figure 18. Flow visualization of plasma actuator DBD-03 at the trailing edge from Cx=70% to 101% at a Re = 5 x 10^4. Image A: actuator off, B: 4.8 kV_{pp}, C: 7.2 kV_{pp}

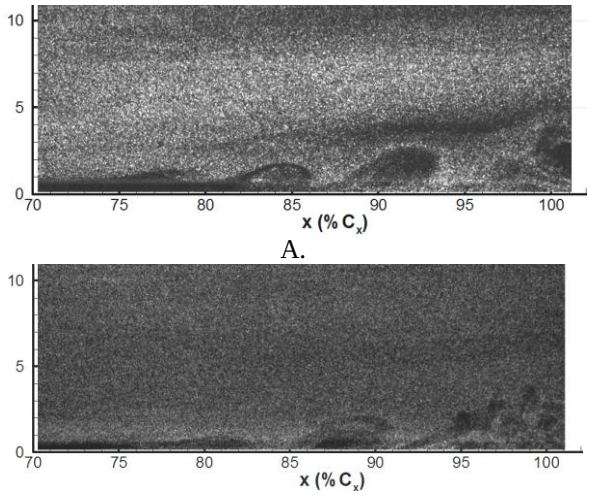

Figure 19. Flow visualization of airfoil with plasma actuator DBD-03 installed. Suction surface near trailing edge is shown at Re=1.0x10^5. Image A: actuator off, B: 7.3 kV$_{pp}$.

CONCLUSIONS

Three different plasma actuator electrode configurations were compared for use in a low Reynolds number separation control system. Two of the actuator configurations were implemented with the intent of generating three-dimensional, or streamwise vorticity to improved moment entrainment from the freestream into the boundary layer. Operation at two different Reynolds numbers was presented here. At the lower Reynolds number of 5x10^4, laminar separation without reattachment was observed with the actuators powered off. At the higher Reynolds number 1.0x10^5 the boundary layer separated and then reattached prior to the trailing edge.

Three parameters were used to compare the performance of each actuator: Suction surface Cp profile, S3F streamwise surface displacement, and drag. At the lowest Reynolds number tested, S3F reattachment locations indicated plasma actuator DBD-02, a spanwise distributed array of linear vertical jets, reattached the flow and moved the mean reattachment upstream as voltage was increased to 7.2kV$_{pp}$. This configuration also resulted in the largest improvement in drag.

At the higher Reynolds number each plasma actuator moved the reattachment point upstream. Plasma actuator configuration DBD-02 shifted the reattachment point upstream in excess of 6% Cx, likely significantly further as the mean reattachment point moved out of the field of view. Plasma actuator configuration DBD-03 shift the reattachment point upstream 8% Cx. Each actuator tested at Re=1.0x10^5 showed an increase in drag as the separation length decreased with increased voltage. This is considered to be due to an increase in turbulent boundary layer length.

Several conclusions can be made from the results of this study:

1. The spanwise distributed array of linear vertical jets (DBD-02) are deemed the most effective in the two flow conditions presented here. However, plasma actuator DBD-01, a spanwise array of cross-stream jet showed promise and it is possible that a different spanwise spacing of the jets would yield better results.
2. Alternative DBD plasma actuator electrode configurations to the standard asymmetric electrode configuration must be considered and studied in more detail as they show potential for performance improvements.
3. The electrode configuration that will provide the most effective separation control at low Reynolds number will likely change with flow conditions. This points towards electrode configurations and power electronics that enable induced velocity jet vectoring. A configuration that uses jet vectoring could create the effects of configurations DBD-01, and DBD-02, and enable switching between jet orientations based on flow condition.

It should be mentioned that the success of the two spanwise distributed arrays, used here in hopes of generating three dimensionality and streamwise vorticity, point towards the conclusion that longitudinal vorticity was generated. However, further study is necessary to verify the control mechanism that led to reattachment.

ACKNOWLEDGMENT

The authors would like to thank Dr. Richard Rivir for the use of a substantial amount of the test and measurement equipment used for this work. Dr. Sergey Fonov and his coworkers at Innovative Scientific Solutions Inc. are acknowledged for fabricating the S3F used in this work and training and assistance on the use of S3F technology. Thank you to Dr. Rivir, and Dr. Joseph Shang for sharing their knowledge of DBD plasma actuators with the lead author.

REFERENCES

[1] Lake, J., "Flow Separation Prevention on a Turbine Blade in Cascade at Low Reynolds Number" PhD Dissertation, Air Force Institute of Technology, 1999.

[2] Mahmood, G., Hill, M., Nelson, D., "Local Heat Transfer and Flow Structure On and Above a Dimpled Surface in a Channel", ASME 2000-GT-230, 2000.

[3] Sondergaard, R., Rivir, R., Bons, J., "Control of Low-Pressure Turbine Separation Using Vortex-Generator Jets," *Journal of Propulsion and Power, 18,* 2002, pp. 889-895.

[4] Bons, J., Sondergaard, R., Rivir, R., "Turbine Separation Control Using Pulsed Vortex Generator Jets," *Journal of Turbomachinery, 123*, 2001, pp. 198-206.

[5] Johnston, J. P., and Nishi, M., "Vortex-Generator Jets: Means for Flow Separation Control," *AIAA Journal, 28,* 1990, pp. 989-994.

[6] Moreau, E., "Airflow control by non-thermal plasma actuators", *Journal of Physics D: Applied Physics, 40,* 2007, pg 605-636.

[7] Enloe, C., McLaughlin, T., VanDyken, R., Kachner, K., Jumper, E., Corke, T., "Mechanisms and Responses of a Single Dielectric Barrier Plasma Actuator: Plasma Morphology" AIAA Journal V. 42, No. 3, pp 589-594 2004.

[8] Enloe, C., McLaughlin, T., VanDyken, R., Kachner, K., Jumper, E., Corke, T., Post, M., Haddad, O. "Mechanisms and Responses of a Single Dielectric Barrier Plasma Actuator: Geometric Effects." AIAA Journal V. 42, No. 3, pp. 595-604 2004.

[9] Enloe, C., McLaughlin, T., Baughn, J., "Parameterization of Temporal Structure in the Single-Dielectric-Barrier Aerodynamic Plasma Actuator", AIAA Journal, 44, pp. 1127-1136, 2006.

[10] Rivir, R., White, A., Carter, C., Ganguly, B., Jacob, J., Forelines, A., Crafton, J., "AC and Pulsed Plasma Flow Control, AIAA Paper No. AIAA-2004-847, January, 2004.

[11] Pons, J., Moreau, E., and Touchard, G., "Asymmetric surface barrier discharge in air at atmospheric pressure: electric properties and induced airflow characteristics", *Journal of Phy. D: Appl. Phys., 38*, pg 3635-3642.

[12] Fridman, A., Chirokov, A., and Gutsol, A., "Non-thermal atmospheric discharges", *Journal of Physics D: Applied Physics, 38*, 2005, R1-R24.

[13] Roth, J., Sherman, D., and Wlidkenson, S., "Boundary Layer Flow control with a One Atmosphere Uniform Glow Discharge Plasma," Paper No. AIAA-1998-0328, January 1998.

[14] Porter, C., Baughn, J., McLaughlin, T., Enloe, C., Font, G. "Plasma Actuator Force Measurements" AIAA Journal, V. 45, July 2007, pg 1562-1570.

[15] Sondergaard, R., Rivir, R., Bons, J., "Control of Low-Pressure Turbine Separation Using Vortex-Generator Jets", *Journal of Propulsion and Power, 18*, pp. 889-895, 2002.

[16] Shang, J., Personal Correspondence, July 2008.

[17] Rivir, R.B., Sondergaard, R., Bons, J.P., and Yurchenko, N. 2004. Control of Separation in Turbine Boundary Layers, AIAA Paper No. 2004-2201.

[18] Huang, J., Corke, T., and Thomas, F., "Plasma Actuators for Separation Control of Low Pressure Turbine Blades", AIAA Paper No. 2003-1027, January, 2003.

[19] Huang, J., Corke, T., and Thomas, F., 2006. "Unsteady Plasma Actuators for Separation Control of Low-Pressure Turbine Blades", AIAA Journal, 44, pp. 1477-1487.

[20] Rizzetta, D.P. and Visbal, M.R., "Simulation of Plasma-Based Flow-Control Strategies for Transitional Highly Loaded Low-Pressure Turbines", AIAA Paper No. AIAA-2007-938, June, 2007.

[21] Rizzetta, D. P., and Visbal, M. R., "Numerical Investigation of Plasma-Based Flow Control for Transitional Highly Loaded Low-Pressure Turbine" *AIAA Journal, 45*, pp. 2554-2564, 2007.

[22] Roy, S., and Wang, C., "Bulk flow modification with horseshoe and serpentine plasma actuators", J. Phys. D: Appl. Phys. 42 (2009), pp. 1-5.

[23] Crafton, J., Fonov, S., Forlines, A., Goss, L., "Skin Friction Measurements Using Elastic Films", *AIAA Aerospace Sciences Meeting*, AIAA, Orlando, FL, 2010, AIAA-2010-42.

[24] Jacob, J., Ramakumar, K., Anthony, R., Rivir, R., "Control of Laminar and Turbulent Shear Flows Using Plasma Actuators" *4th International Symposium on Turbulence and Shear Flow Phenomena*, Williamsburg, VA June 27-29, 2005.

[25] Santhanakrishnan, A., and Jacob, J., "Flow Control with Plasma Synthetic Jet Actuators" *J. Phys. D: Appl. Phys. 40* (2007) pp 637-651.

[26] Santhanakrishnan, A., and Jacob, J., "Effect of Plasma Morphology on Flow Control Using Plasma Synthetic Jet Actuators" AIAA Paper No. 2007-783.

[27] Santhanakrishnan, A., and Jacob, J., "Characterization of Linear Plasma Synthetic Jet Actuators". AIAA Paper No. 2008-538.

[28] Santhanakrishnan, A., Reasor, J., and Lebeau, R. "Characterization of linear plasma synthetic jet actuators in an initially quiescent medium". *Physics of Fluid 21*, 2009, DOI:10.1063/1.3097004.

[29] Porter, C., Abbas, A., Cohen, K., McLaughlin, T., and Enloe, C., "Spatially Distributed Forcing and Jet Vectoring with a Dielectric Barrier Discharge Plasma Actuator," AIAA Paper No. 2008-1374.

[30] Porter, C., Abbas, A., Cohen, K., McLaughlin, T., Enloe, C., "Spatially Distributed Forcing and Jet Vectoring with a Plasma Actuator" *AIAA Journal, 47*, (2009), pp. 1368-1378.

[31] Bolitho, M., and Jacob, J., "Thrust Vectoring Flow Control Using Plasma Synthetic Jet Actuators," AIAA Paper No: 2008-1368.

[32] Sherman, D. M. "Manipulating Aerodynamic boundary layers using an electrohydrodynamic effect generated by a One Atmosphere Uniform Glow Discharge Plasma", August 1998, Master's Thesis, University of Tennessee, Knoxville, p. 52.

[33] Lin, J. C. and Pauley, L. L., "Low-Reynolds Number Separation on an Airfoil," *AIAA Journal, 34*, pp. 1570-1577.

[34] Selig M. S. and Mcgranahan, B. D., "Wind Tunnel Aerodynamic Tests of Six Airfoils for Use on Small Wind Turbines." National Renewable Energy Laboratory Subcontractor Report, NREL/SR-500-34515, 2004.

[35] List, J., Byerley, A., McLaughlin, T., Van Dyken, R., "Using a Plasma Actuator to Control Laminar Separation on a Linear Cascade Turbine Blade", *41st Aerospace Sciences Meeting*, AIAA Paper No. AIAA-2003-1026.

[36] McQuilling, M., Wolff, M., Fonov, S., Crafton, J., Sondergaard, R., "An Experimental Investigation of a Low-Pressure Turbine Blade Suction Surface Using a Shear and Stress Sensitive Film", *Experiments in Fluids*, V. 44, No. 1, pp. 73-88.

[37] McQuilling, M., Wolff, M., Fenov, S., Crafton, J., and Sondergaard, R., "An Experimental Investigation of Suction Surface Flow Features on a High-Lift LPT", AIAA Paper No. 2008-79.

[38] McQuilling, M., Wolff, M., Fonov, S., Crafton, J., Sondergaard, R., "An Experimental Investigation of a Low-Pressure Turbine Blade Suction Surface Using a Shear and Stress Sensitive Film", *Experiments in Fluids*, V. 44, No. 1, pp. 73-88.

[39] McQuilling, M., Wolff, M., Fenov, S., Crafton, J., and Sondergaard, R., "An Experimental Investigation of Suction Surface Flow Features on a High-Lift LPT", AIAA Paper No. 2008-79.

[40] Marks, C., Nessler, C., Sondergaard, R., Wolff, M., Crafton, J., Fonov, S., "High Lift LPT Blade Suction Surface Flow Investigation Using Surface Stress Sensitive Film, *45th AIAA Joint Propulsion Conference & Exhibit*, AIAA Paper No. 2009-5106, Denver, CO, 2009.

[41] Drela, M., and Youngren, H., 2001. XFOIL 6.9 User Primer. Accessed on January 4, 2009. http://web.mit.edu/drela/Public/web /xfoil/xfoil_doc.txt

[42] Goett, H., "Experimental Investigation of the Momentum Method for Determining Profile Drag," NACA Report No. 660, 1939.

[43] Roth, J., Sherman, D., and Wilkinson, S., "Electrohydrodynamic Flow Control with a Glow-Discharge Surface Plasma," *AIAA Journal, 38*, pp. 116.

APPENDIX F

Proceedings of ASME Turbo Expo 2013
GT2013
June 3-7, 2013, San Antonio, USA

GT2013-95000

ENDWALL LOSS REDUCTION OF HIGH LIFT LOW PRESSURE TURBINE AIRFOILS USING PROFILE CONTOURING – PART I: AIRFOIL DESIGN

M. Eric Lyall
Air Force Research Laboratory
Wright-Patterson AFB, OH, USA

Paul I. King
Air Force Institute of Technology
Wright-Patterson AFB, OH, USA

John P. Clark
Air Force Research Laboratory
Wright-Patterson AFB, OH, USA

Rolf Sondergaard
Air Force Research Laboratory
Wright-Patterson AFB, OH, USA

ABSTRACT

This paper presents the reasoning for and the design process of contouring a high lift front-loaded low pressure turbine (LPT) airfoil near the endwall to reduce the endwall loss. The test airfoil, L2F, was designed to the approximate gas angles with 38% larger pitchwise spacing than the widely studied Pack B airfoil. Being more front-loaded with a higher stagger angle, L2F is shown to produce more endwall losses than Pack B. It is suggested that the high endwall loss of L2F is due to the high stagger angle, not front-loading as usually suggested in the literature. A procedure is presented to approximate the front-loading and stall resistance of L2F and obtain a low stagger version of that airfoil, designated L2F-LS. A contoured airfoil is then designed by transitioning L2F into L2F-LS at the endwall to obtain a benefit from the reduced stagger angle at the endwall. The contouring process generates a fillet, so the contoured airfoil is referred to as L2F-EF ("Endwall Fillet"). Predictions in this paper suggest endwall loss reductions between 17% and 24% at Re = 100,000. Linear cascade experiments in Part II [1] of this paper indicate that L2F-EF reduces endwall losses more than 20% compared to L2F. The overall conclusion is that the stagger angle has a significant effect on endwall loss and should be considered for designing high lift LPT airfoils at the endwall.

NOMENCLATURE

BLFP	boundary layer force parameter
C_{ax}	axial chord
C_p	pressure coefficient, $C_p = \left(P_s - P_{s,in}\right)/0.5\rho\, U^2_{in,st}$
H	airfoil height, or span
M	Mach number
P_s	static pressure
P_t	total pressure
RANS	Reynolds-averaged Navier-Stokes
Re	Reynolds number based on inlet velocity and axial chord
s	suction surface distance coordinate
S	cascade pitchwise spacing
SS_L	suction surface length
U	mean velocity
x,y,z	cascade coordinate directions
Y	total pressure loss coefficient, $\left(P_{t,in} - P_t\right)/0.5\,\rho U^2_{in,st}$
Z_w	Zweifel loading coefficient, $Z_w = 2\left(\frac{S}{C_{ax}}\right)\cos^2\alpha_{ex}\left(\tan\alpha_{in} - \tan\alpha_{ex}\right)$

Greek

α	cascade gas angle, measured from axial
δ_{99}	99% boundary layer thickness
λ	stagger angle
τ	shear stress

Subscripts and Superscripts

2D	midspan or profile conditions, two-dimensional
ew	endwall
ex	exit location
in	inlet location
p	peak suction
ps	passage
st	streamwise direction
w	wall

U.S. Air Force Public Affairs Office Case No. 88ABW-2010-6254

INTRODUCTION

Elevated endwall loss limits the practical loading levels of high lift LPT airfoils. Several passive flow control methodologies have been attempted to reduce endwall losses, including boundary layer fences, leading edge bulbs and fillets, and non-axisymmetric endwall contouring. (Langston [2] provides a brief overview of these methods.) Although the concepts are quite different, all these loss reduction methods attempt to manipulate the vortex structures of the endwall flow to reduce the total pressure loss. Among these flow control techniques, the literature reports that non-axisymmetric endwall contouring has been the primary technique applied to high lift LPT profiles. Praisner et al. [3] and Knezevici et al. [4] found, however, that the endwall loss remained beyond practical limits for the high lift Pack DF profile (a representative high lift design), even after implementing non-axisymmetric endwall contouring. Other approaches may need to be considered to reduce the endwall loss of high lift designs to acceptable levels.

Unlike past high lift LPT studies focusing on endwall contouring, the current work examines the effect on endwall loss of the profile shape at the endwall. A loss reduction method that focuses on the airfoil can be combined with endwall contouring methods to potentially give further performance improvements. As will be shown, reducing the stagger angle at the endwall can reduce endwall losses. This paper documents how to contour the profile near the endwall for linear cascades of airfoils to obtain the beneficial effect of the reduced stagger angle. The following section shows the cascade nomenclature and sign convention used in this study.

CASCADE NOMENCLATURE

Figure 1 shows the cascade definitions. The flow angle sign convention is consistent with Wilson and Korakianitis [5]. The stagger setting, λ, is defined as a positive angle. For all experiments and calculations in this study, the aspect ratio is $H/C_{ax} = 3.5$. The following section describes the testbed airfoil used in this study, L2F.

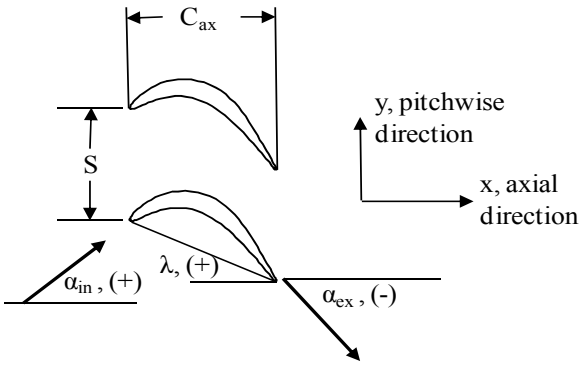

Figure 1. Cascade definitions

DESCRIPTION OF THE L2F AIRFOIL

The L2F airfoil is one from a family of airfoils designed at the Aerospace Systems Directorate of AFRL to study low Reynolds number and high lift LPT aerodynamics (Lyall et al., [6]). The design intent of L2F was to achieve good low Reynolds number performance compared to the widely studied Pratt & Whitney Pack B airfoil while increasing the aerodynamic lift. McQuilling [7] designed the L2F airfoil to the approximate Pack B gas angles with 38% larger pitchwise spacing. Both airfoils are compared in Fig. 2. Besides different pitchwise spacing, Table 1 shows that the L2F stagger angle is 8.7˚ larger than for Pack B.

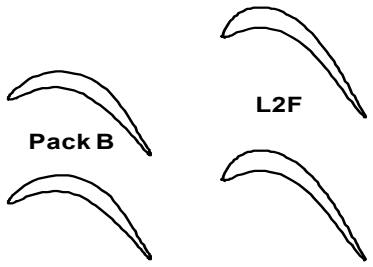

Figure 2. Comparison of Pack B and L2F profiles

Table 1. Pack B and L2F geometric and flow properties

	S/C_{ax}	α_{in}, deg	α_{ex}, deg	λ, deg	Z_w
Pack B	0.885	35.00	-58.48	25.90	1.13
L2F	1.221	35.00	-58.12	34.60	1.57

The Reynolds lapse data of Fig. 3 show that L2F performs quite well at low Reynolds number compared to Pack B. The difference is significant, considering that L2F has 38% larger pitchwise spacing than Pack B. The good low Reynolds number performance of L2F can be attributed to its front-loaded pressure distribution shown in Fig. 4. As shown, peak suction for L2F and Pack B occurs approximately at $0.25C_{ax}$ and $0.65C_{ax}$, respectively.

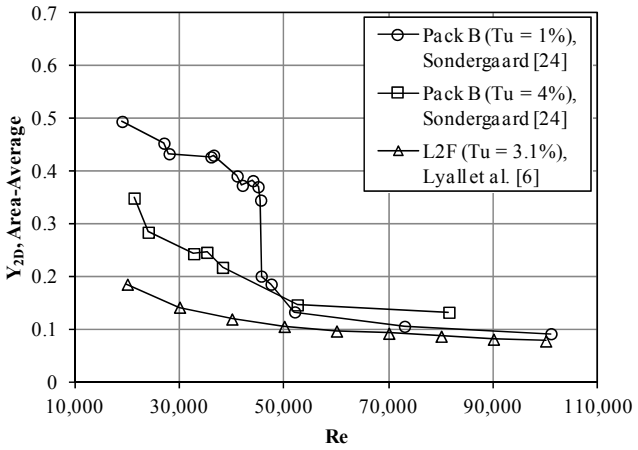

Figure 3. Comparison of Pack B and L2F midspan Reynolds lapse

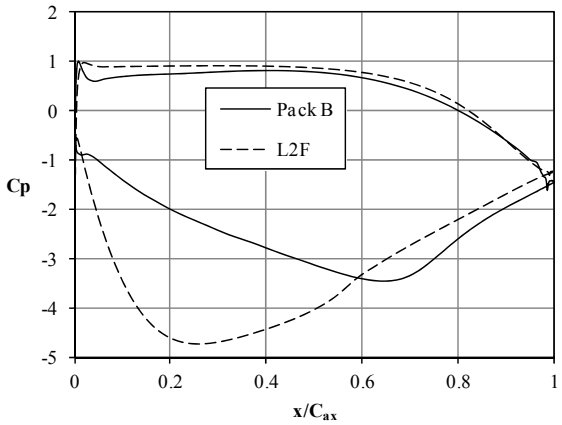

Figure 4. Pack B and L2F pressure loading (Leo Code)

Unfortunately, high lift airfoils such as L2F with good low Reynolds number performance often produce unacceptably high endwall loss. Table 2 shows the ratio of endwall loss (Y_{ew}) of L2F to that of Pack B, computed using the design code Leo (code is discussed in the following section). Data for the Pack DA and Pack DF airfoil 4% turbulence cases of Zoric et al. [8] are also included for reference. Pack DA and Pack DF are LPT airfoils that are aft and front-loaded, respectively, designed to the same approximate gas angles as Pack B. As shown, Y_{ew} of the front-loaded L2F and Pack DF airfoils exceeds that of Pack B by nearly 40%. On the other hand, Pack DA actually produces less endwall loss than Pack B. One also notes in Table 2 that the airfoils with high endwall loss, L2F and Pack DF, have larger stagger angles than the airfoils with less endwall loss, Pack B and DA.

Table 2. Effect of pressure loading and stagger angle on Y_{ew} at Re = 80,000

	S/C_{ax}	Z_w	λ, °	$Y_{ew}/Y_{ew,\,(Pack\ B)}$
L2F (Leo)	1.221	1.57	34.6	1.37
Pack DA, [8]	1.105	1.37	26.0	0.93
Pack DF, [8]	1.105	1.37	35.4	1.39
Pack B	0.885	1.13	25.9	1.00

To offer an explanation for why the high stagger airfoils produce more endwall loss than Pack B, Fig. 5 shows the effect of the static pressure field on the inlet boundary layer flow of the low stagger Pack B and high stagger L2F airfoils. The Cp contours are drawn in a plane at half the inlet boundary layer thickness. Accordingly, the streamlines are released from the same plane as they enter the flow domain. As shown for both airfoils in Figs. 5a and 5b, the streamlines indicate that the inlet boundary layer fluid cannot enter the high-pressure region of the passage, as indicated by the Cp = 0.5 contour line. For the high stagger L2F airfoil, the Cp = 0.5 line becomes nearly orthogonal to the incoming boundary layer fluid near the leading edge, suggesting a stronger pressure blockage compared to Pack B. To further illustrate the increased blockage of L2F, Fig. 6 shows close-up images of leading edge

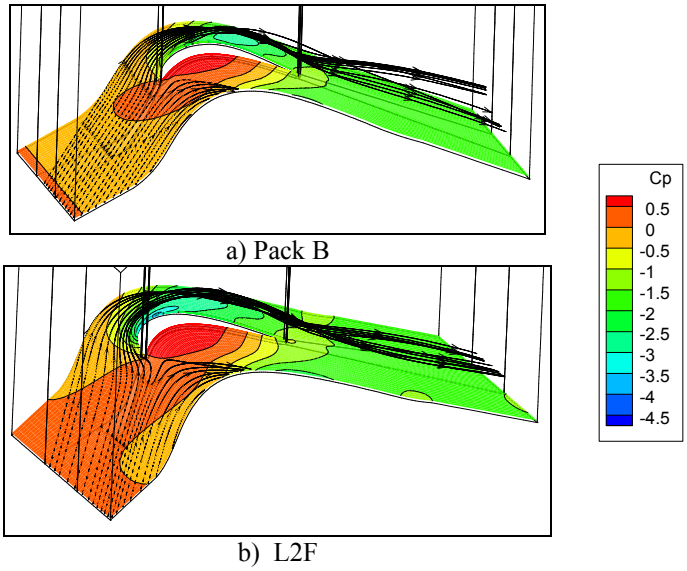

a) Pack B

b) L2F

Figure 5. Effect of the static pressure field on the inlet boundary layer flow for the Pack B and L2F profiles (Streamlines initiated at ½ the inlet boundary layer thickness)

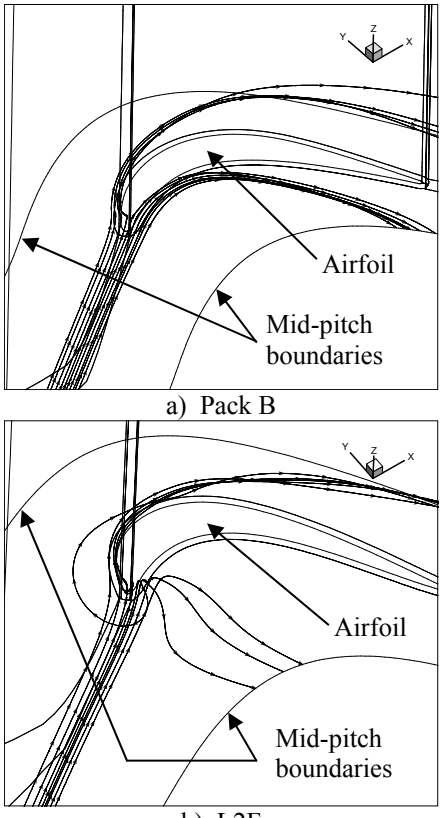

a) Pack B

b) L2F

Figure 6. Leading edge streamlines showing more entrainment of inlet boundary layer fluid for L2F compared to Pack B (Streamlines released at the edge of the inlet boundary layer)

streamlines released from the edge of the inlet boundary layer as opposed to half the inlet boundary layer thickness. As shown for Pack B, the streamlines pass through the passage. For L2F, however, fluid is still being entrained in the horseshoe vortex, a direct result of the increased blockage.

Several studies including those of Weiss and Fottner [9], Zoric et al. [8], Praisner et al. [3], and Knezivici et al. [4] have all shown that front-loading increases endwall loss. The front-loaded airfoils in all these studies had higher stagger angles than the companion aft-loaded airfoils. Although increasing the stagger angle is the most common method to apply front-loading, thickening the leading edge region while limiting the stagger angle can also be used to apply front-loading (cf., Korakianitis and Papagiannidis [10]). Considering that the results in this section suggest that increasing the stagger angle increases endwall loss, L2F is contoured at the endwall to reduce the stagger angle and maintain front-loading consistent with the latter method of front loading. The design intent is to reduce the pressure blockage at the endwall, thereby weakening the inlet boundary layer separation and reducing endwall losses. The following section discusses the codes used to modify L2F.

DESIGN CODES

This section discusses the design codes used to contour the L2F airfoil at the endwall. AFRL's Turbine Design and Analysis System (TDAAS) is a 2D code that was used to define the new profile shape for use at the endwall. The codes Wand and Leo (Aerodynamic Solutions, [11]) are the grid generator and flow solver, respectively, used for evaluating passage and endwall performance. The following sections briefly describe each code.

Turbine Design and Analysis System (TDAAS)

The TDAAS system employs the profile generator of Clark et al. [12]. That algorithm uses Bezier curves in conjunction with typical leading- and trailing-edge specifications (e.g., wedge angles, edge radii of curvature, gage areas, and uncovered turning) to define airfoil shapes using a small number of control points according to the method described by Casey [13]. Once the profile was defined, the grid generator and flow solver of Dorney and Davis [14] was used with an ad hoc implementation of Praisner and Clark's [15] separated flow transition model to determine airfoil performance. The RANS equations were closed using the Baldwin-Lomax [16] algebraic model. Graphical User Interfaces (GUIs) and both design optimization (Vanderplaats, [17]) and design-of-experiments techniques (Santner et al., [18]) were used during the design process to define the shape of the profile.

The grid generator of Dorney and Davis [14] produces multi-block structured OH grids, with O-type grids used for discretizing the boundary layer and H-grids used for the remainder of the domain. Approximately 7,000 grid points gave grid-independent results for 2D passages, with y^+ levels less than unity on airfoil surfaces.

The flow solver of Dorney and Davis [14] is density-based and is used to solve the RANS equations using an implicit dual time stepping, time-accurate approach. The time-integration scheme is second-order accurate with convergence being obtained when the pressure field downstream of the trailing edge becomes steady periodic. Spatial discretization is third-order accurate using finite differences. Exit Mach numbers were elevated to $M_{ex} = 0.2$ to reduce stiffness of the governing equations while maintaining incompressible flow. Reynolds numbers were controlled by adjusting the fluid density via the pressure.

Wand Code

Wand functions as the preprocessor, generating the computational grid and assigning boundary conditions for use with the flow solver Leo. Grids can be for either 2D or 3D applications. Typical 2D grids have structured multi-block OHH topologies. O-type grids discretize the airfoil boundary layers with H-grids used for the remainder of the domain. Grid topologies are referred to as OHH instead of OH because of the addition of extra H-grid blocks upstream and downstream of the leading and trailing edges, respectively. Full passage grids are constructed by using multiple 2D grids along the airfoil span, referred to as k-planes. Grid-independent results are achieved using approximately 12,000 and 800,000 points for 2D and 3D domains, respectively. The grids are refined at the walls such that the y^+ levels are less than unity.

Besides generating computational grids, the Wand code can also be used to design 3D airfoils. For example, a designer may define profiles at the endwall, at midspan and at the tip to control the spanwise work distribution. The WAND code uses spline interpolation to generate the mesh along the span, thus shaping the whole airfoil that passes through the defining profiles. We used this method to contour the L2F airfoil near the endwall to reduce the stagger angle.

Leo Code

The flow solver LEO is a compressible finite volume code. The code employs a cell-vertex discretization scheme that is second order accurate in space. Time integration can be for either steady or time accurate simulations. For the current study that focuses on single blade rows, all solutions are steady. For convergence acceleration the code employs local time stepping and multi-grid techniques. The code also uses a preconditioner to reduce stiffness of the governing equations and accelerate convergence for low Mach number flows. Nevertheless, exit Mach numbers were elevated to $M_{ex} = 0.2$ to reduce stiffness of the governing equations while maintaining incompressible flow. The Reynolds number was varied by adjusting the pressure to change the fluid density. The RANS equations are closed using the fully turbulent k-ω model (Wilcox, [19]).

CONTOURED AIRFOIL DESIGN

The premise for designing the contoured airfoil is that the high stagger angle of L2F is a significant cause of elevated endwall loss for that airfoil in Table 2. Therefore, the idea is to reduce the stagger angle at the endwall.

Designing the contoured airfoil was a two-step process. First, a low-stagger version of L2F, L2F-LS, was designed for use at the endwall. Secondly, the spanwise length required to transition from L2F in the middle of the airfoil to L2F-LS at the endwall was determined. As will be shown, the contouring process generates a fillet predominantly on the pressure surface at the endwall. The contoured airfoil will therefore be referred to as L2F-EF (L2F-"endwall fillet"). The following sections describe the design processes.

L2F-LS Profile Design

For designing a low stagger version of L2F, it is desired to match the gas angles, pitchwise spacing and stall resistance (the desirable attribute of L2F, see Fig. 3). The stagger angle is arbitrarily set to $\lambda = 25.8^\circ$, similar to Pack B. Matching the gas angles and pitchwise spacing was straightforward, but matching the stall resistance was not. A new non-dimensional parameter, referred to as the boundary layer force parameter (BLFP), was derived to provide a quantifiable measure of front-loading and stall resistance.

The reasoning used for deriving BLFP is similar to the reasoning used for the separated flow transition model of Praisner and Clark [15]. Those authors formulated their model to predict the length of the separation bubble as a function of momentum thickness Reynolds number just prior to separation. Their model relied on the premise that the length of the separation bubble scales with the state of the boundary layer at separation. Furthermore, their model suggests that thinner boundary layers with higher wall shear stress will produce smaller separation bubbles, thus making profiles more stall resistant. This idea can be extended by considering that the adverse pressure gradient eventually drives the wall shear to zero as the separation bubble forms. Thus, a scale parameter that compares the friction force in the boundary layer prior to peak suction to the adverse pressure gradient aft of peak suction may provide insight into stall resistance of LPT profiles.

The ratio of the friction force prior to peak suction to the pressure force aft of peak suction can be written as,

$$\mathrm{BLFP} = \frac{\dfrac{\tau_{w,p}}{\delta_{99,p}}}{\dfrac{P_{s,ex} - P_{s,p}}{SS_L - s_p}} \tag{1}$$

where $\tau_{w,p}$ is the wall shear stress, $\delta_{99,p}$ is the 99% boundary layer thickness, $P_{s,ex} - P_{s,p}$ is the pressure rise from peak suction to the trailing edge, and $SS_L - s_p$ is the suction surface distance from peak suction to the trailing edge. Using flat plate similarity solutions to provide scales for the friction force (cf., Schlichting and Gersten, [20]),

$$\frac{\tau_{w,p}}{\delta_{99,p}} \approx \frac{\rho\, U_p^2}{s_p}. \tag{2}$$

Using static pressure coefficients,

$$P_{s,ex} - P_{s,p} = \left(Cp_{ex} - Cp_p\right)\frac{\rho U_{in,st}^2}{2}. \tag{3}$$

Substituting Eqs. (2) and (3) into Eq. (1),

$$\mathrm{BLFP} = \frac{\left(SS_L - s_p\right)}{s_p\left(Cp_{ex} - Cp_p\right)}\frac{U_p^2}{U_{in,st}^2}. \tag{4}$$

Since we are only seeking a scaling parameter, the factor of two in Eq. (3) was neglected when obtaining Eq. (4). Assuming inviscid flow for a streamline with flow accelerating from $U_{in,st}$ to U_p,

$$\frac{U_p^2}{U_{st,in}^2} = 1 - Cp_p. \tag{5}$$

Substituting Eq. (5) into Eq. (4) and rearranging, the final form of BLFP is,

$$\mathrm{BLFP} = \frac{\left(1 - Cp_p\right)\left(1 - s_p/SS_L\right)}{s_p/SS_L\left(Cp_{ex} - Cp_p\right)}. \tag{6}$$

Given the surface coordinates of the profile and the pressure loading distribution, BLFP can be calculated for any airfoil. The suction surface can be defined starting from the stagnation point near the leading edge out to the maximum axial coordinate defining the profile. For convenience, the minimum axial coordinate is usually near the stagnation point and will also work well as the starting point for defining the suction surface. Due to difficulties in computing Cp values at trailing edges, Cp_{ex} can be defined using the exit static pressure downstream of the blade row. In the following discussion of BLFP for Pack B and L2F, the suction surface is defined using the minimum and maximum axial coordinates of the profiles. Data of Fig. 4 determined the Cp_p values and the outlet static pressure of LEO predictions were used to compute Cp_{ex} values. Although the LEO calculations were viscous, inviscid Cp predictions will also work for calculating BLFP.

Figure 7 shows the effects of peak suction location and aerodynamic lift on BLFP using Cp's from both the Pack B and L2F airfoils. Although s_p/SS_L is a singular value for both airfoils, it was treated as a parameter to generate the two curves. Approximate values of s_p/SS_L for Pack B and L2F are indicated on the chart. BLFP for Pack B and L2F is 2.27 and

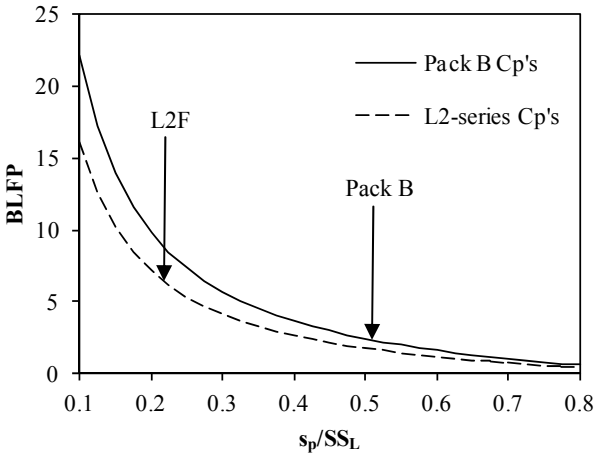

Figure 7. Effect of peak suction and lift on BLFP

5.90, respectively. As shown, BLFP increases as profiles are front-loaded to move the peak suction location closer to the leading edge. Based on the derivation of BLFP, the physical implication is that the suction surface boundary layer prior to peak suction becomes thinner for more front-loaded profiles resulting in separation bubbles that more easily reattach, thus increasing stall resistance. The increased Zweifel number of L2F causes the BLFP curve to be offset below that of Pack B in Fig. 7. The different peak suction locations, however, compensates for increased loading to increase the stall resistance of L2F compared to Pack B (see Fig. 3). Lyall [21] provides a more extensive discussion of BLFP.

Regarding the design of the low stagger version of L2F, L2F-LS, $BLFP_{new} \geq BLFP_{L2F}$ is the constraint required to approximate the stall resistance of L2F. Together, the constraints that $\lambda = 25.8^{\circ}$ and $BLFP_{new} \geq BLFP_{L2F}$ were implemented in TDAAS to produce a new baseline high lift profile. The new baseline profile is shown in Fig. 8 compared to L2F. Furthermore, the new baseline profile has BLFP = 6.74, 14% larger than the L2F BLFP number. As shown, the constraint that limits the stagger angle combined with the large pitchwise spacing and front-loading of L2F results in an extremely thick profile. The suction surface of the new profile is also highly curved, extending upstream of the leading edge. The primary effect of the large profile thickness is that the stagnation point moves from just under the leading edge for L2F to the front side of the new profile. Flow passing over the leading edge of the new profile causes an undesirable pressure surface separation bubble.

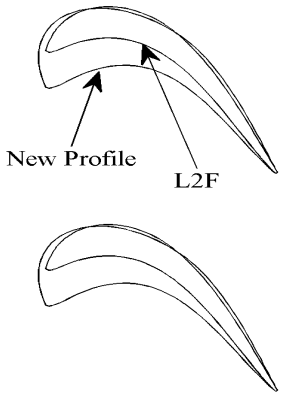

Figure 8. Comparison of the new baseline profile with L2F

Blanco et al. [22] has shown that pressure surface separation bubbles can increase endwall loss. In practice, profiles are often modified to eliminate pressure surface separation bubbles. Figure 9 shows several variations of the baseline profile pressure surface. The idea is to manipulate the airfoil shape to occupy the space of the separation bubble that occurs for the baseline design. The modifications shown are cubic Bezier curves extending from the leading edge to approximately $0.82C_{ax}$, aft of bubble reattachment for the baseline profile. Full passage calculations using the Leo code indicated that Mod 2 in Fig. 9 minimized the losses among the cases considered, so that design was designated as the L2F-LS profile to be used at the endwall of the contoured airfoil.

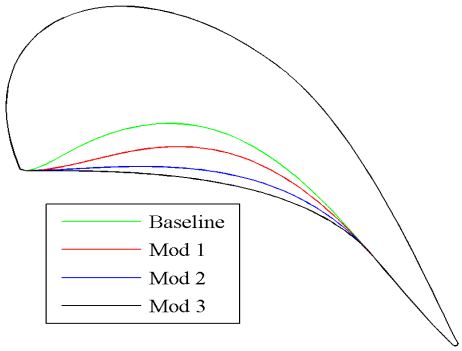

Figure 9. Pressure surface modifications to eliminate the pressure surface separation

Figure 10 shows Y contours based on profile calculations using Leo to show the elimination of the pressure surface separation bubble. As shown, the high loss region adjacent to the pressure surface of the baseline profile is absent for the L2F-LS profile.

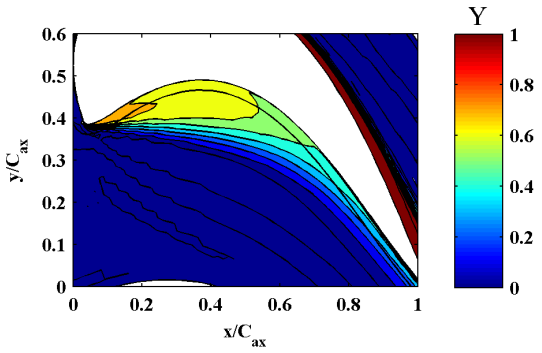

a) Baseline new profile design

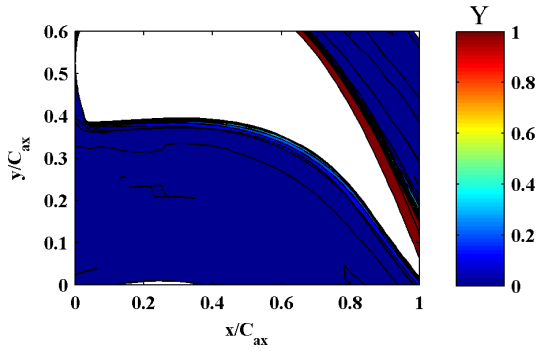

b) L2F-LS profile

Figure 10. Y contours to show the elimination of the pressure surface separation bubble (Computed using Leo, Re = 100k)

Having discussed the L2F-LS design process, Fig. 11 shows the low Reynolds number performance predicted using TDAAS. No experimental data were available to validate the predictions for L2F-LS, but the TDAAS predictions are in good agreement with experiments for L2F. As shown, L2F-LS performs quite well at low Reynolds number and satisfies the design intent of a high lift stall resistant airfoil compared to Pack B, similar to L2F. The profile loss of L2F-LS, however, is consistently higher than for L2F, indicating that L2F-LS may not be a good choice for use in the middle of LPT airfoils. The increased profile loss of L2F-LS may be due to its significantly longer perimeter around the profile compared to L2F. Although BLFP suggests stall resistance, it does not in general indicate the overall level of profile loss. Also similar to L2F, the stall resistance of L2F-LS is attributed to a front-loaded pressure distribution, shown in Fig. 12. The BLFP constraint resulted in the front-loaded pressure distribution for L2F-LS. For convenience, geometric and flow properties are summarized in Table 3 for Pack B, L2F and L2F-LS.

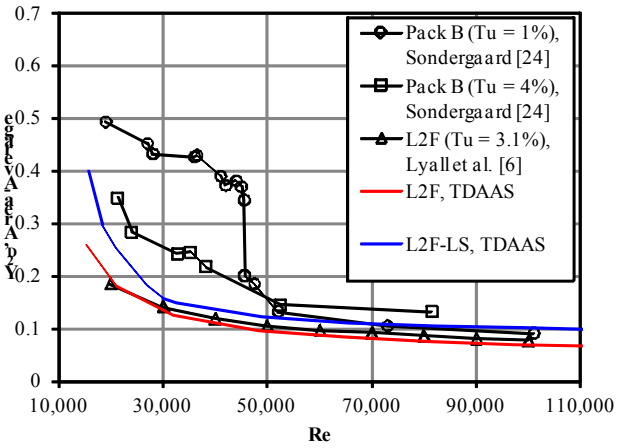

Figure 11. L2F-LS Reynolds lapse compared to L2F and Pack B

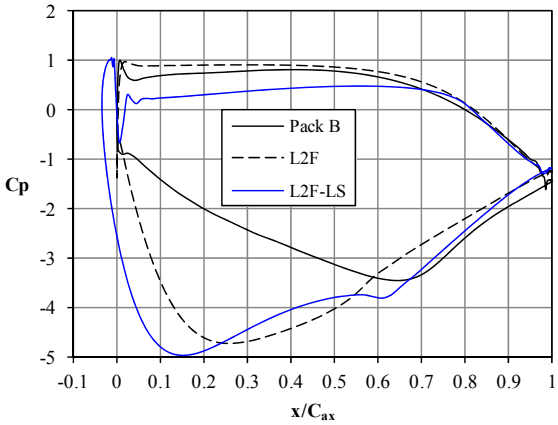

Figure 12. L2F-LS pressure loading compared to L2F and Pack B

Table 3. Pack B, L2F and L2F-LS geometric and flow properties

	Pack B	L2F	L2F-LS
S/C_{ax}	0.885	1.221	1.221
α_{in}, deg	35.00	35.00	35.00
α_{ex}, deg	-58.48	-58.12	-57.44
λ, deg	25.90	34.60	25.80
Z_w	1.13	1.57	1.60
BLFP	2.27	5.90	6.74

The newly designed L2F-LS profile will be used at the endwall of the contoured airfoil (L2F-EF, "EF is for endwall fillet") in an attempt to reduce the endwall loss of L2F. The following section outlines the process for determining the transition from L2F at the middle of the airfoil to L2F-LS at the endwall.

Contoured L2F-EF Airfoil Design

The transition between the high and low stagger L2-series profiles resulted in a fillet shape at the endwall, predominantly on the airfoil pressure surface. The contoured L2F-EF airfoil is visualized in Fig. 13 using airfoil coordinates in k-planes near the endwall that were generated using the WAND code. The thick blue line in Fig. 13 illustrates the transition from L2F-LS at the endwall to the L2F profile. The point where the blue line straightens indicates the fillet height. To generate the fillet shape using Wand, the L2F-LS profile was defined at the endwall with L2F defined at the desired fillet height. A second L2F profile was defined 2% span on towards midspan. Together, the profile shapes defined along the span functioned as control points for a spline interpolation that defined the whole airfoil. As shown in Fig. 13, the contoured airfoil near the endwall appears smooth.

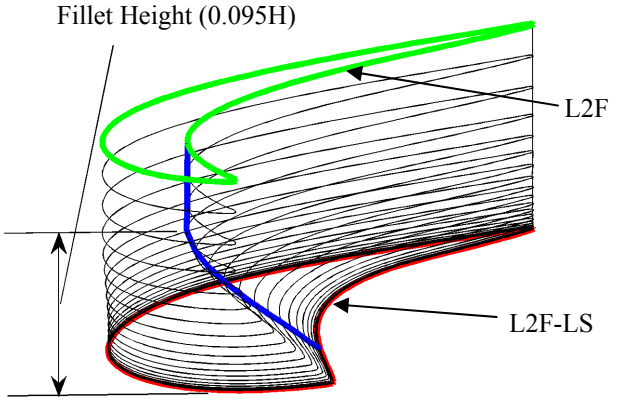

Figure 13. Illustration of the L2F-EF airfoil near the endwall to show the fillet shape

One might expect the fillet height to influence the overall total pressure loss. Based on the premise that a reduced stagger angle can reduce endwall losses, a benefit may not be realized if the fillet height is too small. As shown in Fig. 11, however,

the L2F-LS profile defined at the endwall will likely produce more profile losses than L2F, suggesting excessive profile loss if the fillet height is too large. Figure 14 shows the results of a sensitivity study of the fillet height on the overall passage loss, Y_{ps}. As shown, Y_{ps} is fairly insensitive to the fillet height. Nevertheless, the case for the fillet height of approximately z/H = 0.095 produced minimum losses among the cases considered, so that design was chosen for L2F-EF shown in Fig. 13.

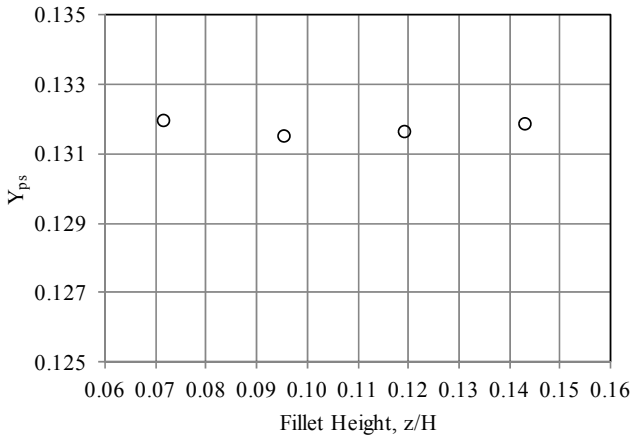

Figure 14. Sensitivity of L2F-EF passage loss to the fillet height, Re = 100k (Computed using Leo)

Having discussed the design of the L2F-LS profile and the contoured L2F-EF airfoil, the focus of the following section is on full passage and endwall performance of the newly designed airfoils. As will be shown, the reduced stagger angle at the endwall can reduce endwall losses.

RESULTS AND DISCUSSION

The purpose of designing the new L2F-LS profile and the contoured L2F-EF airfoil was to determine if a benefit can be obtained from reducing the stagger angle of high lift front-loaded LPT airfoils. The discussion begins by comparing straight L2F and L2F-LS airfoils to show the beneficial effect of the stagger angle on endwall loss. Secondly, results for the contoured L2F-EF airfoil are shown to demonstrate that contouring the airfoil near the endwall to reduce the stagger angle can also be beneficial.

All results were computed using fully turbulent Leo calculations while assuming a 99% inlet boundary layer thickness of $0.088C_{ax}$, consistent with experiments in Part II [1] of this paper. Loss results are based on mass-weighted averages taken an axial chord downstream of the blade row in the axial direction. Furthermore, 2D CFD models were used to compute the profile loss, Y_{2D}, to eliminate endwall effects and obtain a clean estimate of the profile loss. Midspan loss does not in general equal profile loss for finite length airfoils, so separate 2D and 3D CFD models were deemed necessary (cf., Sharma and Butler [23]). Endwall loss, Y_{ew}, is calculated as the passage loss, Y_{ps}, minus Y_{2D}.

The use of fully turbulent RANS calculations also requires further comment. Most notably, separation bubbles on the suction surfaces of the high lift airfoils are usually eliminated by assuming full turbulence. Hence, results from the Leo code under-predict the Reynolds number dependency of the total pressure loss in an absolute sense. However, results are presented for a range of Reynolds numbers to compare airfoils. The L2F and L2F-LS airfoils are compared in the following section.

Effect of the Stagger Angle on Endwall Loss

Predicted Y_{ew} and Y_{ps} calculations using LEO for L2F and L2F-LS are shown in Fig. 15. As shown, there is little difference in Y_{ps} between the two profiles for Re > 80,000. Y_{ew} of L2F-LS is significantly lower compared to L2F at high Re, yet excessive Y_{2D} causes Y_{ps} to be nearly equivalent for the two profiles. The results using the LEO code indicating high profile loss for L2F-LS are in agreement with TDAAS predictions in Fig. 11. At low Re, however, the low stagger L2F-LS airfoil is predicted to have a stronger Re dependency in Y_{ew} than L2F, leading to increased Y_{ps} at low Re. Considering results of Y_{ps} across the whole Re range, L2F can arguably be considered the better performing profile. The low Y_{ew} of L2F-LS, however, is a desirable design feature. As shown in Fig. 16, L2F-LS produces over 20% less Y_{ew} than L2F for Re > 70,000. The results of Figs. 15 and 16 support the hypothesis that the stagger angle, λ, has a significant effect on Y_{ew}.

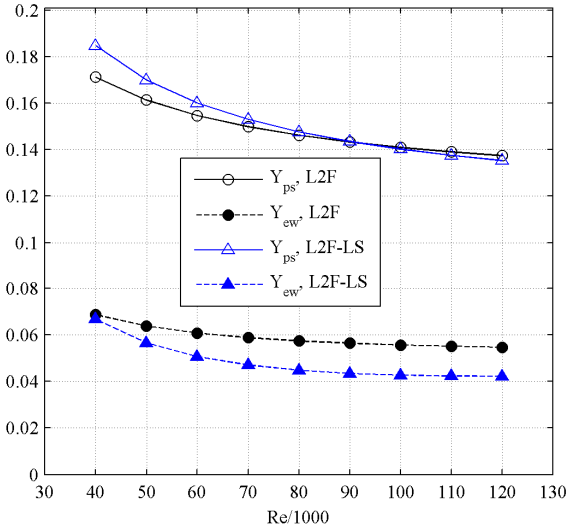

Figure 15. Comparison of L2F and L2F-LS endwall and passage performance

The following section discusses the performance of the contoured L2F-EF airfoil. The design intent of this airfoil was to preserve the good midspan performance of L2F while exploiting the beneficial effect on endwall loss of the reduced L2F-LS stagger angle.

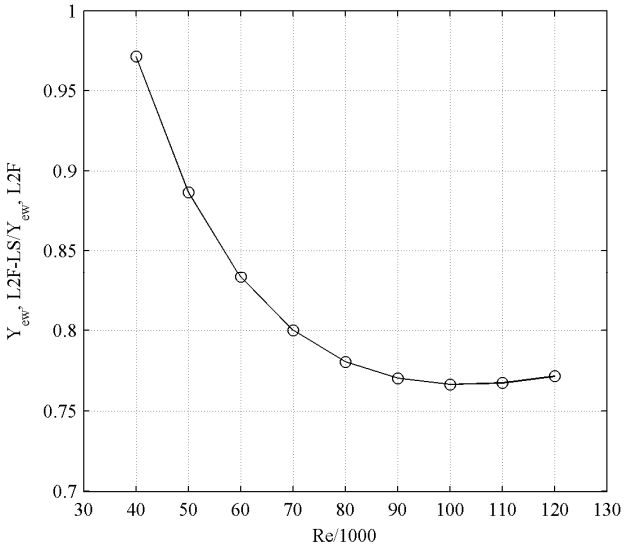

Figure 16. Endwall loss reduction of L2F-LS compared to L2F

Performance of the Contoured L2F-EF Airfoil

Figure 17 compares the reduction in Y_{ew} of L2F-EF with that of L2F-LS. At high Re, the L2F-EF airfoil does not provide as much loss reduction as L2F-LS, but well over half of the loss reduction is retained using the fillet. Because of the transition between the two profile shapes, it is not surprising that L2F-EF does not have as much of a reduction in Y_{ew} as L2F-LS. Nevertheless, the L2F-EF predictions suggest a significant loss reduction for all Re examined. At Re ≈ 56,000, the two curves intersect due to a strong Re dependency for L2F-LS at low Re. The addition of the fillet of the L2F-EF airfoil partially retains the weaker Re dependency of Y_{ew} shown in Fig. 15 for L2F, yet at high Re Y_{ew} is higher than for L2F-LS.

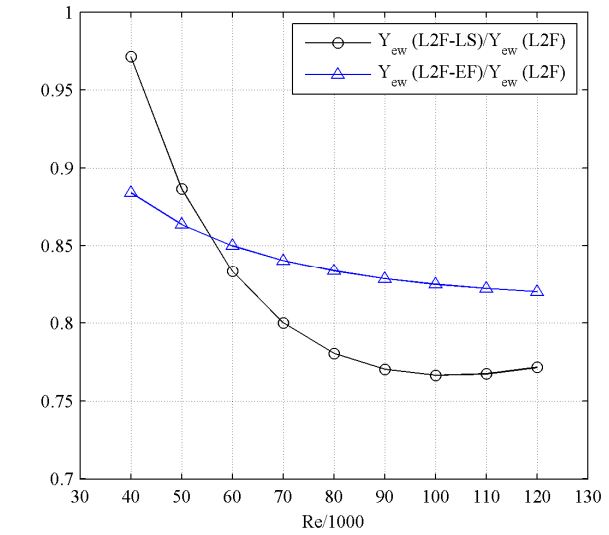

Figure 17. Comparison of Y_{ew} reduction between L2F-LS and L2F-EF

Although L2F-EF does not reduce Y_{ew} as much as L2F-LS at high Re, the results still suggest that contouring high lift airfoils to reduce the stagger angle at the endwall can significantly reduce Y_{ew}. The L2F-LS curve in Fig. 17 likely bounds the endwall loss reduction that can be achieved by reducing the stagger angle through profile contouring. At Re = 100,000 used for experiments in Part II [1] of this paper, Fig. 17 suggests an endwall loss reduction in the range of 17% to 24%. As will be shown in Part II [1], the experimental mass-averaged endwall loss reduction is approximately 23%.

Keeping in mind that for high lift LPT airfoils to be practical, they must perform as well as the conventional lift airfoils they are intended to replace. The following section compares the performance of the L2-series airfoils just described to the conventional lift Pack B airfoil.

Comparison of L2-Series Airfoils with Pack B

Fig. 18 compares Y_{ps} of the high lift L2-series airfoils with that of Pack B. As shown, both L2F and L2F-LS have noticeably higher Y_{ps} than Pack B for all Re considered. Although Y_{ps} of L2F-EF is also higher than for Pack B, Y_{ps} is significantly reduced. According to Zoric et al. [8], Re = 80,000 at the Pack B design condition. At the design point, predicted Y_{ps} of L2F is nearly 10% higher than for Pack B. The addition of the fillet used for L2F-EF reduces Y_{ps} to within 2.5% of Pack B at the design point. At the low and high extremes of Re, the predicted difference in Y_{ps} between L2F-EF and Pack B is less than 2%. Considering that Pack B is expected to begin to stall for Re < 50,000 (See Fig. 3), it is likely that L2F-EF will actually perform much better at low Re than Pack B.

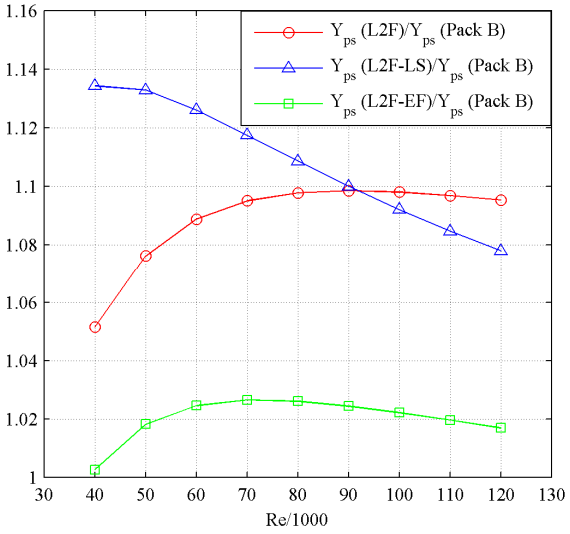

Figure 18. Comparison of L2-series passage loss (Y_{ps}) to that of the conventionally loaded Pack B airfoil

Figure 19 shows that elevated Y_{ew} is why Y_{ps} of L2F-EF is predicted to remain slightly higher than for Pack B. At the Pack B design point of Re = 80,000, Fig. 19 shows that Y_{ew} for

L2F-EF is estimated to be 14% higher than for Pack B. However, the difference between L2F-EF and Pack B is a significant improvement compared to L2F that has approximately 37% higher Y_{ew} than Pack B. Other endwall loss reduction methods (e.g., non-axisymmetric endwall contouring) are likely needed for L2F-EF to be practical.

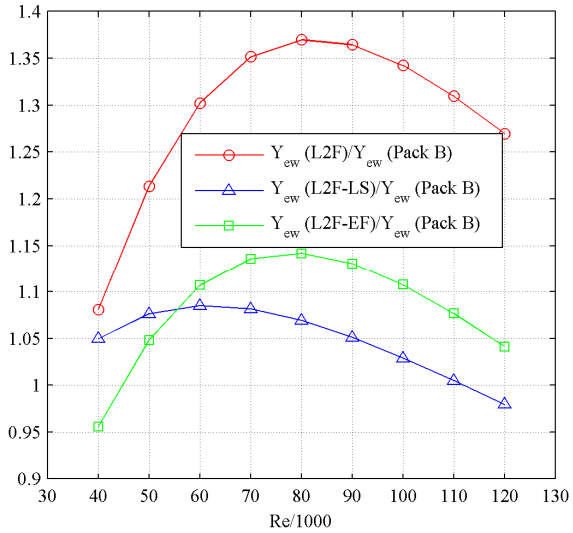

Figure 19. Comparison of L2-series endwall loss (Y_{ew}) to that of the conventionally loaded Pack B airfoil

SUMMARY AND CONCLUSIONS

In this paper results indicated that the stagger angle has a significant influence on endwall losses of front-loaded high lift LPT airfoils. A new high lift front-loaded airfoil, designated L2F-LS, was designed as a low stagger version of the primary testbed airfoil, L2F. These L2-series airfoils have 38% larger pitchwise spacing than the conventional lift airfoil, Pack B. L2F-LS was designed using a new non-dimensional boundary layer force parameter (BLFP) to approximate the front-loading and stall resistance of L2F, as well as the pitchwise spacing and gas angles. L2F-LS produced over 20% less endwall loss than L2F for Re > 70,000, indicating that reducing the stagger angle of high lift front-loaded airfoils can reduce the endwall loss. L2F-LS, however, produced no net reduction in passage loss due to increased profile loss.

The contoured L2F-EF (L2F-"Endwall Fillet) airfoil was designed to exploit the good profile and endwall performance of L2F and L2F-LS, respectively. The contouring was between 9.5% span and the endwall. Design predictions at Re = 100,000, the experimental Reynolds number of Part II [1] of this paper, estimated endwall loss reductions in the range of 17% to 24%. Experiments in Part II [1] indicate an approximate 23% endwall loss reduction for L2F-EF compared to L2F. Thus, the design predictions in this paper and experiments in Part II [1] indicate that contouring high-lift front-loaded LPT airfoils at the endwall to reduce the stagger angle can reduce endwall losses. Such a design modification results in a fillet predominantly on the pressure surface. It is suggested that non-axisymmetric endwall contouring could provide additional performance improvements to L2F-EF.

Whereas this paper focused on the effect of the stagger angle on endwall loss and how it can be exploited, the focus of Part II [1] is on showing the effect experimentally and explaining why the stagger angle influences endwall loss. Those experiments support the claim in this paper that the loss reduction is due to a weakened inlet boundary layer separation for L2F-EF compared to L2F.

As a final note, much work remains before such a modification can be applied to a real machine. At present it is unknown how the modification will perform in an annular cascade, as well as with realistic skewed inlet boundary layers. Also, whether or not a significant weight penalty is incurred due to thickening the ends of the airfoil will likely depend on how the airfoil is manufactured, e.g., hollow or solid airfoils. At the tip, the flow turning is usually smaller than at the hub, so less thickening will be required. Implementation may also be simpler using shrouded blades for rotors.

REFERENCES

[1] Sangston, K., Little, J., Lyall, M.E., and Sondergaard, R, 2013, "Endwall Loss Reduction of High Lift Low Pressure Turbine Airfoils Using Profile Contouring – Part II: Validation," ASME Paper GT2013-95002.

[2] Langston, L.S., 2001, "Secondary Flows in Axial Turbines –A Review," Annals New York Academy of Sciences, Vol. 934, *Heat Transfer in Gas Turbine Systems*, pp. 11-26.

[3] Praisner, T.J., Grover, E.A., Knezevici, D.C., Popovic, I., Sjolander, S.A., Clark, J.P., and Sondergaard, R., 2008, "Toward the Expansion of Low-Pressure-Turbine Airfoil Design Space," ASME Paper GT2008-50898.

[4] Knezevici, D.C., Sjolander, S.A., Praisner, T.J., Allen-Bradley, E., and Grover, E.A., 2009, "Measurements of Secondary Losses in a High-Lift Front-Loaded Turbine Cascade with the Implementation of Non-Axisymmetric Endwall Contouring," ASME Paper GT2009-59577.

[5] Wilson, D.G., and Korakianitis, T., 1998, "The Design of High-Efficiency Turbomachinery and Gas Turbines," 2nd Edition. Upper Saddle River, New Jersey: Prentice Hall Inc.

[6] Lyall, M.E., King, P.I., Sondergaard, R., Clark, J.P., and McQuilling, M.W, 2012 "An Investigation of Reynolds Lapse Rate for Highly Loaded Low Pressure Turbine Airfoils with Forward and Aft Loading," *ASME J. of Turbomachinery*, Vol. 134, pp. 051028-1:051028-9.

[7] McQuilling, M.W., 2007. "Design and Validation of a High Lift Low-Pressure Turbine Blade," PhD Thesis, Wright State University, Dayton, Ohio.

[8] Zoric, T., Popovic, I., Sjolander, S.A., Praisner, T., and Grover, E., 2007, "Comparative Investigation of Three Highly Loaded LP Turbine Airfoils: Part I – Measured Profile and Secondary Losses at Design Incidence," ASME Paper GT2007-27537.

[9] Weiss, A.P., and Fottner, L, 1995 "The Influence of Load Distribution on Secondary Flow in Straight Turbine

Cascades," *ASME J. of Turbomachinery*, Vol. 117, pp. 133-141.

[10] Korakianitis, T., and Papagiannidis, P., 1993, "Surface-Curvature-Distribution Effects on Turbine-Cascade Performance," *ASME J. of Turbomachinery*, Vol. 115, pp. 334-340.

[11] Aerodynamic Solutions, 2012, "http://www.aerodynamic-solutions.com/," Pleasanton, California.

[12] Clark, J. P., Koch, P. J., Ooten, M. K., Johnson, J. J., Dagg, J., McQuilling, M. W., Huber, F., and Johnson, P. D., 2009, "Design of Turbine Components to Answer Research Questions in Unsteady Aerodynamics and Heat Transfer," AFRL Report No. AFRL-RZ-WP-TR-2009-2180.

[13] Casey, M. V., 1994, "Computational Methods for Preliminary Design and Geometry Definition in Turbomachinery," in Turbomachinery Design Using CFD, AGARD Lecture Series 195, pp. 1-1:1-22.

[14] Dorney, D. J. and Davis, R. L., 1992, "Navier-Stokes Analysis of Turbine Blade Heat Transfer and Performance," *ASME J. of Turbomachinery*, Vol. 114, pp. 795-806.

[15] Praisner, T. J. and Clark, J. P., 2007, "Predicting Transition in Turbomachinery, Part I – A Review and New Model Development," *ASME J. of Turbomachinery*, Vol. 129, pp. 1-13.

[16] Baldwin, B., and Lomax, H., 1978, "Thin Layer Approximation and Algebraic Model for Separated Turbulent Flows," AIAA Paper No. AIAA-78-257.

[17] Vanderplaats, G. N., 1984, Numerical Optimization Techniques for Engineering Design: With Applications, McGraw-Hill, New York.

[18] Santner, T. J., Williams, B. J., and Notz, W. I., 2003, The Design and Analysis of Computer Experiments, Springer-Verlag, New York.

[19] Wilcox, D.C., 1998, "Turbulence Modeling for CFD," 2nd Edition. La Cañada, California: DCW Industries Inc.

[20] Schlichting, H. and Gersten, K., 2000, "Boundary Layer Theory," 8th Edition. New York, New York: Springer-Verlag.

[21] Lyall, M.E., 2012 "Effects of Front-Loading and Stagger Angle on Endwall Losses of High Lift Low Pressure Turbine Vanes," PhD Dissertation, Air Force Institute of Technology, Wright-Patterson Air Force Base, Ohio.

[22] Blanco, E., Hodson, H.P., Vazquez, R., and Torre, D., 2003, "Influence of the State of the Inlet Endwall Boundary Layer on the Interaction between Pressure Surface Separation and Endwall Flows," Proc. Instn Mech. Engrs Vol. 217, Part A: *J. of Power and Energy*, pp. 433-441.

[23] Sharma, O.P., and Butler, T.L., 1987, "Predictions of Endwall Losses and Secondary Flows in Axial Flow Turbine Cascades," *ASME J. of Turbomachinery*, Vol. 109, pp. 229-236.

[24] Sondergaard, R., 2008, "LPT Flow Control at AFRL," AIAA Paper No. AIAA2008-4156.

Proceedings of ASME Turbo Expo 2013
GT2013
June 3-7, 2013, San Antonio, USA

APPENDIX G

GT2013-95002

ENDWALL LOSS REDUCTION OF HIGH LIFT LOW PRESSURE TURBINE AIRFOILS USING PROFILE CONTOURING – PART II: VALIDATION

Keith Sangston and Jesse Little
University of Arizona
Tucson, AZ, USA

M. Eric Lyall and Rolf Sondergaard
Air Force Research Laboratory
Wright-Patterson AFB, OH, USA

ABSTRACT

The hypothesis, posed in Part I [1], that excessive endwall loss of high lift low pressure turbine (LPT) airfoils is due to the influence of high stagger angles on the endwall pressure distribution and not front-loading is evaluated in a linear cascade at Re = 100,000 using both experimental and computational studies. A nominally high lift and high stagger angle front-loaded profile (L2F) with aspect ratio 3.5 is contoured at the endwall to reduce the stagger angle while maintaining the front loading. The contouring process effectively generates a fillet at the endwall, so the resulting airfoil is referred to as L2F-EF (Endwall Fillet). Although referred to as a fillet, this profile contouring process is novel in that it is designed to isolate the effect of stagger angle on endwall loss. Total pressure loss measurements downstream of the blade row indicate that the use of the lower stagger angle at the endwall reduces mixed out mass averaged endwall and passage losses approximately 23% and 10% respectively. This is in good agreement with computational results used to design the contour which predict 18% and 7% loss reductions. The endwall flow field of the L2F and L2F-EF models is measured using stereoscopic particle image velocimetry (PIV) in the passage. These data are used to quantify changes in the endwall flow field due to the contouring. PIV results show that this loss reduction is characterized by reduced inlet boundary layer separation as well as a change in strength and location of the suction side horseshoe vortex (SHV) and passage vortex (PV). The endwall profile contouring also produces a reduction in all terms of the Reynolds stress tensor consistent with a decrease in deformation work and overall flow unsteadiness. These results confirm that the stagger angle has a significant effect on high-lift front-loaded LPT endwall loss. Low stagger profiling is successful in reducing endwall loss by limiting the development and migration of the low momentum fluid associated with the SHV and PV interaction.

NOMENCLATURE

C	chord [m]
CTKE	Normalized turbulent kinetic energy
$C\lambda_{CI}$	Normalized swirling strength
$C\omega$	Normalized vorticity
$C\omega_s$	Normalized secondary vorticity
$CRe_{y'z'}$	Normalized Reynolds shear stress in y′z′ plane
H	airfoil height, or span [m]
$L_{in,st}$	Integral length scale [m]
M_{in}	Inlet Mach number
P_s	static pressure [Pa]
P_t	total pressure [Pa]
Re	Reynolds number based on inlet velocity and axial chord
S	cascade pitchwise spacing [m]
$Tu_{in,st}$	Turbulence intensity
$U_{in,st}$	Inlet velocity [m/s]
V_s	Secondary velocity [m/s]
x, y, z	cascade coordinate directions [m]
U, V, W	Ensemble average Cartesian velocity components [m/s]
u, v, w	Turbulent fluctuations [m/s]
Y	total pressure loss coefficient, $\left(P_{t,in} - P_t\right)/\left(0.5\,\rho U_{in,st}^2\right)$ Multiply by $\cos^2(\alpha_{ex})/\cos^2(\alpha_{in})$ to rescale based on exit conditions

U.S. Air Force Public Affairs Office Case No. 88ABW-2013-0693

< >	Denotes ensemble average

Greek

α	cascade gas angle, measured from axial [deg]
δ_{99}	99% boundary layer thickness [m]
θ	boundary layer momentum thickness [m]
λ_{CI}	swirling strength
ω	vorticity [1/s]

Subscripts and Superscripts

2D	midspan or profile conditions, two-dimensional
ax	axial direction
ew	endwall
ex	exit location
in	inlet location
ps	passage
st	streamwise direction
′	PIV coordinate system

Acronyms

LPT	low pressure turbine
OP	outer plane
PIV	particle image velocimetry
PS	pressure side
PV	passage vortex
SHV	suction side horseshoe vortex
SS	suction side
TKE	turbulence kinetic energy

INTRODUCTION

The pressure distribution is an important parameter for high lift LPT airfoils, primarily because it is manipulated to preserve low Reynolds number (Re) performance [2,3]. Front-loading increases stall resistance at low Re. Front-loading can be achieved in two ways; increasing the stagger angle [4] or for a fixed stagger angle, thickening the leading edge [5]. Several studies have concluded that front-loading increases endwall loss [3,6-8], however the profiles in all of these studies are designed with increased stagger angles compared to the companion aft-loaded profiles. To our knowledge, no studies in the literature have isolated pressure loading and stagger angle effects on endwall loss.

In response to the possible confounding effects of the stagger angle and pressure distribution, Part I of a companion paper investigates a pair of airfoils with similar front-loaded pressure distributions, but different stagger angles [1]. The low stagger airfoil (L2F-LS) produces significantly less endwall loss, but no net reduction in passage loss is achieved due to increased profile loss. Therefore, to achieve a net passage loss reduction, a design procedure is undertaken to decrease the stagger angle of a high lift front-loaded airfoil only at the endwall to reduce the endwall loss while maintaining good midspan loss. The method used for reducing the stagger angle at the endwall is referred to as profile contouring. Although the intent is to exploit the benefits of a reduced stagger angle and not develop a fillet design, the profile contouring process effectively results in a fillet-like shape. The modified airfoil is therefore referred to as L2F-EF. The focus of the current paper is to validate and explain the reduced endwall loss due to this design modification.

Several passive flow control methods have been used for reducing endwall loss, including boundary layer fences, endwall contouring, and leading edge bulbs and fillets. For all of these methods, the goal is to favorably influence the development of the rotational component of the endwall flow in ways that reduce total pressure loss. However, the reasoning for using each method can be quite different. Prümper [9] proposed boundary layer fences as a means of hindering the cross passage boundary layer flow and reducing endwall loss. Harvey et al. [10] implemented nonaxisymmetric endwall contouring to reduce endwall total pressure loss. In this case, the cross passage pressure gradient was weakened to reduce the strength of the passage vortex (PV). As described by Langston [11], the concept of leading edge bulbs is to strengthen the suction side horseshoe vortex (SHV), which has the opposite sense of the passage vortex (PV), thus weakening the overall vortex system that comprises the endwall flow.

Past studies have also investigated fillets for turbine applications. Zess and Thole [12] designed a leading edge fillet for reducing the horseshoe vortex of a high pressure turbine first stage vane. Those authors demonstrated computationally and experimentally that the leading edge vortex was eliminated, thus delaying formation of the PV. The addition of the fillet also reduced the unsteadiness. They did not report an overall passage loss. On the other hand, Becz et al. [13] did investigate the passage loss of a filleted blade, showing that a fillet and leading edge bulb produced nearly equivalent loss reductions for their cascade.

In this paper, it is shown that the profile contouring approach described here produces a mixed out mass averaged endwall loss reduction of 22.6%, leading to an overall passage loss reduction of 9.9% for our 3.5 aspect ratio passage. Stereoscopic PIV results map out the endwall flow and turbulence development inside the passage. Profile contouring decreases the inlet boundary layer separation and reduces the strength of the PV, similar to the effect demonstrated by Zess and Thole [12]. It delays the roll up of the secondary flow and reduces the amount of fluid it convects, similar to the phenomena witnessed with the use of endwall contouring performed by Knezevici et al [14]. It is also found to increase the strength of the SHV in agreement with the concept suggested by Langston [11]. The contouring produces a reduction in magnitude for all components of the Reynolds stress tensor indicating a decrease in the overall unsteadiness of the endwall vortex system. Detailed loss mechanisms are beyond the scope of this paper, but the reduced inlet boundary layer separation suggests that less low energy fluid will be entrained in the PV, leading to a reduction in exchange between low and high energy fluid within the passage.

FACILITY AND EXPERIMENTAL TECHNIQUES

Experiments are carried out in the AFRL low speed wind tunnel. This facility is an open-circuit, suction wind tunnel located in the Aerospace Systems Directorate at Wright-Patterson Air Force Base. The tunnel has an 8:1 contraction ratio and a test section with dimensions 0.85m x 1.22m. A linear cascade of seven L2F airfoils is fixed within the test section by a rigging that includes a Plexiglas splitter plate extending upstream and downstream to simulate the endwall of a turbine (Fig. 1). Table 1 outlines the cascade geometry and relevant flow properties. The boundary layer shape factor suggests that the inlet boundary layer is transitional. Although the state of the inlet boundary layer can affect the overall level of losses produced, it was kept constant to facilitate comparisons with previous work. The inner and outer end-flow adjusters are used to maintain a uniform airflow velocity across the width of the test section.

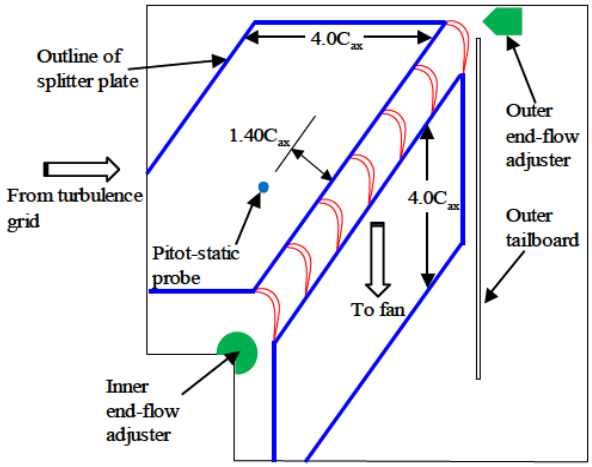

Figure 1. Wind tunnel test section schematic.

Table 1. Cascade geometry and flow properties

Cascade Geometry	
Axial chord, C_{ax}	152.4 mm
Pitch/axial chord, S/C_{ax}	1.221
Span/axial chord, H/C_{ax}	3.5
Inlet Turbulence Conditions, 1.4C_{ax} Upstream	
Turbulence intensity, $Tu_{in,st}$	3.0%
Streamwise integral length scale, $L_{in,st}$	0.26 C_{ax}
Inlet Flow Conditions, 1.4C_{ax} Upstream	
Re, ($U_{in,st}$ and C_{ax})	100,000
Mach number, M_{in}	0.03
Inlet Boundary Layer Parameters, 1.4C_{ax} Upstream	
δ_{99}/H	0.025
Re_θ	655
Shape factor	2.2
Flow Angles	
Inlet flow angle (from axial), α_{in}	35°
Predicted mean profile exit angle, α_{ex}	-58.12°

The L2F-EF airfoil is designed by smoothly transitioning the airfoil from the high stagger L2F profile in the 2D inlet flow region mid-span to the low stagger L2F-LS profile near the endwall. Figure 2 shows the transition between the two airfoil shapes. The effective fillet that results is visualized using airfoil coordinates in k-planes near the endwall that were generated using the WAND code for use with the LEO flow solver [1]. The thick blue line illustrates the transition spline between the two profiles. The point where the blue line straightens indicates the maximum fillet height (z/H=0.095), with the profile being purely the L2F design above that level. Note that when the L2F and L2F-LS profiles are overlaid, the two suction surfaces intersect twice. To simplify the design, the profile aft of the first intersection defaults to the L2F design. This allowed the transition to be implemented by manufacturing endwall gloves in the form of a fillet that could be slipped over the L2F base profile. Thus, the suction surfaces of the tested airfoils are slightly different near the endwall than the airfoil modeled in CFD. This difference is expected to be insignificant since close to the endwall, the cross-passage boundary layer flow is dominant, and slight deviations in the suction side profile are not important.

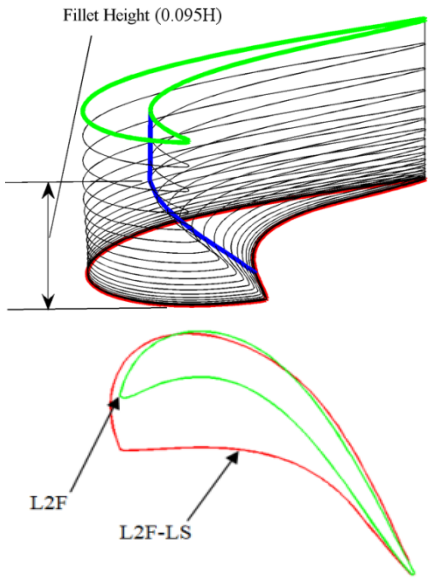

Figure 2. Comparison of L2F and L2F-LS near the endwall.

Stereolithography models of the fillet are fabricated to mimic the design of the L2F-EF airfoil. Fillets are attached to the three center airfoils in the wind tunnel. Relevant spanwise planes showing the fillet geometry are provided in Fig. 2. Figure 3 shows a close-up CAD model of the fillet attached to the L2F leading edge. The fillet is designed by subtracting the geometry of the straight L2F airfoil from L2F-EF geometry.

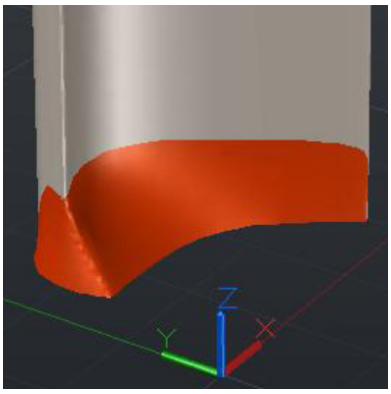

Figure 3. CAD model of the fillet modification used to mimic the L2F-EF airfoil design.

An upstream stationary pitot-static probe and a kiel probe in the exit measurement plane are used to measure total pressure loss. At 3.2 mm diameter, the kiel probe is less than 2% of the blade pitch, providing sufficient resolution within the wakes. The ambient pressure is measured with a laboratory barometer and freestream fluid temperature is measured using type J thermocouples. An IFA300 constant temperature anemometer is used with single normal hot-film probes (TSI 1211-20) for obtaining velocities and turbulence measurements at the inlet. The velocities for setting the inlet Reynolds number (Re) are measured using the upstream pitot-static probe. A TSI 1299-20-18 triple sensor hot-film probe is used to obtain velocity and turbulence measurements downstream of the blade row for the case without the fillet to provide validation for the PIV. The three sensors of the triple probe are contained within a 2 mm measurement diameter. The probe stem is 4.6 mm in diameter.

All uncertainties are estimated at 95% confidence. Uncertainties for Re and total pressure loss coefficients are estimated using the partial derivative and root-sum-square method of Kline and McClintock [15]. The loss coefficients at each point are estimated to within ± 0.01, approximately 1% of the inlet dynamic head. Re is also estimated to be within about 1% of the measured value. The uncertainty of mean velocities for the exit flow field is estimated to be within 1.5% of the measured values. In the experiment, average flow angles relative to the probe axis are typically within 10˚. Angle measurements on the calibration stand for the triple-probe are within ± 0.9˚ of the actual velocity vector for ±18˚ pitch and yaw, indicating reasonable bias error.

Stereoscopic PIV is used to obtain quantitative measurements of the velocity fields in the passage. Images are acquired and processed using a LaVision PIV system operating DaVis 8.0. A Vicount smoke generator is used to create uniform seeding by filling the entire bay housing the open-loop wind tunnel with a lingering cloud of particles. A dual-head New Wave Solo PIV-120 Nd:YAG laser is used in conjunction with spherical and cylindrical lenses to form a thin light sheet that allows PIV measurements. The light sheet is directed upward through the bottom of the acrylic splitter plate and manually positioned at the location of interest. Stereo-PIV data are acquired at various planes, but the majority of the results presented here are located at x′/C = 0.25, 0.5, 0.75, and 1.0 corresponding to Planes 1-4 respectively as shown in Fig. 4. The planes are situated so that they cross the chord line of the L2F airfoils at regular intervals within the passage. This orientation is chosen so that the normal to the planes is more in line with the turning flow, which better captures the in-plane flow characteristics and improves camera visibility. Note that two coordinate systems are used in this analysis. The x-y coordinate system represents the cascade axial and pitchwise directions respectively, while the x′-y′ chord based coordinate system is used to represent the PIV results. The z-axis extends out of the page. The viewing perspective is for an observer looking upstream (see Fig. 4b).

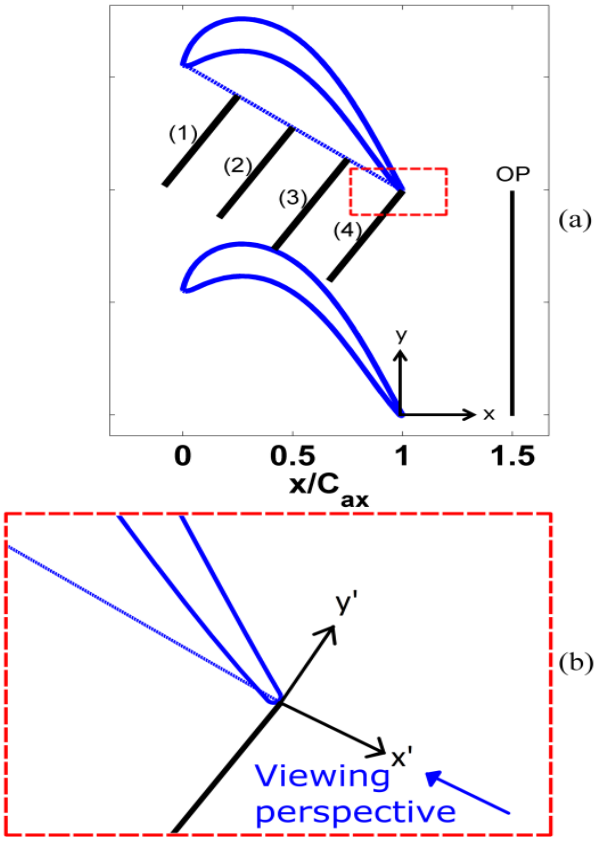

Figure 4. (a) Plane locations, orientations, and cascade coordinate system and (b) inset showing rotated coordinate system used for PIV data representation in the passage.

The time separation between laser pulses used for particle scattering is set according to the flow velocity, camera magnification and correlation window size. Two images corresponding to the pulses from each laser head are acquired by Cooke Corporation pco.1600 14 bit cameras with pixel resolution of 1600 x 1200. The cameras are equipped with scheimpflug mounts, 105mm Nikon lenses, 532nm optical filters and are tripod mounted at various locations/orientations to provide maximum optical access in the passage.

For each image pair, subregions are cross-correlated using decreasing window size (32^2-16^2 pixel^2) multi-pass processing with 50% overlap. The resulting velocity fields are post-processed to remove spurious vectors using an allowable vector range and median filter. Removed vectors are replaced using an interpolation scheme based on the average of neighboring vectors. A 3x3 Gaussian smoothing filter is also applied to the calculated velocity fields. The PIV data are nominally sampled at 15 Hz, but this rate varies considerably due to PC performance thus guaranteeing independent samples.

Ensemble-averaged statistics are calculated from 2000 instantaneous velocity fields. The average spatial resolution of PIV data is 0.58mm ($3.8x10^{-3}C_{ax}$). Near surface measurement resolution is strongly dependent on the measurement plane and camera orientation. The accuracy for measurements of instantaneous velocity is less than 3% of the inlet velocity. This is calculated by assuming negligible laser timing errors and a conservative correlation peak estimation error of 0.1 pixels. Spatial derivatives of velocity are calculated using a 2nd order accurate central difference scheme.

PIV VALIDATION

PIV measurements are validated at the outer plane (see Fig. 4, OP) with respect to triple probe data. Results from both measurement techniques are provided in Fig. 5. Secondary velocity vectors, (V_s and W) are superimposed on floods of secondary vorticity, $C\omega_s$ defined by:

$$C\omega_s = \frac{C_{ax}}{U_{in,st}}\left(\frac{\partial W}{\partial y} - \frac{\partial V_s}{\partial z}\right) \qquad (1)$$

where

$$V_s = Vcos(58°) + Wsin(58°) \qquad (2)$$

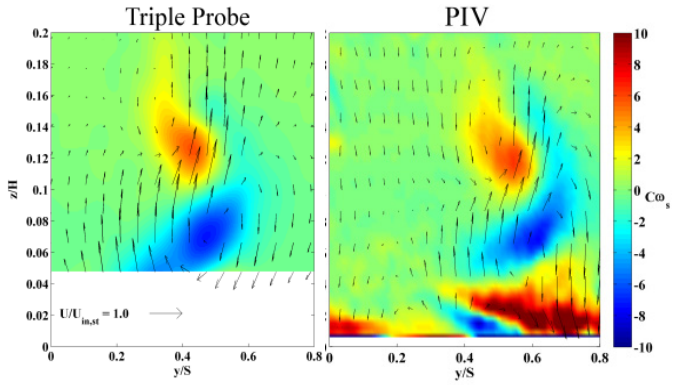

Figure 5. Comparison of hot wire and PIV data near OP for L2F. PIV data is acquired at x/C_{ax}=1.50 while hot wire data is at x/C_{ax}=1.58 explaining the shift in the vortex system.

Note that because of access constraints, the triple probe data is only acquired above z/H=0.05 hence the area with no data in Fig. 5a. The PIV data shows this region contains significant secondary vorticity. Near surface laser-based measurements of this type should be highly scrutinized due to unavoidable reflection issues. These effects are observed here below z/H=0.005, thus secondary vorticity data centered on z/H=0.02 is believed to be valid. Similar flow characteristics near the endwall have been observed for a different front-loaded profile [8].

Both the secondary velocity vectors and the secondary vorticity magnitude are consistent between the two measurement techniques. However, inspection shows the triple probe features are shifted left by y/S≈0.15. This discrepancy is attributed to a necessary offset between the two measurement planes. Optical accessibility required the PIV data to be sampled at the OP shown in Fig. 4(a), which is $0.08C_{ax}$ upstream of the triple probe data. This offset is consistent with the shifted triple probe data features that result from strong flow turning/mixing at this location.

The uncertainties in measurements of mean velocity are calculated using 95% confidence intervals for each PIV plane [16]. A sample is provided at the OP in Fig. 6. Results are cast as a percentage of local velocity. In this case, the maximum relative error is ~5% and occurs near the surface (z/H<0.05) in the region associated with strong secondary vorticity discussed above. The error above z/H=0.05 is substantially less (~1%). Confidence intervals in the passage at planes 1-4 (see Fig. 4) show maximum values on the order of 3% (not shown).

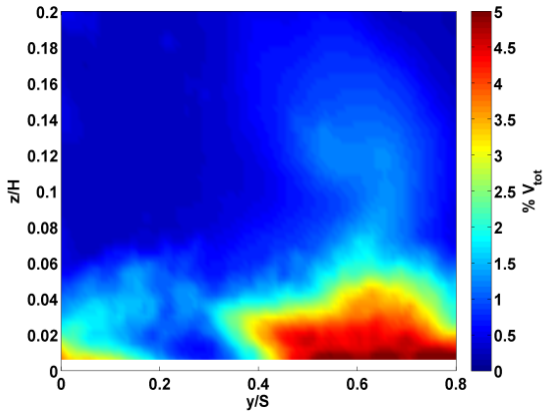

Figure 6. 95% confidence interval as a percentage of inlet velocity for PIV data at OP.

PIV MEAN FLOW RESULTS

Stereoscopic PIV is used to provide detailed information on the influence of the endwall fillet on the flow field in the passage. Data has been acquired at various planes, but only floods associated with y′-z′ planes identified in Fig. 4 are presented in the interest of brevity. The cascade geometry and especially the fillet installation create challenges for optical accessibility. Black and white contour values are employed to distinguish between a solid boundary and obstructed line of sight respectively. This convention is only valid on the left and right side of all images. White regions at the top and bottom of images have been masked to remove vector calculation due to laser reflections or insufficient signal. The suction and pressure sides of the blades are denoted by SS and PS respectively.

Figure 7 shows four planes of PIV data separated by 0.25C for both the L2F and L2F-EF case. The in-plane velocity

vectors, calculated from W′ and V′ are shown on top of out-of-plane vorticity, ω′. The flow is dominated by the V′ (horizontal) component of velocity in the irrotational region of the upstream portion of the passage (Plane 1, x′/C=0.25) in both cases. The endwall boundary thickness is greater in the L2F case and the core of the PV is visible. The PV of the L2F-EF case is discernible beside the fillet and a reduction in endwall boundary layer thickness is already apparent. Plane 2 (x′/C=0.50) shows the beginnings of an irrotational clockwise swirl due to both the PV and the solid wall boundary (PS). This behavior is substantially less apparent in the fillet case. The PV core in the L2F-EF is now clearly visible and the reduction in the spanwise extent of rotational endwall flow in comparison to L2F persists. The first clear evidence of the SHV with opposite sense of rotation is found in Plane 3 (x′/C=0.75). It is considerably stronger than the L2F case. This observation is consistent in other planes not shown. This observation and the associated reduction in total pressure loss is in agreement with suggestions by Langston using leading edge bulbs that strengthen the SHV yet lead to an overall reduction in endwall loss [11]. At plane 3, the PV is now centered in the field of view in both cases and a spanwise compression of the flow pattern due to the fillet is clear. Also note the variation in irrotational swirl between the two cases. The L2F case is plagued by laser reflections near the PS (right side) which give rise to the checkered vorticity pattern at y′/S>-0.05. This pattern is an unphysical product of the PIV processing algorithm and has no influence on the primary endwall flow features under consideration. The irrotational region of plane 4 (x′/C=1) is dominated by motion in the negative y′ direction consistent with the expected flow turning. Clear evidence of flow climbing up the SS is also apparent. Note that laser reflections near the SS in the L2F-EF case have caused some unphysical vorticity values here. As in the L2F case for plane 3, these have little influence on the interpretation of the primary endwall flow features. The decreased spanwise extent of the PV and increased strength of the SHV in the fillet case are consistent with upstream planes. Also note evidence of a SS corner vortex at Plane 4 which appears significantly stronger in the L2F-EF case. Considerable uncertainty is associated with this feature due to its near wall location, thus we only note its appearance and do not place emphasis on its behavior.

Swirling strength, which represents a measure of the rotational rate of local fluid elements, is employed for both vortex identification and tracking. Unlike vorticity, which identifies both rotation and shear, this technique ignores regions of pure shear and highlights regions of pure rotation. This is one of a class methods based on critical point analysis of the local velocity gradient tensor and its eigenvalues [17], which for these data only include derivatives in the z′ and y′ directions. The parameter of interest is the imaginary component of the eigenvalues which is nonzero only if:

$$\frac{\partial V'}{\partial z'}\frac{\partial W'}{\partial y'} - \frac{1}{2}\frac{\partial V'}{\partial y'}\frac{\partial W'}{\partial z'} + \frac{1}{4}\left[\left(\frac{\partial V'}{\partial y'}\right)^2 + \left(\frac{\partial W'}{\partial z'}\right)^2\right] < 0 \quad (3)$$

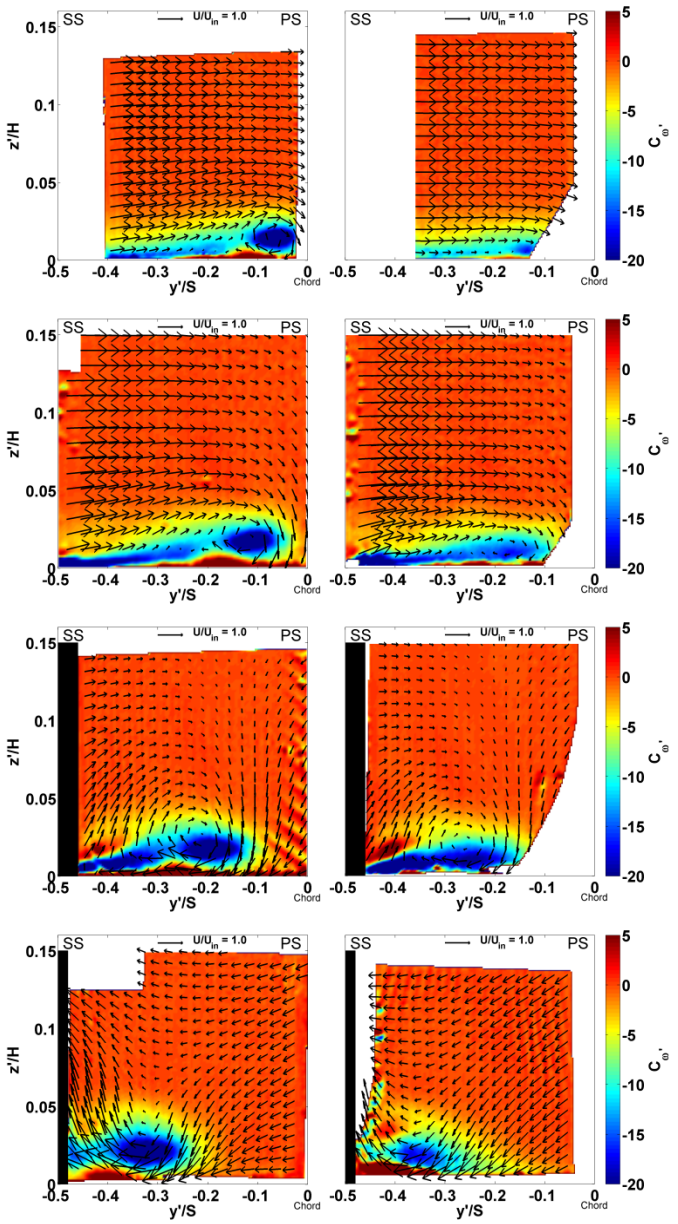

Figure 7. In-plane velocity vectors superimposed on out-of-plane vorticity floods for both L2F (left) and L2F-EF (right) at Planes 1-4 (top to bottom).

The normalized magnitude of the imaginary component of the eigenvalues, $C\lambda_{CI}$, is shown in Fig. 8, where normalization is performed as in vorticity. The colorbar values have been multiplied by a factor of 100 for plotting convenience. As in the floods of vorticity, black and white regions represent the airfoil surface and obstructed line of sight respectively. Again, this convention is only valid on the left and right side of all images.

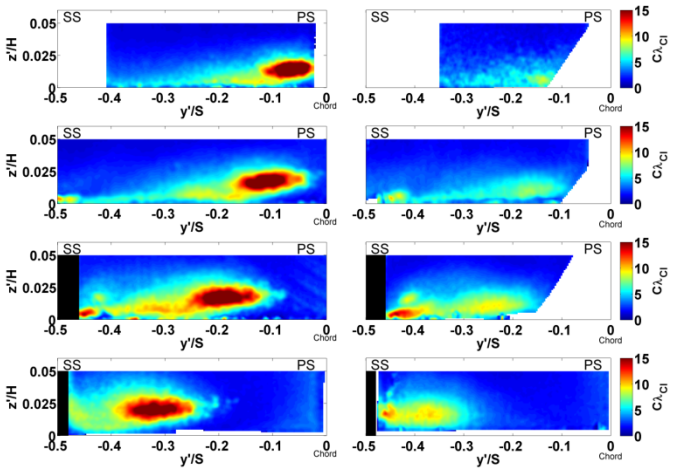

Figure 8. Swirling strength for both L2F (left) and L2F-EF (right) at Planes 1-4 (top to bottom).

The difference in both the progression and strength of the PV between the L2F and L2F-EF cases is now readily apparent. In addition to decreasing its spanwise extent, it is now clear that one of the primary effects of the fillet is to reduce the rotational rate of the PV. The swirling strength of the L2F-EF PV is approximately half of the L2F case throughout the passage. This stems from a reduction in boundary layer overturning due to adjustment of both the stagnation point and cross-passage endwall pressure gradient. The decreased rate of rotation is expected to have substantial effect on turbulent quantities which are discussed subsequently. The SHV is more difficult to see using swirling strength due to removal of the sign of rotation. Additionally, the SHV is surrounded by substantially less shear since it is above the endwall boundary layer. This makes it more amenable to visualization using vorticity alone.

The maximum value of swirling strength in the PV and SHV regions is used to estimate the vortex locations. The trajectory for each is plotted in Fig. 9. In this case, a location for all measured planes (ΔC=12.5%) is plotted to provide better tracking of the flow features. The cross passage location (Fig. 9a) shows that the PV trajectory is essentially parallel between the two cases with nominal separation of ~10mm (~0.053S). The PV in the fillet case is actually closer to the suction surface which seems counterintuitive from a loss production standpoint considering that one of the primary goals of some active control techniques (e.g. blowing) is to distance the PV from the suction surface [18]. The SHV persists over a longer distance through the passage in the fillet case consistent with the increased strength observed in Figs. 7 and 8. The spanwise progression of the PV and SHV is shown in Fig. 9b. There is little variation between the two SHV cases, but the previous observations on spanwise PV extent now become readily apparent. The fillet case is consistently lower in spanwise extent throughout the passage. Apparently, in the L2F-EF case, the reduction in rotation rate, spanwise extent and overall unsteadiness (shown in a subsequent section) are enough to overcome the closer proximity of PV to the suction surface thereby reducing total pressure loss.

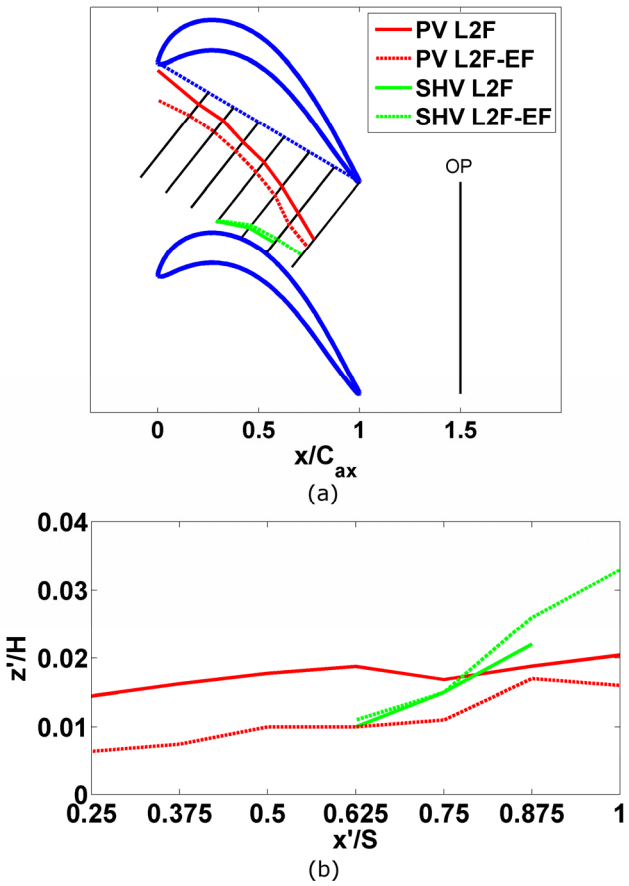

Figure 9. Paths of the PV and SHV in the passage for both L2F and L2F-EF.

PIV TURBULENCE RESULTS

The deformation work or turbulence production term in the mean kinetic energy equation has been shown to be key to accounting for loss production by transfer of energy from the mean flow to the turbulence and eventually on to viscous dissipation [18,19]. The out-of-plane velocity gradient, $\partial/\partial x'$, is not captured with the existing data set. In lieu of the production term, select components of the Reynolds stress tensor are employed to shed light on flow physics. A detailed analysis of loss production mechanisms is beyond the scope of this work. However, comparisons between turbulent statistics of the two cases give some additional insight into the fillet performance.

Figure 10 shows the TKE data for the Planes 1-4 defined as

$$\mathrm{CTKE} = \frac{1}{2}\frac{(\langle u'^2\rangle+\langle v'^2\rangle+\langle w'^2\rangle)}{U_{in,st}^2} \qquad (4)$$

As before, black and white regions correspond to solid boundaries and line of sight obstruction respectively. Again, this convention is only valid on the left and right side of all images. The high TKE regions near the SS of the L2F-EF case

at plane 1 and 4 arise from contamination of the image by laser reflections and are unphysical.

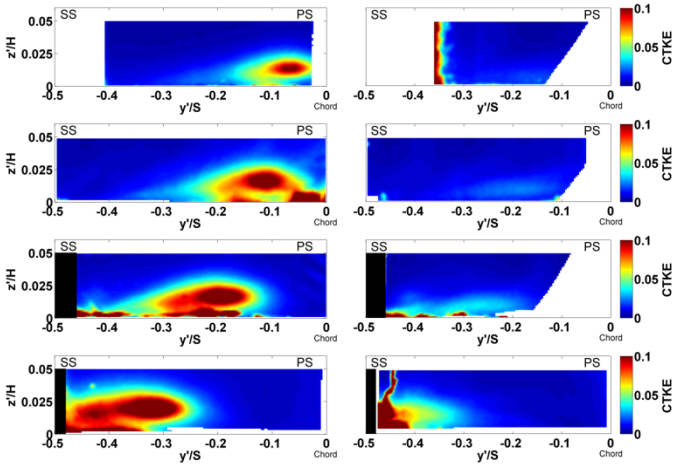

Figure 10. TKE for both L2F (left) and L2F-EF (right) at Planes 1-4 (top to bottom).

Regions of high TKE in the L2F case are aligned with regions of high swirling strength suggesting the dominant components of TKE are contained within the PV. The floods of high TKE are found to gradually increase through the passage. Individual maps of the Reynolds normal stresses (not shown) indicate slight dominance by the <w′w′> component over the <v′v′> component throughout. The out-of-plane normal stress, <u′u′>, is generally lower in magnitude, but gradually increases down the passage reaching values of similar order as the other components as the flow becomes uncovered by the adjacent blade (x′/C=1). Note that the "bi-modal" distribution of TKE most apparent at x′/C=1 stems from the <v′v′> component. The <w′w′> and <u′u′> stresses remain aligned with the PV core throughout.

TKE in the L2F-EF case also increases down the passage, but is limited to values less than half of the L2F case throughout. Individual floods of each Reynolds normal stress for the fillet case (not shown) illustrate reduction for all components throughout the passage. In addition, the dominant contributor to TKE is now the <v′v′> component. The <w′w′> case which was previously dominant for L2F is now found to be almost negligible in comparison to <v′v′> and <u′u′>. As in the L2F case, the <u′u′> component gradually increases throughout the passage and reaches values near <v′v′> at x′/C=1. Note that we do not observe any clear bi-modal TKE features in the fillet case. This stems from the strong reduction of <w′w′> due to endwall contouring. Additional analysis on the Reynolds normal stresses and their relation to loss production in the passage is intended for a future publication. At present, it suffices to say that the L2F-EF profile produces a substantial decrease in overall flow unsteadiness. This is expected if the primary generator of TKE is the PV as seen here. This behavior is consistent with observations for other fillet designs [12].

The Reynolds shear stresses also contribute to turbulence production, but only the in-plane component (<v′w′>) is shown in Fig. 11 in the interest of brevity and is defined as

$$CRe_{y'z'} = -\frac{< v'w' >}{U_{in,st}^2} \qquad (5)$$

The colorbar values have been multiplied by a factor of 10 for plotting convenience. The Reynolds shear stress magnitudes are approximately 25% of the normal stresses, but the velocity gradient associated with deformation work can be large enough to have a substantial impact on loss production [19] warranting examination. The <v′w′> component is found to be dominant inside the passage especially at Planes 1 (x′/C=0.25) and 2 (x′/C=0.5) which is expected given the plane orientation and PV characteristics. The <v′w′> stress has a kidney shape with strongest regions on the SS of the PV where the negative rotation of the vortex interacts with the previously undisturbed endwall boundary and eventually the SHV. A weaker negative region is also present on the PS of the PV.

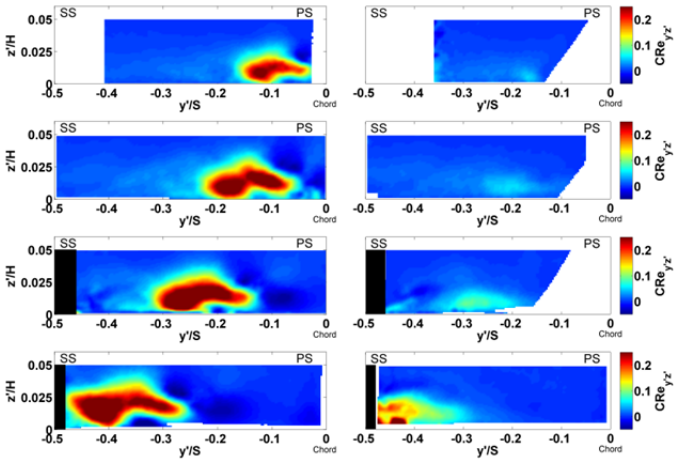

Figure 11. In-plane Reynolds stress for both L2F (left) and L2F-EF (right) at Planes 1-4 (top to bottom).

The <v′u′> component of the Reynolds stress tensor (not shown) is dominantly negative and increases downstream reaching similar levels in absolute value as <v′w′> at x′/C=0.75 and 1. Strong regions of <v′u′> are aligned with the SS of the PV and its core. The <w′u′> component also gradually increases in absolute value down the passage, but still remains weaker than the others. It possesses both positive and negative regions on the SS and PS of the PV respectively.

As with the normal stresses, the fillet reduces the magnitude of all shear stresses in the passage, but the greatest reduction is seen on the <v′w′> component (Fig. 11) which goes from the dominant shear stress to levels slightly below the other components. The L2F-EF case for <v′w′> has magnitude less than half of L2F. In addition, the kidney shape in L2F is no longer visible. Detailed analysis on the effects of both normal and shear stresses on loss production is a subject of future work. Here, it suffices to say that the fillet has created a

reduction in all turbulent stresses consistent with overall reduction in unsteadiness and turbulence production.

TOTAL PRESSURE RESULTS

Figure 12 shows total pressure loss contours with and without the fillet at OP. Two low energy cores are present for both cases with similar magnitude. The dominant loss core without the fillet, midwake at z/H = 0.18, moves closer to the endwall to z/H = 0.14 with the fillet consistent with swirling strength results inside the passage (Figs. 8 and 9). The second loss core without the fillet, approximately at z/H = 0.08, moves slightly away from the endwall to z/H = 0.10, resulting in the pair of loss cores covering a smaller area with the fillet. The extent of the endwall loss contours in the y direction is not substantially affected by the fillet, but the spanwise extent is considerably decreased. Thus, the overall effect of the fillet can be described as a spanwise compression of the endwall flow at OP. The smaller area coverage of the loss cores suggests that less low energy fluid is contained in the wake, directly resulting from a weakened inlet boundary layer separation (or equivalently a reduced vortex system) due to the low stagger angle at the endwall.

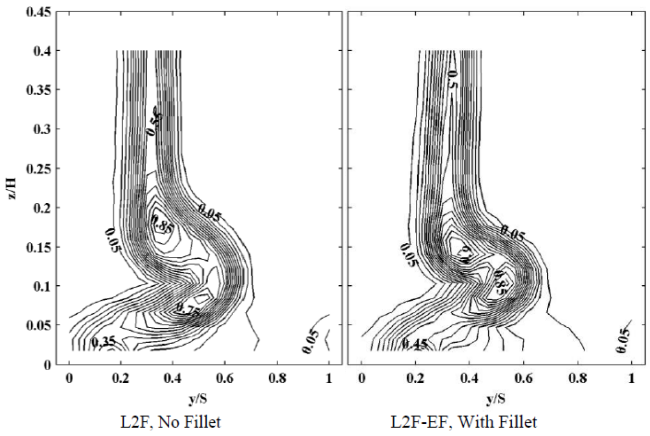

Figure 12. Comparison of L2F and L2F-EF Y contours (Re = 100k) (ΔY = 0.05).

Table 2 shows integral parameters capturing the overall effect on total pressure loss characteristics for both the computational and experimental efforts. Y_{ps} is based on the entire passage after subtracting off the inlet boundary layer loss using the method of Sharma and Butler [21]. Note that for experimental Y_{ps}, changes in Y and the velocity field were assumed negligible between z/H = 0.4 and z/H = 0.5, so we assumed symmetry to obtain Y_{ps} from half the passage. The profile loss, Y_{2D}, was obtained from independent cascade experiments with the splitter plate of Fig. 1 removed while using straight L2F airfoils. Removing the splitter plate gave a significantly higher passage aspect ratio, H/C_{ax} = 5.75 compared to H/C_{ax} = 3.5 for the endwall experiments (see Table 1), to reduce endwall effects on midspan measurements. Sharma and Butler [20] pointed out that midspan loss measurements in almost all cascade tests suffer from endwall effects, so the higher aspect ratio experiments were an attempt to get an improved estimate of the L2F profile loss. The endwall loss, Y_{ew}, is defined as

$$Y_{ew} = Y_{ps} - Y_{2D} \qquad (6)$$

The experimental loss results are mixed out mass averages assuming constant area and no external forces, consistent with Harrison [22]. The computational loss results are design outputs based on mass averages taken one axial chord downstream of the blade row where the flow is also well mixed and consistent with the results of Part I [1]. Finally, Table 2 also shows the predicted and measured passage mass averaged exit flow angles to show the effect of the fillet on turning.

Table 2. Experimental and computational L2F loss breakdown with and without the fillet (Re = 100k).

	L2F	L2F-EF	Diff
Experimental			
Y_{ps}	0.142	0.128	-9.9%
Y_{2D}	0.080	0.080	0%
Y_{ew}	0.062	0.048	-22.6%
α_{ex}	-58.28°	-57.98°	+0.3 deg
Computational			
Y_{ps}	0.141	0.131	-7.1%
Y_{2D}	0.085	0.085	0%
Y_{ew}	0.056	0.046	-17.9%
α_{ex}	-57.43	-57.55	-0.12 deg

The experimental results show a mass average reduction of Y_{ew} by approximately 23% in comparison to the CFD at ~18%. The reduction in the overall passage loss, Y_{ps}, is nearly 10% for the experimental case and 7% for the CFD for our 3.5 aspect ratio passage. The experimental results fall between the predicted Y_{ew} reductions for L2F-LS (the straight low stagger airfoil) and L2F-EF of Fig. 15 in Part I [1]. These losses are on the same order of those reported by Knezevici, who used endwall contouring as a means of loss reduction for a similar front-loaded airfoil [8]. Regarding flow turning, the difference in the exit gas angle with and without the fillet is quite small and within the experimental uncertainty of the triple probe. Both experiments and CFD indicate that the fillet has a negligible influence on flow turning. Overall, the results of Table 2 support the stereo-PIV measurements in the passage indicating that profile contouring to implement a low stagger angle at the endwall can effectively reduce endwall losses while retaining high-lift front-loading.

CONCLUSIONS

The hypothesis, posed in Part I [1], that excessive endwall loss in high lift LPT airfoils is due to high stagger angles and not front-loaded pressure distributions has been validated in a linear cascade at Re = 100,000 using both experimental and computational studies. A nominally high lift and stagger angle

front-loaded profile (L2F) with aspect ratio 3.5 is contoured at the endwall predominantly on the pressure surface. The performance of this new low stagger profile, L2F-EF, reduces endwall loss consistent with computational predictions. The primary effect of the fillet on loss cores at the exit of the passage is to produce a spanwise compression of the endwall vortex system. Total pressure loss measurements downstream of the blade row show that this results in mixed out mass average endwall and passage loss reductions of approximately 23% and 10% respectively. This is in good agreement with computational results used to design the contouring which predict 18% and 7%.

Detailed information on the passage flow field is acquired using stereoscopic PIV at various planes oriented normal to the chord line. The spanwise compression of the loss cores and overall loss reduction by the fillet results from a substantial weakening of the inlet boundary layer separation. This reduction in inlet boundary layer separation is due to a stronger suction side horseshoe vortex and weaker passage vortex presumably due to the fillet placement primarily on the blade pressure surface. The location of the suction side horseshoe vortex is not strongly affected by the fillet although an increase in strength allows it to be tracked further down the passage. The fillet pushes the passage vortex closer to the suction surface of the adjacent blade seemingly incompatible with a reduction in total pressure loss. The effect of this undesirable location is overcome by the weaker passage vortex rotation rate and its reduced spanwise extent, both of which are consistent with the measured total pressure contours at the passage exit. The endwall fillet reduces TKE throughout the passage as well as the magnitude of each individual Reynolds normal stress. The most striking reduction is in the <w′w′> component which is the dominant TKE contributor for L2F, but almost negligible for L2F-EF. All Reynolds shear stress magnitudes are also reduced by the fillet. This is most apparent in the <v′w′> case which is dominant for L2F, but slightly weaker than its counterparts for L2F-EF. Detailed analysis of loss production mechanisms is beyond the scope of this work. However, the reduction in magnitude of each component in the Reynolds stress tensor is consistent with a decrease in deformation work and overall flow unsteadiness which are key to accounting for total pressure loss in the passage.

These results confirm that the stagger angle has a significant effect on high-lift front-loaded LPT endwall loss and offer insight into strategies for further reduction and understanding of loss production. In summary, low stagger profiling is successful in reducing endwall loss by limiting the development and migration of the low momentum fluid associated with the passage vortex.

ACKNOWLEDGEMENTS

The support of Jesse Little and Keith Sangston by the Air Force Summer Faculty Fellowship Program during the PIV measurement campaign is greatly appreciated. The assistance of Derick Endicott during data acquisition and Jeff Downie during fillet design/fabrication was vital to the success of this work.

REFERENCES

[1] Lyall, M. E., Clark, J. P., King, P. I., and Sondergaard, R., 2013, "Endwall Loss Reduction of High Lift Low Pressure Turbine Airfoils through use of Profile Contouring - Part I: Airfoil Design," GT2013-95000.

[2] McQuilling, M. W., 2007, "Design and Validation of a High Lift Low-Pressure Turbine Blade," Ph.D. Thesis, Wright State University, Dayton, OH.

[3] Praisner, T. J., Grover, E. A., Knezevici, D. C., Popovic, I., Sjolander, S. A., Clark, J. P., and Sondergaard, R., 2008, "Toward the Expansion of Low-Pressure-Turbine Airfoil Design Space," GT2008-50898.

[4] Korakianitis, T., 1993, "Prescribed-Curvature-Distribution Airfoils for the Preliminary Geometric Design of Axial-Turbomachinery Cascades," *ASME Journal of Turbomachinery*, Vol. 115, pp. 325-333.

[5] Korakianitis, T., and Papagiannidis, P., 1993, "Surface-Curvature-Distribution Effects on Turbine-Cascade Performance," *ASME Journal of Turbomachinery*, Vol. 115, pp. 334-340.

[6] Weiss, A. P., and Fottner, L., 1995, "The Influence of Load Distribution on Secondary Flow in Straight Turbine Cascades," *ASME Journal of Turbomachinery*, Vol. 117, pp. 133-141.

[7] Zoric, T., Popovic, I., Sjolander, S. A., Praisner, T., and Grover, E., 2007, "Comparative Investigation of Three Highly Loaded LP Turbine Airfoils: Part I – Measured Profile and Secondary Losses at Design Incidence," GT2007-27537.

[8] Knezevici, D. C., Sjolander, S. A., Praisner, T. J., Allen-Bradley, E., and Grover, E. A., 2009, "Measurements of Secondary Losses in a High-Lift Front-Loaded Turbine Cascade with the Implementation of Non-Axisymmetric Endwall Contouring," GT2009-59677.

[9] Prümper, H., 1972, "Application of Boundary Layer Fences in Turbomachinery," AGARD-AG-164, pp. 311-331.

[10] Harvey, N. W., Rose, M. G., Taylor, M. D., Shahpar, S., Hartland, J., and Gregory-Smith, D. G., 2000, "Non-Axisymmetric Turbine Endwall Design: Part I – Three-Dimensional Linear Design System," *ASME Journal of Turbomachinery*, Vol. 122, pp. 278-285.

[11] Langston, L. S., 2001, "Secondary Flows in Axial Turbines –A Review," Annals New York Academy of Sciences, Vol. 934, *Heat Transfer in Gas Turbine Systems*, pp. 11-26.

[12] Zess, G. A., and Thole, K. A., 2002, "Computational Design and Experimental Evaluation of Using a Leading Edge Fillet on a Gas Turbine Vane," *ASME Journal of Turbomachinery*, Vol. 124, pp. 167-175.

[13] Becz, S., Majewski, M. S., and Langston, L. S., 2003, "Leading Edge Modification Effects on Turbine Cascade Endwall Loss," GT2003-38898.

[14] Knezevici, D. C., Sjolander, S. A., Praisner, T. J., Allen-Bradley, E., and Grover, E.A., 2008, "Measurements of Secondary Losses in a Turbine Cascade with the

Implementation of Non-Axisymmetric Endwall Contouring," GT2008-51311.
[15] Kline, S. J., and McClintock, F. A., 1953, "Describing Uncertainties in Single Sample Experiments," *Mechanical Engineering*, Vol. 75.
[16] Benedict, L., and Gould, R., 1996, "Towards better uncertainty estimates for tublence statistics," *Experiments in Fluids*, Vol. 22, pp. 129-136.
[17] Adrian, R., Christensen, K., and Liu, Z., 2000, "Analysis and interpretation of instantaneous turbulent velocity fields," *Experiments in Fluids*, Vol. 29, pp. 275-290.
[18] Benton, S., Bons, J., and Sondergaard, R., 2012, "Secondary Flow Loss Reduction throught Blowing for a High-Lift Front-Loaded Low Pressure Turbine Cascade," GT2012-68812.
[19] MacIsaac, G. D., Sjolander, S. A., and Praisner, T. J., 2012, "Measurements of Losses and Reynolds Stresses in the Secondary Flow Downstream of a Low-Speed Linear Turbine Cascade," *ASME Journal of Turbomachinery*, Vol. 134(061015).
[20] Moore, J., Shaffer, D. M., and Moore, J. G., 1987, "Reynolds Stresses and Dissipation Mechanisms Downstream of a Turbine Cascade," *ASME Journal of Turbomachinery*, Vol. 109, pp. 258-267.
[21] Sharma, O.P., and Butler, T.L., 1987, "Predictions of Endwall Losses and Secondary Flows in Axial Flow Turbine Cascades," *ASME Journal of Turbomachinery*, Vol. 109, pp. 229-236.
[22] Harrison, S., 1990, "Secondary Loss Generation in a Linear Cascade of High-Turning Turbine Blades," *ASME Journal of Turbomachinery*, Vol. 112, pp. 618-624.

APPENDIX H

Proceedings of ASME Turbo Expo 2012
GT2012
June 11-15, 2012, Copenhagen, Denmark

GT2012-68709

ENDWALL LOSS AND MIXING ANALYSIS OF A HIGH LIFT LOW PRESSURE TURBINE CASCADE

M. Eric Lyall
Air Force Institute of Technology
Wright-Patterson AFB, OH, USA

Paul I. King
Air Force Institute of Technology
Wright-Patterson AFB, OH, USA

Rolf Sondergaard
Air Force Research Laboratory
Wright-Patterson AFB, OH, USA

ABSTRACT

A high lift LPT profile designated L2A is used as a test bed for studying the origin of endwall mixing loss and the role of vortical structures in loss development. It is shown analytically and experimentally that the mixing forces within the endwall wake can be decoupled into either mean flow or turbulent forces, and can be further classified as either reversible or irreversible. Among the irreversible forces, mean flow shear is negligible compared to turbulent shear, suggesting that turbulence dissipation is the dominant cause of loss generation. As a result, the mean flow components of the vortical structures do not generate significant mixing losses. Rather than mixing effects, the mean flow of the vortices cause the suction surface boundary layer to separate inside the passage, thereby generating the large low energy regions typical of endwall flows. Losses are generated as the low energy regions mix out. This vortex separation effect is demonstrated with an experiment using a profile fence and pressure surface modification near the endwall. The findings in this paper suggest that profile modifications near the endwall that suppress suction surface separation may provide loss reductions additive to those that weaken vortical structures, such as endwall contouring.

NOMENCLATURE

a_{ij}	turbulence anisotropy tensor, $\langle u_i u_j \rangle - \frac{2}{3} k \delta_{ij}$
C_{ax}	axial chord
C_p	pressure coefficient, $C_p = (P_s - P_{s,in})/0.5\rho U^2_{in,st}$
$C\omega_s$	secondary vorticity coefficient, Eq. (15)
e	internal energy
$F_{<uv>'}$	secondary mixing force due to <uv>′, Eq. (17)
$F_{<uw>'}$	secondary mixing force due to <uw>′, Eq. (18)
$F_{M'}$	secondary mixing force due to mean flow friction, Eq. (16)
h	enthalpy
H	airfoil height, or span
IMF	irreversible mean force, Eq. (11)
ITF	irreversible turbulent force, Eq. (13)
k	turbulent kinetic energy, $k = 0.5(\langle u^2 \rangle + \langle v^2 \rangle + \langle w^2 \rangle)$
M	Mach number
MW_{st}	mechanical work along streamline, Eq. (14)
L	turbulence integral scale
$\vec{n}$	unit vector in mean flow direction
P_s	static pressure
P_t	total pressure
RANS	Reynolds-averaged Navier-Stokes
Re	Reynolds number based on inlet velocity and axial chord
Re_θ	inlet boundary layer momentum thickness Reynolds number
RMF	reversible mean force, (See Table 1)
RTF	reversible turbulent force, Eq. (12)
S	cascade pitchwise spacing
S_{ij}	instantaneous strain rate tensor, $0.5\left(\frac{\partial v_j}{\partial x_i} + \frac{\partial v_i}{\partial x_j}\right)$
s_{ij}	fluctuation strain rate tensor, $0.5\left(\frac{\partial u_j}{\partial x_i} + \frac{\partial u_i}{\partial x_j}\right)$
SKE	secondary kinetic energy, $0.5(V'^2 + W^2)$
t	time variable

U.S. Air Force Public Affairs Office Case No. 88ABW-2012-0315

TKE same as k, used in text for convenience

Tu turbulence intensity, $\sqrt{< u^2 >}/U \times 100\%$

u_i fluctuation velocity vector, v_i - U_i

U_i mean velocity vector, v_i - u_i

v_i instantaneous velocity vector

U,V,W cascade mean velocities

U′,V′,W secondary mean velocities

x_i Cartesian index notation direction coordinate

x,y,z cascade coordinate directions

x′, y′, z secondary coordinate directions

Y total pressure loss coefficient,

$$Y = \left(P_t - P_{t,in} \right) / 0.5\rho\, U_{in,st}^2$$

Z_w Zweifel loading coefficient,

$$Z_w = 2\left(\frac{S}{C_{ax}} \right) \cos^2\alpha_{ex} \left(\tan\alpha_{in} - \tan\alpha_{ex} \right)$$

Greek

α cascade gas angle, measured from axial

δ_{ij} Kronecker delta

δ_{99} 99% inlet boundary layer thickness

ε_{ijk} alternating unit tensor

ρ fluid density

υ fluid kinematic viscosity

ω_i mean vorticity vector, $\varepsilon_{ijk}\partial_j U_k$

Subscripts and Superscripts

ex exit location

i,j,k Cartesian indices, can be 1, 2, or 3

in inlet location

st streamwise direction

x,y,z direction indicators for axial, pitchwise, and spanwise directions, respectively

$( )'$ prime indicates secondary coordinate system

Operator Symbols

∇ gradient operator of scalar field

Δ difference operator

$\langle\ \rangle$ averaging operator

INTRODUCTION

Recently, there has been increased interest in increasing the aerodynamic load on turbine airfoils to reduce weight. Turbines operate with an overall favorable pressure gradient, but with diffusion on the airfoil suction surfaces, increasing the aerodynamic load with highly curved airfoils and stronger adverse pressure gradients can cause stall at higher Reynolds numbers. Stall refers to a separation bubble that does not reattach upstream of the trailing edge. McQuilling [1] showed that with laminar-turbulent transition modeling and manipulation of the pressure loading distribution, high lift profiles can be designed that preserve midspan low Reynolds number performance. In linear cascade studies using profiles with similar gas angles as the L2A in the present study, Praisner et al. [2] and Knezevici et al. [3] showed that such designs increase endwall loss beyond practical limits. In both of these studies, the authors applied non-axisymmetric endwall contouring in an attempt to mitigate the elevated endwall losses, yet the losses remained too high for use in engines.

The purpose of this paper is to elucidate the causes of elevated endwall loss for high lift LPT airfoil designs and to suggest an alternative approach for reducing mixing losses. Past endwall loss reduction methods such as endwall contouring have generally focused on weakening vortical structures. Vortices are often viewed in the literature as loss-generating mechanisms, yet the way they contribute to loss is unclear.

In this paper we examine endwall flow and losses in terms of both mixing effects and the interaction of vortices with the profile suction surface. Past endwall loss studies have considered mixing effects, but interaction of the endwall flow with the profile has not received much attention. To study mixing we decompose the mixing forces locally within the flow field. The interaction of vortices with the profile is studied using profile boundary layer fences and a pressure surface modification. Because of the no-slip condition, little can be done to reduce endwall boundary layer losses for a given surface area, so the focus of this work is on aspects of freestream mixing.

ENDWALL LOSS STUDIES

The mean endwall flow field is comprised of several vortical structures with the passage vortex being dominant. Although large scale unsteady flow features may be present, turbulence is also quite high in the endwall region. As a result, past endwall loss studies have generally focused on dissipation of the vortical structures by studying the secondary kinetic energy (SKE) and the role of turbulence.

The Role of Secondary Kinetic Energy

In the mean flow field, the rotational energy at the endwall is typically quantified by the magnitude of SKE. Using the mass-averaged exit flow angle, or the mean camber line angle at the trailing edge as the primary reference direction (depends on researcher), SKE is defined as half the sum of squared mean velocity components normal to the primary reference direction (See Fig. 2). The mathematical definition is given as,

$$\mathrm{SKE} = \frac{1}{2}\left(V'^2 + W^2 \right). \qquad (1)$$

Moore and Adhye [4] measured SKE at three downstream planes of a low speed linear turbine cascade. They suggested that the increased loss is almost entirely explained by a decrease in SKE at downstream planes. More recently, MacIsaac et al. [5] also reported endwall flow loss development downstream of a low speed linear turbine cascade. They observed that reduction in SKE only accounted for 42% and 64% of the mixing losses in the second and third downstream mixing planes, respectively. The lack of correlation between

SKE and loss was attributed to streamwise gradients in the exit flow that were not captured by computing SKE.

The differing conclusions of these two studies regarding SKE may be due to boundary conditions. It is worth noting that the Moore and Adhye [4] cascade had an aspect ratio of unity, whereas the MacIsaac et al. [5] cascade had an aspect ratio of 2.8. Besides incompressible flow, no other geometric or flow conditions were matched. The significant differences in test conditions provide a good pair of test cases for assessing the utility of SKE as an indicator of passage loss. The differing conclusions suggest that SKE may not be a good indicator of measured losses. We do not present SKE measurements in the present study.

The Role of Turbulence

Gregory-Smith et al. [6] investigated the role of TKE in total pressure loss within and downstream of a low speed linear cascade of turbine airfoils. The through-passage integrated turbulence energy increased tenfold, but it only accounted for about 25% of the total pressure loss. They concluded that dissipation (presumably mean flow and turbulent) through viscous action is very significant. MacIsaac et al. [5], however, found that the integrated TKE in three measurement planes downstream of their linear turbine cascade remained approximately constant, indicating that the growth of TKE is not correlated with increasing downstream total pressure loss.

Moore et al. [7] studied turbulent Reynolds stresses in downstream mixing in a low speed linear turbine cascade. They found that the integrated deformation work term that exchanges mean flow and turbulent kinetic energy (TKE) (also called the turbulence production term) agreed very closely with the rate of total pressure loss production. Their data also showed that contours of TKE identified the boundary of the airfoil wake similar to loss coefficient contours, but the peaks were not aligned. MacIsaac et al. [5] also studied the turbulence production in downstream measurement planes of a low speed linear turbine cascade. Their results supported Moore et al. [7], in that turbulence production (not simply TKE) plays a significant role in the mixing process and loss production. MacIsaac et al. [5] pointed out that the magnitude of the turbulence production term should be comparable to the dissipation term.

Relation of Present Work to Past Mixing Loss Studies

The mixing analysis in this paper is related to the work of MacIsaac et al. [5] and Moore et al. [7], but the governing equation we use is quite different. These authors applied the mean kinetic energy equation for a turbulent flow given by Hinze [8]. That equation has a gradient of the product of a convection velocity and total pressure, a term that is difficult to measure. Moore et al. [7] assumed the convection velocity constant so it could be factored out for computing area averages of the total pressure gradient downstream of the blade row. In this paper we solve for the total pressure gradient to study mixing locally in the flow field.

MIXING ANALYSIS

For incompressible and adiabatic cascade flows the overall work is zero. For these conditions the first law of thermodynamics can be written as,

$$\frac{\Delta P_t}{\rho} = -\Delta e \,, \tag{2}$$

where e is internal energy. We see that the passage total pressure loss will be due to an increase in internal energy. Considering a differential element in the flow field, the equation governing the internal energy of an incompressible, adiabatic, turbulent flow can be written as,

$$\frac{D\langle e\rangle}{Dt} = 2\upsilon\left[\langle S_{ij}\rangle\langle S_{ij}\rangle + \langle s_{ij}s_{ij}\rangle\right] , \tag{3}$$

where $\langle e\rangle$ is the mean internal energy, $\langle S_{ij}\rangle$ is the mean strain rate tensor, and s_{ij} is the fluctuation strain rate tensor. The quantities $2\upsilon\langle S_{ij}\rangle\langle S_{ij}\rangle$ and $2\upsilon\langle s_{ij}s_{ij}\rangle$ are the mean flow and turbulence dissipation rates, respectively. These dissipation terms are caused by shear stresses in the fluid. To decouple the roles of the mean and turbulent flow fields in loss production, one could locally measure both dissipation rates to obtain a direct measure of internal energy production and total pressure loss. Integrating the local dissipation measurements across the passage would yield the overall total pressure loss production rate. Unfortunately, measurement of the turbulence dissipation rate is very difficult even for simple flows due to the need to measure instantaneous fluctuation gradients.

An alternative method to quantify local influences on total pressure can be derived from the RANS momentum equation,

$$\frac{\partial U_i}{\partial t} + U_j\frac{\partial U_i}{\partial x_j} = -\frac{1}{\rho}\frac{\partial P_s}{\partial x_i} + \upsilon\frac{\partial^2 U_i}{\partial x_j\partial x_j} - \frac{\partial\langle u_i u_j\rangle}{\partial x_j} . \tag{4}$$

The convection term on the left hand side can be replaced using the following identity given by Panton [9],

$$U_j\frac{\partial U_i}{\partial x_j} = \frac{\partial}{\partial x_i}\left(\frac{1}{2}U_jU_j\right) + \varepsilon_{ijk}\omega_j U_k \,, \tag{5}$$

where ω_j is the local vorticity vector. Note that the second term on the right hand side of Eq. (5) can also be written as $\vec{\omega}\times\vec{U}$. Assuming steady mean flow and substituting Eq. (5) into Eq. (4), we obtain an expression for the spatial total pressure derivatives,

$$\frac{\partial P_t}{\partial x_i} = \mu\frac{\partial^2 U_i}{\partial x_j\partial x_j} - \rho\varepsilon_{ijk}\omega_j U_k - \rho\frac{\partial\langle u_i u_j\rangle}{\partial x_j} . \tag{6}$$

Equation (6) can be interpreted as a local description of the force balance in the flow field that causes changes in total pressure. The first term on the right hand side represents a force due to viscous diffusion, an irreversible mean flow friction force (IMF). The second term came from the vector identity of Eq. (5) and represents a coriolis force. This vector identity decomposed the convection term present in the inviscid Euler equations and as a result, is a reversible mean force (RMF). The last term of Eq. (6) requires more attention.

Following Pope [10], the Reynolds stress tensor can be decomposed as,

$$\left\langle u_i u_j \right\rangle = \frac{2}{3} k \delta_{ij} + a_{ij} \tag{7}$$

where $k = 0.5\left\langle u_i u_i \right\rangle$. This decomposition splits the Reynolds stress tensor into isotropic and anisotropic parts, $\frac{2}{3} k \delta_{ij}$ and a_{ij}, respectively. The isotropic stress cannot cause shear and as a result, represents a reversible turbulent force (RTF). This is analogous to the absence of pressure from the vorticity equation because of its inability to cause shear. On the other hand, a_{ij} represents a deviatoric shear stress and as a result, accounts for an irreversible turbulent force (ITF). In summary, we have irreversible mean forces (IMF), irreversible turbulent forces (ITF), reversible mean forces (RMF), and reversible turbulent forces (RTF) that define the total pressure spatial derivatives.

For experiments, it is convenient to non-dimensionalize equations for establishing similarity and to enable scaling. In this study, spatial variables were scaled using the axial chord. Total pressure was scaled by twice the inlet dynamic head. Velocities were scaled by the inlet mean velocity magnitude and turbulence quantities by the square of the inlet mean velocity magnitude. In non-dimensional variables, Eq. (6) can be expressed as,

$$\frac{\partial P_t}{\partial x_i} = \frac{1}{Re} \frac{\partial^2 U_i}{\partial x_j \partial x_j} - \varepsilon_{ijk} \omega_j U_k - \left(\frac{2}{3} \frac{\partial k}{\partial x_j} \delta_{ij} + \frac{\partial a_{ij}}{\partial x_j} \right). \tag{8}$$

For convenience, the index notation terms of Eq. (8) are written out explicitly in Table 1 with non-dimensional variables for the x-direction. The forms of the total pressure derivatives in the y and z directions are implied. To expand the index notation terms, substituting 1, 2, or 3 for the indices (i.e., i, j, and k) refers to the x, y, and z coordinate directions, respectively. Table 2 lists the scales used for non-dimensionalization.

Because Eq. (8) is an alternative form of the RANS momentum equation (a vector equation), taking the dot product of Eq. (8) with the mean velocity vector will result in a mechanical energy equation. The forces will generate work in the flow. By taking the dot product of Eq. (8) with a unit vector in the mean flow direction, we obtain a measure of the change in total pressure along the local streamline, referred to as the mechanical work,

$$MW_{st} = \nabla P_t \cdot \vec{n}, \tag{9}$$

where,

$$\nabla P_t = \frac{\partial P_t}{\partial x} \vec{i} + \frac{\partial P_t}{\partial y} \vec{j} + \frac{\partial P_t}{\partial z} \vec{k}, \tag{10}$$

and $\vec{n}$ is the unit vector in the mean flow direction. MW_{st} is our focus for determining the dominant mixing effects. Upon carrying out the calculation of MW_{st} by hand, one finds that the second term on the right hand side of Eq. (8) (i.e., term defining RMF) is orthogonal to the mean velocity vector. Thus, RMF has no role in changing the mechanical energy of the flow. The remaining mixing effects are decoupled according to,

$$IMF = IMF_x n_x + IMF_y n_y + IMF_z n_z, \tag{11}$$

Table 1. Expansion of Eq. (8) for the x-direction

$\frac{\partial P_t}{\partial x} = IMF_x + RMF_x + RTF_x + ITF_x$	
IMF_x	$\frac{1}{Re}\left(\frac{\partial^2 U}{\partial x^2} + \frac{\partial^2 U}{\partial y^2} + \frac{\partial^2 U}{\partial z^2} \right)$
RMFx	$(-1)(\omega_y W - \omega_z V)$
RTF_x	$\left(-\frac{2}{3} \right) \frac{\partial k}{\partial x}$
ITF_x	$(-1)\left(\frac{\partial a_{uu}}{\partial x} + \frac{\partial a_{uv}}{\partial y} + \frac{\partial a_{uw}}{\partial z} \right)$

Table 2. Summary of Scaling Variables

Quantity	Scale
P_t	$\rho U_{in,st}^2$
Velocity	$U_{in,st}$
Flucuation/Re Stress	$U_{in,st}^2$
Distance	C_{ax}

$$RTF = RTF_x n_x + RTF_y n_y + RTF_z n_z, \tag{12}$$

$$ITF = ITF_x n_x + ITF_y n_y + ITF_z n_z, \tag{13}$$

and,

$$MW_{st} = IMF + RTF + ITF. \tag{14}$$

EXPERIMENTAL METHODS

The experiments were conducted in the AFRL low speed wind tunnel facility located at Wright-Patterson Air Force Base. This wind tunnel is an open loop induction type, with the flow that enters a bell-mouth contraction passing through a turbulence-generating grid, through a cascade and exiting via a fan. The turbulence grid is comprised of a lattice of horizontal and vertical 25.4 mm round bars, with 76.2 mm center spacing. The turbulence grid produces a turbulence intensity of Tu = 2.9%, with an integral scale of L_{in} = 19.7 mm at about $1.4C_{ax}$ upstream of the cascade, where C_{ax} is axial chord. The center blade of the cascade is approximately 90 bar diameters downstream of the grid.

A schematic of the test section is given in Fig. 1. The cascade is comprised of seven airfoils. The outer tailboard is used to set the exit angle at Re = 100,000, the Reynolds number used in this study. A splitter plate assembly provides inlet boundary layer control for endwall studies. The distance between the splitter plate and the tunnel roof causes an effective span to axial chord ratio of 3.5. The splitter inlet plate leading edge was designed according to the recommendations of Narasimha and Prasad [11].

Figure 2 shows the cascade and secondary flow coordinate systems. The secondary coordinate system is indicated with primes and rotated 58˚ off axial, the approximate exit angle for tests with and without fences. Exit measurements were taken $0.58C_{ax}$ downstream of the blade row, placing the center airfoil

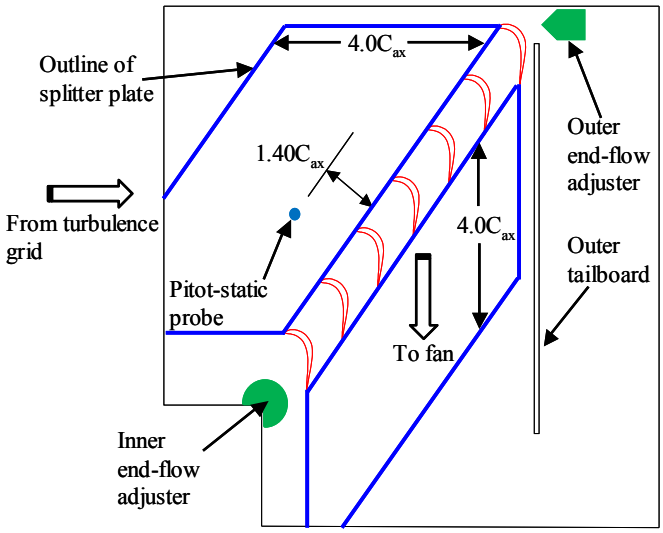

Figure 1. Schematic of AFRL low speed wind tunnel test section

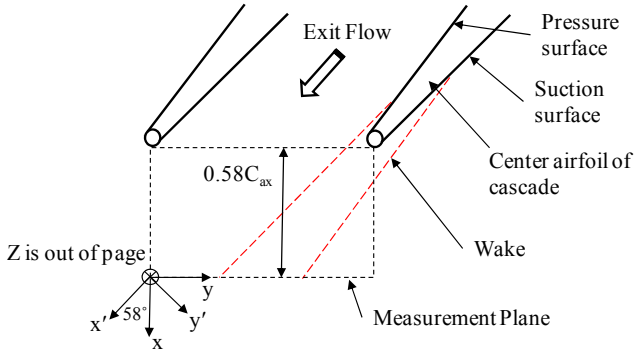

Figure 2. Schematic depicting the cascade and secondary flow (primed) coordinate system definitions

wake near the middle of the measurement plane. Table 3 summarizes the cascade geometry and flow conditions. One notes in Table 3 that the inlet boundary layer thickness is quite small. Though the inlet boundary layer thickness will influence the overall measured losses downstream of the blade row, this paper focuses on the physics of how losses are generated and not on the overall losses.

Figure 3 shows the pressure loading of the L2A profile. The pressure loading is based on fully turbulent calculations by Lyall et al. [12], and shows that the profile is aft loaded with peak suction at 0.60C$_{ax}$. This profile was designed at the Propulsion Directorate of the Air Force Research Laboratory for studying low Reynolds number and high lift aerodynamics. It was designed to have the same gas angles as the Pratt & Whitney Pack B profile.

Except for ambient pressures, data were sampled using National Instruments hardware and software. An upstream stationary pitot-static probe and a kiel probe in the exit measurement plane were used to measure total pressure loss. At 3.2 mm diameter, the kiel probe was less than 2% of the

Table 3. Cascade Geometry and Flow Conditions

Axial chord, C_{ax}	152.4 mm
Pitch/axial chord, S/C_{ax}	1.221
Span/axial chord, H/C_{ax}	3.5
Zweifel coefficient, Z_w	1.59
Inlet flow angle (from axial), α_{in}	35°
Mean exit flow angle without fence (from axial), α_{ex}	-57.7°
Inlet turbulence Intensity, Tu_{in}	2.9%
Streamwise integral scale at inlet, $L_{in,st}$	0.13C$_{ax}$
Max exit Mach number, M_{ex}	0.053
Re, ($U_{in,st}$ and C_{ax})	100,000
Inlet boundary layer parameters, 1.4C$_{ax}$ upstream	
δ_{99}/H	0.025
Re_θ	655
Shape factor	2.2

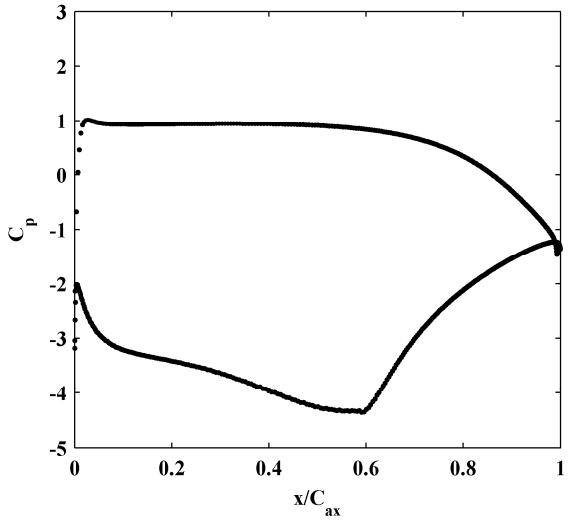

Figure 3. Pressure loading of the L2A profile, taken from Lyall et al. [12]

blade pitch, providing sufficient resolution within the wakes. The ambient pressure was measured with a laboratory barometer, and freestream fluid temperatures were measured using type J thermocouples. An IFA300 constant temperature anemometer was used with single normal hot-film probes (TSI 1211-20) for obtaining velocities and turbulence measurements at the inlet. The velocities for setting the inlet Reynolds number were measured using the upstream pitot-static probe. A TSI 1299-20-18 triple sensor hot-film probe was used to obtain velocity and turbulence measurements downstream of the blade row. The three sensors of the triple probe were contained within a 2 mm measurement diameter. The probe stem was 4.6 mm in diameter.

All hot-film probes were calibrated using a TSI Model 1127 velocity calibrator. Typical calibration curves included 18

points, spanning the measured velocity range in the experiment. Calibrations spanned 2 < U < 14 m/s and 5 < U < 29 m/s for inlet and exit measurements, respectively. During calibration, the triple sensor probe was placed in a zero pitch/yaw configuration for the entire velocity range. An analytical technique, similar to that described by Lekakis et al. [13], combined with the table look-up procedure of Gieseke and Guezennec [14] was used for obtaining velocity magnitudes and angles, given effective cooling velocities. In the experiment, average flow angles relative to the probe axis were typically within 10˚. Angle measurements on the calibration stand were within ± 0.9˚ of the actual velocity vector for ±18˚ pitch and yaw, indicating reasonable bias error.

All uncertainties were estimated at 95% confidence. Uncertainties for the Reynolds number and total pressure loss coefficients were estimated using the partial derivative and root-sum-square method of Kline and McClintock [15]. The loss coefficients at each point were estimated to within ± 0.01, approximately 1% of the inlet dynamic head. The Reynolds number was also estimated to be within about 1% of the measured value. The uncertainty of mean velocities for the exit flow field was estimated to be within 1.5% of the measured values. Sampling times were also sufficiently long to ensure independence of the samples in the presence of unsteadiness. When acquiring data for computing three-dimensional mixing forces, it was important to control the precision error to allow quality gradient calculations within the turbulence field. Approximately 7,000 independent samples were acquired at each measurement location to limit the mean-square fluctuation to within 3.5% of the measured values.

Three-dimensional mixing forces were obtained from triple sensor hot-film measurements. Derivatives were calculated using second order centered finite differences given by Tannehill et al. [16] for three-point stencils without interpolation between measurement points. For computing the derivatives, the grid spacing was set at $\Delta x = 0.083C_{ax}$, $\Delta y = 0.028C_{ax}$, and $\Delta z = 0.042C_{ax}$ within the measurement plane. Forty five independent quantities comprised of velocity and turbulence measurements were required to compute the mechanical work, MW_{st}, at a single position. The combined uncertainty in MW_{st} due to the separate measurements was estimated using the sequential perturbation technique of Moffat [17].

Results of MW_{st} with 95% confidence bands at 20% span, along with total pressure loss coefficients for reference are shown in Fig. 4. Positive and negative MW_{st} indicates energy addition to and extraction from the mean flow, respectively. As will be shown in the results section, the differences in the mixing forces that sum together to give MW_{st} are larger than the error bars, indicating that meaningful conclusions can be obtained regarding the role of the different mixing forces. The Reynolds stress measurements had the largest uncertainty.

RESULTS AND DISCUSSION

The experimental results are presented in three subsections. The first includes a discussion of the flow field to provide a basis for discussing mixing and loss development. Mixing forces are discussed next, whereby the mean flow and turbulence effects are decoupled. The final subsection presents an experiment in the lab using profile fences and a pressure surface modification. The purpose of this latter experiment was to investigate the influence on loss development due to interaction of the secondary flow with the profile suction surface.

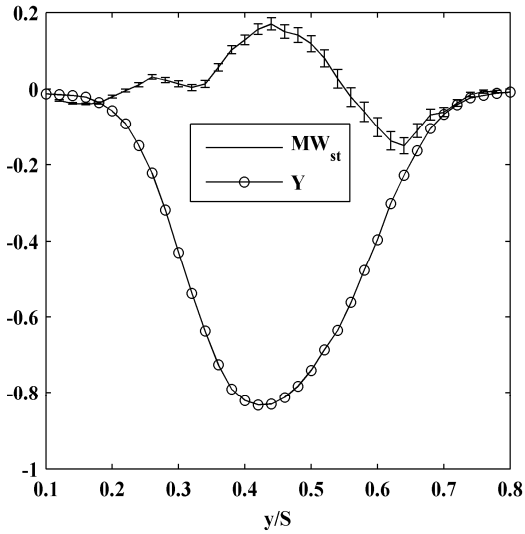

Figure 4. Mechanical work and loss coefficients at 20% span in the measurement plane (See Fig. 2)

Flow Field Description

Secondary flow formation is well documented so only a brief discussion will be given here, based on Langston's [18] review. Several variations of endwall flow models exist, but we will only consider the dominant features. Upstream of the leading edge, the inlet endwall boundary layer separates, forming a horseshoe vortex. The pressure side leg of the horseshoe vortex is swept across the passage towards the adjacent suction surface by the cross passage pressure gradient, eventually becoming the passage vortex. The passage vortex climbs the suction surface and separates as it rotates. Meanwhile, the suction side leg of the horseshoe vortex remains close to the suction surface and rotates in opposite sense to the passage vortex. Langston [18] also points out that the suction side leg may orbit around the axis of the passage vortex. In this paper, we will focus on mixing effects of the secondary flow structures downstream of the blade row, and also the interaction with the suction surface.

Figure 5 gives surveys of secondary velocity vectors (V′, W), secondary vorticity coefficients and total pressure loss coefficients. The wake behind the center blade of the cascade is shown where the right side of the wake corresponds to the suction surface (see Fig. 2). The secondary vorticity coefficients were computed using the method described by Hodson and Dominy [19],

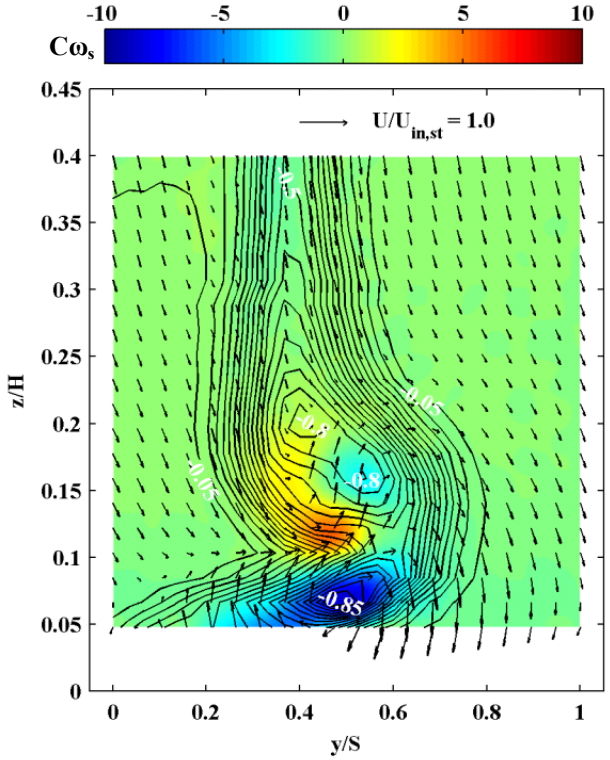

Figure 5. Secondary vorticity, total pressure loss coefficients (ΔY = 0.05 for contours), and secondary velocity vectors within the measurement plane (See Fig. 2)

$$C\omega_s = \frac{\partial W}{\partial y} - \frac{\partial V'}{\partial z}, \qquad (15)$$

where the variables were non-dimensionalized with the scales of Table 2. The positive axis of vorticity is out of the page. Equation (15) will not equal the magnitude of the vorticity vector in the streamwise direction, x′, but provides a measure of the relative strength of the streamwise vorticity across the measurement area. Also note that there is a z component of the secondary velocity vectors approaching midspan, a region in the measurement area where the z component may be expected to be nearly zero. This z component is due to the extra blockage of the wind tunnel boundary layer at z/H = 1.0, compared to the relatively thin boundary layer on the tunnel splitter plate at z/H = 0 (See Fig. 1). In this wind tunnel using the splitter plate, the z component of velocity approaching midspan is smaller for cascades that have less secondary loss.

The center of the passage vortex in Fig. 5 is approximately at y/S = 0.48 and z/H = 0.07, as indicated by the secondary velocity vectors. The passage vortex extends approximately to z/H = 0.10. Strong negative vorticity is present inside the passage vortex. The secondary velocity vectors midwake beyond the passage vortex show a spanwise migration of flow towards midspan. Those vectors indicate that this migrating flow extends to approximately z/H = 0.20. The boundary layer on the suction surface will be skewed due to this migrating flow. Furthermore, the spanwise migration of flow turns away from the suction surface and separates, generating a weaker negative vorticity core at y/S = 0.55 and z/H = 0.16. Rather than separate negative vorticity cores, it is more common for the spanwise migrating flow and the passage vortex to be merged, generating a single negative vorticity core within the secondary flow. Zoric et al. [20], however, show data for cascades with the same gas angles as L2A with both merged and separate negative vorticity cores. For incoming turbulence levels of Tu = 1.5%, Zoric et al. [20] show that the Pack B cascade generates a single merged region of negative vorticity while the Pack D-A cascade has two negative vorticity cores, similar to L2A in this study. Also note in Fig. 5 that there is a region of positive vorticity that has a peak magnitude at y/S = 0.45 and z/H = 0.12 and extends to nearly z/H = 0.20. This region of positive vorticity (commonly referred to as the shed vorticity) is due to the skewing of the profile boundary layer by the spanwise flow migration.

The total pressure loss coefficients of Fig. 5 show that there are two regions of low energy cores in the flow field, which is typical of endwall flows. The low energy core closest to the endwall is approximately collocated with the passage vortex, at y/S = 0.48 and z/H = 0.07. A larger low energy region is approximately centered at y/S = 0.45 and z/H = 0.18 and contains two minima.

In the following sections of this paper, we will investigate the components of Eq. (8) that influence MW_{st} in Eq. (9). We focus on the irreversible effects of mixing. Secondly, we will investigate how the low energy regions form, but focus on the largest low energy region centered at y/S = 0.45 and z/H = 0.18. We suggest that the largest low energy region forms inside the passage as the spanwise flow migrating towards midspan separates from the suction surface. Later this idea is investigated using profile fences and a pressure surface modification.

Decomposition of Mixing Forces

Figure 6 shows MW_{st} obtained at 20% span within the large low energy region of Fig. 5. Recall from Eq. (14) that IMF, ITF, and RTF sum together to give MW_{st}. One first notes that the irreversible mean force due to viscous diffusion, IMF, is negligibly small. Secondly, the dominant mixing effect is the irreversible turbulent shear force, ITF. The reversible turbulent force, RTF, plays a secondary role in mixing at this spanwise location. At the positive peak in MW_{st} (y/S = 0.44), the ratio of mean to turbulent shear forces is IMF/ITF = 0.003. This negligible mean flow shear suggests that turbulence dissipation is the dominant cause of losses at 20% span. We will investigate the shear effects within the measurement plane of Fig. 2 to show that mean flow shear remains negligible compared to turbulent shear at other spanwise locations.

We define some additional terms for convenience to describe the relative strength of shear effects. Consider mixing in the downstream main flow direction, x′ of Fig. 2. By inspection of Table 1 and applying the secondary coordinate system, $IMF_{x'}$ will define the mean flow shear force in the main flow direction. $IMF_{x'}$ results from viscous diffusion, or second

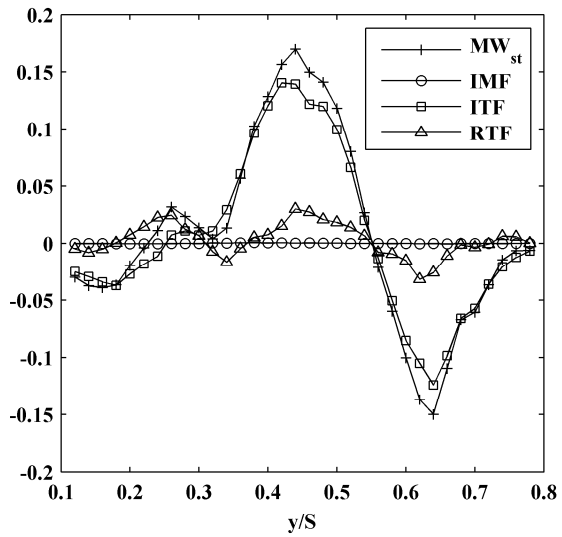

Figure 6. Decomposition of the mixing forces at 20% span in the measurement plane (See Fig. 2)

derivatives of the U′ velocity. We define a new mean flow shear force parameter as,

$$F_{M'} = \frac{1}{Re}\left(\frac{\partial^2 U'}{\partial y^2} + \frac{\partial^2 U'}{\partial z^2}\right), \qquad (16)$$

with non-dimensional variables according to Table 2. The diffusion term in the x′ direction was neglected. Also note in Eq. (16) the second derivative in the y direction as opposed to y′. This change reflects the measurement plane orientation in the y direction. $F_{M'}$ will therefore have a smaller magnitude than expected for $IMF_{x'}$.

Using similar reasoning as for defining $F_{M'}$, we define two new turbulent shear force parameters. Recognizing in Eq. (7) that $\langle u_i u_j \rangle = a_{ij}$ when $i \neq j$, these parameters are defined by,

$$F_{<uv>'} = -\frac{\partial \langle uv \rangle'}{\partial y}, \text{ and} \qquad (17)$$

$$F_{<uw>'} = -\frac{\partial \langle uw \rangle'}{\partial z}, \qquad (18)$$

with non-dimensional variables according to Table 2. The turbulent shear parameters are defined separately to isolate effects due to each Reynolds stress component. The sum of $F_{<uv>'}$ and $F_{<uw>'}$ will have a smaller magnitude than $ITF_{x'}$ due to the derivative in the y direction as opposed to y′. The implication of Eqs. (16-18) is that if $F_{M'}/(F_{<uv>'} + F_{<uw>'})$ is negligible, then $IMF_{x'}/ITF_{x'}$ will also be negligible. For the full area traverse, the velocity and turbulence data were refined using cubic spline interpolation for computing derivatives.

Figure 7 shows flood plots of the newly defined mixing force variables. Contours of Y and secondary velocity vectors are included for reference. Figure 7a shows the combined effects of $F_{<uv>'}$ and $F_{<uw>'}$. On the outer perimeter of the wake, the mixing forces are negative, indicating energy extraction from the mean flow. On the inside of the wake, the mixing

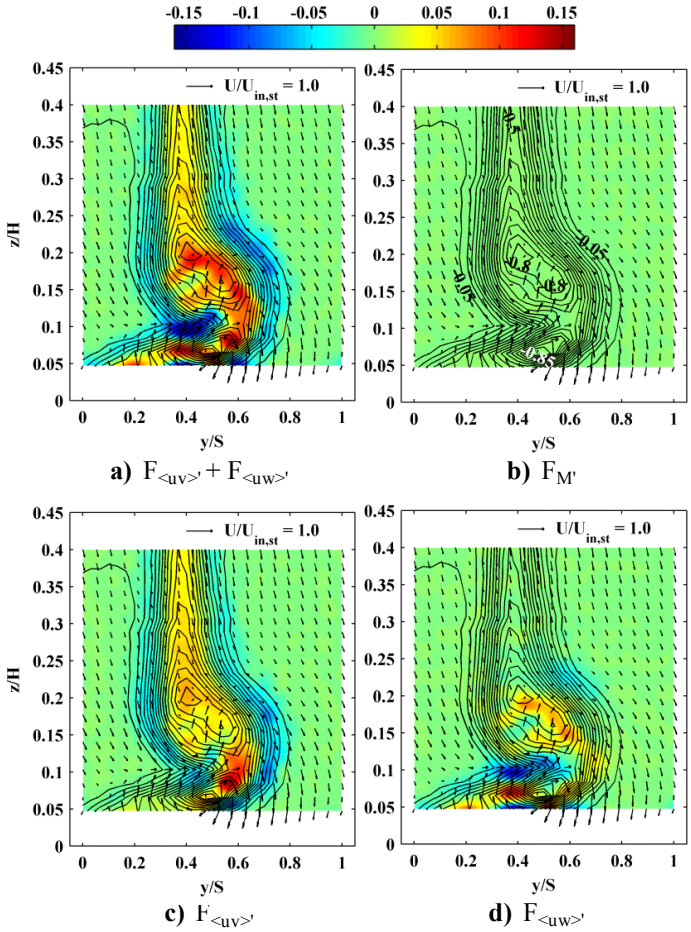

Figure 7. Flood plots of mixing force variables overlaid with Y contours and secondary velocity vectors

forces are positive and adding energy to the mean flow. In Fig. 7b, the mean flow viscous force, $F_{M'}$, has a negligible influence across the whole measurement area, thus supporting the original idea that mean flow viscous shear and dissipation has little effect on losses. From Figs. 7c and 7d, we see that $F_{<uv>'}$ remains significant over most of the measurement area. $F_{<uw>'}$, however, is insignificant from z/H = 0.25 on towards midspan and has little influence on mixing in this region.

Between z/H = 0.25 and the endwall (z/H = 0), the region where both $F_{<uv>'}$ and $F_{<uw>'}$ are significant, the mixing forces vary significantly across the measurement area. This variation is enhanced mainly because $F_{<uv>'}$ and $F_{<uw>'}$ do not always carry the same sign. Where both quantities carry the same sign, energy extraction or addition is enhanced to speed up mixing. One such area is y/S = 0.4 and z/H = 0.10 in Fig. 7a. At this location, energy extraction is quite strong. Figures 7c and 7d show that $F_{<uv>'}$ and $F_{<uw>'}$ both extract energy from the mean flow at this location. On the other hand at y/S = 0.4 and z/H = 0.15 in Fig. 7a, the overall mixing force is depressed within the large low energy region. Figures 7c and 7d reveal that $F_{<uv>'}$ and $F_{<uw>'}$ are of opposite sign at this position to slow down mixing.

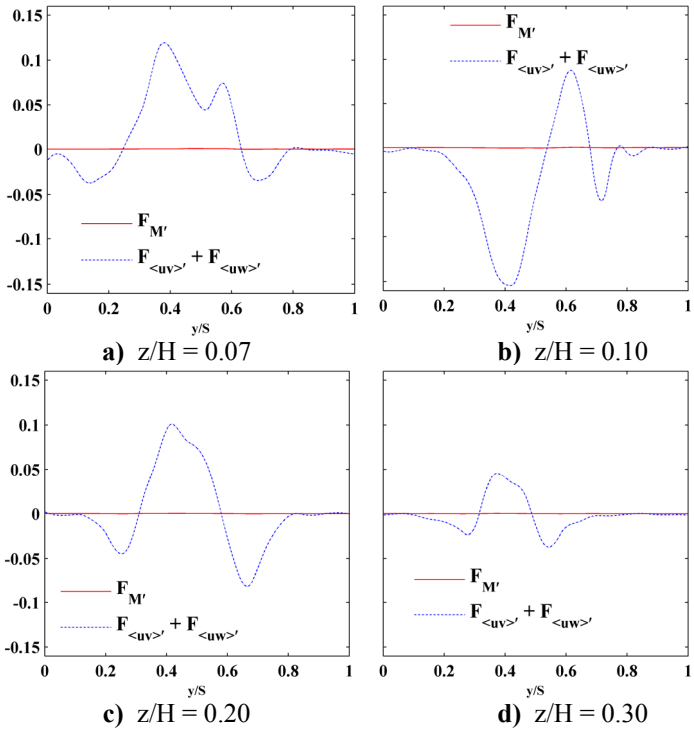

Figure 8. Mean flow and viscous effects for various spanwise positions

Figure 8 shows mixing forces obtained from Fig. 7 at several spanwise positions. The z/H = 0.07 position in Fig. 8a corresponds to the approximate center of the passage vortex. At this spanwise location, the turbulent shear forces mostly add energy to the mean flow and $F_{M'}$ is negligible. Recall from Fig. 5 that the strongest secondary vorticity is within the passage vortex. As an additional check of the magnitude of mean flow shear, $F_{M'}$ was recalculated at z/H = 0.07 with both V′ and W as opposed to U′. The change in $F_{M'}$ calculated with V′ and W was negligible, indicating weak mean flow shear effects inside the passage vortex despite the presence of strong secondary vorticity. At z/H = 0.10 in Fig. 8b, energy extraction by the turbulent forces dominates. At z/H = 0.20 and 0.30 in Figs. 8c and 8d, respectively, the variation of turbulent mixing forces is geometrically similar across the pitch with smaller magnitudes closer to midspan. At all spanwise locations, $F_{M'}$ is negligible.

Figures 6 through 8 provide insight into how and where mixing losses are produced in the airfoil wake. Analytically, shear effects in the flow can be decoupled into those that change internal energy and those that change mechanical energy (cf., Panton [9]). Both effects occur simultaneously. The turbulence and mean flow dissipation rates are shear effects that change the internal energy of the flow, leading to the net total pressure loss across the blade row (Eqs. 2 and 3). Because the turbulence dissipation rate is difficult to measure, we used an equation describing the mechanical energy of the flow (MW_{st} in Eqs. 9 and 14) as a basis for determining the strength of the shear effects in the flow field. The magnitudes of shear effects that change the mechanical energy indicate the presence and relative strength of dissipation effects. The implication of negligible mean flow shear in Figs. 6 through 8 is that turbulence dissipation is the dominant cause of mixing losses. Furthermore, turbulent shear is strongest in the secondary flow between z/H = 0.25 and the endwall, suggesting higher dissipation rates in this region.

In this section we decomposed the mixing effects of the mean and turbulent flow fields of the airfoil wake. The mean flow component of the vortex structures will have a negligible effect on mixing loss. This conclusion applies to the freestream away from bounding walls. Also, large-scale unsteadiness has been included with the turbulence effects in this analysis. Although mixing losses are negligible for mean flow structures, they do play a role in loss production, primarily in how they interact with the suction surface inside the passage. Most of the paper so far has focused on mixing, but effects inside the passage give rise to the mixing process. We discuss the interaction of the secondary flow with the profile suction surface in the following section.

The Influence of Secondary Flow Separation From the Profile

Recall the midwake secondary velocity vectors of Fig. 5 that indicate a spanwise migration of the secondary flow along the profile suction surface. This spanwise flow turns away, or separates from the profile and circulates back towards the endwall. It is suggested that this separation is responsible for generating the expansive low energy regions typical of endwall flows. Energy is lost via viscous dissipation as the separated flow mixes with high-energy fluid.

We investigated the use of profile fences to inhibit the spanwise flow towards midspan on the suction surface, thus isolating the secondary flow from the midspan flow. To the authors' knowledge, Prümper [21] was the first to investigate fences for turbomachinery applications, testing approximately 400 different fence designs. The optimum design consisted of a profile fence and it reduced the area averaged passage loss by 50% for an annular cascade of vanes of aspect ratio unity. We are not advocating the use of fences, but they can elucidate the influence of the secondary flow on energy deficit formation within the passage.

As partially shown in Fig. 9, boundary layer fences were installed on the three center airfoils of the cascade. The center airfoil of the cascade is shown on the left in Fig. 9. Because measurements were obtained in the wake of the center airfoil, its fence was cut to wrap around to the pressure surface to enable attachment without altering the shape of the suction surface. The neighboring airfoil fences, however, were attached to the suction surfaces.

Plumber's putty was applied to the pressure surface of the airfoil adjacent to the center blade suction surface near the endwall. The putty narrowed the passage to reduce the cross-passage pressure gradient and improve the isolating effect of the fence. This application of a thickened or "spooned" profile pressure surface is different than commonly used in practice. Blanco et al. [22] describes how "spooning" the profile is used

Figure 9. Image of cascade airfoils with fence and pressure surface modifications

to reduce the interaction between the pressure surface separation bubble and the endwall flow. Based on the transitional computational model used by Lyall et al. [12] and surface flow visualization, the L2A profile does not have a pressure surface separation bubble at design incidence. The plumber's putty shown in Fig. 9 was applied by hand, so its appearance is not smooth in the picture. Smoothness is not important in creating a reduced cross-passage pressure gradient.

The fences were installed at 4.2% span from the endwall, a distance above the inlet boundary layer thickness. Bloxham's [23] particle image velocimetry measurements on the L1A profile, which has the same gas angles as L2A in the present study, indicated that the spanwise flow of the passage vortex remains close to the suction surface inside the passage. Using Bloxham's [23] measurements as a guide, the sheet metal fences were cut to extend into the flow 8.5% pitch from the suction surface. The leading edges of the fences were at $0.65C_{ax}$ from the leading edges of the profiles (aft of peak suction).

The effect of the fence and putty on the endwall wake is shown in Fig. 10. One first notes in Fig. 10b that applying the fence and putty caused a nearly two-dimensional flow from z/H = 0.12 on towards midspan. The strong region of positive vorticity in Fig. 10a that has a peak magnitude approximately centered at y/S = 0.45 and z/H = 0.12, is essentially eliminated using the fences and putty. This positive region of vorticity was eliminated because of the absence of spanwise flow along the profile that would normally skew the boundary layer. Furthermore, because of the absence of the spanwise flow, there is no ability for flow separation to propagate towards midspan. The absence of spanwise flow is why the large low energy region of Fig. 10a that is approximately centered at y/S = 0.45 and z/H = 0.18, is nearly eliminated using the fences and putty. Without fences and putty, significant endwall effects propagate to approximately 30% span, but to only 12% span with a fence. The secondary velocity vectors also indicate a slight improved average turning in Fig. 10b of approximately less than 0.5˚.

The mass-averaged passage loss was reduced by 12.9% using the fences and putty. An experiment using only fences (not shown in Fig. 10), showed that the putty contributed to

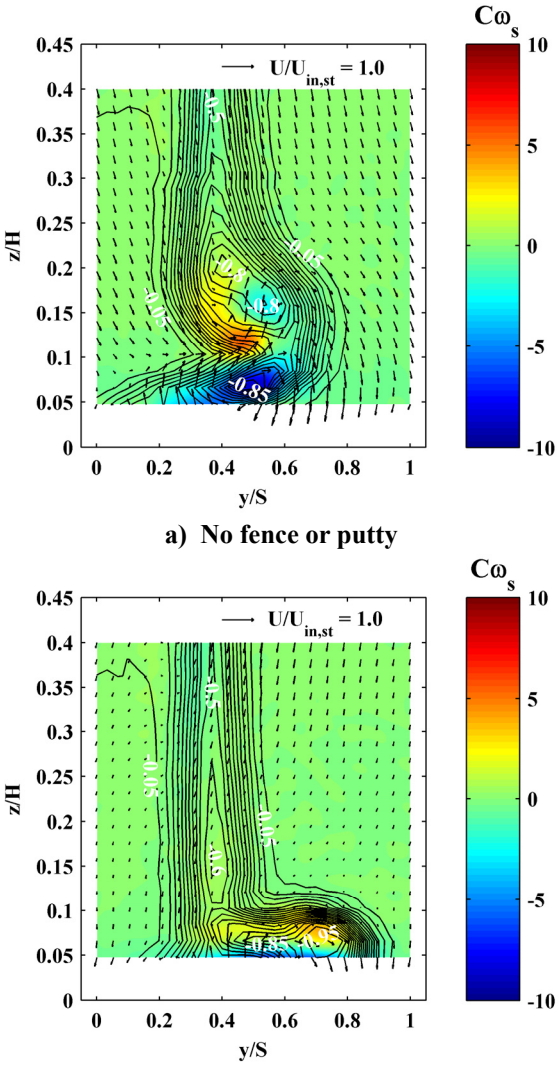

Figure 10. Flood plots of secondary vorticity, Y contours, and secondary velocity vectors with and without fences and putty

about 3% of the loss reduction. The authors note that measurements below 4.8% span were not included in the estimate, so the loss reduction may be lower when including measurements all the way to the wall. The purpose of the experiment with the fences and putty, however, was not to develop a loss reduction design, but to bring attention to the importance of the interaction of the secondary flow with the profile suction surface. Inside the passage, the secondary flow vortices climb the profile suction surface and then separate. Losses are generated by mean flow and turbulence dissipation as the separated flow mixes out, forming the low energy cores typical of endwall flows. Mixing continues within and downstream of the blade row.

Past attempts at reducing endwall losses for high lift profiles have generally focused on weakening the vortex structures, such as using non-axisymmetric endwall contouring (e.g., Praisner et al. [2] and Knezevici et al. [3]). Any

modifications to the profile near the endwall that suppress separation of the secondary flow may provide loss reductions additive to those that weaken vortical structures. Such modifications may not be straightforward and need to be researched.

CONCLUSIONS

In this paper, the origin of cascade mixing losses and the role of secondary flow vortical structures in loss development were investigated. For incompressible and adiabatic cascade flows, losses are generated by mean flow dissipation and turbulence dissipation. Turbulence dissipation, however, is difficult to measure and was not attempted. Keeping in mind that shear stress results in dissipation, an approach was developed to study components of the mixing forces. Among the shear forces that drive mixing and generate loss, turbulent shear was dominant over mean shear, suggesting that turbulence dissipation is the dominant cause of losses.

Due to negligible mean flow shear, the mean flow components of the vortical structures in the secondary flow (e.g., the passage vortex) do not contribute significantly to the mixing loss. Rather, the secondary flow causes the suction surface boundary layer to separate near the endwall. Low energy cores, typical of endwall flows, form inside the passage due to dissipation effects as the separated flow mixes out. An ad hoc experiment using profile boundary layer fences and a pressure surface modification eliminated a large portion of this separation, containing endwall effects to within 12% span. Endwall effects propogated to 30% span without the fences and pressure surface modification. Thus, interaction of the secondary flow with the profile suction surface is very important for loss development.

Modifications that limit the suction surface separation near the endwall can provide loss reductions additive to those that weaken vortical structures, such as endwall contouring. These modifications may not be straightforward and research is needed to investigate the problem.

REFERENES

[1] McQuilling, M.W., 2007. "Design and Validation of a High Lift Low-Pressure Turbine Blade," PhD Thesis, Wright State University, Dayton, Ohio.

[2] Praisner, T.J., Grover, E.A., Knezevici, D.C., Popovic, I., Sjolander, S.A., Clark, J.P., and Sondergaard, R., 2008, "Toward the Expansion of Low-Pressure-Turbine Airfoil Design Space," ASME Paper GT2008-50898.

[3] Knezevici, D.C., Sjolander, S.A., Praisner, T.J., Allen-Bradley, E., and Grover, E.A., 2009, "Measurements of Secondary Losses in a High-Lift Front-Loaded Turbine Cascade with the Implementation of Non-Axisymmetric Endwall Contouring," ASME Paper GT2009-59577.

[4] Moore, J. and Adhye, R.Y., 1985, "Secondary Flows and Losses Downstream of a Turbine Cascade," *J. of Engineering for Gas Turbines and Power*, Vol. 107, pp. 961-968.

[5] MacIsaac, G.D., Sjolander, S.A., and Praisner, T.J., 2010, "Measurements of Losses and Reynolds Stresses in the Secondary Flow Downstream of a Low-Speed Linear Turbine Cascade," ASME Paper GT2010-22727.

[6] Gregory-Smith, D.G., Walsh, J.A., Graves, C.P., and Fulton, K.P., 1988, "Turbulence Measurements and Secondary Flows in a Turbine Rotor Cascade," *J. of Turbomachinery*, Vol. 110, pp. 479-485.

[7] Moore, J., Shaffer, D.M., and Moore, J.G., 1987, "Reynolds Stresses and Dissipation Mechanisms Downstream of a Turbine Cascade," *J. of Turbomachinery*, Vol. 109, pp. 258-267.

[8] Hinze, J.O., 1975, "Turbulence," 2nd Edition. New York, New York: McGraw Hill.

[9] Panton, R.L., 1996, "Incompressible Flow," 2nd Edition. New York, New York: John Wiley & Sons, Inc.

[10] Pope, S.B., 2000, "Turbulent Flows," 1st Edition. Cambridge, UK: Cambridge University Press.

[11] Narasimha, R., and Prasad, S.N., 1994, "Leading Edge Shape for Flat Plate Boundary Layer Studies," *Experiments in Fluids*, Vol. 17, No. 5, pp. 358-360.

[12] Lyall, M.E., King, P.I., Sondergaard, R., Clark, J.P., and McQuilling, M.W., 2011, "An Investigation of Reynolds Lapse Rate for Highly Loaded Low Pressure Turbine Airfoils with Forward and Aft Loading," ASME Paper GT2011-46328.

[13] Lekakis, I.C., Adrian, R.J., and Jones, B.G., 1989, "Measurement of Velocity Vectors with Orthogonal and Non-Orthogonal Triple-Sensor Probes," *Experiments in Fluids*, Vol. 7, pp. 228-240.

[14] Gieseke, T.J., and Guezennec, Y.G., 1993, "An Experimental Approach to the Calibration and Use of Triple Hot-Wire Probes," *Experiments in Fluids*, Vol. 14, pp. 305-315.

[15] Kline, S.J., and McClintock, F.A., 1953, "Describing Uncertainties in Single Sample Experiments," *Mechanical Engineering*, Vol. 75.

[16] Tannehill, J.C., Anderson, D.A., and Pletcher, R.H., 1997, "Computational Fluid Mechanics and Heat Transfer," 2nd Edition. Philadelphia, Pennsylvania: Taylor & Francis.

[17] Moffat, R.J., 1988, "Describing the Uncertainties in Experimental Results," *Experimental and Thermal Fluid Science*, Vol. 1, pp. 3-17.

[18] Langston, L.S., 2001, "Secondary Flows in Axial Turbines –A Review," Annals New York Academy of Sciences, Vol. 934, *Heat Transfer in Gas Turbine Systems*, pp. 11-26.

[19] Hodson, H.P., and Dominy, R.G., 1987, "Three-Dimensional Flow in a Low-Pressure Turbine Cascade at its Design Condition," *J. of Turbomachinery*, Vol. 109, pp. 177-185.

[20] Zoric, T., Popovic, I., Sjolander, S.A., Praisner, T., and Grover, E., 2007, "Comparative Investigation of Three Highly Loaded LP Turbine Airfoils: Part I – Measured Profile and Secondary Losses at Design Incidence," ASME Paper GT2007-27537.

[21]Prümper, H., 1972, "Application of Boundary Layer Fences in Turbomachinery," AGARD-AG-164, pp. 311-331.

[22]Blanco, E., Hodson, H.P., Vazquez, R., and Torre, D., 2003, "Influence of the State of the Inlet Endwall Boundary Layer on the Interaction between Pressure Surface Separation and Endwall Flows," Proc. Instn Mech. Engrs Vol. 217, Part A: *J. of Power and Energy*, pp. 433-441.

[23]Bloxham, M.J., 2010, "A Global Approach to Turbomachinery Flow Control: Loss Reduction Using Endwall Suction and Midspan Vortex Generator Jet Blowing," PhD Dissertation, The Ohio State University, Columbus, Ohio.

APPENDIX I

SURFACE STRESS SENSORS FOR CLOSED LOOP

LOW REYNOLDS NUMBER SEPARATION CONTROL

A dissertation submitted in partial fulfillment of the
requirements for the degree of
Doctor of Philosophy

By

CHRISTOPHER ROY MARKS
B.S.M.E., Michigan State University, 2001
M.S.M.E. Wright State University, 2006

_____

2011
Wright State University

ABSTRACT

Marks, Christopher, Roy. Ph.D. Department of Mechanical and Materials Engineering, Wright State University, 2011. Surface Stress Sensors for Closed Loop Low Reynolds Number Separation Control.

Low Reynolds number boundary layer separation causes reduced aerodynamic performance in a variety of applications such as MAVs, UAVs, and turbomachinery. The inclusion of a boundary layer separation control system offers a way to improve efficiency in conditions that would otherwise result in poor performance. Many effective passive and active boundary layer control methods exist. Active methods offer the ability to turn on, off, or adjust parameters of the flow control system with either an open loop or closed loop control strategy using sensors. This research investigates the use of a unique sensor called Surface Stress Sensitive Film (S3F) in a closed loop, low Reynolds number separation control system. S3F is an elastic film that responds to flow pressure gradients and shear stress along its wetted surface, allowing optical measurement of wall pressure and skin friction. A new method for installing the S3F sensor to assure a smooth interface between the wall and wetted S3F surface was investigated using Particle Image Velocimetry techniques (PIV). A Dielectric Barrier Discharge (DBD) plasma actuator is used to control laminar boundary layer separation on an Eppler 387 airfoil over a range of low Reynolds numbers. Several different DBD plasma actuator electrode configurations were fabricated and characterized in an open loop configuration to verify separation control of the Eppler 387 boundary layer. The open loop study led to the choice of a spanwise array of steady linear vertical jets generated by DBD plasma as the control system flow effecter. Operation of the plasma actuator resulted in a 33% reduction in section drag coefficient and reattachment of an otherwise separated boundary layer. The dissertation culminates with an experimental demonstration of S3F technology integrated with a control system and flow effecter for closed

loop, low Reynolds number separation control. A simple On/Off controller and Proportional Integral (PI) controller were used to close the control loop.

Table of Contents

List of Figures

List of Tables

Nomenclature

C_d	section drag coefficient
C_f	skin friction coefficient
C_h	Stanton number
C_p	pressure coefficient
C_x	axial chord length (meters)
d_a	actual displacement (pixels)
d_e	S3F tangential displacement error (pixels)
$\overline{d_e}$	filtered error signal (pixels)
d_i	displacement at index *i* (pixels)
d_m	mean displacement (pixels)
d_r	reference displacement (pixels)
d_x	S3F tangential displacement in the streamwise direction (pixels)
$\overline{d_x}$	filtered streamwise displacement (pixels)
d_y	S3F normal displacement (pixels)
e(t)	error signal
E	Energy consumption in an open loop configuration (Joules)
E_f	Energy consumption with feedback flow control (Joules)
f_o	S3F first natural frequency (Hz)
f_s	sampling frequency (Hz)
h	S3F thickness (meters)
i	instantaneous current (Amps)
K_D	derivative term gain
K_I	integral term gain

K_P	proportional term gain
L	length
LS	laminar separation location
m	filter window size
P	pressure or power (Pa or Watts)
Pr	Prandtl number
P_t	total pressure (Pa)
q	dynamic pressure (Pa)
$r(t)$	reference signal
Re	Reynolds number
t	time (sec)
TR	turbulent reattachment location
u	local velocity or S3F displacement (m/s or px)
u_e	local velocity (m/s)
$u(t)$	controller output signal
v	instantaneous voltage
$\|V\|$	velocity magnitude
V_{in}	inlet velocity (m/s)
w	correlation window size (pixels)
x	length scale or horizontal dimension
y	vertical dimension
z	spanwise dimension

Greek

α	angle of attack (deg.)
δ	ratio of pressure gradient to shear stress (1/m)

δ boundary layer thickness

ε exposure time (sec.)

ε_b mean bias error (px)

ε_{RMS} RMS error (px)

η non-dimensional length in the airfoil normal direction

μ viscosity of air (kg/m·s)

μ_m shear modulus (Pa)

ρ density of air or S3F (kg/m^3)

τ_x shear stress in the streamwise direction (Pa)

τ_w wall shear stress (Pa)

φ variable of integration

Subscripts

in inlet condition

w value in the wake

Acknowledgements

My biggest thank you goes to my wife, Kristen. She has been my greatest supporter, runs our household, and raises our son Josh while working full-time! Every day I am amazed at the amount of work you can accomplish, and your breadth of knowledge! I look forward to the great times our family will have together. Thank you also goes to my parents and family who have supported me, and taught me the most important skills I use every day as an engineer from day one.

I would like to thank my advisor Dr. Mitch Wolff for his support and willingness to mentor me in this PhD effort, career, and life. I appreciate all the fruitful conversations we have had in your office over the extent of this work. I would also like to thank my supervisors while I worked at AFRL. Thanks to Dr. Rolf Sondergaard for his mentorship in the AFRL/RZ low speed wind tunnel facility. Your breadth of knowledge is amazing…thank you for sharing some of it with me. The generous support from Charles Stevens, and Dr. Sondergaard at AFRL/RZTT will never be forgotten. Dr. Rich Anthony is acknowledged for spending several late nights fabricating high quality plasma actuators with me!

Thank you to my dissertation committee members, Rolf Sondergaard, James Menart, Mark Reeder, and Joe Shang. I appreciate your willingness to take the time to advise and educate me with such busy schedules.

1. Introduction

The field of flow control is broad and encompasses systems with many different specific engineering objectives unique to a particular application, such as separation control, lift enhancement, and noise reduction. Even though specific applications have unique design goals, all flow control systems operate by altering the natural flow field around a wetted surface or object in order to obtain a performance improvement. Flow control systems are generally classified as either passive or active. Passive techniques are usually fixed to the surface of which the flow is being controlled. They have the benefit of being simple, but cannot be turned off. Examples of passive techniques include surface treatments like dimples, or vortex generators. Active control methods can be turned on and off, removing any penalty at off-design conditions, but require additional complexity and weight. Both an active flow control actuator and also a sensor are required. The added complexity of an active control system has no doubt limited their use to date. Significant research is under way in all areas of flow control, from actuators to sensors, to control logic for closed loop active control systems. In this work a new type of separation control sensor is investigated for use at low Reynolds number with the objective of using it to close the control loop in a separation control system.

1.1. Low Reynolds number fluid dynamics

Reynolds number is a non-dimensional parameter representing the ratio of inertial forces to viscous forces in a fluid, given by:

$$\mathrm{Re} = \frac{\rho U x}{\mu} \tag{1.1}$$

where x is the characteristic length. Equation (1.1) scales by a length parameter. For a fixed density, viscosity, and freestream velocity, e.g. two vehicles operating at the same flight

conditions, the Reynolds numbers increases as the size of the vehicle increases. At high Reynolds numbers, fluid inertial effects dominate; at low Reynolds number viscous effects (i.e. boundary layer behavior) play a larger role. The focus of this work is low Reynolds number flows which are classified, as others have (see Lissaman 1983 and Gad-el-Hak 2000), to be flows with Reynolds number between 10^4 and 10^6. At these conditions boundary layer behavior plays a large role in aerodynamic losses of an object, and the transition process is more sensitive to free stream disturbances and aberrations of the airfoil geometry (Mueller et al. 1983).

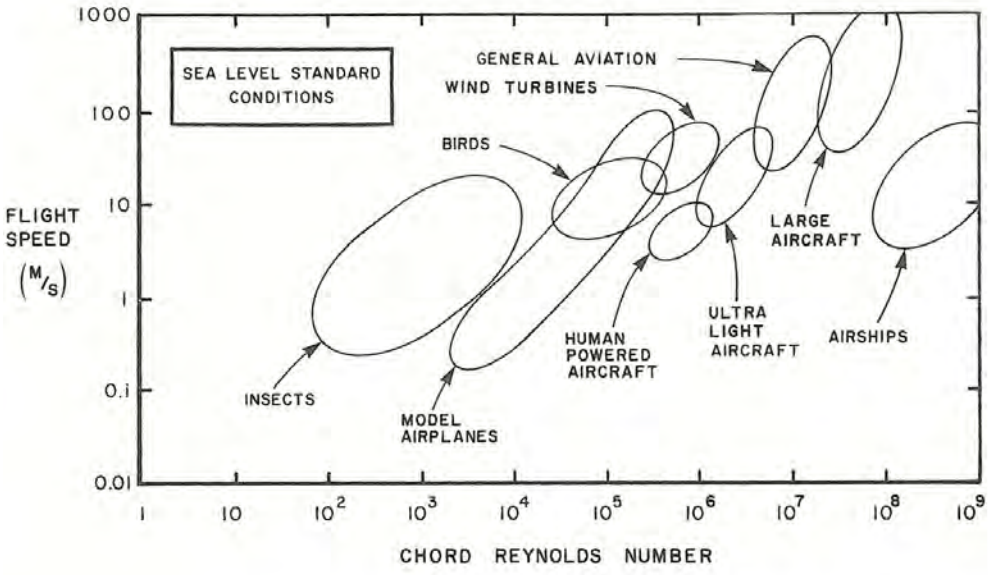

Figure 1.1 Flight Reynolds number spectrum at sea level (from Lissaman 1983).

In this range of Reynolds numbers, the maximum lift-to-drag ratio for smooth airfoils decreases by two orders of magnitude as Reynolds number decreases (McMasters and Henderson 1980, Gad-el-Hak 2000). Turbomachinery components such as compressors, and low pressure turbines also suffer a lapse in performance as Reynolds number decreases as shown in Figure 1.2. According to Sharma (1998) the efficiency of LP turbines at take off conditions has steadily increased over the last 25 years, but the same trend did not apply to LP turbines at cruise altitude conditions. At cruise altitude, Reynolds number drops below 100,000 and in some cases below

25,000 (Bons et al. 2000, Sondergaard et al. 2002). Considering that over a typical mission (either military or civilian aircraft) the bulk of engine operation is at cruise altitude, improving performance at these flight conditions is a priority. At such low Reynolds numbers, viscous forces along the surface of the blades have a stronger effect on the fluid flow. An adverse pressure gradient due to high aerodynamic loading coupled with low Reynolds flow has the potential to separate flow over the suction surface of the blade. Flow separation is detrimental to the efficiency of the turbine blade. A breakdown of LP turbine blade losses presented in Curtis et al. (1997) indicated that the suction side surface of a LP turbine blade accounts for 60% of the blade loss. Researchers have been developing methods of designing blades that increase the low Reynolds number performance as well as methods of controlling the flow and improving efficiency in conditions that would otherwise result in degraded performance.

At low Reynolds number, separation, transition and reattachment can all occur within a short distance and dramatically affect the performance of lifting surfaces (Gad-el-Hak 2000). Depending on flow conditions, such as freestream turbulence, Reynolds number, surface curvature, roughness, and pressure distribution, the boundary layer can remain laminar beyond the minimum pressure location. The adverse pressure gradient beyond the minimum pressure

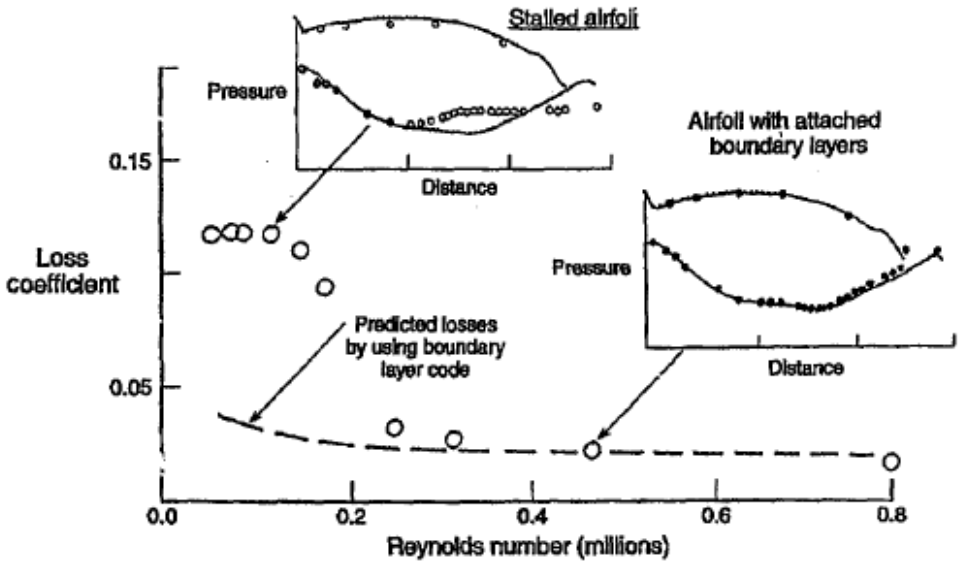

Figure 1.2 High losses in LP turbine measured in a cascade at low Reynolds number (from Sharma 1998).

point on the suction surface can cause the laminar boundary layer to separate and become a free shear layer. When a laminar boundary layer separates, it rapidly undergoes transition to a turbulent flow (Lissaman 1983). The separated shear layer is unstable and depending on the Reynolds number and flow conditions, in some cases reattaches, forming a closed separation bubble. In other cases the free shear layer will remain separated over the remainder of the airfoil.

Mueller (1985) describes several types of flow behavior which result at low Reynolds number:

1. "Laminar separation occurring at
    a. high angle of attack and for which the separated boundary layer does not reattach, and the airfoil may be considered fully "stalled".
    b. low angles of attack in which the flow remains attached for a portion of the blade in which there is a favorable pressure gradient, but separates after the maximum thickness in the presence of an adverse pressure gradient.
2. Natural transition of the boundary layer to turbulent prior to reaching the surface of the blade in which there is an adverse pressure gradient. The transition of the laminar boundary layer near the leading edge to a higher energy turbulent boundary layer allows the boundary layer to remain attached. This behavior is accompanied by higher lift and lower overall drag coefficients.
3. An extension of the laminar separation case in which the separated laminar free shear layer may in some cases reattach shortly after separation, or more often may become turbulent and then reattach."

The description by Mueller was in the context of external flow such as those over aircraft airfoils, but a similar situation occurs in turbomachinery as well. In turbomachinery airfoil performance is also affected by three dimensional effects, periodic unsteadiness, and an adverse passage pressure gradient in compressors, and a favorable pressure gradient in turbines (Mayle 1991).

1.1.1. Laminar Separation Bubbles and Separation

As mentioned above, the presence of an adverse pressure gradient can lead to separation of the boundary layer from the surface. In this case the boundary layer becomes a separated shear layer. If conditions are right, the separated shear layer will transition to turbulent and reattach to the surface. The area between the separation point and reattachment point is referred to as a laminar separation bubble. Laminar separation bubbles have a large effect on the behavior of the boundary layer, and thus performance of an airfoil (Tani 1964). The diagram of Horton (1968) illustrates the characteristics of a closed reattaching laminar separation bubble. The description is of the mean flow structure, but in reality the structure is dynamic. Along the surface of the airfoil the shear stress will reach zero at the separation point. Downstream of the separation point is a region labeled dead-air. The flow is of course, not completely stagnant, but is the main recirculation area. This region has a relatively low, negative shear stress. At the downstream end of the laminar separation bubble is a region labeled reverse flow vortex. In this area the shear stress decreases further to a minimum before recovering to cross zero at the reattachment point. The scanning PIV measurements of Burgmann et al. (2006) of a SD7003 airfoil showed this reverse flow vortex can consist of several vortices with spanwise variation. The vortices under

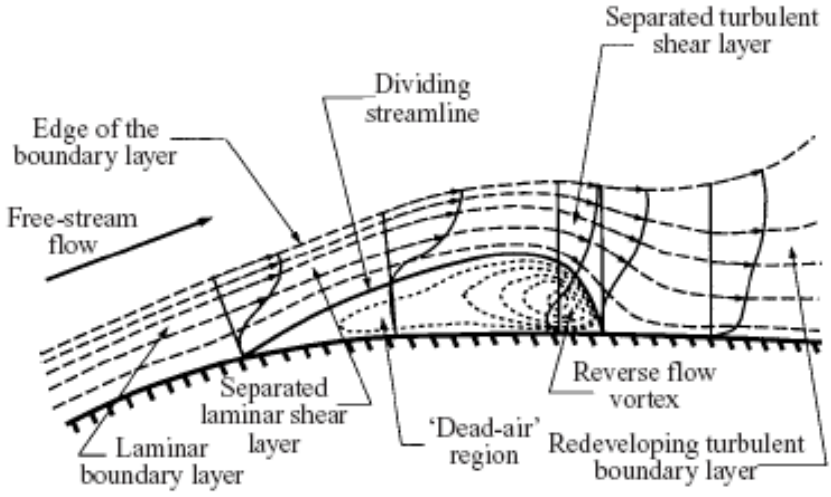

Figure 1.3 The time averaged flow structure of a laminar separation bubble (Horton 1968).

the right conditions burst from the separation bubble and travel downstream. There is a complex mutual interaction between vortex bursting and reattachment location via the pressure distribution (Bergmann et al. 2006).

A separation bubble is often described as long or short. Tani in his 1964 review of the subject explains that two types of bubbles should be distinguished by their effect on pressure distribution, and not on their length. A long bubble has a large affect on the pressure distribution, compared to that of an inviscid flow. The sharp pressure peak of an airfoil may be diminished or non-existent, significantly decreasing its lift. A short bubble has little effect on the peak pressure on the suction surface, which continues to increase as angle of attack is increased up to stall (Tani 1964).

Lin and Pauley (1996) point out that if the local Reynolds number is sufficiently high, boundary layer transition is caused by amplification of Tollmein-Schlichting instabilities. This is natural transition (viscous-type) of the attached boundary layer. Numerical simulations by Lin and Pauley suggest that if the boundary layer separates, Kelvin-Helmhotz (inviscid) instabilities will develop and cause the shear layer to rollup. They point out that it is expected that unsteadiness in the separation bubble will be dominated by large-scale vortex rollup and shedding, and not small-scale turbulence like many researchers often describe.

1.2. **Methods of flow control**

Gad-el-hak (2001a) defines flow control as "…the ability to manipulate a flowfield actively or passively to effect a desired change…" The control of low Reynolds number aerodynamic flows is of interest in many design domains such as air vehicles, turbomachinery, and wind turbines. Micro-air-vehicles (MAV) which have small length scales and operate at low flight speed present numerous low speed aerodynamic design challenges such as lift and control surfaces, thrust generation, and power plants (Gad-el-Hak 2001b).

Flow control is categorized as either passive or active, and active techniques can be further categorized as has been done by several groups (see Gad-el-Hak 2000, Wright et al. 2002). Gad-el-Hak divides active flow control into predetermined and reactive. Predetermined active flow control does not require sensors; however, the actuators are still turned on and off and for predetermined situations, either based on time or condition. Thus predetermined control is an open loop control strategy. Reactive flow control on the hand, requires a sensor to either provide feedback or on/off control of the sensor (Gad-el-Hak 2000).

Feedback control based systems consist of a flow effecter (or actuator), sensor, and control logic. The control strategy used with reactive flow control systems very considerably with regard to control logic complexity and synthesis of the model. Synthesis of the control system can range across physics based models, low-dimensional models, black-box models of the flow, and model free methods. Many physics based models are generated from solutions of the Navier-Stokes equations, however, the requirement of massive computing power to solve the equations limits their practical use (Henning and King 2007). Black-boxed based models describe simplified models developed by studying the input and output relationship of the plant (Brehm et al. 2006). Model-free controller synthesis for adaptive flow control shows promise in non-linear flow control environments since prior knowledge of the steady state input-output-map is not required (King et al. 2006 and Becker and King 2007).

Examples of low-dimensional models are Galerkin, and proper orthogonal decomposition (POD) based controllers (Henning and King 2007). POD is a technique used to identify the large scale motions of turbulent flows and is also known as Karhunen-Loeve decomposition. Lumley (1967) first applied POD to the study of turbulent flows (Pope 2008). It is based on orthogonal decomposition of the fluctuating velocity field, and a significant property of POD is that the first N modes of a POD contain more energy than any other orthogonal decomposition (Pope 2008).

The drawback of POD based analysis is that the optimal basis functions calculated are only optimal for certain flow conditions, which means they will change based on flow speed and

whether or not control is turned on (Gunes and Rist 2004; Gross and Fasel 2007). Glauser et al. (2004) and Pinier et al. (2007) describe the development of feedback control systems using proper orthogonal decomposition (POD) and modified linear stochastic measurement (mLSM) for control of separated flows. The methods described in Pinier et al. (2007) uses surface pressure measurements to estimate the first mode *global* POD coefficients and use them to demonstrate that the first mode is sufficient to use in a proportional feedback loop to control flow over a NACA 4412 airfoil. The use of global POD coefficients means the eigenfunctions have a greater "knowledge" of flow states, improving performance at different flow conditions.

An analytical approach to flow control is presented in the computational study of Alam et al. (2006). The method uses a distributed array of wall shear stress sensors; the wall shear stress distribution is viewed as the solution to a linear parabolic PDE with forcing. Two actuators on each end of the shear sensor provide separation and reattachment control via a feedback loop. The method was demonstrated computationally as a method to control separation of flow over a backward facing step.

If the system is relatively simple and has only one input and output, a mature class of control methods called proportional integral differential (PID) feedback controllers can be used. A PID controller has the general form:

$$u(t) = K_P e(t) + K_I \int e(t)dt + K_D \frac{de(t)}{dt}$$

where $u(t)$ is the controller output signal, and $e(t)$ is the error term equal to the difference between the reference $r(t)$ and the sensor $y(t)$ signal. K_P, K_I, and K_D are gains adjusted to tune the system response. K_P is the proportional gain and multiplication by the error results in adjustment of the controller output signal proportional to the amount of error. K_I is the integral gain and adjustment of K_I increases or decreases the controller output signal in proportion to the time history of error. K_D is the derivative term gain and is a prediction of future error. Variations of

this type of controller are systems that use only two of the elements making them PI or PD controllers.

Adjustment of the controller gain is done a variety a ways, often iteratively. The gain can be adjusted manually to obtain a stable response, or automatically based on a time response and desired output characteristics. In computational studies by Brehm et al. (2006) and Gross and Fasel (2007), control of laminar separation in a low pressure turbine cascade is simulated using a proportional differential (PD) feedback controller. Brehm et al. (2006) used one downstream pressure transducer as the input, and the control signal drove harmonic wall normal blowing. Values of K_P, K_D and other controller parameters were adjusted and set by defining an objective function and monitoring it as controller parameters were incrementally adjusted. Gross and Fasel (2007) compared the use of steepest decent algorithm versus simultaneous perturbation stochastic approximation (SPSA) demonstrating a self adaptive controller.

1.2.1. Recent Low Reynolds Number Research

A number of numerical and experimental studies have been carried out recently, with the focus on control of low Reynolds number laminar separation. Closed loop studies have been mostly limited to computational work as in the case of the Direct Numerical Simulation (DNS) study of Rist and Augstin (2006) on a flat plate, and the numerical work of Brehm et al. (2006), and Gross and Fasel (2007) applied to airfoils and LP turbine blades. Most control strategies employ an instability generating mechanism upstream of the separation point. The study by Rist and Augstin (2006) used a DNS analysis of a laminar separation bubble over a flat plate with an adverse pressure gradient to demonstrate the use of unsteady force to control laminar separation bubbles. Low amplitude boundary layer disturbances, mimicking suction or blowing, and generated at optimum frequencies control the size of the bubble by inducing earlier laminar-turbulent transition. The artificial, unsteady forcing generates instability waves that lead to spanwise vorticity which enhances wall-normal energy transfer, prior to full onset of turbulence.

Rist and Augustin recommend, based on linear stability theory (LST), that an actuator should not be placed in a region of favorable pressure gradient, but should be placed just upstream of the separation point, at an optimum neutral point based on linear stability theory. They used DNS to verify predictions from LST and found that even though transition is a nonlinear phenomena, most disturbance growth followed LST closely. The authors suggest that LST can be used as an effective method to estimate the effect of choosing different forcing frequencies (Rist and Augustin 2006).

Experimental studies using feedback control from a sensor signal often use simple controllers that trigger on an actuator when the sensor signal reaches a predetermined threshold value. The literature is dominated with feedback flow control methods that use a pressure signal to determine when to turn on a flow effecter. Patel et al. 2003 described an active stall control system using deployable vortex generators at Reynolds number of 6.0×10^5. The pressure signal from a pressure transducer sampled at 500 Hz was used to detect the onset of flow separation and trigger deployment of the vortex generators. A threshold value of the standard deviation of the pressure signal was determined and stored in onboard memory. Deployment of the actuators was based on comparing current standard deviation with the threshold values. In Patel et al. 2007 an additional method of using the pressure signal for flow control is described in experiments that use high bandwidth pressure sensors for feedback control of the flow over a NACA 0015 airfoil with plasma actuators located near the leading edge. The Amplitude Sense Peak and Control (ASPC) method uses a plasma actuator located at the leading edge that is cycled on and off as angle of attack is changed. The method takes advantage of experimental observation that the unsteady plasma actuator driving frequency is only detected in the pressure signals at an angle of attack that is just prior to separation , or at angles of attack in which separation would occur without flow control. This method enabled the authors to detect separation or the onset of separation.

Becker et al. 2007 uses the readings from two fast response pressure transducers to detect whether the flow state is attached or separated over the flap of a generic high lift airfoil

configuration. They infer the boundary layer state by the difference in the pressure coefficient calculated from the two pressure transducers. A separated flow case has a delta C_p of near zero, and a fully attached flow has a delta C_p significantly greater than 1.

An alternate way of measuring separation and reattachment regions is by surface shear stress. The surface shear stress is equal to zero at boundary layer separation and reattachment points. In regions of attached flow the shear stress is positive; in regions of separation the shear stress is negative. A sensor that can measure surface shear stress is a natural fit for separation control systems. Recently, Poggie et al. 2010 demonstrated the use of a shear stress sensitive sensor array in a large scale wind tunnel. An array of hot film sensors was used to detect stall and plasma actuators to reattach flow at a Reynolds number of 0.9×10^6 to 1.7×10^6. When the hot-film signal exceeded a threshold value indicating the separation point was over the plasma actuator panel, the actuators were triggered on. Lack of the use of shear stress sensors for flow control is due to limited sensor technology that is mature, small scale, robust, and can be mounted to a surface in a clean manor. Shear stress sensors will be discussed further in the next section.

1.3. **Sensor Technology**

There are many different classes of flow control for different design conditions, each with different sensor and actuator needs. This fact makes it impossible to define a single set of requirements for all sensors in all aspects of active flow control (Wright et al. 2002).

Useful flow control sensors are shear stress, pressure, and temperature sensors. Pressure sensors can be point sensors as in the case of either diaphragm type, or piezoelectric, or field sensors as in the case of pressure sensitive paint (PSP). Piezoelectric transducers are typically smaller and have quicker response than the diaphragm type (Barlow et al. 1999). The small sizes of modern piezoelectric transducers make them a viable option as a flow control sensor if mounted flush to a surface with no tubing. A group at Notre Dame has recently experimented

with using pressure transducers as stall detection sensors. Their technique uses frequency analysis of the pressure signal to detect flow separation. Both Fourier transforms based methods and wavelet transform techniques have been investigated (Bowles and Corke 2009). Several groups have also used microphones as sensor for flow control over a backward facing step.

Thermal based sensors for separation control take advantage of the Reynolds analogy, which states that wall shear and heat transfer rate are proportional:

$$\frac{C_h}{C_f} = f\left(\mathrm{Pr}, \frac{x}{L}, geometry\right) \tag{1.2}$$

where C_h is the Stanton number, and Pr is the Prandtl number (White 1991). The Stanton number is the non-dimensional wall heat transfer coefficient, and the Prandtl number is a non-dimensional ratio of viscous to thermal diffusion rates. For flat plate flow, with either turbulent or laminar boundary layer:

$$\frac{C_f}{C_h} = 2\,\mathrm{Pr}^{2/3} \tag{1.3}$$

In the presence of strong pressure gradient, this relationship breaks down (White 1991).

A shear sensor can be used as a flow control sensor in several ways. If the temporal resolution is high enough, frequency analysis of the sensor signal could indicate separation based on large fluctuations in shear (or power). The mean signal from an array of sensor could be used as indication of separation point based on wall shear stress magnitude (or direction for optical based sensors).

Shear stress measurement techniques can be divided into direct and indirect methods. Examples of direct methods are floating surface balances, surface stress sensitive film, and oil-film interferometry. These methods are called direct because the parameter being measured directly responds to skin friction (Liu et al. 2008). Indirect methods require an empirical or theoretical relation between a parameter measured by the sensor and shear stress. An example of

an indirect method is thermal based shear stress sensors which use the Reynolds analogy to relate wall heat transfer to wall-shear stress.

An early method to measure skin friction was described by Preston (1954) and utilizes a Pitot tube in the boundary layer and either a static port on the model surface or on a second probe. Preston originally describes its use to measure the skin friction in a turbulent boundary layer, but the probe can also be used in a laminar boundary layer with an equation provided by Bechert (1996). The accuracy of the technique is dependent on the logarithmic law of the wall, and requires a probe size that is much smaller than the boundary layer thickness.

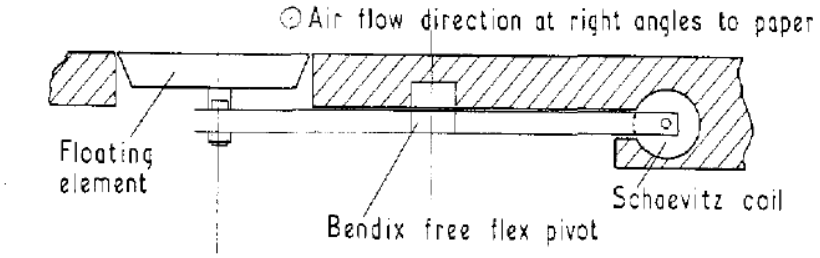

Figure 1.4 Example of skin friction force balance utilizing a floating surface element (Headley 1969).

Another method to measure skin friction described in Headley (1968) involves directly measuring skin friction with a measuring plate and balance, which is reported to date back to Schultz-Grunow in 1940. This method is shown in Figure 1.4, and of course, requires a large apparatus and correspondingly large test specimen. The other drawback of the technique is that it measures the integrated skin friction over a surface area, rather than a point measurement.

Another approach to the floating surface element was presented by Schmidt et al. (1988) who describe a micromachined floating-element sensor that uses a differential capacitor and integrated pair of matched transistors for readout. The prototype sensor featured a 500 μm x 500 μm floating element with overall chip dimensions of 4 mm x 5mm. The prototype had an on-chip sensitivity of 47 μV/Pa. A more recent development to the micromachined floating-element sensor was the use of integrated photodiodes, fabricated using wafer-bonding technology

(Padmanabhan et al. 1995). This new sensing scheme was developed after finding that environmental exposures impose high levels of drift on the capacitive readout shemes. The photodiodes measure in-plane displacement of a 120 μm x 120 μm x 7 μm floating element sensor. A reported shear stress sensitivity of 0.1 Pa and range of 0-5 Pa make them suitable for low shear stress boundary layers.

Tanner and Blows (1976) describes a method of measuring skin friction in air flows by the interferometric thickness measurements of silicone oil films flowing over body surfaces. The method is compared to the Preston tube method in Tanner (1977). The film is displaced over time due to the skin friction of the freestream gas flow, thus by measuring the change in thickness over time, skin friction can be deduced. The technique is more difficult to setup than Preston tube, but it useful for any boundary layer thickness, or state (laminar, transitional, turbulent).

Fernholz et al. (1996) gives a description of four measuring techniques: surface fence, wall hot wire, wall pulsed wire, and oil-film interferometry, with tabular comparison shown in Table 1.1. Each of the techniques are indirect with the exception of oil-film interferometry.

Table 1.1. Comparison of four skin-friction measuring techniques (from Fernholz et al. 1996)

	Surface fence	Wall hot wire	Wall pulsed wire	Oil-film interferometry
Measured quantity	Pressure difference	Heat transfer	Time of flight	Movement of fringes
Calibration necessary	Yes	Yes	Yes	No
Mean value	Yes	Yes	Yes	Yes
Temporal resolution	Unclear	$>$ 10 kHz	$\simeq$ 20 Hz	No
Cross correlation	No	Yes	No	No
Spatial resolution $\Delta x,\ \Delta z$ (mm)	$<$ 1, 3	$<$ 0.5, 0.5	1.5, 0.5	$<$ 1, 1
Direction of τ_w	Yes	Yes	Yes	Possible
APG	Yes	Yes (but no instantaneous reverse flow)	Yes	Yes
Reverse Flow	Yes	No	Yes	Yes
FPG	Yes (but restricted)	Yes	Probably yes	Yes
Transitional flow	Unclear	Yes	Probably yes	Yes
Laminar flow	Yes	Yes	Probably yes	Yes
3D flow	Yes	Yes	Yes	Yes
Accuracy (estimated)	$\pm$4%	$\pm$4%	$\pm$4%	$<\pm$4%

Wall shear stress can also be measured with wall mounted hot wire and hot-film probes. These probes can be used in experimental setups in which the conductivity of the fluid is higher

than the conductivity of the wall material. The benefits of hot-films are their high temporal resolution in contrast to only mean wall shear stress measurements by Preston tube.

Another device is the surface fence or sublayer fence in which a surface of height, not to exceed $H^+ \approx 5$, is placed in the viscous sublayer. The only measurement is the pressure difference upstream and downstream of the fence which requires a precision manometer or pressure transducer. Each fence requires a calibration procedure, with the skin friction being a function of pressure difference Δp. Reported accuracy of a surface fence is about ± 4% (Fernholtz et al. 1996), but accuracy will likely decrease if the turbulent structure of the flow differs significantly from the calibration turbulent structure.

Montelpare and Ricci (2004) used a thermographic technique to locate local boundary layer separation phenomena. Their experimental work demonstrated the feasibility of using thermography for locating the laminar separation point and length of a laminar separation bubble on an Eppler 387 airfoil in a wind tunnel. They qualitatively located the bubble region visually based on the surface temperature, but required a quantitative technique to clearly identify the separation location and reattachment point. The local minimum and maximum of the first derivative of the temperature distribution was used to identify the separation point and length of the laminar separation bubble. The authors found that the separation and reattachment point agreed well with numerical and experimental locations, with separation point showing the best correlation.

A non-intrusive optical method to measure low values of wall shear stress was described by Gregory et al. in 2008. The technique builds upon the laser thermal tuft flow visualization method first reported in Baughn et al. (1995) and later patented by the U. S. Air Force (Rivir et al. 1999). The thermal tuft technique as used for flow visualization uses a laser to heat a spot on the surface immersed in a fluid flow. The surface which is coated with thermochromic liquid crystals changes temperatures and takes on a tuft shape as the heated air changes the surface temperature around the spot. The laser spot was ≈3 mm in diameter and the tuft points downstream. The

thermal tuft technique was used by Baughn et al. (1995) to obtain boundary layer separation location by noting that at the separation or reattachment point the tuft is circular, rather than tear dropped in the downstream direction. It was demonstrated in the early work that the thermal tuft could be used as a qualitative surface sensor, and Baughn et al. in (2006) reported that the length of the thermal tuft can be used to measure wall shear stress. Additional experimental and theoretical results are were reported in Gregory et al. in (2008) which confirmed the potential of the thermal tuft technique as a quantitative wall shear stress sensor especially at low values of shear stress less than 1 Pa. Gregory et al. (2008) reports that to date, the thermal tuft technique has only been used with steady laminar flow, and only to measure time averaged values due to the slow response of the heat transfer mechanism involved.

MEMS based separation control sensors have been proposed in a variety of packages. The most promising packaging consists of arrays of shear stress sensors mounted to flexible substrates with high spatial resolution. Most of these designs use thermal techniques to measure shear stress. Jiang et al. (2000) described a fabrication process that uses many of the techniques used to fabricate integrated circuit (IC). They were able to create a flexible 80μm thick sensor array consisting of 100 vacuum-insulated diaphragm-type thermal shear-stress sensors inside a 1 cm x 3 cm area. Each sensor was on the order of 20 μm square. The sensitivity of the sensors is about 100 mV/Pa. Measurements with sensor installed on the surface of a cylinder demonstrated that the sensor could be used for separation location detection.

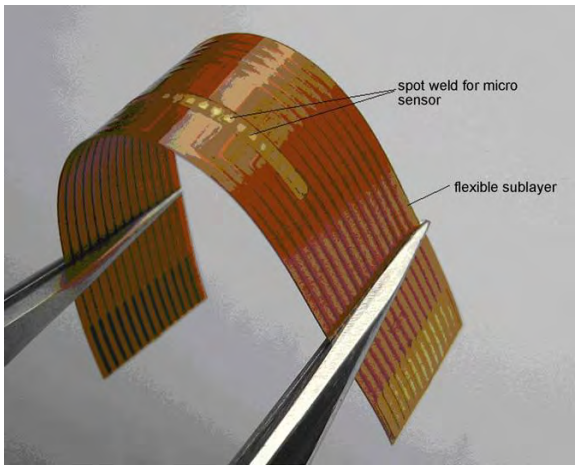

Figure 1.5 MEMS thin film sensor Liu et al. 2007.

Another MEMS array of thermal shear stress sensor is based on the principles of thermal anemometry shown in Figure 1.5. The flexible array of sensors consists of platinum thin film

resistors on a silicon nitride base. Current passes through the resistors which operate as constant current thermal anemometers with bandwidth of about 1 kHz. The sensors were shown to have the potential to accurately identify flow separation location around a cylinder based on mean or RMS sensor voltage output (Liu et al. 2007).

Another type of MEMS sensor in a cluster configuration was described by Kahng et al. (2000). The sensor cluster consists of local shear stress, pressure, and temperature on an airfoil. The shear sensor is heat transfer based, and is 300 microns square mounted on a flexible polyimide sheet. The reported typical sensitivity of the sensor is 150 mV/Pa.

Seifert and Melton (2004) describe a method they used to detect turbulent boundary layer separation using an array of hot film sensors. Their method of detecting separation utilizes analysis of the spectra from their wall mounted hot film sensors. The algorithm is based on the intermittent disappearance of high frequency content from the spectra as separation condition approaches.

Grobe and Schroder (2008) describe a shear stress measuring device based on micro-pillars or thin cylindrical beams that bend due to fluid forces against them. The pillars are made of an elastomer material and wall shear stress is obtained by relationship between pillar deflection and local surface friction. Diameters of the pillars are in the range of microns and an array of pillars offers the potential of high spatial resolution surface shear stress measurements. The height of the pillars is limited to the height of the viscous sublayer to ensure a linear relation between the wall shear stress and the near wall velocity gradient. Grobe et al (2006) report that intrusiveness of the sensor has been investigated using μPIV which has shown that the flow past the pillar is in the Stokes regime for typical low to moderate Reynolds number flows. There is only a local impact on the flow field in an area two to four diameter downstream of the pillar (Grobe et al. 2006). Typical lateral spacing of the pillars is 15-25 diameters (Grobe and Schroder 2008). In order to measure the mean and fluctuating components of shear, the dynamic characteristics of the pillars must be designed properly. Grobe and Schroder (2008) report the potential for

measurements at time scales on the order of a few kHz with properly designed pillars. The shear stress is calculated ensuring the sensor is in the viscous sublayer where the mean velocity gradient in turbulent flows can be approximated by a linear relationship between shear stress and mean velocity gradient in the vicinity of the wall up to wall distances of $y \leq 7 \cdot y^{+}$ (Grobe and Schroder 2008).

Gnanamanickam and Sullivan (2008) describe a similar optical based wall shear stress sensor to that of Grobe and Schroder. Their shear stress sensor employs a micro pillar array made from silicone rubber that is glued to the surface of a wall bounded flow. The micro pillars extend into the viscous sublayer and deflect an amount proportional to the wall shear stress. They state that if silicone based rubber is used as the pillar material, the resonant frequency of the pillars are on the order of 100 kHz. Research investigating spacing of the micro pillars to eliminate interference is ongoing. Micropillar based shear stress sensors will be susceptible to surface contamination which will need to be further investigated. Regardless, micropillar based sensors show promise as spatial shear stress sensors with high temporal resolution that will be required for controlling turbulent flows.

A sensor capable of measuring surface shear stress field with high spatial resolution has been under development by Innovative Scientific Solutions Inc. The technology is called Surface Stress Sensitive Film (S3F). S3F is an optical sensor that uses a low shear modulus elastomeric film that is inherently sensitive to both surface tangential stress (shear) and pressure gradient. Optical measurements of markers on the surface of the film and embedded luminescent molecules are used to determine the tangential stress and pressure gradient on the film. S3F has been used to measure surface stresses in a variety of aerodynamic (e.g. Fonov et al. 2006) and hydrodynamic (Crafton et al. 2008) flows. The system requires an illumination source, image acquisition system, and processing system.

S3F was used extensively in this work, and a detailed background and discussion of S3F is included in the experimental arrangement shown in Section 2.3.3 of this document.

1.4. **Actuation methods**

Passive techniques have the benefit of consuming no power or mass flow, but are "active" during all operating conditions. For this reason passive control application requires careful consideration and design in order to obtain the best performance over all operating conditions. Active flow control techniques on the other hand offer a flow control mechanism that can be turned on or off as needed. The disadvantage is their consumption of power or core mass flow, potentially reducing the benefit of the device. The best active flow control methods will consume a minimal amount of power compared to net performance improvements. The most efficient control schemes will always be operational as it was pointed out by Pinier et al. (2007) that it is more energy efficient to keep flow attached, than to reattach separated flow.

Researchers have been investigating the use of both passive and active flow control techniques to mitigate low Reynolds number flow separation for many years. Many of the techniques have shown large performance improvement in open loop configurations. With the intent of improving low pressure turbine blade efficiency at low Reynolds number Lake et al. (1999) investigated the use of surface dimples and v-grooves as a passive flow control technique on the suction side surface of a Pack-B LP turbine blade. Surface treatments have the same effect as dimples on golf balls, used to decrease drag at their flight Reynolds number of $\approx 10^5$ (White 1999). The increased surface roughness enhances momentum transfer between the boundary layer and freestream leading to earlier transition to turbulence, decreasing or eliminating the effects of flow separation. The experiments of Lake et al. (1999) demonstrated a 58% decrease in loss coefficient at low Reynolds number using dimples. The drawback of surface treatments is a negative parasitic effect at higher Reynolds number. Bons et al. (2000) and Sondergaard et al.

(2002) have investigated the use of both steady and unsteady vortex generator jets, which would provide the ability to control flow only when beneficial and remove the parasitic effect at off-design conditions. Vortex generating jets (VGJs) function by ejecting a small jet of air from the blade surface at a skewed angle to the freestream, thus generating streamwise vortices. VGJs have received a large amount of attention as a turbomachinery flow control mechanism because they are believed to be relatively straightforward to implement in a turbine engine. High pressure (HP) turbines utilize film cooling techniques that use bleed air ejected from the surface of the turbine blade, and employing VJGs could be an extension of this technology. Both steady VGJs (Sondergaard, et al. 2002) and pulsed VGJs (Bons et al. 2001; 2008) have been investigated experimentally. Investigations with steady blowing have shown a reduction in blade wake pressure loss between a factor of two and three. Pulsed VGJs offer the greatest promise with lab tests showing that mass flow requirements are almost negligible and an order of magnitude less than steady VGJs (<0.01% of core mass flow) (Bons et al. 2001). Experimental work indicated that the mechanism of control has to do with the starting and ending transitions of the pulsing cycle rather than the injected stream itself (Bons et al. 2001). Sondergaard et al. 2002 investigated the potential to reduce the LP turbine blade count by increasing blade spacing using VGJs to maintain attached boundary layers. Over the Reynolds number levels investigated, 25,000-75,000, the authors found they could maintain design level wake pressure loss with pitch settings of 150% of design pitch. This demonstrates the potential for decreasing blade count in future LP turbines, or removing existing stages when flow control techniques are used.

As the ability to fabricate precision devices of increasingly smaller sizes has continually improved, a new field of multidisciplinary study known as Micro Electro Mechanical Systems (MEMS) has emerged. MEMS devices show promise as flow control sensors, and actuators, especially in the field of relaminarization since MEMS devices can be fabricated on the order of turbulent length scales. For low speed flows this is on the order of hundreds of microns and of tens of milliseconds (Kumar et al. 1999). Kumar et al. in 1999 describe MEMS zero mass flux

vortex generators developed by Jacobson (1995) and shown in Figure 1.6. The piezoceramic devices consists of cantilevers that expand and contract to create counter-rotating vortices, and when operated continuously forms a continuous jet. The size of the device is on the order of a dime and aligns flush with a surface for zero drag penalty.

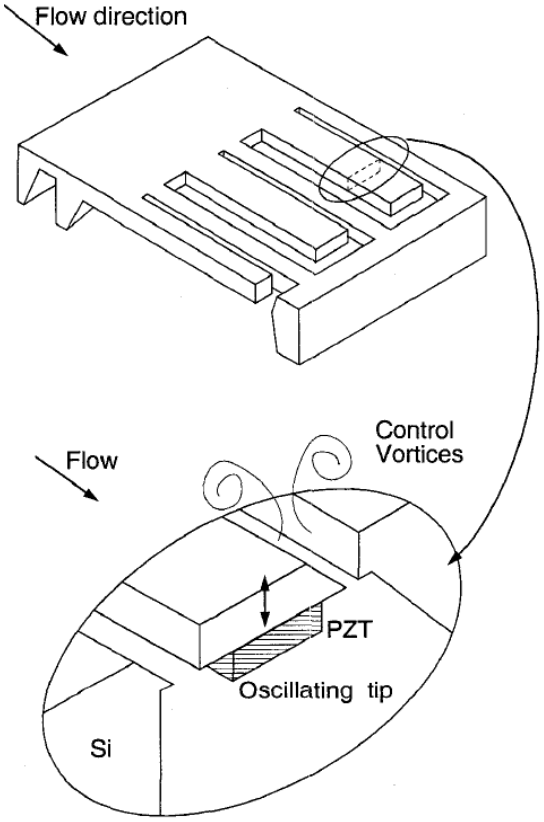

Figure 1.6 MEMS zeros mass flux vortex generator from Kumar et al. (1999).

Synthetic jet actuators generated by small flush mounted surface devices have been investigated for separation control of external flows (Smith et al. 1998; Amitay et al. 1998; Amitay et al. 1999), and internal flows (Amitay et al. 2000). The topic has been reviewed in Glezer and Amitay (2002). They function by providing an alternating suction and blowing force at the wall produced typically by an oscillating diaphragm over a cavity embedded in the wall. Using only the working flow, they produce a train of vortices whose interaction with the cross flow creates a synthetic jet. When operated at high actuation frequencies, they can produce a "virtual" surface shape change which can be used in flow control applications. Synthetic jets have also been generated by using plasma actuators, which have no moving parts, with an annular electrode configuration by Santhanakrishnan and Jacob (2008), and more recently in a linear arrangement by Santhanakrishnan et al. (2009). The use of dielectric barrier discharge (DBD) plasma actuators for flow control have been investigated for a variety of flow control applications, see Corke et al. (2005), and has become a popular research topic because they offer a low power, on demand active flow control method.

The following section discusses DBD plasma actuators and their potential use for flow control in more detail.

1.4.1. Dielectric Barrier Discharge plasma actuators

Several projects have been undertaken to demonstrate that DBD plasma actuators can be used for low Reynolds flow control. The focus of this section is a brief background of DBD plasma actuators that have been presented in the literature for flow control applications. Common and alternate electrode configurations are discussed, as well as application of DBD plasma actuators for low Reynolds separation control around LP turbine blades.

1.4.1.1. DBD Plasma Actuator Background and Overview

A simple schematic of an asymmetric configuration of DBD is shown in Figure 1.7. This configuration has been studied significantly in recent literature.

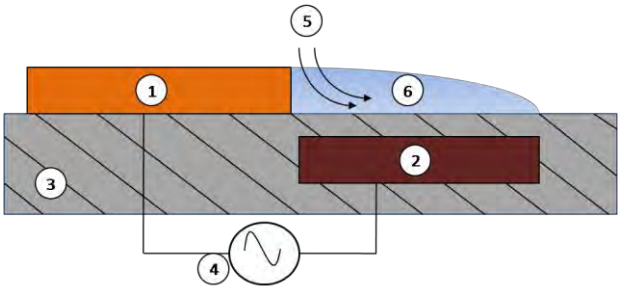

Figure 1.7. Asymmetric configuration of DBD plasma actuator.

The encapsulated electrode is typically grounded and the voltage potential is alternated between positive and negative. Typically high voltage AC is applied to the electrodes with voltage amplitudes of several kV_{p-p} to tens of kV_{p-p} and frequencies from around 1 kHz to tens of kilohertz.

In the case of the surface DBD, examination of the voltage and current (Pons et al. 2005), and optical measurements (Enloe et al. 2004a, 2004b, 2006) have both indicated that the plasma in the electrode gap is generated through a succession of microdischarges, randomly distributed in time and space (Moreau 2007). Moreau gives a simple explanation for the discharge mechanism known as the Townsend mechanism. Moreau's explanation is paraphrased here; under an applied electric field, the electrons located in the electron gap accelerate towards the anode and ionize the gas by collisions with neutral particles. An electron avalanche develops due to the multiplication of electrons as they move towards the anode, colliding with neutrals, releasing more electrons (Figure 1.8). A discharge current is then created, which is unique to the type of discharge present (i.e. corona, DBD) (Moreau 2007).

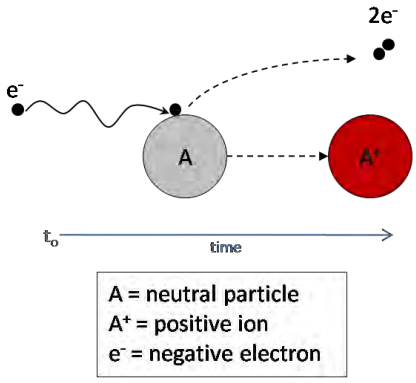

Figure 1.8 Ionization of neutral particles (as described in Moreau 2007).

For detailed information and background on the physics of the plasma discharge, readers should refer to other papers (e.g. Enloe et al. 2004a, 2004b, 2006), the topical review paper by Fridman et al. (2005) and a paper by Moreau (2007).

The generation of an induced velocity by the DBD and its low power requirement make it a viable candidate for flow control applications. An electrostatic force (Enloe 2004b):

$$\vec{F} = \rho_e \vec{E} = -(\varepsilon_0/\gamma_D^2)\phi\vec{E} \qquad (1.4)$$

acts on the charged species located in the plasma which results in an electric wind in the form of a wall jet.In equation 1.4, ρ_e is the net charge density, E is the electric field, ε_0 is the permittivity of free space,and γ_D is the debye length. The thrust produced by the force has been reported to be in the range of 10 mN or less (Enloe et al. 2006). The induced air flow can be several meters per second, but larger velocities have been generated (Moreau 2007). The induced velocity and power have both been observed to be proportional to $V_{app}^{7/2}$ (Enloe et al. 2004a). An induced

velocity and low power requirement are what make a DBD a viable candidate for low speed flow control applications.

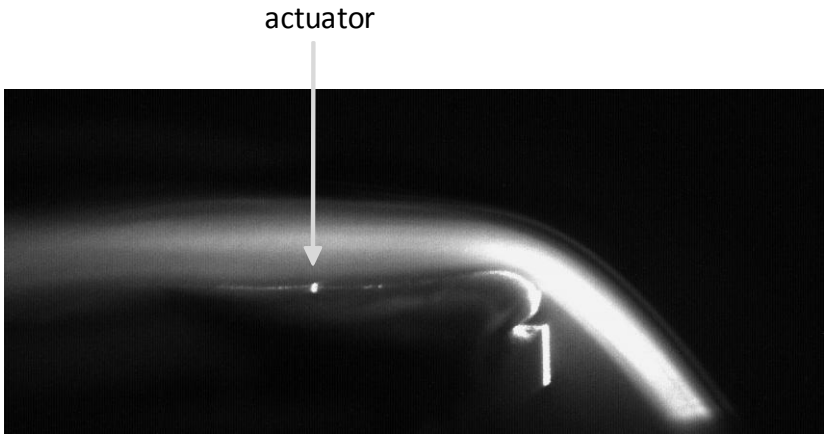

a.) Power off

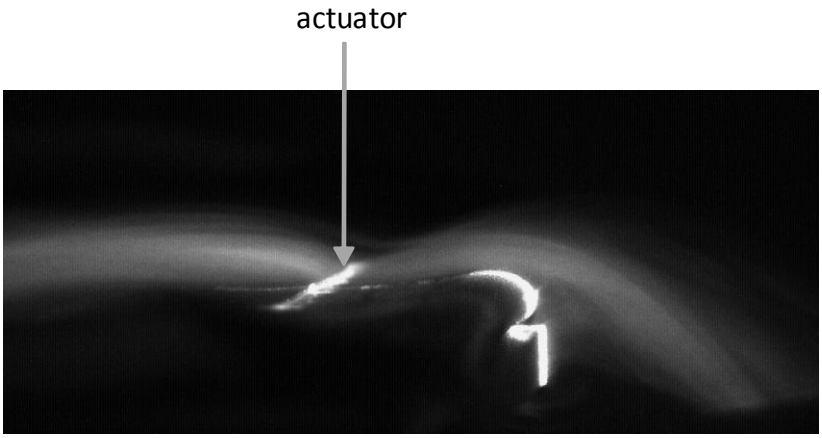

b.) Power on

Figure 1.9. Visualization of the induced velocity generated by a DBD plasma actuator single asymmetric electrode configuration. Top image: actuator off. Bottom image: actuator on. Flow is from left to right.

1.4.1.2. Alternate DBD Plasma Actuator Configurations

A majority of fundamental research and application of DBD plasma actuators for flow control have utilized the linear asymmetric electrode arrangement illustrated in Figure 1.7. This configuration generates an induced velocity in the form of thin wall jet over the buried electrode.

Figure 1.9 shows flow visualization of the induced velocity generated by a linear asymmetric electrode arrangement. The images are of a plasma actuator operating on a benchtop. The flow here is generated by the fog formed from dropping dry ice in water. The fog is naturally flowing over the plasma actuator from left to right in the images. The plasma has the effect of pulling the fog towards the buried electrode and ejecting in the form of a thin tangential wall jet. This configuration is effective at reenergizing the boundary layer by transferring momentum from the freestream to the boundary layer. The height of the jet is typically only several millimeters above the surface (Pons et al. 2005). This configuration was used experimentally by Huang et al. (2006) to reattach and decrease the length of a separation bubble over the Pack-B airfoil. The jet was oriented downstream along the surface of the airfoil just upstream from separation adding momentum to the boundary layer with the objective of overcoming the adverse pressure gradient aft of the negative pressure peak. Huang et al. concluded the actuator acted as a turbulent trip, promoting earlier transition to a turbulent boundary layer. A nearly analogous computational study by Rizzetta and Visbal (2007) found the same steady actuator configuration mounted facing upstream more effective then the downstream facing plasma actuator. They predicted that the upstream jet created a local small scale separation and subsequent formation of vorticity and turbulent mixing. It should be noted that both Huang et al. and Rizzetta and Visbal investigated pulsed configurations in their studies and found them to be more effective while using less power. Their performance gain was attributed to the generation of more coherent spanwise vortical structures that transferred high momentum fluid from the outer boundary layer to the blade surface (Huang et al. 2006, Rizzetta and Visbal 2007).

As alternatives to the asymmetric electrode arrangement several researchers have proposed different electrode configurations with the objective of improved control authority. The objective of alternative electrode configurations over the traditional linear plasma jet is generation of induced jets with three dimensionality and vorticity for enhanced boundary layer control. Longitudinal vortices generated by vortex generators are known to be efficient at eliminating or

reducing boundary layer separation by increasing cross-stream mixing of streamwise momentum (Johnston et al. 1990). Roy and Wang (2009) have proposed horseshoe and serpentine electrode configurations in a numerical study that showed promise for generating induced flows with three-dimensionality.

Plasma synthetic jet configurations have been proposed in both annular (Jacob et al. (2005), Santhankrishnan and Jacob (2007)) and linear configurations (Santhanakrishnan and Jacobs (2008), Santhanakrishnan et al (2009), Sherman (1998)). Santhanakrishnan and Jacobs experimentally studied both a steady and pulsed annular arrangement. Steady operation behaved like a synthetic jet in crossflow, and pulsed operation formed multiple counter-rotating vortex rings. Linear plasma synthetic jets were experimentally and numerically studied by Santhanakrishnan et al. (2009) in quiescent air using PIV. The researchers found similar findings as the annular array in that steady operation resulted in a zero-mass flux jet, and unsteady operation resulted in counter-rotating vortical structures. They also found a low peak velocity located close to the actuator compared to the higher velocities observed with traditional synthetic jets.

Porter et al. (2008, 2009) investigated improving upon the linear plasma synthetic jet by modifying the shape of the buried electrode to produce spanwise variation or "waviness" in the normal jet. They create spanwise waviness in the vertical jet by removing portions of the buried electrode (either diamond or square shapes) at specified spatial frequency. This limits the extent of the plasma to areas in which the bottom electrode has not been removed creating spanwise variation in the body force. They found that their electrode arrangements had the ability to generate vertical jets with spanwise spatial variation (Porter et al. 2009).

Jet vectoring is another interesting approach to generating increased vorticity and mixing by controlling the direction of the jet produced by linear plasma synthetic jets. Variations of jet vectoring have been suggested by Porter et al. (2008, 2009), Bolitho and Jacobs (2008), and Sherman (1998). The work of Porter et al. is very interesting in that they vary the voltage applied

to each of the two exposed electrodes that form a linear plasma synthetic jet. They demonstrate ≈ +/- 60 degrees of jet directional control by varying the voltage between exposed electrodes. In addition they demonstrate oscillation of the jet by frequency modulation, greatly expanding the design space of linear plasma synthetic jets.

1.5. Current Study

The objective of this research is to investigate the feasibility and technological challenges associated with using a new type of sensor in a closed loop separation control system. The sensor is based on surface stress sensitive film (S3F) technology which is sensitive to both surface shear stress and pressure gradient. Wright et al. in their 2002 paper outline two important challenges that must be addressed to use discrete sensors in flow control applications:

1. development of accurate, durable shear stress sensors
2. integration of a high-density sensor suites into aerodynamic surfaces.

This research has addressed both challenges by investigating the use of a new type of shear stress sensor technology for use as a sensor in a flow control system. This work focuses on several specific objectives:

1. Obtain the experimental suction surface *Cp* and boundary layer behavior of an Eppler 387 (E387) airfoil model at low Reynolds number over a range of small angles of attack that result in laminar boundary layer flow separation.
2. Study a new method of surface stress sensitive film installation over a curved surface to reduce the effect of the film on the boundary layer and surface being studied.
3. Compare several different dielectric barrier discharge plasma actuator geometries for low Reynolds number separation control on the E387 airfoil model.
4. Develop a first generation closed loop low Reynolds number separation control system using S3F as the separation control sensor.

This work culminates with an experimental demonstration of a separation control system comprised of an S3F sensor and linear vertical jets generated by dielectric barrier discharge (DBD) plasma actuators as the flow control mechanism.

2. Methodology

This chapter discusses the methodology used to complete this research. In order to reach the end goal of demonstrating S3F in a closed loop separation control system, several major milestones were completed:

- wind tunnel setup and modification
- fabrication and initial testing of airfoil models in a small scale wind tunnel
- development and testing of high sensitivity S3F based wall shear stress sensor
    - S3F based sensor system design – packaging & experimental arrangement
    - S3F development and fabrication by ISSI Inc., Dayton, OH
    - S3F testing in the AFRL/RZ wind tunnel, WPAFB, OH
- development of the actuator and flow control method (open loop experiments)
- detailed development of closed loop control method – software and hardware

Each of these milestones will be discussed in relevant sections of this chapter.

2.1. Experimental Facility

This research was performed at the Air Force Research Laboratory (AFRL) Propulsion Directorate‟s Low Speed Wind Tunnel (LSWT) facility located at Wright-Patterson Air Force Base, Ohio. The LSWT facility is comprised of two wind tunnels, the first is a large, variable angle linear cascade facility primarily used for aerodynamic investigation of turbomachinery components. The 2-D linear cascade has been used in numerous previous efforts (see for example Sondergaard et al. 2002; Bons et al. 2002; McQuilling 2007). The tunnel features a variable angle test section that is 0.85m tall by 1.22m wide at the inlet and typically houses 6-7 linear turbine blades with an axial chord of 17.8 cm. An optional turbulence generation grid can be used to increase the freestream turbulence up to a maximum of approximately 12%. A recent

upgrade to the facility has included the development, installation, and characterization of a unique, internally mounted, periodic wake generator which has been described in Nessler et al. (2009a; 2009b).

A second, straight test section wind tunnel was relocated to the LSWT facility to use in this effort. The wind tunnel is referred to as the Developmental Wind Tunnel (DWT). The DWT has good optical access, and an airspeed range of 4.5 – 65 m/s generated with a 7.5 kW electric motor. The inlet has a series of flow straighteners and turbulence-reducing screen followed by a 9.5:1 contraction providing an advertised turbulence level of less than 0.2%. The test section dimensions are 30.5 cm x 30.5 cm x 61 cm.

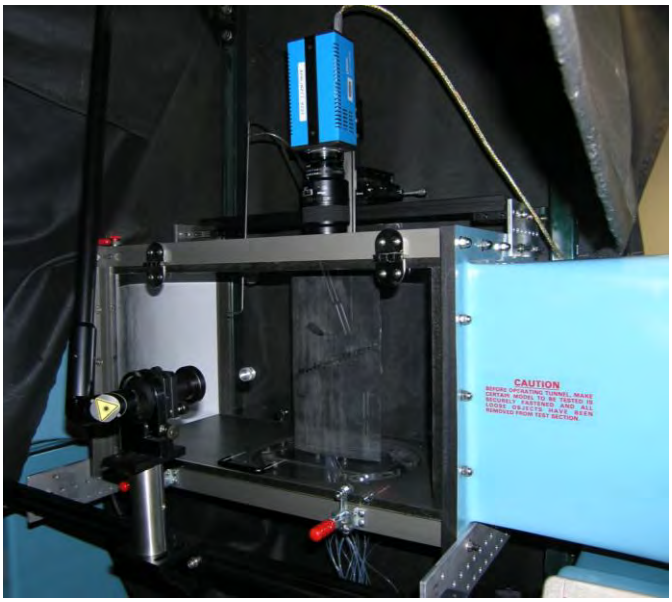

Figure 2.1 Airfoil 1 mounted in the DWT test section and setup up for PIV, flow visualization, and C_p measurements.

In order to complete the experiments in this research, several modifications to the wind tunnel were made. The bottom of the wind tunnel had an aluminum disk insert for mounting models or a sting. This metal disk was replaced with a clear acrylic disk to provide optical access from below, and lower mounting holes for the airfoil. An optical table was positioned in front of the wind tunnel section to mount equipment and isolate it from wind tunnel vibration. Four

mounting plates were fabricated and added to the top and bottom of the wind tunnel test section. The lower mounting plates were extended out from under the test section to create a cantilevered mounting. An optical plate was attached to the cantilevered mount. The two optical mounting plates provided both a surface that was disconnected and free from wind tunnel motion, and one that was rigidly attached to the wind tunnel test section. The PIV laser and S3F lamp power supply were mounted on the optical table, and the S3F lamp, S3F camera, and sheet forming laser lenses were mounted to the optical plate fixed to the wind tunnel test section. Several traverses were used around the test section. A microtraverse controlled by a custom Labview VI was used to position instruments in the wake of the test specimen. A manual traverse that moved in the wind tunnel longitudinal direction was located above the test section and used to mount a camera. Another manual traverse was mounted on the optical board and used to position either a camera or laser sheet.

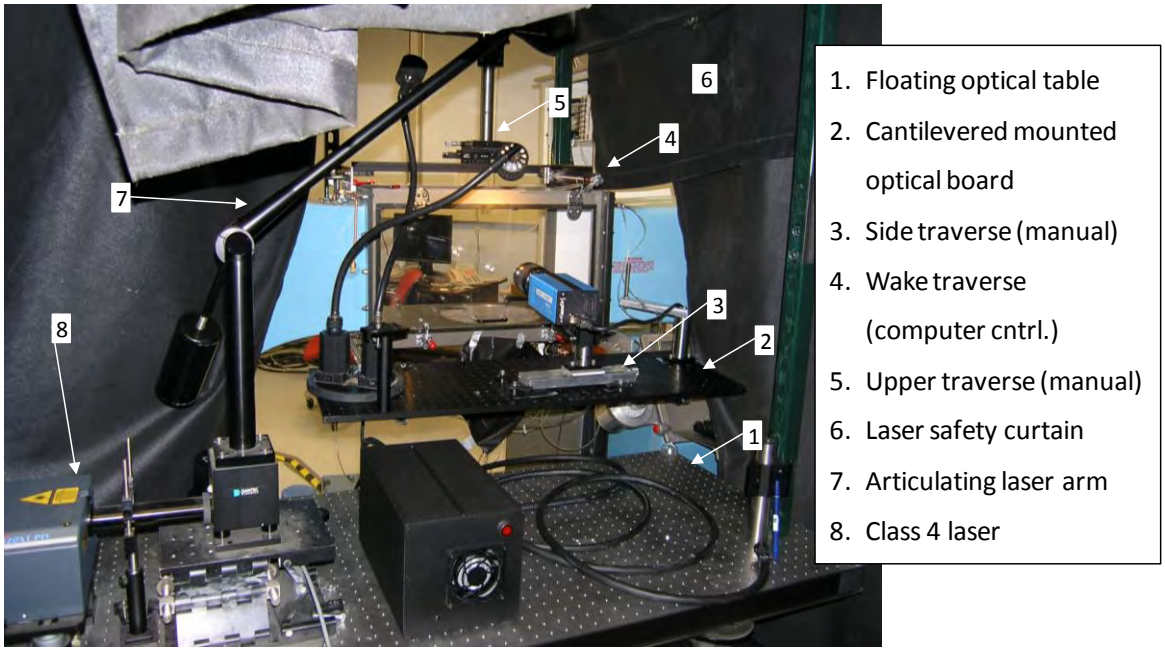

Figure 2.2 Modifications to wind tunnel

2.1.1. Data acquisition

A precompiled Labview application was provided with the wind tunnel to set the motor speed. In order to measure the wind tunnel freestream velocity and other parameters a National Instruments data acquisition rack was set up. The rack consisted of a PXI-1010 chassis with the cards shown in Table 2.1. A MC-4SA Servo amplifier system and NI PXI-7344 motion controller was used to control a National Aperature MM4M-EX200 micro traverse. The micro traverse was mounted over a downstream slot which enabled wake traverses.

Table 2.1 PXI-1010

Device	**Description**	**Function**
PXI-8335	MXI-3 Interface	Interface to PC, 1.5 Gbit/s serial data rate
PXI-7344	Motion Controller	Control of microtraverse
PXI-5052E	Multifunction I/O	16 bit, 333 kS/s digitization of analog S*CX*I signals
S*CX*I-1121		Pressure Signal Acquisition

2.2. **Airfoil**

A generic low Reynolds number airfoil called the Eppler 387 (E387) was used in this work to make the research basic and applicable across design domains. Selig and McGranahan (2004) reported that the airfoil geometry was originally designed for model sailplanes in the 1960s by Richard Eppler, but has also been used to compare one low speed wind tunnel facility with another. For this reason the airfoil is well represented in literature and has been tested in numerous wind tunnel facilities such as those at: Princeton, NASA Langley, and the University of Illinois at Urbana-Champaign. In addition to experimental data, several researchers have performed computational studies, both RANS and DNS, using the Eppler 387 airfoil.

The Eppler 387 airfoil has been extensively tested at the University of Illinois at Urbana-Champaign and results have been presented in several reports. A 2004 report by Seilig and McGranahan focused on the use of the blade geometry as a wind turbine, presented aerodynamic force measurements. The group at UIUC tested the blade at a range of low Reynolds numbers from 100,000 to 500,000. Researchers at NASA Langley (McGhee et al. 1988) also tested the blade at low Reynolds numbers down to 60,000. Both facilities report a mean separation bubble on the suction surface at a Reynolds number of 100,000 and zero degree angle of attack. The NASA Langley data provides pressure coefficient as well as laminar separation location and turbulent reattachment location identified from oil flow visualization.

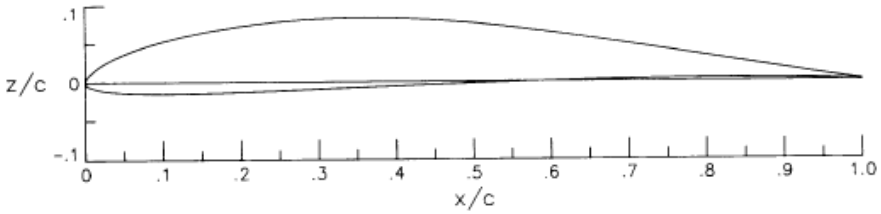

Figure 2.3. Eppler 387 airfoil section shape. (from McGhee et al. 1988)

Figure 2.4 shows pressure coefficient data taken in the NASA Langley tunnel at a Reynolds number of 100,000, and at angles of attack from -3 to +2 degrees. The pressure coefficient indicates laminar boundary layer separation at an angle of attack of -3 degrees, with turbulent reattachment near the trailing edge as angle of attack is increased to -2 degrees and above. Reattachment location moves upstream as angle of attack is increased. Figure 2.5 and Figure 2.6 show pressure coefficient at angles of attack of 0 degrees and 2 degrees overlaid with oil flow visualization indicated laminar separation and turbulent reattachment locations. For the larger angle of attack, the length of the separation bubble has decreased slightly as angle of attack increased. The separation point has moved forward as angle of attack increased. Based on the measurements at UIUC and NASA Langley the E387 was chosen because of laminar separation

on the suction surface at small angles of attack. The Langley data taken at a Reynolds number of 60,000 indicated laminar flow separation at angles of attack near zero. The experiments reported in this work were in the range of Re = $1.5x10^5$ to $5.0x10^4$, so both a laminar separation bubble and non-reattaching boundary layer separation were possible by adjusting the wind tunnel speed with the angle of attack fixed. Both of these low Reynolds flow phenomena have been observed in previous LP turbine investigations in the AFRL/RZ LSWT linear cascade at roughly the same freestream velocities. This allowed previous work using S3F, in terms of film sensitivity, to be directly applicable to the present study. It will also make scaling the experiments for future studies in the large linear turbine cascade tunnel easier.

Several researchers have performed computational studies on the E387 airfoil geometry to test numerical methods of simulating unsteady low Reynolds number flows over airfoils. Lin and Pauley (1996) performed a computational study using an unsteady 2D incompressible Navier-Stokes equation code. They found that periodic vortex shedding occurred at each Reynolds

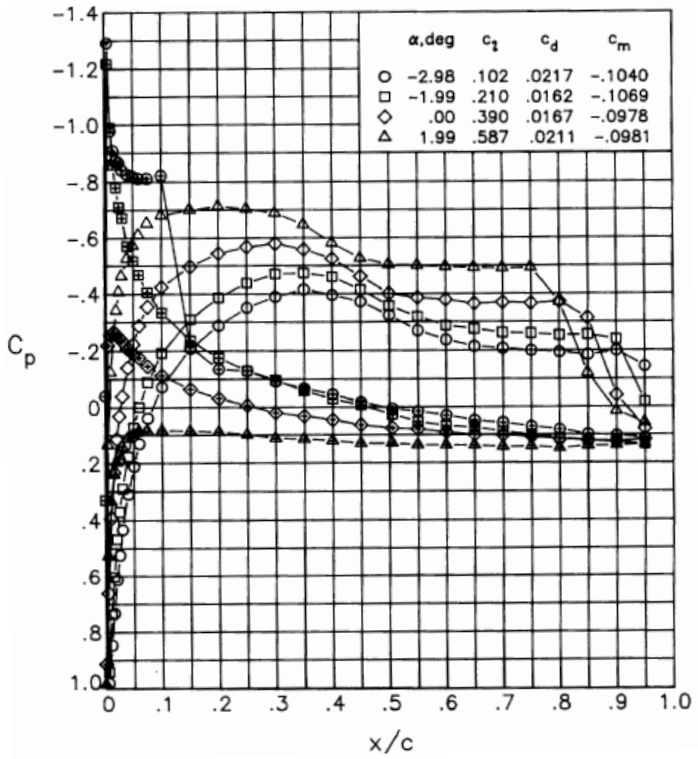

Figure 2.4 Eppler 387 Pressure Coefficient at Re = 100,000 (from McGhee et al. 1988).

number they studied, 6 x 10^4, 1 x 10^5, and 2 x 10^5 at several small angles of attack. The results from Lin and Pauley lead them to suggest that two dimensional large-scale structures in the form of vortex shedding control the laminar separation bubble and omnipresent small-scale turbulence plays only a secondary role. Hall and Mohseni (2007) and Sahin, Hall, and Mohseni (2008) also performed numerical studies on the flow around the Eppler 387 airfoil. In the first paper the authors presented results using a time-accurate, three-dimensional, finite element based code, with no turbulence model. Calculations were performed at a Reynolds number of 6.0 x 10^4 and at various angles of attack. Surface pressure coefficient and surface shear stress was presented at angles of attack of 2, 4, and 6 degrees. The second paper by Sahin, Hall and Mohseni in 2008 present DNS simulation of the flow around the Eppler 387. Computations were made at a

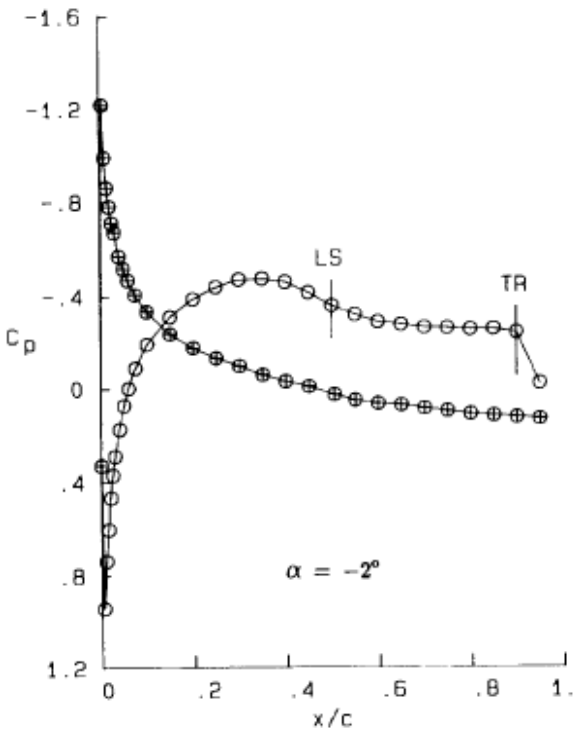

Figure 2.5. Pressure coefficient data at -2° angle of attack with laminar separation and turbulent reattachment point identified by oil flow visualization (from McGhee et al. 1988).

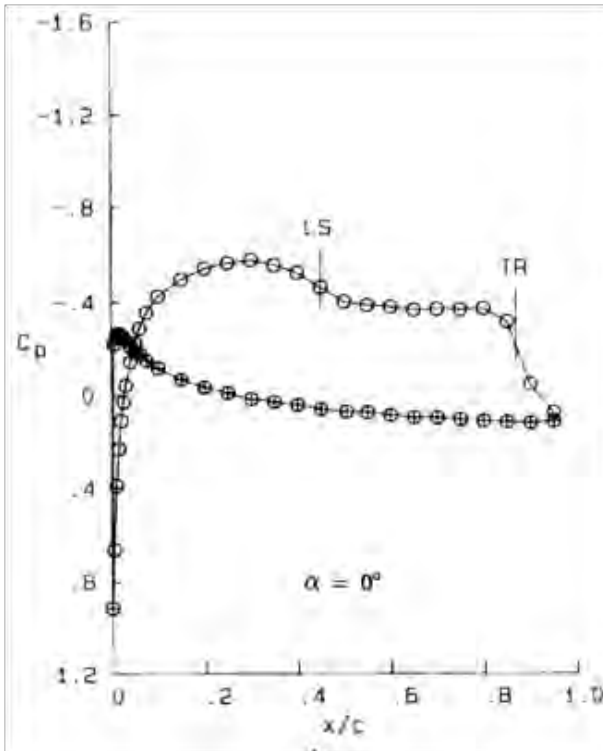

Figure 2.6. Pressure coefficient data at zero angle of attack with laminar separation and turbulent reattachment point identified by oil flow visualization (from McGhee et al. 1988).

Reynolds number of 6.0 x 10^4, using both three dimensional and two-dimensional DNS. The authors indicate that the two dimensional simulations indicated a large, abrupt decrease in surface pressure just before reattachment as was found in other numerical studies. The three dimensional simulation agreed with the experimental data by McGhee et al. in that the size of the abrupt decrease was smaller. This was attributed to the lack of spanwise flow structure in the two-dimensional simulation, as the three dimensional simulation indicated the formation of half-moon type vortices in the laminar shear layer, with no regular spanwise structure. The vortices were observed to interact with each other and burst into the freestream causing a momentum exchange between the airfoil boundary layer flow and freestream. They report these findings were consistent with experimental observations by Bergmann et al. (2006) who used scanning PIV to investigate the spanwise structure and dynamics of the roll-up of vortices within the separation bubble of the SD7003 airfoil.

An axial chord length of 16.51 cm (6.5 inches) was chosen for the experiments since the inlet velocity at the Reynolds numbers being investigated was inside the operating range of the wind tunnel and agrees well with velocities over a LP turbine blade in previous experiments using S3F. The airfoil models were rapid prototyped out of a mixture of ABS and Polycarbonate and were mounted across the full height of the wind tunnel and fixed at the top and bottom.

2.2.1. Wind tunnel models

Two different test articles were fabricated, both with the E387 airfoil geometry. The first airfoil was an unmodified E387 airfoil, and the second airfoil had a cavity formed in the suction surface in which a removable S3F carrier was mounted, these are referred to as Airfoil 1 and Airfoil 2. An end cap was attached to the top end of each airfoil with two screws. The end cap had a circular extrusion that extended into a hole in the top wall of the wind tunnel test section. A bolt held the top of the airfoil to the wind tunnel wall, and two screws at the bottom end of the airfoil rigidly fixed the airfoil in the test section.

The S3F carrier that was installed in Airfoil 2 was 3D printed out of a mixture of ABS and polycarbonate and was very flexible due to its 1.3mm maximum thickness. The flexibility of the carrier enabled it to conform to the curvature of the airfoil suction surface. The leading edge of the S3F carrier and corresponding cavity on the airfoil were notched. This provided a secure, tight, and smooth interface along the interface between the S3F carrier and airfoil suction surface. Each carrier was hand sanded to ensure a tight fit into the airfoil cavity. Early tests used spray adhesive to attach the S3F carrier to the airfoil. Adhesive did not prove to be a reliable method to attach the S3F carrier because of small amounts of S3F residue left on the bottom of the S3F carrier during filling of the S3F cavity. Instead the notch at the leading edge of the S3F carrier and two small, countersunk screws placed at approximately C_x = 90% were used to reliably secure the S3F carrier to the airfoil. Drawings of Airfoil 2 are shown in Figure 2.7 and Figure 2.8.

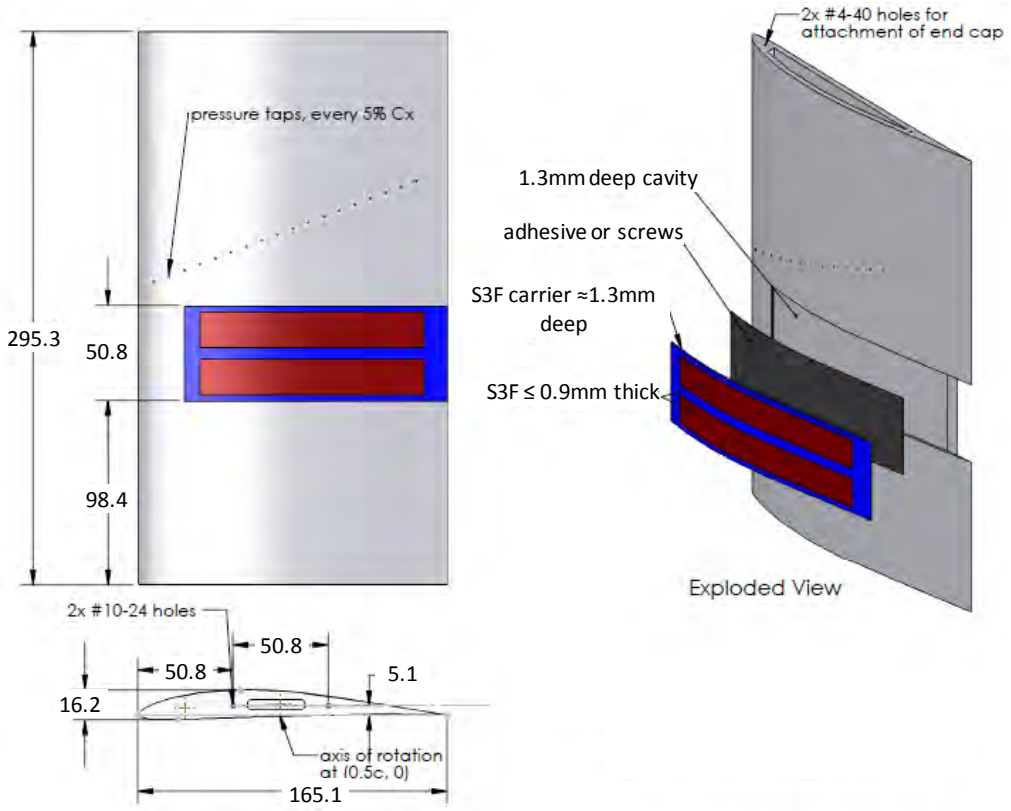

Figure 2.7 Drawing of Airfoil 2 showing the pressure tap locations and S3F location (all dimensions in millimeters).

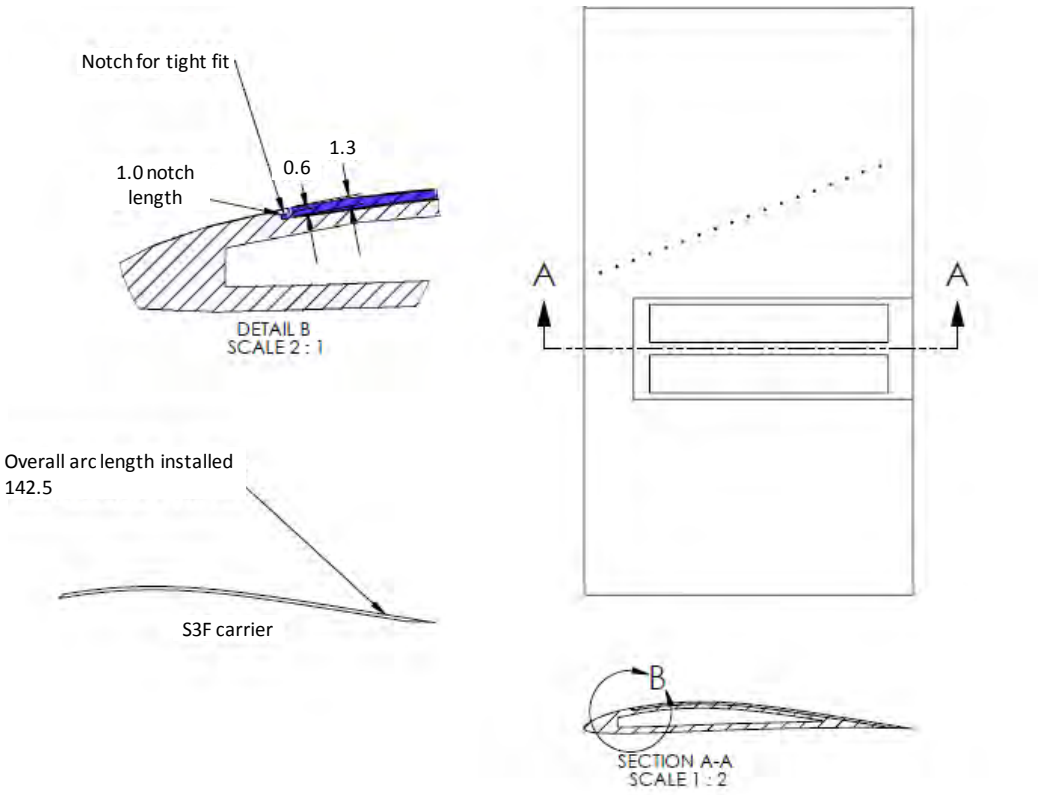

Figure 2.8 Drawing showing S3F carrier installation on Airfoil 2 (dimensions in mm).

2.3. Experimental Techniques

This section explains the experimental methods used to acquire pressure data, particle image velocimetry, flow visualization, and S3F data. A detailed background and explanation of the S3F method is provided.

2.3.1. Pressure Measurements

Pressure measurements were used to calculate the inlet velocity, surface pressure coefficient and drag. Two LabVIEW VIs were created, one to obtain static surface pressures to calculate pressure coefficient, and one to measure the pressure in the airfoil wake to calculate drag. While LabVIEW software automated the entire drag measurement process, the C_p measurements

required human intervention to adjust a manual pressure selector valve to choose the correct pressure port when prompted by Labview.

Pressure taps located every 5% axial chord on the suction surface of each model, starting from 5% chord to 90% chord, were placed during printing of the airfoil models. The pressure tap holes were purposely printed undersized and then manually enlarged during the plumbing process. Pressure taps had an internal diameter of 0.91 mm and were staggered in the spanwise direction to reduce the chance for imperfections of upstream taps to contaminate the downstream tap measurements. The pressure lines of Airfoil 1 were completely enclosed inside the body of the airfoil and exited through a hole at the bottom of the wind tunnel. During testing of the S3F method the hollow cavity in Airfoil 2 was filled in an effort to stiffen the model. This meant the pressure lines could not be passed through the inside of the airfoil. Instead the pressure lines were run along the pressure side of the airfoil and covered with a smooth layer of tape. Even though the pressure lines were extremely small diameter, this method modified the pressure surface geometry and effected the flow field. This will be discussed further in the section on airfoil characterization.

An array of AllSensor low pressure transducers were used for pressure measurements with nominal 0.05% and maximum 0.25% linearity full scale. A mounting plate, shown in Figure 2.9, with three 0-125 Pa (31.1 Pa/V) and three 0-249 Pa (62 Pa/V) pressure transducers was fabricated and mounted under the wind tunnel. The mounting plate included 5V supply voltage distribution and BNC connectors for signal transmission to the NI data acquisition rack. The 0-125 Pa transducers were used for wake pressure measurements and inlet dynamic pressure measurements. The 0-249 Pa transducer was used for C_p measurements. A barometer and thermometer were located on site to measure atmospheric conditions.

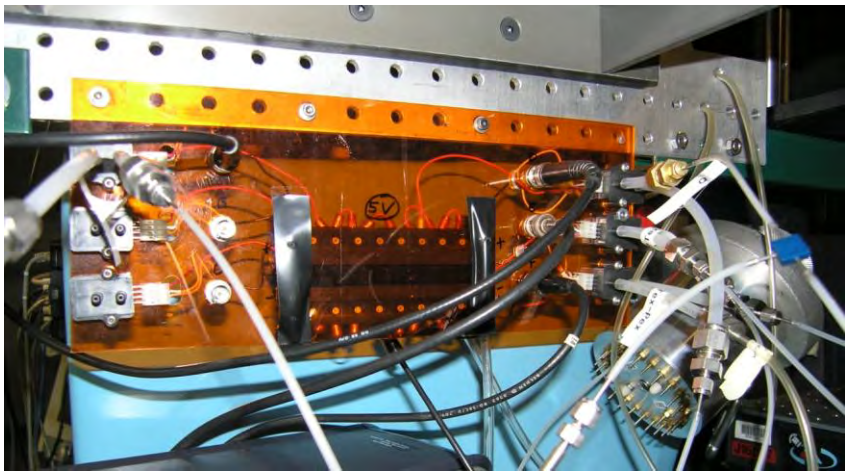

Figure 2.9 Pressure transducer mounting plate.

2.3.1.1. Pressure Coefficient Measurements

The upstream static and total pressures were measured via a Pitot-static probe located 101 mm (≈ 2/3 C_x) upstream from the leading edge of the airfoil. The pressure taps were plumbed to a manual selector valve and then to the pressure transducer mounting plate. Static pressure was calculated using:

$$Cp = \frac{P_i - P_{t,in}}{q_{in}} \tag{2.1}$$

with no corrections. P_i is the pressure at the each pressure tap, $P_{t,in}$ is inlet total pressure, and q_{in} is the inlet dynamic pressure. Pressure tap locations used on each airfoil are shown in Table 2.2. Check marks in the table indicate locations where measurements were made. The locations on Airfoil 2 between 25% and 35% axial chord listed as "blocked" indicate tap location that were covered up when plasma actuators were installed on the airfoils.

Table 2.2 Pressure tap locations.

	Tap Location - C_x%								
	5	10	15	20	25	30	35	40	45
Airfoil 1	√	√	√	√	√	√	√	√	√
Airfoil 2	-	-	-	-	Blocked	Blocked	Blocked	√	√
	50	55	60	65	70	75	80	85	90
Airfoil 1	√	√	√	√	√	√	√	√	√
Airfoil 2	√	√	√	√	√	√	√	√	√

Data was acquired at a 1000 Hz sampling frequency and the mean pressures over the sampling period were used in the calculation of C_p. Typically, data was recorded for a minimum of 4 seconds at each port, with a 9 second settling time before the start of recording at the next measurement location. This method provided very repeatable pressure coefficient measurements.

Uncertainty in the C_p measurements is nominally 1.5% at the pressure minimum, and 3.1% in the trailing edge area at Re = $5x10^4$. At Re = 1.0 x 10^5 uncertainty in C_p is nominally 0.5% at the pressure minimum and 1.1% in trailing edge area.

2.3.1.2. Drag Measurements

Drag was calculated by wake traverses using the method of Jones (Goett, 1939):

$$C_d = \frac{2}{C_x}\int^{W} \frac{\sqrt{P_{T,w} - p_w}}{\sqrt{P_{T,in} - p_{in}}}\left(1 - \frac{\sqrt{P_{T,w} - p_{in}}}{\sqrt{P_{T,in} - p_{in}}}\right) dz \qquad (2.2)$$

using a Pitot-static probe located in a slot $0.5C_x$ downstream from the trailing edge.
No corrections were applied to the data. Uncertainty in the drag measurements, omitting errors related to the probes, is less than 1%.

2.3.2. Particle Image Velocimetry & Flow Visualization

The modern digital 2D PIV technique has developed into a method that is quite common in experimental fluid dynamic laboratories. Fluid velocity fields can be obtained relatively quickly, with high spatial resolution, using a non-intrusive optical measurement method. Four main pieces of equipment are required: a high power laser, digital camera, flow seeder, and control and post processing software. The beam from a high power laser is formed into a thin laser sheet to illuminate a two dimensional cross section of fluid flow seeded with light scattering particles. A digital camera records the light scattered from the particles in two consecutive exposures. The time between the exposures is short, and set based on the velocity of the flow being measured and

the size of the field of view. Cross correlation methods are used to determine the particle displacement in individual regions across the entire field of view. The fluid velocity across the entire field of view is then calculated using local particle displacement divided by the time between the two consecutive exposures.

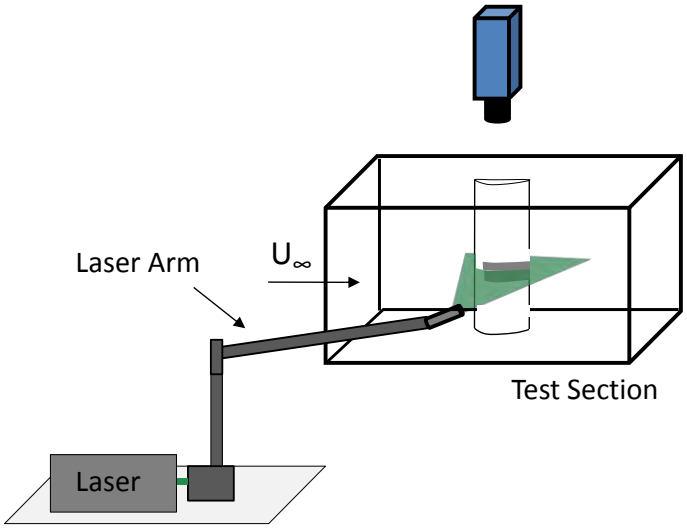

Figure 2.10 General PIV Experimental Arrangement

2.3.2.1. PIV Experimental Setup

A New Wave Solo - 120 dual-head Nd:YAG laser capable of dual 120 mJ pulses was used for flow illumination. The laser beam was transmitted from the laser aperture to the wind tunnel test section using a Dantec articulating laser arm. A Dantec sheet forming optics module was mounted to the end of the articulating arm and used to form a thin laser sheet with 1 mm nominal thickness. The laser sheet was positioned to cut through a cross section of the airfoil span at the edge of the S3F film. A pulse generator was used to control system timing which was set to 10 Hz. The time between consecutive exposures was a function of flow velocity and optical magnification factor. A high resolution, PCO 1600 camera with 1600 x 1200 pixel resolution was used to acquire images.

Instantaneous and ensemble averaged flow fields were calculated using Dantec Flowmanager processing software. Multi-pass adaptive cross correlation was used to analyze the images with interrogation domains of 128, 64, and 32 pixels with a 50% overlap.

PIV experiments in the LSWT linear cascade have used fog from a theatrical fog generator for flow seeding, but that method proved unacceptable in the smaller DWT. Two issues precluded the use of the fog generator in the DWT: condensation on the airfoil leading edge and inadequate room ventilation to remove fog generator odor. Different clean seeding methods for PIV have been investigated by Reeder et al. (2009) and inspired the use of water particles generated by a commercial boiler. A Sussman MBA9 9kW electric boiler was used to generate steam that was directed into the inlet of the wind tunnel (See Figure 2.11). The steam was injected approximately 1-2 meters upstream of the inlet. A separate tank and water pump provided a virtually endless supply of water to the boiler. This seeding method worked nearly analogous to the propylene/water fog generator except that a much higher laser power setting was required for adequate illumination. Flow visualization images were acquired with the same setup as the PIV technique.

The PIV technique is very useful for obtaining high spatial resolution fluid velocity fields, but the method is not without limitations. General limitations of the technique encountered in this work were:

1. Laser reflection makes it difficult to obtain fluid velocity very close to the airfoil surface. Measurements were generally limited to greater than 1mm from the wall.
2. The time between consecutive exposures must be set to one value, but the actual flow field may have large velocity gradients. The experimenter must choose a time delay that provides adequate particle displacement (generally on the order of 10 pixels) in the region of greatest interest. In the separated flows measured in this work the delay time had to be set long enough to enable some measurement of the flow in the separated regions as well as freestream.

3. It is sometimes a challenge to get flow seeding reliably in the field of view. It is also difficult to reliably get seeding in regions of separated flow. If the seeding is inadequate in the separated regions the velocity will measure zero and potentially bias calculations in neighboring regions.

Figure 2.11 Flow seeding equipment.

2.3.2.2. Benchtop DBD Plasma Actuator Flow Visualization

Several different DBD plasma actuator electrode configurations were fabricated and tested in an effort to improve flow effecter control authority over the traditional asymmetric DBD plasma actuator electrode arrangement. A simple method to visualize the induced velocity of each arrangement on a bench top in quiescent flow was devised and used to compliment wind tunnel data.

A schematic of one flow visualization arrangements is shown in Figure 2.12. The plasma actuators were fixed to a Nylon sheet using adhesive transfer tape. The laser beam from a Class 3A laser diode was expanded into a sheet and used to illuminate planes across the plasma actuator. A small plastic container was filled with a mixture of water and dry ice that created a fog that was naturally pumped through a tube and out a series of orifices. The end of the tube was set up so that the fog would flow across the plasma actuator. Various digital camera and lens combinations were used to capture the plasma on and plasma off images showing the wall jets generated by each plasma actuator arrangement.

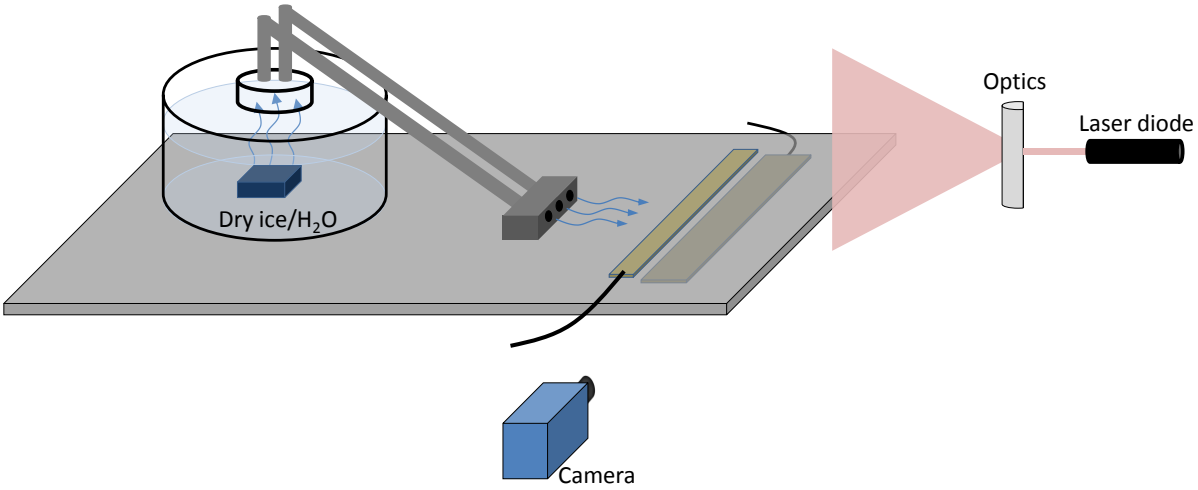

Figure 2.12 Benchtop plasma actuator flow visualization diagram.

2.3.3. The S3F Method

The S3F method uses an elastic film designed and manufactured by ISSI Inc. to measure wall pressure and wall shear stress in fluid flows. The film has two types of sensors; the first is used to measure normal force (pressure) on the film by a fluorescent probe embedded in the S3F. The second consists of markers distributed across the surface of the film. Marker displacement under load from the fluid flow is recorded using a digital camera and compared to a flow-off image to

determine film tangential displacement field. Recently Fonov et al. 2010 used stereo photogammetry to measure and reconstruct the deformed S3F surface which enables measurement of normal and tangential displacement using only cross correlation techniques. Once the S3F deformation field is measured, the normal and tangential wall forces can be calculated from the film displacement by solving an inverse elasticity problem using FEA (Fonov et al. 2006).

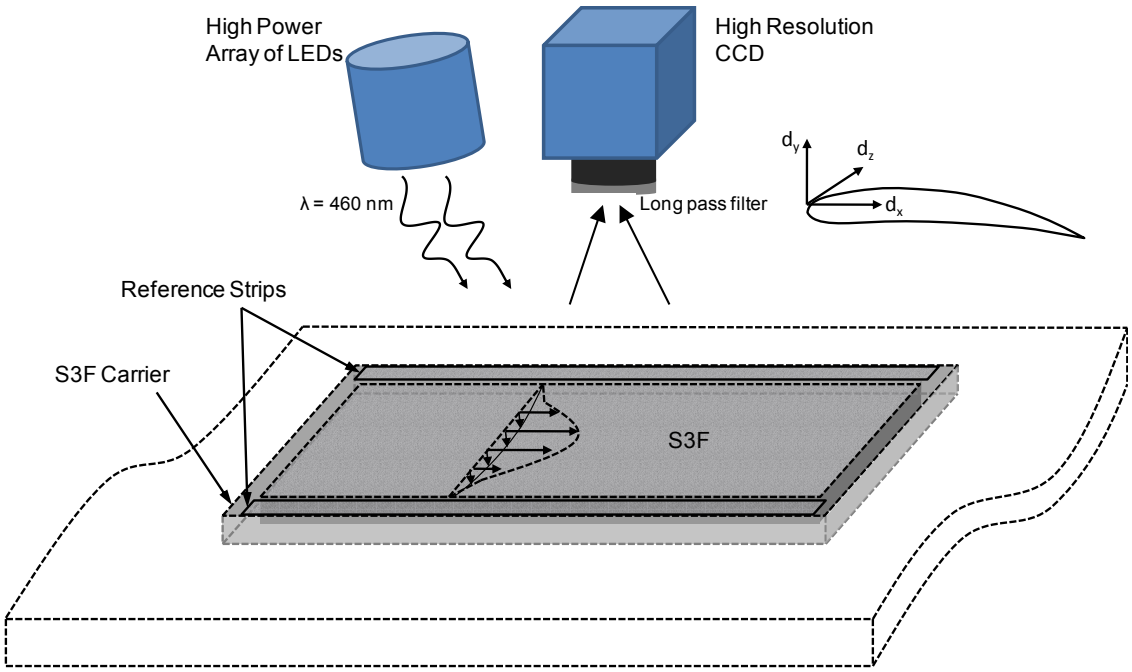

Figure 2.13. S3F Experimental Setup

Through analysis of the response of S3F using both experimental and analytical techniques ISSI has determined that with spatial loading frequencies (thickness/contact surface) below 0.1, film response can be modeled mathematically by (from Crafton et al. 2010):

$$d_X = \frac{h}{\mu_m}\left(\tau_X - \frac{h}{2}\frac{\partial P}{\partial x}\right) \qquad d_Y = \frac{h}{\mu_m}\left(\frac{h^2}{3}\frac{\partial^2 P}{\partial x^2} - \frac{h}{2}\frac{\partial \tau_X}{\partial x}\right) \tag{2.3}$$

In Equation (2.3), the surface normal (d_y) and tangential (d_x) reaction of the film is written in terms of the film thickness (h), shear modulus (μ_m), tangential stress (τ_x), and normal stress (P).

These equations give insight into designing a film to have a higher response to shear than pressure, or vice-versa. The tangential reaction of the film is a function of tangential stress and pressure gradient scaled by thickness. A thin film will have a higher relative response to shear forces than to pressure gradients. Conversely, a thicker film will show a higher response to pressure forces over shear forces (Crafton et al. 2010). Equation (2.3) was derived by ISSI Inc. based on the theory of elasticity and observed response of S3F to various surface forces (Fonov et al. 2011).

Another important insight from Equation (2.3) is that in the presence of small pressure gradients, shear stress is linearly related to tangential displacement. This key attribute was used in this work to develop the separation control sensor and will be discussed further in Sections 2.4 and 3.4.3.

The frequency response of the S3F is described by ISSI Inc. with a simple mass-spring-damper model that assumes the film is purely elastic (Crafton et al 2008). The first natural frequency of tangential oscilliation of the film is calculated by:

$$f_0 = \frac{1}{2\pi}\sqrt{\frac{\mu_m}{\rho h^2}} \quad (2.4)$$

The film frequency response is thus a function of shear modulus (μ_m), density (ρ), and thickness (h), which enables the frequency response to be adjusted in the range of 0.3 to 10 kHz (Crafton et al. 2008).

S3F has been fabricated with a shear modulus as low as 8 Pa and as high as several thousand Pascal, and thickness from 0.1mm to 1mm (Crafton et al. 2008). The ability to fabricate S3F with wide ranges of material properties allows a film to be fabricated with response characteristics that are designed for a particular flow environment using Equations 2.2-2.3.

Quantifying and improving upon the sources of uncertainty of S3F measurements is an on-going effort. Crafton et al. (2010) identified the dominant error sources of shear stress

measurement to be tangential displacement and film thickness. Experiments using fully developed channel flow resulted in skin friction measurements with an error of about 6% full scale (Crafton et al. 2010.).

Several methods are used by ISSI Inc. to obtain film properties, and each of these measurements has a direct effect on skin friction and pressure measurements. The film thickness is measured either by optical absorption, or an ultrasonic or capacitive thickness gage. Crafton et al. (2010) estimates the accuracy of these thickness measurement devices to be about 1 μm plus 1% of the reading. ISSI uses two different methods to measure the shear modulus of the S3F. One method is by static loading, the other is by dynamic loading. The static loading method involves determination of the shear modulus by measuring the displacement of a small load applied to the film surface as the system is rotated. An example of this method is shown in Figure 2.14. The second approach uses dynamic modeling in which an oscillating tangential load is applied to the film and the frequency is varied until the displacement amplitude reaches a maximum. The frequency obtained using this technique is the first tangential natural frequency of the film and the shear modulus is calculated using the equation shown in Figure 2.15. ISSI estimated the uncertainty in shear modulus to be ± 10% for the ultra low shear modulus films used in this work.

An additional error source when using S3F is the stability of the film properties. Crafton et al.

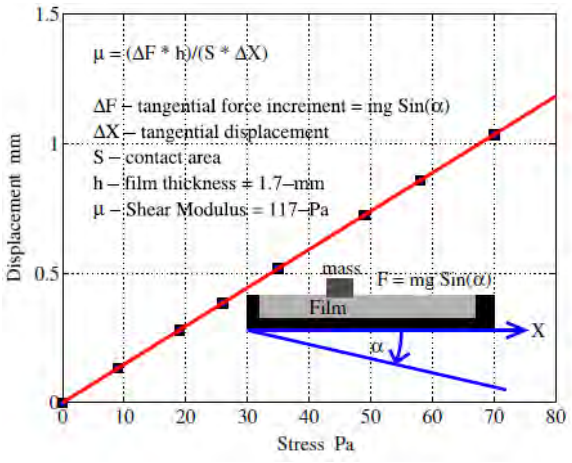

Figure 2.14 S3F calibration by static loading (from Crafton et. al 2008)

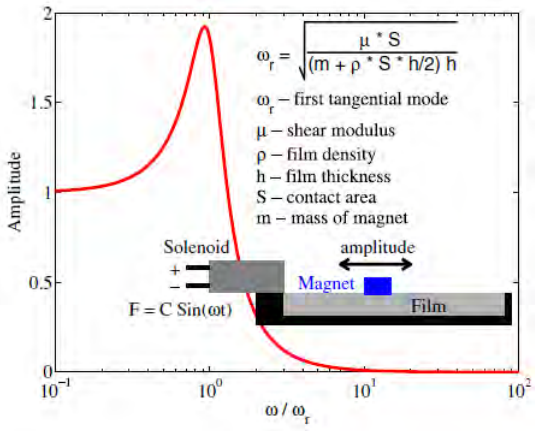

Figure 2.15 S3F calibration by dynamic loading (from Crafton et. al. 2008).

(2008) reported a significant change in shear modulus over the first day as the polymer initially cured. From day 1 to 10 the shear modulus changed 0.21% per day and experimental results indicated that over the remaining 118 day period the shear modulus change per day decreased even further.

The use of S3F at low Reynolds number, and in sea level air flows can push the limits of the technique (McQuilling 2007). Experiments using S3F have been reported in several studies found in open literature. Crafton et al. (2008) used the film for skin friction measurements in a hydrodynamic setting at high Reynolds number. Experiments were undertaken with a point sensor design installed in the wall of a water tunnel at Penn State University. The point sensor was packaged into a 76mm diameter plug inserted into the tunnel test section window. The S3F filled a 30 mm diameter x 1 mm diameter cavity. The bottom of the cavity was made of glass and below the glass window were LEDs for illumination and a CCD camera.

Figure 2.16 shows a picture of the point sensor concept as well as response of the film. The film was used in a zero pressure gradient boundary layer, so the film was designed for a large response to shear force versus normal force. The response plot shows that there is a non-uniform response along the edges of the sensor, but is uniform in the center up to approximately four film thicknesses from the boundary. Their work confirmed that the film displacement is linearly related to skin friction when the pressure gradient is negligible. The S3F skin friction measurements agreed with drag balance measurements with 5% rms difference, for one of the sensors used. The other sensor saw a larger deviation thought to be bias error. Source of error as pointed out by Crafton et al. (2008) are uncertainties in material properties, stability of the polymer, and experimental error sources caused by movement of the camera versus film over a series of data runs. In the work of McQuilling (2007, 2008a, 2008b), markers were added below the film and around the film in order to provide a reference channel for canceling out movement of the camera and optical system versus the film. The markers were fixed to the model, so any movement of the markers during the flow-on and flow-off images is associated with movement

between the model and the camera and are cancelled out. McQuilling (2007) used the film to study the flow over the suction surface of a low pressure turbine blade at low Reynolds number. The work of McQuilling (2008a) demonstrated the potential of S3F in flow velocities below 7 m/s. It was found that the sensitivity of the film was critical due to an order of magnitude variation of shear stress gradients from leading edge to trailing edge in the streamwise direction. McQuilling et al. (2008b) demonstrated the use of S3F applied to a L2F highly loaded LP turbine blade in a linear cascade to establish the separation location for CFD transition model validation. The studies by McQuilling et al. (2007; 2008b) demonstrated the potential of S3F for identification of flow features along the suction side surface of a blade at low velocity and also identified measurement uncertainties that need further investigation.

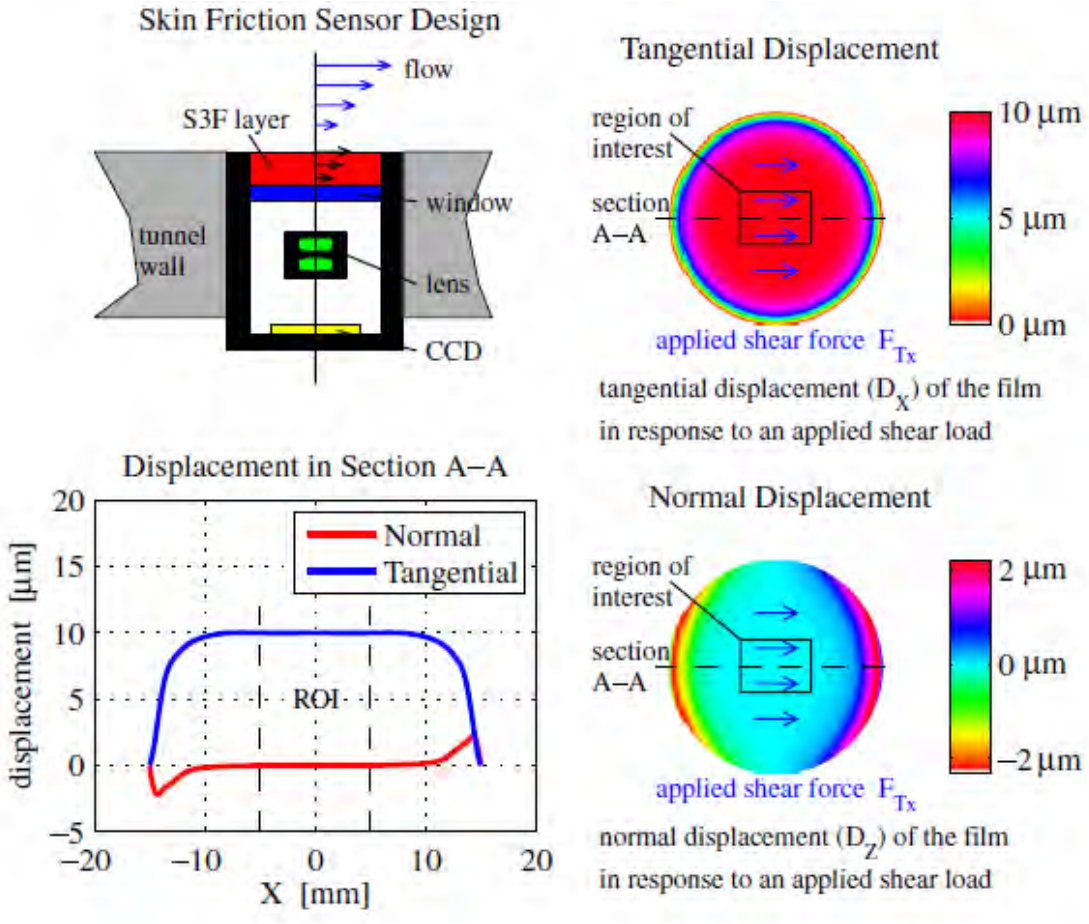

Figure 2.16 Design and response of S3F point sensor used by Crafton et al. (2008).

Two different applications of S3F film resulted in two different shear stress profiles along the surface of the blade. Sensitivity to tunnel vibration and deformation of the turbine blades in the wind tunnel was identified as a potential source of uncertainty with the technique (McQuilling 2008b).

Separate from fabrication and design of the film itself, another difficulty with the S3F technique is ensuring that S3F is cleanly mounted on the test article and that it does not affect the boundary layer or characteristics of the flow it is being used to study. The installation method could influence the pressure and skin friction over the surface. If the film is applied externally to an object (e.g. glued on) and not placed in a relief, the film will increase the thickness or shape of the object, which in turn will modify the pressure distribution. The film roughness may also affect the skin friction and transition point in the boundary layer if it differs in roughness from the base surface.

Previous studies have touched on the intrusiveness of the sensor. McQuilling (2007) applied S3F in a cavity along the suction surface of a LP turbine blade and irregularities in the data were observed that may have been due to disturbance of the flow by the S3F not being perfectly flat or flush with the blade surface. Measurements on the L1A LP turbine profile in the summer of 2009 compared the separation and reattachment location indentified from S3F measurements with the suction surface pressure profile measured using pressure taps at a different spanwise location. The reattachment and separation location indicated by shear measurement agreed within several percent of the chord with the pressure tap data.

An objective of this research was to improve the way S3F is installed on curved surfaces. S3F has been installed to surfaces by spraying, gluing, and filling a cavity.

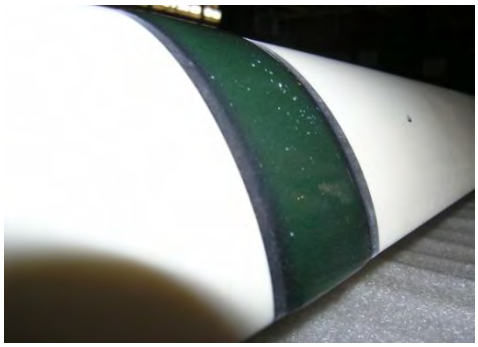

a.)

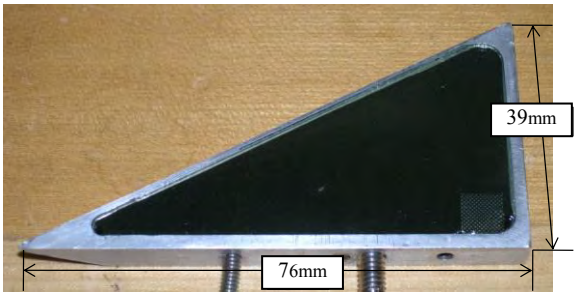

b.) [a.]

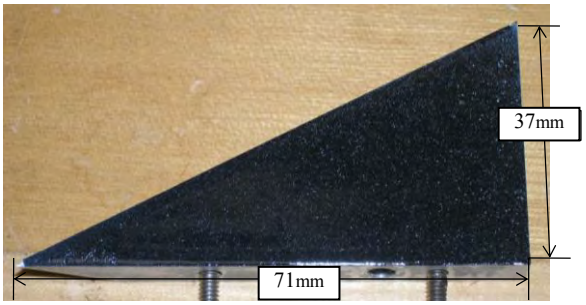

[b]c.)

Figure 2.17 Samples of S3F applied by a.) gluing to a surface , b.) filling a cavity, c.) spray-on with an airbrush.

Forming the S3F in a cavity has worked well, but is difficult when the surface is curved. To simplify installing S3F on curved surfaces, a new method has been developed and demonstrated. Rather than forming the S3F in a cavity on the curved surface, it is formed in a flexible flat plate prior to installation onto the airfoil. The flat plate is referred to as the S3F carrier. In our experiments the S3F carrier was rapid prototyped with a single cavity, then lightly sanded for a smooth fit into a cavity on the suction surface of the airfoil as is shown in the drawing of Figure 2.8 and the photo in Figure 2.18. The S3F carrier was painted black prior to being filled with S3F to reduce reflection of light. The S3F carrier was filled with S3F at ISSI Inc. then installed in the airfoil and held in place with two flat head screws near the trailing edge.

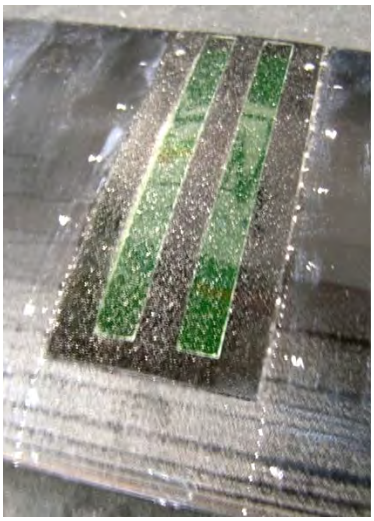

Figure 2.18 Example of S3F carrier filled and installed on Airfoil 2.

The S3F experimental arrangement is shown in Figure 2.13. S3F was installed along the suction surface of the E387 as was shown in Figure 2.7. Images were acquired with a commercial, high resolution CCD camera (PCO 4000) with a resolution of 4008 x 2680 pixels. A Nikkor 200 mm f4 lens with long pass filter was fitted to the camera and rigidly fixed to the wind tunnel test section. A Novatron flashlamp with flash-on time on the order of several hundred microseconds, and an ISSI Inc. high power LED lamp (460 nm wavelength) was used to illuminate the S3F. The Novatron flashlamp provided a high intensity light source, but repetition rate was limited to 0.33 Hz. The high power LED lamp can be operated in steady mode or high speed pulsed mode driven by an external signal generator and was used in the closed loop control experiments.

Images were transferred to CPU RAM over a high speed Cameralink interface (255 MB/s) via a NI PCIe-1429 image acquisition board. A Labview based software program controlled image acquisition and calculated film displacement using single pass cross-correlation. Frame rate (sampling speed) and exposure was controlled by a Quantum Composer 9300 Pulse generator. A slower, but potentially more accurate image analysis software program (ISSI Inc.) was available to calculate S3F displacement for comparison with the Labview based software.

2.4. **Sensor System**

A general description and background on the S3F method was given in Section 2.3.3. This section focuses on the use of S3F in a separation control system, specifically in the experimental conditions of this research.

2.4.1. System Design Considerations

S3F is naturally sensitive to both pressure gradient and shear stress, however; in low pressure gradients Crafton et al. showed that film tangential response is essentially uncoupled from pressure gradient (Crafton et al. 2008). This implies that tangential displacement itself can be used as a direct indicator of shear stress direction and magnitude. Exploiting the direct relationship between S3F tangential displacement and shear stress enables the use of S3F as a separation sensor. The data from an S3F sensor could be analyzed and used in a separation control system in several ways that will be discussed in later sections.

In this investigation the tangential S3F displacement is used directly as a separation sensor output signal. Several factors put a limit on sensor speed: illumination intensity, camera frame rate, image processing speed, film response, and experimental setup. The factors are not independent of one another.

Image processing speed was set by the system hardware and image processing algorithm. The camera frame rate was limited by image sensor resolution and magnification factor required to sense film displacement. A high resolution camera was required to achieve adequate film displacement, which had a maximum resolution frame rate of only 5 fps. The intensity of the pulsed light source set a minimum exposure time of approximately 40ms.

The determination of appropriate S3F material properties for a given application is a trade-off between film displacement, frequency response, and pressure gradient effects. Equation (2.3) implies that for a given surface load, thinner films have a higher response to shear stress than

pressure gradient. Thinner films also have a higher frequency response, but lower overall tangential film displacement. The optics system must provide a large enough magnification so that film displacement is detectable and uncertainty acceptable. In this proof of concept research effort the light source and camera were mounted external to the test article as shown in Figure 2.19. A better packaging concept for an S3F based sensor for flow control is currently being analyzed by ISSI Inc. Any useful sensor package for flow control will need to include an integrated method to measure film displacement rather than an external camera and light source. In this experiment, the length scale of the airfoil, target experimental Reynolds number, and properties of air required that a very sensitive S3F, with high magnification factor be used. Ultimately, a miniaturized version of the discrete skin friction sensor system similar to the description in Crafton et al. (2008) would be a more useful package when integrated into an aerodynamic surface. This type of sensor would be useful in a variety of aerodynamic systems, with potential for using thinner films, higher frequency response, and increased sensor sampling speed. Unfortunately a discrete, small form factor sensor package that would fit on an airfoil was not available in time for this research.

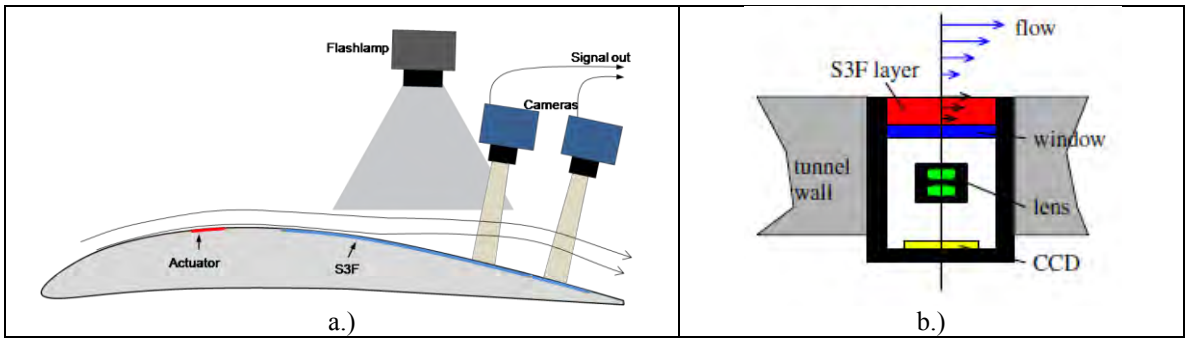

Figure 2.19 a.) Prototype S3F Separation Sensor used in current study. b.) Discrete S3F based skin friction sensor from Crafton et al. (2008)

The shear stress on the surface of the airfoil is low, on the order of 1 Pa. Figure 2.20 gives estimates of tangential film response for a 1 Pa shear stress with a 100 Pa/m pressure gradient over a range of S3F thicknesses and shear modulus calculated using Equation (2.3). The film must have an extremely low shear modulus (< 100 Pa) to provide adequate tangential

displacement on the order of 1 px. Ultra low shear modulus S3F refers to S3F with shear modulus approximately 100 Pa or less. A high resolution camera and high focal length lens was required to obtain a high image magnification factor. Image field of view height was on the order of 15mm, magnification factor >100 px/mm, and film thickness 0.9mm enabling measurement of displacements on the order of tens of microns.

Figure 2.21 shows S3F frequency response versus thickness and shear modulus. Ultra low shear modulus S3F has a frequency response as high as 500 Hz if thin films are used, and lower frequency response around 50 Hz if thicker films are used. Another factor that effects S3F instantaneous measurements is film response to load changes, and image exposure time. As exposure time increases the wind on image is capturing marker track over time rather than a crisp image of instantaneous marker position. A comparison of marker appearance with a 100ms exposure and 50 ms exposure is shown in Figure 2.22. The longer exposure time results in more markers blurring which adds noise to the cross correlation calculation and also potentially changing the cross correlation peak shape, affecting the accuracy of the peak finding method.

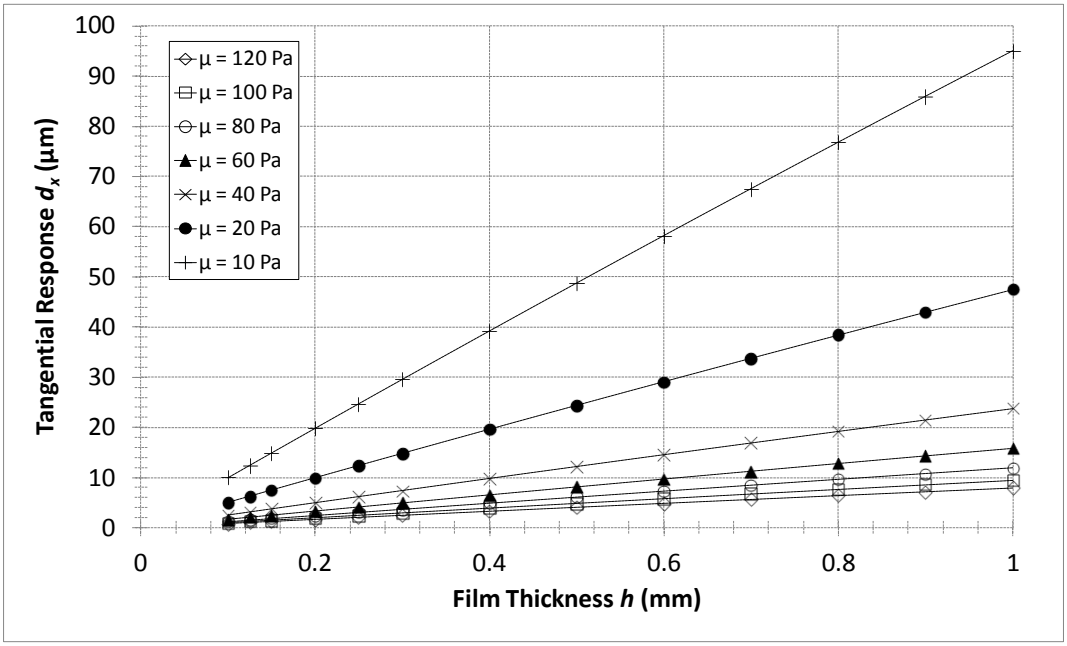

Figure 2.20 S3F tangential displacement for a 1 Pa surface shear stress and 100 Pa/m pressure gradient.

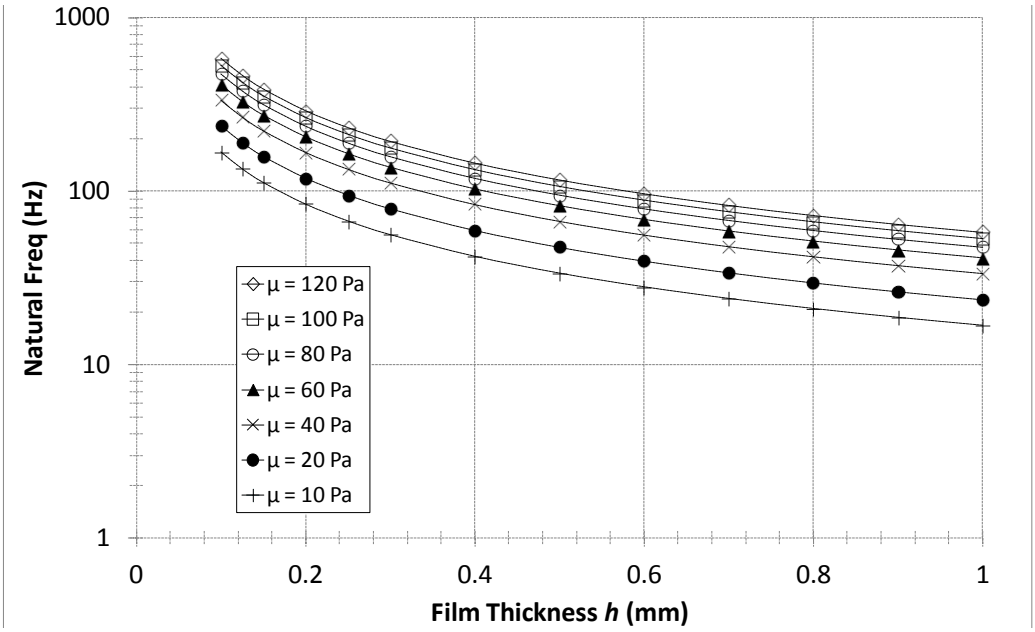

Figure 2.21. S3F frequency response.

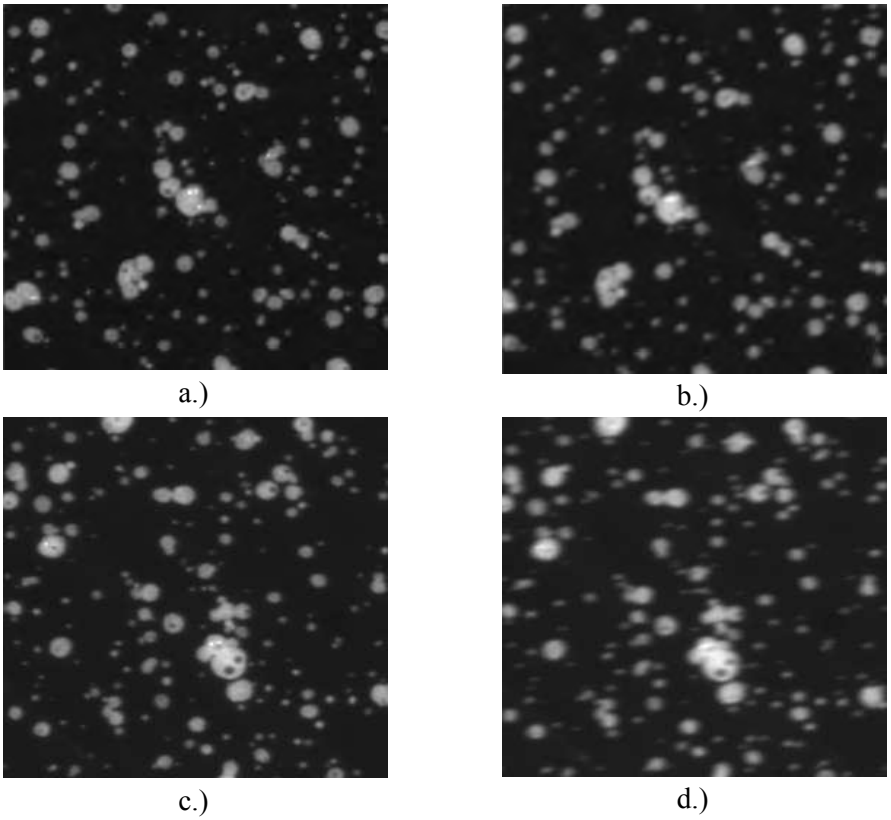

Figure 2.22 Effect of exposure time on image quality. Image a) wind-off, 50ms b.) wind-on 50ms c.) wind-off 100ms d.) wind-on 100ms

The S3F based separation sensor assumes that pressure gradient is low and the S3F tangential displacement is an indicator of surface shear stress direction and magnitude. In reality the pressure gradient over the surface of the airfoil also contributes to tangential film displacement introducing spatial error into the sensor signal. The error is dependent on film properties, pressure gradient, and shear stress. Figure 2.23 shows the error associated with assuming the film tangential displacement is linearly related to shear stress *only,* in the presence of a pressure gradient. β is the ratio of pressure gradient in Pa/m to shear stress in Pa. For thin films the error is below 10 percent even with a high pressure gradient to shear stress ratio. At higher film thicknesses, even a moderate loading ratio will result in significant local error.

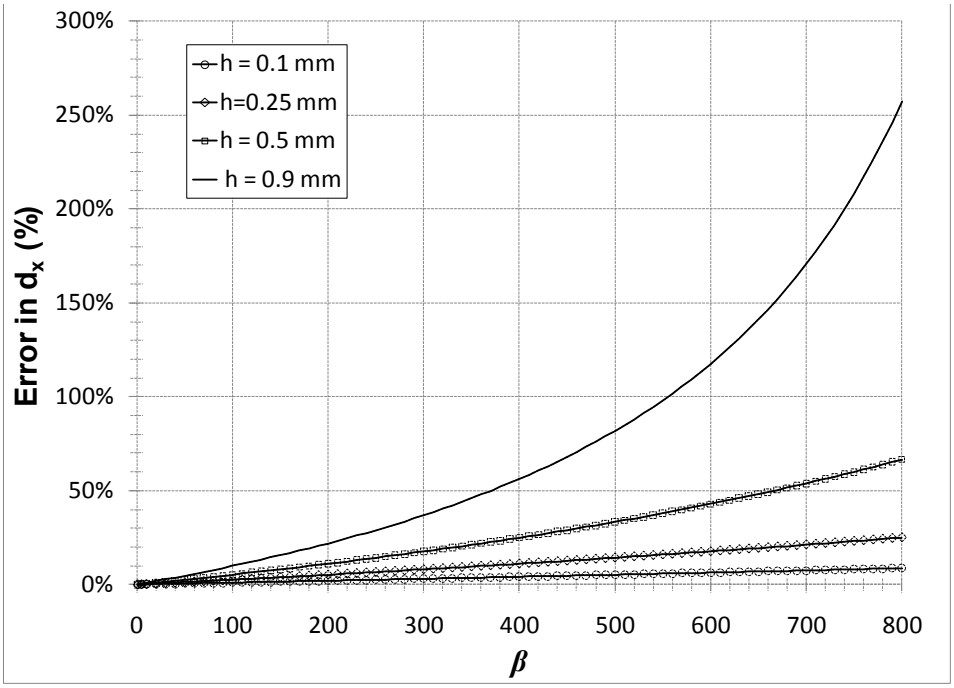

Figure 2.23. Error in tangential displacement when ignoring pressure gradient for various film thicknesses and shear stress.

2.5. Signal Analysis

Film tangential displacement is determined by calculating the shift of particles in the "wind-on" and "wind-off" images. Since the objective here is to use S3F as a separation control sensor

the image processing speed was essential. Two dimensional cross-correlation was chosen for its relative simple digital implementation and efficiency compared to other techniques.

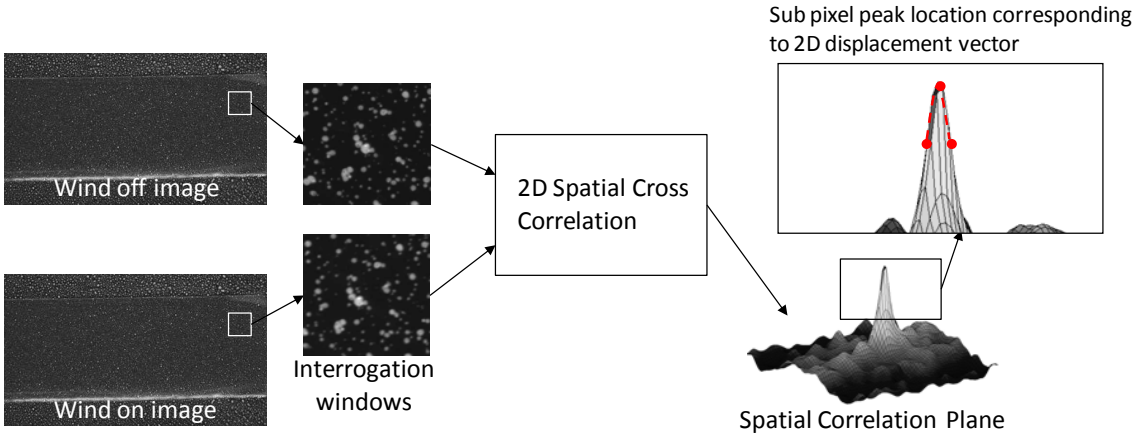

Figure 2.24 Two dimensional film displacement calculation using cross correlation.

The two images are divided into interrogation regions of size *N x N* each containing an adequate number of markers. Image correlation can be accomplished using statistical methods or frequency based methods. Frequency based methods are much quicker requiring $O[N^2 log_2 N]$ operations compared to $O[N^4]$ for statistical based methods (Raffel et al. 2007). Since processing speed was critical in this application frequency domain based cross-correlation was used.

In practice the frequency based process is outlined in Figure 2.25. The FFT of the two regions are calculated, complex conjugate multiplication of the two Fourier coefficients, then inverse FFT results in a cross-correlation plane. The plane has dimensions N x N equivalent to the original interrogation region.

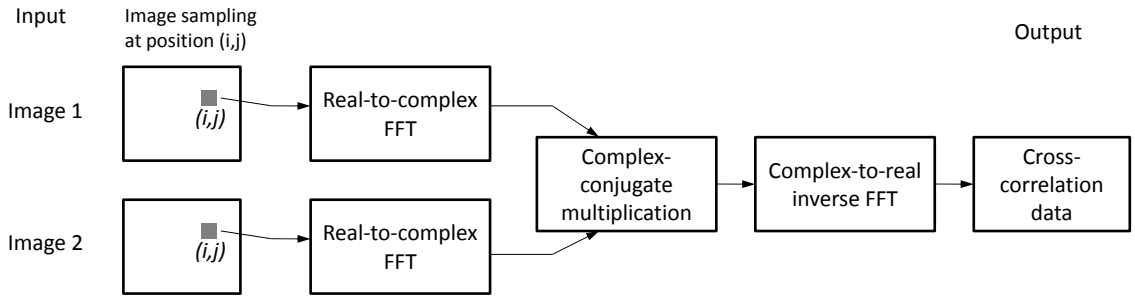

Figure 2.25 Implementation of cross-correlation using fast Fourier transforms (from Raffel et al. 2007)

The mean particle displacement is located at the maximum value in the correlation plane which is located at an integer value. Many methods have been proposed to locate particle displacement to sub-pixel accuracy. Displacement location to sub-pixel accuracy was achieved by using a three point Gaussian curve fitting function around the correlation peak (Willert and Gharib, 1991; Huang et al. 1997):

$$x = x_0 + \frac{\ln R_{x_0-1,y_0} - \ln R_{x_0+1,y_0}}{2 \cdot \ln R_{x_0-1,y_0} + 2 \cdot \ln R_{x_0+1,y_0} - 4 \cdot \ln R_{x_0,y_0}} \tag{2.5}$$

$$y = y_0 + \frac{\ln R_{x_0,y_0-1} - \ln R_{x_0,y_0+1}}{2 \cdot \ln R_{x_0,y_0-1} + 2 \cdot \ln R_{x_0,y_0+1} - 4 \cdot \ln R_{x_0,y_0}} \tag{2.6}$$

Several key system parameters significantly influence processing speed and accuracy. Most noticeably marker size and density places a bound on interrogation window size. Smaller interrogation window sizes result in a faster processing speed, but are only possible when SNR is high, and particle diameters and densities are appropriate. Increasing marker density increases the probability of valid displacement detection, and marker diameter affects displacement uncertainty with simulations indicating that diameters between 2-3 pixels are optimum (Raffel et al. 2007).

2.6. **Signal Preprocessing**

The additional processing times associated with multi-pass and other advanced processing techniques are not acceptable for the current study because of the additional time required to process the data with each additional pass. For this study only one pass is used, but several methods of improving the signal to noise ratio and reducing errors were evaluated: bias correction, thresholding, and correlation multiplication.

In order to better understand the impact of each of these signal enhancement methods 500 interrogation windows were analyzed. The interrogation windows were generated from a sample image of the fluorescent paint marker pattern taken with the same camera and optical

arrangement used in the actual experiments. Marker displacement was artificially generated by shifting one image a distance d_a in image processing software.

The mean bias error ε_b and RMS error ε_{RMS} were calculated. Bias error was calculated using:

$$\varepsilon_b = d_m - d_a \tag{2.7}$$

where d_m is the sample mean displacement, and d_a is the actual displacement. The RMS error was calculated as the standard deviation of the sample displacements:

$$\varepsilon_{RMS} = \sqrt{\frac{1}{N}\sum_{i=1}^{N}(d_i - d_m)^2}\,. \tag{2.8}$$

Sources of mean bias error include systematic errors having to do with the calculation of displacement vectors, such as inadequate curve fit for sub-pixel peak detection. This type of error is systematic. Random errors are due to a number of factors such as improper marker distribution, non-uniform illumination and reflection from markers, and camera noise (Huang et al. 1997).

The use of Fourier transforms assumes the signal is periodic, when in reality it is not. Bias correction corrects for the assumption of periodicity. As the wind-on image is shifted in relation to the wind-off (template) image, only a fraction of the signal contributes to the actual correlation value resulting in displacement biased to a lower magnitude. This can be overcome by applying a weighting function to the correlation plane. The method outlined in Raffel et al. (2007) was used to correct for bias. A weighting function was generated by convolving the image sampling function with itself. The weighting function was then divided out of the correlation plane. Correcting for bias in the correlation plane increased the mean displacement decreasing the overall mean error with little effect on the RMS error. Bias correction was used in the signal analysis code because of the reduction in error with little additional processing time.

Thresholding of the image signal was accomplished by defining a lower threshold value τ, and regions of the image that were below the threshold were forced to zero. The main objective of thresholding is to remove background noise from the images. In addition to removing

background noise, large markers with smaller signal values were effectively decreased in size, essentially acting as a filter. Increasing threshold value reduced the RMS error at values above d_a = 0.5 px, but the trend was little to no improvement in mean bias error.

Correlation multiplication (Hart et al. 2000) involves multiplying the correlation planes of two adjacent, partially overlapped interrogation windows. As long as the displacement gradient is small, this multiplication has the effect of reducing noise and amplifying the correlation peak. For this simple investigation two adjacent correlation planes offset by 50% were multiplied with each other. The calculation of an extra correlation plane has the negative impact of essentially doubling the time it takes to calculate one displacement vector.

Single pass correlation of 500 interrogation windows with markers artificially shifted provides an estimate of the uncertainty due correlation calculation. Figure 2.26 compares the effect of thresholding, correlation multiplication, and a combination of thresholding and correlation multiplication with a standard 2D cross-correlation. Correlation multiplication by itself shows a definite improvement in mean bias error at all sub-pixel displacements, and a bias towards lower magnitudes at displacements larger than one pixel compared to the baseline. Correlation multiplication decreases the RMS error, and in combination with thresholding decreases the RMS error by 50% or more at displacements greater than one pixel. For sub-pixel marker displacement thresholding resulted in a decrease in RMS error, but an increase in mean bias error.

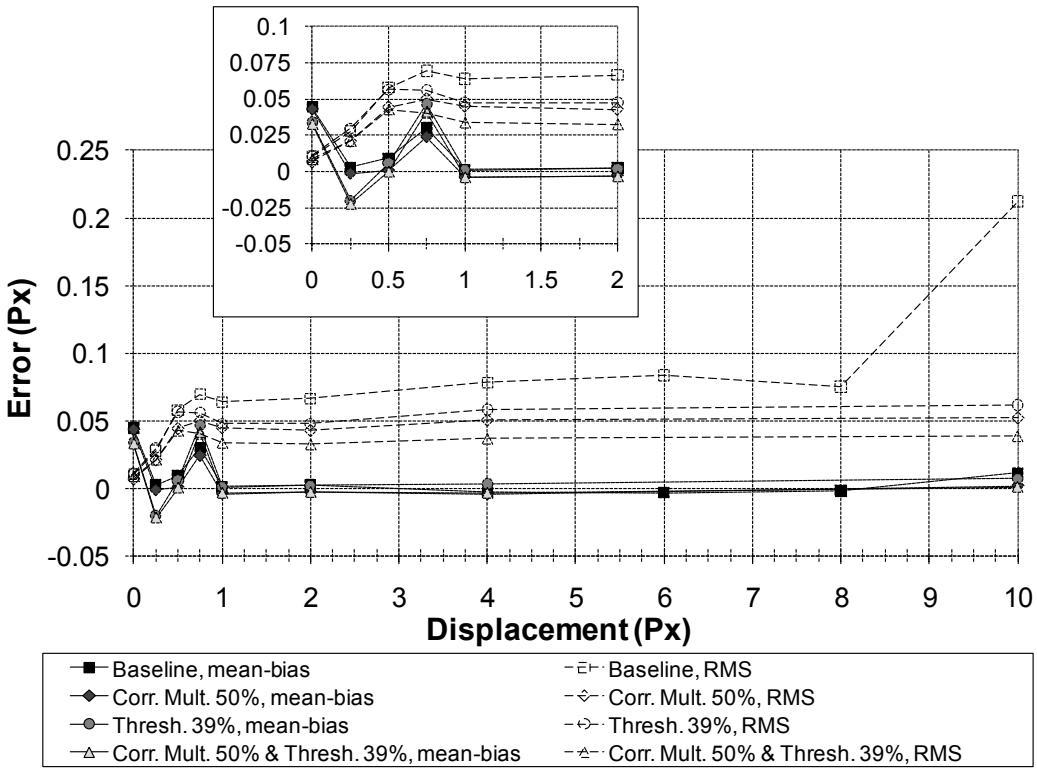

Figure 2.26 Comparison of noise reduction processing techniques.

The plot of Figure 2.27 gives mean and RMS error for subpixel and integer marker displacement using correlation multiplication which is equivalent to the method used in the separation control system software. Peak error is at sub-pixel displacement with nearly 9% ε_{rms} and 3.2% ε_b. Both types of errror significantly decrease as displacement increases up to a marker displacement of 10 pixels.

Figure 2.28 compares error in the displacement calculation using two different correlation window sizes. RMS error is higher for the smaller interrogation windows size. Bias error is higher for the larger interrogation window size at sub-pixel displacement, with comparable, very small amount of error at integer displacements.

Other sources of error in the displacement calculation include airfoil movement relative to the camera. Airfoil motion was compensated for by calculating the displacement of markers just above and below the S3F. The top and bottom region of markers were rigidly fixed to the airfoil. The displacement of the airfoil itself was subtracted from the calculated S3F displacement along

the midspan using 2D interpolation. An investigation into the uncertainty associated with correcting for airfoil movement was undertaken by installing a flat plate with markers into the cavity of the airfoil in which the S3F carrier was installed. Images of marker displacement with the wind tunnel on were recorded and displacement analyzed using ISSI Inc. hybrid cross correlation/optical flow software, then correcting for displacement using the method described above in Matlab. Marker displacement after correction for airfoil motion should have resulted in zero displacement. The analysis indicated that second order curve fits of airfoil motion in the streamwise direction worked better than linear or third order curve fitting. First order curved fits were used in the spanwise (vertical) direction. Analysis indicated a mean displacement error of approximately +/- 0.015 pixels could be obtained using averages of 25, 50, and 100 images. This is an estimate of the accuracy of the airfoil rotation correction method.

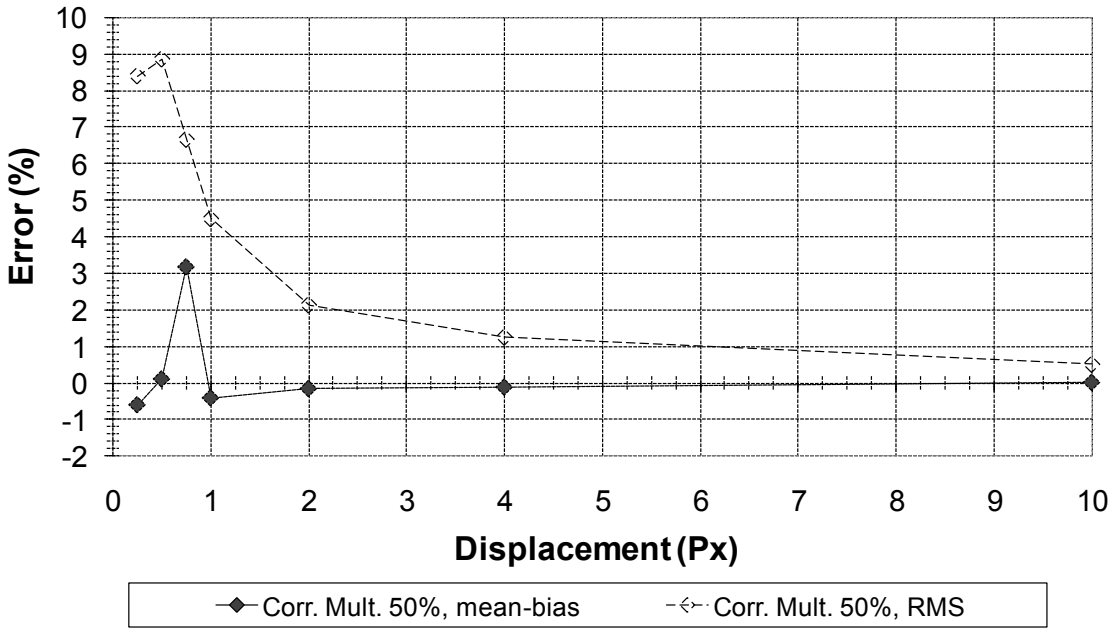

Figure 2.27 Percent error of single pass correlation using correlation multiplication with 50% overlap.

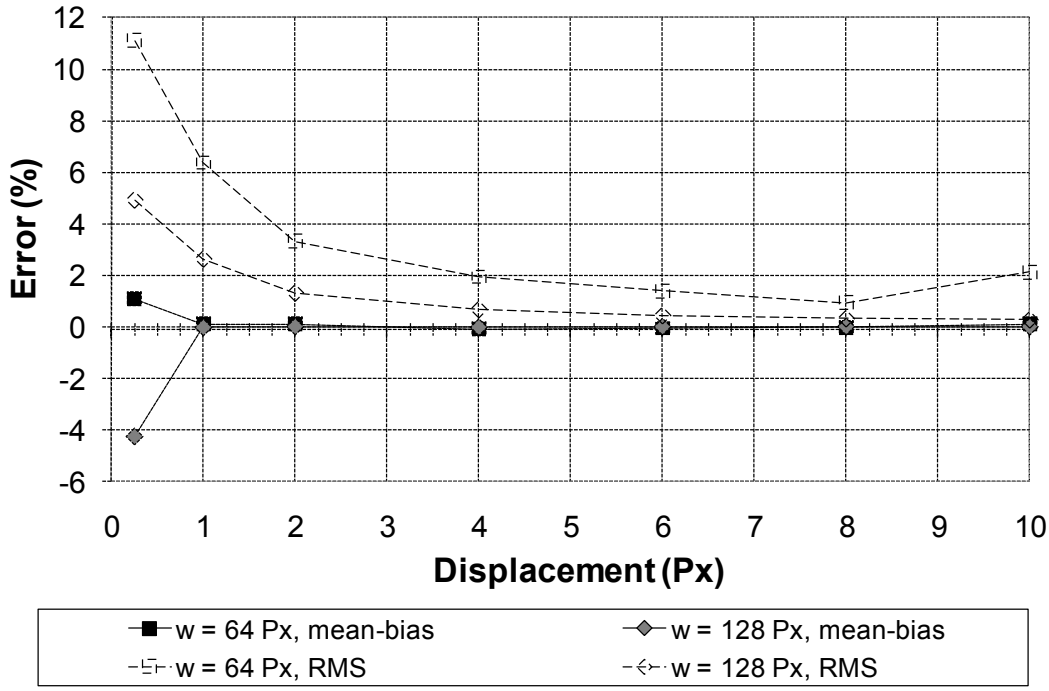

Figure 2.28 Comparison of error in displacement calculation using single pass cross correlation for two different interrogation region sizes.

2.7. Separation Control System Software

A custom LabVIEW virtual instrument was developed to read and analyze images of the S3F, record wind tunnel conditions, send plasma actuator control signals, and execute the closed loop separation control system logic. The film tangential displacement was calculated using frequency domain, single pass cross correlation described in Sections 2.5 and 2.6. A screenshot of the Labview separation software GUI is shown in Figure 2.29, and a top level system diagram of the system is shown in Figure 2.30.

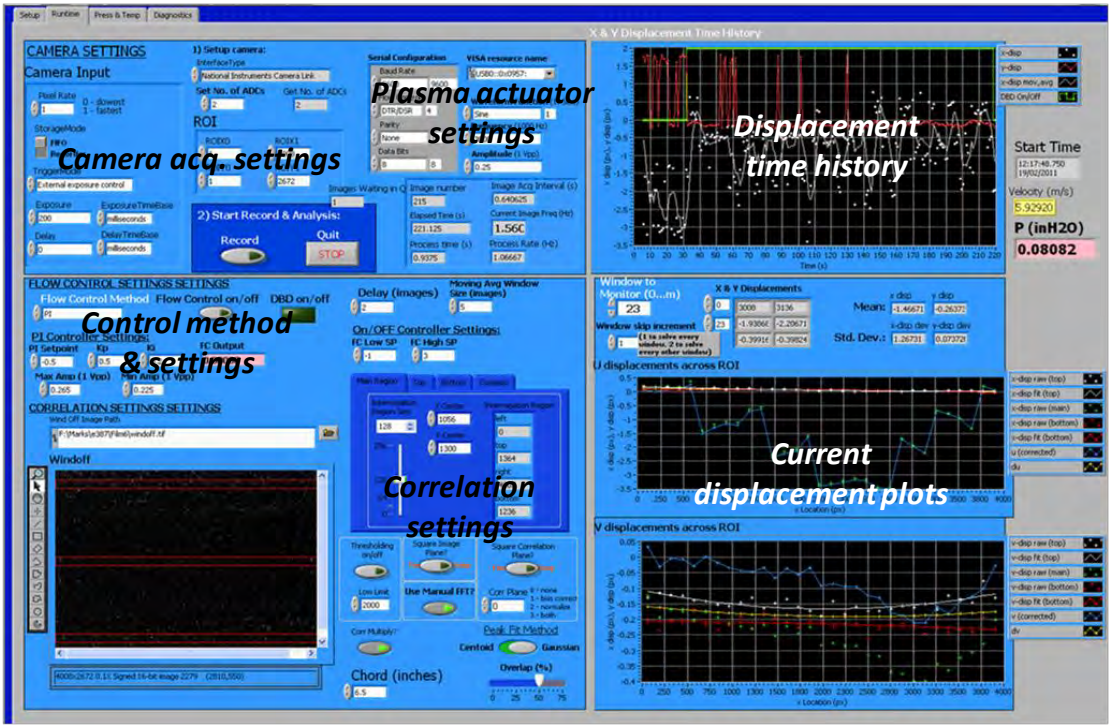

Figure 2.29 Screenshot of Separation Control Software GUI.

The software GUI can be described as having seven different functional areas. Each area is labeled in Figure 2.29 with the exception of the screen in which the pressure transducer and thermocouple data acquisition parameters are input. The region labeled *Camera acq. settings* is where PCO camera specific parameters such as region of interest, exposure control, and number of ADCs, are input. *Plasma actuator setting* is the region where variables associated with the plasma actuator signal are input. The control method and variables associated with each particular control method are contained in the area labeled *Control method and settings.* *Correlation settings* contains input parameters for the cross correlation method and correction methods, such as interrogation region size, and regions of interest settings. On the right side of the screen are plots that are updated in real time after each calculation of film displacement. The top plot is the time history of film displacement at the monitoring point. The bottom plot is film displacement across the entire view, at the top, bottom, and middle regions of interest. The data displayed in each plot is saved to the hard drive after each run.

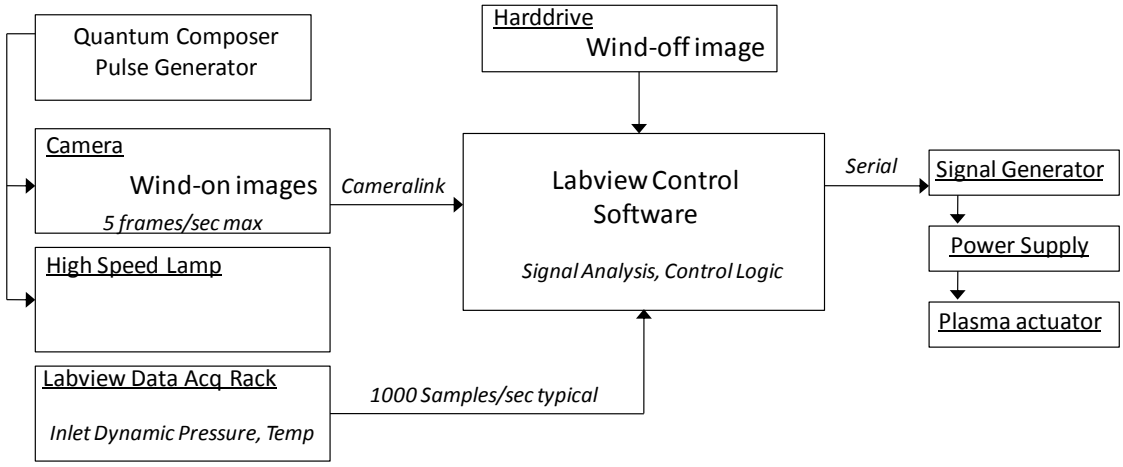

Figure 2.30 Top level system diagram.

The top level system diagram shows signal sources, paths, and interaction between the equipment used in the separation control system. A flow chart of command and control system logic pertaining to control of the plasma actuator executed during each time step is shown in Figure 2.31. Two different control methods were implemented in the code: On/off control and PI control. The wind-off image is recorded prior to execution of the separation control code. Upon execution of the separation control code, and during initialization of variables, the regions of interest in the wind-off image are loaded into computer RAM. This occurs only once during initial execution of the software. The wind-on images are transferred to the computer immediately after each exposure using camera FIFO protocol via a high speed Cameralink interface. A high resolution PCO 4000 scientific camera that has 4008 x 2600 pixel CCD image sensor was used in the experiments to obtain high magnification rates required to detect film displacement. While the PCO 4000 provided high resolution, low noise data, the features of the camera limited frame rate and processing speed. Data representing each image was large and can only be transferred to computer RAM as 16 bit data. The camera had the ability to only record a portion of the image sensor array by defining one region of interest. Because the motion of the airfoil relative to the camera needs to be calculated and corrected for during each exposure, three different regions of interest were required: a top region just above the S3F, a middle region

along the mid span of the S3F, and a bottom region just below the S3F. Since only one region of interest can be designated with the PCO 4000, the full image data was transferred to the computer RAM upon each exposure. The use of a high resolution camera with the ability to transfer 8bit image data and multiple regions of interest, rather than the entire image, would increase the sampling rate over the system described and used in this work.

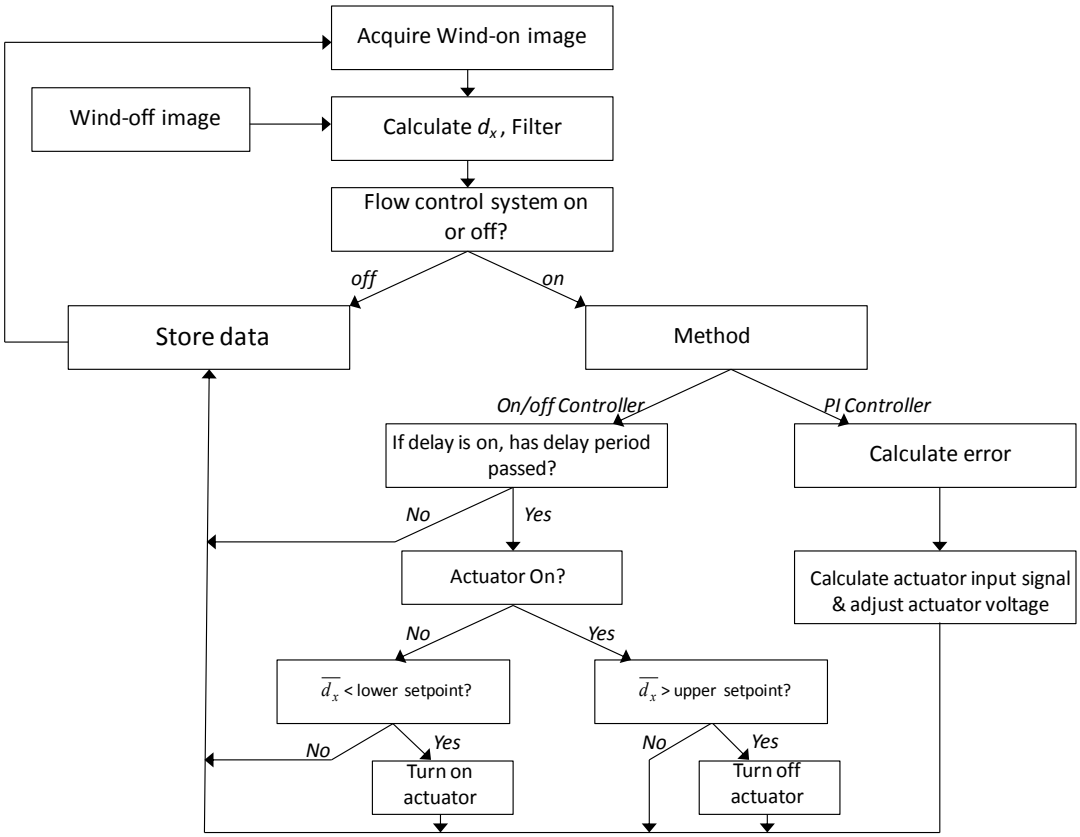

Figure 2.31 Command and control system software flow chart.

Sampling speed was limited by the experimental setup and hardware, ultimately set by the high resolution camera and illumination requirements to approximately 3 Hz. Sampling rates were typically kept to 0.5-2.5 Hz and were sufficient for experimental setup and control method used. The most appropriate way to increase the sensor system speed is by creating a miniature discrete sensor package similar to Figure 2.19b which would improve system speed by:

1. Increasing the frame rate by using lower resolution image sensors
2. Eliminate the need for airfoil/camera motion correction

3. Decrease the illumination intensity required.

In addition, a real time processor using GPUs optimized to perform the FFTs required for cross correlation would increase processing speed and allow the use of more accurate multi-pass algorithms that achieve higher accuracy.

Figure 2.32 shows a typical mean displacement field near the suction surface trailing edge calculated by both the ISSI Inc. software which uses a hybrid optical flow/cross correlation method, and by single pass cross correlation. The ISSI Inc. image processing algorithm uses phase correlation to estimate displacement to an integer value, and then an optical flow based method to estimate the displacement to sub integer (pixels) levels (Fonov et al. 2004). It was reported that the hybrid approach is similar to the method proposed by Cheng-Yuan et al. (1998) (Fonov et al. 2004). At a Reynolds number of Re = 1.0 x 10^5, Figure 2.32 clearly shows a reattachment region with a definite zero crossing location at approximately C_x=94% using both image analysis techniques. The hybrid optical flow/cross correlation method results in larger overall displacement magnitude and a more continuous signal when displacements are small near the zero crossing point. The smoother displacement signal calculated by the hybrid optical flow/cross correlation software is not surprising due to a multi-pass approach and spatial filtering. The mean biasing is evident in the single pass cross correlation signal in regions of near zero displacement. At the lower Reynolds number, peak displacement of the single pass cross correlation agrees well with the ISSI Inc. software calculation, but between 83% C_x and 94% C_x where the displacement is near zero, the single pass cross correlation method results in a signal that oscillates about zero. S3F in a filled cavity will show edge effects in an area approximately three to four film thicknesses from the edges (Crafton et al. 2008), and the edge of this region has been highlighted with a dark dashed line in Figure 2.32.

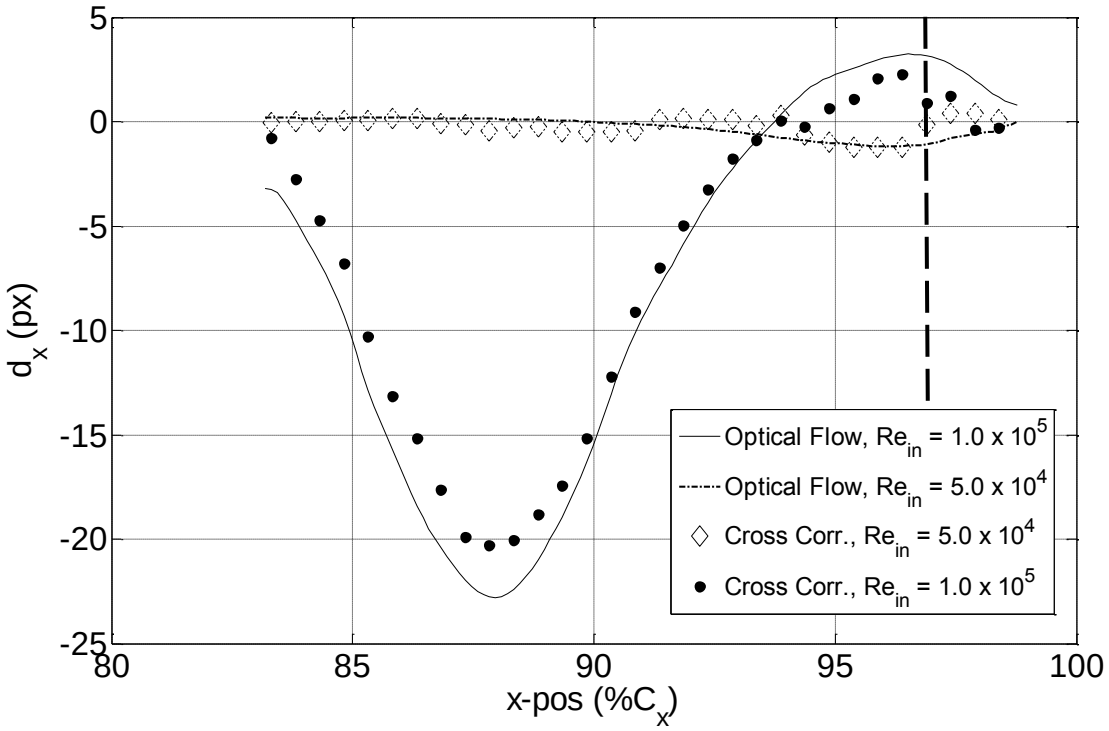

Figure 2.32. Comparison of mean streamwise displacement, ε = 200ms, Fs=1 Hz, correlation multiplication on.

S3F #6 had an estimated first natural frequency of 16 Hz, meaning signals at frequencies greater than twice the natural frequency would be significantly filtered out. Depending on damping characteristics, the film could also oscillate if loaded at a frequency near the natural frequency. Film displacement was also dependent on exposure time since longer exposure resulted in larger particle blurring as is seen in the raw images of Figure 2.22. A comparison of mean displacement field with exposure times of 50ms – 200ms is shown in Figure 2.33. The longer exposure time resulted in an 8% increase in peak displacement at an exposure of 200ms versus 50ms. The zero crossing location varied by less than 0.5%C_x, but the longer exposure image crossed zero at more than one location, indicating larger error in the correlation calculation. This could be due to mean bias error due to inadequate sub-pixel peak fitting. A minimum exposure time of 40ms was used for flow control experiments because it provided adequate marker illumination with the high speed S3F LED lamp.

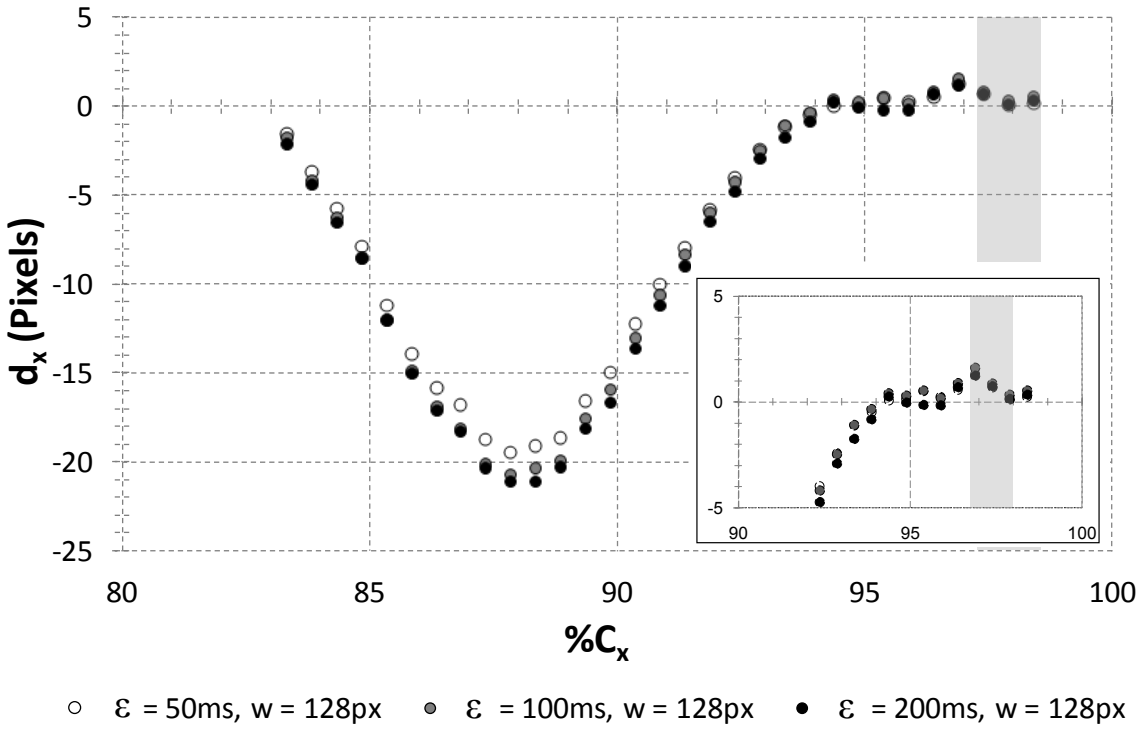

Figure 2.33 Effect of exposure time on calculated mean displacement, Re = 1.0x10^5, 100 samples using single pass cross correlation.

3. Airfoil Characterization

Airfoil characterization involved determining the behavior of the unmodified and modified airfoils in the AFRL/RZ low speed wind tunnel. This was accomplished by comparing suction surface C_p, drag, and PIV images with data from other facilities. Suction surface C_p was measured on the unmodified Airfoil 1 to determine an angle of attack that produced laminar boundary layer separation. The criteria for choosing angle of attack were:

- low angle of attack to minimize flow blockage
- laminar separation with and without reattachment in the Reynolds number ranged studied ($1.5 \times 10^5 - 5 \times 10^4$).

Included in this chapter are the experimental measurements on each airfoil and a comparison of PIV measurements on a clean version of Airfoil 2 compared with S3F installed on Airfoil 2.

3.1. Airfoil 1

The objective of this baseline dataset was to obtain the pressure coefficient on the suction surface of the rapid prototyped model and compare it with inviscid distribution to identify approximate separation and reattachment locations. Data was taken at angles of attack between 2.5° and -1.5° in order to determine an angle of attack that resulted in a laminar boundary layer separation on the suction surface.

Suction surface pressure coefficients at various low angles of attack are presented in Figure 3.1 - Figure 3.5 at Reynolds numbers of 1.5×10^5, 1.4×10^4, and 6.0×10^4. Experimental results measured in the AFRL/RZ DWT compared to XFOIL inviscid solution, and experimental measurements by McGhee et al. (1988) taken in the NASA Langley low turbulence wind. For angles of attack in which no NASA experimental data was available, the closest angle of attack to that used at AFRL was included in the plot for reference. The XFOIL airfoil analysis code was

used to obtain inviscid surface pressure distributions to compare with measured surface pressure coefficients. XFOIL was developed by Mark Drela of MIT in 1986. It is an open source airfoil design and analysis software capable of inviscid or viscous solutions. The inviscid solution uses a linear-vorticity stream function panel method in which the equations are closed with an explicit Kutta condition. Karman-Tsien compressibility correction is included, valid up to sonic conditions (Drela and Youngren 2001).

Figure 3.1 and Figure 3.2 show the suction surface pressure distribution at small angles of attack with Re = 1.0 x 10^5 and Re = 6 x 10^4. The laminar boundary layer separation is evident by the plateau in pressure coefficient in the area of C_x = 45-55%. The separation point moves upstream as angle of attack is increased. At the higher Reynolds number of 1.0 x 10^5 the boundary layer reattaches at angles of attack greater than -1.5°. As angle of attack increases the reattachment point moves upstream.

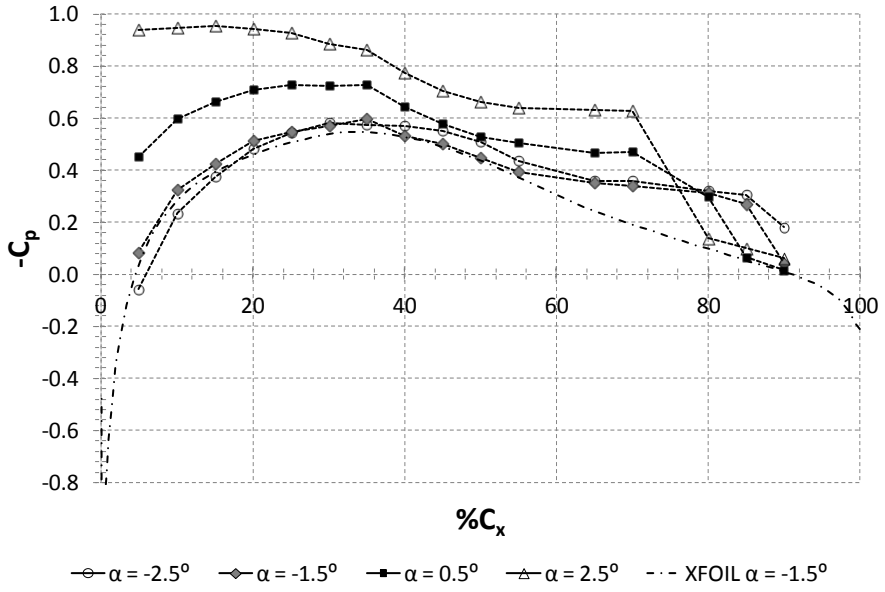

Figure 3.1 Suction surface C_p at small angles of attack, Re = 1.0 x 10^5.

At the lower Reynolds number of 6 x 10^4 the boundary layer separates in the area of C_x = 45-55% with the separation point moving upstream as angle of attack increases. The boundary layer does not appear to reattach until angles of attack larger than 0.5°.

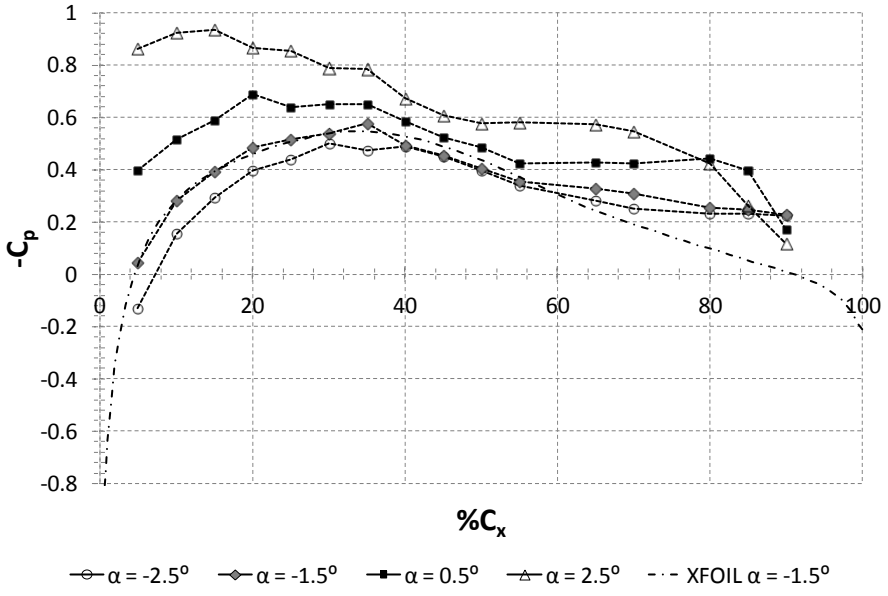

Figure 3.2 Suction surface C_p at small angles of attack, Re = 6 x 10^4.

Figure 3.3 compares data taken in the AFRL/RZ LSWT facility Developmental Tunnel with measurements in the NASA Langley wind tunnel from McGhee et al. (1988) at a Re = 1.0 x 10^5. In general, the loading was higher in the AFRL/RZ DWT and closer to the inviscid loading predicted in XFOIL, except in the region of laminar boundary layer separation.

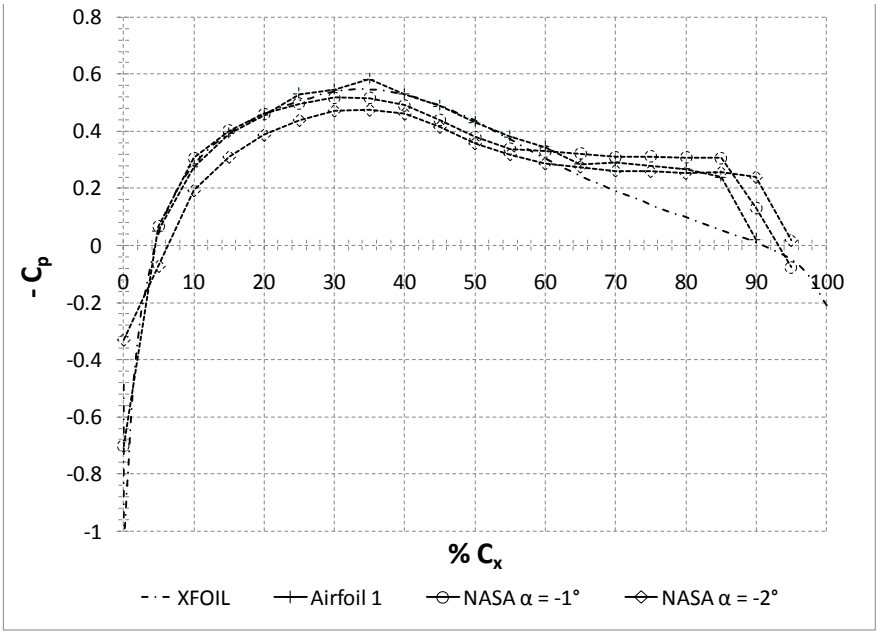

Figure 3.3 Comparison of NASA Langley measurements compared with AFRL/RZ LSWT measurements at α = -1.5°, Re = 1 x 10^5.

Figure 3.4 compares data taken in the two facilities at a Reynolds number of 1.0 x 10^5. The trend is similar to the lower Reynolds number data. The AFRL/RZ DWT data has a higher loading than the data from McGhee et al. The data taken in the DWT has lower loading than predicted in XFOIL, but higher than the data in McGhee et al.

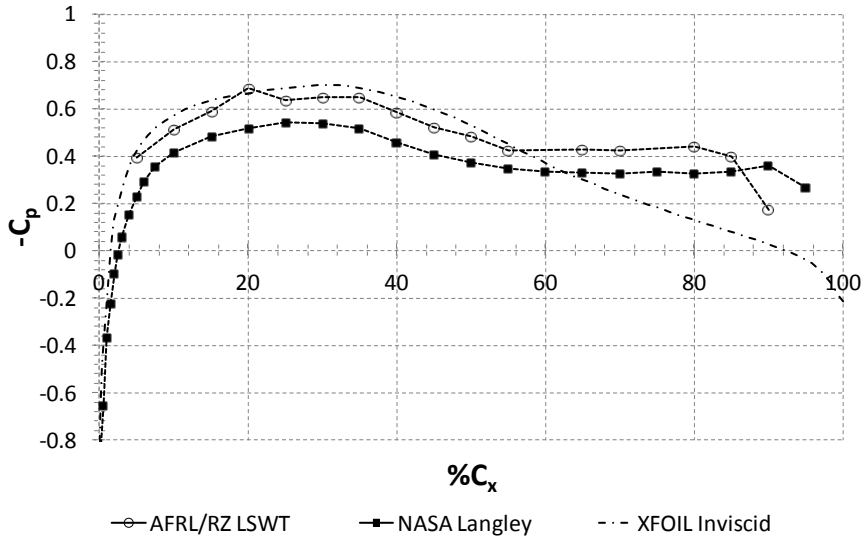

a.) α = 0.5°

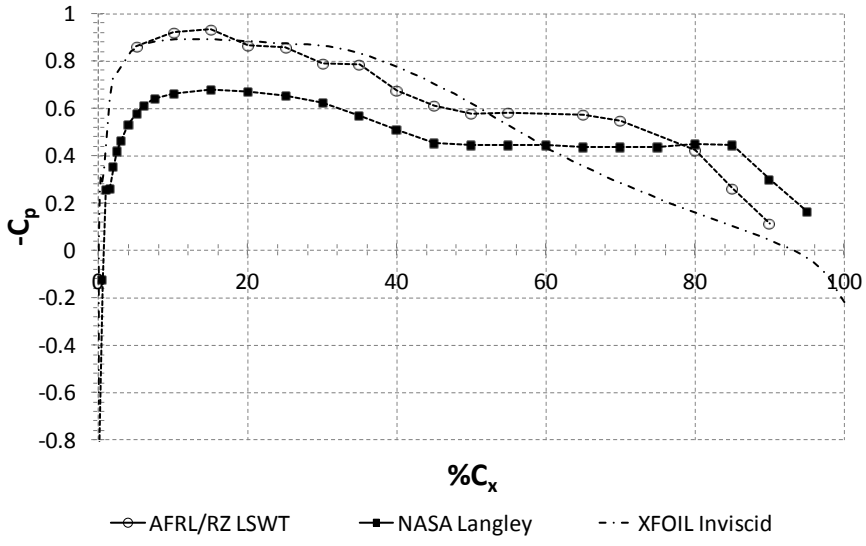

b.) α = 2.5°

Figure 3.4 Suction surface pressure distribution compared to NASA Langley at Re = 6.0 x 10^4 and small angles of attack.

The pressure distributions are obviously effected by boundary layer separation and deviations from the inviscid profile were used to estimate separation and reattachment locations (listed in Table 3.1). The pressure coefficient measurements on Airfoil 1 were jagged and not smooth along the chord. This was most profound at C_x = 20% and 35%. Testing indicated that this variation was not due the sampling period, as the measurements were repeatable. It is assumed that the measurement anomalies were due to irregularities at the pressure ports or the internal pressure tubing.

The baseline C_p data indicated that an angle of attack of -1.5° would provide the desired boundary layer behavior on the suction surface: the presence of a separation bubble at Reynolds number of 1.0 x 10^5, and separation without reattachment at a Reynolds number of 6.0 x 10^4. These two conditions allowed ample testing of the separation control system, both in an open loop configuration, and a closed loop configuration.

Table 3.1. Summary of approximate separation reattachment location on Airfoil 1 based on C_p measurements.

Reynolds Number	Angle of attack	Approx. separation location (C_x)	Approx. reattachment location (C_x)
1.0 x 10^5	-1.5°	55%	90%
6.0 x 10^4	-1.5°	55%	None

Figure 3.5 shows the suction surface pressure coefficient on Airfoil 1 over a Reynolds number range of 1.5 x 10^5 to 6 x 10^4, and α = 1.5°. The plot shows that the separation point does not move significantly with Reynolds number, but reattachment moves upstream as Reynolds number increases. Airfoil loading increases as the Reynolds number increases and the extent of separation is reduced.

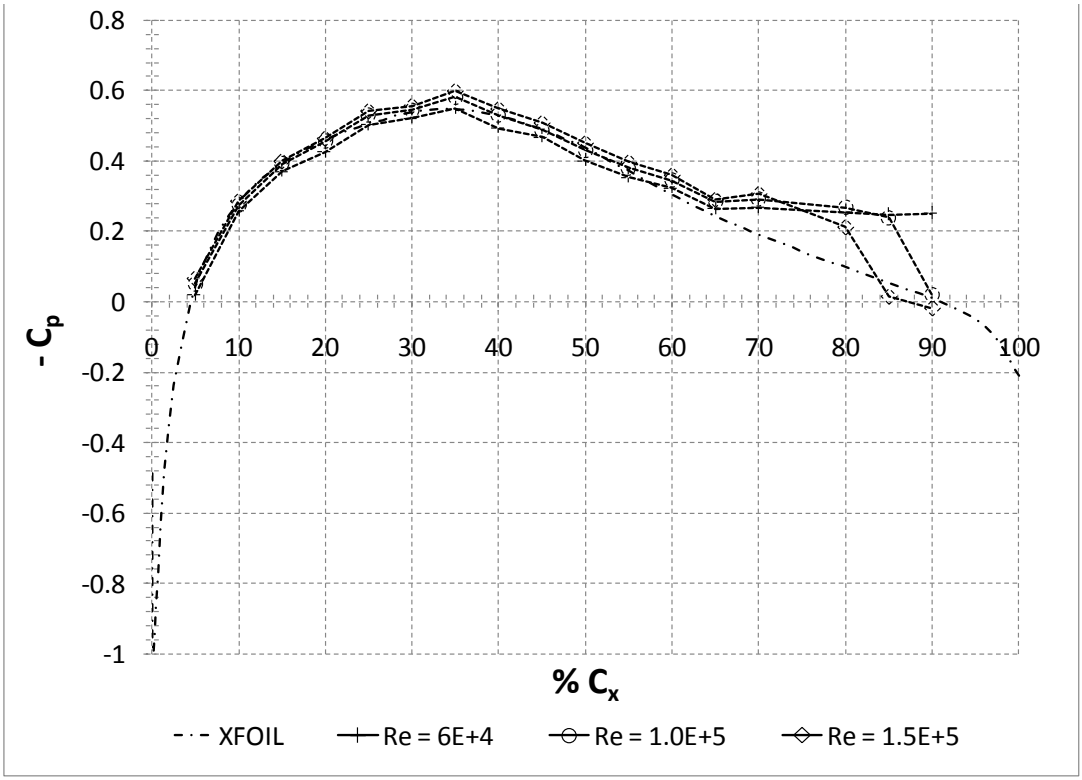

Figure 3.5 Airfoil 1 suction surface C_p at α = -1.5° and various Reynolds numbers.

3.2. **Airfoil 2**

The airflow around Airfoil 2 was expected to be different than Airfoil 1 due to the addition of pressure lines along the pressure side of the airfoil. In this section C_p measurements are compared to the measurements of Airfoil 1 in the AFRL/RZ DWT facility. Drag measurements between Airfoil 1 and Airfoil 2 are compared with measurements in other facilities, and PIV over the suction surface of Airfoil 2 with and without S3F installed is compared.

3.2.1. C_p measurements

C_p measurements over the suction surface of Airfoil 2 at Reynolds numbers of Re=1.5x10^5, 1.0x10^5 and 6x10^4 are show in Figure 3.6. This data was obtained with a "clean" airfoil, meaning that no S3F or plasma actuators were installed. A flat plate was installed in the cavity in which S3F is typically installed. The inviscid suction surface profile is shown as well for comparison.

The peak loading at each Reynolds number is higher than the inviscid profile. Airfoil 2 Cp data is smoother along the chord direction than was observed in Airfoil 1. As Reynolds number decreases peak loading on the suction surface decreases, resulting in a decrease in lift. At each Reynolds number laminar flow separation occurs at approximately C_x=55%. Reattachment points vary for each Reynolds number tested. At the highest Reynolds number the reattachment point is at C_x = 85%. After the reattachment point the pressure coefficient again plateaus and deviates from the inviscid value indicating either separation at the trailing edge or erroneous data. This phenomenon did not occur on Airfoil 1. At a Reynolds number of 1.0×10^5 the plateau beginning at C_x=55% is sharp with transition in the area of C_x=80%, then recovering to the inviscid profile at C_x=90%. At the lowest Reynolds number the boundary layer separates, but it is unclear whether reattachment occurs near the trailing edge due to lack of pressure taps beyond C_x=90%.

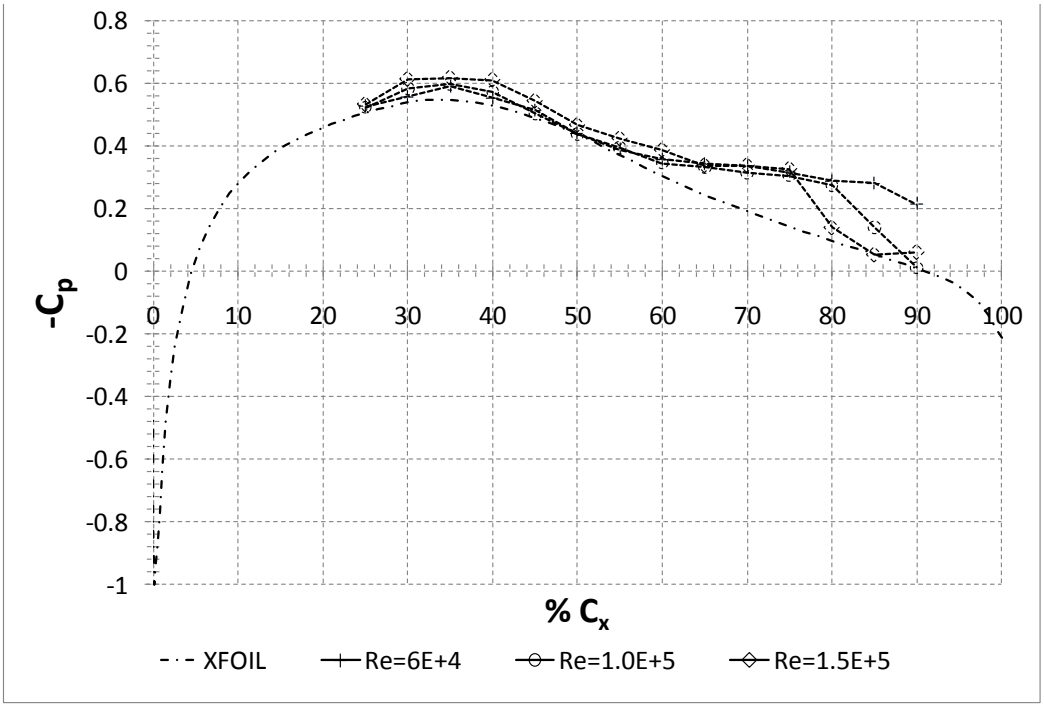

Figure 3.6 Airfoil 2 suction surface C_p at various Reynolds numbers.

The comparison of Airfoil 1 and Airfoil 2 shown in Figure 3.7 indicates that the laminar separation of Airfoil 2 is different than Airfoil 1, both in transition and reattachment location. It is difficult to determine from the C_p plots exactly where the separation and reattachment points

are, but it appears Airfoil 2 separates slightly upstream from the Airfoil 1 separation point with a higher peak loading. Both airfoils reattach by C_x = 90% with Airfoil 2 transitioning further upstream.

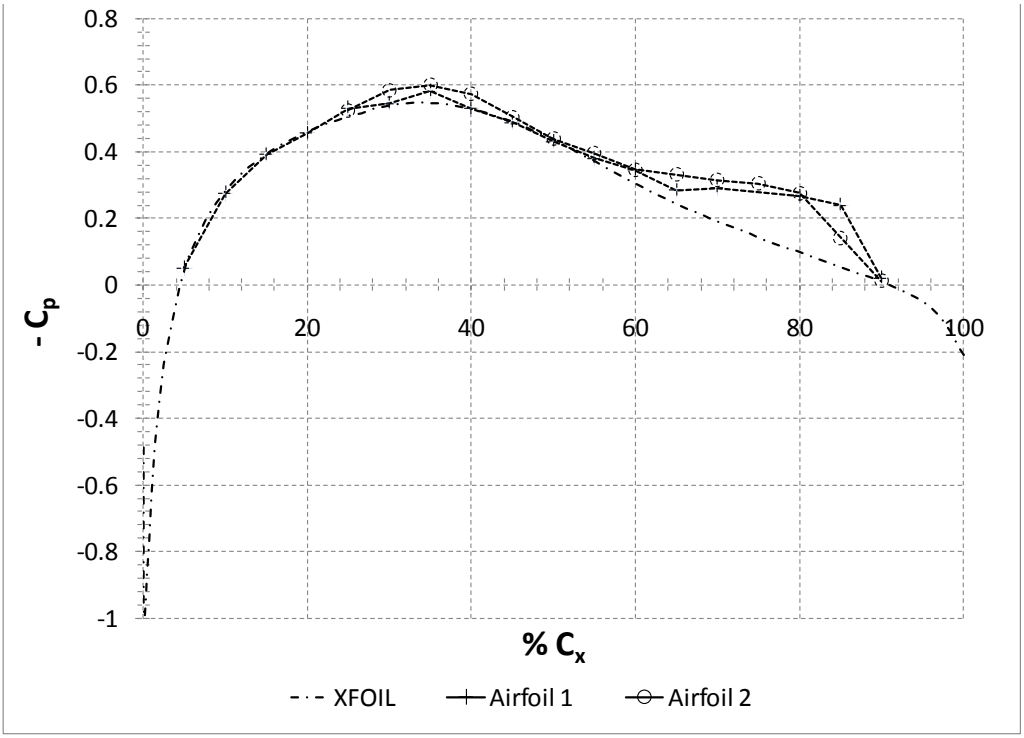

Figure 3.7 Comparison of Airfoil 1 and Airfoil 2 suction surface C_p at Re = 1.0x10^5.

3.2.2. PIV – No S3F Installed

Baseline PIV was taken on the modified airfoil with a flat plate installed in the S3F mounting cavity as shown in Figure 3.8. Data was taken at three different inlet Reynolds numbers: 1.5x10^5, 1.0 x 10^5, 6 x 10^4. Data shown here were taken with four different camera views and assembled together into one plot extending from approximately 42% C_x to 100% C_x. Each individual view had a magnification factor of 54.85 px/mm resulting in a 29.2 x 21.9mm field of view. A minimum of 250 images were used to calculate the mean flowfield.

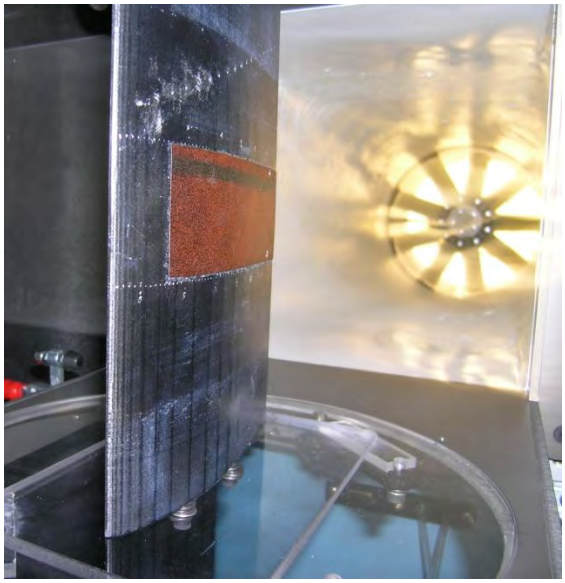

Figure 3.8 Flat plate mounted in the S3F cavity of Airfoil 2.

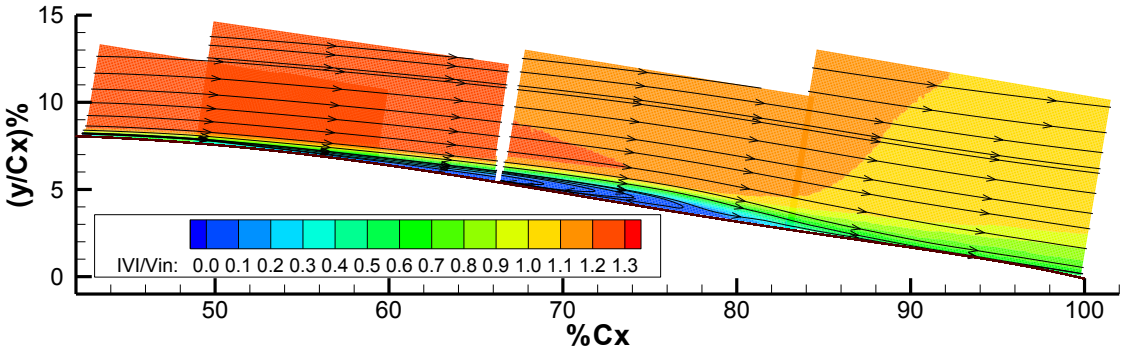

Figure 3.9 Airfoil 2, Flat plate installed, Re = 1.5 x 10^5

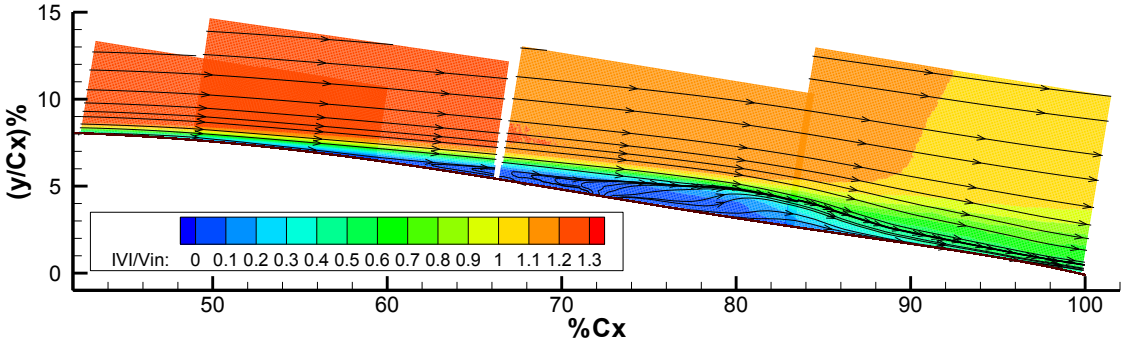

Figure 3.10 Airfoil 2, Flat plate installed, Re = 1.0 x 10^5

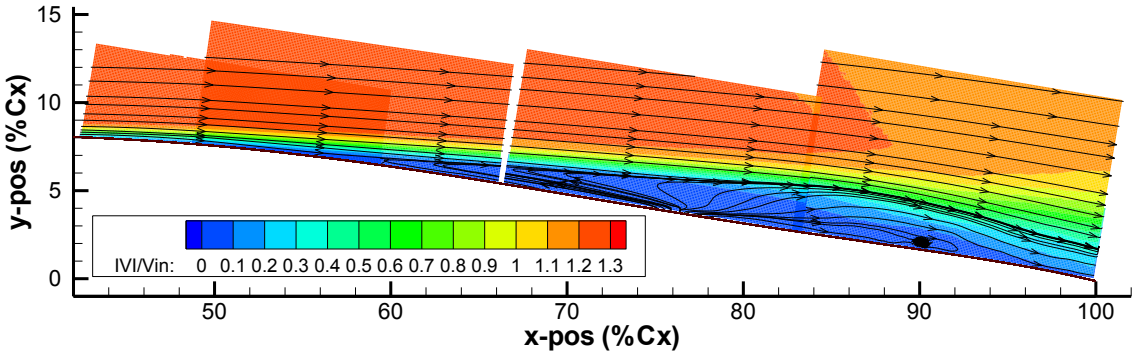

Figure 3.11 Airfoil 2, Flat plate installed, Re = 6 x 10^4

The mean PIV fields shown in Figure 3.9-Figure 3.11 provide more precise identification of the separation and reattachment locations compared to C_p measurements. A summary of the mean reattachment and separation points on Airfoil 2 is shown in Table 3.2. It is obvious that the higher spatial fidelity PIV data allows for a more precise determination of boundary layer behavior. The PIV data indicates that there is a small shift upstream in the separation location at the lowest Reynolds number. Mean separation bubble length increased as Reynolds number decreased. At the highest Reynolds number tested the reattachment point is at approximately C_x=82% and shifts downstream as Reynolds number is decreased. It was not obvious from the C_p data, but the mean flow does reattach just prior to the trailing edge at the lowest Reynolds number tested. The C_p data at Re = 1.5 x 10^5 at C_x=90% decreased creating a plateau that implied separation near the trailing edge. No trailing edge separation was observed in the PIV data.

Table 3.2 Comparison of approximate mean separation and reattachment locations on Airfoil 2

Inlet Reynolds Number	Separation		Reattachment	
	C_p	PIV	C_p	PIV
1.5 x 10^5	55%	56%	85%	82%
1.0 x 10^5	55%	56%	90%	86%
6 x 10^4	55%	54%	Unknown	97%-99%

In order to better understand the boundary layer behavior at the lowest Reynolds number Re = 6 x 10^4, five instantaneous PIV velocity fields at the trailing edge are shown in Figure 3.12.

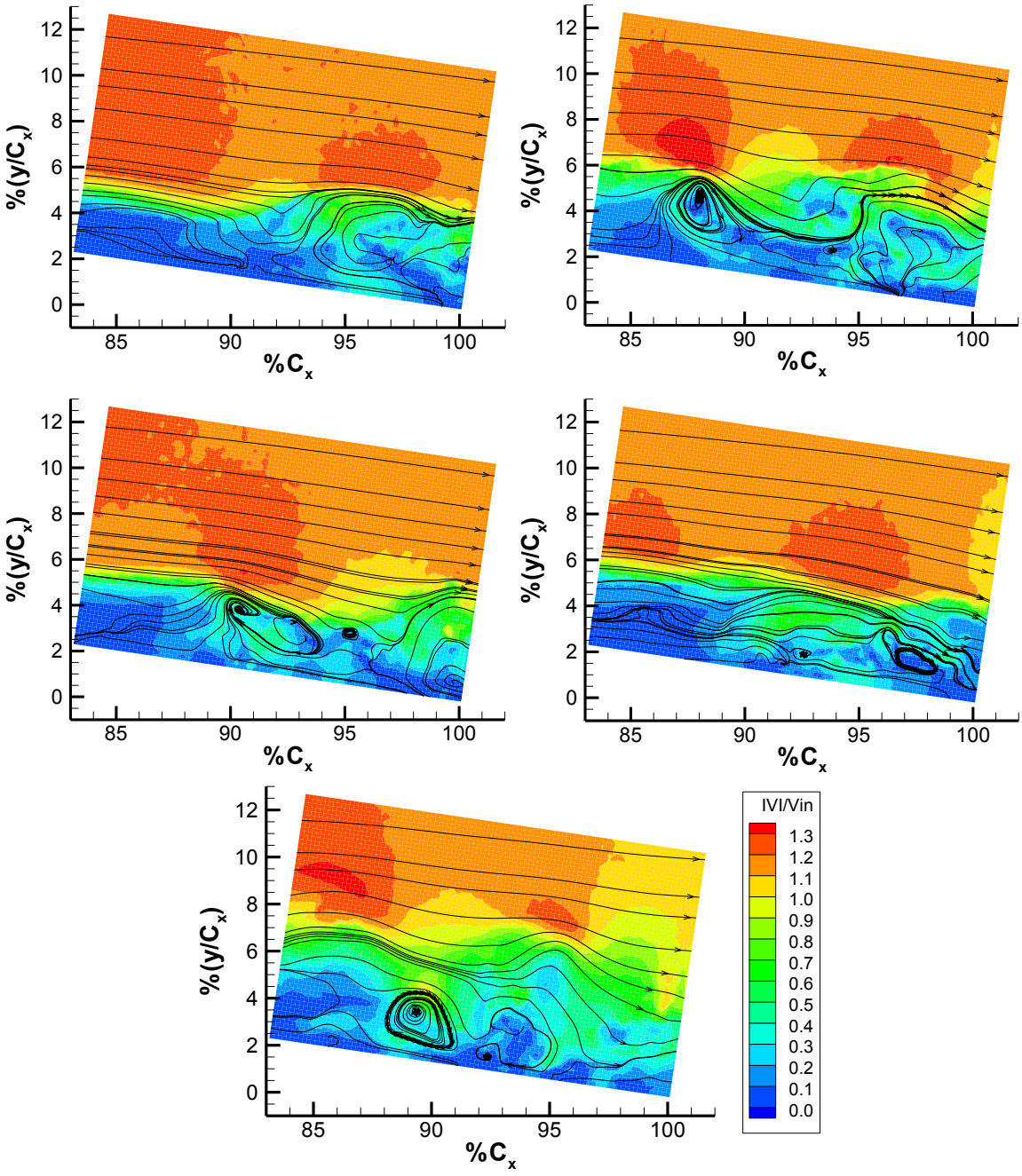

Figure 3.12 A sample of five instantaneous velocity fields in the trailing edge region at Re = 6 x 10^4

Vortex shedding of the separated shear layer results in large vortices that develop and travel along the suction surface. Selected instantaneous PIV images in Figure 3.12 show that the shear

layer behavior is complex. The boundary layer near the trailing edge cannot be labeled reattached or separated unless considering time averaged data.

Examining the instantaneous velocity fields of Figure 3.12 shows that in some instances the shed vortex remains coherent and laminar, with areas that have begun to break down and transition to turbulence; in other instances the vortices are larger and appear to have merged. The large eddies, which are on the order of 4%C_x had a large instantaneous effect on the flowfield and on boundary layer thickness. The unsteady numerical study of Lin and Pauley (1996) agreed with the PIV observations. Their study of the Eppler 387 at Re = 6.0 x 10^4 at a 4 degree angle of attack showed periodic shedding downstream of the separation point. Vortex pairing occurred at locations downstream of the separation point, where the shed vortices interacted and merged into one. Vortex pairing is believed to be due to the adverse pressure gradient which slows the leading vortex and allows the trailing vortex to close on the leading vortex and ultimately merge (Winert and Browand 1974; Lin and Pauley 1996).

3.2.3. Drag Measurements

Drag was measured by a wake traverse along the span of the airfoil. The installation of the pressure lines along the pressure surface resulted in better C_p measurements than on Airfoil 1, but at the cost of spanwise variation in drag. The addition of pressure tubing along the pressure side of the airfoil is clearly seen in the plot of drag along the span shown in Figure 3.13. Variation in losses is most significant on the pressure side of the airfoil in the region where the pressure tubes exit from the airfoil surface.

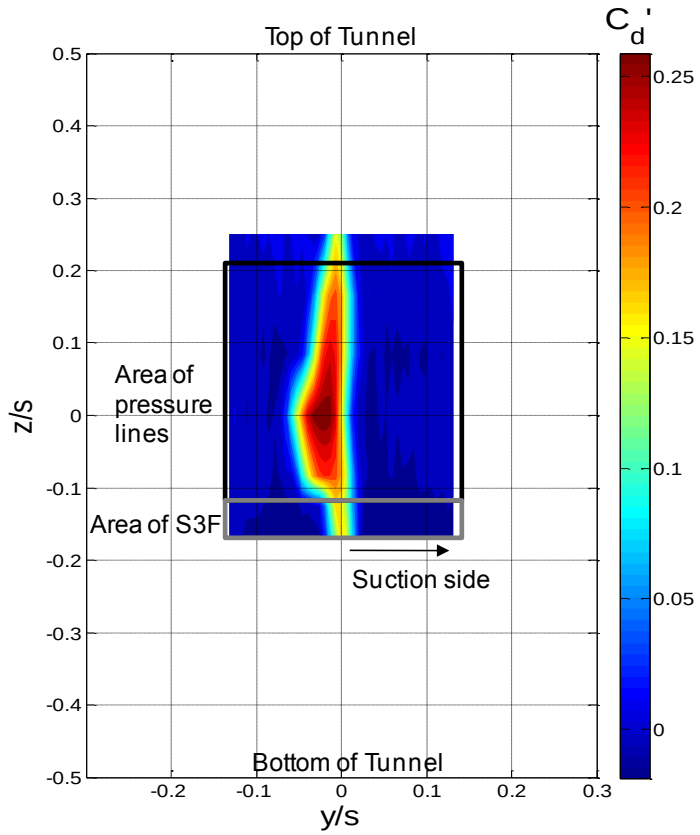

Figure 3.13 Spanwise variation in wake due to pressure lines on Airfoil 2, Re = 1.0 x 10^5.

The pressure tubes were covered with a piece of tape in order to make them more streamline with the flow (Figure 3.14). All measurements presented in this paper were obtained on the suction side of the airfoil where spanwise variation is less significant.

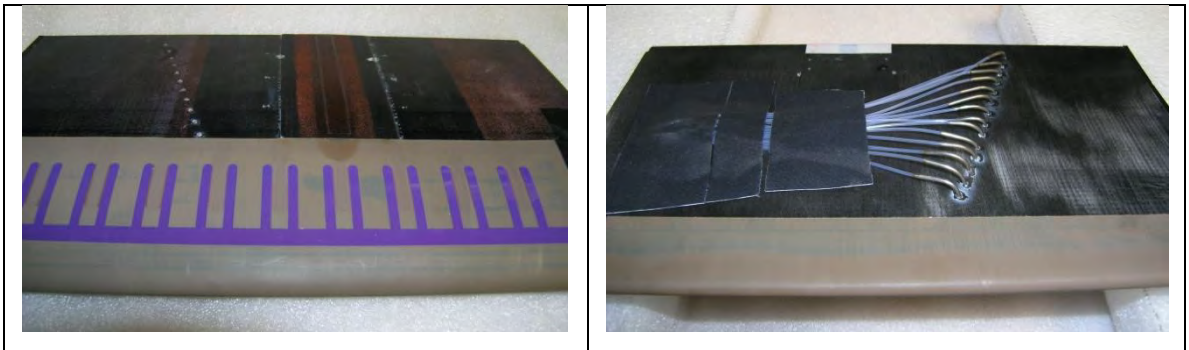

A.) B.)

Figure 3.14 Images of Airfoil 2 A.) suction side surface and B.) pressure side surface with plasma actuator installed.

Figure 3.15 shows the wake velocity deficit in the region of the airfoil with S3F installed from *z/s* = -0.13 to -0.17 indicating the spanwise variation is minimal, especially on the suction surface (y/s > 0). This is the region in which S3F, PIV, and flow visualization images were recorded. Even with the spanwise variation in drag, the airfoil was considered to be adequate for the flow control experiments since laminar separation still existed as expected on the suction surface.

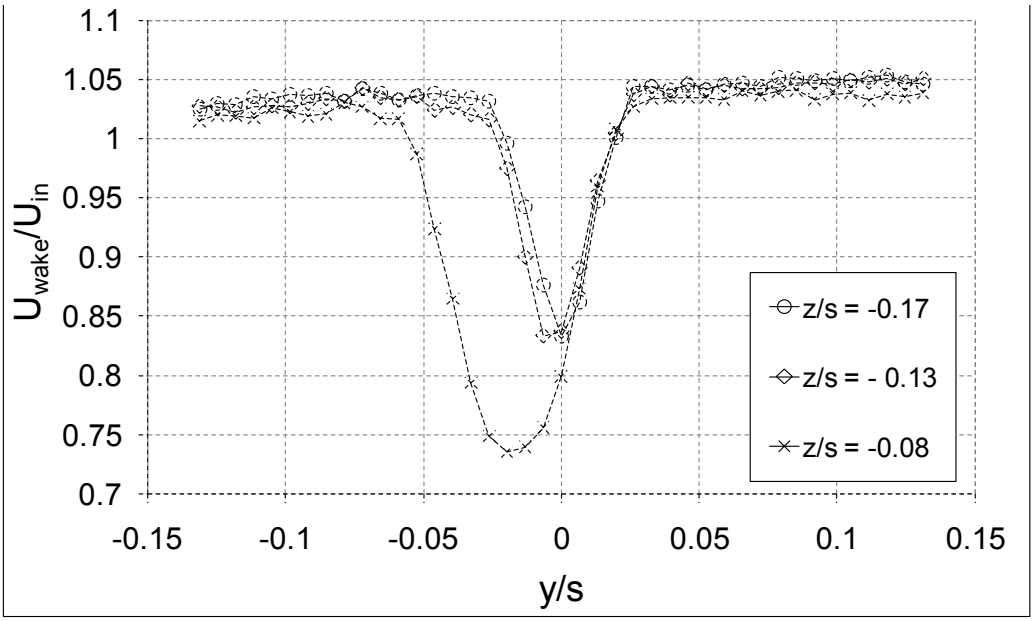

Figure 3.15 Wake velocity deficit in the area of S3F and PIV measurements at Re = 1.0 x 10^5.

A comparison of drag coefficient in the area of the S3F and PIV measurements is shown in Figure 3.16. There is a significant spread in data between all facilities. Section drag measured on Airfoil 1 at Re = 1.0 x 10^5 is between the drag values measured at NASA Langley and U. of Illinois. Data from each facility was significantly lower than the U. of Stuttgart data. As expected Airfoil 2, which had pressure tubing exposed on the pressure side of the airfoil, had a higher drag coefficient at the lowest Reynolds number compared to Airfoil 1, but surprisingly not significantly higher than the value measured at the U. of Stuttgart.

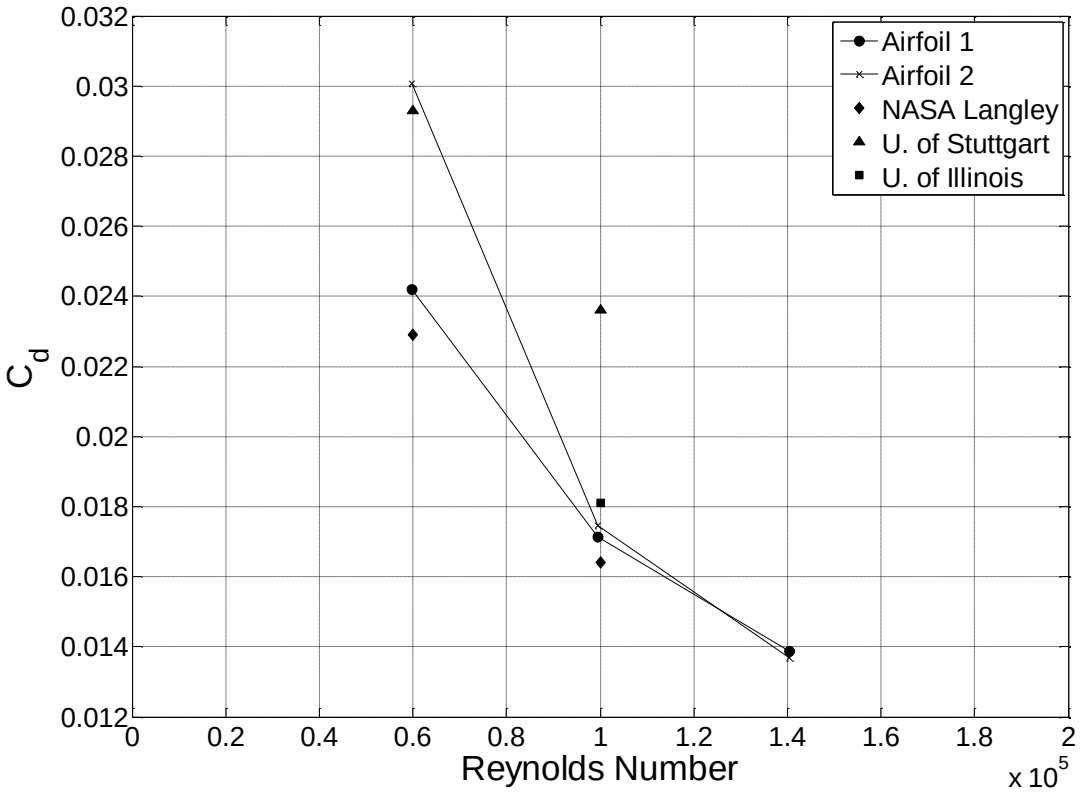

Figure 3.16 Comparison of drag measurements of Airfoil 2 compared to other facilities. Measurements were at z/s = -0.13 in area of S3F and PIV.

3.2.4. Summary

C_p measurements were taken on Airfoil 1 at several small angles of attack to determine an appropriate angle of attack for the separation control experiments. The measurements indicated that laminar separation occurred in the AFRL/RZ DWT consistent with measurements in the NASA tunnel, but that loading was slightly higher in the DWT. At $\alpha = 1.5°$ laminar separation could be obtained by varying Reynolds number. C_p measurements were recorded for Airfoil 2 and indicated that installation of the pressure lines along the pressure surface changed the reattachment point compared to Airfoil 1. Airfoil 2 did however, exhibit laminar boundary layer separation and reattachment on the suction surface consistent with the unmodified version of the E387 at the same angle of attack and Reynolds numbers. PIV data was recorded on Airfoil 2 in order to determine mean separation and reattachment points with better spatial resolution. Drag

measurements on both Airfoil 1 and Airfoil 2 were compared to E387 data from other facilities. Airfoi1 1 drag measurements were within the spread of data taken at other facilities. Airfoil 2 drag did not vary considerably from Airfoil 1 except at the lowest Reynolds number recorded, where drag was 25% higher on Airfoil 2, than Airfoil 1.

3.3. Clean Installation of S3F on Airfoil 2

PIV was used to obtain velocity field measurements in the area of the S3F and compared to PIV without the S3F installed in order to investigate whether the new method of S3F attachment significantly affected boundary layer behavior. The new S3F installation method was described in Section 2.2.1. The focus of the comparison was at Reynolds numbers of 1.0×10^5 and 6.0×10^4. This section also includes a comparison of mean velocity measurement with a plasma actuator installed on the airfoil to gage if either the S3F or plasma actuator had a significant effect on the boundary layer.

To simulate an airfoil with no S3F installed, the cavity was filled with a black flat plate. Mean velocity data for this case was shown in Section 3.2.2. S3F carriers were 3D printed with a single cavity, then lightly sanded for a smooth fit into a cavity on the suction surface of the airfoil. The S3F carrier was painted black prior to being filled with S3F to reduce reflection of light. The S3F carrier was filled with S3F at ISSI Inc. then installed in the airfoil and held in place with two flat head screws near the trailing edge.

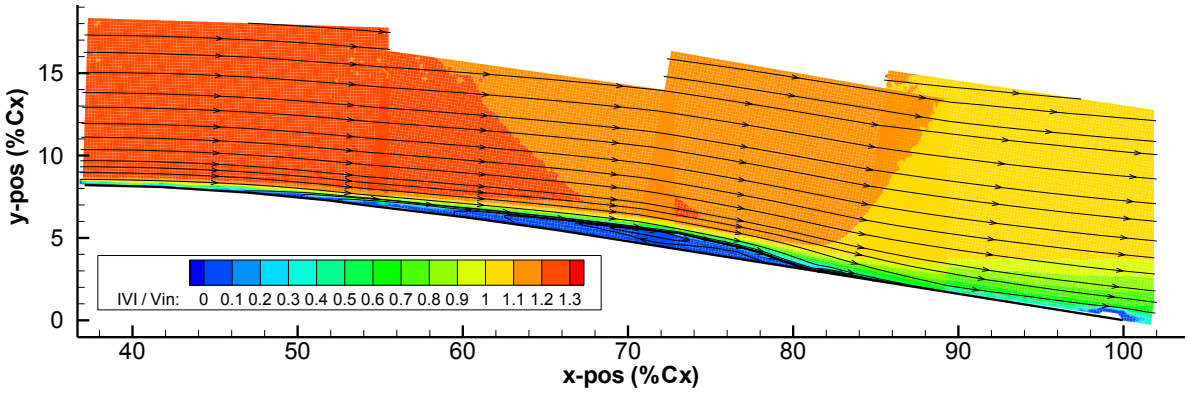

Figure 3.17 Airfoil 2, S3F #4, Re = 1.5 x 10^5

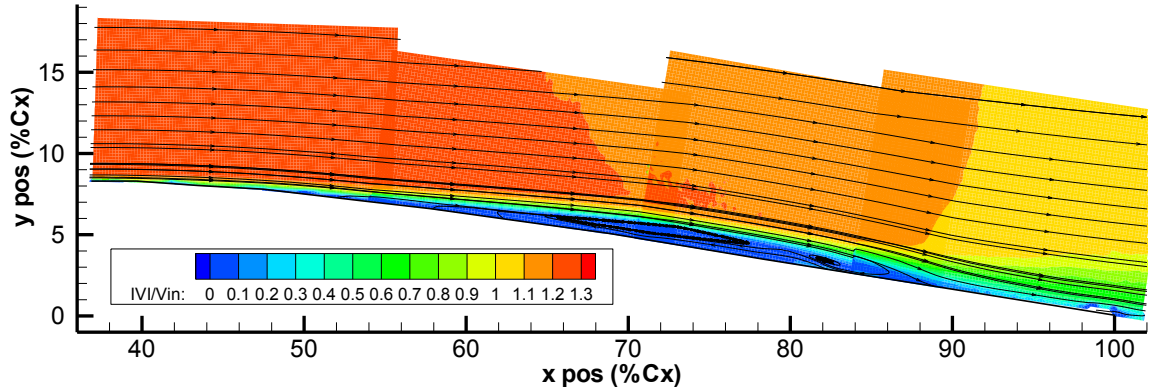

Figure 3.18 Airfoil 2, S3F #4, Re = 1.0 x 10^5

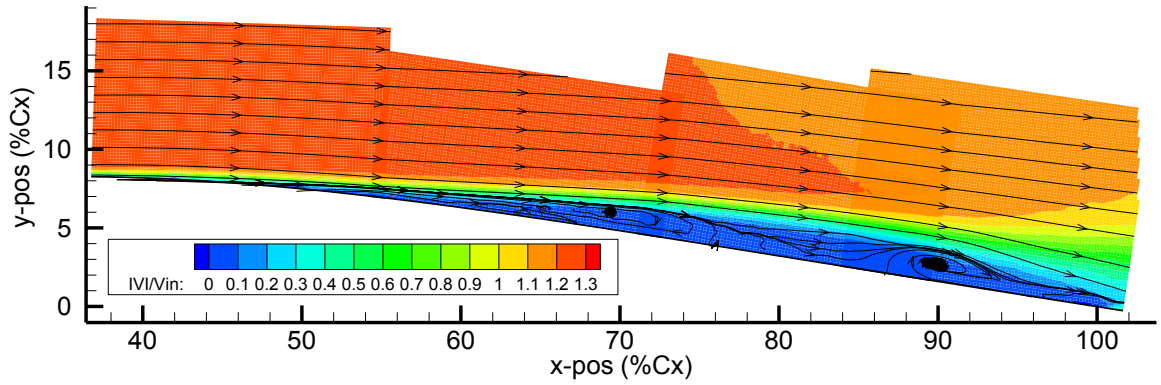

Figure 3.19 Airfoil 2, S3F #4, Re = 6 x 10^4

Mean non-dimensional velocity fields over the suction surface of Airfoil 2 with S3F #4 installed are shown in Figure 3.17 through Figure 3.19. The laser sheet was aligned with the top edge of the S3F. Streamlines have been overlaid on the plots in order to visualize the flow field.

At the highest Reynolds number tested Re = 1.5 x 10^5 the boundary layer separates at approximately C_x=54%. A thin mean laminar separation bubble extends to approximately C_x=82%. At Re = 1.0 x 10^5 the separation bubble is thicker and extends to approximately C_x=89%. Streamlines in the separation bubble indicate a clockwise recirculation until C_x≈78%, followed by a second vortex at the trailing edge of the mean separation bubble with a core at C_x=82%. This mean vortex is most likely an indication of the location in which vortices that that have rolled up in the separated shear layer shed from the rear of the separation bubble. At a Re = 6 x 10^4 the extent of separation is nearly to the trailing edge of the airfoil. The mean streamlines show a more complex shape. It appears that a main recirculation region forms under the separated shear layer. Near the trailing edge a vortex is located with a core at C_x= 90%. The PIV data implies that even at Re = 6 x 10^4 there is mean boundary layer reattachment near the trailing edge of the airfoil, with a strong reverse flow vortex centered about C_x= 90%.

Mean velocity profiles normal to the airfoil surfaces are shown in Figure 3.20 through Figure 3.23. The figures compare velocity profiles measured on Airfoil 2 with and without (clean) the S3F installed. Also included in the figures is data taken with a plasma actuator installed on the airfoil. This data is labeled "DBD" in the figures and has been included to give perspective into the change due to installation of the S3F compared to changes due to adding flow effecter to an airfoil.

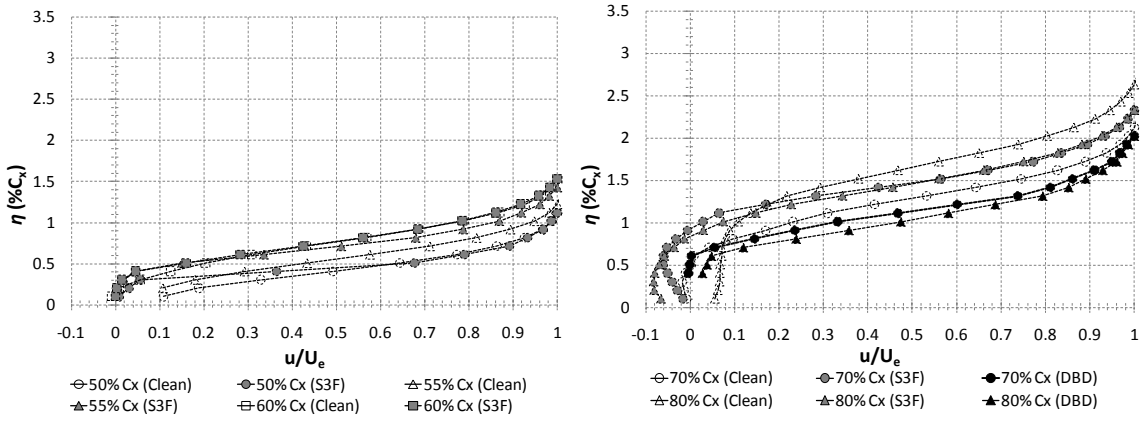

a.) *b.)*

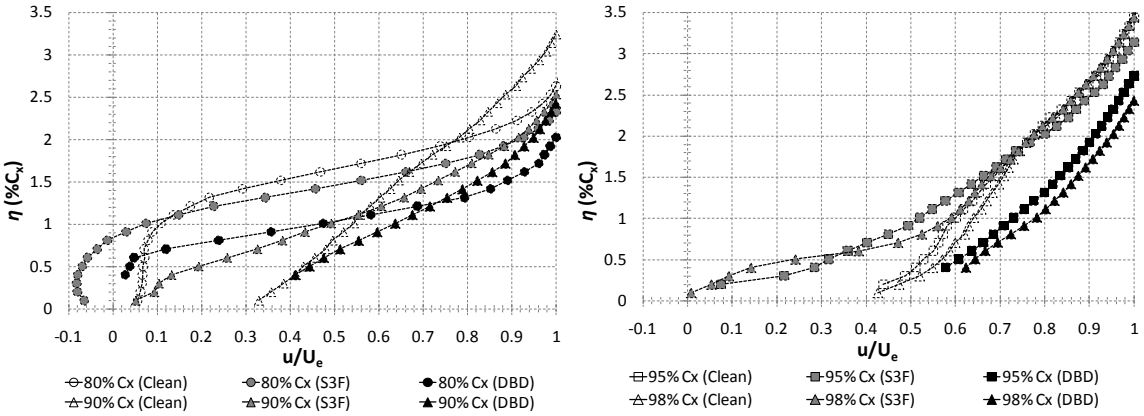

c.) *d.)*

Figure 3.20 Suction surface boundary layer profiles with and without S3F installed, Re = 1.0x10^5.

Figure 3.20 shows mean boundary layer profiles normal to the airfoil. At upstream positions near the separation point (Figure 3.20a), the boundary layer has an inflection point very near the airfoil surface due to an adverse pressure gradient. The airfoil with S3F installed had a thicker, fuller boundary layer. It is interesting note that beyond the separation point, by C_x=60%, the boundary layer thickness is nearly equal for both cases. The separation point appears to be slightly further upstream when the S3F is installed. No data was available near the separation point with plasma actuator installed. It should be noted that the laminar boundary layer thickness in the region of separation is very thin relative to the size of the image field of view. The uncertainty could be quite high owing to the large velocity gradient between the free stream and the near wall flow. Mean velocity profiles in the region of the separation bubble are shown in Figure 3.20b. There is significant spread in the boundary layer height between the three cases shown. In general, the boundary layer is thicker when the plasma actuator is not installed. The velocity profiles at C_x=80% without the airfoil installed is positive without reverse flow near the wall. This could be erroneous data as it would imply the mean boundary layer has reattached. By C_x=90% the boundary layer has reattached for each case. The boundary layer is much thicker without S3F or the plasma actuator installed through the trailing edge. Near the trailing edge at

C_x=95%-98% the boundary layers are fuller and resemble turbulent boundary layers. When the plasma actuator is installed the boundary layer has the smallest thickness and fullest profile.

Boundary layer thickness has been plotted in Figure 3.21 and compared to predictions for a flat plate laminar boundary layer by Blasius, and 1/7th power law turbulent boundary layer prediction. The Blasius prediction for boundary layer thickness agrees with PIV obtained mean velocity data up to the separation point near 55% axial chord. The boundary layer thickness grows rapidly after separation. In the region of turbulent reattachment at C_x=90%, and to the trailing edge, the boundary layer thickness is higher for the clean airfoil. This is implies transition to turbulence occurs further downstream for the clean case, compared to the cases with S3F and a plasma actuator installed. In summary, both the S3F and the plasma actuator had the effect of decreasing boundary layer thickness downstream of the laminar separation point. Installation of the plasma actuator had the largest overall effect on boundary layer thickness at Re = 1.0 x 10^5.

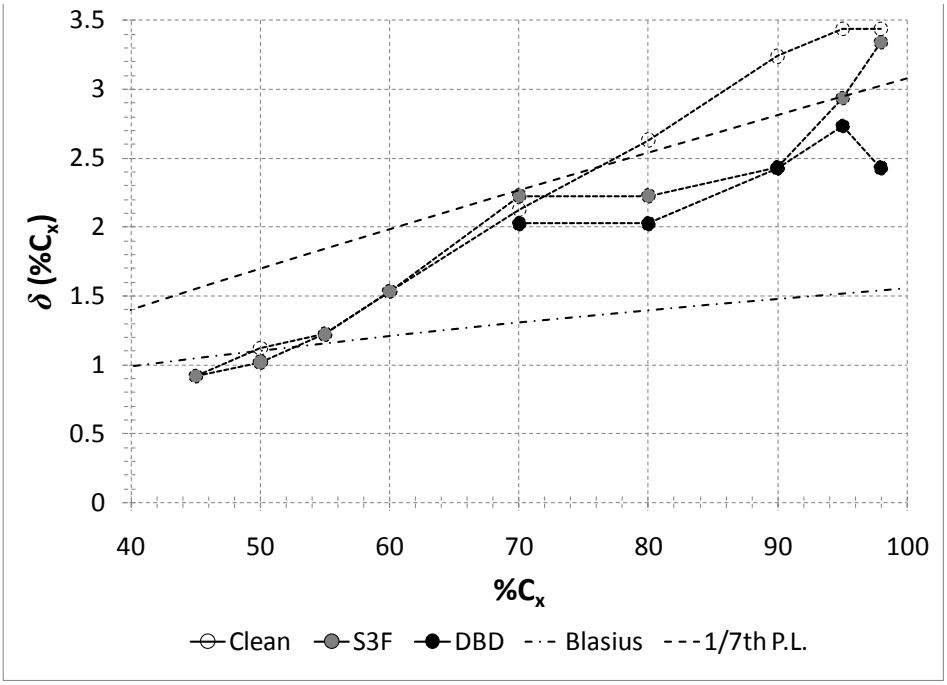

Figure 3.21 Boundary layer thickness with and without S3F installed, Re = 1.0x10^5.

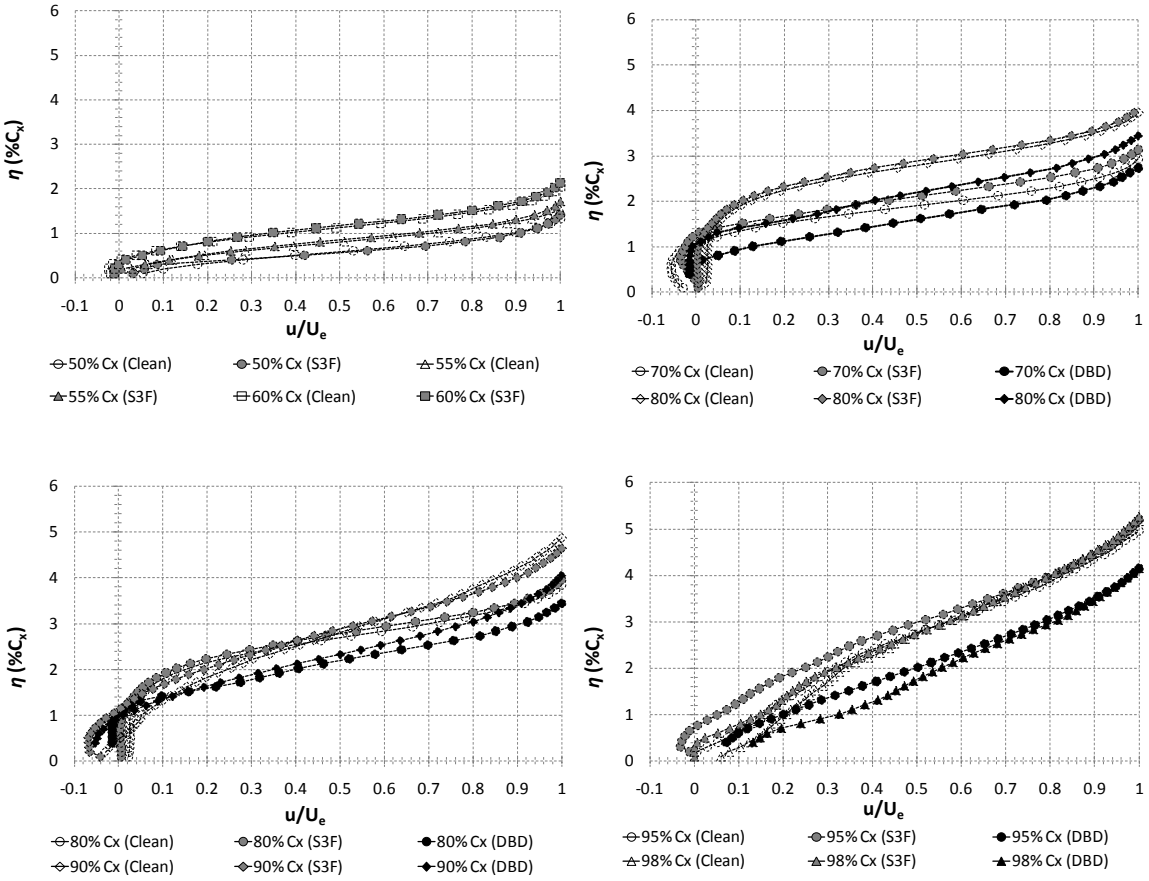

Figure 3.22 Suction surface boundary layer profiles with and without S3F installed, Re = 6 x 10^4.

Figure 3.22 shows the surface normal velocity profiles at Re = 6 x 10^4. Near the separation point the boundary layer profiles are very similar. Laminar boundary layer separation has occurred by C_x=60%. Boundary layer thickness has nearly doubled by C_x=80%. The near wall velocity is nearly zero, but each case shows a small positive velocity. This could be due to a mean bias in the measurement due to lack of reliable seeding in this region of very low velocity. At C_x=90% each profile has a negative velocity near the wall indicating that the mean boundary layer is separated. The reattachment point varies between all three cases. When the plasma actuator was installed the mean boundary layer reattachment occurred upstream of C_x=95%. With the S3F installed the boundary layer does not appear to reattach until approximately

C_x=98%, slightly downstream of the clean case. Mean boundary layer thickness is shown in Figure 3.23.

The installation of the S3F had a much smaller effect on boundary layer thickness at Re = 6 x 10^4, compared to the higher Reynolds number. On the other hand, the plasma actuator decreased boundary layer thickness by approximately 20%. Boundary layer thickness was not far off from the Blasius prediction up to the separation point. The $1/7^{th}$ power law prediction did not compare well to the boundary layer thickness near the trailing edge of the airfoil.

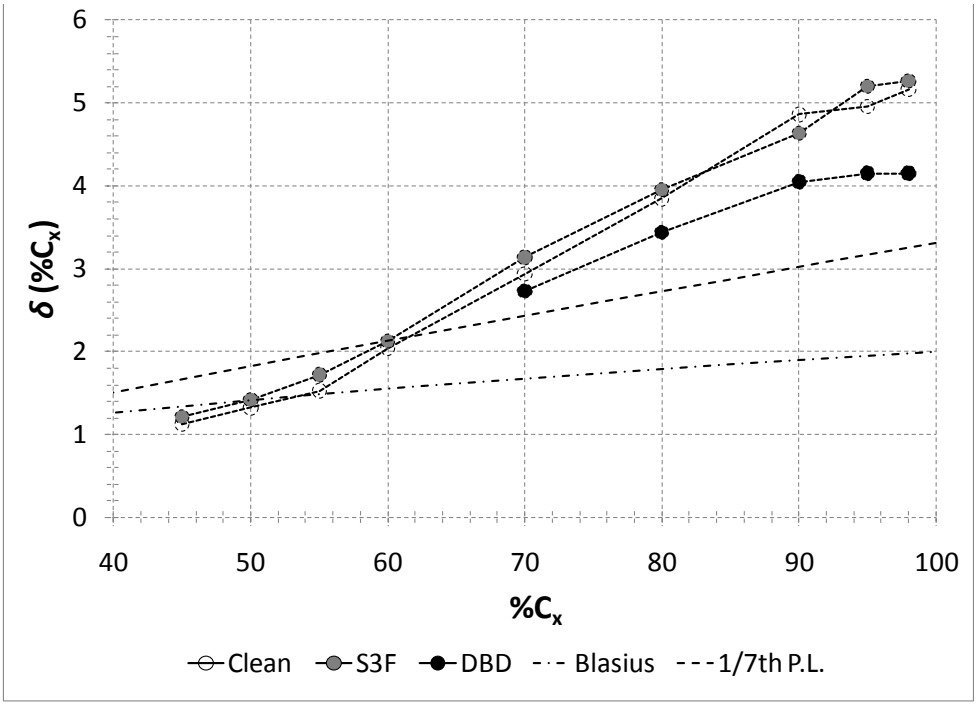

Figure 3.23 Boundary layer thickness with and without S3F installed, Re = 6 x10^4.

3.3.1. Summary

Comparisons of mean boundary layer thickness and velocity profiles using 2D-PIV have been made for three cases: Clean, S3F installed, and Plasma actuator installed. At both Reynolds numbers, installation of the plasma actuator had the largest effect on boundary layer thickness compared to installation of the S3F. Boundary layer thickness up to the laminar separation

location was consistent with Blasius's prediction for a flat plate boundary layer, at both Reynolds numbers. In the trailing edge region at Re = 1.0 x 10^5 the boundary layer thickness was in the range of $1/7^{th}$ power law prediction for a turbulent boundary layer. At the lower Reynolds number of 6 x 10^4 the $1/7^{th}$ power law prediction for boundary layer thickness was much lower than the actual boundary layer thickness calculated from PIV data. This agrees with instantaneous PIV velocity measurements that showed large coherent vortices along the trailing edge of the airfoil, rather than a developed turbulent boundary layer.

3.4. **S3F Development**

A total of six different S3F formulations summarized in Table 3.3 were fabricated and installed on Airfoil 2 over the period of this research. Frequency response was approximated using Equation (2.4) and shear modulus measurements were provided by ISSI Inc. The method used to measure such low shear modulus was improved over the course of the work by S3F #5 ISSI Inc. reported the uncertainty in the shear modulus measurement was +/-10%.

Table 3.3 S3F Properties

Version	Shear Modulus (Pa)	Mag Factor (px/mm)	Thickness (mm)	Freq. Response (Hz)	Notes
S3F #1	110	97	0.6	93	TiO_2 particles, two 20mm wide strips
S3F #2	110	-	0.6	93	Attempt to decrease shear modulus, no significant change
S3F #3	118	144	0.9 / 0.45	64	Effort to increase pixel disp., ↓S3F width to 10 mm, ↑Mag factor, ↑S3F thk, S3F extended to C_x = 98% but with T.E. thickness change
S3F #4	100	157	0.9	59	C_x = 42%-98% with uniform thickness, switch to one strip, switch to fluorescent paint markers
S3F #5	37 +/- 10%	145-147 typ.	0.9	32	Fluorescent paint markers
S3F #6	7.7 +/- 10%	156	0.9	16	Fluorescent paint markers

The S3F parameters as well as the carriers were modified in an effort to improve measurements at the low Reynolds numbers and length scale used in the experiments. Creating the S3F and filling the plastic S3F carrier flush to the surface required skill, and often several attempts were made to achieve the desired film properties and fill quality. ISSI Inc. improved the method to generate the S3F at such low shear modulus over the period of the research effort. By the third version (S3F #3) the films were consistently fabricated with shear modulus in the range of 100 Pa.

Initially the width of the S3F strip was 20mm and 0.6 mm thick for both S3F #1 and #2. The width of the S3F set the maximum magnification factor for a given camera and lens combination since part of the S3F carrier above and below the S3F was required in the field of view to correct for airfoil and camera movement. In an effort to increase displacement the width of the S3F was reduced to 10 mm and the thickness increased to 0.9mm. The increase in thickness was at the expense of frequency response, but it remained well above the camera maximum frame rate. By S3F #4 it was realized that the high magnification factors being used required a smaller diameter and denser distribution of markers on the film. In order to increase marker density and decrease marker diameter, fluorescent paint was used rather than titanium oxide particles. A comparison of images of S3F with Titanium Oxide markers versus fluorescent paint markers is shown in Figure 3.24.

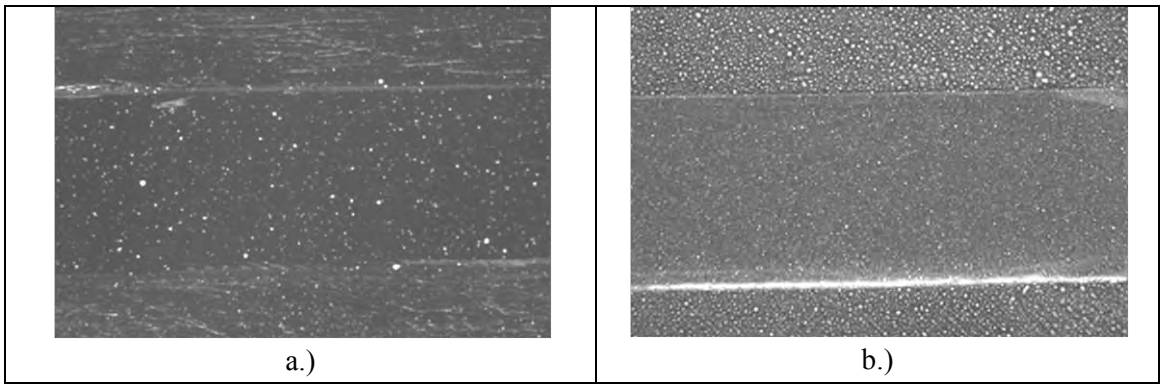

Figure 3.24 Sample images of S3F with different markers: a.) TiO_2 particles b.) Fluorescent paint. Nikon 200mm F4 lens, f/32 aperture, 0.6ms exposure, 550 nm long pass filter.

By experimenting with new methods of fabricating S3F, ISSI Inc. was able to produce an even more sensitive film for version #5. This resulted in a significant decrease in shear modulus from 100 Pa to 37 Pa for S3F #5. Film displacement increased and measurements were made at a Reynolds number down to $5x10^5$. S3F #6 resulted in the lowest shear modulus film tested, having a mean shear modulus of 7.7 Pa along the centerline of the film. ISSI Inc. also observed a larger variation in shear modulus across the film than in previous formulations. Film displacement increased significantly, but frequency response decreased to approximately 16 Hz.

3.4.1. Skin friction

This section discusses the skin friction values inferred from S3F tangential displacement presented in the following sections. Predicting the skin friction on the suction surface of an airfoil with laminar separation and reattachment is difficult in the absence of numerical simulation. Here the discussion is limited to phenomenological and order of magnitude comparisons.

As a laminar boundary layer develops along the surface of an airfoil it will reach a critical point at which it transitions to a turbulent boundary layer. The critical point in which laminar to turbulent transition occurs is strongly dependent on the pressure gradient (Schlichting & Gersten 2000). The boundary thickness increases along the surface of the airfoil and the rate of increase is larger in the turbulent downstream boundary layer than in the laminar boundary layer. As the boundary layer thickness increases, the wall shear stress decreases; however, a turbulent boundary layer has a higher wall shear stress than a laminar boundary layer.

As a rough order of magnitude estimate of skin friction over the E387 airfoil, flat plate estimates of both laminar and turbulent boundary layers are used. The local skin friction in the boundary layer of a flat plate at zero incidences is calculated by solution of the Blasius equation to be:

$$C_f(x) = \frac{0.664}{\sqrt{\mathrm{Re}_x}} \tag{3.1}$$

with boundary layer thickness approximated by:

$$\delta_{99} \approx 5.0\sqrt{\frac{\upsilon \cdot x}{U_\infty}} \tag{3.2}$$

.

The local skin friction and boundary layer height of a flat plate with a turbulent boundary layer can be approximated by the 1/7 power law estimate:

$$C_f(x) \approx \frac{0.027}{\mathrm{Re}_x^{1/7}} \tag{3.3}$$

and

$$\delta_{99} \approx 0.16 \cdot \frac{x}{\mathrm{Re}_x^{1/7}} \tag{3.4}$$

.

The boundary layer on the E387 airfoil will differ from the flat plate estimates given in Equations (3.1)-(3.4) due to an adverse pressure gradient on the suction surface beginning at the negative pressure peak. The adverse pressure gradient causes a point of inflection in the boundary layer profile with increasing downstream pressure ultimately leading towards negative flow at the wall and separation (White 1991). Equations (3.1)-(3.4), however, do give an order of magnitude estimate of the shear stress and boundary layer thickness expected over the E387 suction surface.

3.4.2. S3F measurements on airfoil 2

Measurements with S3F #4-#6 are compared in this section at a Reynolds number of 1.0×10^5. These films had shear modulus of 100, 37, and 7.7 Pa which resulted in significant difference in tangential displacement magnitude. Figure 3.25-Figure 3.27 show the mean tangential film displacement at Re = 1.0×10^5 calculated using ISSI Inc."s hybrid cross correlation/optical flow method (Fonov, 2004). Each plot shows a zero crossing location implying mean boundary layer

reattachment. The zero crossing location is different for each S3F and varies between C_x = 92% and 96%.

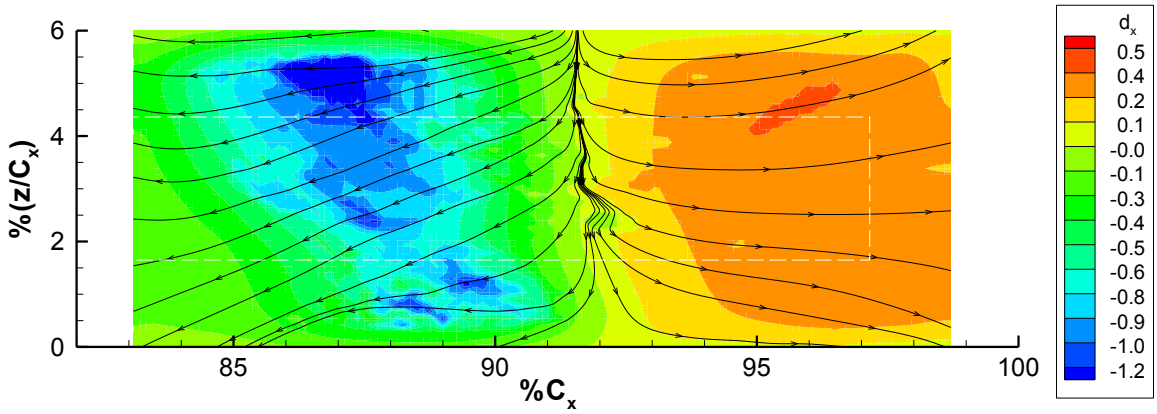

Figure 3.25 S3F #4 mean streamwise displacement in pixels, Re = 1.0x10^5, μ_m = 100 Pa.

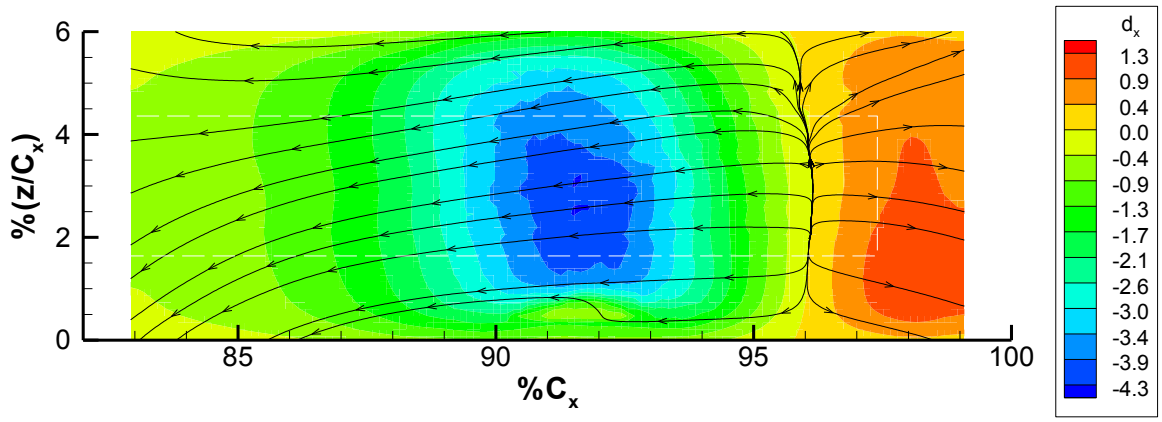

Figure 3.26 S3F #5 mean streamwise displacement in pixels, Re = 1.0x10^5, μ_m = 37 Pa.

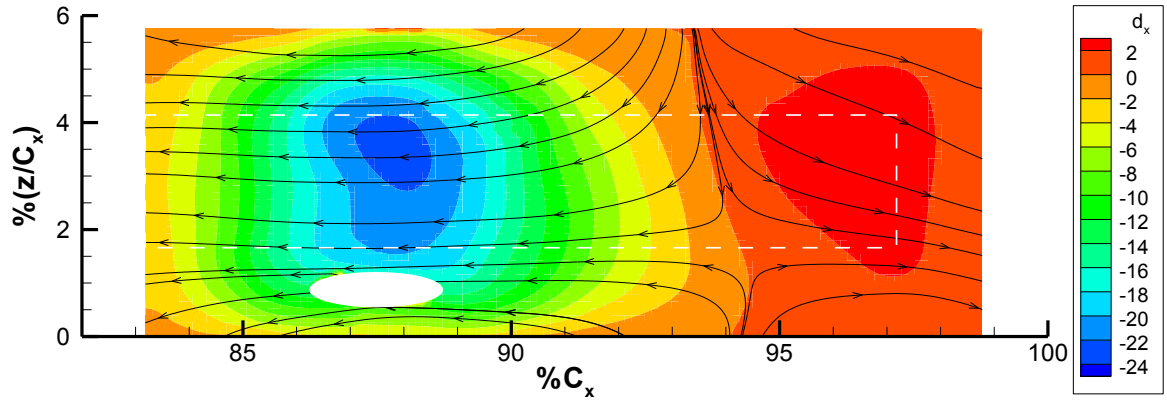

Figure 3.27 S3F #6 mean streamwise displacement in pixels, Re = 1.0x10^5, μ_m = 7.7 Pa.

Figure 3.28 gives estimates of the skin friction coefficient. A word of caution is necessary here when evaluating the skin friction coefficient in Figure 3.28. The skin friction has been calculated assuming shear stress is a linear function of tangential displacement. Crafton et al. (2008) has verified this is true in flow with zero pressure gradients, and this is assumed true in flows with small pressure gradients as well. The E387 suction surface likely has locally high pressure gradients that negate this assumption, especially near the reattachment point.

The minimum skin friction value is nearly identical for S3F #5 and S3F #6, but with different spatial location. S3F #4 has the same shape as the other two films, but with a higher minimum value. The zero crossing location of S3F #4 at C_x = 91.5% is in very good agreement with PIV data. The estimated turbulent boundary layer skin friction using 1/7th power law is included in the plot for reference. A summary of minimum and maximum S3F tangential displacement, skin friction coefficient, and reattachment location is shown in Table 3.4.

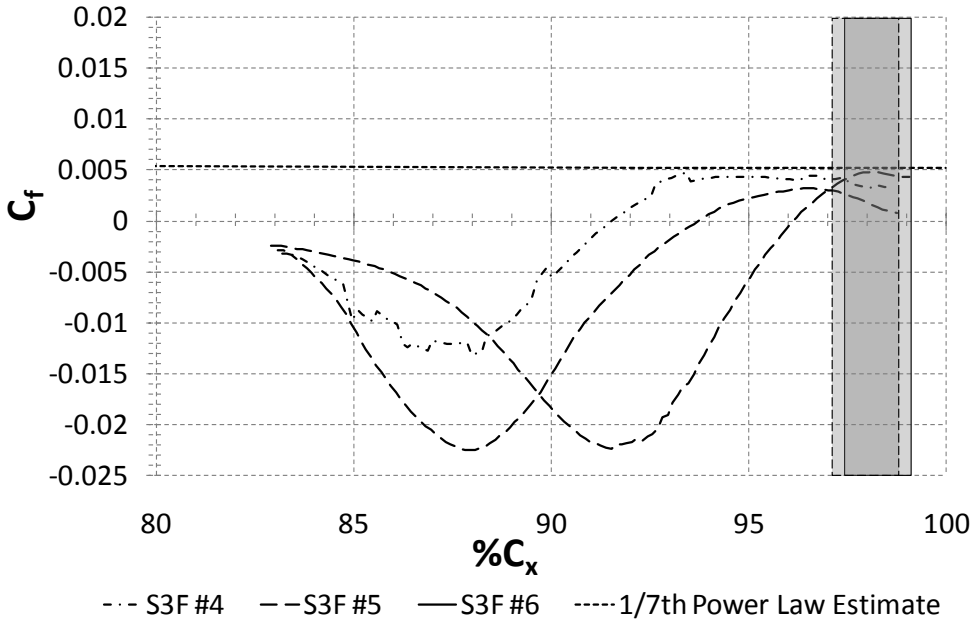

Figure 3.28 Estimate of S3F #6 mean skin friction coefficient, Re = 1.0 x 10^5.

Table 3.4 Summary of mean parameters near the trailing edge region for S3F #4-#6, Re=1.0x10^5.

	$d_{x,max}$ (px)	$d_{x,min}$ (px)	$C_{f,max}$ (estimated)	$C_{f,min}$ (estimated)	$\%C_{x,reattach}$
S3F #4	0.36	-1.02	0.005	-0.013	91.8
S3F #5	0.95	-4.28	0.004*	-0.022	96.2
S3F #6	3.17	-22.62	0.003	-0.023	93.7

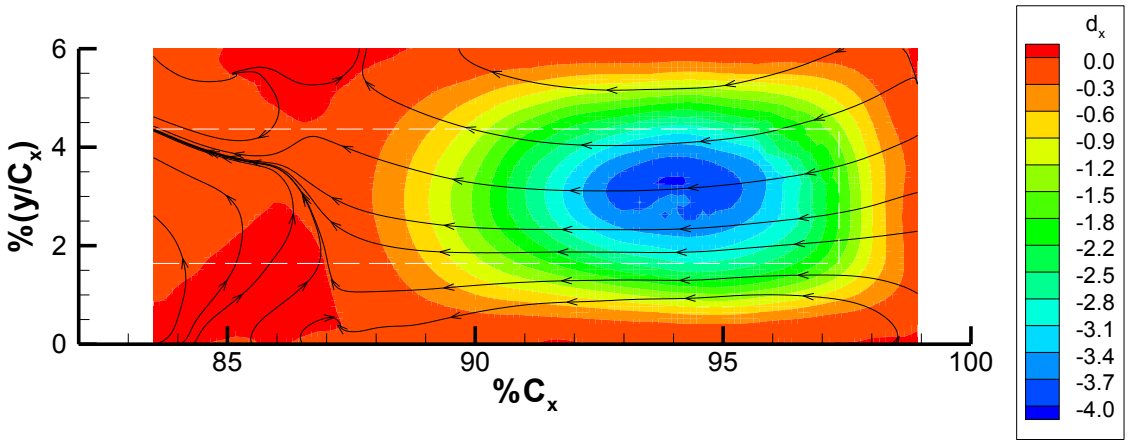

Figure 3.29 S3F #6 mean streamwise displacement in pixels with plasma actuator installed, Re = 6x10^4.

S3F #6 tangential displacement at a lower Reynolds number of 6 x 10^4 is shown in Figure 3.29 and an approximation of skin friction coefficient assuming linear relationship between shear stress and tangential displacement in Figure 3.30. A plasma actuator is installed on the airfoil which is expected to change the boundary layer characteristics compared to a clean airfoil as was discussed in Section 3.3. No zero crossing is indicated in the measurements which would imply that the mean boundary is separated to extent of the S3F near 99% C_x or that the pressure gradient near the trailing edge is large enough relative to shear stress that the tangential displacement is actually a coupled response between pressure gradient and shear stress. PIV data discussed in Section 3.3 showed that a mean reattachment point was in the area of 95% C_x with the plasma actuator installed. There was also a reverse flow vortex in the mean data at Re = 6 x 10^4 centered about 90% C_x. In the absence of simultaneous pressure gradient data it is unclear whether the local minimum in tangential displacement at Re = 6 x 10^4 observed in Figure 3.29 and Figure 3.30 is due primarily to shear stress or a coupling of shear stress and pressure. Regardless of whether the local minimum was created by a coupling of forces or not, it was hypothesized that this minimum would shift spatially depending on reattachment location. This would make the tangential film displacement useful at the lower Reynolds number even if the shift in minimum is due to a coupled forcing affect. Further discussion on the potential impact of ignoring pressure gradient will be discussed in the next section.

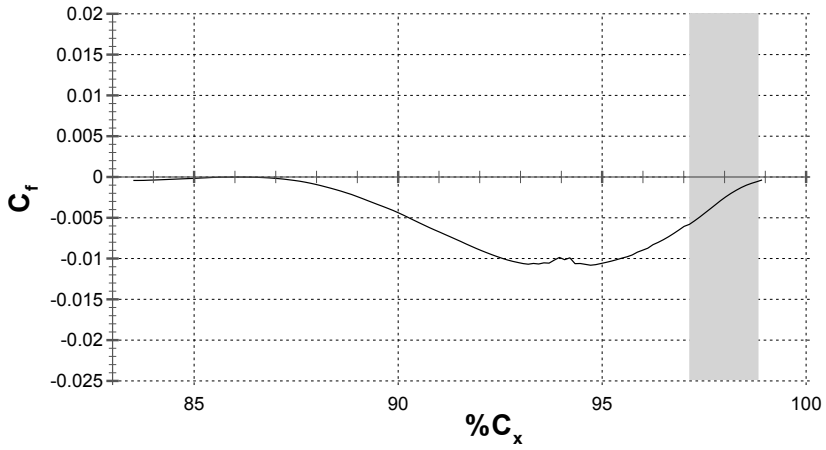

Figure 3.30 Estimate of mean skin friction coefficient measured by S3F #6 with plasma actuator installed, Re = $6x10^4$.

3.4.3. Assumption of a linear relationship between d_x and C_f

Measurements of S3F #5 tangential displacement in the streamwise direction were obtained with four different overlapping camera views. The S3F midplane, mean streamwise tangential displacements of each individual camera view were assembled into one plot shown in Figure 3.31. Individual images were analyzed using ISSI Inc. image processing software. The combined plot of Figure 3.31 demonstrates that the experimental measurement method was repeatable, as the wind tunnel had to be turned off, the camera repositioned, image view located, and magnification factor calculated for each view. Regions assumed to have edge effects are shaded gray. The shape and direction of S3F displacement is consistent with shear stress magnitude and direction expected along a surface with laminar separation and reattachment. A zero crossing at approximately 52% C_x indicates flow separation and reversal followed by a region of low negative displacement in the separation bubble. The shear stress decreases to a minimum point at approximately 90.5% C_x before increasing to a zero crossing at 96% C_x. The region surrounding the minimum from 82% C_x to 96% C_x is typical of a recirculation area in a laminar separation bubble just upstream from the reattachment point (see Figure 5.15). At the

upstream edge of the S3F is actually two zero crossings, the first is on the edge of the region expected to experience edge effects.

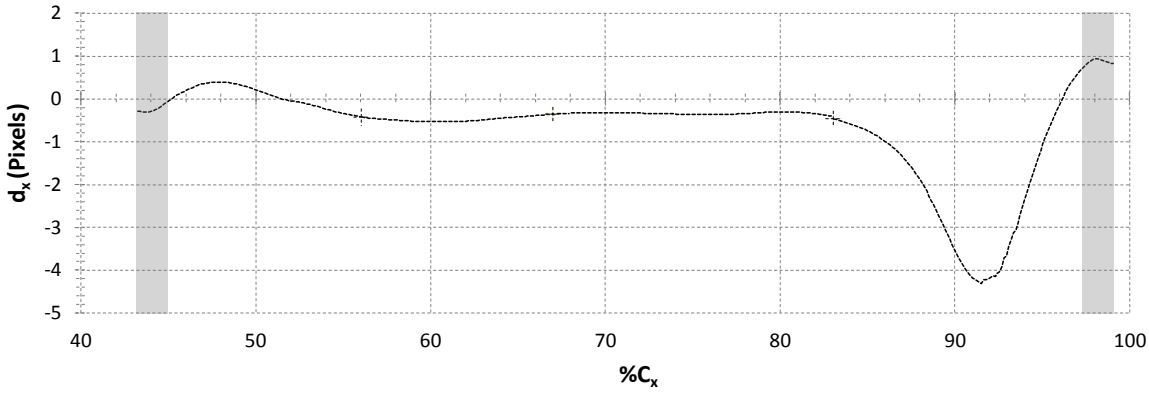

Figure 3.31 S3F #5 streamwise film tangential displacement along the suction surface at Re = 1.0 x 10^5. The plot is a combination of four different views, with division between each view marked with the symbol '+'.

Using S3F tangential displacement directly to indicate suction surface boundary layer features assumes that the pressure gradient has a negligible effect on S3F tangential displacement. This assumption may be valid along portions of the S3F and not others depending on the ratio of pressure gradient to local shear stress. The pressure gradient on the S3F was approximated from pressure coefficient measurements on Airfoil 2. Equation (2.3) was used to estimate skin friction coefficient compared to ignoring pressure gradient effects. Pressure tap measurements were available up to C_x=90%, and the inviscid profile calculated in XFOIL was used to estimate the pressure coefficient from C_x=90% to the trailing edge of the S3F. Static pressure measurements were available every 5% C_x to approximate the pressure gradient and linear interpolation was used to estimate the pressure gradient between pressure tap locations. Pressure distributions used in the comparison are shown in Figure 3.32. The Airfoil 2 C_p (clean) measurements refer to no plasma actuator or S3F installed on the airfoil. The measured C_p was also shifted three degrees downstream in order to understand the effect of the reattachment point shifting downstream. The inviscid pressure distribution calculated in XFOIL has also been included in the comparison. An estimation of skin friction coefficient based on Blasius"s solution for laminar boundary layer

on a flat plate, and the 1/7th power law estimate of turbulent boundary layer shear stress is plotted in each image.

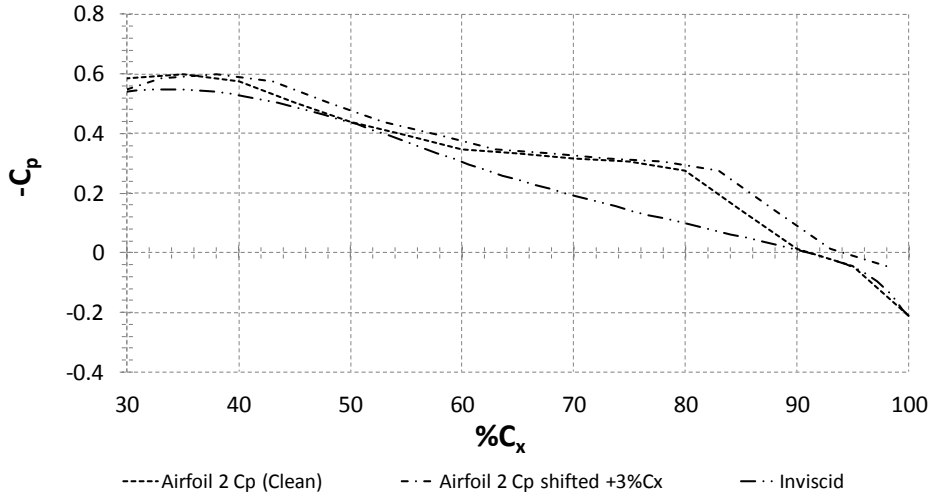

Figure 3.32 C_p profiles at Re = 1.0 x 10^5 used to estimate surface pressure gradient.

The location of highest pressure gradient along the S3F is in the area of the reattachment point, but near the separation point the shear stress is low relative to pressure gradient which can result in a shift in perceived separation point.

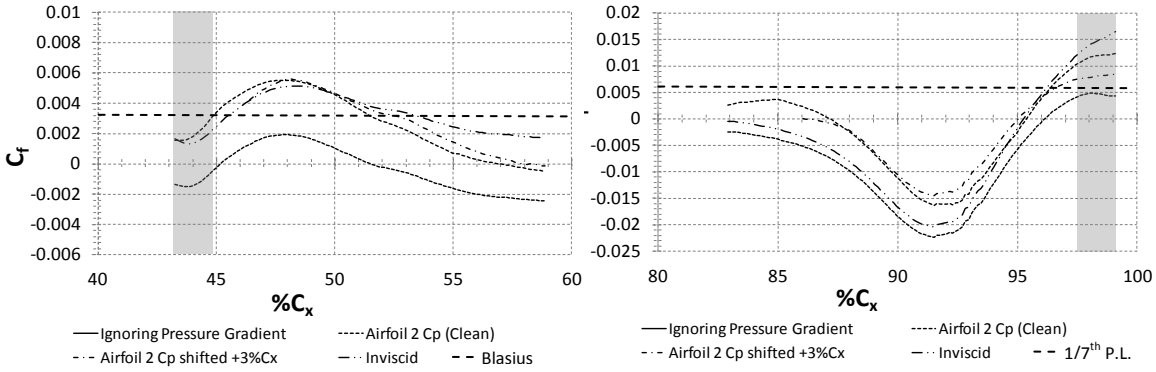

Figure 3.33 Estimation of the effect of pressure gradient on S3F indicated separation and reattachment points, S3F #5, Re = 1.0 x 10^5.

Figure 3.33 shows the potential effect of pressure gradient on the tangential displacement of the S3F near the reattachment and separation points at a Re = 1.0x10^5. Near the separation point the perceived separation point is at 51.5% C_x, but depending on the pressure gradient the separation point could shift in excess of 6% C_x downstream. Both the measured clean Airfoil 2

C_p and the shifted C_p result in a separation point of 57% C_x and 58% C_x respectively. Near the trailing edge of the airfoil each of the pressure gradients shift the reattachment point upstream less than 1% C_x. It is worth noting that when considering pressure gradient in the skin friction estimate upstream of the separation point, the skin friction coefficient is nearly twice as high as Blasius"s estimate. Downstream of the reattachment point the estimated skin friction ignoring pressure gradient is within 16% of the $1/7^{th}$ power law estimate, but including pressure gradient in the estimation results in significantly higher skin friction. It is apparent that if the pressure gradient is included in the estimation of skin friction from S3F tangential displacement, the pressure gradient must be accurately located spatially. Pressure gradient location has a large effect on estimated skin friction when using Equation (2.3).

A similar comparison is made at the trailing edge of S3F #6. The perceived reattachment point based on raw S3F tangential displacement is approximately 94% C_x, 2% C_x further upstream than the measurements of S3F #5. The pressure gradients resulted in a larger shift in reattachment point, as much as 2% C_x, and also decreased the minimum skin friction coefficient.

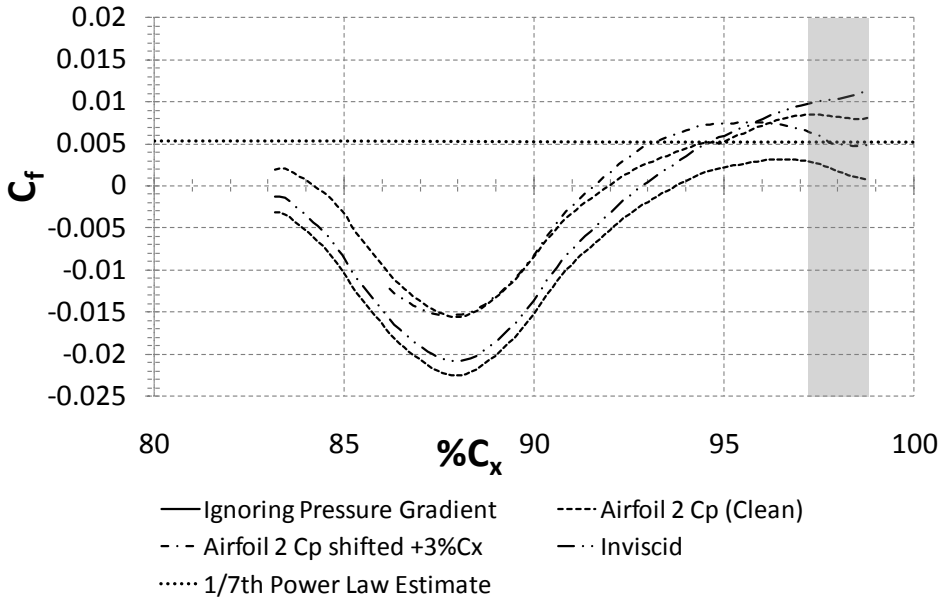

Figure 3.34 Effect of pressure gradient on S3F estimated separation and reattachment points, S3F #6, Re = 1.0 x 10^5.

3.5. Chapter Summary

Six different formulations of S3F were tested for use as a separation control sensor on the E387 at Reynolds numbers below 1.0 x 10^5. The measured tangential displacement and estimated skin friction coefficient of the final three films were compared. Each film showed a similar mean displacement shape, but location of minimum tangential displacement and zero crossing location varied by as much as 4% C_x at Re = 1.0 x 10^5. At Re = 6 x 10^4 the reattachment point was indicated by S3F tangential displacement. It is hypothesized that regardless of whether the minimum in tangential displacement was due to primarily shear stress or a coupled loading with pressure gradient, the minimum point would shift spatially with reattachment location and still provide a useful separation control sensor. Estimations of skin friction coefficient that included pressure gradient showed that the mean separation point could shift spatially in excess 6% C_x from the perceived separation point based on tangential displacement. Near the reattachment point the inclusion of pressure gradient only shifted the mean zero crossing 2% C_x.

4. Open Loop Actuator Investigation

The objective of the open loop study was to verify that a plasma actuator could mitigate boundary layer separation on the E387 airfoil and determine an appropriate flow control strategy for the closed loop investigation. Two different plasma actuator electrode arrangements were compared to an asymmetric electrode arrangement that is often used for flow control. The two alternate plasma actuator electrode arrangements were chosen with the intent of generating streamwise vorticity, and improving separation control authority using a DBD plasma actuator. This chapter includes flow visualization of the induced velocity from each actuator configuration, pressure coefficient, profile drag, and flow visualization at various voltage amplitudes.

4.1. Description of Experiment

Three different electrode configurations shown in Figure 4.1were evaluated in an open loop configuration. The first actuator arrangement, DBD-01 was a spanwise array of 11 linear actuators spaced 20.6 mm on center, mounted parallel to the flow. This configuration produced an array of cross stream jets with the intent of generating longitudinal vorticity (Roth et al. 2000). The second actuator, DBD-02 was a spanwise array of linear plasma synthetic vertical jets spaced 23.8 mm on center. Vertical jet arrangements can be created as annular or linear configurations, and operated steady or pulsed (Jacobs et al. 2005, Santhanakrishnan and Jacob, 2007a, 2007b, 2008, 2009). DBD-03 is a single asymmetric electrode across the span of the airfoil centered at 35% C_x. This type of geometry produces a downstream jet along the span of the airfoil. Figure 4.1 includes a schematic, photograph, and relative length of each discharge compared to the baseline, for each actuator electrode configuration installed in the AFRL/RZ DWT.

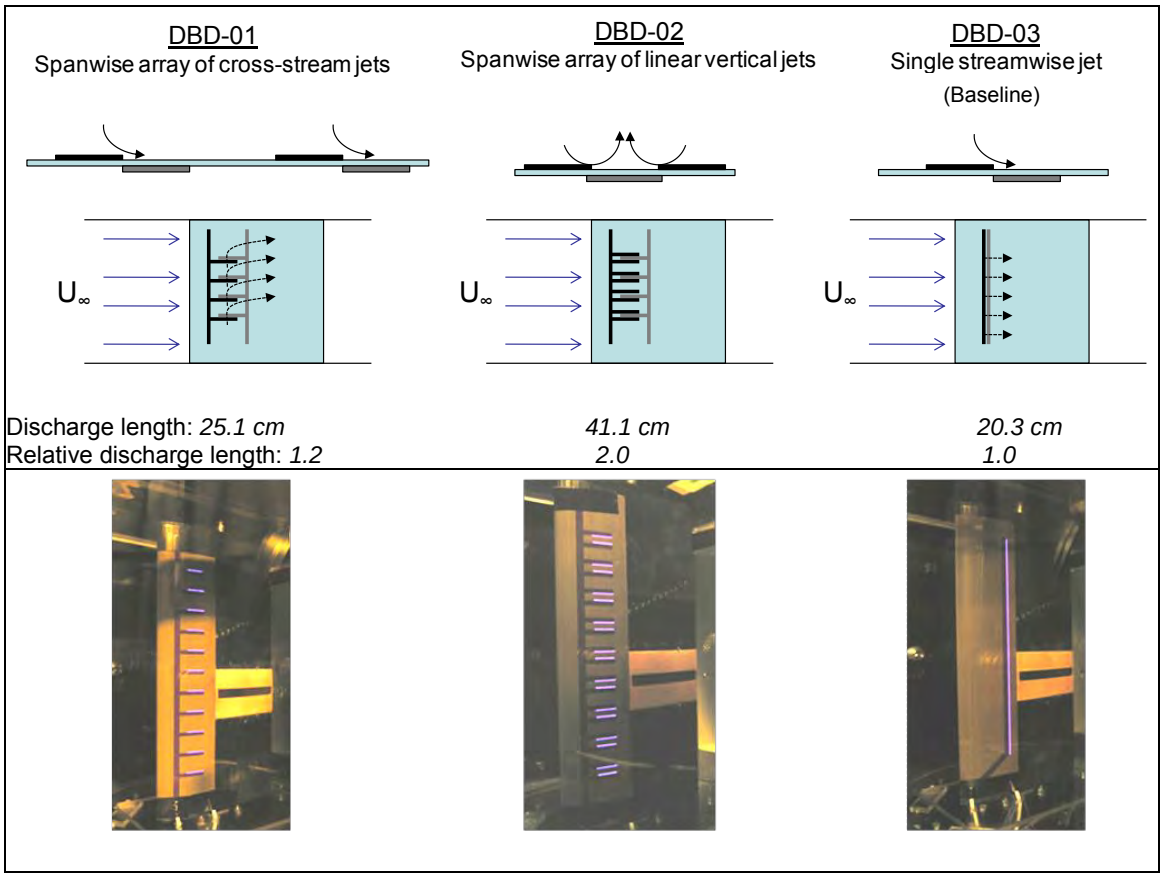

Figure 4.1 Schematic of each plasma actuator electrode configuration and photograph of each actuator installed and powered in the wind tunnel.

S3F #5 was used in the open loop study. In this study the S3F tangential surface displacement was used as a direct indicator of shear stress direction.

A PCO 4000 camera with 4008 x 2672 pixel resolution was used to obtain S3F flow-on and flow-off images. The image field of view was 27.3mm x 18.2 mm with a magnification factor of 146.6 px/mm. Airfoil deformation and motion relative to the camera on the order 25-50 μm (3.5-7 pixels) was corrected for using 2D interpolation using the method discussed in Section 2.6. Displacement maps were calculated using ISSI Inc. hybrid cross correlation/optical flow software. The displacement fields were then corrected for airfoil motion in Matlab.

The plasma actuators were fabricated in the U.S. AFRL Propulsion Directorate‟s thin film lab by photolithography and etching double-sided copper clad Kapton. The Kapton was 5 mil thick and the copper electrodes were 1.4 mil thick. The top and bottom electrodes were formed flush

with each other with no overlap. The plasma actuators were attached to the airfoil suction surface by 2 mil thick adhesive transfer tape and were wrapped around the entire leading edge of the airfoil to reduce the chance of tripping the boundary layer. Surface irregularity added by the plasma actuators on the suction surface was reduced to a 36 μm (1.4 mil) step up at the exposed electrode and an approximately 178 μm (7 mil) step down at the trailing edge of the actuator. Nonetheless, variation in extent of the mean laminar separation bubble was observed between different installations of the plasma actuators onto the airfoil.

A schematic of the power circuit is shown in Figure 4.2. The electrodes were powered by two Titan Series power supplies from Compact Power. Each of the power supply output voltages were increased by an Industrial Test Equipment Co. transformer to kilovolt levels. In this work the DBD plasma actuators were operated in steady mode with continuous sinusoidal waveforms at a frequency of 3 kHz. Measurements showed that it took approximately 200ms to achieve steady state actuator voltage amplitudes.

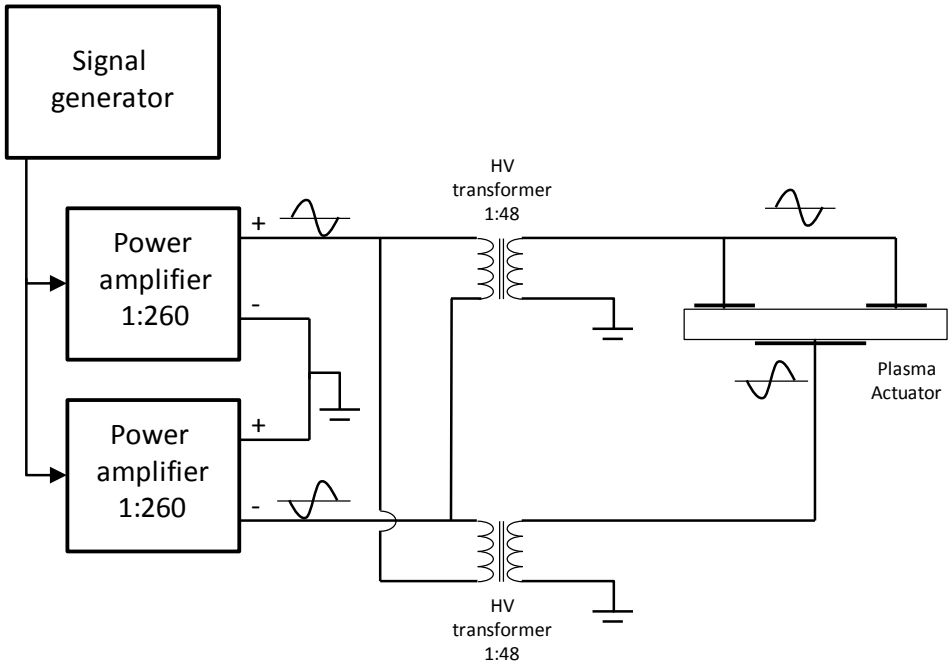

Figure 4.2 Plasma actuator circuit.

The top and bottom electrode voltages were measured using two Northstar PVM-11 high voltage probes with 1000:1 attenuation. The current was measured using a Pearson Model 4100 current monitor (1 Volt/Amp) placed on the top electrode power lead. The signal from each probe was measured using a Tektronix TSD 3054B oscilloscope. The power dissipation was calculated by numerically integrating the product of instantaneous voltage and current:

$$P = \frac{1}{\Delta t}\int_0^T v \cdot i \, dt. \tag{6.1}$$

The average power was obtained by considering the power dissipation over 10 complete periods of signal history. Figure 4.3 shows a plot of typical power dissipation versus applied voltage for the plasma actuator. The power dissipation is proportional to $V_{pp}^{3.5}$ and is consistent with the measurements of other researchers found in literature (Enloe et al. 2004). Figure 4.3 also shows the power dissipation per meter of discharge. Operation of the plasma actuator permanently changed the surface of the Kapton dielectric and left an image on the surface that was assumed to represent the extent of discharge. The image left on the Kapton surface was used to measure the discharge length. Each buried electrode had two areas of plasma along each spanwise edge totaling 41.1 cm of discharge length.

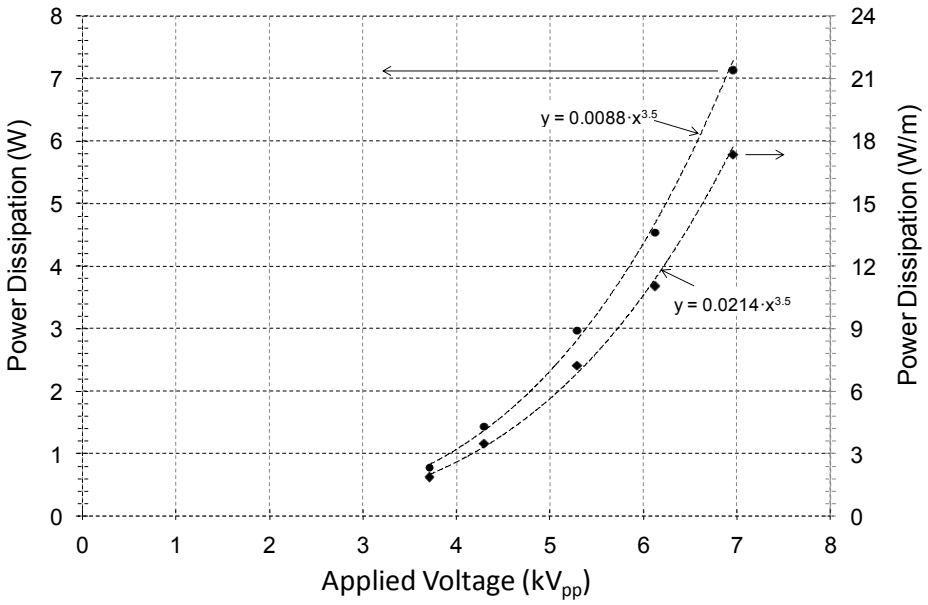

Figure 4.3 Typical actuator power dissipation

4.2. **Open Loop Study Results and Discussion**

4.2.1. Benchtop flow visualization

Flow visualization of the induced velocity generated with each plasma actuator electrode configuration is shown in Figure 4.4-Figure 4.6. In each figure an actuator was fixed to a flat plate with a uniform layer of adhesive transfer tape and placed on a bench top. The flow visualization method was explained in Section 2.3.2.

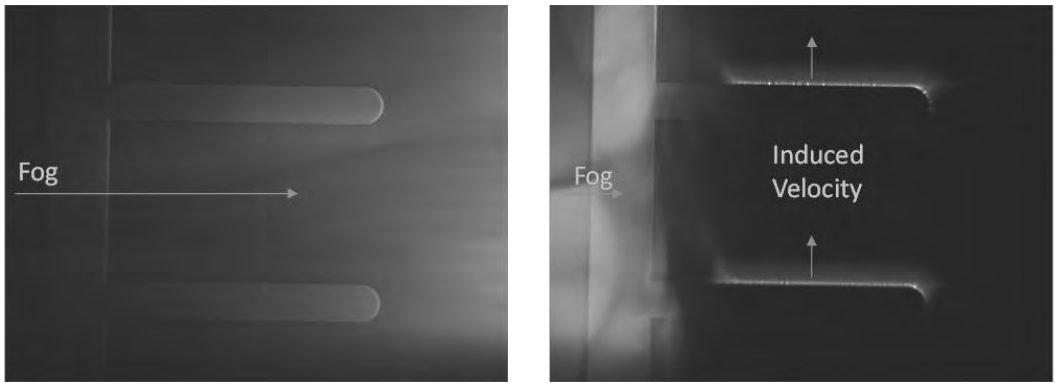

A. Series of lateral jets powered off B. Series of lateral jet powered on

Figure 4.4 Flow visualization using CO_2 generated fog of the plasma actuator electrode configuration DBD-01. Arrows indicate location of induced velocity from each discharge.

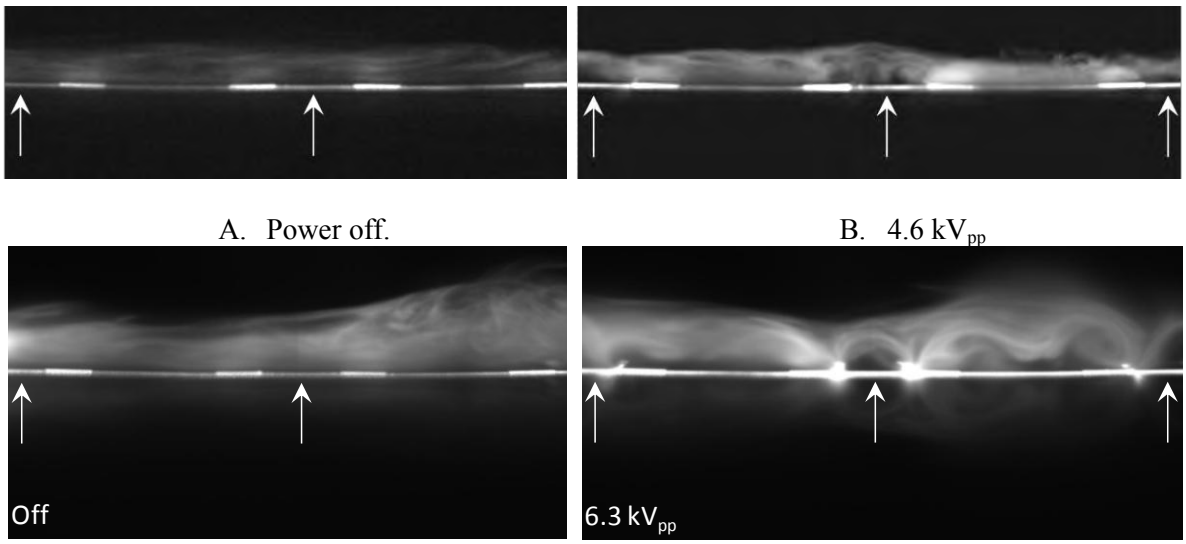

A. Power off. B. 4.6 kV_{pp}

Figure 4.5 Flow visualization using CO_2 generated fog of the plasma actuator electrode configuration DBD-02. Arrows indicate the location of each vertical jet.

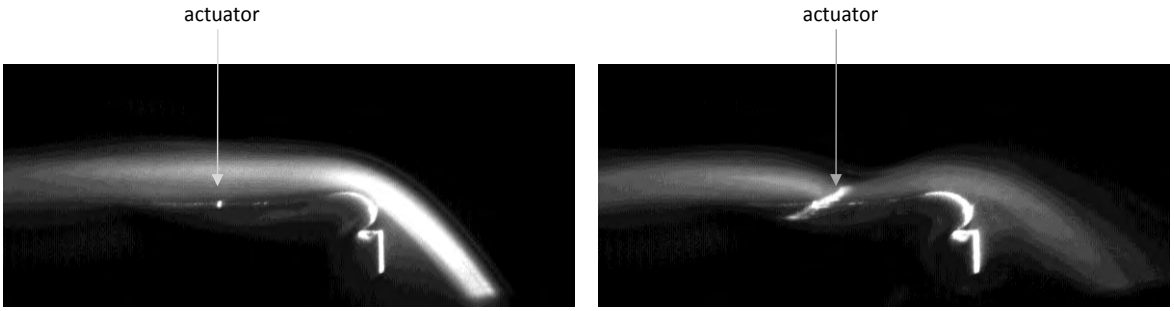

Figure 4.6 Flow visualization using CO_2 generated fog of the plasma actuator electrode configuration DBD-03.

In Figure 4.4 and Figure 4.6 the fog is flowing left to right, and in Figure 4.5 the flow is traveling towards the reader. The image of Figure 4.5 shows a strong jet in the spanwise direction that prevents the fog from reaching the illuminated plane. The potential for streamwise vorticity lies in the interaction between the freestream fluid flow and cross stream wall jets.

In Figure 4.5 two different actuator voltages are shown along with corresponding power off images taken just before each power on image. At the lower voltage vortical structures are observed in the region of the plasma marked by the middle arrow. Induced velocity jets are formed in the region of plasma at the inner edge of the exposed upper electrodes, directed towards each other. At the higher voltage the plasma area at the inner edge of the exposed electrodes looks like a pair of sinks, entraining fluid and drawing it through the plasma region and ejecting it into the vertical jet between electrodes. At the higher voltage an interaction between vertical jets is clearly observed producing streamwise vortical structures in between the vertical jets. No effort to optimize the electrode configuration was made, but this type of spanwise configuration of vertical jets has great potential as a flow effecter due to the potential for generating three-dimensional vorticity and boundary layer instability.

The arrangement of Figure 4.6 produces a tangential wall jet and was discussed in detail in Section 1.4.1.

4.2.2. Flowfield

Data was taken at four different Reynolds numbers with a focus here on performance at Re = 5 x 10^4, and Re = 1.0 x 10^5. At the lower Reynolds number the laminar boundary layer separates and large eddies are formed in the separated shear layer; the flow however, does not fully reattach. At the higher Reynolds number the boundary layer separates then transitions to turbulent and reattaches. The closed separation bubble sheds vortices which travel down the suction surface to the trailing edge. The large scale Kelvin-Helmholtz instabilities that develop in the separated shear layer lead to periodic vortex shedding observed in Figure 4.7. Previous analysis has shown that time averaged measurements of the laminar separation look very similar to measurements of a traditional laminar separation bubble (Lin and Pauley 1996, Selig and McGranahan 2004).

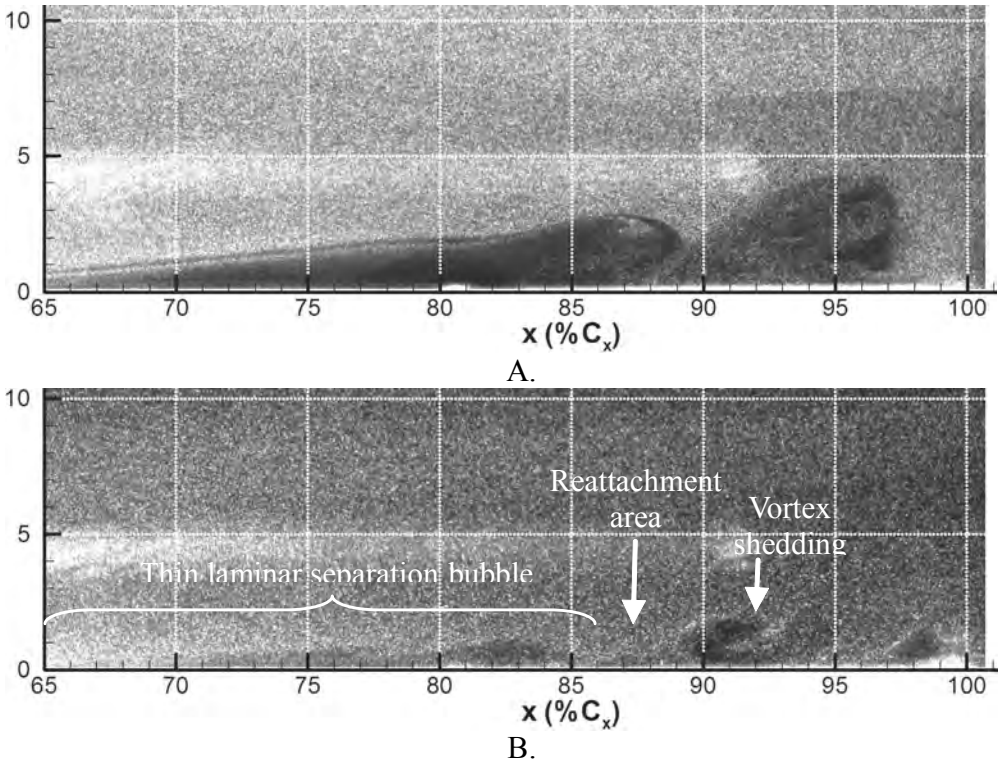

Figure 4.7 Flow visualization over the E387 suction surface from C_x = 67% to trailing edge with DBD-01 installed. Image A is at Re = 5 x 10^4. Image B is at Re = 1.0 x 10^5.

Figure 4.8 shows the suction surface C_p distribution with each plasma actuator installed at each Reynolds number tested along with inviscid results obtained in XFOIL. The C_p distribution is consistent across each plasma actuator installed with regard to the presence of laminar separation without reattachment at Reynolds numbers tested below $6.0x10^4$, and laminar separation with reattachment for Reynolds numbers tested equal to $1.0x10^5$ and higher. Differences between the C_p profiles include a higher peak C_p for DBD-01 as compared to DBD-02 and DBD-03, with DBD-03 having the lowest peak C_p. In addition,

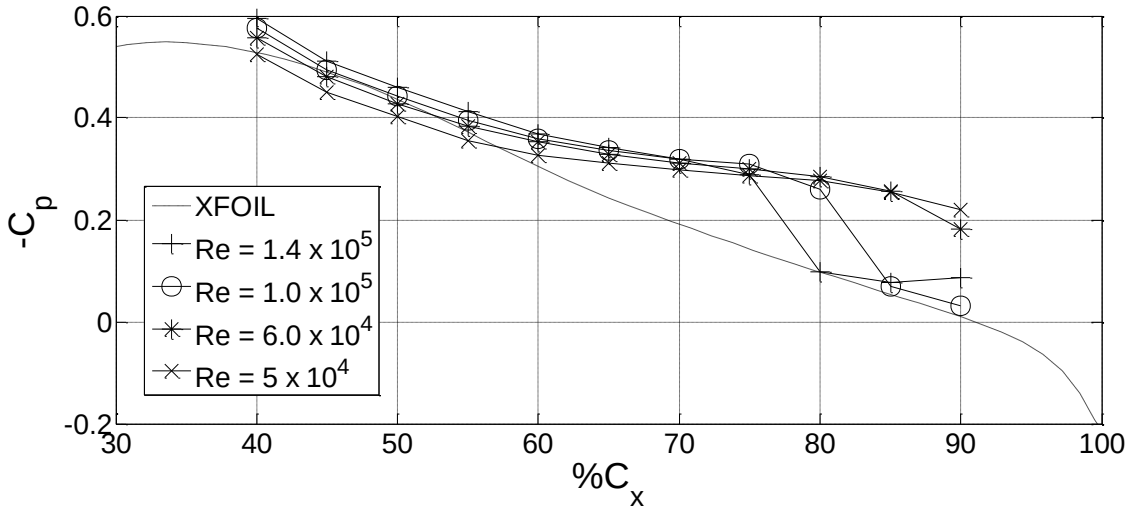

A.

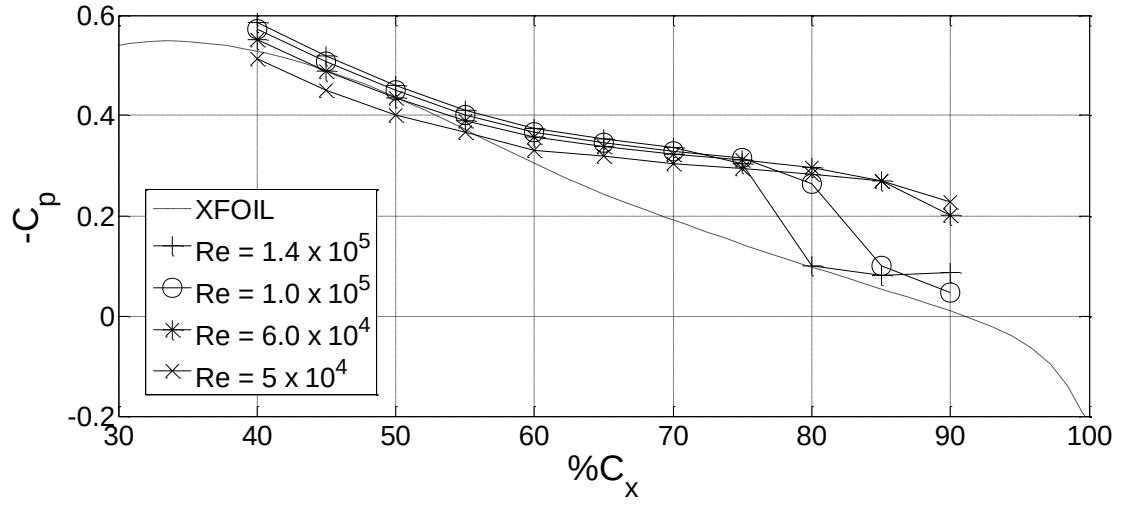

B.

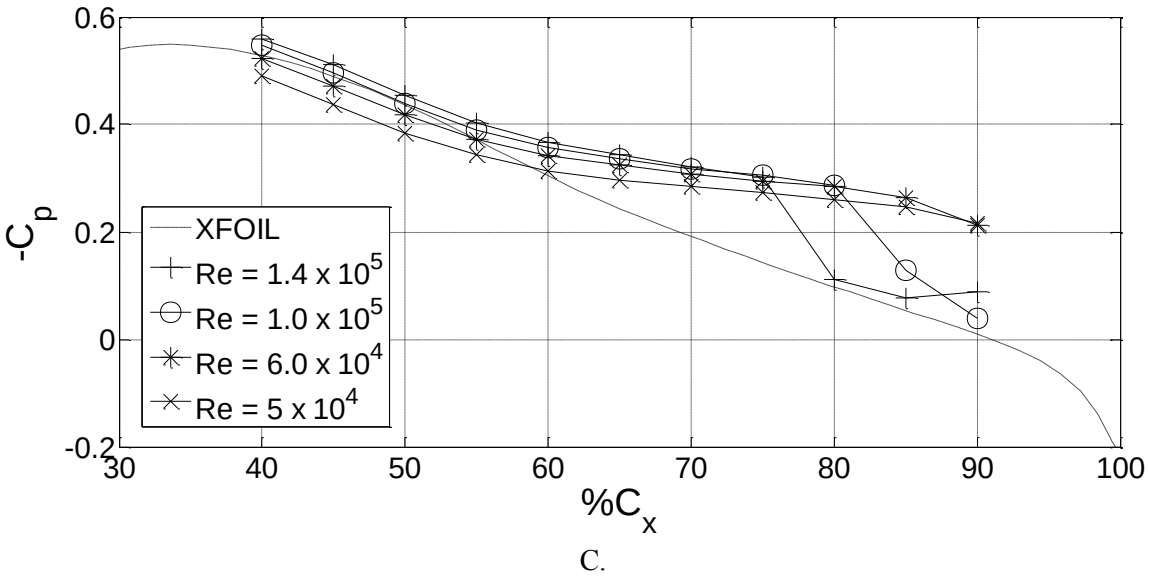

C.

Figure 4.8 Suction surface C_p distribution with plasma actuators powered off. Plot A: DBD-01, B: DBD-02, C: DBD-03.

C_p plots indicate a difference in reattachment location for the three different plasma actuators tested. This difference is most noticeable in the C_p plot of DBD-03 at Re=1.0x10^5 in which the reattachment point noticeably shifts downstream 5% axial chord to C_x≈90%. It is important to keep in mind the spatial resolution of C_p data due to the limited amount of pressure taps. The S3F displacement field vector plots of Figure 4.12 indicate that the reattachment point is not uniform along the span, so a discrepancy of several percent axial chord is not unexpected. The difference in max C_p is likely due to the shift in mean reattachment location. The difference in data for each case is presumably due to two things: variation in the quality of installation of each plasma actuator, and the possibility that the electrode geometry caused small scale perturbations in the laminar boundary layer.

A summary of the separation and reattachment locations (extracted from C_p data) is provided in Figure 4.9 for each plasma actuator configuration tested.

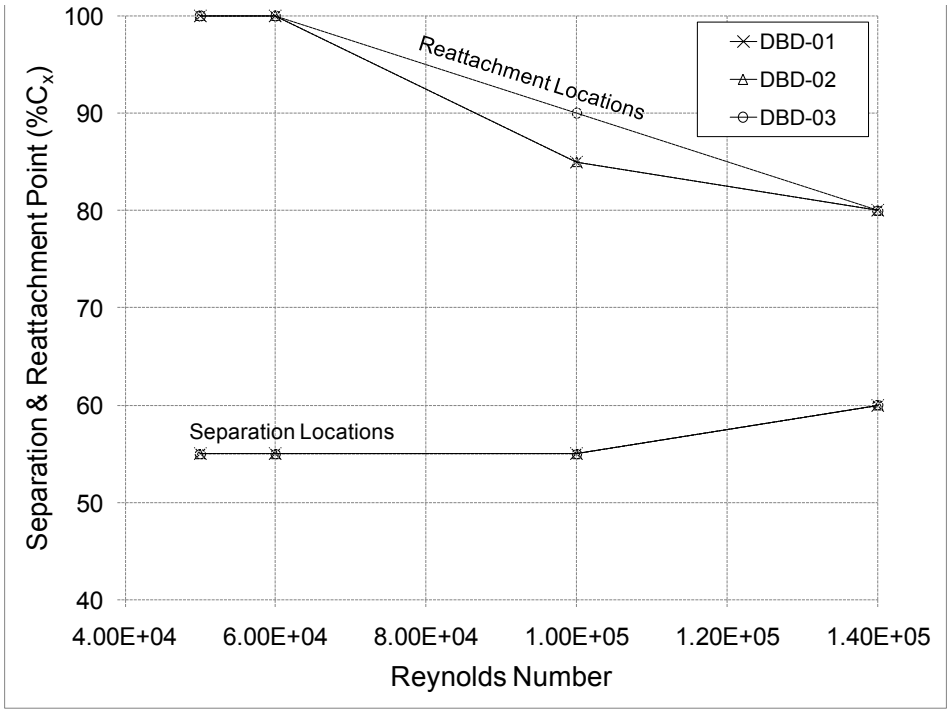

Figure 4.9 Mean suction surface separation and reattachment points for each plasma actuator configuration tested powered off.

4.2.3. Results at Re = 5 x 10^4

C_p and wake profile plots for each plasma actuator tested at a Reynolds number of 5x10^4 are shown in Figure 4.10 and Figure 4.11 respectively. A range of input voltages are shown in each plot. DBD-01 and DBD-02 drastically improve the surface pressure distribution with the time averaged measurements. With DBD-01 the highest actuator voltage flattened out the pressure plateau indicating a reduction in separation bubble length, but the pressure coefficient near the trailing edge did not recover to the inviscid profile. Operation of the plasma actuator has changed the loading on the airfoil suction surface. A similar trend was observed with DBD-02, except flattening of the pressure coefficient occurred at a lower voltage. Powering on DBD-03 resulted in a movement of the reattachment point upstream, but with a much less significant change in pressure coefficient compared to the first two plasma actuators.

Powering on each actuator resulted in a significant narrowing of the airfoil wake. The wake of DBD-01 decreased in width as input voltage increased to 5.6 kV_{pp}, and then increased width as

voltage was amplified further. As the voltage of DBD-02 was increased beyond 4.2 kV_{pp} the wake gradually increased in width up to a voltage of 5.6 kV_{pp}. At input voltages above 5.6 kV_{pp} the wake began to narrow at its base with a significant increase in peak velocity deficit. Increasing the voltage of DBD-03 did not decrease the wake considerably beyond the lowest input voltage applied.

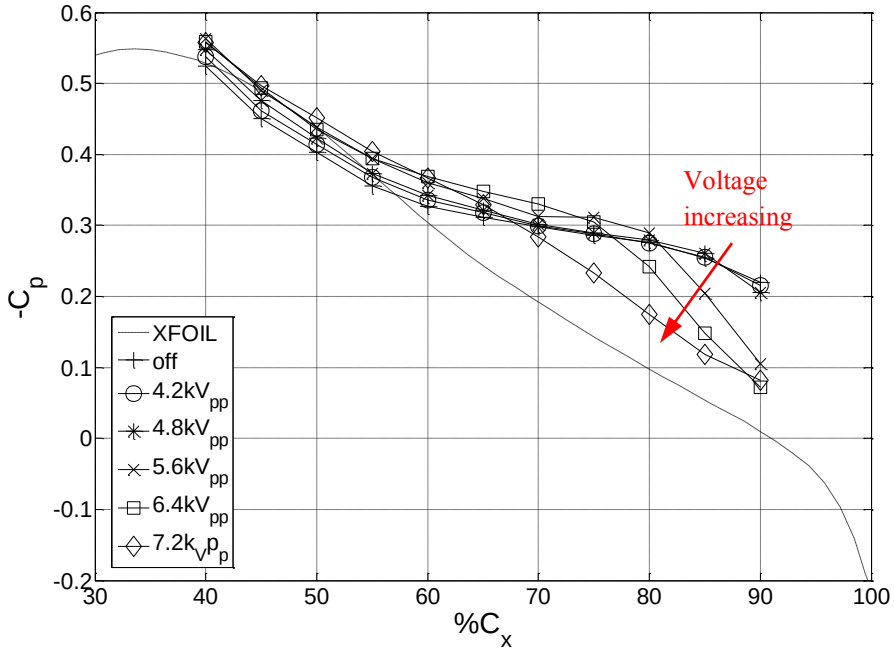

a.) DBD-01

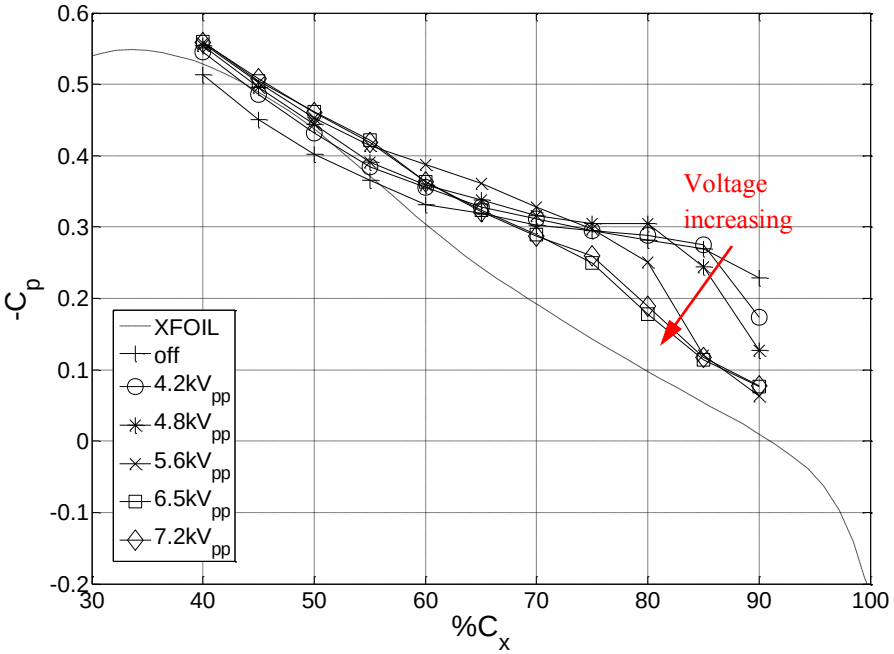

b.) DBD-02

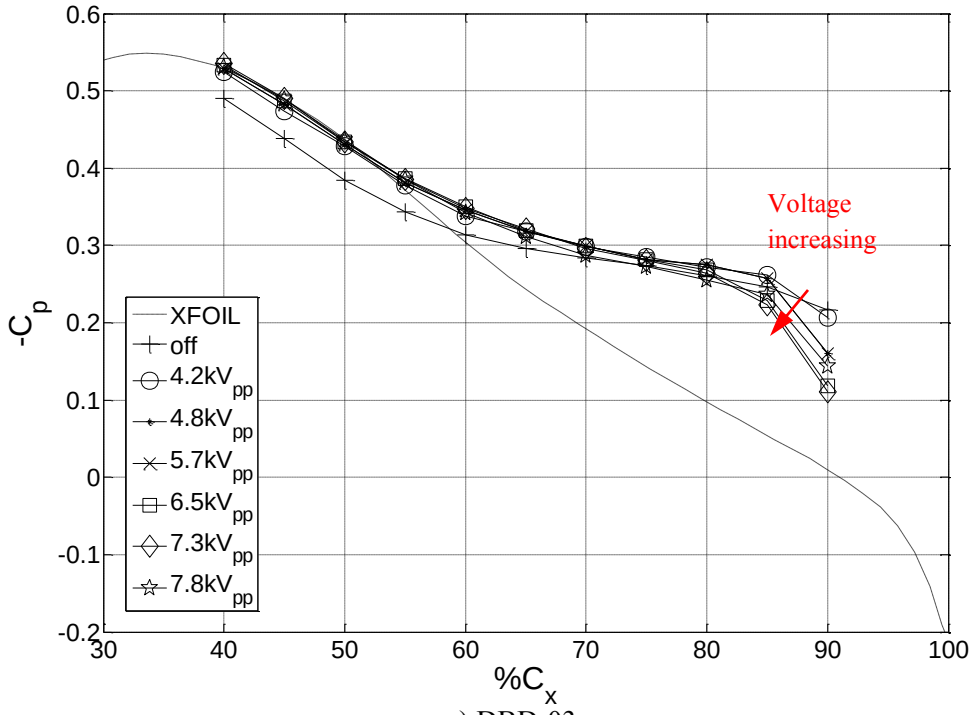

c.) DBD-03

Figure 4.10 Suction surface Cp distribution for each plasma actuator tested at 5 x 10^4.

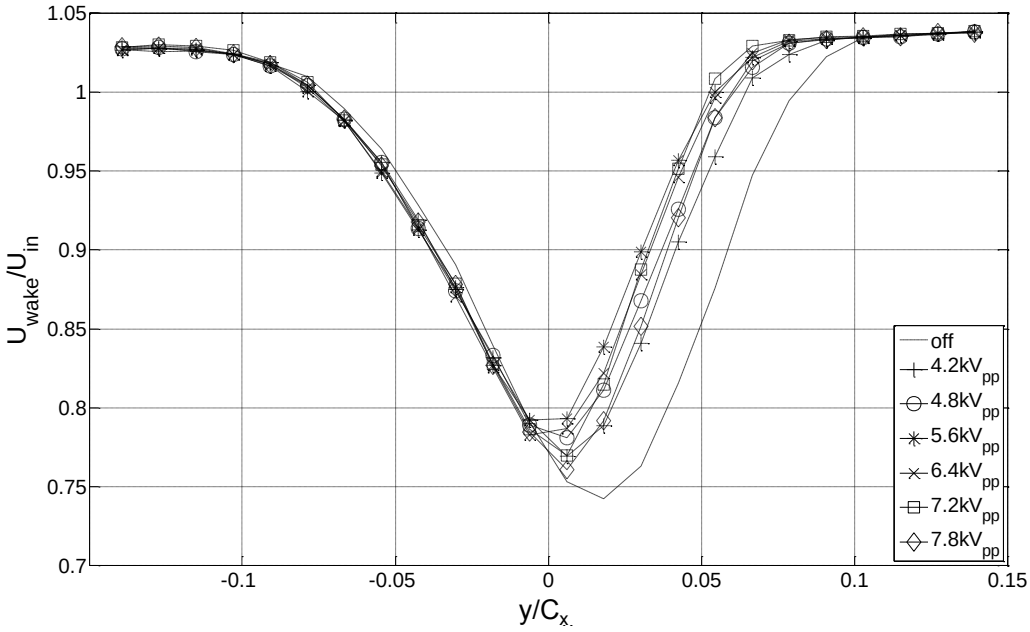

a.) DBD-01

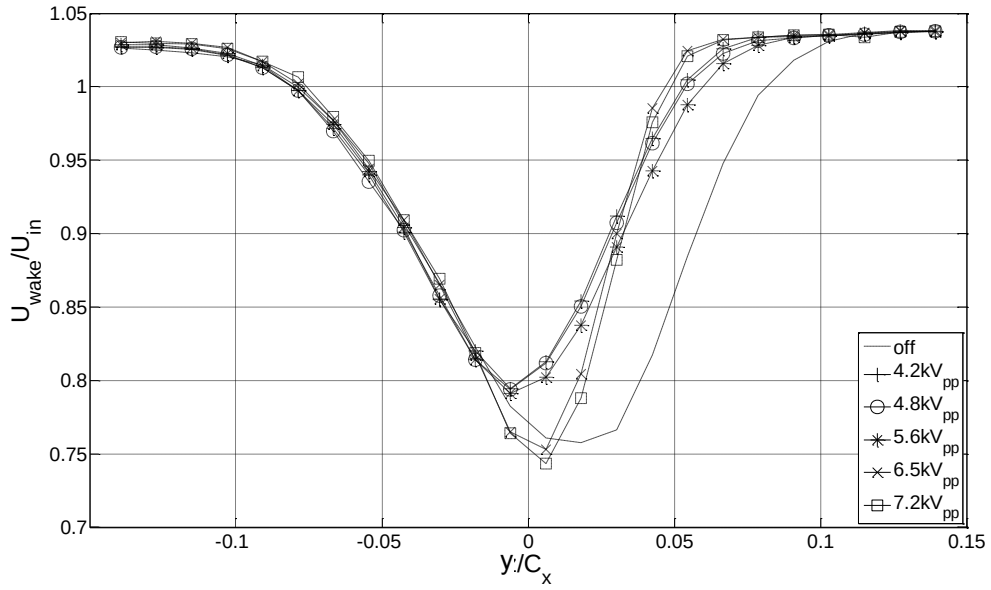

b.) DBD-02

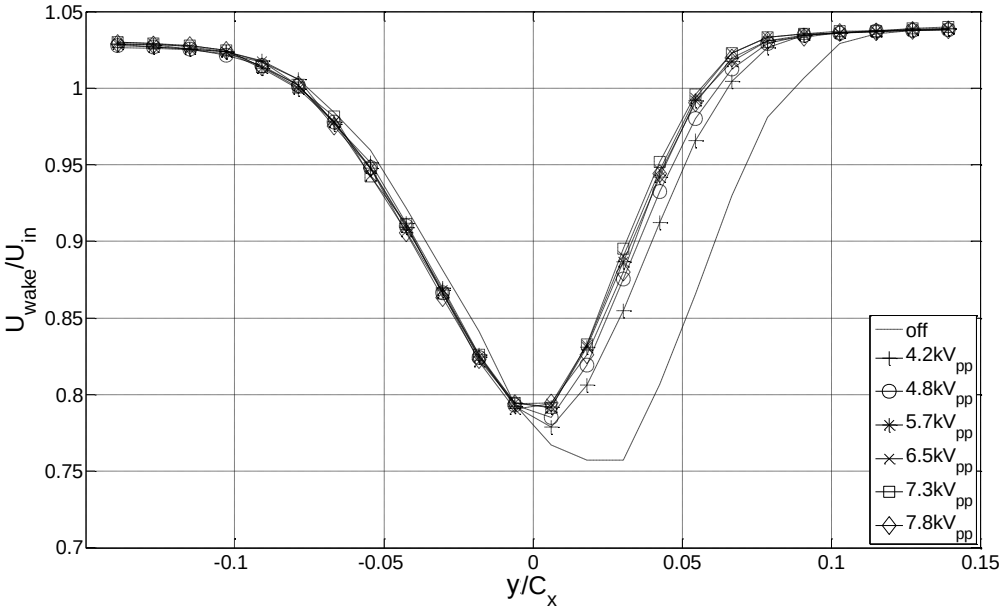

c.) DBD-03

Figure 4.11 Wake profile for each plasma actuator tested at 5 x 10^4.

The use of S3F allows a unique view of the surface tangential displacement which directly corresponds to surface shear stress direction. Figure 4.12 is a series of mean surface tangential displacement vector plots obtained from S3F for DBD-01 actuator off and a range of applied plasma actuator voltage. The plots clearly show the effect of the plasma actuator. For actuator

off conditions a strong reverse flow vortex is present at the trailing edge of the airfoil with a dead air region of separated flow just upstream from the vortex. As the plasma actuator is turned on the reverse flow vortex gradually shifts upstream with increase in voltage. There is a significant upstream shift and movement of the reverse flow vortex out of the view at the highest applied voltage of 7.2 kV_{pp}. At the highest voltage the mean flow appears to be reattached at $C_x \approx 93\%$ indicated by a zero crossing and downstream pointing displacement vectors. Figure 4.13 shows mean S3F tangential streamwise displacement for each plasma actuator tested at a spanwise location at z = 5.5%C_x (reference views in Figure 4.12).

From data in Figure 4.10 - Figure 4.15 the following conclusions are made for operation at Re=5 x 10^4:

DBD-01 – array of cross stream jets:

- Narrowing of the wake when the actuator is turned on indicates a decrease in drag and decrease in separation angle
- Mean S3F streamwise displacement in Figure 4.12 indicate that boundary layer reattachment and subsequent decrease in separated region does not occur until an applied voltage of 5.6 kV_{pp} and higher.
- C_p measurements agree with S3F in that there is no reattachment and/or minimal shift in reattachment point until higher actuator voltages are applied.

DBD-02 – array of vertical jets:

- C_p, S3F, and wake profile data all indicate that DBD-02 has a much larger effect on the flow at lower applied voltages compared to DBD-01.
- The reverse flow vortex moves upstream several percent chord when the plasma actuator is turned on at the lowest voltage. This is an improvement over DBD-01 and implies that the separated boundary layer is reattached or nearly reattached at the trailing edge at a voltage of 4.2 kV_{pp}. When the voltage is increased to 5.6 kV_{pp} the mean flow is clearly reattached as shown in the C_p and S3F data.

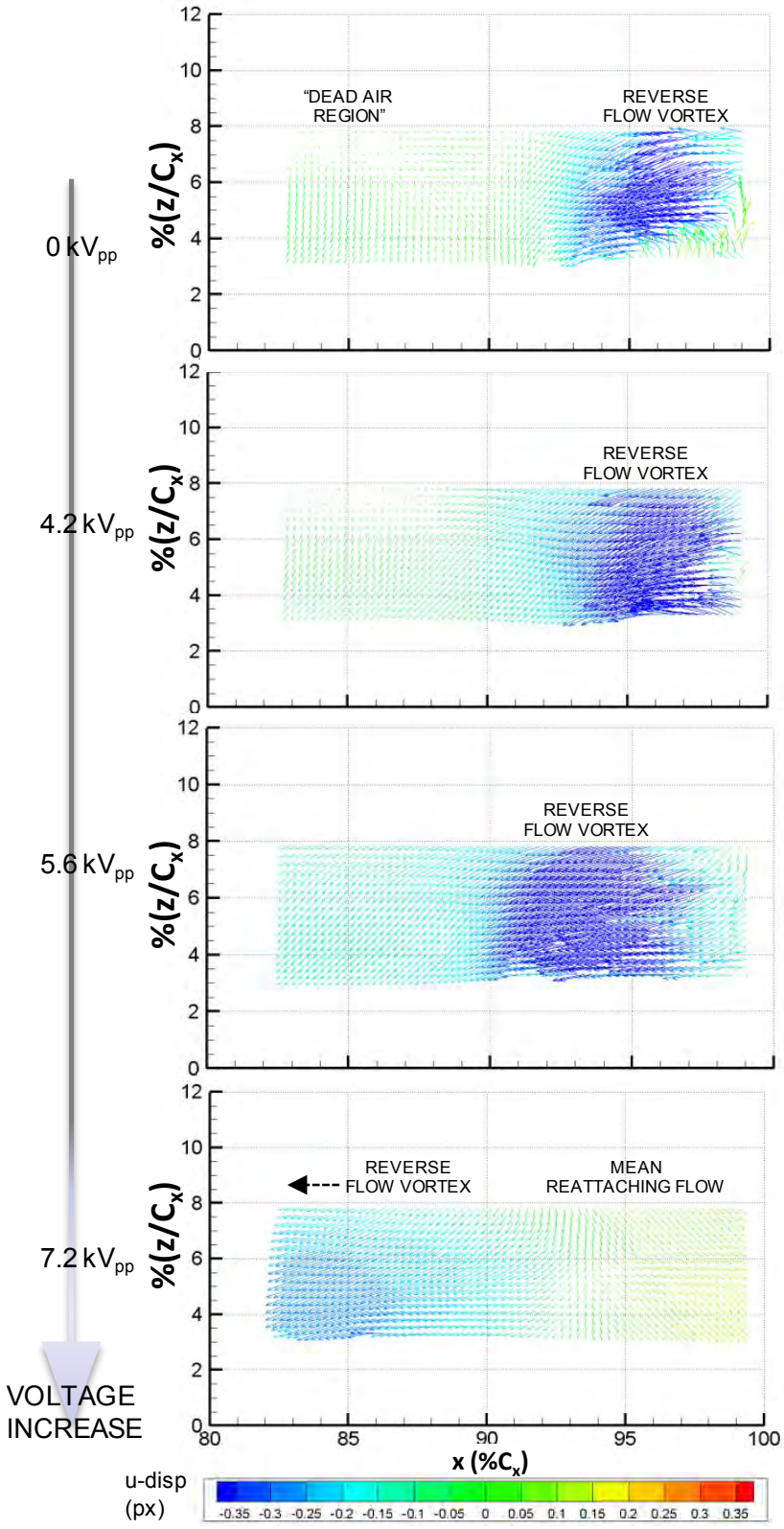

Figure 4.12 S3F measured surface tangential displacement of airfoil with DBD-01 installed. Flow speed is Re = 5 x 10^4 with various plasma actuator voltages

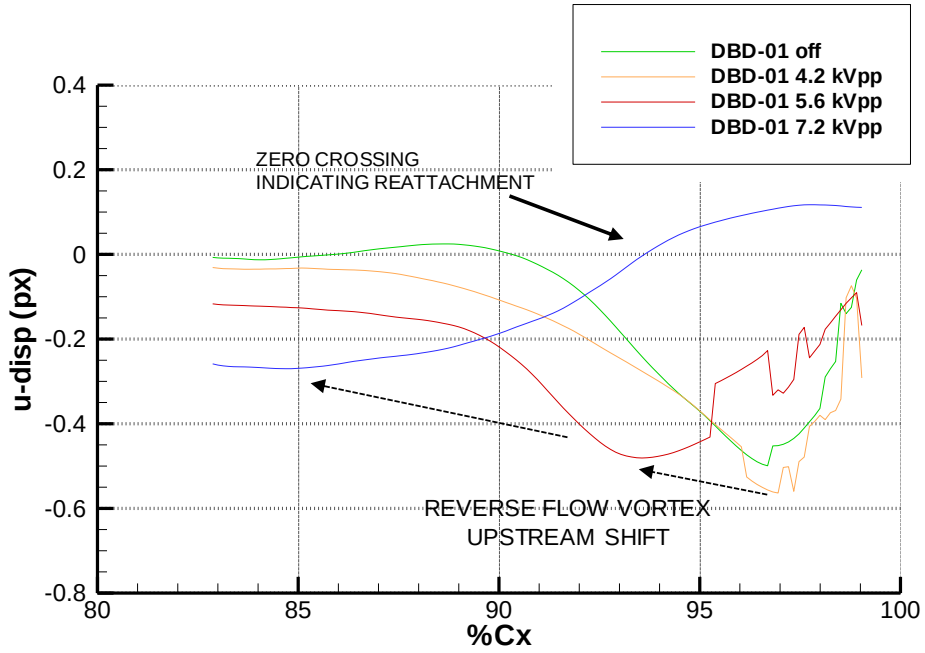

Figure 4.13 S3F streamwise disp. of DBD-01 at Re = 5 x 10^4 & various plasma actuator voltages.

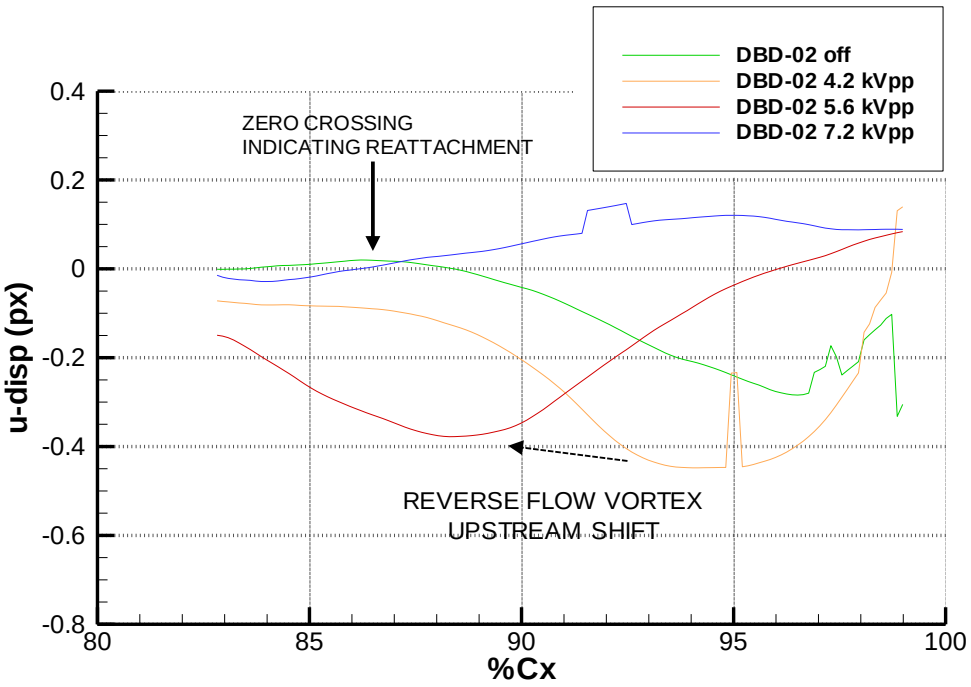

Figure 4.14 S3F streamwise disp. of DBD-02 at Re = 5 x 10^4 & various plasma actuator voltages.

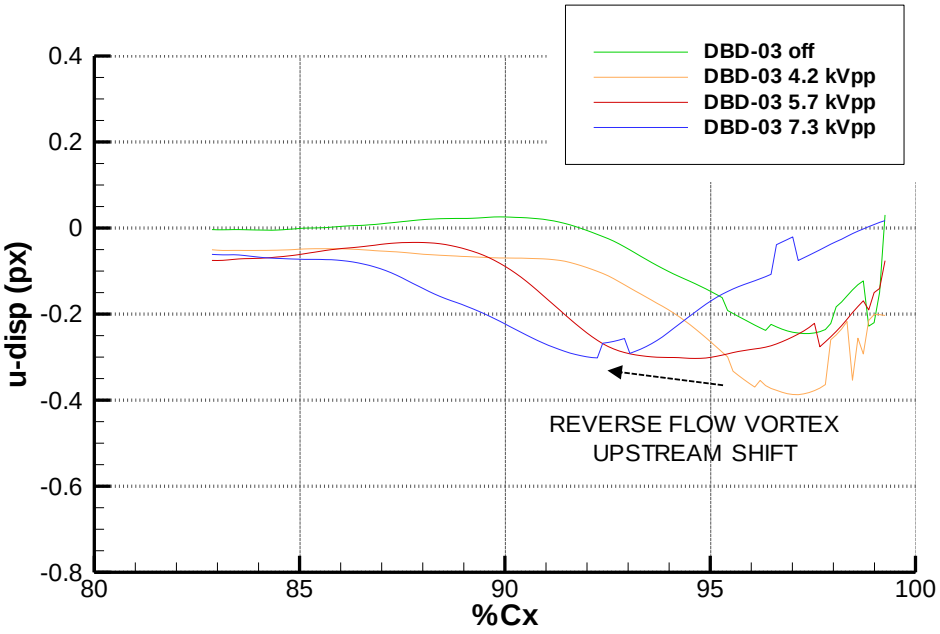

Figure 4.15 S3F streamwise disp. of DBD-03 at Re = 5 x 10^4 & various plasma actuator voltages.

DBD-03 – downstream jet:

- DBD-03 has the least significant change in C_p distribution and S3F streamwise displacement when the actuator is turned on and voltage is increased.
- Decrease in wake profile at the lowest plasma actuator voltage indicates that there is an effect on the separated flow by the actuator.

4.2.4. Results at Re = 1.0 x 10^5

Figure 4.16 shows C_p profiles at Re = 1.0 x 10^5 for which there is laminar separation with reattachment when the actuator is powered off. The C_p profiles for each plasma actuator show an effect on suction surface C_p distribution when the actuator is turned on. The wake profiles (omitted here) however, show no decrease in wake width or depth with actuation; instead they remain constant or grow wider.

When the actuator is powered on the mean reattachment point gradually moves upstream as much as 5%C_x for DBD-01. The plateau region of the C_p distribution is flattened as voltage is

increased for DBD-02 and DBD-03, first with a shift upstream of the reattachment point, then overall smoothing of the pressure gradient. As the pressure coefficient in the separated region is smoothed out the pressure profile does not approach the inviscid profile, instead it is lower. The S3F streamwise displacement in Figure 4.18 agrees with the C_p distributions in that there is a larger shift in reattachment point caused by DBD-02 and DBD-03, than for DBD-01. In fact, based on S3F data at the trailing edge and C_p data, the mean flow reattaches far upstream of C_x=80% for DBD-02 with an applied voltage of 7.3 kVpp. This is a significant decrease in the extent of the mean separation bubble length. Earlier transition to turbulence with less dominance from large scale inviscid type instability and more viscous small scale turbulence in the boundary layer would support the increase in wake velocity deficit seen in DBD-02 at Re=1.0 x 10^5.

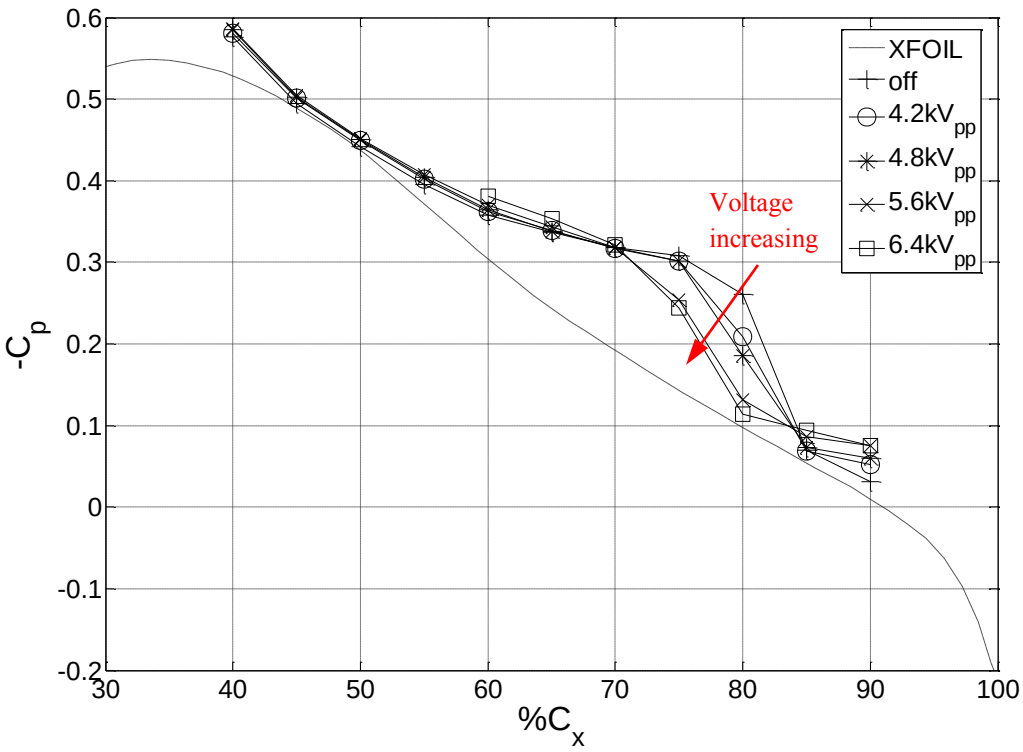

a.) DBD-01

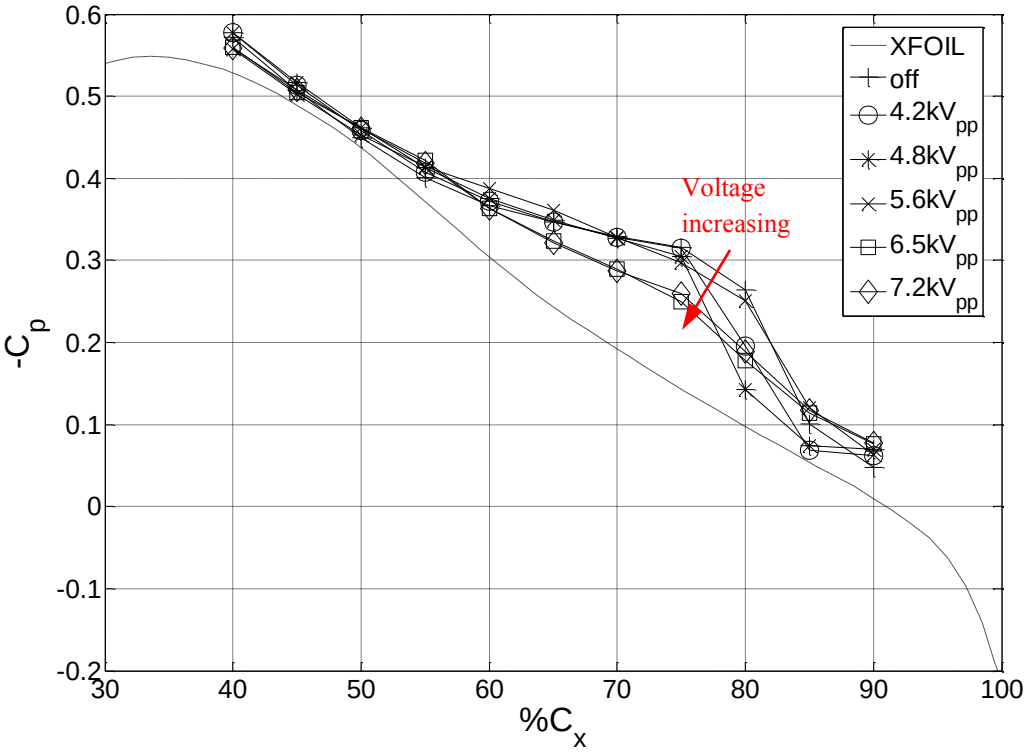

b.) DBD-02

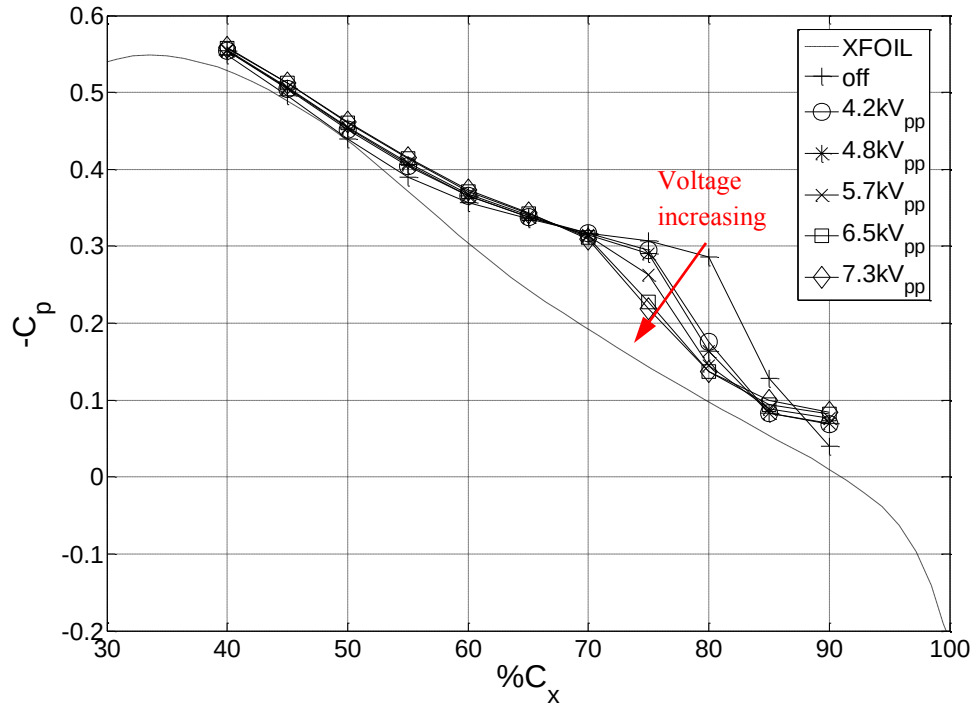

c.) DBD-03

Figure 4.16 Suction surface Cp distribution for each plasma actuator tested at Re = 1.0 x 10^5.

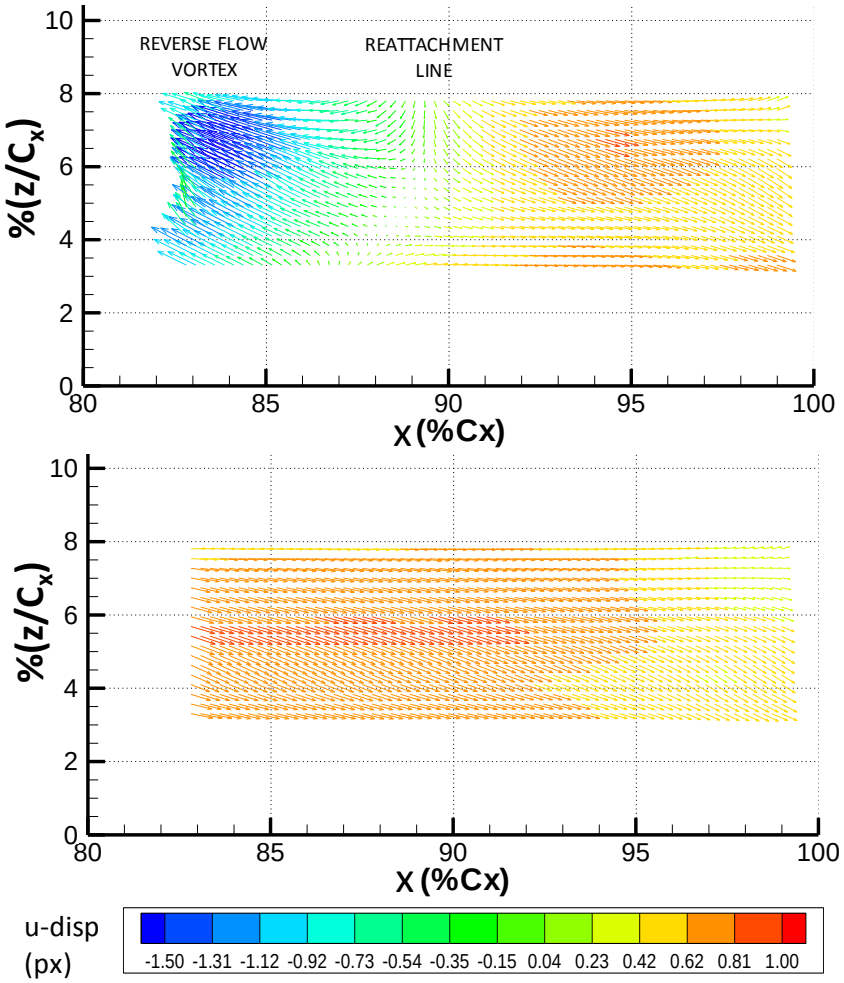

Figure 4.17 S3F tangential displacement of DBD-02 at Re = 1.0 x 10^5 for Top: Actuator off, Bottom: 7.2 kVpp.

Based on the plots of Figure 4.16 - Figure 4.18 the following conclusions are made for operation at Re = 1.0 x 10^5:

- All three plasma actuators move the mean reattachment point upstream as voltage is increased.
- C_p data indicates an upstream shift in reattachment point for DBD-01 of at least 5% C_x. S3F data indicates an upstream shift in mean reattachment of nearly 4% C_x at the S3F midpoint, but the reattachment point is not uniform along the airfoil span.
- C_p data of DBD-02 shows a significant upstream shift in reattachment location as plasma actuator voltage is increased. The plateau in C_p that marks the separation bubble smoothes out significantly at a voltage of 6.5kVpp and above. The peak velocity deficit in the wake

increases with voltage. S3F data shows a significant upstream shift in mean reattachment location as the voltage is increased culminating with a reattachment point upstream of the view which ends at C_x=83%.

- Powering on plasma actuator DBD-03 shifts the reattachment point upstream with increases in voltage providing further upstream shift in reattachment. S3F indicates a nearly 8% upstream shift in mean reattachment point as voltage is increased to 7.3 kVpp.

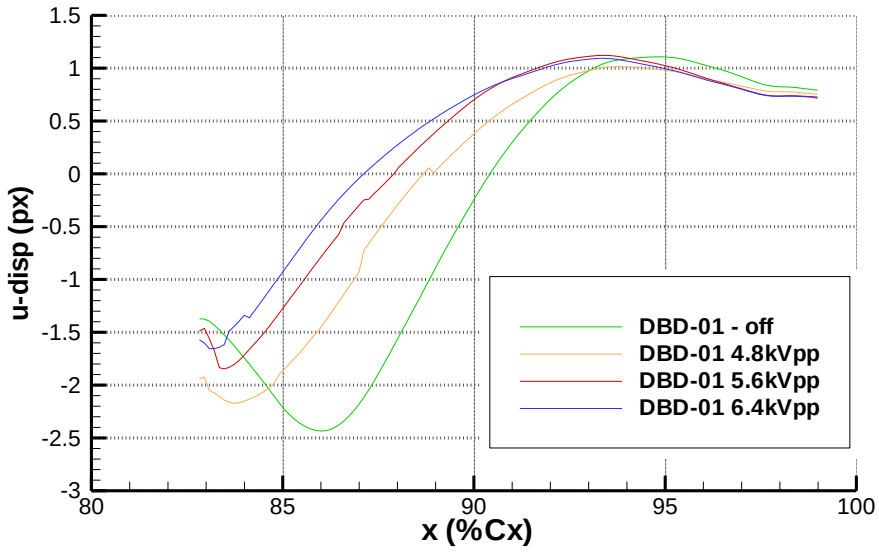

a.) DBD-01

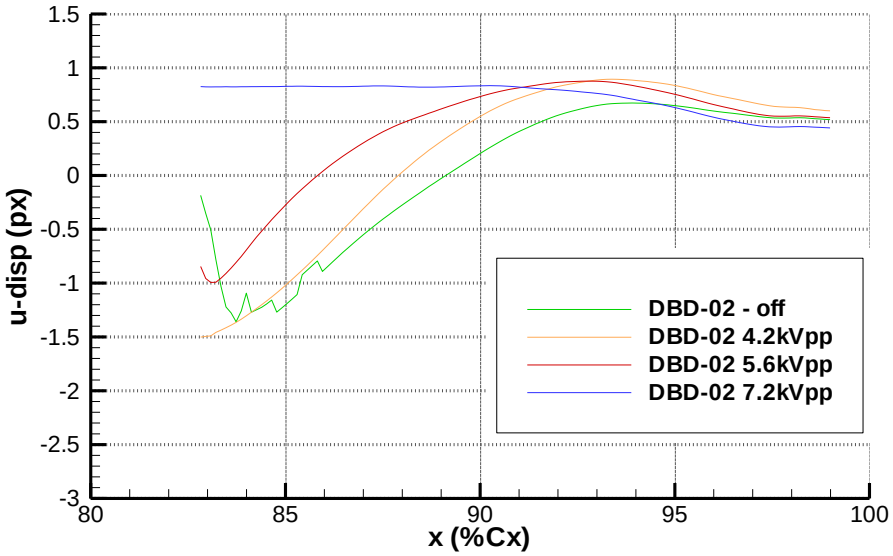

a.) DBD-02

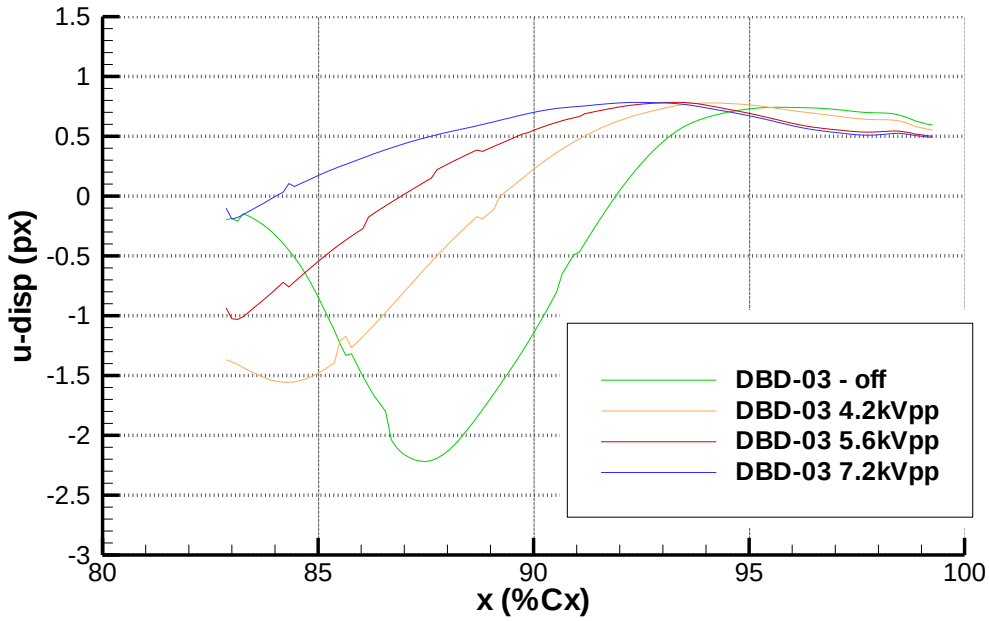

Figure 4.18 S3F tangential displacement at Re = 1.0 x 10^5 and various plasma actuator voltages.

4.2.5. Discussion

Each actuator clearly had an effect on suction surface laminar boundary layer separation as summarized in the plots of Figure 4.19 that show the S3F indicated mean reattachment points. At the lower Reynolds number 5.0x10^4 in which there was laminar separation without reattachment, powering on actuators DBD-01 and DBD-02 clearly resulted in a significant upstream shift in mean reattachment location. Electrode configuration DBD-02, the spanwise array of linear vertical jets led the actuators tested with reattachment at C_x=87%. This is confirmed by C_p data that shows significant smoothing of the plateau in pressure gradient that marked flow separation. DBD-03 did not definitively result in mean reattachment at the highest voltage tested, but did result in a significant decrease in wake width when the actuator was powered.

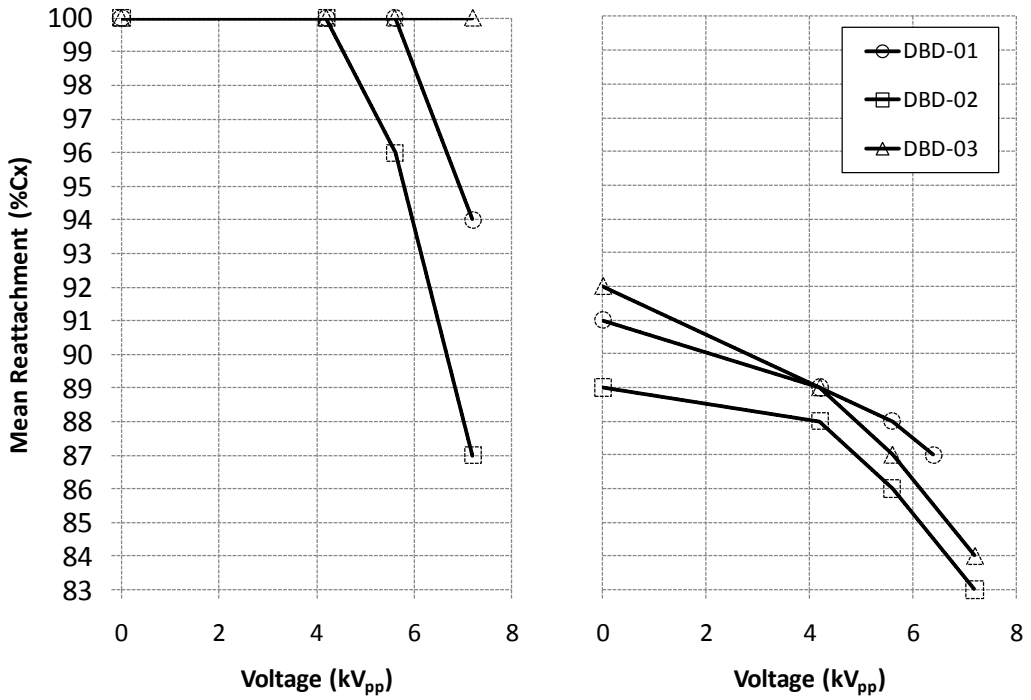

Figure 4.19 S3F indicated shifts in mean reattachment locations with increase in voltage

At the higher Reynolds number, $1.0x10^5$, laminar boundary separation with mean reattachment was present with the plasma actuator off. In these flow conditions powering on DBD-03 significantly shifted the mean reattachment line upstream 8%C_x. Less of an upstream shift was observed for DBD-01, the spanwise array of cross stream jets, however S3F data was not obtained at 7.2kVpp to compare to the other actuators, and further upstream shift may have resulted. Electrode configuration DBD-02 had the largest apparent effect with an S3F indicated shift in mean reattachment point beyond the field of view (reattachment at C_x<83%).

Drag data is presented in Figure 4.20 for each actuator tested. Powering on each actuator resulted in a decrease in drag at Re = 5 x 10^4, with each actuator reaching a minimum drag value. DBD-02, the spanwise array of linear vertical jets reached its minimum at the lowest plasma actuator voltage, with a 33% reduction in drag. DBD-03 the downstream facing jet also had a significant decrease in drag 30% at Re=$5.0x10^4$. At the Re=$1.0x10^5$ powering on the actuators did not result in a decrease in drag. In fact the drag gradually increased with increase in voltage for

each actuator. This is most likely due to the increased length of turbulent boundary layer as the separation bubble decreases in length, resulting in no improvement in drag. The drag plot shown in Figure 4.20 also displays the difference in drag due to variation in the quality of installation of each plasma actuator on the airfoil. The airfoil with DBD-03 has the largest initial drag when the plasma actuator is powered off. For a fair comparison of drag reduction between actuators, the power dissipation should be considered. Each actuator configuration had different electrode dimensions, discharge length, and power dissipation across the span. An estimate of the discharge length for each configuration was provided in Figure 4.1. A summary of peak drag reduction and corresponding power dissipation compared to the baseline electrode configuration is listed in Table 4.1.

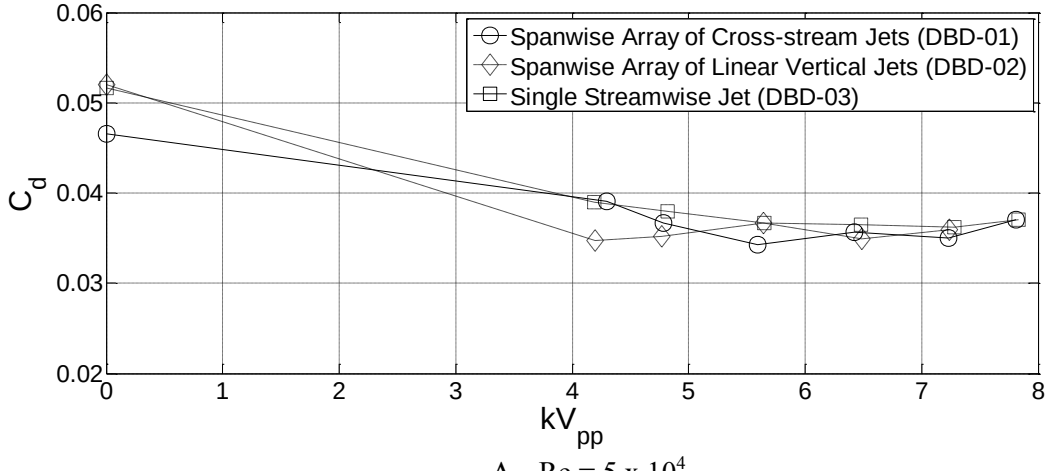

A. Re = 5 x 10^4

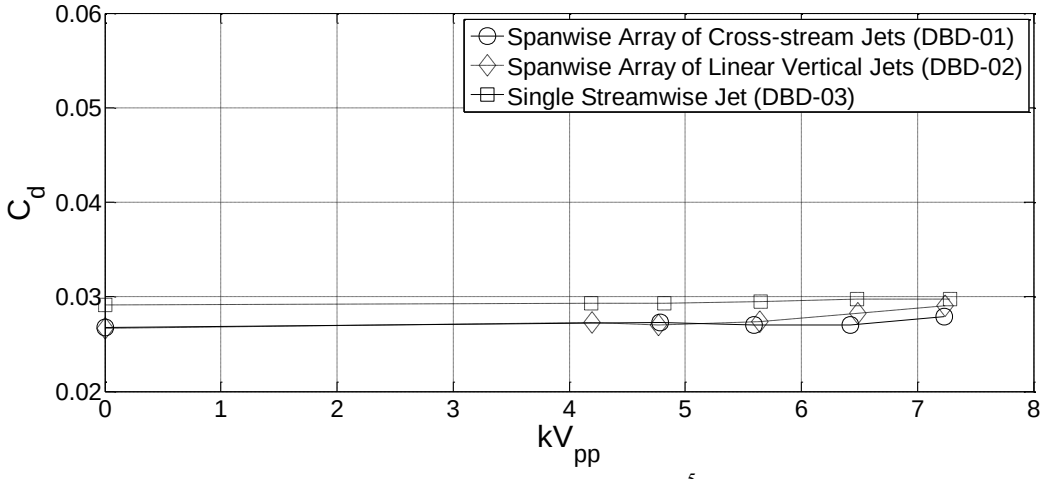

B. Re = 1.0 x 10^5

Figure 4.20 Section drag for each plasma actuator tested.

Table 4.1 Comparison of the peak drag reduction of each plasma actuator configuration at Re = 5 x 10^4.

	Relative length	Voltage (kV_{pp})	Change in C_d (%)	Change in Power vs. Baseline (%)
DBD-01	1.2	5.6	-27%	-51%
DBD-02	2.0	4.2	-33%	-70%
DBD-03	1.0	7.3	-30%	0%

Flow visualization images are shown in Figure 4.21-Figure 4.23 in order to further understand the effect of each actuator. Figure 4.21shows a large decrease in separation and boundary layer thickness as the actuator power is increased. At the lower actuator voltage a decrease in separation angle, and smaller, less dominate large scale inviscid structures in the separated shear layer are observed. At the higher voltage a thin separation bubble is formed. This explains the earlier minimum observed in drag. As the voltage increases past 5.6 kV_{pp} and the separated boundary layer reattaches, no additional gains are made in drag due to increased turbulent boundary layer length.

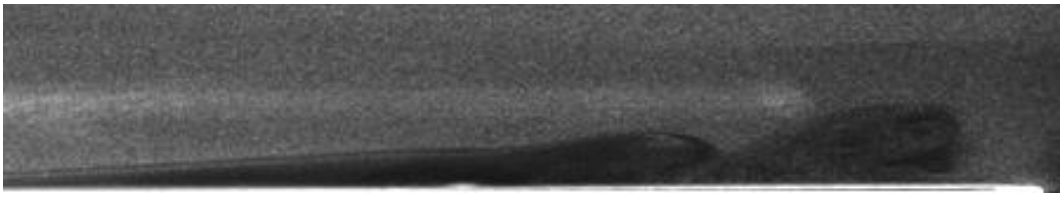

a.)

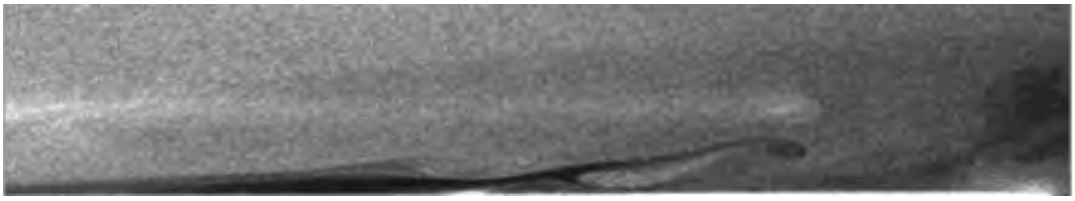

b.).

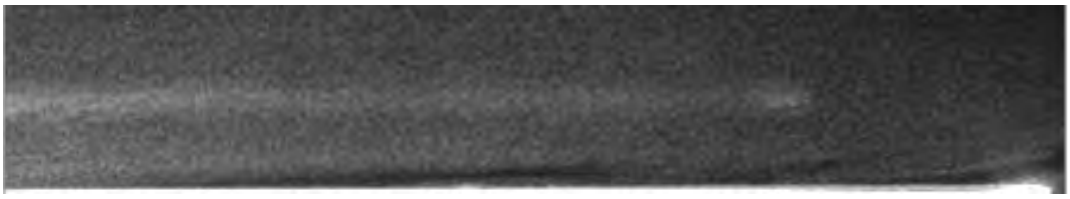

c.)

Figure 4.21 Flow visualization of plasma actuator DBD-01 at the trailing edge from C_x=65% to 101% at a Re = 5 x 10^4. Image A: actuator off, B: 5.6 kV_{pp}, C: 7.2 kV_{pp}

In Figure 4.22 flow visualization in the area of the plasma actuator and boundary layer separation is shown. The actuator on image is very interesting and shows eddies formed downstream of the actuator. The laser sheet in this case was placed centered with one of the plasma actuator vertical jets. The eddies were only observed at the highest voltage tested 7.3 kV_{pp}. The linear vertical jet is aligned with the streamwise direction and is expected to introduce three dimensional vorticity by creating a local separation region. This bottom image in Figure 4.22 clearly shows that, at the least spanwise coherent eddies form entraining higher momentum flow from the freestream to the wall.

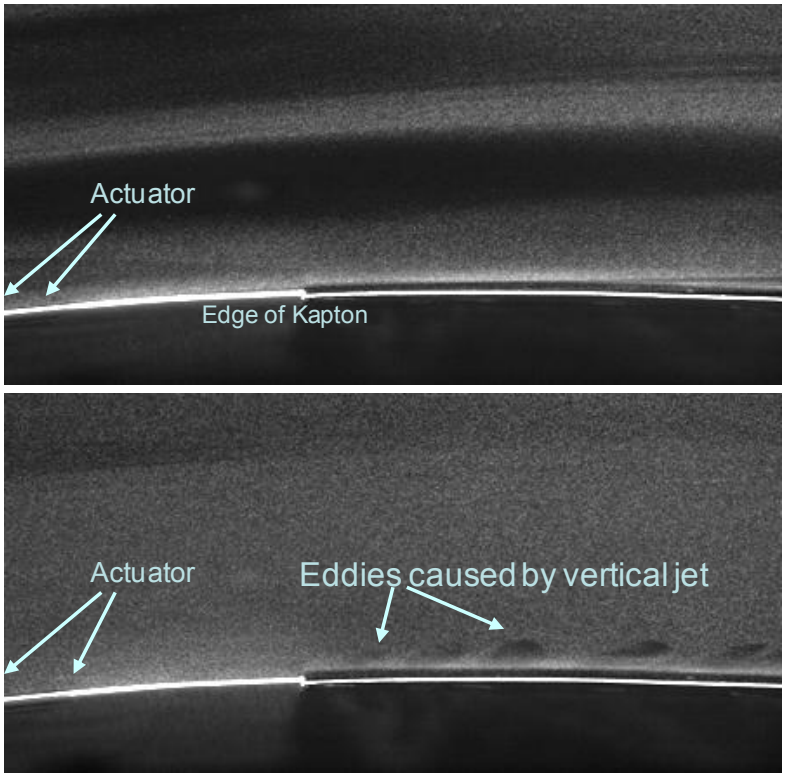

Figure 4.22 Flow visualization showing spanwise coherent unsteadiness generated by the vertical jets of DBD-02 with Re=5x10^4. Top: actuator off, Bottom: actuator voltage 7.2 kVpp. View is from approximately C_x=30% to 60%.

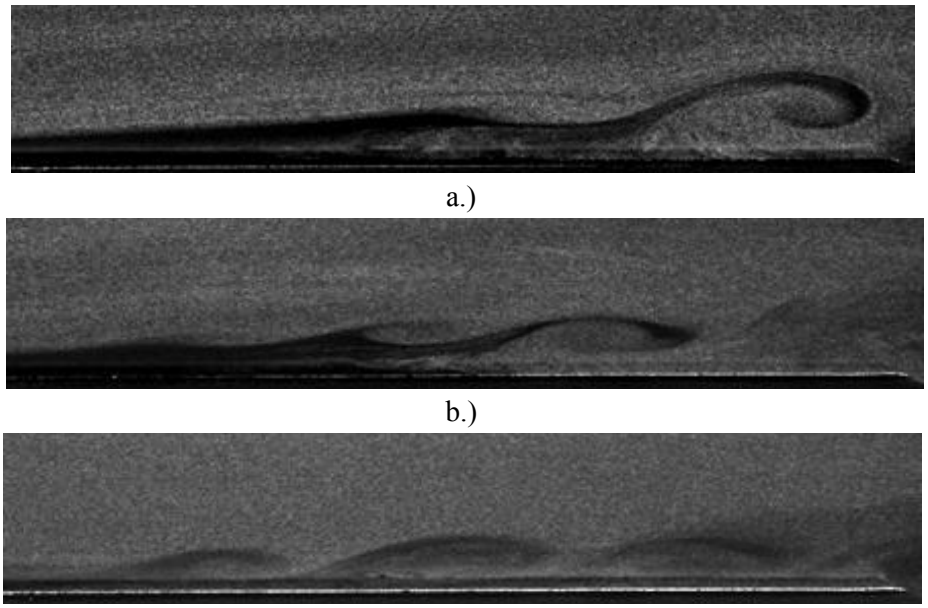

a.)

b.)

c.)

Figure 4.23 Flow visualization of plasma actuator DBD-03 at the trailing edge from C_x=70% to 101% at a Re = 5 x 10^4. Image A: actuator off, B: 4.8 kV_{pp}, C: 7.2 kV_{pp}.

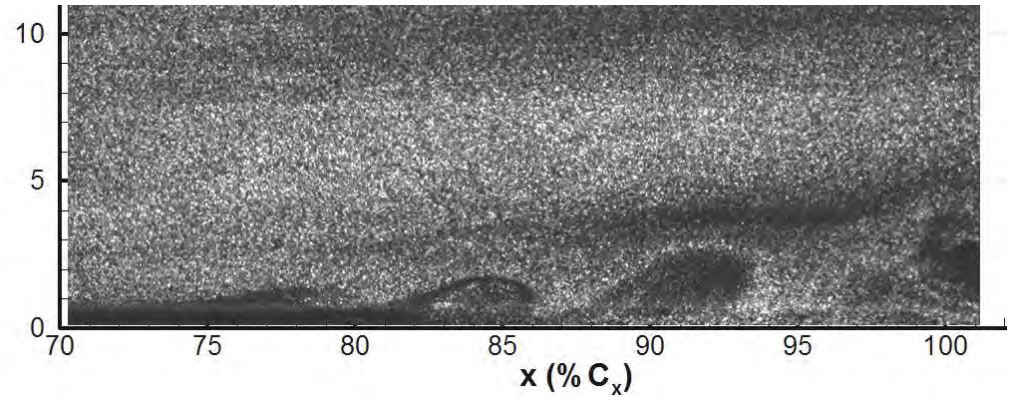

a.)

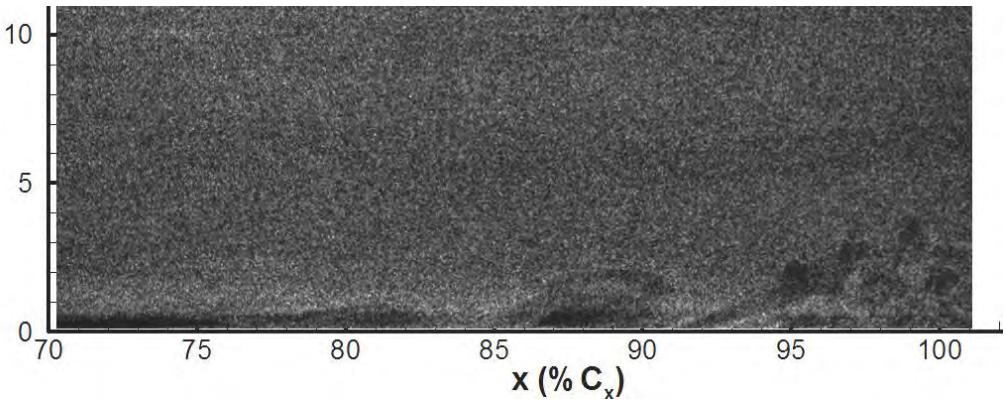

b.)

Figure 4.24 Flow visualization of airfoil with plasma actuator DBD-03 installed. Suction surface near trailing edge is shown at Re=1.0x10^5. Image A: actuator off, B: 7.3 kV_{pp}.

The effect of plasma actuator DBD-03 at the trailing edge is shown in Figure 4.23. This plasma actuator was least effective at the lowest Reynolds number tested. The flow visualization indicates that as voltage is increased the separated shear layer develops into a boundary layer with large scale streamwise structures. This orientation acts as a wall jet entraining momentum from the freestream and adding momentum to the boundary layer. The flow visualization in this study indicates the configuration was less effective at promoting transition and reattachment of the boundary layer. The large scale inviscid structures are maintained and do not appear to break up into small scale structures. It did however, decrease drag by 30%. At the higher Reynolds number of $Re=1.0x10^5$ in which a mean reattaching separation bubble was present in the actuator off case, the plasma actuator DBD-03 was very effective at moving the reattachment point upstream (see Figure 4.24).

5. Closed Loop System

Feedback closed loop separation control experiments are described in this chapter. S3F #6 was used as the separation control sensor, and a spanwise array of linear vertical jets generated by DBD plasma actuator (DBD-04) were used as the flow effecter. The plasma actuator electrode geometry was identical to DBD-02 and mounted at the same location on the airfoil. All data presented in this chapter was taken with the DBD-04 and S3F #6 installed on Airfoil 2. In some situations observations from the experiments presented in this chapter may be compared with measurements from other chapters.

5.1. Boundary Layer Flow Behavior

Examples of instantaneous flow visualization are shown in Figure 5.1 with the plasma actuator and S3F installed. At a Reynolds number of 1.0×10^5 a laminar boundary layer separates, transitions to turbulent and reattaches. In the area of reattachment vortices are shed from the separation bubble and travel downstream along the boundary layer. The boundary layer reattachment location is approximately 85% C_x and which is further upstream than the measurements in Chapter 3 and 4. This is likely due to variation in the attachment of the plasma actuator to the airfoil.

At $Re = 6.0 \times 10^4$ and below the boundary layer behavior is complex and very unsteady near the trailing edge as was discussed in detail in Chapter 3. The boundary layer often did not reattach and large coherent eddies were observed convecting down the separated shear layer leading to instances of both reattached and separated boundary layer near the trailing edge.

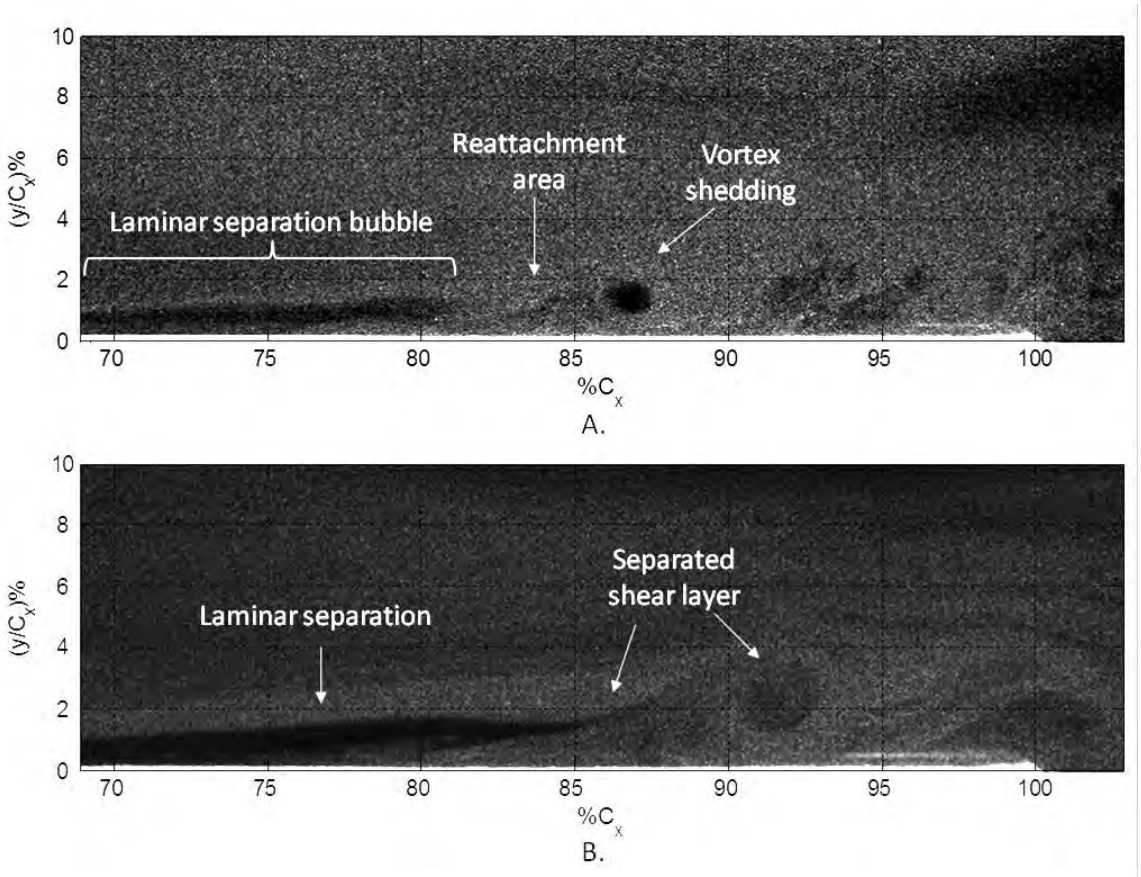

Figure 5.1. Flow visualization over the E387 suction surface trailing edge region with actuator installed and powered off. Image A is at Re = 1.0 x 10^5. Image B is at Re = 6.0 x 10^4.

Mean static pressure across the trailing edge region of the airfoil suction surface with the actuator installed is shown in Figure 5.2 for various Reynolds numbers compared to the inviscid solution calculated in XFOIL. The plateau in suction pressure gradient beginning near C_x=55% is characteristic of boundary layer separation. At a Reynolds number of 1.0x10^5 the pressure recovers in the vicinity of C_x = 80-85% which is characteristic of boundary layer reattachment. At the two lower Reynolds numbers, the mean reattachment point moves downstream towards the trailing edge, or does not reattach. The loading on the suction surface of the airfoil increases as Reynolds number increases. The reattachment points have moved upstream significantly compared to the open loop experiments. This is due to variation in attachment of the plasma

actuator. The plasma actuator was wrapped around the leading edge. Any change in the shape at the leading edge or a discontinuity could move the reattachment point upstream.

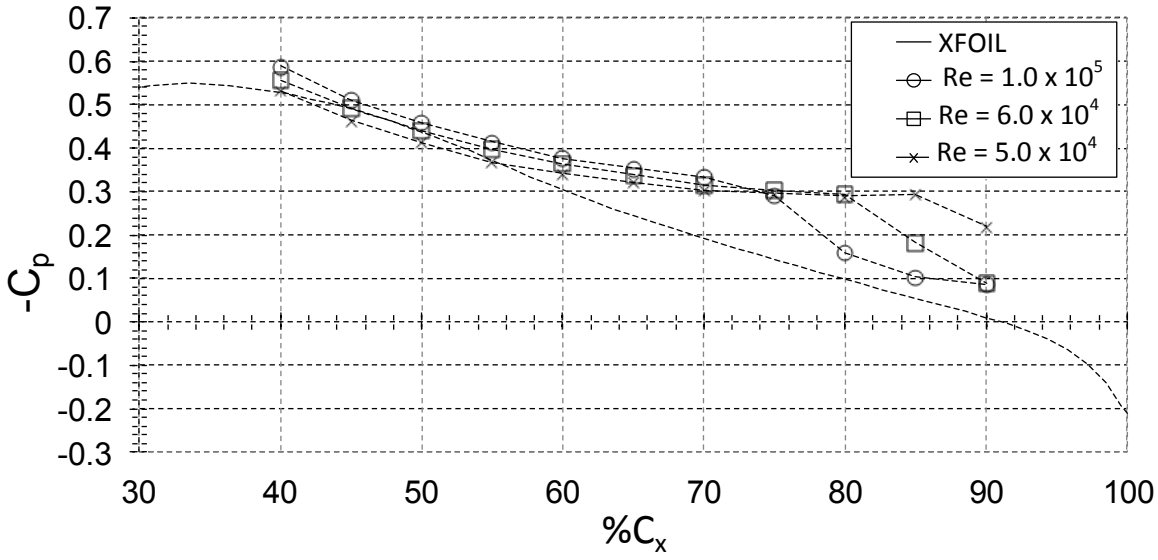

Figure 5.2. Example of Suction Surface C_p in the trailing edge region at various Reynolds numbers with actuator installed.

Mean velocity fields calculated by particle image velocimetry (PIV) are shown in Figure 5.3-Figure 5.4. The laser plane was at the top edge of the S3F. At least 500 images were used to calculate the mean fields. The mean reattachment point at a Reynolds number of 1.0 x 10^5 is between C_x = 85 & 90%. In contrast to observations made using instantaneous flow visualization, the boundary layer reattaches and forms a mean reattaching separation bubble at a Reynolds number of 6.0 x 10^4 with reattachment between C_x = 90 & 95%.

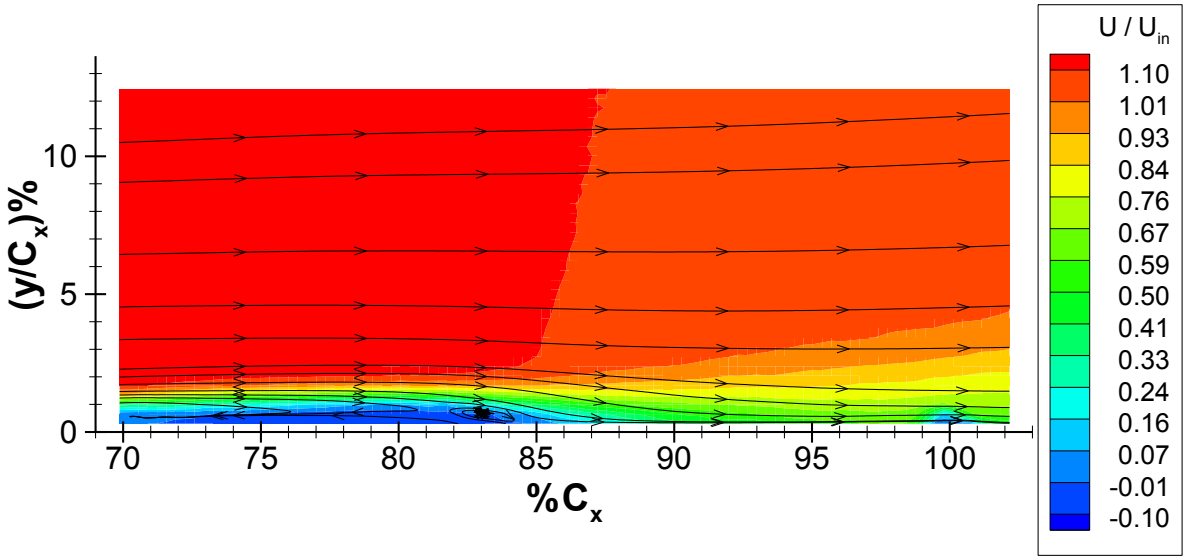

Figure 5.3. PIV mean velocity field at Re = 1.0x10^5 with plasma actuator off.

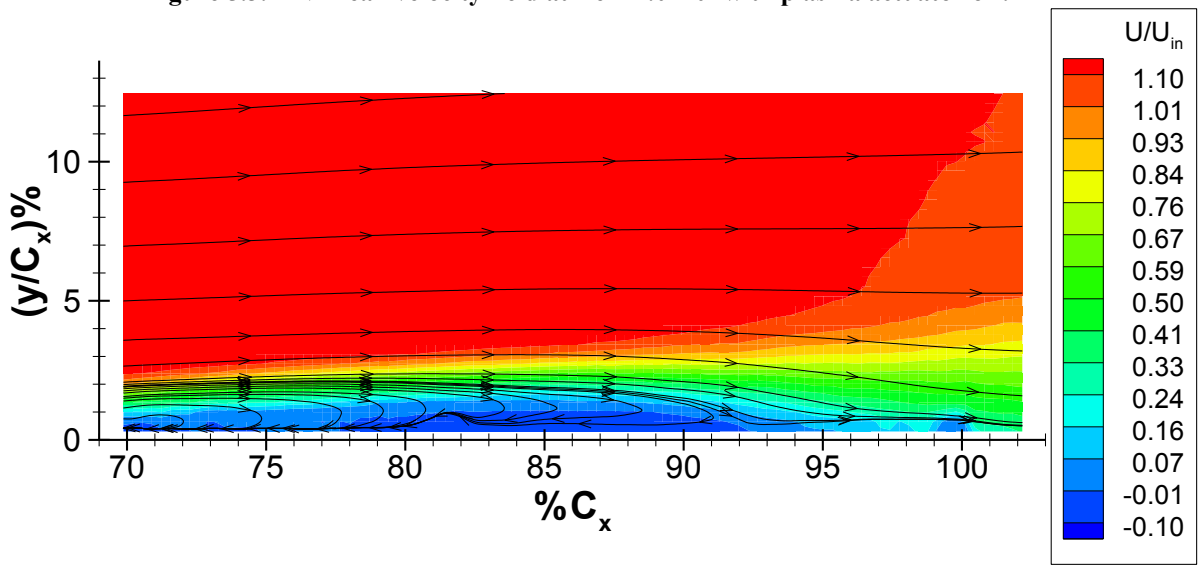

Figure 5.4. PIV mean velocity field at Re = 6.0x10^4 with plasma actuator off.

5.2. Flow Effecter

A spanwise array of steady linear vertical jets generated by a DBD plasma actuator was used as the flow effectors based on the results of the open loop control study. The control authority of the spanwise array of linear vertical jets was considered adequate for the current closed loop experiments over the entire Reynolds number range (1.0 x 10^5 – 6.0 x 10^4) considered here. The

actuator was mounted upstream of the separation point and consisted of 9 linear vertical jets spaced 23.8mm on center and extending approximately 20.3mm in the streamwise direction. The actuator electrode geometry was identical to DBD-02, and fabricated and installed using the same method as was described in Chapter 4. For consistency the data reported in this chapter has been obtained using the same plasma actuator (DBD-04).

Figure 5.5. Plasma actuator configuration mounted in the wind tunnel.

The mean velocity field obtained by PIV with the actuators on at Reynolds numbers of 1.0×10^5 and 6×10^4 are shown in Figure 5.6 and Figure 5.7. Comparing the actuator on images with the actuator off images clearly shows an upstream shift in the mean reattachment point and significant decrease in the thickness of the separation bubble. In fact the separation becomes so thin that it becomes difficult to identify a precise mean reattachment point. At a Reynolds number of 1.0×10^5 the plasma actuator with an applied voltage of 6.4 kV_{pp} moves the mean reattachment point upstream approximately 5% C_x, from 86% to approximately $C_x = 81\%$. At the lower Reynolds number of 6×10^4 the upstream shift in reattachment point is approximately 10% C_x from $C_x = 93\%$ to $C_x = 83\%$ with a 6.4 kV_{pp} voltage.

Mean boundary layer velocity profiles normal to the airfoil surface with the actuator powered on and off are shown in Figure 5.8 and Figure 5.9. Mean boundary layer thickness with the plasma actuator powered on and off are shown in Figure 5.10.

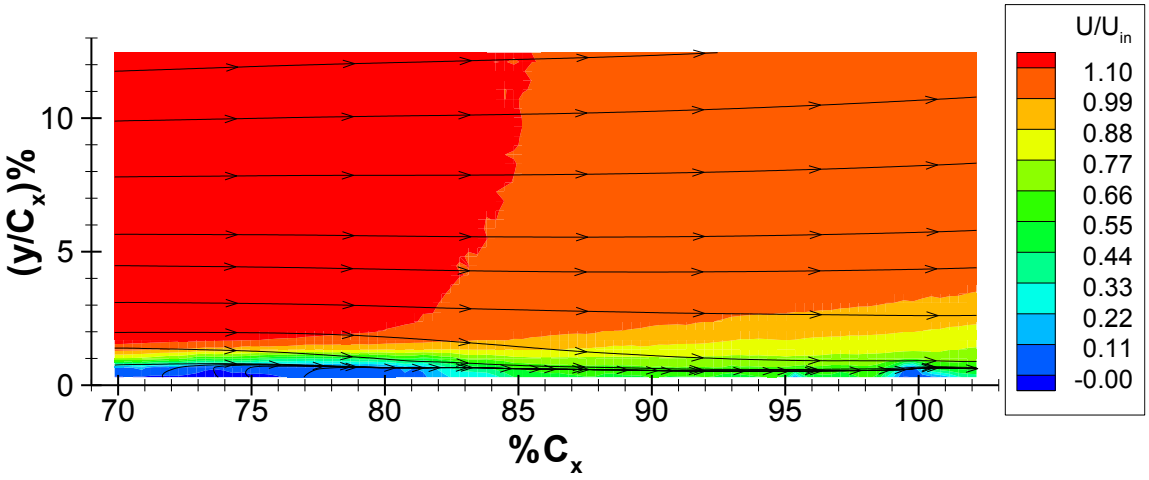

Figure 5.6 PIV mean velocity field at Re = 1.0x10^5 with plasma actuator on, V = 6.4 kV$_{pp}$

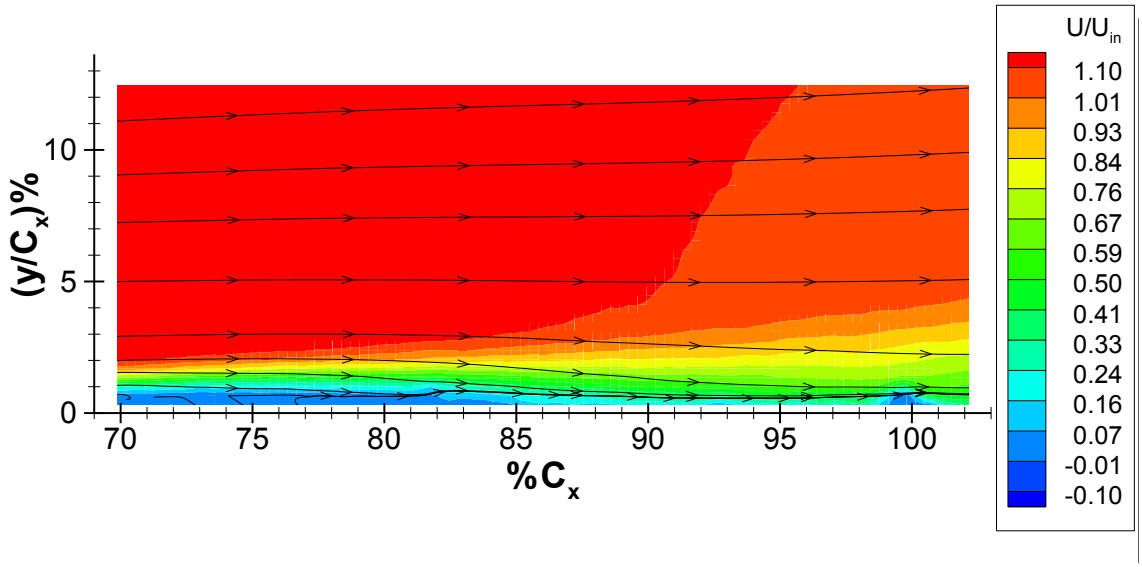

Figure 5.7. PIV mean velocity field at Re = 6.0x10^4 with plasma actuator on, V = 6.4 kV$_{pp}$.

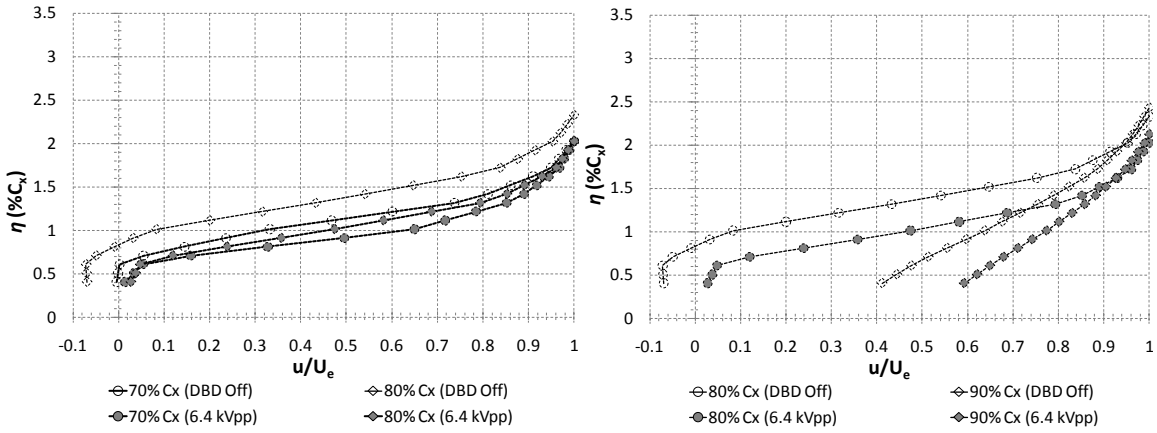

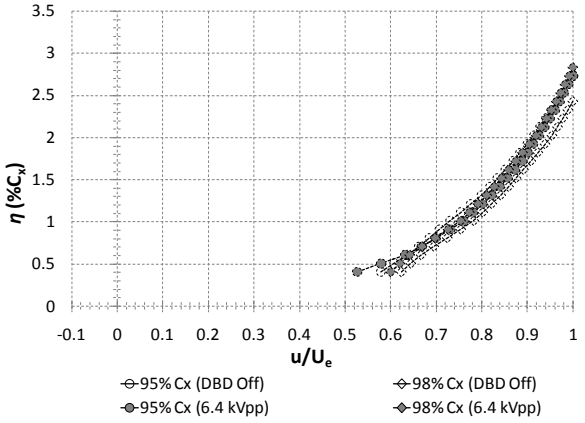

c.)

Figure 5.8 Suction surface PIV velocity profiles near the trailing edge with plasma actuator power on and off, Re = 1.0 x 10^5.

At a Reynolds number of 1.0 x 10^5 turning on the plasma actuator results in earlier reattachment and a fuller boundary layer profile at C_x = 90%. The boundary layer thickness is also smaller with the plasma actuator on until the trailing edge of the airfoil where the boundary layer thicknesses are nearly equal.

At the lower Reynolds number of 6 x 10^4 the boundary layer thickness is significantly reduced, with an approximately 10% upstream shift in reattachment location. Mean boundary layer thickness with the plasma actuator on in Figure 5.10b is very similar to the predicted turbulent boundary layer thickness on a flat plate. In a mean sense, the large scale inviscid structures have broken down into small scale turbulence near the trailing edge of the airfoil as shown in the image of Figure 5.11.

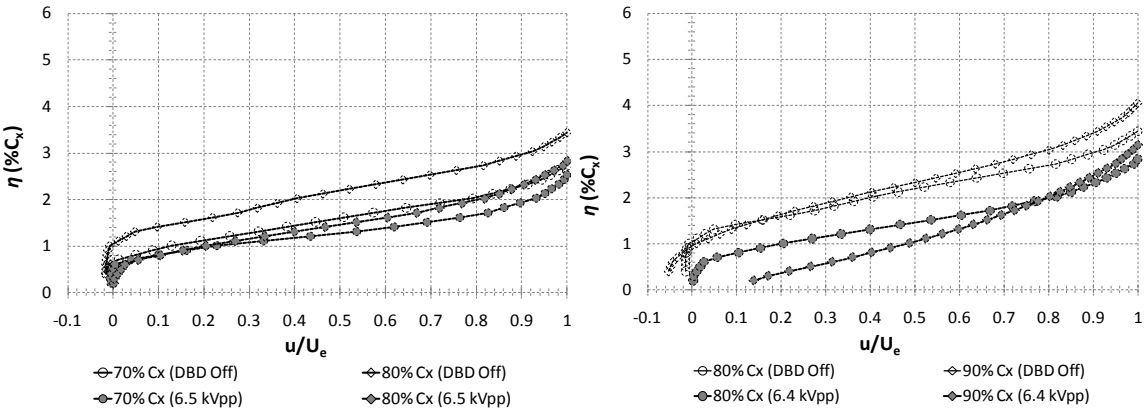

a.) b.)

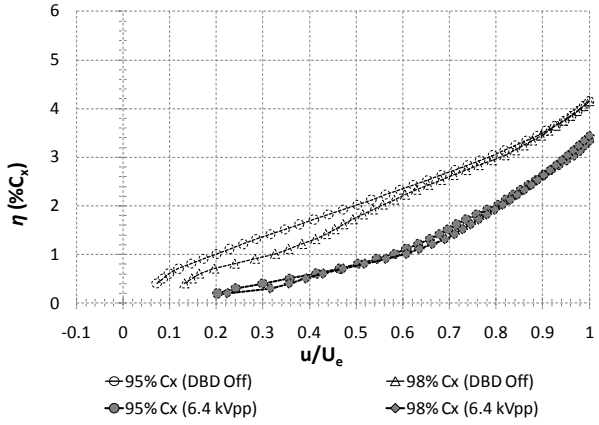

c.)

Figure 5.9 Suction surface PIV velocity profiles near the trailing edge with plasma actuator power on and off, Re = 6 x 10^4.

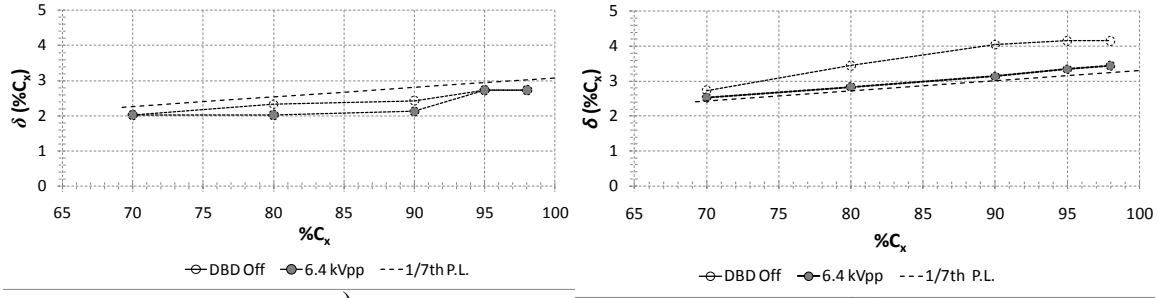

a.) b.)

Figure 5.10 Boundary layer thickness with plasma actuator powered on and off at a.) Re = 1.0 x 10^5, and b.) Re = 6 x 10^4.

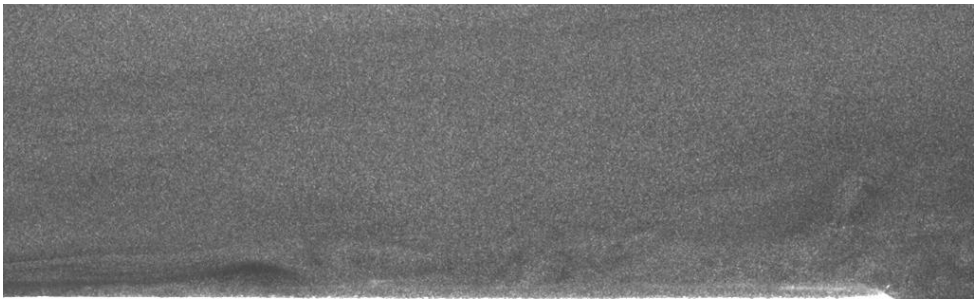

Figure 5.11 Flow visualization over the trailing edge portion of the airfoil with plasma actuator on 6.4 kV_{pp}. View is from C_x ≈ 70 – 103 %

5.3. Control Method

A system block diagram of the feedback separation control system is shown in Figure 5.12.

A simplistic approach was taken in this work to develop a simple controller with the objective of

demonstrating that the S3F can be used a separation control sensor. An on/off controller and a PI controller were implemented.

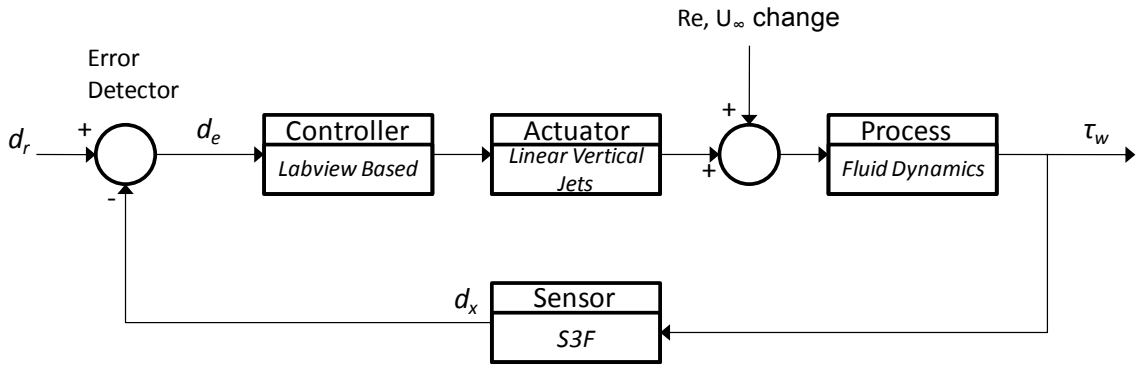

Figure 5.12. Feedback Control System Diagram

5.3.1. System Response

Several measurements were made to understand the sensor response. Mean S3F response at several different plasma actuator voltages is shown in Figure 5.13. Time resolved response at candidate monitoring points is shown in Figure 5.14. The time resolved response of the S3F when the wind tunnel speed is rapidly decreased from a Reynolds number of 1.0 x 10^5 to 6 x 10^4 is shown in Figure 5.15.

Figure 5.13 show a mean nonlinear response in tangential displacement at candidate monitoring points, typically located just downstream of the mean reattachment point. Also included in the response plots are mid-S3F line plots across the camera field of view at select plasma actuator voltages. The higher Reynolds number of 1.0 x 10^5 shows a linear response with increase in actuator voltage until a 5.5 kV_{pp} applied voltage in which a further increase in actuator voltage resulted in little change in shear displacement. The plateau in the response curve is consistent with observations using the same plasma actuator electrode geometry (DBD-02) during the open loop plasma actuator electrode investigation of Chapter 4. This implies there is a threshold voltage of approximately 5.5 kV_{pp} above which there is very little additional decrease in separation length. A maximum upstream shift in reattachment point of 6.1 %C_x was observed at

Re = 1.0 x 10^5 with 7.2 kV_{pp} applied voltage. The reattachment location implied by the S3F tangential displacement is further downstream than was observed with PIV. With the plasma actuator off the mean zero crossing location was at 90% C_x with an upstream shift to approximately 84% C_x with 7.2 kV_{pp} applied voltage. At the lower Reynolds number the same linear range is visible but a drop off in shear displacement occurs at the highest plasma actuator voltage. The mean displacement actually changes to a negative value. Mean reattach point shifted upstream to as high as 89% C_x with a 6.4 kV_{pp} applied voltage. This is an upstream shift of approximately 9% C_x. The upstream shift in reattachment point is consistent with PIV measurements that indicated a 10% upstream shift; however, the location of zero crossing is nearly 7% further upstream than the reattachment point measured with PIV.

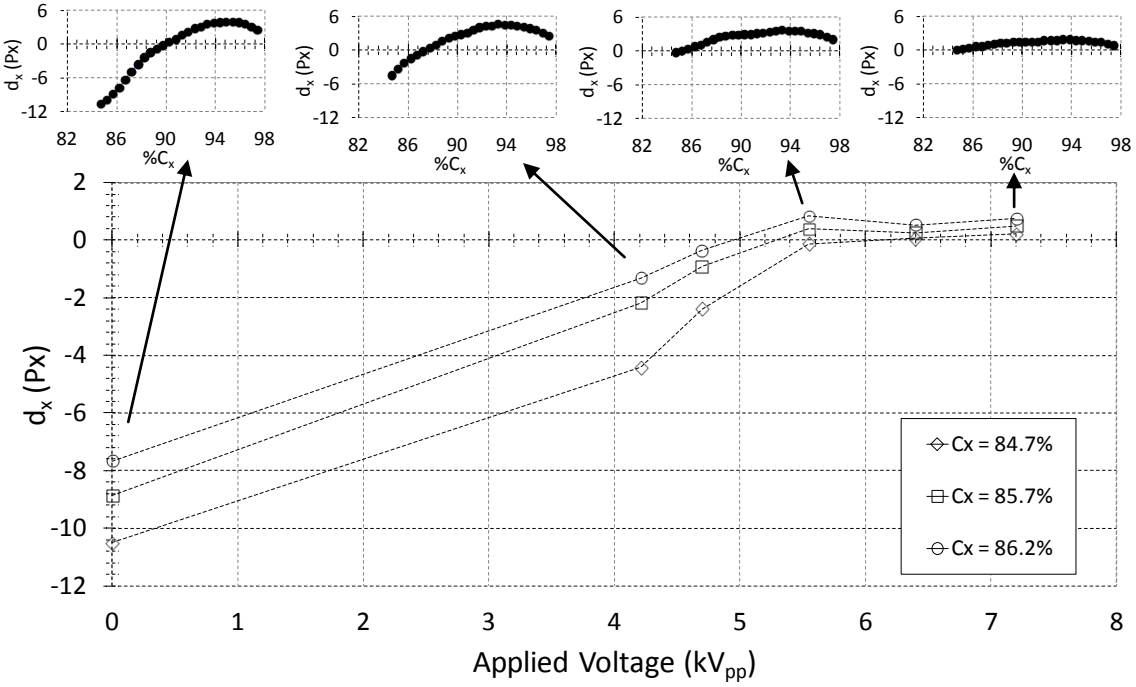

a.)

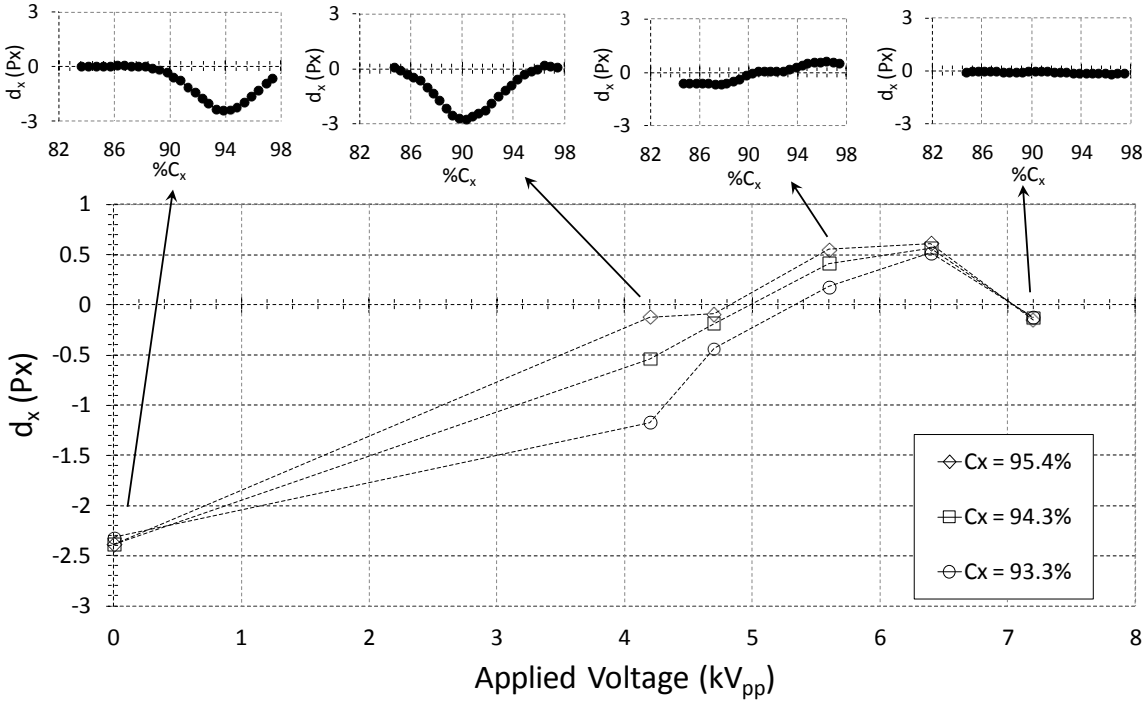

b.)

Figure 5.13 S3F mean response at various sensor locations, a.) Re = 1.0 x 10^5, b.) Re = 6 x 10^4.

Understanding the response of the S3F at a high level of plasma actuator voltage is complicated. Several factors could play a role in the change in S3F tangential displacement: frequency response of the S3F, pressure gradient effects, changes in pressure gradient and shear stress, and uncertainty in the displacement calculation. A mean negative displacement at Re = $6.0x10^4$ and the highest actuator voltage could be due to the uncertainty in the single pass cross correlation method as displacement approaches zero.

The time resolved response of the S3F when the plasma actuator is powered on shows that the film responds to load change within 1 second. The response at an applied voltage of $7.2kV_{pp}$ is interesting since it resembles a damped system, with no oscillation. This could mean that the frequency response characteristics of the film are responsible for the near zero displacement reading.

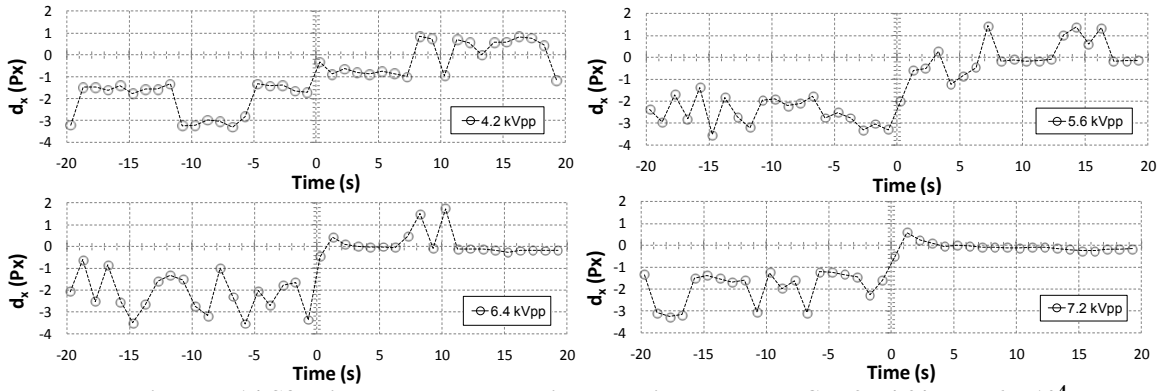

Figure 5.14 S3F time response at various applied voltages, C_x = 95.4 %, Re=6 x 10^4.

The response of the highly sensitive, ultra low shear modulus, viscoelastic S3F may require further development and material property testing to fully understand. Nonetheless, the response of the S3F shown in Figure 5.13 makes it useful in a feedback separation control system. With the plasma actuator off the S3F tangential displacement is certainly negative, and when the plasma actuator is turned on the S3F tangential displacement moves positive or towards zero.

The S3F behavior is certainly useful as a sensor for On/off control of the plasma actuator. In order to better understand the time resolved S3F signal response as flow conditions change and separation control is turned on the wind tunnel speed was reduced from a speed at which the S3F displacement was positive and the boundary layer attached to a speed in which the boundary layer is separated over the monitor point. The sampling speed was set to 2.5 Hz and a point at C_x=95.4% was monitored. In one case the actuator was triggered to come on as separation was detected at the S3F monitor point, and the other flow control was left off. The results of both cases are shown in Figure 5.15. At a Reynolds number of 1.0x10^5 the S3F tangential displacement oscillates from just around zero to approximately 3.5 pixels. Oscillation of the signal is consistent with unsteadiness in the boundary layer downstream of the laminar separation bubble observed in the flow visualization in Figure 5.1b. The frequency of oscillation is not accurate due to the low natural frequency of the S3F, and slow sampling speed. For the two cases shown, the magnitude of displacement at a Re = 1.0x10^5 is not the same indicating either error in the measurement, or a small change in the boundary layer behavior between runs due to the

sensitivity of the laminar boundary layer to minute changes in freestream unsteadiness. When the tunnel speed is decreased the S3F displacement quickly decreases to a negative displacement implying the reattachment point has moved downstream of the monitor point. There is a 6 second transient response period from the time the tunnel inlet Reynolds number reaches 6 x 10^4 until the displacement reaches a consistent value centered about approximately -3 px. For the case in which the plasma actuator is triggered on at an S3F filtered displacement of -1 px the boundary layer separation is significantly diminished within approximately 1.5 second. The actuator significantly increases the S3F displacement at the monitor point to a value that fluctuates between positive and negative with a mean value of -0.1 px.

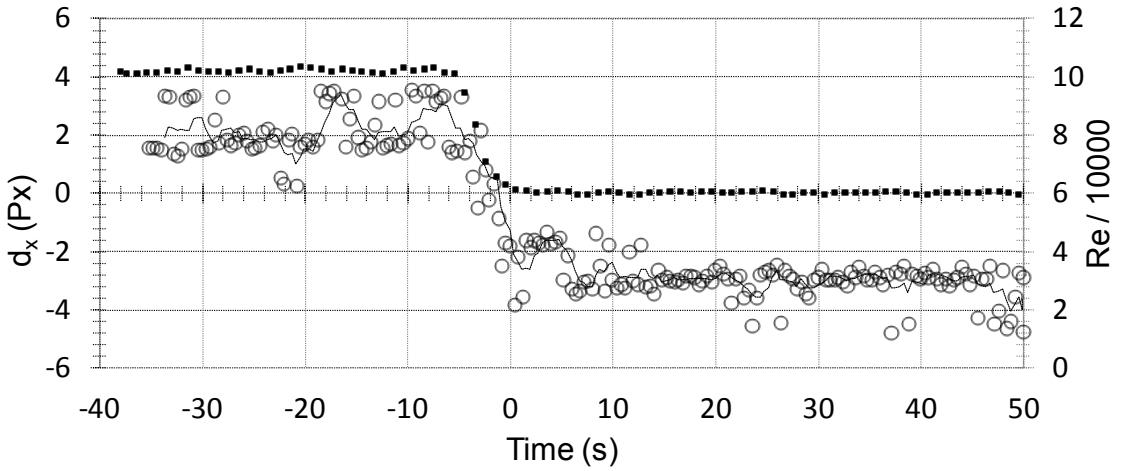

a.) Actuator off

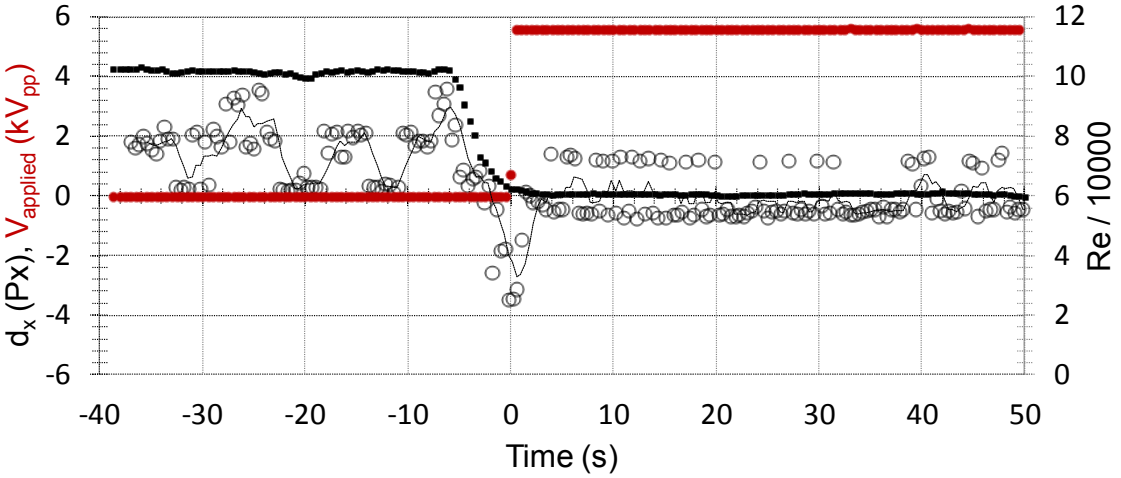

b.) Actuator on, v = 5.6 kV_{pp}

Figure 5.15. Comparison of S3F response for a sudden drop in free stream velocity, with and without flow control. Triggering of plasma actuator at d_x = -1 px, f_s=2.5 Hz, monitor point at 95.4%C_x.

5.3.2. On/off Controller

As a first demonstration of the closed loop system, the S3F sensor signal was used with an on/off controller. This is similar to the stall control system demonstrated by Poggie et al. (2010) using hot film gauges, but with the ability to turn the actuator back off when flow conditions become more favorable. The system used the S3F signal as a trigger to turn on and off the plasma actuator at a predetermined sensor low and high signal level using the logic flow shown in Figure 2.31. If the S3F displacement changed to a value less than the lower set point the actuator would be turned on to a predetermined value. If the displacement increased to a value higher than the upper set point the actuator would be turned off. When the displacement was between the upper and lower set points the actuator would remain at its previous setting. Due to the unsteady signal and latency of the boundary layer response, delay logic was built into the controller. Once the actuator state changed, no control changes could be made for a period of t_d. This assured that the system did not oscillate. The sensor signal was low pass filtered to reduce noise.

Two examples of the on/off controller with different values of actuator voltage are shown in Figure 5.16-Figure 5.17. In both examples the sampling frequency was set to 2.5 Hz and the wind tunnel speed was set to provide a Reynolds number of 1.0 x 10^5 then decreased to the 6 x 10^4. The sensor location was at C_x = 95.4%. In the first case the actuator was set to 4.7 kV_{pp} and the sensor signal implies that flow separation was removed in under 2 seconds. With the actuator on, the S3F displacement at the monitoring point was 0.1 pixels. As the wind tunnel speed was increased and the controller detected a positive displacement larger than the upper set point the actuator was powered off. After several seconds the displacement begins to oscillate in a similar manner as previous studies.

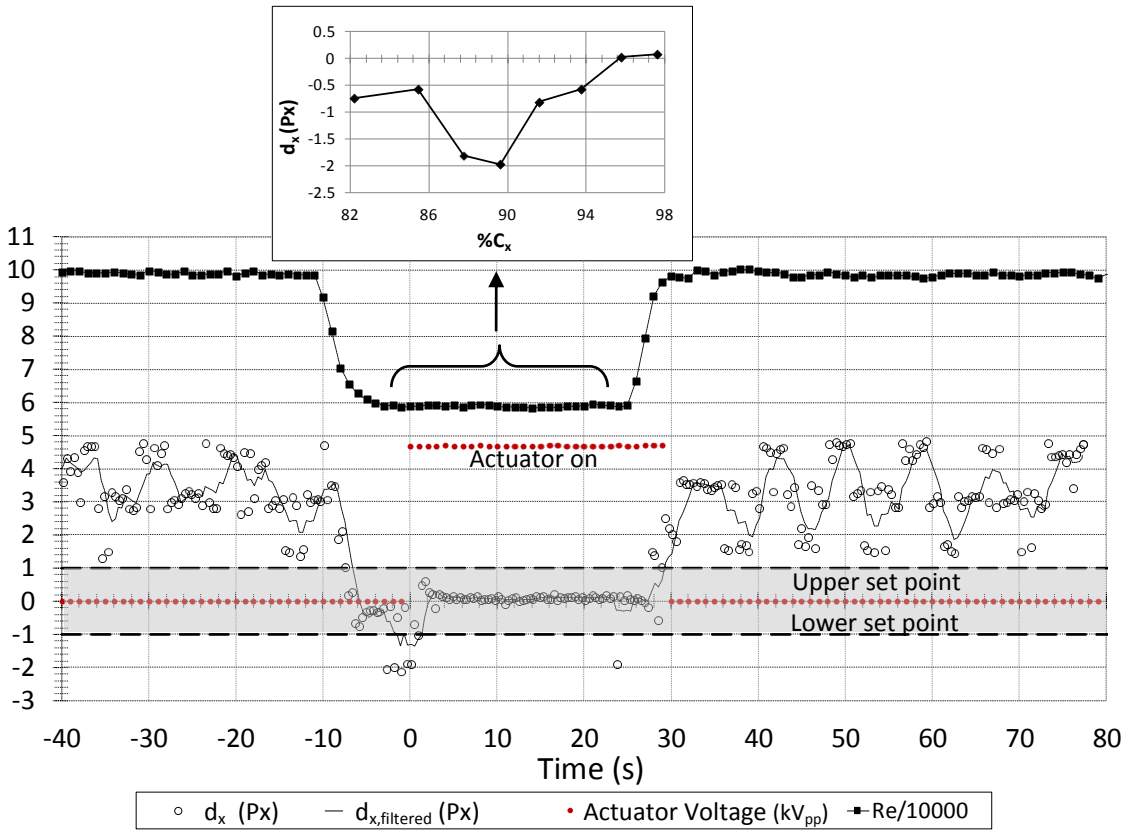

Figure 5.16. On/off controller, f_s = 2.5 Hz, v = 4.7 kVpp.

In the case shown in Figure 5.17 the plasma actuator voltage was set to 5.6kV$_{pp}$ and the upper set point increased to 2 pixels. When the plasma actuator was turned on the displacement reaches a positive value and then oscillates about zero after approximately 10 seconds in a similar manner as was observed in Figure 5.16. The change in S3F displacement after a delay of approximately 10 seconds suggests a difference in boundary layer response between Figure 5.16 and Figure 5.17, even though conditions were the same.

As a final demonstration of the On/off controller, the wind tunnel speed was arbitrarily varied between Re = 1.0 x 10^5 and 5 x10^4 as shown in Figure 5.18.

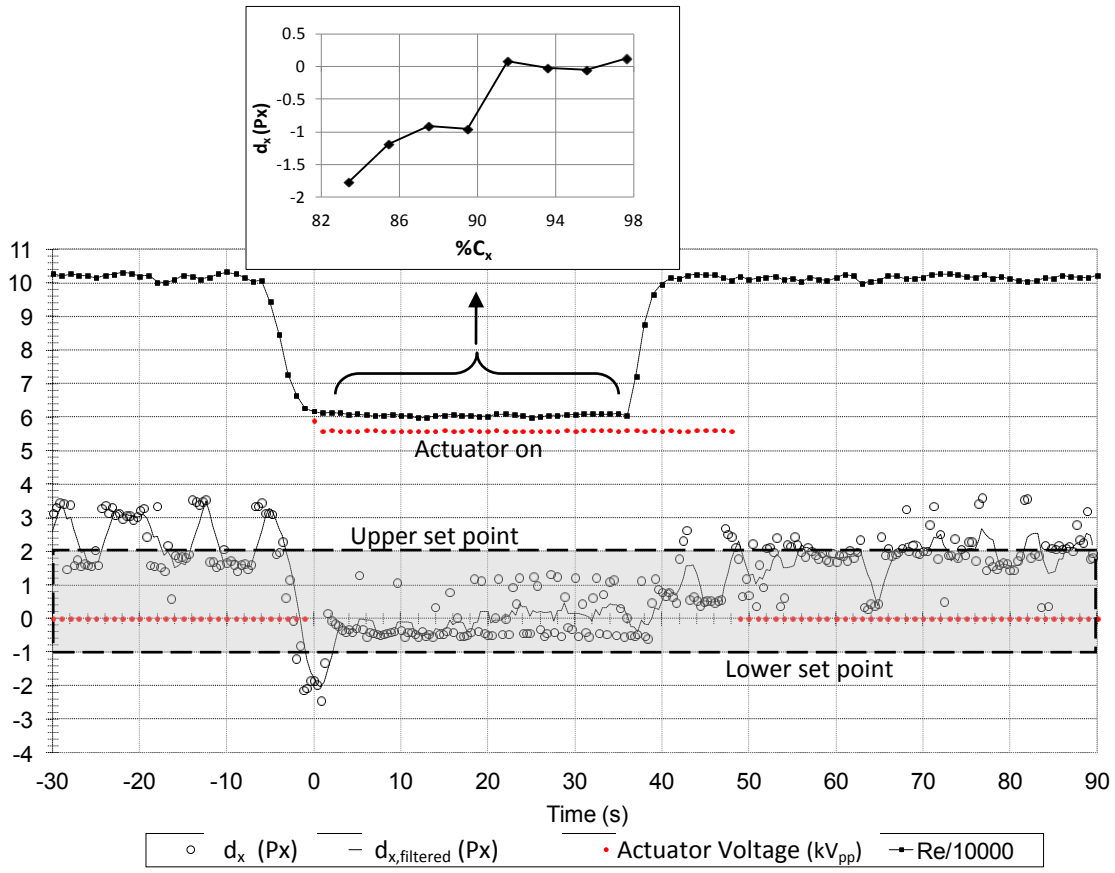

Figure 5.17. On/off controller, f_s=2.5Hz, v = 5.6 kVpp.

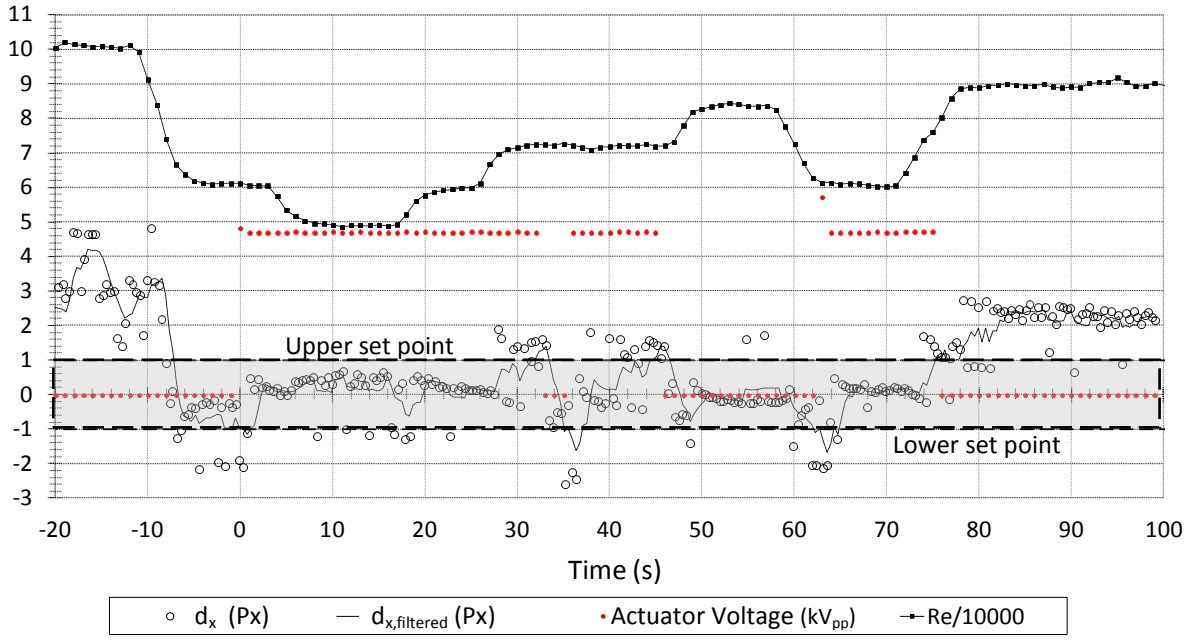

Figure 5.18 On/off controller, f_s = 2.5 Hz, actuator v = 4.7 kV_{pp} with arbitrary tunnel speed.

5.3.3. PI Controller

A proportional integral (PI) controller was implemented to demonstrate closed loop control with a simple automatic controller. The standard form of a PI controller is given by:

$$u(t) = K_P \cdot d_e(t) + K_I \cdot \int_0^t d_e(\varphi) d\varphi \tag{5.1}$$

where *u(t)* is the output signal.

A discrete version of the PI controller was implemented in the control software. First the sensor signal was low pass filtered, compared to the reference value, then PI controller output calculated by:

$$u(t) = K_P \cdot \bar{d}_e(t) + K_I \cdot \sum_{i=1}^{k} \bar{d}_e(t_i) \cdot \Delta t \tag{5.2}$$

where $\bar{d}_e(t)$ is the low passed filtered error signal calculated by:

$$\bar{d}_e(t) = d_r - \bar{d}(t) \tag{5.3}$$

$$\bar{d}(t) = \frac{1}{m} \cdot (d(t) + d(t-1) + d(t-2) \cdots d(t-m-1)). \tag{5.4}$$

The controller gains were manually tuned, first by adjusting the proportional gain, then by adding and increasing the integral gain until a satisfactory response was obtained. It is important to remember that the PI controller used here was un-optimized and a better controller would likely yield better performance. The system sampling rate was typically between 0.5 Hz and 2.5 Hz, which was limited by the hardware available.

Only one interrogation window in the field of view was used to simulate a discrete shear stress sensor. In a first example shown in Figure 5.19 the sampling rate was 0.5 Hz, the reference displacement d_r was 0 pixels at C_x=96%, and the output signal was limited to 0.94 (5.6 kV_{pp}). When the control system is turned on the controller commands maximum actuator output and boundary layer separation was eliminated. After approximately 30 seconds from the start of

control the response becomes unsteady and the mean increases slightly resulting in a reduction of the output signal. The reason for the unsteadiness in unknown but assumed to be due to a change in boundary layer behavior. The time resolved reattachment point of the boundary layer with flow control on is spatially unsteady due to the shedding of vortices that form in the separated shear layer as shown in Figure 5.1. The simple un-optimized PI controller used here does a reasonable job at maintaining the set point even with the highly unsteady signal. At t=200s an impulse disturbance is introduced by increasing the flow velocity to a Reynolds number of $1.0x10^5$. At the higher Reynolds number the sensor signal would typically be much higher than zero, but the disturbance happens in too short of a time scale to overcome the inherent damping in the system. At t=230s a step disturbance is introduced for 30 seconds resulting in a significant increase in sensor signal. The controller responds by decreasing the output signal to maintain the set point. As the disturbance is removed the controller increases the output signal. The PI controller response is slow, but necessary due to the unsteady input signal.

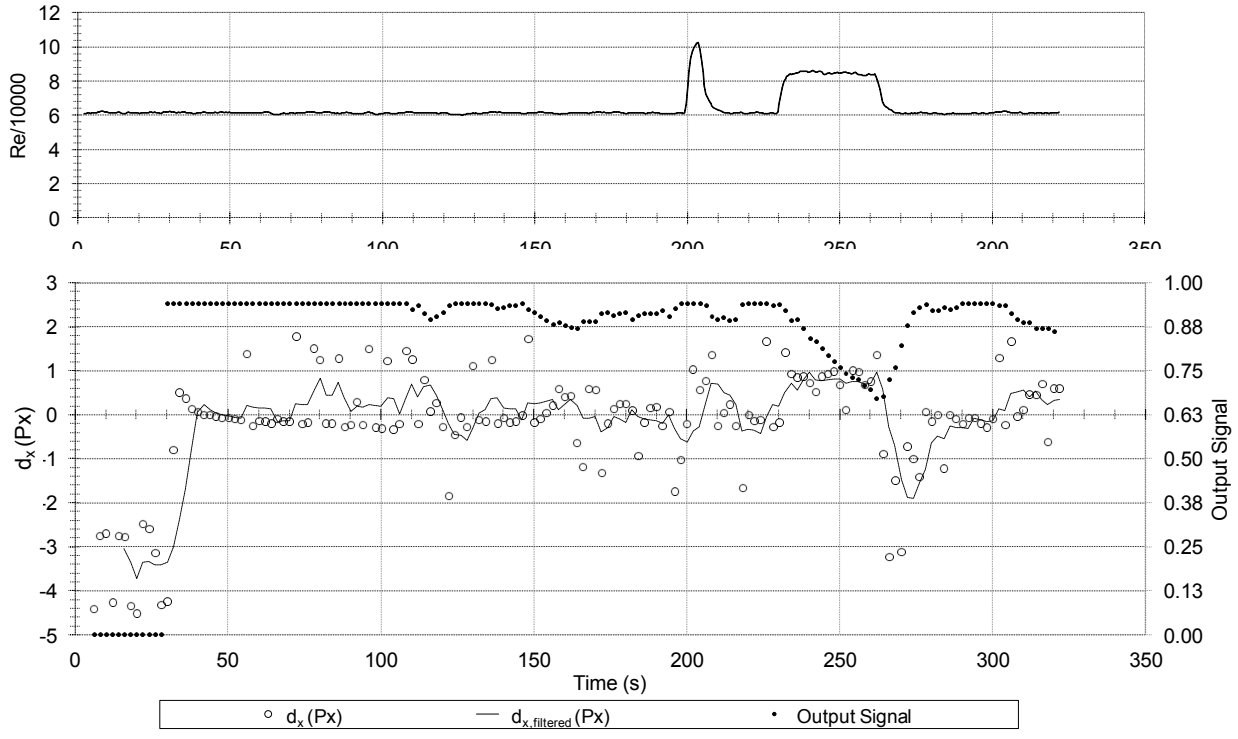

Figure 5.19. Controller response to external disturbances. Set point d_r = 0 px at C_x = 96%.

As a second example of the PI controller the wind tunnel was set to a speed providing a Re = 6.0 x 10^4, and the controller turned on. The output signal was increased over the previous example. Figure 5.20 shows the system response and the top three plots show the mean tangential displacement across the full sensor field of view at three different phases of the run. Three distinct phases of boundary layer response are shown. The first phase is with the feedback control system off. Reverse flow is observed at the trailing edge corresponding to a mean reversed flow vortex inside a separation area. When the control system is turned on the PI controller commands maximum actuator output and the separation is eliminated. After the initial

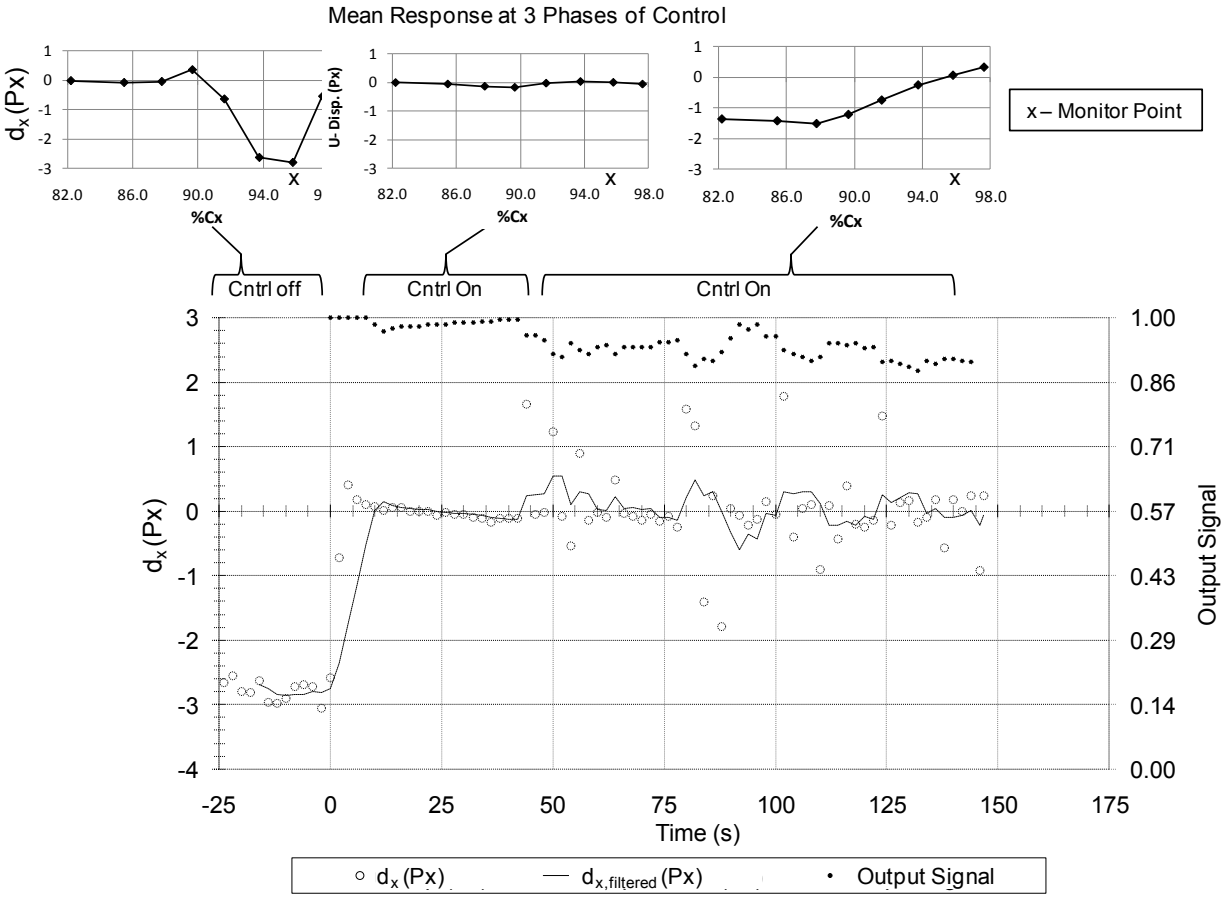

Figure 5.20. Example of separation control using a PI controller at Re = 6.0x10^4, f_s=0.5 Hz.

transient response to the actuator step disturbance, the controller begins to decrease the actuator output signal. As the output signal is adjusted the response begins to oscillate with the controller

trying to respond and maintain the reference value. The response in Phase 3 shows a mean reattachment point in the vicinity of the monitor point. The unsteadiness in the signal is most likely due to shedding of vortices.

The example provided here using a PI controller demonstrates that the S3F sensor signal can be used in a closed loop separation control system. The use of a different type of controller, hardware, and S3F packaging could provide a higher sampling rate, and quicker system response. The system response time using the ultra low S3F in this study are slow and would only make the use of the S3F sensor here useful in a limited number of flight environments. Future efforts should work towards increasing the S3F based sensor sampling speed.

5.3.4. Energy savings

The objective of an active flow control system with feedback is to save energy by turning the actuator off when it is not required, or reducing power when conditions require less control authority. The energy consumption of the two feedback control methods demonstrated here were calculated and compared to simply turning on the plasma actuator at a predetermined condition.

Energy consumption was calculated by numerically integrating the power dissipation of the plasma actuator over time. Instantaneous power dissipation was estimated from the applied voltage using the equation in Figure 4.3. The energy consumption saving is dependent on the profile length. The two different situations were analyzed: On/off controller with arbitrary tunnel speed which was shown in Figure 5.18, and the PI controller experimental run shown in Figure 5.20.

The region used in the calculation of energy consumption without and without the On/off controller is shown in Figure 5.21 and Figure 5.22 respectfully. If the plasma actuator is turned on, and left on, at a predetermined threshold value, 200 J of energy would be used. If an On/off controller is used only 113 J of energy are consumed resulting in a 44% reduction in energy consumption over a 78 second period.

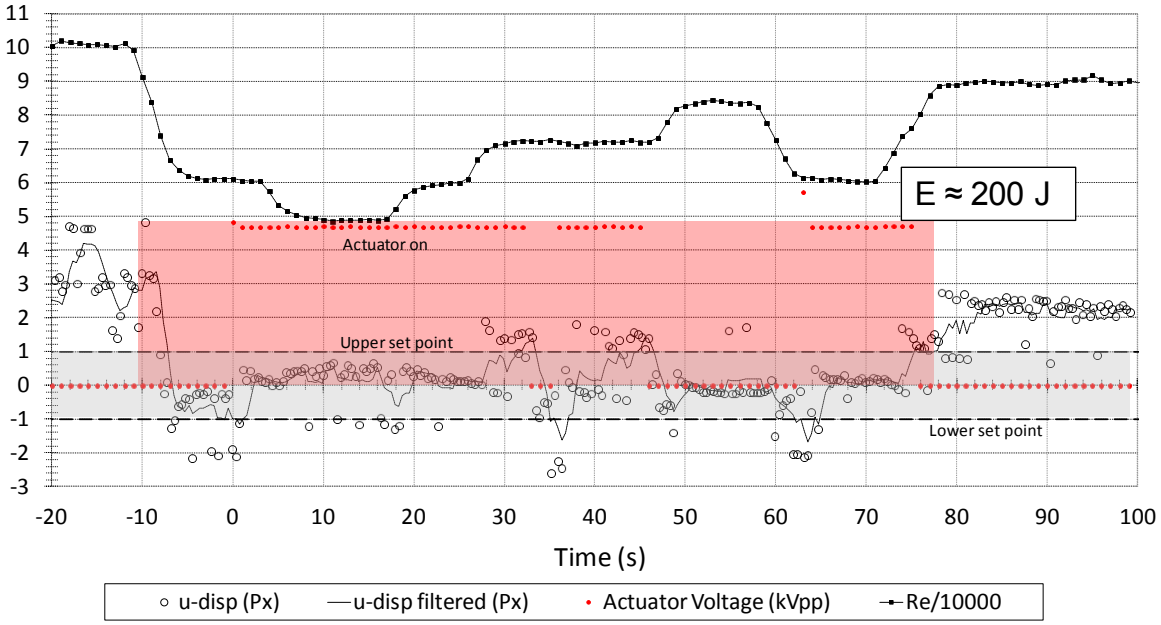

Figure 5.21 Energy consumption calculation without an On/off feedback controller.

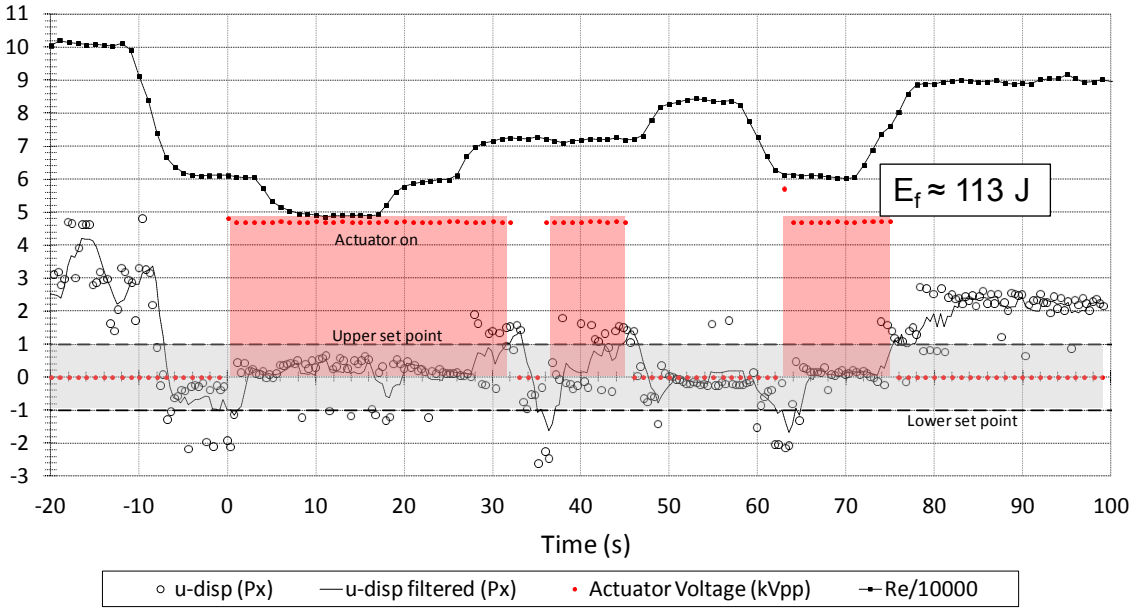

Figure 5.22 Energy consumption calculation with an On/off feedback controller.

In the case of the PI controller, the energy dissipation is shown in Figure 5.23. The use of the PI controller would result in a 34% reduction in energy consumption for140 seconds of operation. As operation time increases energy consumption will increase. Large savings in energy

consumption can be realized using an automatic controller with a plasma actuator because actuator power dissipation scales proportional to $V^{3.5}$. The potential for even larger savings are possible if the plasma actuator is operated in an unsteady mode (Huang et al. 2006).

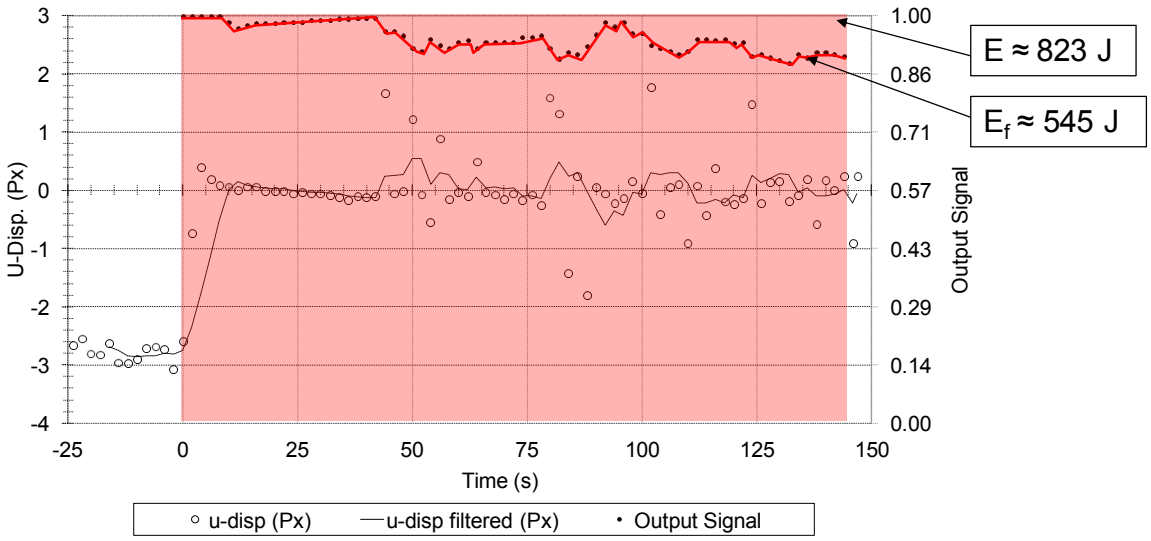

Figure 5.23 Energy consumption calculation using a PI controller.

6. Conclusions

The overall goal of this study was to investigate using the sensitivity of S3F to surface shear stress as a low Reynolds number separation control sensor. Several objectives were listed in the introduction of the document, and they are repeated here with conclusions.

Objective 1: Obtain the experimental suction surface Cp and boundary layer behavior of an Eppler 387 (E387) airfoil model at low Reynolds number over a range of small angles of attack that results in laminar boundary layer flow separation.

The E387 airfoil is a generic representation of a low Reynolds number airfoil and was useful because of laminar flow separation on the suction surface at small angles of attack. E387 suction surface C_p, flow visualization, PIV, and section drag was measured in the AFRL/RZ DWT facility at low angles of attack. This data provided a thorough understanding of the E387 airfoil suction surface boundary layer, and led to a choice of angle of attack and confirmation that the airfoil could be used for a separation control study. The extent of separation could be adjusted by varying the Reynolds number. At a Reynolds number of 1.0×10^5 a mean laminar separation bubble was formed on the suction surface. At Reynolds numbers below approximately 6×10^4 the boundary layer separated and did not reattach.

Objective 2: Study a new method of surface stress sensitive film installation over a curved surface to reduce the effect of the film on boundary layer and surface being studied.

A new method of installing S3F over a curved surface was demonstrated in this study. The new technique originated at ISSI Inc. and uses a thin, flexible S3F carrier. A cavity in the S3F carrier is filled with S3F level and flush to the surface prior to installation on the airfoil. This method simplifies installation of S3F onto a curved surface. Velocity field data were measured

by PIV on the suction surface of the airfoil with the S3F installed, and compared to the velocity field without the S3F installed, and with a plasma actuator installed on the airfoil. The velocity field data indicated that the S3F installation decreased the boundary layer thickness, but not as much as installation of the plasma actuator. The change in the boundary layer was more severe at higher Reynolds numbers.

Objective 3: Compare several different dielectric barrier discharge plasma actuator geometries for low Reynolds number separation control on the E387 airfoil model.

Three different plasma actuator electrode configurations were compared for use in a low Reynolds number separation control system. Two of the actuator configurations were implemented with the intent of generating three-dimensional, or streamwise vorticity to improve momentum entrainment from the freestream into the boundary layer. Operation at two different Reynolds numbers was presented in the study. At the lower Reynolds number of 5×10^4, laminar separation without reattachment was observed with the actuators powered off. At the higher Reynolds number 1.0×10^5 the boundary layer separated and then reattached prior to the trailing edge.

Three parameters were used to compare the performance of each actuator: suction surface C_p profile, S3F streamwise surface displacement, and drag. At the lowest Reynolds number tested, S3F reattachment locations indicated plasma actuator DBD-02, a spanwise distributed array of linear vertical jets, reattached the flow and moved the mean reattachment upstream as voltage was increased to $7.2 kV_{pp}$. The pressure coefficients did not recover to the inviscid profile predicted in XFOIL. This configuration also resulted in the largest improvement in drag at the lowest applied voltage.

At the higher Reynolds number each plasma actuator moved the reattachment point upstream. Plasma actuator configuration DBD-02 shifted the reattachment point upstream in excess of 6% C_x, likely significantly further as the mean reattachment point moved out of the field of view.

Plasma actuator configuration DBD-03 shifted the reattachment point upstream 8% C_x. Each actuator tested at Re=1.0x10^5 showed an increase in drag as the separation length decreased with increased voltage. This is considered to be due to an increase in turbulent boundary layer length. Several conclusions can be made from the results of the open loop study:

1. The spanwise distributed array of linear vertical jets (DBD-02) are deemed the most effective in the two flow conditions presented here. However, plasma actuator DBD-01, a spanwise array of cross-stream jet showed promise and it is possible that a different spanwise spacing of the jets would yield better results.
2. Alternative DBD plasma actuator electrode configurations to the standard asymmetric electrode configuration must be considered and studied in more detail as they show potential for performance improvements.
3. The electrode configuration that will provide the most effective separation control at low Reynolds number will likely change with flow conditions. This points towards electrode configurations and power electronics that enable induced velocity jet vectoring. A configuration that uses jet vectoring could create the effects of configurations DBD-01, and DBD-02, and enable switching between jet orientations based on flow condition.

It should be mentioned that the success of the two spanwise distributed arrays, used here in hopes of generating three dimensionality and streamwise vorticity, point towards the conclusion that longitudinal vorticity was generated. However, further study is necessary to verify the control mechanism that led to reattachment.

Objective 4: Develop a first generation closed loop low Reynolds number separation control system using S3F as the separation control sensor.

In order to use S3F as a sensor on the E387 airfoil, an appropriate experimental setup that enabled measurement of low values of film displacement had to be determined. This required the

testing of six different S3F formulations on the E387, and integration of the S3F method into a LabVIEW environment. It was hypothesized that the S3F tangential displacement itself could be used as an input to the separation control system. Calculation of tangential displacement was by single pass cross correlation. The sensitivity of the S3F was significantly increased over time by the manufacturer, but this resulted in a decrease in S3F frequency response. During the course of this work the S3F shear modulus was decreased from approximately 100 Pa to 7.7 Pa. A high speed Cameralink interface was used to transfer images from a high resolution scientific grade camera. A high resolution camera was required to resolve film displacement in the current setup. The use of high resolution camera and the hardware used to calculate S3F displacement set the maximum sampling speed to approximately 3 Hz. Alternate S3F sensor packaging configurations are under development by ISSI Inc. that could potentially increase sampling rate. A comparison of S3F tangential displacement with Cp and PIV data indicated that tangential film displacement itself could be used to infer reattachment location. At a Reynolds number of 1.0×10^5 a zero crossing was observed that moved upstream in relation to a shift in mean reattachment point. At the lower Reynolds number a strong minimum point was observed that shifted upstream with reattachment point, inferring an upstream shift in reattachment. Examining the mean frequency response of the S3F at two different Reynolds numbers showed a non-linear response curve. Time resolved response of the S3F indicated that the S3F responded in less than 1 second, which was the limit of the sampling rate. The use of S3F with two different, simple, un-optimized feedback controllers was demonstrated in the AFRL/RZ DWT. An On/off controller and PI controller were used to control boundary layer separation as the inlet Reynolds number was reduced from $Re = 1.0 \times 10^5$ to $Re = 6 \times 10^4$. Decreasing the wind tunnel speed resulted in an increase in the extent of separation. The objective of feedback active control systems over open loop configurations is better control with reduced energy consumption. The energy consumption of two arbitrary experimental runs, one using the On/off controller, and the other using the PI controller was calculated. The On/off controller resulted in a 77% reduction in energy

consumption over a 78 second operating period. The PI controller resulted in a 34% reduction in energy consumption over a 140 second period. The amount of energy savings is directly dependent on the length of the run. The un-optimized PI controller power saving substantially increased over time.

The use of the tangential displacement from an S3F sensor has been used in this study to control Low Reynolds number flow separation over an E387 airfoil. Future work should focus on increasing frequency response, sampling rate, and repackaging the system into an all-in-one discrete sensor that includes S3F and displacement detection system. This work has demonstrated that a repackaged system, small enough to cleanly integrate into aircraft surfaces, would make a useful flow control sensor for a variety of aerodynamic systems.

References

ALAM, M. AND SANDHAM, N.D. 2000. Direct Numerical Simulation of `Short' Laminar Separation Bubbles with Turbulent Reattachment. *Journal of Fluid Mechanics 403*, 223-250.

AMITAY, M., SMITH, B. L. AND GLEZER, A., 1998. Aerodynamic flow control using synthetic jet technology. *AIAA Paper 98-0208.*

AMITAY, M., KIBENS, V., PAREKH, D. E. AND GLEZER, A., 1999. The Dynamics of Flow Reattachment over a Thick Airfoil Controlled by Synthetic Jet Actuators. *AIAA Paper 99-1001.*

AMITAY, M., PAREKH, D., PITT, D., KIBBENS, V., AND GLEZER, A., 2000. Control of Internal Flow Separation Using Synthetic Jets Actuators. *AIAA Paper No. 2000-0903*.

BARLOW, J., RAE, W., AND POPE, A., 1999. "Low-Speed Wind Tunnel Testing", 3rd Edition, John Wiley & Sons, New York.

BAUGHN, J. W., BUTLER, R. J., BYERLEY, A. R., AND RIVIR, R. B. 1995. An Experimental Investigation of Heat Transfer, Transition and Separation on Turbine Blades at Low Reynolds Number and High Turbulence Intensity. *ASME Paper 95-WA/HT-25*.

BAUGHN, J. W., BYERLEY, A. R., AND GREGORY, J. W. 2006. An Optical Method for Measuring Low Wall Shear Stresses Using Thermal Tufts. *AIAA Paper 2006-0647*.

BECHERT, D. 1996. Calibration of Preston Tubes. *AIAA Journal 34*, 205-206.

BECKER, R., AND KING, R., 2007. Adaptive Closed-Loop Separation Control on a High-Lift Configuration Using Extremum Seeking. *AIAA Journal, 45*, pp 1382-1392.

BOLITHO, M., AND JACOB, J., 2008. Thrust Vectoring Flow Control Using Plasma Synthetic Jet Actuators. *AIAA Paper No: 2008-1368.*

BONS, J., SONDERGAARD, R., AND RIVIR, R., 2001. Turbine Separation Control Using Pulsed Vortex Generator Jets *J. of Turbomachinery 123*, 198-206.

BOWLES, P. AND CORKE, T. 2009. Stall detection on a leading-edge plasma actuated pitching airfoil utilizing onboard measurement. *AIAA Paper 2009-93.*

BREHM, C., GROSS, A., AND FASEL, H. 2006. Closed-Loop Control of Low-Pressure Turbine Laminar Separation. *3rd AIAA Flow Control Conference, 5-8 June, San Francisco, CA.*

BURGMANN, S., BRUCKER, C., AND SHRODER, W. 2006. Scanning PIV Measurements of a Laminar Separation Bubble. *Experimental Fluids 41*, 319-326.

CHENG-YUAN, T., YI-PING, H., ZEN, C. 1998. Robust two-stage approach for image motion estimation. *Electronic Letters, 34*, pp. 1091-1093.

CORKE, T., AND POST, M., 2005. Overview of Plasma Flow Control: Concepts, Optimization, and Applications. *AIAA Paper No. 2005-563.*

CRAFTON, J., FONOV, S., JONES, E., GOSS, L., FORLINES, A., AND FONTAIN, A. 2008. Measurements of skin friction in water using surface stress sensitive films. *Meas. Sci. Technol. 19*, 801-811.

CRAFTON, J., FONOV, S., FORLINES, A., AND GOSS, L., 2010. Skin Friction Measurements Using Elastic Films. *AIAA Paper 2010-42.*

CURTIS, E., HODSON, H., BANIEGHBAL, M., DENTON, J., HOWELL, R., AND HARVEY, N., 1997. Development of Blade Profiles for Low-Pressure Turbine Applications. *J. of Turbomachinery 119*, 531-538.

DRELA, M., AND YOUNGREN, H., 2001. XFOIL 6.9 User Primer. Accessed on January 4, 2009. http://web.mit.edu/drela/Public/web /xfoil/xfoil_doc.txt.

ENLOE, C., MCLAUGHLIN, T., VANDYKEN, R., KACHNER, K., JUMPER, E., CORKE, T. 2004a. Mechanisms and Responses of a Single Dielectric Barrier Plasma Actuator: Plasma Morphology. *AIAA Journal 42,* 589-594.

ENLOE, C., MCLAUGHLIN, T., VANDYKEN, R., KACHNER, K., JUMPER, E., CORKE, T., POST, M., HADDAD, O., 2004b. Mechanisms and Responses of a Single Dielectric Barrier Plasma Actuator: Geometric Effects. *AIAA Journal 42*, 595-604.

ENLOE, C., MCLAUGHLIN, T., BAUGHN, J., 2006. Parameterization of Temporal Structure in the Single-Dielectric-Barrier Aerodynamic Plasma Actuator. *AIAA Journal, 44,* 1127-1136.

FERNHOLZ, H., JANKE, G., SCHOBER, M., WAGNER, P., AND WARNACK, D., 1996. New developments and applications of skin-friction measuring techniques. *Measurement Science Technology 7*, 1396-1409.

FRIDMAN, A., CHIROKOV, A., AND GUTSOL, A., 2005. Non-thermal atmospheric discharges, *Journal of Physics D: Applied Physics, 38*, R1-R24.

FONOV, S., JONES, G., CRAFTON, J., FONOV, V., AND GOSS, L. 2006. The development of optical techniques for the measurement of pressure and skin friction. *Meas. Sci. Technol. 17*, 1261-1268.

FONOV, S., CRAFTON, J., FORLINES, A., GOSS, L. 2010 Demonstration of a Surface Stress Sensitive Films for Skin Friction Measurements in a Variety of Flows. *27th AIAA Aerodynamic Measurement Technology and Ground Testing Conference, AIAA Paper No. 2010-4800.*

FONOV, S., 2011. Personal communication.

FONOV, V., FONOV, S., JONES, G., CRAFTON, J. 2004. Image Processing Technique for Shear-Stress Optical Measurements. *11th International Symposium on Flow Visualization*, University of Notre Dame, USA.

GAD-EL-HAK, M. 2000. Flow Control Passive, Active, and Reactive Flow Management 1-2. Cambridge University Press.

GAD-EL-HAK, M. 2001a. Flow Control: The Future. *Journal of Aircraft 38*, 402-418.

GAD-EL-HAK, M. 2001b. Micro-Air-Vehicles: Can They Be Controlled. *Journal of Aircraft 38,* 419-429.

GLAUSER, M., HIGUCHI, H., AUSSEUR, J., AND PINIER, J. 2004. Feedback Control of Separated Flows. AIAA Paper 2004-2521.

GLEAZER, A., AND AMITAY, M. 2002. Synthetic Jets. *Annu. Rev. Fluid Mech. 34*, 503-529.

GNANAMANICKAM, E. P., AND SULLIVAN, J. P. 2008. Image Based Sensor for Distributed Wall Shear Stress Measurement. *46th AIAA Aerospace Sciences Meeting and Exhibit, 7-10 January 2008, Reno, NV*.

GOETT, H., 1939. Experimental Investigation of the Momentum Method for Determining Profile Drag. NACA Report No. 660.

GROSS, A., AND FASEL, H. 2007. Self-Adaptive Closed-Loop Control of Low-Reynolds Number Laminar Separation. *25th AIAA Applied Aerodynamics Conference*, 25-28 June 2007, Miami, FL.

GREGORY, J. W., BAUGHN, J. W., PORTER, C. O, AND BYERLEY, A. R. 2008. Optical Method for Measuring Low Wall Shear Stresses Using Thermal Tufts. *AIAA Journal 46*, 1088-1095.

GROBE, S., AND SCHRODER, W. 2008. Mean wall-shear stress measurements using the micro-pillar shear-stress sensor MPS^3. *Measurement Science and Technology 19*, 1-12.

GROBE, S, SCHRODER, W., AND BRUCKER, C., 2006. Nano-Newton drag sensor based on flexible micro-pillars. *Measurement Science and Technology 17,* 2689-97.

GUNES, H., AND RIST, U., 2004. Proper orthogonal decomposition reconstruction of a transitional boundary layer with and without control. *Physics of Fluids 16,* 2763-2784.

HALL, J., AND MOHSENI, K., 2007. Numerical simulation of an airfoil at Low Reynolds number. *45th AIAA Aerospace Sciences Meeting,* 8-11 January, Reno, NV. AIAA Paper 2007-1269.

HART, D. (2000). PIV error correction. *Exp. Fluids 29*, 13-22.

HEADLEY, J. 1968. Skin Friction Balance. Journal of Scientific Instruments (Journal of Physics E) 2, 360.

HENNING, L., AND KING, R. 2007. Robust Multivariable Closed-Loop Control of a Turbulent Backward-Facing Step Flow. *Journal of Aircraft 44,* 201-208.

HORTON, H.P. 1968. Laminar Separation in Two and Three-dimensional Incompressible Flow. *PhD Dissertation*, University of London.

HORTON, H.P. 1969. A Semi-empirical Theory for the Growth and Bursting of Laminar Separation Bubbles. C.P. No. 1073.

HUANG, H., DABIRI, D., GHARIB, M., 1997. On errors of digital particle image velocimetry. *Measurement Science Technology*, *8*, pp. 1427-1440.

HUANG, J., CORKE, T., AND THOMAS, F., 2003. Plasma Actuators for Separation Control of Low Pressure Turbine Blades. *AIAA Paper 2003-1027*.

HUANG J., CORKE, T., AND THOMAS, F. 2006. Unsteady Plasma Actuators for Separation Control of Low-Pressure Turbine Blades. *AIAA Journal 44*, 1477-1487.

JACOB, J., RAMAKUMAR, K., ANTHONY, R., RIVIR, R. 2005. Control of Laminar and Turbulent Shear Flows using Plasma Actuators. *4th International Symposium on Turbulence and Shear Flow Phenomena,* June 27-29 2005, Williamsburg, VA.

JACOBSON, S. A. 1995. An Experimental Investigation Towards the Active Control of Turbulent Boundary Layers. Ph.D. Thesis, Stanford, CA, 1995.

JIANG, F., LEE, G., TAI, Y., HO, C., 2000. A flexible micromachine-based shear-stress sensor array and its application to separation-point detection. *Sensors and Actuators 79*, 194-203.

JOHNSTON, J., AND NISHI, M., 1990. Vortex Generator Jets – Means for Flow Separation Control. *AIAA Journal, 28*, pp. 989-994.

KAHNG, S., SCOTT, M., BEELER, G., BARTLET, J., AND COLLINS, R., 2000. An Integrated MEMS Sensor Cluster System for Aerospace Applications. NASA Langley Research Center, Doc ID: 20040086577.

KING, R., BECKER, R., FEUERBACH, G., HENNING, L., PETZ, R., NITSCHE, W., LEMKE, O., NEISE, W. 2006. Adaptive Flow Control Using Slope Seeking. *14th Mediterranean Conference on Control and Automation, IEEE*.

KUMAR, S. M., REYNOLDS, W. C., AND KENNEY, T. W. 1999. MEMS Based Transducers for Boundary Layer Control. *IEEE Proceedings of the 12th International Workshop on Micro Electro Mechanical Systems – MEMS*, 17-21 Jan. 1999, Orlando, FL.

LAKE, J., KING, P, AND RIVIR, R., 1999. Reduction of Separation Losses on a Turbine Blade with Low Reynolds Number. *AIAA Paper 99-0242.*

LIN, J. C., AND PAULEY, L. L., 1996. Low-Reynolds-Number Separation on an Airfoil. *AIAA Journal 34*, 1570-1576.

LISSAMAN, P. B., 1983. Low-Reynolds-Number Airfoils. *Ann. Rev. Fluid Mechanics 15*, 223-239.

LIU, K., YUAN, W., DENG, J., MA, B., AND JIANG, C. 2007. Detecting boundary-layer separation point with a micro shear stress sensor array. *Sensors and Actators A 139*, 31-35.

LIU, T., WOODIGA, S., NOTEFORT, J., CONN, K., AND SHEN, L. 2008. Mapping Skin Friction Fields in Complex Flows Using Luminescent Oil. *46th AIAA Aerospace Sciences Meeting and Exhibit*, Reno, NV. AIAA Paper 2008-267.

LUMLEY, J. 1967. The structure of inhomogeneous turbulence. In A. M. Monin and V. I. Tatarski (Eds.), *Atmospheric Turbulence and Wave Propagation*, pp. 166-178. Moscow: Nauka.

MAYLE, R. E., 1991. The Role Laminar-Turbulent Transition in Gas Turbine Engines. *J. of Tubomachinery 113*, 509-531.

MCGHEE, R. J., WALKER, B. S. AND MILLARD, B. F. 1988. Experimental Results for the Eppler 387 Airfoil at Low Reynolds Numbers in the Langley Low-Turbulence Pressure Tunnel. *NASA Technical Memorandum 4062,* NASA Langley Research Center.

MCMASTER, J. H., AND HENDERSON, M. L., 1980. Low Speed Single Element Airfoil Synthesis. *Technical Soaring 6,* 1-21.

MCQUILLING, M. W. 2007. Design and Validation of a High-Lift Low-Pressure Turbine Blade. *PhD Dissertation*, Wright State University.

MCQUILLING, M., WOLFF, M., FONOV, S., CRAFTON, J., SONDERGAARD, R., 2008a. An Experimental Investigation of a Low-Pressure Turbine Blade Suction Surface Using a Shear and Stress Sensitive Film. *Experiments in Fluids 44*, 73-88.

MCQUILLING, M., WOLFF, M., FENOV, S., CRAFTON, J., AND SONDERGAARD, R., 2008b. An Experimental Investigation of Suction Surface Flow Features on a High-Lift LPT. *AIAA Paper No. 2008-79*.

MOREAU, E., 2007. Airflow control by non-thermal plasma actuators. *Journal of Physics D: Applied Physics 40*, 605-636.

MONTELPARE, S., AND RICCI, R. 2004. A Thermographic Method to Evaluate the Local Boundary Layer Separation Phenomena on Aerodynamic Bodies Operating at Low Reynolds Number. *International Journal of Thermal Sciences 43*, 315-329.

MUELLER, T. J., POHLEN, L. J., CONIGLIARO, P. E., AND JANSEN, B. J., JR. 1983. The Influence of Free-Stream Disturbances on Low Reynolds Number Airfoil Experiments. *Experiments in Fluids 1,* 3-14.

MUELLER, T. J. 1985. Low Reynolds Number Vehicles. AGARD-AG-288.

NESSLER, C., MARKS, C., SONDERGAARD, R., AND WOLFF, M., 2009a. An Investigation of Losses on a Highly Loaded Low Pressure Turbine Blade with Unsteady Wakes. *47th AIAA Aerospace Sciences Meeting*, Orlando, FL.

NESSLER, C., MARKS, C., SONDERGAARD, R., AND WOLFF, M., 2009b. PIV Investigation of Periodic Unsteady Wakes over a Highly Loaded Low Pressure Turbine Blade. *AIAA Joint Propulsion Conference*, Denver, CO.

PADMANABHAN, A., GOLDBERG, H., BREUER, K., SCHMIDT, M., 1995. A Silicon Micromachined Floating-Element Shear-Stress Sensor with Optical Position Sensing by Photodiodes. *IEEE 8th International Conference on Solid State Sensors and Actuators, and Eurosensors IX.* Stockholm, Sweden, Jun 25-29, 1995.

PATEL, M. P. TILMAN, C. P., NG, T. T., 2003. Active Transparent Stall Control Systems for Air Vehicles. *Journal of Aircraft, 40*, pp. 993-997.

PATEL, M. P., SOWLE, Z. H., CORKE, T. C., HE, C., 2007. Autonomous Sensing and Control of Wing Stall Using a Smart Plasma Slat. *Journal of Aircraft, 44*, pp 516-527.

PINIER, ‚J., AUSSEUR, J., GLAUSER, M., AND HIGUCHI, H. 2007. Proportional Closed-Loop Feedback Control of Flow Separation. *AIAA Journal 45,* 181-190.

POGGIE, J., TILMAN, C., FLICK, P., SILKEY, J., OSBORNE, B., ERVIN, G., MARIC, D., MANGALAM, S., MANGALAM, A., 2010. Closed-Loop Stall Control System. *Journal of Aircraft, 47*, pp. 1747-1755.

PONS, J., MOREAU, E., AND TOUCHARD, G., 2005. Asymmetric surface barrier discharge in air at atmospheric pressure: electric properties and induced airflow characteristics, *Journal of Phy. D: Appl. Phys.,38*, 3635-3642.

POPE, S., 2008. *Turbulent Flows*. Cambridge University Press, New York.

PORTER, C., ABBAS, A., COHEN, K., MCLAUGHLIN, T., AND ENLOE, C., 2008. Spatially Distributed Forcing and Jet Vectoring with a Dielectric Barrier Discharge Plasma Actuator. *AIAA Paper No. 2008-1374*.

PORTER, C., ABBAS, A., COHEN, K., MCLAUGHLIN, T., ENLOE, C., 2009. Spatially Distributed Forcing and Jet Vectoring with a Plasma Actuator. *AIAA Journal, 47,* pp. 1368-1378.

PRESTON, J. 1954. The Determination of Turbulent Skin Friction by Means of Pitot Tubes. *Journal of the Royal Aeronautical Society 58,* 109-121.

RAFFEL, M., WILLERT, C., WERELEY, S., AND J. KOMPENHANS, 2007. Particle Image Velocimetry: A Practical Guide. Springer.

REEDER, M., CRAFTON, J., ESTEVADEORDAL, J., DELAPP, J., MCNIEL, C., PELTIER, D., AND REYNOLDS, T., 2009. Clean seeding for flow visualization and velocimetry measurements. *Exp. Fluids,* DOI:10.1007/S00348-009-0.

RIVIR, R. B., BAUGHN, J. W., BUTLER, R. J., BYERLEY, A. R., AND TOWNSEND, J. L. 1999. Thermal Tuft Fluid Flow Investigation Apparatus with a Color Alterable Thermally Responsive Liquid Crystal Layer. *U.S. Patent No. 5963292*.

RIZZETTA, D.P. AND VISBAL, M.R., 2007b. Numerical Simulation of Plasma-Based Flow Control for Transitional Highly Loaded Low-Pressure Turbine. *AIAA Journal 45*, 2554-2564.

ROTH, J., SHERMAN, D., AND WILKINSON, S., 2000. Electrohydrodynamic Flow Control with a Glow-Discharge Surface Plasma. *AIAA Journal, 38*, p. 116.

ROY, S., AND WANG, C. 2009. Bulk flow modification with horseshoe and serpentine plasma actuators. *J. Phys. D: Appl. Phys. 42*, DOI:10.1088/0022-3727/42/3/032004.

SAHIN , M., HALL, J., MOHSENI, K. 2008. Direct Numerical Simulation of Separated Low-Reynolds Number Flows around an Eppler 387. *46th AIAA Aerospace Science Meeting*, 7-10 January, Reno, NV. AIAA Paper 2008-422.

SANTHANAKRISHNAN, A., AND JACOB, J., 2007a. Flow Control with Plasma Synthetic Jet Actuators. *J. Phys. D: Appl. Phys. 40,* pp 637-651.

SANTHANAKRISHNAN, A., AND JACOB, J., 2007b. Effect of Plasma Morphology on Flow Control Using Plasma Synthetic Jet Actuators. *AIAA Paper No. 2007-783*.

SANTHANAKRISHNAN, A., AND JACOB, J., 2008. Charactarization of Linear Plasma Synthetic Jet Actuators. AIAA Paper No. 2008-538.

SANTHANAKRISHNAN, A., REASOR, J., AND LEBEAU, R. 2009. Characterization of linear plasma synthetic jet actuators in an initially quiescent medium. *Physics of Fluid 21*. DOI:10.1063/1.3097004.

SCHLICHTING AND GERSTAN, 2000. Boundary Layer Theory. Springer.

SCHMIDT, M., HOWE, R., SENTURIA, S., AND HARITONIDIS, J., 1988. Design and Calibration of a Microfabricated Floating-Element Shear-Stress Sensor. *IEEE Transactions on Electron Devices 35*, 750-757.

SEIFERT, A. AND PACK-MELTON, L. 2004. Control and Identification of Turbulent Boundary Layer Separation, NASA Langley Research Center Doc ID: 20040111309.

SELIG M. S. AND MCGRANAHAN, B. D. 2004. Wind Tunnel Aerodynamic Tests of Six Airfoils for Use on Small Wind Turbines. National Renewable Energy Laboratory Subcontractor Report, NREL/SR-500-34515.

SHARMA, O., 1998. Impact of Reynolds Number on LP Turbine Performance. *Proceedings of 1997 Minnowbrook II Workshop on Boundary Layer Transition in Turbomachines*, NASA/CP-1998-206958.

SHERMAN, D. M. 1998. Manipulating Aerodynamic boundary layers using an electrohydrodynamic effect generated by a One Atmosphere Uniform Glow Discharge Plasma, August 1998, *Master's Thesis, University of Tennessee*, *Knoxville*.

SMITH, D., AMITAY, M., KIBENS. K., PAREKH, D., AND GLEZER, A., 1998. Modification of lifting body aerodynamics using synthetic jet actuators. *AIAA Paper 98-0209.*

SONDERGAARD, R., RIVIR, R., AND BONS, J., 2002. Control of Low-Pressure Turbine Separation Using Vortex-Generator Jets. *J. of Propulsion and Power 18*, 889-895.

TANI, I., 1964. Low-Speed Flows Involving Bubble Separations. *Progress in Aerospace Sciences 5*, 70-103.

WHITE, F., 1991. *Viscous Fluid Flow,* 2nd ed., McGraw-Hill, Inc., Boston.

WILLERT, C., AND GHARIB, M., 1991. Digital particle image velocimetry. *Exp. Fluids, 10*, pp 181-193.

WINANT, C. D., AND BROWAND, F. K., 1974. Vortex Pairing: The Mechanism of Turbulent Mixing-Layer Growth at Moderate Reynolds Number. *Journal of Fluid Mechanics, 63, Pt. 2,* pp. 237-255.

WRIGHT, K. D., WASHBURN, A. E., JORDAN, J. D., LEIGHTY, B. D., WALTKINS, A. N., INGRAM, J. L., OGLESBY, D. M., FLEMING, G. I., SCOTT, M. A., BALLA, R. J., HART, R. C., HERRING, G. C., FLETCHER, M. T., SCHWARTZ, R. J., 2002. Measurement Technology for Use in Active Flow Control. *22nd AIAA Aerodynamic Measurement Technology and Ground Testing Conference,* 24-26 June 2002, St. Louis, MO.

LIST OF ACRONYMS

Acronym	Description
AFOSR	Air Force Office of Scientific Research
IHPTET	Improved High Performance Turbine Engine Technology
LDV	Laser Doppler Velocimetry
LPT	Low Pressure Turbine
PIV	Particle Image Velocimetry
TRF	Turbine Research Facility
VAATE	Versatile Affordable Adaptive Turbine Engines
VGJ	Vortex Generator Jet